

**'THE BREAKDOWN TO TURBULENCE OF A FORCED  
VORTEX FLOW AT A PIPE ORIFICE: THE NON-LINEAR  
EVOLUTION OF INITIALLY AXISYMMETRIC VORTICES'**

**By Paul Stanley Addison**

**A Thesis Submitted for the Degree  
of Doctor of Philosophy**

**Department of Civil Engineering  
The University  
Glasgow**

**© P.S. Addison 1993**

ProQuest Number: 13818422

All rights reserved

INFORMATION TO ALL USERS

The quality of this reproduction is dependent upon the quality of the copy submitted.

In the unlikely event that the author did not send a complete manuscript and there are missing pages, these will be noted. Also, if material had to be removed, a note will indicate the deletion.



ProQuest 13818422

Published by ProQuest LLC (2018). Copyright of the Dissertation is held by the Author.

All rights reserved.

This work is protected against unauthorized copying under Title 17, United States Code  
Microform Edition © ProQuest LLC.

ProQuest LLC.  
789 East Eisenhower Parkway  
P.O. Box 1346  
Ann Arbor, MI 48106 – 1346

*Thesis  
9613  
copy 1*

GLASGOW  
UNIVERSITY  
LIBRARY

TO MY PARENTS – JOSEPHINE AND STANLEY ADDISON

AND

TO MY WIFE – STEPHANIE

## DECLARATION

I hereby declare that the following thesis has been composed by myself, that it is a record of work carried out by myself, and that it has not been presented in any previous application for a higher degree.

Paul S Addison, July 1993

## ACKNOWLEDGEMENTS

I am most grateful to my mother, father and wife, for all the support and encouragement they have given to me during the course of my studies.

I would like to thank my supervisors, Dr. D.A. Ervine, Dr. A.H.C. Chan and Dr. K.J. Williams whose encouragement and advice has been invaluable throughout the course of the research programme.

I would also like to express my gratitude to Mr. A. Gray, (Hydraulics technician), for his assistance with the design and fabrication of the apparatus. His detailed knowledge, and extremely high standard of work, were crucial to the success of the experimental work.

I would also like to thank Mr. I. Dickson, (Civil Engineering Electronics technician), Mr. J. McGuire, (Civil Engineering technician) and Mr P. Miller, (Electronics Department technician), for their assistance.

I would like to thank Mr. A. Burnett, Departmental Superintendent, for the procurement of materials during the project, and express my gratitude to the remainder of the Glasgow University technical staff.

I would like to thank Professor D. Muir Wood for allowing the use of the facilities within the Civil Engineering Department.

I would like to thank Dr. L. Jendele and Mrs. M. Stewart for their helpful comments and suggestions regarding the software aspects of my work.

I would like to express my grateful thanks to the University of Glasgow for providing financial assistance, in the form of a scholarship, during the course of this research.

I would like to thank Dr. Tom Mullin of Oxford University's Physics Department for useful discussions relating to experimental work involving non-linear dynamics.

Last but not least I would like to thank Professor K. Dickinson for the use of the facilities in the Department of Civil and Transportation Engineering at Napier University, Edinburgh, during the final stages of this work.

## ABSTRACT

The primary purpose of this research is to investigate non-linear and chaotic behaviour of water in a pipeline at the transition region from laminar to turbulent flow. Turbulence was generated in the flow by the use of an orifice plate which generated coherent vortices and subsequent break-down into turbulence, downstream of the orifice. The flow regime was pulsatile. This was decided specifically to obtain better control of the experimental apparatus, better control of the frequency of vortices shedding from the orifice, and because of its wider range of practical applications discussed in section 1.3.

The mechanism of vortex breakdown has been addressed many times over the past century. The process by which vortices interact and degenerate is essentially non-linear. New techniques from the field of non-linear dynamics have emerged which can yield some quantitative information about the complexity of non-linear phenomena. This thesis aims to test some of these techniques, together with more traditional methods, on the experimental time series data obtained from axisymmetric vortex breakdown of a pulsed flow at a pipe orifice.

An experimental rig was designed and constructed in the Civil Engineering Department, at the University of Glasgow, to produce, accurately controllable, pulsed flows within a pipe system at an orifice plate. The apparatus was designed to allow a range of parameters to be varied over the course of the investigation. Computer algorithms were written by the author to analyse the resulting data, obtained from Laser Doppler Anemometry readings. Flow visualisation techniques were also used to give a qualitative understanding of the system.

Evidence was found for the development of initially axisymmetric pulsed vortex flows to a relatively low dimensional chaotic state prior to breaking down to a more complex turbulent state. The flow complexity was probed by investigating the dynamics of phase space attractors reconstructed from time series taken at various spatial locations within the developing flow field. The two techniques used for this were the Grassberger-Procaccia dimension and the Lyapunov exponent. Reconstruction of the attractors was performed using the minimum mutual information function.

The flow complexity was used in conjunction with Turbulent Intensities within the flow and the development of the flow velocity profile, to provide a comprehensive picture of the flow field development for pulsed vortex flows. In addition, the techniques from the field of non-linear dynamics were thoroughly tested in the experimental environment. The problem of noise, and its effect on the results produced has been analysed in detail.

THE BREAKDOWN TO TURBULENCE OF A FORCED  
VORTEX FLOW AT A PIPE ORIFICE: THE NON-LINEAR  
EVOLUTION OF INITIALLY AXISYMMETRIC VORTICES

<u>CONTENTS</u>	<u>Page</u>
ACKNOWLEDGEMENTS	i
ABSTRACT	iii
LIST OF SYMBOLS	xv
LIST OF TABLES AND FIGURES	xix
<u>CHAPTER 1: GENERAL INTRODUCTION</u>	1
1.1 BACKGROUND TO THE WORK	2
1.2 OUTLINE OF THE INVESTIGATION	3
1.3 PRACTICAL APPLICATIONS OF THE WORK	4
1.4 RELATED WORK	6
1.5 THESIS OUTLINE	7
<u>CHAPTER 2: LITERATURE SURVEY AND REVIEW OF THEORY</u>	9
2.1 INTRODUCTION	12
2.2 THE FLOW OF FLUID IN A PIPE	13
2.2.1 Basic Definitions	13
2.2.2 Laminar Pipe Flows	14
2.2.3 Turbulent Pipe Flow	15
2.2.3.1 The Reynolds Stress and Prandtl Eddy Length	17
2.2.3.2 Correlation and Intermittency	18
2.2.4 Head Loss and the Friction Factor	20

	<u>Page</u>	
2.2.5	Stability Theory	22
2.2.6	Structures Present in Transitional Pipe Flow: The Puff and the Slug	25
2.2.7	Entrance Flow Development	27
2.2.8	Pulsatile Pipe Flow	28
2.2.9	Orifice Flow Phenomena in Pipes	30
2.2.9.1	Numerical Solution of Low Reynolds Number Orifice Flows	32
2.2.9.2	Flow Pulsations at an Orifice	32
2.3	VORTEX FLOWS	33
2.3.1	Introduction	33
2.3.2	Vorticity	34
2.3.3	The Rankine Vortex and the Diffusion of Vorticity	37
2.3.4	Flow Separation and Vortex Motion	37
2.3.5	The Strouhal Number	40
2.3.6	Forced Vortex Flows	41
2.3.7	Flow Behaviour in Pipes, at Orifice Plates and Sudden Expansions	43
2.3.8	Flow Induced Vibrations	47
2.4	NON-LINEAR DYNAMICAL SYSTEMS	48
2.4.1	Introduction	48
2.4.2	Dynamical Systems	49
2.4.3	Phase Space and Poincare Sections	51
2.4.4	Strange Attractors	52
2.4.5	Examples of Mathematical Systems Exhibiting Chaotic Motion	54
2.4.6	Real Systems with Strange Attractors	59
2.4.6.1	Fluid Dynamics	59
2.4.6.2	Other Areas	60
2.4.7	Mathematical Routes to Turbulence	61
2.4.8	Modelling Real Non-linear Systems	64
2.5	THE TESTING OF NON-LINEAR DYNAMICAL SYSTEMS	65
2.5.1	Characterisation of Attractors	65
2.5.2	The Fast Fourier Transform	65
2.5.3	Experimental Attractor Construction	66
2.5.4	The Dimension of an Attracting Set	69

	<u>Page</u>
2.5.5 The Grassberger-Procaccia Dimension	72
Estimate and its Implementation	
2.5.5.1 Regions of Behaviour on the Attractor	72
2.5.5.2 Attractors and Noise	73
2.5.5.3 Other Factors Affecting the	74
Estimation of Dimension	
2.5.6 The Lyapunov Exponent	74
2.5.6.1 The Lyapunov Exponent as	75
a Dynamical Measure	
2.5.6.2 The Kaplan-Yorke Conjecture	76
2.5.7 Alternative Methods of Analysis	77
2.6 NONLINEAR DYNAMICS AND FLUIDS	78
2.6.1 Introduction	78
2.6.2 The Fractal Nature of Fluid Systems	79
2.6.3 Chaotic Behaviour of Vortex Systems	80
2.6.4 Pipe Flows at Transition	82
2.7 SUMMARY	83
<b><u>CHAPTER 3: EXPERIMENTAL APPARATUS</u></b>	<b>122</b>
3.1 GENERAL INTRODUCTION	124
3.2 EXPERIMENTAL APPARATUS	124
3.2.1 General Layout of the Apparatus	124
3.2.2 Design of the Test Rig	125
3.2.3 Water Temperature and Viscosity	127
3.2.4 Laser Table Design	128
3.2.5 Piston Design	128
3.2.6 Entrance Piece Design	130
3.2.7 Pipe Specifications	131
3.2.8 The Orifice Plate	131
3.2.9 Pipe Alignment	133
3.2.10 Pipe Deflection and Expansion	134
3.2.11 Water Tank Specifications	136
3.2.12 Test Procedure	138

	<u>Page</u>
3.3	MOTOR CONTROL 140
3.3.1	Introduction 140
3.3.2	Original Motor-Gearbox Arrangement 141
3.3.3	Modified Motor-Gearbox Arrangement 142
3.3.4	Reduction of Background Noise by Physical Means 143
3.3.5	Generation of a Pulsatile Fluid Flow 143
3.3.6	The A.C. Inverter and Function Generator 144
3.3.7	The Drive Shaft Limit Switches 145
3.4	INSTRUMENTATION - THE L.D.A. SYSTEM 146
3.4.1	Introduction 146
3.4.2	Components of the L.D.A. System 146
3.4.3	Principles of the L.D.A. System 147
3.4.4	Experimental Practice 149
3.5	DATA ACQUISITION 151
3.5.1	Introduction 151
3.5.2	Acquisition Hardware 152
3.5.3	Analog to Digital Conversion 153
3.5.4	Computer Specifications 153
3.5.5	Software 154
3.5.6	Sampling and Manipulation of the Data 155
3.6	FLOW VISUALISATION APPARATUS 156
3.6.1	Introduction 156
3.6.2	Light Box Design 156
3.6.3	Experimental Practice 157
3.7	SUMMARY 158
<u>CHAPTER 4; PRELIMINARY RESULTS AND CALIBRATION</u> 178	
4.1	INTRODUCTION 179

	<u>Page</u>
4.2 CALIBRATION OF APPARATUS AND PRELIMINARY RESULTS	179
4.2.1 The Inverter Frequency - Pipe Reynolds Number Relationship	179
4.2.2 Centre-line Velocity Results	180
4.2.3 Parabolic Hagen-Poiseuille Flow	181
4.2.4 Selection of Forcing Frequency and Amplitude	182
4.2.5 Pulsatile Laminar Flow	184
4.2.6 Natural Frequency Results and the Strouhal Number	185
4.3 CALIBRATION OF THE COMPUTER ALGORITHMS	187
4.4 DERIVED RELATIONSHIPS	187
4.4.1 Pipe, Orifice and Reynolds Number Relationships	187
4.4.2 The Wake Reynolds Number	189
4.4.3 The Forcing Frequency - Pipe Reynolds Number Relationship	191
4.4.4 Vortex Shedding Velocity and Wavelength	191
4.4.5 Forcing Amplitude Relationship	192
4.5 OUTLINE OF THE EXPERIMENTAL WORK	192
<u>CHAPTER 5: FLOW VISUALISATION RESULTS</u>	206
5.1 INTRODUCTION	208
5.2 BACKGROUND TO FLOW VISUALISATION	208
5.2.1 The Technique of Flow Visualisation	208
5.2.2 Interpretation of the Flow Phenomena	209
5.2.3 Illumination of the Flow	211
5.2.4 Information from Film	212
5.2.5 Geometrical and Refractive Properties of the Pipe	213
5.2.6 Flow Visualisation at a Pipe Orifice	213
5.3 PRELIMINARY TESTS	214
5.4 NATURAL, UNFORCED FLOW RESULTS AT THE 13.00mm ORIFICE PLATE	215

	<u>Page</u>
5.5 FORCED FLOW RESULTS: THE 13mm ORIFICE	216
5.5.1 Flows at the Orifice Plate	216
5.5.2 Downstream Dissipation of the Disturbances	217
5.6 FORCED FLOW RESULTS: THE 9.75 AND 16.25mm ORIFICE PLATES	218
5.6.1 The 9.75mm Orifice	219
5.6.2 The 16.25mm Orifice	219
5.7 VIDEO RESULTS	220
5.7.1 Introduction	220
5.7.2 Contents of the Video Film	221
5.7.3 Overall Picture of the Flow Processes	223
5.7.4 Categorisation of the Flow	225
Visualisation Results	
5.8 VORTEX WAVELENGTH AND VELOCITY RESULTS	227
5.9 SUMMARY	229
<u>CHAPTER 6: MAIN L.D.A. RESULTS AND ANALYSES</u>	252
6.1 INTRODUCTION	255
6.2 TEST SET A:	257
THE 13mm ORIFICE PLATE, VARIOUS REYNOLDS NUMBERS	
6.2.1 Frequency Spectra, Centre-line Velocities and Turbulence Intensities	257
6.2.2 Minimum Mutual Information and Attractor Construction	260
6.2.3 Dimension and Lyapunov Exponent Results	263
6.3 TEST SET B:	264
THE 13mm ORIFICE PLATE, VARIOUS FORCING AMPLITUDES	
6.3.1 Frequency Spectra, Centre-line Velocities and Turbulence Intensities	264
6.3.2 Minimum Mutual Information and Attractor Construction	266
6.3.3 Dimension and Lyapunov Exponent Results	267

	<u>Page</u>
6.4 TEST SET C:	268
THE 9.75mm ORIFICE PLATE, VARIOUS REYNOLDS NUMBERS	
6.4.1 Frequency Spectra, Centre-line Velocities and Turbulence Intensities	268
6.4.2 Minimum Mutual Information and Attractor Construction	270
6.4.3 Dimension and Lyapunov Exponent Results	271
6.5 TEST SET D:	271
THE 16.25mm ORIFICE PLATE, VARIOUS REYNOLDS NUMBERS	
6.5.1 Frequency Spectra, Centre-line Velocities and Turbulence Intensities	271
6.5.2 Minimum Mutual Information and Attractor Construction	272
6.5.3 Dimension and Lyapunov Exponent Results	273
6.6 TEST SET E:	274
A COMPARISON OF THE VARIOUS ORIFICE PLATES AT A PIPE REYNOLDS NUMBER OF 256	
6.6.1 A Comparison of the 9.75mm, 13.00mm and 16.25mm Orifice Plates: Frequency Spectra, Centre-line Velocities Turbulence Intensities, Minimum Mutual Information, Dimension and Lyapunov Exponent Results	274
6.6.2 A Comparison of all the Orifice Plates used in the Study: Frequency Spectra, Centre-line Velocities and Turbulence Intensities.	275
6.7 TEST SET F:	276
ACROSS FLOW RESULTS FOR THE 13mm ORIFICE PLATE AT A PIPE REYNOLDS NUMBER OF 256	
6.7.1 Frequency Spectra, Centre-line Velocities and Turbulence Intensities	277
6.7.2 Minimum Mutual Information and Attractor Construction	277
6.7.3 Dimension and Lyapunov Exponent Results	278

	<u>Page</u>
6.8 TEST SET G:	278
A CHECK ON THE REPEATABILITY OF THE EXPERIMENT	
6.9 OTHER ANALYSES	279
6.9.1 Autocorrelation Results	279
6.9.2 Probability Distributions of Selected Attractor Slices	279
6.9.3 Return Map Results	280
6.10 SUMMARY	280
<u>CHAPTER 7: ANALYSIS OF THE RESULTS</u>	390
7.1 INTRODUCTION	392
7.2 ANALYSIS OF PULSATILE FLOW BEHAVIOUR AT A PIPE ORIFICE AT LOW REYNOLDS NUMBERS	392
7.2.1 An Overview of the Flow Mechanisms	392
7.2.1.1 The Flow Processes in the Pipe Generated by the Orifice Plate	392
7.2.1.2 The Evolution of Shed Vortices	395
7.2.1.3 The Relationship Between Flow Type, Orifice Diameter and Reynolds Number	397
7.2.2 The Centre-Line Velocity and Turbulence Intensity	399
7.2.2.1 Directly Dissipating Flows	399
7.2.2.2 Initially Interacting Flows	399
7.2.3 Transverse Measurements of Velocity and Turbulence Intensity for Initially Interacting Flows	403
7.3 THE EVIDENCE FOR CHAOTIC BEHAVIOUR	404
7.3.1 Preliminary Analyses: The First Minimum in Mutual Information, Autocorrelation Function, Attractor Plots, Return Maps and Probability Density Functions	404
7.3.2 Downstream Development of the Lyapunov Exponent, Dimension and Turbulence Intensity	408

	<u>Page</u>
7.4 THE ROLE OF THE NEW TECHNIQUES IN DESCRIBING TRANSITIONAL FLUID PHENOMENA	410
7.4.1 Introduction	410
7.4.2 The Description of Non-Random Flows	411
7.4.3 The Practical Application of the Techniques from Non-Linear Dynamics	412
7.5 FURTHER NOTES ON THE CHARACTERISATION ALGORITHMS	412
7.5.1 Introduction	412
7.5.2 The Grassberger-Procaccia Dimension Algorithm and Noise	413
7.5.3 The Lyapunov Exponent Algorithm and Noise	413
7.5.3.1 Positive Lyapunov Exponents Caused by Noise	414
7.5.3.2 Coincident Trajectories	420
7.6 SUMMARY	421
 <u>CHAPTER 8: CONCLUSIONS</u>	 443
8.1 INTRODUCTION	444
8.2 MAIN CONCLUSIONS	445
8.2.1 Non-Linear Dynamics and Fluid Flow	445
8.2.2 The Characterisation Techniques	447
8.3 SUGGESTIONS FOR FUTURE RESEARCH	449
 <u>APPENDICES</u>	
 APPENDIX 1 - DERIVATION OF THE LAMINAR PIPE FLOW EQUATION FROM THE NAVIER STOKES EQUATIONS EXPRESSED IN CYLINDRICAL COORDINATES	   451
 APPENDIX 2 - COMPUTER PROGRAMS AND ALGORITHM CONSTRUCTION	 456
 APPENDIX 3 - A NOTE ON THE GEOMETRIC AND REFRACTIVE PROPERTIES OF THE PIPE	 481

	<u>Page</u>
APPENDIX 4 - OBSERVATIONS ON NUMERICAL METHOD DEPENDENT SOLUTIONS OF A MODIFIED DUFFING OSCILLATOR	488
APPENDIX 5 - A NOTE ON THE USE OF THE GRASSBERGER-PROCACCIA DIMENSION ALGORITHM TO CHARACTERIZE THE SOLUTION OF A NUMERICALLY MODELLED JOURNAL BEARING SYSTEM	506
APPENDIX 6 - FURTHER NOTES ON THE GRASSBERGER-PROCACCIA DIMENSION ALGORITHM	508
REFERENCES	517

## LIST OF SYMBOLS

The following list contains all the symbols used in this thesis. In some instances a symbol may have more than one definition, which one is appropriate will be apparent from its context within the text.

<b>A</b>	- 1. Area
	- 2. Constant
<b>A<sub>g</sub></b>	- Cross Sectional Area of the Pipe Glass
<b>A<sub>o</sub></b>	- Cross sectional Area of the Orifice Aperture
<b>A<sub>p</sub></b>	- Cross Sectional Area of the Pipe
<b>A<sub>pis</sub></b>	- Cross Sectional Area of the Piston Chamber
<b>A<sub>w</sub></b>	- Cross Sectional Area of the Water in the Pipe
<b>C<sub>d</sub></b>	- Orifice Discharge Coefficient
<b>C<sub>f</sub></b>	- Coefficient of Thermal Expansion
<b>C<sub>r</sub></b>	- Correlation Integral
<b>C<sub>ξ</sub></b>	- Correlation Function
<b>D</b>	- Diameter
<b>D<sub>o</sub></b>	- Orifice Diameter
<b>D<sub>p</sub></b>	- Pipe Diameter (Internal)
<b>D<sub>c</sub></b>	- Capacity Dimension
<b>D<sub>GP</sub></b>	- Grassberger–Procaccia Dimension
<b>D<sub>i</sub></b>	- Information Dimension
<b>D<sub>KY</sub></b>	- Kaplan–Yorke Dimension
<b>E<sub>g</sub></b>	- Youngs Modulus for Glass
<b>F( )</b>	- Function
<b>H</b>	- Head
<b>H<sub>d</sub></b>	- Dynamic Head
<b>H<sub>e</sub></b>	- Elevation Head
<b>H<sub>l</sub></b>	- Head Loss
<b>H<sub>nl</sub></b>	- Net head loss
<b>H<sub>p</sub></b>	- Pressure Head
<b>I</b>	- Information
<b>I<sub>xx</sub></b>	- Second Moment of Area About x– Axis
<b>K</b>	- Pressure Loss Coefficient

<b>L</b>	– 1. Lyapunov Exponent
	– 2. Length
<b>Mom.</b>	– Momentum
<b>N</b>	– Arbitrary Number
<b>P</b>	– Pressure
<b>P(x)</b>	– The Probability of the Occurrence of 'x'
<b>P*</b>	– Piezometric Pressure
<b>Q</b>	– Flow Rate
<b>R</b>	– Radius
<b>Re</b>	– Reynolds Number
<b>Re<sub>crit</sub></b>	– Critical Reynolds Number
<b>Re<sub>chao</sub></b>	– Reynolds Number for Chaotic Motion
<b>Re<sub>o</sub></b>	– Orifice Reynolds Number
<b>Re<sub>p</sub></b>	– Pipe Reynolds Number
<b>Re<sub>w</sub></b>	– Wake Reynolds Number
<b>S</b>	– Strouhal Number
<b>T</b>	– Temperature
<b>T.I.</b>	– Turbulence Intensity
<b>Point– T.I.</b>	– Point Turbulence Intensity
<b>H.G.– T.I.</b>	– Hagen– Poiseuille Turbulence Intensity
	(See Text for Details)
<b>U</b>	– Flow Velocity
<b>U<sub>o</sub></b>	– Average Orifice Flow Velocity
<b>U<sub>p</sub></b>	– Average Pipe Flow Velocity
<b>U<sub>z</sub></b>	– Axial Flow Velocity
<b>U<sub>r</sub></b>	– Radial Flow Velocity
<b>U<sub>s</sub></b>	– Sedimentation Velocity
<b>U<sub>θ</sub></b>	– Tangential Flow Velocity (Swirl)
<b>U'</b>	– Fluctuating Flow Component
<b>U'<sub>osc</sub></b>	– Oscillating Flow Component (Pulsatile Flows)
<b>W</b>	– Mass per Unit Length
<b>Z<sub>e</sub></b>	– Entrance Length

- $dt$  - Time Increment  
 $d_p$  - Distance moved by particle (Flow Visualization)  
 $e$  - Exponential Function  
 $f$  - Frequency  
 $f_d$  - Doppler Frequency  
 $f_f$  - Forcing Frequency  
 $f_i$  - Inverter Frequency  
 $f_n$  - Natural Frequency  
 $f_s$  - Sampling Frequency  
 $f_{shed}$  - Vortex Shedding Frequency  
 $f_v$  - Vortex Frequency  
 $g$  - Gravitational Acceleration  
 $h$  - Height  
 $i$  - 1. Complex Number  $(-1)^{\frac{1}{2}}$ ,  
           2. Index ie.  $X_i$   
 $j$  - Index ie.  $X_j$   
 $k$  - Thermal Difussivity  
 $l$  - Prandtl Eddy Length  
 $l_v$  - Vortex Wavelength  
 $n$  - Phase Space Embedding Dimension  
 $r$  - Radial Distance  
r.m.s. - Root Mean Squared Value  
 $t$  - Time  
 $t_e$  - Exposure Time  
 $x$  - Cartesian Spatial Coordinate  
 $y$  - Cartesian Spatial Coordinate  
 $z$  - Cartesian Spatial Coordinate  
  
 $\Gamma$  - Circulation  
 $\Sigma$  - Summation Sign  
 $\Theta$  - Heaveside Function  
 $\Phi$  - Probability Distribution Function  
 $\Upsilon$  - Time Delay  
 $\Omega$  - Angular Velocity

- $\alpha$       – 1. Area Ratio
- 2. Strain
- $\beta$       – Diameter Ratio
- $\delta$       – Deflection
- $\delta\mu$      – Feigenbaum Universal Number
- $\epsilon$       – 1. Pipe Wall Roughness
- 2. Box Length (Dimension Calculations)
- $\epsilon_0$      – Separation at Time Zero
- $\epsilon_t$      – Separation at Time 't'
- $\eta$       – Pipe Centreline Velocity Factor  
          (Schiller's Theory)
- $\theta$      – Angular Measurement
- $\lambda$      – Pipe Friction Factor
- $\mu$       – Absolute Viscosity
- $\nu$       – Dynamic Viscosity
- $\xi$       – Delay
- $\pi$       – Pi = 3.141592654...
- $\rho$       – Fluid Density
- $\tau$       – Shear Stress
- $\tau_i$      – Instantaneous Shear Stress
- $\tau_R$      – Reynolds Stress
- $\omega$      – Vorticity Vector
  
- $\dot{x}$       – Denotes the First Derivative  
          with respect to Time of 'x'
- $\ddot{x}$      – Denotes the Second Derivative  
          with respect to Time of 'x'
- $\bar{x}$       – Denotes the Average Value of 'x'
- $x'$       – Denotes the Fluctuating Component of 'x'
- $\tilde{x}$      – Disturbance, as used in Stability Theory

## LIST OF TABLES AND FIGURES

<u>CHAPTER 2</u>	<u>Page</u>
<u>Figure 2-1: Typical Pipe Section Detail Showing the Cylindrical Coordinate System</u>	85
<u>Figure 2-2: Parabolic Velocity Profile of Laminar Newtonian Pipe Flow</u>	85
<u>Figure 2-3: Elements of Turbulent Flow</u>	86
<u>Figure 2-4: Turbulent Mixing Length and Velocity Fluctuations</u>	87
<u>Figure 2-5: The Autocorrelation Function</u>	87
<u>Figure 2-6: Spectrum of Eddy Lengths Associated with Turbulent Flow</u>	87
<u>Figure 2-7: Intermittency</u>	88
<u>Figure 2-8: The Moody Diagram</u>	89
<u>Figure 2-9: Intermittency Factor Versus Pipe Reynolds Number</u>	89
<u>Figure 2-10: The Occurrence of Puffs and Slugs in a Pipe</u>	90
<u>Figure 2-11: Leading and Trailing Edges of a Turbulent Slug</u>	90
<u>Figure 2-12: The Development of the Velocity Profile at a Pipe Entrance for Laminar Flow</u>	90
<u>Figure 2-13: Pressure Drop in a Pipe Due to the Presence of an Orifice Plate</u>	91

	<u>Page</u>
<u>Figure 2-14: Pressure Loss Coefficients for Various Orifice Diameters</u>	91
<u>Figure 2-15: Numerical Solution of Low Reynolds Number Orifice Flows</u>	92
<u>Figure 2-16: Flow Streamlines at an Orifice as a Function of the Forcing Cycle</u>	92
<u>Figure 2-17: Closed Curve APB in a Fluid</u>	93
<u>Figure 2-18: Regions of Formation, Stability and Instability in the Wake of a Cylinder, for Three Reynolds Numbers</u>	93
<u>Figure 2-19: Flow Separation</u>	94
<u>Figure 2-20: Vortex Flows</u>	95
<u>Figure 2-21: Vortices Generated at the Edge of a Jet Flow</u>	95
<u>Figure 2-22: Viscous Flow Separation at Obstacles</u>	96
<u>Figure 2-23: The Roll-up Process in Kelvin-Helmholtz Instability</u>	97
<u>Figure 2-24: The Karman Vortex Street Generated in the Wake of a Cylinder</u>	97
<u>Figure 2-25: The Strouhal Number Versus the Reynolds Number for a Circular Cylinder and a Flat Plate</u>	97
<u>Figure 2-26: Frequency Spectra of Natural and Locked Vortex Flow</u>	98

	<u>Page</u>
<u>Figure 2-27: Frequency Locking Phenomena as Observed by Ho and Huang</u>	98
<u>Figure 2-28: Schematic Diagram of a Trip-Induced Transition Pattern in a Pipe Showing the Effect of Increasing Disturbance Height</u>	98
<u>Figure 2-29: Flows at a Pipe Orifice as the Reynolds Number is Increased</u>	99
<u>Figure 2-30: Flow at a Sudden Expansion within a Pipe</u>	100
<u>Figure 2-31: Reattachment Length Versus Upstream Pipe Reynolds Number for Sudden Expansion Flow in a Pipe</u>	100
<u>Figure 2-32: Reattachment Length Versus Upstream Pipe Reynolds Number for Sudden Expansion Flow in a Pipe</u>	101
<u>Figure 2-33: Centre-line Velocity and Turbulence Intensity Results of Khezzar, Replotted by the Author</u>	101
<u>Figure 2-34: Relaminarizing of Sudden Expansion Flow in a Pipe</u>	102
<u>Figure 2-35: 'x-t' Time Trace Solutions for the Duffing Oscillator</u>	103
<u>Figure 2-36: Phase Space Portraits of Solutions to the Duffing Oscillator</u>	104
<u>Figure 2-37: Poincare Sections of the Duffing Oscillator Solutions of Figure 2-44</u>	104
<u>Figure 2-38: The Cantor Set, Fractals and Dimension</u>	105

	<u>Page</u>
<u>Figure 2-39: The Logistic Map</u>	106
<u>Figure 2-40: The Henon Attractor</u>	107
<u>Figure 2-41: The Lorenz Equations</u>	108
<u>Figure 2-42: The Attractor of the Rossler Equations</u>	110
<u>Figure 2-43: The Attractor of the Rossler Hyper-Chaos Equations</u>	109
<u>Figure 2-44: The Attractor of the Truncated Navier-Stokes Equations</u>	110
<u>Figure 2-45: Schematic Diagrams of the Rayleigh-Benard and Taylor-Couette Experiments</u>	111
<u>Figure 2-46: The Belousof-Zhabotinskii Attractor</u>	111
<u>Figure 2-47: The Hopf Bifurcation</u>	111
<u>Figure 2-48: A Comparison of the Phase Portraits of the Actual and Modelled Dripping Faucet System</u>	112
<u>Figure 2-49: The Fluid Elastic Vibration System</u>	112
<u>Figure 2-50: Power Spectra Associated with Vortex Shedding at a Cylinder</u>	113
<u>Figure 2-51: Broadening of Power Spectra Bases as the Chaotic State Is Approached</u>	113
<u>Figure 2-52: The Method of Time Delays in Attractor Construction</u>	114
<u>Figure 2-53: The Mutual Information and its Effect on the Reconstructed Attractor</u>	115

	<u>Page</u>
<u>Figure 2-54: The Grassberger-Proccacia Dimension Estimate</u>	116
<u>Figure 2-55: Regions of Behaviour on the Attractor</u>	117
<u>Figure 2-56: Definition Sketch of Trajectory Separation for the Lyapunov Exponent Calculation</u>	118
<u>Figure 2-57: The Effect of Reynolds Number Increase on the Dimension of the Taylor-Couette System</u>	118
<u>Figure 2-58: The Fractal Nature of a Turbulent Jet</u>	118
<u>Figure 2-59: Vortex Shedding Results from an Airfoil</u>	119
<u>Figure 2-60: Lyapunov Exponents Taken Across the Flow for Vortex Shedding at an Airfoil</u>	120
<u>Figure 2-61: Power Spectra Associated with Vortex Shedding at a Cylinder</u>	120
<u>Figure 2-62: Intermittent Pipe Flow Results</u>	121
 <u>CHAPTER 3</u>	
<u>Table 3.1: Tank Deflection Test Results</u>	138
<u>Figure 3-1: General Layout of the Experimental Apparatus</u>	160
<u>Figure 3-2: Plan View of the Experimental Apparatus</u>	161
<u>Figure 3-3: Sketch of the Layered Structure of the Experimental Rig to Eliminate Vibrations from the Surroundings</u>	162
<u>Figure 3-4: Cutaway Section of Piston Casing Showing Piston</u>	163

	<u>Page</u>
<u>Figure 3-5: Pipe Entrance Piece</u>	164
<u>Figure 3-6: Pipe Coupling Detail</u>	165
<u>Figure 3-7: Two Views of a Typical Pipe Support</u>	166
<u>Figure 3-8: Orifice and End Plate Detail</u>	167
<u>Figure 3-9: Method of Aligning the Pipe in the Vertical Plane</u>	168
<u>Figure 3-10: Schematic Diagram of the Horizontal Alignment of the Pipe</u>	169
<u>Figure 3-11: Pipe Cross Section Details</u>	169
<u>Figure 3-12: Schematic Diagram of the Original Piston-Motor Control Arrangement</u>	170
<u>Figure 3-13: Schematic Diagram of the Modified Piston-Motor Arrangement</u>	171
<u>Figure 3-14: Physical Methods of Noise Reduction on the Rig</u>	172
<u>Figure 3-15: Signal Generator and Multimeter</u>	173
<u>Figure 3-16: Data Acquisition and Flow Chart</u>	174
<u>Figure 3-17: L.D.A. Operation</u>	175
<u>Figure 3-18: Laser Intersection with the Pipe</u>	176
<u>Figure 3-19: Light Box used in the Flow Visualisation</u>	177

<u>CHAPTER 4</u>	<u>Page</u>
<u>Table 4.1: Pipe-Orifice Relationships</u>	190
<u>Table 4.2: Outline of the Experimental Tests</u>	195
<u>Figure 4-1: Inverter Frequency - Pipe Reynolds Number Relationship</u>	196
<u>Figure 4-2: Centre-line Velocity Comparison</u>	196
<u>Figure 4-3: L.D.A. Velocity Profiles</u>	197
<u>Figure 4-4: Relative Amplitude Tests</u>	199
<u>Figure 4-5: Preliminary Pulsatile Flow Test Results</u>	203
<u>Figure 4-6: Strouhal Number Results - 13.00mm Orifice Plate</u>	204
<u>Figure 4-7: Strouhal Number Results - All Orifice Plates</u>	204
<u>Figure 4.8: Wake and Jet Flows at an Orifice Plate</u>	205
<u>CHAPTER 5</u>	
<u>Figure 5-1: Flow Visualization Set-Up</u>	231
<u>Figure 5-2: Lamp versus Flash Illumination</u>	231
<u>Figure 5-3: Natural Unforced Vortex Flows at the 13mm Orifice Plate</u>	232
<u>Figure 5-4: The 13mm Orifice Plate - Various Reynolds Numbers</u>	234
<u>Figure 5-5: Downstream Dissipation of the Disturbances</u>	237

	<u>Page</u>
<u>Figure 5-6: Downstream Dissipation of the Disturbances</u>	238
<u>Figure 5-7: The 9.75mm Orifice - Various Reynolds Numbers</u>	239
<u>Figure 5-8: The 16.25mm Orifice - Various Reynolds Numbers - Illumination in the Vertical Plane</u>	240
<u>Figure 5-9: The 16.25mm Orifice - Various Reynolds Numbers - Illumination in the Horizontal Plane</u>	241
<u>Figure 5-10: Sketch of the Flow Processes at the 13.00mm Orifice Plate - Various Reynolds Numbers</u>	243
<u>Figure 5-11: Sketch of the Flow Processes at the 13.00mm Orifice Plate - Various Forcing Amplitudes</u>	245
<u>Figure 5-12: Sketch of the Flow Processes at the 9.75mm Orifice Plate - Various Reynolds Numbers</u>	246
<u>Figure 5-13: Sketch of the Flow Processes at the 16.25mm Orifice Plate - Various Reynolds Numbers</u>	247
<u>Figure 5-14: Sketch of the Flow Processes at the 6.50mm, 19.50mm and 22.75mm Orifice Plates</u>	248
<u>Figure 5-15: Catagorisation of the Flow Processes</u>	249
<u>Figure 5-16: Downstream Wavelength Results</u>	250
<u>Figure 5-17: Normalised Vortex Wavelength and Velocity Results</u>	251
 <u>CHAPTER 6</u>	
<u>Figure 6-1: Frequency Spectra - 13.00mm Orifice - <math>Re_p = 128</math></u>	282

	<u>Page</u>
<u>Figure 6-2: Frequency Spectra - 13.00mm Orifice - <math>Re_p = 256</math></u>	287
<u>Figure 6-3: Frequency Spectra - 13.00mm Orifice - <math>Re_p = 384</math></u>	291
<u>Figure 6-4: Frequency Spectra - 13.00mm Orifice - <math>Re_p = 256</math></u>	295
<u>Figure 6-5: Frequency Spectra - 13.00mm Orifice - <math>Re_p = 256</math></u>	297
<u>Figure 6-6a: Centreline Velocities - 13.00mm Orifice</u> <u>Various Reynolds Numbers</u>	299
<u>Figure 6-6b: Normalised Centreline Velocities - 13.00mm Orifice</u> <u>Various Reynolds Numbers</u>	299
<u>Figure 6-7a: Point-Turbulence Intensities- 13.00mm Orifice</u> <u>Various Reynolds Numbers</u>	300
<u>Figure 6-7b: H.C.-Turbulence Intensities - 13.00mm Orifice</u> <u>Various Reynolds Numbers</u>	300
<u>Figure 6-8a: Minimum Mutual Information - 13.00mm Orifice</u> <u>Various Reynolds Numbers</u>	301
<u>Figure 6-8b: Normalised Minimum Mutual Info.- 13.00mm Orifice</u> <u>Various Reynolds Numbers</u>	301
<u>Figure 6-9: Individual Minimum Mutual Information Plots</u> <u>13.00mm Orifice - <math>Re_p = 256</math></u>	302
<u>Figure 6-10: Time Series Plots - 13.00mm Orifice - <math>Re_p = 256</math></u>	304
<u>Figure 6-11: Attractor Plots - 13mm Orifice - <math>Re_p = 256</math></u>	307
<u>Figure 6-12: 'log(r) - log(Cr)' Plots</u> <u>13mm Orifice - <math>Re_p = 256</math></u>	309

	<u>Page</u>
<u>Figure 6-13: Dimension Results - 13.00mm Orifice</u> <u>Various Reynolds Numbers</u>	316
<u>Figure 6-14: Lyapunov Exponent Results - 13.00mm Orifice</u> <u>Various Reynolds Numbers</u>	316
<u>Figure 6-15: Frequency Spectra - 13.00mm Orifice - <math>Re_p = 256</math></u> <u>0.2 Volts Forcing</u>	317
<u>Figure 6-16: Frequency Spectra - 13.00mm Orifice - <math>Re_p = 256</math></u> <u>1.0 Volts Forcing</u>	321
<u>Figure 6-17a: Centreline Velocities - 13.00mm Orifice</u> <u>Various Forcing Amplitudes</u>	325
<u>Figure 6-17b: Normalised Centreline Velocities -13.00mm Orifice</u> <u>Various Forcing Amplitudes</u>	325
<u>Figure 6-18a: Point-Turbulence Intensities- 13.00mm Orifice</u> <u>Various Forcing Amplitudes</u>	326
<u>Figure 6-18b: H.C.-Turbulence Intensities - 13.00mm Orifice</u> <u>Various Forcing Amplitudes</u>	326
<u>Figure 6-19a: Minimum Mutual Information - 13.00mm Orifice</u> <u>Various Forcing Amplitudes</u>	327
<u>Figure 6-19b: Normalised Minimum Mutual Info.- 13.00mm Orifice</u> <u>Various Forcing Amplitudes</u>	327
<u>Figure 6-20: Attractor Plots - 13mm Orifice</u> <u>0.2 Volts Forcing</u>	328
<u>Figure 6-21: Attractor Plots - 13mm Orifice</u> <u>1.0 Volts Forcing</u>	330

	<u>Page</u>
<u>Figure 6-22: Dimension Results - 13.00mm Orifice</u> <u>Various Forcing Amplitudes</u>	332
<u>Figure 6-23: Lyapunov Exponent Results - 13.00mm Orifice</u> <u>Various Forcing Amplitudes</u>	332
<u>Figure 6-24: Frequency Spectra - 9.75mm Orifice - <math>Re_p = 128</math></u>	333
<u>Figure 6-25: Frequency Spectra - 9.75mm Orifice - <math>Re_p = 256</math></u>	337
<u>Figure 6-26: Frequency Spectra - 9.75mm Orifice - <math>Re_p = 384</math></u>	341
<u>Figure 6-27a: Centreline Velocities - 9.75mm Orifice</u> <u>Various Reynolds Numbers</u>	345
<u>Figure 6-27b: Normalised Centreline Velocities - 9.75mm Orifice</u> <u>Various Reynolds Numbers</u>	345
<u>Figure 6-28a: Point-Turbulence Intensities- 9.75mm Orifice</u> <u>Various Reynolds Numbers</u>	346
<u>Figure 6-28b: H.C.-Turbulence Intensities - 9.75mm Orifice</u> <u>Various Reynolds Numbers</u>	346
<u>Figure 6-29a: Minimum Mutual Information - 9.75mm Orifice</u> <u>Various Reynolds Numbers</u>	347
<u>Figure 6-29b: Normalised Minimum Mutual Info.- 9.75mm Orifice</u> <u>Various Reynolds Numbers</u>	347
<u>Figure 6-30: Attractor Plots - 9.75mm Orifice - <math>Re_p = 128</math></u>	348
<u>Figure 6-31: Attractor Plots - 9.75mm Orifice - <math>Re_p = 256</math></u>	350
<u>Figure 6-32: Attractor Plots - 9.75mm Orifice - <math>Re_p = 384</math></u>	352

	<u>Page</u>
<u>Figure 6-33: Dimension Results - 9.75mm Orifice</u> <u>Various Reynolds Numbers</u>	354
<u>Figure 6-34: Lyapunov Exponent Results - 9.75mm Orifice</u> <u>Various Reynolds Numbers</u>	354
<u>Figure 6-35: Frequency Spectra - 16.25mm Orifice - <math>Re_p = 128</math></u>	355
<u>Figure 6-36: Frequency Spectra - 16.25mm Orifice - <math>Re_p = 256</math></u>	356
<u>Figure 6-37: Frequency Spectra - 16.25mm Orifice - <math>Re_p = 384</math></u>	360
<u>Figure 6-38a: Centreline Velocities - 16.25mm Orifice</u> <u>Various Reynolds Numbers</u>	364
<u>Figure 6-38b: Normalised Centreline Velocities -16.25mm Orifice</u> <u>Various Reynolds Numbers</u>	364
<u>Figure 6-39a: Point-Turbulence Intensities- 16.25mm Orifice</u> <u>Various Reynolds Numbers</u>	365
<u>Figure 6-39b: H.G.-Turbulence Intensities - 16.25mm Orifice</u> <u>Various Reynolds Numbers</u>	365
<u>Figure 6-40a: Minimum Mutual Information - 16.25mm Orifice</u> <u>Various Reynolds Numbers</u>	366
<u>Figure 6-40b: Normalised Minimum Mutual Info.- 16.25mm Orifice</u> <u>Various Reynolds Numbers</u>	366
<u>Figure 6-41: Attractor Plots - 16.25mm Orifice - <math>Re_p = 128</math></u>	367
<u>Figure 6-42: Attractor Plots - 16.25mm Orifice - <math>Re_p = 384</math></u>	368
<u>Figure 6-43: Dimension Results - 16.25mm Orifice</u>	369

Various Reynolds Numbers

<u>Figure 6-44: Lyapunov Exponent Results - 9.75mm Orifice</u>	369
<u>Various Reynolds Numbers</u>	
<u>Figure 6-45: Centreline Velocities - <math>Re_p = 256</math></u>	370
<u>9.75, 13.00 &amp; 16.25mm Orifice Plates</u>	
<u>Figure 6-46a: Point-Turbulence Intensities - <math>Re_p = 256</math></u>	371
<u>9.75, 13.00 &amp; 16.25mm Orifice Plates</u>	
<u>Figure 6-46b: H.G.-Turbulence Intensities - <math>Re_p = 256</math></u>	371
<u>9.75, 13.00 &amp; 16.25mm Orifice Plates</u>	
<u>Figure 6-47a: Minimum Mutual Information - <math>Re_p = 256</math></u>	372
<u>9.75, 13.00 &amp; 16.25mm Orifice Plates</u>	
<u>Figure 6-47b: Normalised Minimum Mutual Information - <math>Re_p = 256</math></u>	372
<u>9.75, 13.00 &amp; 16.25mm Orifice Plates</u>	
<u>Figure 6-48: Dimension Results - <math>Re_p = 256</math></u>	373
<u>9.75, 13.00 &amp; 16.25mm Orifice Plates</u>	
<u>Figure 6-49: Lyapunov Exponent Results - <math>Re_p = 256</math></u>	373
<u>9.75, 13.00 &amp; 16.25mm Orifice Plates</u>	
<u>Figure 6-50: Frequency Spectra - 6.50mm Orifice - <math>Re_p = 256</math></u>	374
<u>Figure 6-51: Frequency Spectra - 19.50mm Orifice - <math>Re_p = 256</math></u>	375
<u>Figure 6-52: Centreline Velocities - <math>Re_p = 256</math></u>	376
<u>All Orifice Plates</u>	
<u>Figure 6-53a: Point-Turbulence Intensities - <math>Re_p = 256</math></u>	377
<u>All Orifice Plates</u>	

	<u>Page</u>
<u>Figure 6-53b: H.C.-Turbulence Intensities - <math>Re_p = 256</math></u> <u>All Orifice Plates</u>	377
<u>Figure 6-54a: Across-Flow Velocities - <math>Re_p = 256</math></u> <u>13mm Orifice Plate</u>	378
<u>Figure 6-54b: Normalised Across-Flow Velocities - <math>Re_p = 256</math></u> <u>13mm Orifice Plate</u>	378
<u>Figure 6-55a: Across-Flow Point-Turbulence Intensities</u> <u>13.00 Orifice Plate - <math>Re_p = 256</math></u>	379
<u>Figure 6-55b: Across-Flow H.C.-Turbulence Intensities</u> <u>13.00 Orifice Plate - <math>Re_p = 256</math></u>	379
<u>Figure 6-56a: Across-Flow Minimum Mutual Information</u> <u>13.00 Orifice Plate - <math>Re_p = 256</math></u>	380
<u>Figure 6-56b: Across-Flow Normalised Minimum Mutual Information</u> <u>13.00 Orifice Plate - <math>Re_p = 256</math></u>	380
<u>Figure 6-57: Across-Flow Dimension Results</u> <u>13.00mm Orifice Plate - <math>Re_p = 256</math></u>	381
<u>Figure 6-58: Across-Flow Lyapunov Exponent Results</u> <u>13.00 Orifice Plate - <math>Re_p = 256</math></u>	381
<u>Figure 6-59: Repeated Centreline Velocity Results</u> <u>13mm Orifice Plate - <math>Re_p = 256</math></u>	382
<u>Figure 6-60: Repeated Point-Turbulence Intensities</u> <u>13.00 Orifice Plate - <math>Re_p = 256</math></u>	382
<u>Figure 6-61: Repeated Minimum Mutual Information</u> <u>13.00 Orifice Plate - <math>Re_p = 256</math></u>	383

	<u>Page</u>
<u>Figure 6-62: Repeated Lyapunov Exponent Results</u> <u>13.00 Orifice Plate - <math>Re_p = 256</math></u>	383
<u>Figure 6-63: Autocorrelation Results - 13mm Orifice Plate</u> <u><math>Re_p = 256</math></u>	384
<u>Figure 6-64: Attractor Trajectory Histogram</u> <u>13.00mm Orifice - <math>Re_p = 256</math></u>	385
<u>Figure 6-65: Return Mappings - 13.00mm Orifice - <math>Re_p = 256</math></u>	386

## CHAPTER 7

<u>Figure 7-1: Regions of Flow Behaviour</u>	423
<u>Figure 7-2: Typical Frequency Spectra Corresponding to</u> <u>the Flow Regions Identified in Figure 1</u>	424
<u>Figure 7-3: Vortex Evolution in Directly Dissipating Flow</u>	425
<u>Figure 7-4: Vortex Evolution in Initially</u> <u>Interacting Vortex Flow</u>	426
<u>Figure 7-5: Schematic Isometric Views of Directly Dissipating</u> <u>and Initially Interacting Vortex Flows</u>	427
<u>Figure 7-6: The Relationship Between Flow Type, Orifice</u> <u>Diameter and Reynolds Number</u>	428
<u>Figure 7-7: The Variation in Centre-Line Velocity and</u> <u>Turbulence Intensity Downstream of the Orifice</u> <u>Plate in Directly Dissipating Flows</u>	431

	<u>Page</u>
<u>Figure 7-8: The Variation in Centre-Line Velocity and Turbulence Intensity Downstream of the Orifice Plate in Initially Interacting Flows</u>	432
<u>Figure 7-9: The Flattening of the Velocity Profile due to the Reynolds Stresses in the Flow</u>	433
<u>Figure 7-10: Turbulence Intensities of Submerged Jet Flows Compared to Experimental Results</u>	434
<u>Figure 7-11: Transverse Flow Measurements</u>	435
<u>Figure 7-12: Phase Portraits of Typical Attractor Types</u>	436
<u>Figure 7-13: The Behaviour of the Attractor Band Probability Distribution Function as the Vortices Develop Downstream of the Orifice Plate</u>	437
<u>Figure 7-14: The Downstream Development of the Lyapunov Exponent, Grassberger-Procaccia Dimension and Turbulence Intensity</u>	438
<u>Figure 7-15: The Lyapunov Exponent and Noise</u>	439
<u>Figure 7-16: The Behaviour of the Average Lyapunov Exponent Calculation</u>	440
<u>Figure 7-17: Lyapunov Exponent versus Time Delay for the Standard Test Results</u>	441
<u>Figure 7-18: The Effect of Noise on the Lyapunov Exponent Calculation</u>	442

## CHAPTER 1

## CHAPTER 1

### GENERAL INTRODUCTION

1.1 BACKGROUND TO THE WORK

1.2 OUTLINE OF THE INVESTIGATION

1.3 PRACTICAL APPLICATIONS OF THE WORK

1.4 RELATED WORK

1.5 THESIS OUTLINE

## 1.1 BACKGROUND TO THE WORK

This work was sparked by the emergent science of non-linear dynamics and chaos, which has captured the imagination of many scientists and a few Engineers, over the last decade. In essence it is a new way or technique of investigating physical phenomena, and may or may not have useful applications in the field of Civil Engineering Hydraulics.

The work is therefore speculative in nature, with no certainty of a useful outcome, and the only previous comparable British experience being work of Dr. Tom Mullin at Oxford university who is currently investigating the transition to turbulence of pipe flows in which turbulence is triggered by puffs of fluid injected cyclically into the pipe. Dr. Mullin has also been prominent in investigating the simpler case of the transition to turbulence of the annular flow of a fluid trapped between two rotating cylinders, (Taylor-Couette flow).

It was decided to investigate a simple, common phenomenon in Hydraulic Engineering, namely flow in a pipe, and to home-in on the transition between laminar and turbulent flows, which was believed to exhibit non-linear and chaotic behaviour at the breakdown into turbulence. The availability of accurate measurement techniques of Laser Doppler Anemometry combined with analysis tools such as Fast Fourier techniques also encouraged the study to proceed.

It should be noted that the breakdown into turbulence can be achieved in a pipe by the use of an orifice plate in the flow. It was found at an early stage that control of the experiment, as well as control of the vortex shedding frequencies from the orifice is best achieved with pulsatile flows in the pipe. The research therefore concentrates on pulsatile flows in a pipe. These are very common within pipeline systems and may be caused by either:-

- 1 - mechanical vibration, both external and internal to the system, (i.e. pump or turbine machinery), or
- 2 - flow related phenomena such as natural vortex shedding from obstructions within the flow field, these include orifice plates, eccentric pipe connections, partially closed valves etc.

The presence of flow pulsations in pipe flows affects many of the engineering

aspects of such flows. These include the pipe friction factor, the sediment transport properties of the flows and the metering of such flows. Very little is known about pulsatile flows as they interact with orifice plates, (or other obstacles), in pipes. This work aims to shed some light on this flow interaction problem.

The primary objectives of this work therefore are twofold:

- 1 - To study the non-linear evolution and breakdown to turbulence of axisymmetric vortices shed from a pipe orifice in pulsatile flow, using Flow Visualisation and Laser Doppler Anemometry. Thereby shedding light upon the mechanisms of flow breakdown and energy loss in such flows.
- 2 - To utilise, and report upon the applicability of, a selection of the emergent analytical techniques from the field of non-linear dynamics. These techniques include algorithms for the attractor construction, dimension, mutual information, first return maps and Lyapunov exponents of the flow system. Such algorithms are in use today to categorise a whole range of non-linear phenomena, from fluid and structural dynamics to biological and chemical systems.

## 1.2 OUTLINE OF THE INVESTIGATION

A brief outline of the research work undertaken by the author, and reported on within this thesis, is given as follows:

- 1 - Low Reynolds number flows are generated at a pipe orifice. The flow is pulsed at the natural vortex shedding frequency to promote the formation of a regular set of vortices at the orifice plate lip.
- 2 - The Reynolds number, forcing amplitude and orifice diameter are systematically varied.
- 3 - Initially, flow visualisation studies are performed to elucidate, in a qualitative manner, the structure of the flow field at the orifice. This included capturing the flow phenomena on photographic and video film.
- 4 - L.D.A. readings are taken within the flow field, to obtain a velocity-time series of the fluid at certain spatial positions within the flow downstream of the orifice.
- 5 - Data analysis is performed on the velocity time series to give quantitative information about the flow at each spatial position.
- 6 - The results from the data analysis were used together with the information

gained from the flow visualisation to present a coherent picture of the route taken by the vortex system to turbulent flow.

### 1.3 PRACTICAL APPLICATIONS OF THE WORK

The work has potential applications in the following areas:

#### 1 – Flows past obstacles.

The pattern of flow breakdown past obstacles is an important topic of study. Such obstacles may include orifice plates in a pipe, sediment build up in a sewer or pipeline deposits in human arteries, to name but a few. The energy losses incurred by such flows together with the effect of these flows on the obstacle is of great importance in many engineering contexts. The work presented herein should provide information on the breakdown of low Reynolds number flows past obstacles. This information will provide a better understanding of such phenomena. By forcing the flow at various frequencies, more control can be gained in the manipulation of the phenomena.

#### 2 – The Behaviour of Pulsatile Pipe Flows at a Constriction.

Pulsatile flows occur in many instances in both the engineering and natural context. Pulsed flows may occur in pipelines due to pumps, or other machinery, or they may occur naturally due to vortex shedding from obstacles within the flow system. It is important, therefore, that the behaviour of such pulsatile flows at obstacles and constrictions, is known. Such knowledge could lead to a better understanding, and prediction, of the energy losses that occur in such circumstances.

One naturally occurring pulsatile flow is that of blood. The phenomena of blood flow is quite different from the flows studied in this thesis, i.e. it is a non-Newtonian fluid, and, arteries and veins are not rigid conduits. However, much work has been done in investigating the effect of flow constrictions on pulsed blood flows, modelling the effect of partially blocked arteries. Furthermore, many of

these investigations have assumed Newtonian fluids and/or rigid conduits for the sake of simplicity.

### 3 - Laminar-Turbulent flow phenomena.

The experiment reported in this thesis has an advantage over traditional pipe flow transition experiments. That is, the transition point at which the flow breaks down into a turbulent state occurs at a fixed spatial position. As opposed to the laminar-turbulent transition of pipes without trigger mechanisms, whereby the flow breaks down intermittently, and the flow field changes at any specific point within the pipe, through time. Therefore, by using an orifice plate and essentially fixing the breakdown position the phenomena is more amenable to study.

### 4 - Increased Sediment Transport Properties of Pulsed Flows

Recent work has shown that, by pulsing pipe flows, an increase in the sediment transport properties of the flow may be obtained, [El Masry and El Shobaky, 1989]. Pulsed pipe flows have a lower critical velocity required to transport sediment, and in some circumstances require less energy to transport a specific amount of sediment than the equivalent non-pulsed flow. This work will provide qualitative and quantitative information on the flow field at an orifice plate for pulsatile pipe flows. Such flow fields may represent an ideal case for a wide variety of constrictions and obstacles that may occur in such pulsed pipe flow used to carry solids.

### 5 - Practical Implications of Nonlinear Dynamical Theories

This work also aims to look for practical applications of the techniques that are being developed in the field of non-linear dynamics. Much has appeared in the literature on non-linear systems in general, most of this in a fluid dynamics context, and the author has attempted to assess the implications of the techniques regarding their use in an engineering context.

Ruelle [1983b] states that the recent improvement of our understanding of the nature of turbulence, and transitional flow phenomena, has three different routes. These are,

- 1 – The injection of new mathematical ideas from the theory of dynamical systems.
- 2 – The availability of powerful computers which permit, amongst other things, experimental mathematics on dynamical systems and numerical simulation of hydrodynamic equations.
- 3 – Improvement of experimental techniques such as laser Doppler anemometry and numerical techniques such as Fourier analysis.

The work of this thesis concerns itself with items (1) and (3).

This investigation uses traditional fluid mechanical means of analysis together with the more recent theories from non-linear dynamics. A comparison is made of the relative attributes of the two areas of analysis.

#### 1.4 RELATED WORK

Two additional pieces of work were undertaken during the course of the main work outlined in this thesis. Both were in the field of non-linear dynamics, and were in effect offshoots from the main work pursued by the author. These are summarised as follows.

- 1 – An investigation was carried out into the applicability of certain numerical methods to find the solutions of a simple non-linear system. Interesting facts came to light regarding the sensitivity of the solution to various factors including the numerical scheme used as well as the initial conditions of the system. The results of this investigation are summarised in Appendix 4, and published by the author, see Addison et al, [1992].

- 2 – The Grassberger–Procaccia dimension algorithm, written by the author, was used in work with Mr. R.D. Brown of Heriot–Watt University, who is currently investigating the non-linear response of journal bearing systems. More details are given in Appendix 5. This work was also published, see Brown, Addison and Chan, [1992].

## 1.5 THESIS OUTLINE

An attempt has been made to make each chapter of this thesis self contained, as far as is possible. Thus all the literature and theory is reviewed in Chapter 2. All the information about the design and construction of the apparatus is presented in Chapter 3, and so on. This modularisation of the thesis, it is hoped, will make it more readable, and make it easier for the reader to access specific information quickly. The remaining chapters contained within this thesis are outlined as follows.

**CHAPTER 2:** Contains a review of the relevant literature to give a background knowledge of the subject area, together with the required theoretical knowledge for the experimental and theoretical work.

**CHAPTER 3:** Presents detailed information about the design, construction and running of the test apparatus. Including the motor control system, the L.D.A. set-up, data acquisition, pipe and piston specifications, and so on.

**CHAPTER 4:** Deals with the calibration of the apparatus and computer algorithms prior to taking the main results. Also contained within this chapter is a section on derived relationships used in the work. Finally a comprehensive outline of the experimental work is given.

**CHAPTER 5:** The results of the flow visualisation study is presented within this chapter. Both photographic and video film is analysed.

**CHAPTER 6:** This chapter presents the results of the main L.D.A. readings.

**CHAPTER 7:** Within this chapter is contained the analysis of the main L.D.A. results of chapter 6.

**CHAPTER 8:** This chapter deals with the conclusions reached from the results and analysis of the work presented herein, and suggestions for future work.

**APPENDICES:** A comprehensive set of appendices are given at the end of the

thesis. They include information on the Navier Stokes equations, algorithm design and listings, related work and the refractive properties of the pipe.

## CHAPTER 2

## CHAPTER 2

### LITERATURE SURVEY AND REVIEW OF THEORY

#### 2.1 INTRODUCTION

#### 2.2 THE FLOW OF FLUID IN A PIPE

##### 2.2.1 Basic Definitions

##### 2.2.2 Laminar Pipe Flows

##### 2.2.3 Turbulent Pipe Flow

###### 2.2.3.1 The Reynolds Stress and Prandtl Eddy Length

###### 2.2.3.2 Correlation and Intermittency

##### 2.2.4 Head Loss and the Friction Factor

##### 2.2.5 Stability Theory

##### 2.2.6 Structures Present in Transitional Pipe Flow: The Puff and the Slug

##### 2.2.7 Entrance Flow Development

##### 2.2.8 Pulsatile Pipe Flow

##### 2.2.9 Orifice Flow Phenomena in Pipes

###### 2.2.9.1 Numerical Solution of Low Reynolds Number Orifice Flows

###### 2.2.9.2 Flow Pulsations at an Orifice

#### 2.3 VORTEX FLOWS

##### 2.3.1 Introduction

##### 2.3.2 Vorticity

##### 2.3.3 The Rankine Vortex and the Diffusion of Vorticity

##### 2.3.4 Flow Separation and Vortex Motion

##### 2.3.5 The Strouhal Number

- 2.3.6 Forced Vortex Flows
- 2.3.7 Flow Behaviour in Pipes, at Orifice  
Plates and Sudden Expansions
- 2.3.8 Flow Induced Vibrations

## 2.4 NON-LINEAR DYNAMICAL SYSTEMS

- 2.4.1 Introduction
- 2.4.2 Dynamical Systems
- 2.4.3 Phase Space and Poincare Sections
- 2.4.4 Strange Attractors
- 2.4.5 Examples of Mathematical Systems  
Exhibiting Chaotic Motion
- 2.4.6 Real Systems with Strange Attractors
  - 2.4.6.1 Fluid Dynamics
  - 2.4.6.2 Other Areas
- 2.4.7 Mathematical Routes to Turbulence
- 2.4.8 Modelling Real Non-linear Systems

## 2.5 THE TESTING OF NON-LINEAR DYNAMICAL SYSTEMS

- 2.5.1 Characterisation of Attractors
- 2.5.2 The Fast Fourier Transform
- 2.5.3 Experimental Attractor Construction
- 2.5.4 The Dimension of an Attracting Set
- 2.5.5 The Grassberger-Procaccia Dimension  
Estimate and its Implementation
  - 2.5.5.1 Regions of Behaviour on the Attractor
  - 2.5.5.2 Attractors and Noise
  - 2.5.5.3 Other Factors Affecting the  
Estimation of Dimension

- 2.5.6 The Lyapunov Exponent
  - 2.5.6.1 The Lyapunov Exponent as a Dynamical Measure
  - 2.5.6.2 The Kaplan-Yorke Conjecture
- 2.5.7 Alternative Methods of Analysis

## 2.6 NONLINEAR DYNAMICS AND FLUIDS

- 2.6.1 Introduction
- 2.6.2 The Fractal Nature of Fluid Systems
- 2.6.3 Chaotic Behaviour of Vortex Systems
- 2.6.4 Pipe Flows at Transition

## 2.7 SUMMARY

## 2.1 INTRODUCTION

Historically, it was the Romans who first thought to obtain a relationship between the dimensions of a pipe and the amount of flow it could carry. This was to allow a tax on water usage to be levied, [Rouse and Ince, 1957]. However, it was not until this century that the flows in pipes could be generally obtained for any Newtonian fluid within a pipe of any diameter.

Pipes and pipe systems play an important role in Civil Engineering. They are used mainly to convey fluids such as gas, oil and water, from one point to another, in some cases they are used to transport suspended solids in fluids such as sewage. In other cases they may be used for the transmission of hydraulic load. Much of the early experimental and theoretical work done on pipe flow was carried out by researchers with Civil Engineering backgrounds, such as Osborne Reynolds and C.F. Colebrook.

Fluid flows may in general be laminar or turbulent. It was Reynolds [1883] who demonstrated the essential nature of the two types of flow, using a flow visualisation chemical within a glass pipe. The transition point between the two types of flow is intermittent in nature, that is, patches of laminar and turbulent flow may be observed in the pipe.

The special case of laminar pipe flow is one of the few exact solutions of the governing equations of fluid flow, known as the Navier–Stokes equations, (Appendix A). However, most fluid flow encountered in the Engineering situation is turbulent, and as such is a very complex phenomenon. The problem of turbulence occupies a vast field of knowledge, (and perhaps ignorance). At present, there is no complete theory of turbulence, only fragments of the whole picture. Recent work in non–linear dynamics has added one more piece to the picture, as will be described in section 2.4.

Although this research spans diverse subject matter from pipe flows, orifice behaviour, vortex structures, turbulence, flow visualisation and non–linear dynamics, it was decided to concentrate mainly on non–linear dynamics, as the other subjects are already well documented in text books and papers.

The chapter begins with basic definitions including laminar and turbulent flows in open pipes but not at a very detailed level. This early section also deals with orifice flow and pulsatile flow in pipes. The literature review touches briefly on vortex flows before reviewing the relatively new field of non-linear dynamics. This includes a brief overview of dynamical systems, chaotic motion, strange attractors and fractals.

The following section deals with the important subject of methods of analysis of non-linear systems including fast Fourier transforms, construction of attractors from experimental data, the Grassberger-Procaccia dimension and Lyapunov exponent. The final section deals with experimental and theoretical work which has been carried out by other investigators, and which is of relevance to the experimental work of this thesis. The use of fractals to describe fluid phenomena is described. Theoretical predictions and experimental evidence of chaotic behaviour in vortex systems is reviewed. Transitional pipe flow studies, which have been analysed using techniques from the field of non-linear dynamics, are also described.

## 2.2 THE FLOW OF FLUID IN A PIPE

### 2.2.1 Basic Definitions

The coordinate system used in the study presented herein is shown in figure 2-1. This cylindrical coordinate system is more suitable for the pipe geometry and also for the axisymmetric nature of the flow conditions.

In most Engineering situations water may be assumed an incompressible fluid. In such a case the continuity condition for incompressible flow applies, that is the volume flow rate, ( $Q = U.A$ ), has the same value at each cross section in the pipe.

The most important flow parameter in the study of the transition to turbulence in a pipe flow is the Reynolds number, which is a measure of the ratio of the

inertial to viscous forces in the flow. The Reynolds number was discovered by Osborne Reynolds [1883], who found that initially laminar flows became unstable and passed into a turbulent state for certain values of the non-dimensional flow parameter, now named in his honour. The Reynolds number is defined thus,

$$Re = \frac{U_p \cdot D_p}{\nu} \quad (2.1)$$

It is simply the product of the average pipe velocity,  $U_p$ , and the pipe internal diameter,  $D_p$ , divided by the liquid kinematic viscosity,  $\nu$ .

Reynolds found the critical value of this parameter,  $Re_{crit}$ , to be around 2300 for pipe flows. Below  $Re_{crit}$  viscous forces dominate and the flow remains laminar, and above which inertial forces tend to dominate the flow and a turbulent state ensues.

### 2.2.2 Laminar Pipe Flows

At Reynolds numbers below  $Re_{crit}$  where viscous forces dominate, viscous fluid flow is laminar. At this stage, the flow streamlines are time independent, and any disturbance in the flow quickly dampens out back to the laminar state.

Viscosity produces stresses within the fluid due to the shearing of faster moving fluid layers over slower ones. The stress between two such layers is related to the rate of shearing of the two layers over each other. In the case of water the viscous stress,  $\tau$ , is linearly related to the rate of fluid shear through the viscosity and is known as a Newtonian fluid, [Rouse & Ince, 1957, p83].

Using the momentum equation, the velocity profile for laminar flow of a Newtonian liquid in a pipe can shown to be parabolic. (The derivation can be found in most introductory fluid mechanics texts.) In fact, the velocity profile being symmetric about the pipe centre-line has the shape of a paraboloid. Referring to figure 2-2, the velocity,  $U_z$ , at a radial distance  $r$  from the central axis of the pipe is given by

$$U_z = U_{z(\max)} \cdot \left[ 1 - \frac{r^2}{R^2} \right] \quad (2.2)$$

where  $U_{z(\max)}$  is the maximum velocity of the flow which occurs at the central axis of the pipe, and is exactly twice the average flow velocity, i.e.

$$\bar{U}_z = \frac{1}{2} \cdot U_{z(\max)} \quad (2.3)$$

Once laminar flows reach a certain critical value of the Reynolds Number they tend to become unstable and breakdown to a turbulent state, whereby the flow contains, in addition to the average flow velocity, a fluctuating component. Turbulent flows, with particular emphasis on pipe flows, will be dealt with in the next section.

### 2.2.3 Turbulent Pipe Flow

Fluid turbulence is a common occurrence in nature, it appears in almost all practical Engineering flow problems, (with the exception of very slow, or viscous flows). Fluid turbulence is also a highly complex phenomenon covering an enormous area of both theoretical and experimental research. At present, the phenomenon of turbulence is still not fully understood. Cvitanovic [1984] has described turbulence as 'the unsolved problem of physics', whereas Ruelle [1983] calls it 'one of the great puzzles of theoretical physics'.

When the Reynolds number of a flow increases above  $Re_{crit}$ , the laminar regime becomes unstable and breaks down into a turbulent state, whereby the flow field becomes full of irregular eddying motions, [Prandtl, 1952]. Turbulent flow is characterised by fluctuating velocity components,  $U'$ , superimposed on the mean velocity components  $\bar{U}$ . In general, the flow velocity,  $U$ , at an instant in time may be described thus,

$$U = \bar{U} + U' \quad (2.4a)$$

For the case of turbulent pipe flows where there is only one component of mean velocity axially in the pipe, the velocities are therefore,

$$U_z = \bar{U}_z + U'_z, \quad U_r = U'_r, \quad U_\theta = U'_\theta \quad (2.4b)$$

The time series trace of the velocities becomes highly irregular and appears to have no discernible pattern, as shown in fig 2-3a. This is true for both an Eulerian and Lagrangian frame of reference.

Turbulence may be described as homogeneous if the average properties of the flow is independent of coordinate position within the fluid. Isotropic turbulence exists when the average statistical properties of the flow, at each point in the flow field are independent of direction, [Batchelor, 1960]. Fully developed turbulent flow in pipes is neither homogenous nor isotropic. The time averaged properties of turbulent pipe flow change at each radial position, however, they do possess axisymmetry and are the same at each cross section along the pipe.

Due to the apparently random nature of turbulent flow, statistical methods are employed in its analysis. One such method is to plot the probability distribution of the fluctuating velocity component, see figure 2-3b. Often turbulent velocity probability distributions approach that of a Gaussian distribution, as shown in the figure.

Since the time average values of the fluctuating velocity components are necessarily zero by definition, a convenient way to characterise the fluctuations is to use the 'turbulence intensity' defined as

$$T.I. = \frac{\left[ \overline{(U')^2} \right]^{\frac{1}{2}}}{\bar{U}} = \frac{U'_{rms}}{\bar{U}} \quad (2.5)$$

whereby the root mean square of the turbulent fluctuation component,  $U'_{rms}$ , is divided by the average flow velocity.

The turbulent flow of fluid in a pipe assumes a flatter velocity profile than the equivalent parabolic laminar profile, (figure 2-3c). From experiment it has been shown that the turbulent profile may be approximated by a simple 'one seventh' power law, (except for a region very close to the wall). This approximation holds for pipe Reynolds numbers up to 100,000, above which the power law exponent progressively reduces in value.

### 2.2.3.1 The Reynolds Stress and Prandtl Eddy Length

In turbulent flow, transfer of momentum between neighbouring layers of fluid becomes important. This momentum exchange gives rise to additional stresses within the fluid. Thus, for a given volume flow rate,  $Q$ , a greater pressure drop is required to drive turbulent flow than would otherwise be required if the flow were laminar. The time averages of these stresses are known as Reynolds stresses,  $\tau_R$ , where,

$$\tau_R = \rho \cdot \overline{U'_x \cdot U'_y} \quad (2.6)$$

An obvious result is that the high values of turbulent shear stresses generally found in real turbulent flows, requires that there exists a strong correlation in the fluctuating velocity components. A completely independent, random variation in both would result in the time average of the product of  $U'_x$  and  $U'_y$  being equal to zero.

As stated above, turbulent flow is full of irregular eddying motions, these motions are highly complex and extremely difficult to define. No one, precise definition of an eddy exists. However, one early attempt to define turbulent flows in terms of characteristic eddy lengths by Prandtl [1952], is known as the mixing

length hypothesis, and will be described below.

Consider the two-dimensional velocity profile in figure 2-4. A turbulent fluctuation  $U_y'$  at position 1 causes a discrete pulse of fluid to move from layer 1 to layer 2 a small distance,  $l$ , (the mixing length). It may be seen that the turbulent fluctuation in the direction of the flow,  $U_x'$ , at position 2, is then

$$U_x' = -l \cdot \frac{dU_x}{dy} \quad (2.7)$$

Combining this expression with that of the Reynolds stress and absorbing the constant of proportionality and the density directly into the value of  $l$ , we arrive at the expression,

$$\tau = l^2 \cdot \left[ \frac{dU_x}{dy} \right]^2 \quad (2.8)$$

The advantage of such a formula is that a plausible guess at the value of  $l$  may be made for certain parts of a turbulent flow field.

### 2.2.3.2 Correlation and Intermittency

Turbulence is described by Robertson [Date Unknown] as 'a random motion which occurs in fluid flows', and further that this 'randomness is of such a nature that the velocity at one instant is still correlated that in the next and in decreasing amounts at succeeding instants'. It is due to this random nature that the solution to the problems of turbulent flows has been in terms of a statistical approach.

The scale of turbulence may be defined quantitatively by using correlation coefficients. The autocorrelation function may be used on an experimental time series of turbulent flow and is defined as

$$C_{\Upsilon} = \frac{\overline{U'_t \cdot U'_{t+\Upsilon}}}{\overline{(U'_t)^2}} \quad (2.9)$$

Where  $U'_t$  is the instantaneous velocity at time  $t$ , and  $\Upsilon$  is the time delay between related velocities, see figure 2-5. A time delay,  $\Upsilon$ , equal to zero leads to the obvious result of the autocorrelation function being equal to unity.

One finds that a turbulent flow time signal is correlated over short time scales indicating that coherent structures exist within the flow, the correlation decreases as the value of time delay increases. Theoretically, the point at which  $C_{\Upsilon}$  becomes equal to zero defines the temporal scale of the largest eddies within the fluid. However, it has been found that the correlation coefficient tends to decay exponentially over its latter part making the value of  $\Upsilon$ , for which  $C_{\Upsilon}$  equals zero, rather vague.

Turbulent flow is composed of many eddies of various sizes. The frequency of eddy fluctuations vary over a large spectral range, (figure 2-6). The larger eddies contain most of the kinetic energy of the flow, these eddies are denoted  $l_e$  in the figure. These large eddies dissipate little energy by viscous effects. Interaction of the large scale eddies with each other generate smaller eddies, this is done by the mechanism of vortex stretching, [Ward-Smith, 1980]. Energy is dissipated by smaller eddies into heat by viscosity, these eddies are denoted  $L_d$  in the figure. The smallest eddies found in a flow are known as Kolmogorov eddies,  $L_k$ . The local Reynolds number of these eddies is unity. There is a continuous transfer of energy from the large scale eddies to the smaller eddies, which dissipate this energy in the form of heat. Large scale eddies are usually quite anisotropic, their size and orientation depending on the method of their generation. However, as one moves down the eddy length scale the smaller eddies become more isotropic, except, of course, near to solid boundaries.

Pipe flows near to the critical Reynolds number may alternate between the laminar and turbulent state, as shown in figures 2.7a and 2.7b. Such a vacillation in the flow regime is known as intermittency. The temporal intermittency factor,

$M_i$ , is defined as

$$M_i = \frac{\text{Duration of Turbulent Flow}}{\text{Duration of Laminar and Turbulent Flow}} \quad (2.10)$$

$M_i$  is equal to zero and unity for wholly laminar and wholly turbulent flows respectively. Intermittency for pipe flow occurs for Reynolds numbers in the approximate range of 2300 to 4000.

There is another type of intermittency associated with turbulent pipe flow which occurs near to the wall, where the pseudo-laminar layer, (or viscous sub-layer, [Davies, 1972]), and the main turbulent flow meet. As one would expect, knowing the random, fluctuating nature of turbulent flow, there is not an abrupt change between the two flow regimes, but rather a region in which turbulent fluctuations penetrate the viscous sub layer from time to time. This results in a temporal intermittency,  $M_i$ , with a spatial variation over a transitional region which is depicted in figure 2-7c.

#### 2.2.4 Head Loss and the Friction Factor

The head loss,  $H_f$ , per unit length of pipe is given by Darcy's equation as follows,

$$H_f = \frac{\lambda \cdot \bar{U}_z^2}{4 \cdot g \cdot R} \cdot dz \quad (2.11)$$

Where the multiplying variable,  $\lambda$ , is the pipe friction factor which depends on the flow regime within the pipe.

In general the flow regimes in a pipe may be split into roughly four definable

areas, these are as follows.

- 1 – Laminar flows for Reynolds numbers below  $Re_{crit}$ , described in section 2.2.2.
- 2 – Intermittent flows, where the flow regime at sections of the pipe changes between the laminar and turbulent state, as outlined in section 2.2.3.2. These occur for flows between approximately 2300 ( $Re_{crit}$ ) and 4000, (after which fully turbulent flows exist).
- 3 – Smooth turbulence, whereby the pipe internal surface discontinuities are masked by the still relatively thick, pseudo-laminar layer, and thus do not affect the main turbulent flow.
- 4 – Rough turbulence, usually occurs at high Reynolds numbers, whereby the pseudo-laminar layer has thinned sufficiently for the pipe surface roughness to affect the main flow.

Each regime has associated with it a different pipe friction factor,  $\lambda$ , the value of which may be obtained using a chart such as the Moody diagram, figure 2–8, or from the Colebrook–White equation, [Colebrooke, 1939],

$$\frac{1}{\sqrt{\lambda}} = -2 \log_{10} \left[ \frac{\epsilon}{3.7 D_p} + \frac{2.51}{R \sqrt{\lambda}} \right] \quad (2.12)$$

Where  $\epsilon/D_p$  is the relative roughness of the pipe wall to the pipe diameter. Using this expression the friction factor for both rough and smooth turbulence may be obtained.

Due to the implicit nature of  $\lambda$  in the above expression, much work has been done to obtain an explicit approximation to it. There now exists many explicit approximations to the Colebrook–White formula, see for example Barr [1975]. Chen and Ackland [1990] have gone further and formulated a continuous equation for the pipe friction factor spanning all four flow regimes.

For undisturbed pipe flow below the critical Reynolds number,  $Re_{crit}$ , the flow is always laminar, and the pipe friction factor is equal to  $64/Re$ , (see appendix 1). Such flows are shown by the preturbulent straight line on the Moody diagram. However, it is to be noticed that the laminar line extends (shown dashed in the

figure) past  $Re_{crit}$ . The reason for this is that laminar flow in a pipe requires that a finite disturbance be input into the flow for the transition to turbulence to take place. Laminar flows above the critical Reynolds number are known as super-laminar flows, and they are highly unstable. Such super-laminar flows have been found experimentally for flows up to Reynolds numbers of 90,000. (Once such super laminar flow has broken down to the turbulent state, the flow Reynolds number must be reduced to below  $Re_{crit}$  for the flow to relaminarise.) More will be said on the stability of laminar pipe flow in the next section.

### 2.2.5 Stability Theory

Much effort has been made to derive theoretically the critical Reynolds number for various flows including axisymmetric pipe flows. Such stability theories have played an important role in the understanding of the transition processes in many fluid situations, [Drazin & Reid, 1981]. It seems appropriate in the present text to briefly outline the general method used in such an activity.

Stability theory has been used successfully to predict critical Reynolds numbers for the case of a flat plate of zero incidence, [Schlichting, 1979, p469]. The case of Hagen-Poiseuille pipe flow, however, has proved to be a much more complex problem.

The general approach is to derive disturbance equations from the Navier Stokes equations, (see equations A1.1–A1.4 in Appendix 1), the disturbances are then put into wave form and the equations solved to find unstable values of the disturbances. The method, as applied to axisymmetric, Newtonian pipe flow, is as follows:

- 1 – The first step is to assume flow conditions, which satisfy the boundary conditions, which for the case of laminar pipe flow is a parabolic axial velocity profile, with both the radius and centre-line velocity set equal to unity for simplicity in the calculations.
- 2 – The Navier Stoke's equations are written for  $U_z$ ,  $U_r$ ,  $U_\theta$  then small disturbances, ( $\check{u}_z$ ,  $\check{u}_r$  and  $\check{u}_\theta$ ), are added to the velocities and the Navier Stokes equations are rewritten for

$$U_z + \check{u}_z, U_r + \check{u}_r, U_\theta + \check{u}_\theta. \quad (2.13)$$

The disturbance equations are then subtracted from the original Navier Stokes equations, leaving a set of disturbance equations.

3 - The disturbance equations are then linearized, by neglecting the products of the disturbance velocity, and the disturbance is modelled by perturbations of the form:

$$(\check{u}_z, \check{u}_r, \check{u}_\theta, \check{p}) = (V_z(r), V_r(r), V_\theta(r), P(r)) \cdot e^{i\alpha(z-ct)} \quad (2.14)$$

This assumes an axisymmetric disturbance which is periodic in the direction of the flow, where temporal growth of the disturbances occurs for a real value of  $\alpha$  and complex  $c$  and spatial growth occurs for a real value of  $c$  and complex  $\alpha$ . These disturbances are known as Tollmein-Schlichting waves, and have been observed experimentally, [Schlichting, 1979, pp473-493].

4 - The resulting equations derived in step (3) are then solved for  $\alpha$ . This is an eigenvalue problem, with homogeneous boundary conditions.

5 - Once a value of  $\alpha$  is obtained the values of  $c_i$  and  $c_r$  can be found.

7- The values of  $\alpha$  and  $c$  thus give the amplitude and speed of propagation and also the type of instability, i.e. temporal or spatial.

For a more in-depth description of the steps involved in stability analysis the reader is referred to White [1974].

At the present time it is generally considered that fluid flow in a pipe is stable for infinitesimal disturbances for all values of  $Re$ , (i.e. small finite amplitude disturbances must be present in the flow for transition to occur), although this has never been rigorously proved, [Stuart, 1979].

Sexl [1927a and 1927b] proceeded to solve the laminar pipe flow disturbance equations for the inviscid solution, (i.e. zero viscosity or very large Reynolds number). Corcos and Sellars [1959] have solved the stability equations for viscous

flow in a pipe subject to axially symmetric disturbances. They found that a finite number of eigenvalues exist for given wave numbers and Reynolds numbers. They concluded that Poiseuille pipe flow damps infinitesimal axially symmetric disturbances and that transition must be triggered by a finite amplitude disturbance in the flow.

Keuthe [1962] noted from experimental studies of flows in pipes, that when initial disturbances are small, their subsequent growth or decay follows linearized theory. However, if the disturbances grow, then at some point in their evolution the non-linear terms neglected in the analysis take over and 'govern the transition process'. Thus, the transition to turbulence becomes a non-linear process. Leite [1957] perturbed laminar air flow in a pipe using an oscillating sleeve surface mounted on the pipe internal wall. This device allowed him to vary the frequency of the disturbances within the flow. He found good agreement with the theoretical results of Corcos and Sellars. Leite also found the following:

- 1 - The disturbances generated exhibited imperfect axial symmetry, the non-symmetric part decayed more rapidly than the symmetric part.
- 2 - The theory of Corcos and Sellars [1959] predicted fairly accurately rates of decay but not rates of propagation.
- 3 - The transition to turbulent flow occurs whenever the amplitude of the disturbance exceeds a threshold value which decreases with increasing Reynolds number.

A similar experimental study, outlined by Lessen et al [1964] and Fox et al [1968], was conducted on water flows within pipes. The disturbances were generated by an oscillating plate placed on the main diameter of the pipe. This work showed up regions of instability for finite disturbances above a critical Reynolds Number,  $Re_{crit}$  of 2150.

It is noted by White [1974] that the linearized stability theory, as outlined in this section, only predicts the breakdown of laminar flows at finite Reynolds numbers, subject to external disturbances. It does not predict the onset of turbulence. Corcos and Sellars [1959] concluded from their theoretical work that stability theory plays only a fragmentary role in the description of transition. Once non-linearities take over, an entirely different analysis seems to be required.

(Echoing the point made by Keuthe, see also Reshotko [1981].) As the disturbances grow, they reach a point at which linearization of the equations is inadmissible, and even qualitative information about further development of the disturbances is lost. The disturbances may grow, settle down to a finite amplitude or decay. If they grow they may appear as turbulent spots which may or may not spread into the flow. As the disturbances grow, and non-linear effects become dominant, they tend to become more three-dimensional in nature, [Klebanoff et al, 1962].

Stability theory is a wide and complex topic and there is only room within this thesis to give it brief coverage. For more detailed information of the subject area the reader is referred to the comprehensive texts on the subject by Lin [1966] and Drazin and Reid [1981].

#### 2.2.6 Structures Present within Transitional Pipe Flow : The Puff and the Slug

Whereas stability theory concerns itself with the initial process of transition, many experiments have concentrated on the next stage in the process, whereby the laminar flow breaks down intermittently to the turbulent state. (See also section 2.2.3.3.) Transition from the laminar state to an intermittently turbulent one is believed to take place at the development region of the laminar flow profile at the pipe inlet, [Smith, 1960]. It may also be caused by disturbances brought in with the flow, [Moss, 1989]. The nature of the breakdown of laminar flow at an arbitrary cross section of a pipe depends, according to Binnie and Fowler [1947], upon the distance of the cross section downstream from the inlet. The phenomenon of intermittency in pipes occurs between pipe Reynolds numbers of 2000 and 3000, [Patel & Head, 1969], and is immediately obvious from the velocity time trace of the pipe fluid, [Rotta, 1956]. Fukuda [1985] gives details of the variation of the intermittency factor with the pipe Reynolds number, as shown in figure 2-9.

Wynanski and Champagne [1973] describes the two types of intermittently turbulent flows that may occur, these are,

- 1 - Puffs - these are generated by large scale disturbances at the inlet.
- 2 - Slugs - these are caused by the instability of the boundary layer to small

disturbances in the entrance region of the pipe.

Figure 2-10 shows the occurrence of puffs and slugs and their dependence on the pipe Reynolds number and level of disturbance.

Puffs occur within a Reynolds number range of 2000 to 2700. Wygnanski et al [1975] have found that the behaviour of the turbulent puff, at large distances from the initial propagating disturbance, is independent of the type of disturbance which caused it. Thus, all puffs at the same value of  $Re_p$  are of equal length. The average velocity of a turbulent puff is approximately equal to the average pipe flow velocity  $U_p$ . Depending upon the value of the pipe Reynolds number, puffs either grow or decay. At a certain value of  $Re_p$  the puffs are stable, and these patches of turbulence interspersed with laminar flow are observed to propagate indefinitely while preserving their lengths. These stable puffs are known as equilibrium puffs and they occur at a pipe Reynolds number of between 2200 [Wygnanski<sup>et al</sup>, 1975] and 2250 [Bandyopadhyay, 1986].

According to Lindgren [1957] and [1969], turbulent slugs are formed when initial small disturbances grow into turbulent spots within the pipe, these develop into turbulence which soon fills the whole cross section of the pipe, and may then grow only in the axial direction. Thus, slugs generally increase in length as they proceed downstream. Downstream of the production area of the slugs there exists a point where the slugs have grown in length and coalesced with each other to produce fully turbulent pipe flow, this occurs for values of  $Re_p$  in excess of 3000. (This is the reason that intermittent flow is generally said to occur for values of  $Re_p$  between 2000 and 3000. Whereas, near to the cause of the turbulent patches, within the inlet region, intermittency may be observed for much larger pipe Reynolds numbers. This is due to the presence of slugs which have not yet grown, to join preceding and succeeding ones, to produce a continuous fully turbulent flow.) Slugs begin to occur at pipe Reynolds numbers in excess of 2700. They have a well defined shape, with leading and trailing edges between the laminar fluid outside the slug and the turbulent fluid within, see figure 2-11. The leading front travelling at velocity greater than the average flow velocity, and the trailing front travelling at a velocity less than the average flow velocity. The difference between the front velocities increases as the pipe Reynolds number increases, thus for higher values of  $Re_p$  the slugs grow more quickly. The bluntness of the

velocity profile within a slug is attributed to the Reynolds stresses in the turbulent flow within the slug. Teitgen [1979] has determined that the fluid flow within the slug has the same characteristics as those of fully developed turbulent flow at the same Reynolds number.

Rubin et al [1979] have found that a slug containing all the attributes of fully developed turbulent pipe flow, is generated by the coalescence of puffs. Thus slugs are in fact trains of puffs, and have a length which is an integer multiple of a puff at the same Reynolds number. Lindgren [1969] went further to suggest that the apparently fully developed turbulence in pipes, with Reynolds numbers up to 6000, were in fact composed of closely packed slugs.

### 2.2.7 Entrance Flow Development

The velocity profile of laminar flow, within the entrance region of a straight pipe of constant cross section, must develop from entrance profile to the parabolic velocity profile of fully developed Hagen–Poiseuille flow, (see figure 2–12). The entrance flow development may be shown very clearly with the aid of flow visualisation, [Japanese Society of Mechanical Engineers, 1988].

The flow profile at the pipe entrance is usually assumed to be of a constant velocity for ease of theoretical manipulation. However, the presence of a smooth entrance to the pipe has the effect of modifying the velocity profile, prior to the fluid entering the pipe, and reducing the entrance length,  $Z_e$ .

There are many theories around to predict  $Z_e$  in terms of the pipe Reynolds number and the pipe internal diameter, see for example Boussinesq [1891 ], Schiller [1922], and Langhaar [1942]. Numerical integration of the basic Navier–Stokes equations by Freidmann et al [1968] finds the entrance length to be

$$Z_e = 0.05600 D_p \cdot Re_p \quad (2.15)$$

This value by Friedmann is recommended by Ward–Smith [1980, pp195–226] in his authoritative account of entrance length theories. This is the formula used to

determine the entrance length required for the experimental investigation reported herein.

The stability of developing laminar flows within the entrance region of pipes has been investigated theoretically by Tatsumi [1952a & b], using the methods of stability theory outlined in section 2.2.5. He found a stability limit at a minimum critical Reynolds number,  $Re_{crit}$ , of 9700, at a point 17 pipe diameters downstream from the entrance.

### 2.2.8 Pulsatile Pipe Flow

Pulsatile flow may be defined as flow with periodic fluctuations of the bulk mass-flow rate. [Oppenheim and Chilton, 1955]. Pulsatile pipe flow consists of a mean velocity component  $\bar{U}$  and an oscillating component,  $U'_o$ , superimposed upon it, thus

$$U = \bar{U} + U'_o \quad (2.16)$$

Unlike the fluctuating component of turbulent flow,  $U'$ , the oscillating component is usually a regular, controllable, periodic function. The simplest example of which is a sinusoidal component,

$$U'_o = U_{amp} \cdot \sin(\omega t) \quad (2.17)$$

where  $U_{amp}$  is the amplitude of the fluctuating component.

The special case, where there is no mean flow component (i.e.  $\bar{U} = 0$ ), is known as oscillatory flow, [Fishler & Brodkey, 1991], and such flows have been described theoretically by Shlichting [1979, pp436–438]. Oscillatory flows may exhibit laminar to turbulent transition phenomena for large values of  $U_{amp}$ , [Kurzweg, 1989].

Pulsatile flows can be found in many pipe flow systems. Such flows often occur

at the inlet and exhaust ducts of reciprocating engines, or in pipe lines fed by reciprocating, or rotary positive displacement pumps or compressors. Pulsating flow may also originate from instabilities in flow systems under certain flow conditions which favour self-excitation, an example of such a self-exciting flow phenomena is that of flow through a partially closed hydraulic valve. The phenomena of flow induced vibrations of hydraulic valves is described in detail by Weaver et al [1978], and D'Netto and Weaver [1987].

Fluctuating components may even be added purposely to the flow, as in the case of transport of solids through pipelines. Such flows may exist as laminar or turbulent flows, under certain conditions [Ramaprian & Tu, 1980], both flow regimes may exist at certain parts of the pulsation cycle. The stability of laminar pulsatile flows has been experimentally investigated and it has been found, by Sarpkaya [1966], that the critical pipe Reynolds number required for transition is higher than the critical Reynolds number of steady Poiseuille flow. Friction factors for fully turbulent pulsatile flows have been obtained experimentally by Baird et al [1971] and Kirmse [1979]. It has been shown by Kirmse that the average value of the friction factor,  $\lambda$ , for such a flow regime is less than the friction factor for a non-pulsating flow at the same Reynolds number. Iguchi [1986] has found turbulent slugs, similar to those of normal intermittent pipe flows, generated in pulsatile pipe flows.

An experimental study by El Masry and El Shobaky [1989] has shown that the transport of solids by fluid flows in pipes may be enhanced by the addition of a pulsatile component to the mean flow velocity. One area of research which has conducted much work on the subject of pulsatile flows is that of blood flow, (a non-Newtonian fluid), where there is a relatively large fluctuating flow component superimposed on the mean flow rate. Work has been conducted on the effect of artery constriction (modelled by a constriction in a pipe) on the breakdown of laminar pulsatile flows by Lieber and Giddens [1989]. While Martinez-Val et al [1990] have looked at the flow regime, of such pulsatile flows, at replacement heart valves.

### 2.2.9 Orifice Flow Phenomena in Pipes

Orifices are the most popular form of flow measurement device used in Civil and Mechanical Engineering, for measuring mass flux rates of incompressible flows. The installation of an orifice plate in a pipeline results in a loss of pressure head in the system at the orifice plate, part of which is recoverable, part irrecoverable.

As the flow passes through the orifice opening it is accelerated and the kinetic energy of the flow increases, this results in a significant pressure drop, (figure 2-13). Much of this kinetic energy is dissipated downstream of the orifice in eddies and this is the mechanism by which the irrecoverable pressure drop occurs. As the flow moves further downstream it decelerates and gradually returns to the upstream velocity profile, this coincides with reduction in the kinetic energy of the flow which in turn causes a recovery of the pressure within the fluid. However, the pressure attains a value less than it would otherwise have been, had the orifice plate been absent from the pipe. The reason for this is that the presence of the orifice plate causes an increase in mixing of the 'flow' due to eddies created at the orifice, these eddies then die out due to viscous diffusion, which in turn loses kinetic energy from the flow to the surroundings in the form of heat, [Bullock<sup>et al</sup>, 1990]. More will be said about the flow mechanisms at an orifice in section 2.3.

The net head loss in the pipe due to the presence of the orifice plate is given by

$$\Delta H_{nl} = K \frac{\bar{U}^2}{2.g} \quad (2.18)$$

where  $K$  is the pressure loss coefficient and is dependent on the orifice geometry and the Reynolds number of the flow. Pressure loss coefficient charts are given by Miller [1978] for various sharp edged orifice plates with various  $D_o/D_p$  ratios and Reynolds numbers in the range 1 to 10,000, (figure 2-14). Charts for more complicated orifice geometries are to be found in the paper by Rao and Sridharan [1972].

At the orifice plate itself there is a large difference between the pressure at the upstream and downstream faces, see figure 2-13. It is this difference which is of particular value for the purpose of flow measurement. Just upstream there is a slight increase in the pressure at the orifice plate. At the downstream face a large drop occurs due to the modification of the velocity profile as the flow is squeezed through the orifice plate and accelerated in the process. The relatively large difference in head across the orifice facilitates the measurement of the flow through the orifice using the standard flow equation:

$$Q = \frac{C_d \cdot A_p \cdot (2 \cdot g \cdot H)^{\frac{1}{2}}}{\left[ 1 - \frac{A_o^2}{A_p^2} \right]^{\frac{1}{2}}} \quad (2.19)$$

where  $C_d$  is the orifice discharge coefficient, see Iversen [1956] and Peterson [1947].

Hodgson [1929] gives a detailed insight into the laws of similarity for orifice flows. A more up to date and comprehensive review of orifice plate theory is outlined by Ward-Smith [1971] in his excellent book on pressure losses in ducted flows.

There exists many designs of orifice plate for the measurement of liquid and gas flows. Much effort has been expended in an attempt to standardise the design of such plates. The position of the pressure tapings, and the bore geometry are the two main criteria which effect the value of the differential pressure observed at the orifice plate. A detailed account of the various designs is not within the scope of this text, for further information the reader is referred to BS1042:1984, and also the following authors: Linford [1961], Sprenkle [1960], Bell and Bergelin [1962], Ward-Smith [1971], West [1962], Yoshitani et al [1985] and Buckingham [1956].

### 2.2.9.1 Numerical Solution of Low Reynolds Number Orifice Flows

The phenomena of steady, incompressible, axisymmetric viscous flow through a square edge orifice in a pipe was first solved numerically by Mills [1968]. To do so, he used a finite difference scheme to solve the Navier Stokes equations for the flow at an orifice. His analysis showed that as the pipe Reynolds number is increased from rest, the downstream recirculation zone increased in size while the upstream zone diminished in size. Figure 2-15a shows the streamlines and vorticity lines obtained by Mills for Reynolds numbers of 0 and 5 respectively. Axial pressure distributions are given in figure 2-15b. Solutions for pipe Reynolds numbers greater than 25 were not attempted due to the inability to distinguish between the actual hydrodynamic instabilities arising in the flow and numerical instabilities arising from the numerical integration method. Mills found good qualitative agreement with the flow patterns he obtained numerically and the experimental results of Johansen [1930].

Nigro et al [1978] have extended the work of Mills to allow for considerable flexibility in the choice of orifice plate geometry. Whereas Mills scheme could only cope with a square edged orifice plate, Nigro et al, claim to be able to solve for slow viscous flows through any orifice plate geometry.

### 2.2.9.2 Flow Pulsations at an Orifice

Flow pulsations cause errors in the metering of flows at orifice plates in pipes. Often there is no obvious indication of pulsations in the flow at the flowmeter. The effect of many forms of flow pulsations, on orifice meters, has been investigated by Oppenheim and Chilton [1955]. BS1042:1984, section 1.4, clause 14 gives guidelines for the practical use of orifice flow meters in pulsating flows.

Downing and Mottram [1977] have presented a theoretical analysis accounting for the metering errors at orifices due to such pulsating flows, (see also Mottram and Robati [1985]). They used this analysis together with experimental results obtained by themselves to define the metering error,  $E_m$ , at an orifice plate due to flow pulsations as,

$$E_m = \left[ 1 - \left( \frac{U_o'_{rms}}{\bar{U}} \right)^2 \right]^{\frac{1}{2}} - 1 \quad (2.20)$$

where  $U_o'_{rms}$  is the root mean square of the fluctuating component of velocity.

Jones and Bajura [1991] have numerically investigated pulsating flows at a pipe orifice in the range,  $0.8 < Re_p < 64$ , and for Strouhal numbers in the range 0.00001 to 100. From the study they concluded the following:

- 1 - The reattachment length varies throughout the forcing cycle, as can be seen in figure 2-16. In the figure, the odd number time steps, (each of one eighth of a cycle), are shown and the change in reattachment length is clearly seen.
- 2 - The reattachment length,  $Z_r$ , increases with the Strouhal number.
- 3 - The flow rate pulsation causes more energy to be dissipated across the orifice plate.

## 2.3 VORTEX FLOWS

### 2.3.1 Introduction

'Vortices are ordered structures in fluid motion, which nature prefers over chaos in certain situations', is how Lugt [1983] describes these commonly occurring flow structures. Such structures exist in nature over many, if not all length scales, from the astronomical scales of the giant vortical spiral galaxies, through the geophysical scales of hurricanes, down to the sub atomic scales of the elementary particles.

Vortex flows occur in all branches of Engineering. Vortex shedding from wing tips are of interest to the Aeronautical Engineer. The Chemical Engineer requires knowledge on the mixing properties of vortex flows. The Biomechanical Engineer concerns him or herself with vortex flows in heart replacement valves. The Civil Engineer is concerned with vortex shedding from structures and the effect from the

resulting flow induced vibrations, and so on.

A vortex is defined as the rotating motion of a multitude of material particles around a common centre, and vorticity as the angular velocity of matter at a point in continuum space.

### 2.3.2 Vorticity

The vorticity vector,  $\omega$ , is defined for Cartesian coordinates as,

$$\omega = \text{curl} (U) = (\omega_x, \omega_y, \omega_z) \quad (2.21a)$$

$$= \left( \frac{\partial U_z}{\partial y} - \frac{\partial U_y}{\partial z}, \frac{\partial U_x}{\partial z} - \frac{\partial U_z}{\partial x}, \frac{\partial U_y}{\partial x} - \frac{\partial U_x}{\partial y} \right) \quad (2.21b)$$

and in cylindrical coordinates as,

$$\omega = \text{curl} (U) = (\omega_r, \omega_\theta, \omega_z) \quad (2.22a)$$

$$= \left[ \frac{1}{r} \cdot \frac{\partial U_z}{\partial \theta} - \frac{\partial U_\theta}{\partial z}, \frac{\partial U_r}{\partial z} - \frac{\partial U_z}{\partial r}, \frac{1}{r} \cdot \frac{\partial}{\partial r} \left[ r \cdot U_\theta \right] - \frac{1}{r} \cdot \frac{\partial U_r}{\partial \theta} \right]$$

(2.22b)

Flows with zero vorticity are known as irrotational.

The circulation of a flow is defined as the flow around a closed curve in a fluid, (see for example the closed curve APB in figure 2-17), and is denoted by the symbol  $\Gamma$ , and is given by the expression,

$$\Gamma_{AB} = \int_A^B U \, dl \quad (2.23)$$

where  $dl$  is the incremental length around the curve, and  $U$  is the velocity at the point considered on the curve. The vorticity,  $\omega$ , is given by the circulation,  $\Gamma$ , divided by the area enclosed by the curve. Thus, for a fluid rotated with a constant angular velocity,  $\Omega$ , about a centre, the circulation around a closed radial curve may be shown to be twice the angular velocity, [Massey, 1984].

For Laminar pipe flows, (section 2.2.2), there are no velocity fluctuations about the mean, ( $U' = 0$ ), and there are no mean radial or swirling flow components, ( $U_r = U_\theta = 0$ ). Thus the vorticity vector, equation 2.22b, reduces to

$$\omega = - \frac{dU_z}{dr} \quad (2.24)$$

Substituting the parabolic Hagen-Poiseuille velocity profile, (eqn. 2.21), for laminar pipe flows for  $U_z$ , gives:

$$\omega = - \frac{d}{dr} \left[ 2 \cdot \bar{U}_z \cdot \left[ 1 - \frac{r^2}{R^2} \right] \right] = \frac{4 \bar{U}}{R^2} \cdot r \quad (2.25)$$

Thus, for such a flow the vorticity is linearly related to the distance from the centre-line, attaining a maximum value at the pipe wall. It is interesting to note that this flow is a very good example of a flow with vorticity but without vortical motion, (i.e. there is no rotation of any of the fluid particles around a common centre).

The case where laminar pipe flow passes through an orifice plate within a pipe gives rise to radial velocities within the flow as the streamlines converge to squeeze the flow through the aperture, and also as they diverge downstream. As the flow approaches the orifice it accelerates and the vorticity increases within the accelerated region of the flow.

The maximum convergence of the flow at an orifice occurs just downstream of the plate. The point at which the streamlines are parallel defines the smallest cross sectional area of the jet of fluid emanating from the orifice, and is known as the *vena contracta*. (This phrase is Latin meaning literally 'contracted vein'). In the case of creeping flows, i.e. flows with a Reynolds number approaching zero, the vena contracta will occur at the orifice aperture.

As described in section 2.2.2 the rate of internal shearing of a Newtonian fluid is directly proportional to the stresses between layers of fluid, related by the fluid viscosity. The shear stress set up between two such layers in laminar pipe flow is

$$\tau = - \mu \frac{dU_z}{dr} \quad (2.26)$$

thus, the viscosity,  $\mu$ , acts to counter the vorticity. Viscosity causes shearing stresses to be set up opposing the shearing of the fluid, defined by the shape of the velocity profile. In effect, the viscosity acts to even out discontinuities in the velocity profile. If viscosity had its way it would reduce the shearing ( $dU_z/dr$ ) to zero. However, due to the no slip conditions at solid boundaries the only way to have zero shearing is to have zero velocity at all points in the flow. Thus, if the driving force of the fluid is removed, the fluid will eventually come to rest due to the action of viscosity, coupled with the no slip boundary condition.

The effect of viscosity,  $\mu$ , to even out the velocity profile and reduce the vorticity is known as diffusion. Viscosity, therefore, causes diffusion of momentum within laminar flows.

### 2.3.3 The Rankine Vortex and the Diffusion of Vorticity

In nature, real vortices tend to possess solid body rotation at their centre due to viscous diffusion, while exhibiting irrotational vortex flow at their extremities. A simple theoretical description of such a vortex is known as a Rankine vortex, which consists of a central core of solid body rotation with the extremities of the vortex consisting of irrotational fluid motion. The theoretical description of the Rankine vortex has been left out of this text, and may be found in most basic Fluid Mechanics texts.

The diffusion of vorticity from a vortex, in a viscous fluid, is a time dependent phenomena. The tangential velocity at a radius,  $r$ , of a vortex, with initial strength,  $\Gamma_0$ , is given by the expression, [Duncan et al, 1963],

$$u_{\theta} = \frac{\Gamma_0}{2\pi r} \left[ 1 - e^{(-r^2/4\nu t)} \right] \quad (2.27)$$

Using the above expression Schaefer and Eskinazi [1959] presented an analytical solution for the velocity field of a vortex street generated in a viscous fluid. They found three basic regions of the vortex shedding, which are summarised in figure 2-18, these are:

- 1 - Formation: The initial development of the vortices in the near wake of the bluff body.
- 2 - Stable Region: A stable region of laminar, periodic flow was found after the formation region.
- 3 - Unstable Region: The stable region eventually lost its stability and broke down to a turbulent flow.

### 2.3.4 Flow Separation and Vortex Motion

Flow separation occurs in many Engineering flows and its effect may, or may not, be beneficial to the system considered. When particles approach each other on the surface streamline from opposite directions, they meet then depart from the

boundary. This phenomenon is called flow separation, see figures 2-19a and 2-19b. When the situation is reversed, and the flow moves towards the boundary an attachment, or reattachment, point is obtained. Both separation and reattachment points are known as stagnation points, shown as S and R, respectively, in the figures. The streamline connecting the separation point with the reattachment point is known as the separation, or limiting, streamline. The occurrence of flow separation is a prerequisite for the generation of discrete vortices in the flow. In boundary layer flows, vorticity is produced at a body surface and from there spreads into the fluid.

As the Reynolds number of a flow increases, convection dominates over diffusion as the main means of transport and dispersal of vorticity, [Rosenhead, 1963]. Convection carries vorticity. Vortices remain attached to the body on which they are formed only for low Reynolds numbers. As the Reynolds number increases, the flow becomes unstable and vortices are shed. The exact value of Reynolds number at which vortices are shed, for a given fluid, is highly dependent upon three factors: the shape of the body, its surface roughness and also the level of background turbulence in the flow. It has been noted by Mair and Maul [1971] that background turbulence may in fact either enhance or suppress the formation and shedding of vortices at a bluff body depending on the relative intensity of the background noise to that of the vortex shedding process.

The phenomenon of vortex separation is to be distinguished from that of flow separation. Vortex separation is always a time dependent process in which vorticity assumes extremal values inside the fluid. Once detached from a body, the core of a vortex rotates like a solid body due to the action of viscous diffusion, even for extremely high Reynolds numbers. In contrast with the theoretical behaviour of inviscid vortex rings which move with constant velocity without decay, real vortex rings lose speed. They decelerate not only through the loss of energy due to friction, but also entrainment of fluid from the surroundings. Vortices with high frequency decay faster than those with relatively smaller frequencies.

Vortices may be generated in a variety of flow situations. However, they exhibit similar qualities. Once vortices have been generated, as for example at the tip of a bluff body, (figure 2-20a), or the end of a splitter plate, (figure 2-20b), they roll up until they are large enough to be convected away by the main flow. The

vortices increase in size as they proceed downstream due to two main effects, vortex merging and entrainment of fluid from the main flow. Viscous diffusion does not normally play a major role in vortex growth.

Vortices in shear layers may interact with each other either by a merging process or a tearing process, [Hernan & Jimenez, 1982]. In the merging process, two eddies (in rare cases three eddies), come into close proximity with each other, begin to rotate about a common centre and eventually become entangled to form a single eddy, (figure 2-20b). The tearing process involves an eddy losing its stability and disintegrating, its vorticity being eventually absorbed by its neighbours.

The presence of vortices in the shear layer tends to make the recirculation zone less well defined. The movement of the vortices on the boundary of the recirculation zone tend to blur its edge, also the reattachment length,  $Z_r$ , fluctuates with the passage of the vortices.

Perry et al [1980], (see also Perry and Lim [1978]), have used flow visualisation to elucidate the flow phenomena at a jet issuing from a tube at low Reynolds numbers. The vortices generated by the jet are shown in figure 2-21. The figure shows the streamlines as would be seen by an observer moving with the mean velocity of the vortices. From the figure, one may discern many of the salient features of the flow. The region of solid body rotation at the centre of each vortex are called centres, labelled C. A saddle point, labelled S, may also be seen in the figure. The complexity of viscous flows approaching obstacles is clearly outlined by Perry and Fairlie [1974]. Figure 2-22a shows the flow patterns in a viscous flow approaching a cylindrical obstruction and figure 2-22b shows the streamline separation pattern of a turbulent boundary layer approaching a building with a causeway beneath it.

Vortices are generated by the amplification of small disturbances in shear flow. One example of this amplification phenomena is that of two horizontal, parallel, infinite streams of fluid flowing over each other with different velocities and densities. The shearing action of the two fluid bodies causes initially very small disturbances to be amplified. This phenomena is known as Kelvin-Helmholtz instability, [Drazin and Reid, 1981, pp14-22]. As the instabilities grow they roll up, due to the action of the two layers, into discrete vortices, see figure 2-23.

One of the most comprehensively studied vortex flows is the Karman vortex street, whereby vortices shed in turn from either side of a circular cylinder in laminar flow, (figure 2-24). These flows are of interest to the Engineer as they can produce results which are directly applicable to the vortex-structure interaction which occur, for example, with chimney stacks in cross winds. See Marris [1964] for a discussion of such flows.

### 2.3.5 The Strouhal Number

The non-dimensional parameter used to describe periodic flows such as those caused by vortex shedding is the Strouhal Number,  $S$ , where:

$$S = \frac{f_{shed} \cdot L}{\bar{U}} \quad (2.28)$$

and where  $f_{shed}$  is the frequency of vortex shedding and  $\bar{U}$  is the average velocity of the flow.  $L$  is a suitable length scale of the object under investigation, such as the diameter of a stationary cylinder or sphere in a cross flow, or for non symmetrical objects such as steel sections of a bridge, it is usually defined as the length perpendicular to the mean flow direction. For orifice flow, the typical length scale,  $L$ , is taken as the diameter of the orifice aperture,  $D_o$ . It has been demonstrated theoretically by Birkhoff (see Birkhoff and Zaran<sup>o</sup>nello [1957], pp290-292) that the vortex shedding from a bluff body, such as a cylinder, is directly proportional to the flow velocity, (by considering the near wake as an oscillator). This relationship has been found by experimental evidence to be the case for large ranges of Reynolds numbers.

Typically, the Strouhal number for vortex shedding at a cylinder is approximately 0.20, where  $L$  is taken as the cylinder diameter. This value remaining fairly constant over a Reynolds number range from 400 to 40,000, for instance see West and Apelt [1990]. A flat plate placed in a uniform flow typically has a Strouhal number around 0.15, (see figure 2-25). For various steel sections, as used in the construction industry, the Strouhal number may vary from approximately 0.12 to 0.16 depending on the geometry involved. More detailed

information on the Strouhal numbers for steel sections may be found in Blevins [1977]. Johansen [1930] found the average Strouhal number to be approximately 0.594 for vortex shedding at an orifice in a pipe with a  $D_o/D_p$  ratio of 0.50. Where the length scale,  $L$ , was taken as the orifice aperture diameter,  $D_o$ . This value remained fairly constant for a range of  $Re_p$  from 111 to 510.

Recently there has been an emergence of flow metering devices which rely on the fact that the Strouhal number remains constant over wide ranges of Reynolds numbers. These devices are known as vortex meters. According to Zanker and Cousins [1977], (who give details of various designs), vortex meters consist of three fundamental parts, these are:

- 1 - The hardware to produce the basic hydrodynamic instability,
- 2 - A method of detecting the resulting vortex shedding frequency, and,
- 3 - A signal processing unit to extract the required flow output.

Vortex meters for pipe flows are advocated by Casperen [1977] for measuring flow rates as they are simple, rugged and may provide accurate measurement if the correct choice is made. However, careful choice of the vortex meter should be made, as shedding frequencies may cause vibration problems which may in turn effect the measuring accuracy and cause mechanical damage.

### 2.3.6 Forced Vortex Flows

Vortices generated within the mixing layer of shear flows tend to form at a dominant, or natural, frequency,  $f_n$ . This frequency is, in general, randomly distributed about a mean, as shown in the frequency spectrum of figure 2-26a. However, by forcing the flow, or the body itself, at, or near to the dominant frequency, the vortex shedding can be made much more regular as indicated by a single 'spike' in the frequency spectrum, (figure 2-26b).

If the forcing frequency,  $f_f$ , is moved away from the natural frequency,  $f_n$ , it causes the shedding frequency,  $f_v$ , to move with it, but only for small changes in  $f_f$  from  $f_n$ . This phenomena is known as frequency locking. Once the forcing frequency moves far from the natural frequency, then either one finds that the

shedding frequency will lock onto a forcing frequency which is a subharmonic of itself, or one finds both frequencies competing with each other in the flow and a beating pattern occurring in the flow pattern. The resulting flow pattern depends very much upon the relative amplitudes of the natural and forcing frequencies.

Ho and Huang [1982] performed a forcing frequency experiment on a mixing layer generated by two streams of fluid moving with different average velocities. They altered the forcing frequency of the flow over a range from  $1.26f_n$  down to  $0.17f_n$ , and found that when  $f_f$  was decreased below a certain limit the response frequency of the vortex shedding,  $f_v$ , switched discontinuously to a higher frequency, in fact back towards  $f_n$ , (see figure 2-27). However, they noticed that the effect of forcing the vortices at  $f_v/2$ ,  $f_v/3$  and  $f_v/4$  was to produce increased merging rates of the vortices and thus greatly increase the spreading rate of the layer.

Vortices forced at  $f_v$  and  $f_v/2$  merged in pairs, the latter frequency causing earlier merging of the vortices. Vortices forced at  $f_v/3$  and  $f_v/4$  merged in triples and quadruples respectively, and the rate of mixing was greatly enhanced. Thus, the resulting coherent structures obtained by this enhanced merging process, (known as collective interaction), have a frequency equal to the forcing frequency.

The vortex shedding frequency is related to the forcing frequency by,

$$f_f = \frac{1}{M} f_v \quad (2.29)$$

$M$  being the mode index, ( $M = 1, 2, 3, 4, \dots$  etc.). According to Ho and Huang, the first merging takes place at a distance  $Z_m$  given as follows,

$$Z_m = N \cdot M \cdot \frac{U_v}{f_v} = N \cdot M \cdot l_v \quad (2.30)$$

where  $N$  is an integer, and  $l_v$  is the vortex shedding wavelength. Thus, for a flow forced at the natural frequency, ( $M = 1$ ), the position of the first merging is an integer multiple of the vortex shedding wavelength.

Experimental investigations into the effect of forcing jets flows by Bradley and Ng [1989] have elucidated some features of forced wakes. They used two different frequencies to force the flow. It was found that by controlling the frequency, amplitude and relative phases of the forcing, that one may induce various modes of vortex development and merging in the downstream flow. Such modes include the pairing of similar sized vortices, pairing of vortices of different sizes, multiple vortex merging, (similar to that observed by Ho and Huang), and vortex shredding. Vortex shredding defines the process whereby one of the disturbances, generated at a subharmonic of  $f_n$ , grows faster than the other disturbance, (not at a subharmonic), and results in the faster growing vortices tearing apart, or 'shredding', the smaller vortices.

It has been suggested [Gharib and Williams–Stuber, 1989] that by forcing a vortex flow, a better environment for examining the nature of the particular system may be attained. They investigated the forced wake of an airfoil, which has a structure essentially of a Karman vortex sheet, and found that the velocity profile downstream adapts to accommodate the forcing of the flow. Nonlinear phenomena such as beating and 'lock-in' have been found in forced Karman vortex sheets by Detemple–Laake and Ecklemann [1989].

### 2.3.7 Flow Behaviour in Pipes, at Orifice Plates and Sudden Expansions

In pipelines it is often the case that the mean flow has a slight angular motion associated with it. This may be caused by the inlet conditions. The presence of an orifice plate in the pipe may accentuate the swirl as the streamlines contract to pass through it. In some circumstances this may lead to cavitation of the flow due to the associated radial pressure drop towards the axis of the pipe, Lugt[1962]. The breakdown of these swirling flows has been examined by Faler and Leibovich [1978]. However, in this text we are concerned with flows which do not have a swirl component at a pipe orifice.

It is also worth mentioning, before we consider orifice flows, that vortex flows may be generated at bluff bodies placed in a pipe. A study by Webb and

Harrington [1956] investigated the behaviour of vortex shedding at an obstacle placed on the pipe wall. They found that, for each Reynolds number investigated, the height of the obstacle determined whether the disturbances grew, or dissipated out, in the flow, see figure 2-28. These obstacles were of the form of non-axisymmetric bluff bodies. The effect of the orifice plate in such flows, which is in effect an axisymmetric bluff body, will be discussed in the following.

Johansen [1929] visually investigated the flow field at an orifice in a pipe for low Reynolds number flows. The glass pipe used in the study had a 27mm bore, and the orifice to pipe diameter ratio was 0.5. A 2% solution of methylene blue in water was used for the purpose. The main conclusions attained by Johansen for the behaviour of the flow at the orifice, as the pipe Reynolds number was increased from rest, are summarised in what follows. (See figure 2-29).

1 - **Creeping Flow ( $Re_o = 10$ )** - For Reynolds numbers approaching zero, the flow remains attached to the orifice lip as it flows over it, and the streamlines are symmetric about the body. Johansen also noted that the velocity appears uniform across the flow at the orifice aperture. (Figure 2-29a).

2 - **Slow Flow ( $Re_o = 30$ )** - The flow begins to separate just behind the orifice lip, and the recirculation zones begin to form. (Figure 2-29b).

3 - **Establishment of Recirculation Zones ( $Re_o = 100$ )** - An increase in Reynolds number causes the flow to detach from the orifice plate lip, reattaching itself further downstream. A vena contracta is formed just downstream of the orifice lip and a recirculation zone is set up. Also, upstream, another smaller recirculation zone is set up due to the detachment of the flow streamlines as they converge prior to passing through the orifice plate aperture. (Figure 2-29c).

4 - **Appearance of Shear Instabilities ( $Re_o = 250$ )** - Instabilities arise in the region of high shear between the main flow and the recirculation zone, (figure 2-29d). These appear as ripples in the flow streamlines and from this point onwards, the streamlines become time dependent.

5 - **Appearance of Imperfect Vortex Rings ( $Re_o = 600$ )** - The instability ripples roll up into incomplete vortex rings. (Figure 2-29e).

6 - Vortex Formation ( $Re_0 = 1000$ ) - A further increase in the  $Re_p$  leads to the rolling up of the instability ripples into discrete vortices, (figure 2-29f). These are convected away by the main flow streaming through the orifice aperture.

7 - Vortex Growth and Breakdown ( $Re_0 = 1600$ , and above) - At high Reynolds numbers the vortices generated at the orifice plate grow rapidly as they proceed downstream, interact with each other and breakdown to a 'violently' turbulent region. This region was seen to extend from one to five orifice diameters downstream of the orifice itself. (Figure 2-29g).

The phenomena, observed by Johansen and cited above, were also observed for other diameter ratios, (these being 0.1, 0.25, 0.75) though not at the same Reynolds numbers. In general the events described above occurred at increasingly higher Reynolds numbers, as the diameter ratio was increased.

Johansen found that, for the case of vortex shedding at a pipe orifice, 'no indication was observed of any tendency for the rings to be shed from the orifice in the form of a spiral'. That is the shedding of one, continuous helical vortex was 'not observed. The vortices shed from a pipe orifice are, therefore, discrete, axisymmetric vortex rings.

The destabilisation of axisymmetric vortex rings is discussed by Baumann et al [1992]. However, their work centred on single vortex rings of one fluid inside another, and perhaps is not relevant in this context where the vortex rings at an orifice are shed in a train, rather like a Karman vortex street, and may interact with each other.

The literature on low Reynolds number, vortex flows at a pipe orifice is very poor, consisting of only Johansen's [1929 & 1933] work. (Bullock et al [1990] have investigated high Reynolds number, fully turbulent flows at a pipe orifice, where  $Re_p = 20,500$ .) It will be instructive, therefore, to look briefly at a similar type of flow, that of flows at a sudden expansion within a pipe, (figure 2-30). This type of flow is also known as a confined jet flow, [Mansoori, 1988].

Back and Roshke [1972] investigated sudden expansion pipe flow for upstream

Reynolds numbers of between 20 and 4200. They found that the reattachment length,  $Z_r$ , of such jets had a variable behaviour depending on the flow regime. The reattachment length versus the upstream pipe Reynolds number is shown plotted in figure 2-31a.

At low Reynolds numbers,  $Z_r$  moved downstream with increasing Reynolds numbers. The variation was seen to be linear in this range as shown in figure 2-31b. At intermediate Reynolds numbers, instabilities in the jet boundary, increased in magnitude and rolled up in to vortex structures. The reattachment zone was determined when the lateral extent of this undulating motion extended to the pipe wall. At higher Reynolds numbers the jet spread more rapidly due to turbulent, random fluctuations and reattachment occurred relatively close to the discontinuity.

Khezzar et al [1986] followed up the work<sup>of</sup> Back and Roshke, using upstream pipe Reynolds numbers in the range, 120 to 40,000. Their results for the reattachment length versus upstream Reynolds number are shown in figure 2-32. They also investigated in detail the flow properties for an Upstream Reynolds number of 40,000. They found that the centre-line flow velocity decreased smoothly from the entrance value,  $U_0$ , to the final value in the large pipe of approximately  $0.32U_0$ . They also presented the turbulence intensities for various cross sections across the flow downstream of the outlet. In figure 2-33, the author has replotted the centre-line velocity results, together with the centre-line turbulence intensities, from the paper of Khezzar et al. From this figure it may be inferred that the turbulent fluctuations play a major part in the modification of the jet centre-line velocity to that of the downstream pipe centre-line velocity. (Compare with results in chapter 6.)

Sibulkin [1962] investigated the turbulent to laminar transition process within a pipe. He generated the 'artificially turbulent flow' using a sudden expansion flow in the pipe. These sudden expansions, (or diffusers as Sibulkin calls them), were of square edge and conical section, as shown in figure 2-34a. The flow conditions could be manipulated so that the flow in the downstream pipe was subcritical, i.e. below  $Re_p$ . Thus, the turbulence generated by the diffuser was dissipated downstream.

Figure 2-34b shows the variation of downstream turbulence intensity at the centre-line, and figure 2-34c gives details of the axial turbulence intensity at various radial positions across the pipe, for three positions downstream of the diffuser, ( $x/d=8, 17$  and  $35$  where  $d$  is the upstream diameter according to Sibulkin). Sibulkin noted that the radial profiles of the turbulence decayed most rapidly at the pipe wall and the centre-line, and least rapidly within the region  $0.4 \leq r/R_p \leq 0.6$ .

Finally, it should be noted that Durst et al [1989] have used both L.D.A. and flow visualisation techniques to investigate piston driven, sudden expansion flows. They have studied both the laminar and transition regimes. The phenomena of vortex roll-up into rings and interaction with solid surfaces were observed visually and detailed L.D.A. measurements were taken, giving an insight into the processes involved.

### 2.3.8 Flow Induced Vibrations

One practical aspect of the phenomena of vortex shedding is that it may give rise to flow induced vibrations. Thus, it seems appropriate to comment briefly on this effect. This type of flow-structure interaction commonly occurs where a flow is impeded by a bluff body or restriction. It is an important factor in certain Civil Engineering design situations, these include bridge deck design, tall buildings, chimneys, partially closed hydraulic valves, bridge piers etc.

In fact, most structures or hydraulic devices may suffer from flow induced vibrations, (caused by vortex shedding), under at least some of their expected operating conditions. It is the role of the Engineer to establish whether these conditions are acceptable to the operation of the structure, or device, in question. The problem of flow induced vibrations may be easily dealt with in certain circumstances by an appropriate change in the shape, and thus modification of the fluid dynamical properties and response characteristics, of the body in question, see for example Konishi et al [1979] and Hanco [1967]. There is, however, not sufficient room herein to go into this subject area in detail, the reader is therefore referred to the many standard texts on the subject.

## 2.4 NON-LINEAR DYNAMICAL SYSTEMS

### 2.4.1 Introduction

It is known that simple, low dimensional dynamical systems may be made to display complicated solution patterns as the control parameter of the system is increased above a critical value, [Lorenz, 1963]. These seemingly random, now called chaotic states, have been found for the post-transient solutions of difference equations and numerically integrated ordinary differential equations (O.D.E.'s). More importantly, such chaotic flows have been found experimentally for all manner of physical systems. These include; fluid flows such as the Taylor-Couette system and Rayleigh-Benard convection, biological systems such as predator prey systems and heart fibrillation patterns, chemical kinetics, electrical circuits and so on.

Chaotic flow is then a universal behaviour which may be realised in non-linear dynamical systems. Most physical systems are non-linear and it is this fact which accounts for the recent interest in the field of non-linear dynamics and further underlines the importance of the work done in this area, [Kuramoto, 1984].

Within the last decade or so scientists and engineers have looked to the new techniques emerging from the field of non-linear dynamics, to provide a framework for explaining the twin phenomena of the transition of a fluid to the turbulent state, and fluid turbulence itself, [Guckenheimer, 1986 and Ruelle, 1983a]. Turbulent flow is characterised by the apparently unpredictable motions of the fluid system, which has, in theory, infinitely many degrees of freedom. However, recent work has suggested that it is possible that turbulent flow could be governed by an underlying mechanism, which has essentially only a few degrees of freedom, [Yorke and Yorke, 1981].

The motion of fluids, governed by the Navier-Stokes equations, is a highly non-linear phenomenon. Almost all natural flows encountered in the engineering context are found to be turbulent. It is fair to say that turbulence was previously regarded as a random process with stochastic analyses tools employed to understand the phenomenon. Now, however, many workers in the field of turbulent flows believe that, in some circumstances at least, turbulence may in fact be a complex

chaotic motion. This belief has been substantiated by the observation of chaotic motion in many real, experimental fluid systems, (see for example Abraham et al [1984]).

For more details of an introductory nature of the subject of chaotic flows and turbulence the reader is referred to Lesieur [1987, Ch.3] and to the articles by Lanford [1981] and Cvitanovic [1984].

#### 2.4.2 Dynamical Systems

Nonlinear dynamics can be applied to two mathematical topics previously thought to be unrelated, these are:

1 – Ordinary Differential Equations, (continuous time),

i.e. Autonomous  $\frac{dX(t)}{dt} = F(X)$  , (2.31a)

and Non-Autonomous  $\frac{dX(t)}{dt} = F(X, t)$  (2.31b)

2 – Mappings, (discrete time intervals),

i.e. Autonomous  $x_{j+1} = f(x_j)$  , (2.32a)

and Non-Autonomous  $x_{j+1} = f(x_j, t)$  (2.32b)

where  $X, x, F$  and  $f$  are  $N$ -dimensional vectors. There are many examples of mathematical non-linear dynamical systems, some of which will be mentioned in this text. The reader will find a more detailed account of such systems in any introductory text on non-linear dynamics, such as Sagdeev et al [1988].

A well studied example of a non-autonomous differential equation is the Duffing Oscillator, [see for example Asfar and Masoud, 1992, Dowell and Pezeshki, 1988, Gottwald et al, 1992, and Rahman and Burton, 1986]. It will be useful to look at it in some detail, and use it to outline some of the basic phenomena of non-linear dynamics.

The Duffing Oscillator has the following mathematical form:

$$\ddot{x} + K\dot{x} + x^3 = B.\cos(t) \quad (2.33)$$

this is a forced non-linear oscillator, with a cubic elastic restoring force.  $K$  and  $B$  are arbitrary control parameters. The superscripted dots denote the first and second derivative of the displacement,  $x$ , with respect to time. Numerically integrating this equation one finds regimes of periodic and nonperiodic solutions, for various values of the control parameters. A suitable scheme for numerical integration such as Runge-Kutta, [O'Neill, 1987], or Newmark method, [Reddy, 1986], could be used. (The author has numerically investigated the effect of various numerical schemes on a modified version of the Duffing oscillator, [Addison et al, 1992]. See also appendix 4.)

For example a periodic solution can be found for the parameter values,  $K = 0.08$  and  $B = 0.20$ , and, nonperiodic solutions for  $K = 0.05$  and  $B = 7.50$ . (Figures 2-35a and 2-35b). The nonperiodic solution is very interesting. It does not repeat itself and appears irregular and unpredictable. However, it is not a random flow, since each time the oscillator is started from a specific set of initial conditions, the resulting time series will be identical, (i.e. it is deterministic). Whereas, a random series will follow a completely different and unpredictable path each time. A slight change in the initial conditions of the nonperiodic solution will rapidly produce an entirely different time series. This phenomena is known as sensitive dependence on initial conditions and is the hallmark of this type of nonperiodic motion, known as chaotic motion.

Figure 2-35c shows the effect of starting the Duffing oscillator from two very close initial conditions, ( $x = 3.0$ ,  $\dot{x} = 4.0$  and  $x = 3.01$ ,  $\dot{x} = 4.0$ ). As can be seen in the figure the resulting time series traces rapidly decorrelate from each

other.

More complex oscillator models may be obtained by coupling together two or more Duffing oscillators, [Yamada and Fujisaka, 1983], or by chaotically exciting one oscillator by the next, [Burton and Anderson, 1989]. However, such systems are outside the scope of this text.

### 2.4.3 Phase Space And Poincaré Sections

The most useful way to depict dynamical systems is by the use of a phase space. The phase space is a 'mathematical space with orthogonal coordinate directions representing each of the variables needed to specify the instantaneous state of the system', [Swinney and Gollub, 1981]. Thus, for the Duffing oscillator, rather than plotting the time series, i.e. the  $x-t$  curve, we may plot the  $x-\dot{x}$  curve in a two dimensional phase space. In figures 2-36a and 2-36b. The phase space trajectories are shown for the periodic and chaotic state of the Duffing oscillator. The trajectories evolve and form a 'phase portrait' of the system in phase space.

The chaotic trajectory of the Duffing oscillator fills up 2-dimensional phase space. However, if the phase space is increased in dimension to 3, (i.e.  $x-\dot{x}-\ddot{x}$  curves), we find that the trajectories do not cross each other, and the phase space does not fill up. Thus, a three dimensional phase space is sufficient to describe the properties of the chaotic solution of the oscillator. (This is because the chaotic solution trajectories actually form an object called an attractor which has a non-integer value of its dimension, between 2 and 3, this will be discussed in more detail in later sections.)

One way to simplify phase diagrams is to use a device known as a Poincare section. It is constructed by sampling the phase trajectories in a 'stroboscopic' fashion. The trajectory is sampled once every cycle of the forcing function. Figure 2-37 contains the Poincare sections of the periodic and chaotic solutions to the Duffing oscillator.

For both the periodic and aperiodic solutions initial conditions far from the

final solutions will produce trajectories which will, after the transients disappear, be attracted to a bounded region in phase space. This region is known as an attractor. For the case of the chaotic flow, where the trajectories never cross, the resulting 'bundle' of non-crossing trajectories form an object known as a strange attractor.

#### 2.4.4 Strange Attractors

Two main phenomena are present in strange attractors, (also known as chaotic attractors), these are Stretching and Folding, as outlined by Roux et al [1983]. The attractor stretches due to the exponential divergence of the trajectories as they evolve, however, as the attractor lies in a bounded region of phase space, it also must exhibit folding. This mechanism of stretching and folding mixes up trajectories in phase space, making long term future predictions of the system impossible unless the condition of the system is known *exactly* at any one point. (Which is not realistic for real systems.)

If two trajectories are started from states that are arbitrarily close they will diverge over a period of time, this divergence is exponential. This initial difference may be thought of as measuring error, i.e. an uncertainty. Thus, as the system evolves through time the error blows up exponentially and the state of the system is essentially unknown after a very short period of time. This sensitive dependence on initial conditions was first elucidated by Lorenz [1963], who used the concept to show that long term future predictions of non-linear dynamical systems, such as the weather, was essentially impossible.

In general, for more complex dynamical systems, the phase space representation may contain many attractors. Which one of these attractors, the final solution settles down to, depends very much on the initial conditions of the system. Each attractor is associated with a region which, if it contains the trajectory at one instant in time, will eventually lead to that trajectory settling on to that attractor. This region is known as the basin of attraction of the attractor.

In systems with more than one strange attractor, the presence of noise may cause the solution trajectory to hop between basins of attraction, this phenomena

together with its associated frequency spectra is discussed by Arrechi [1987]. The reader is also referred to Soliman and Thompson [1991] who make use of basins of attraction to define dynamic ship stability.

Another important feature of a strange attractor, associated with a dissipative dynamical system, is that it contracts volumes in phase space. This is because, even though the attractor exponentially diverges in one orthogonal direction, causing sensitive dependence on initial conditions, on the whole, the attractor contracts in phase space. Thus, any volume of initial conditions is eventually stretched into a thin sheet of ever decreasing volume on the attractor. Thus the volume of a strange attractor, in a phase space of suitable dimension to fully describe the dynamical properties of the system, tends to zero. (See also the section on Lyapunov exponents, section 2.5.6).

Another important property of attractors is their space filling properties. The solution trajectories which form the strange attractor do not intersect each other, when embedded in a suitable dimension of phase-space. However, the trajectories do not fill up space evenly, rather, they fill up space as a fractal. The word fractal is an abbreviation for 'fractional dimension'.

To explain what a fractal structure is, it is helpful to look at a simple example of a fractal, known as the Cantor set, (figure 2-38a). The Cantor set is formed by taking the middle third out of the unit line segment, as shown at the top of the figure. Then the middle third is taken out of the remaining two line segments. Then the middle third is taken from the remaining four line segments, and so on, *ad infinitum*, until we are left with only a set of points, known as the Cantor set or Cantor dust. This set of points fills the unit interval in a special way, and although the length of the Cantor set is zero, it can be shown that the dimension of the set is 0.6309..., (see section 2.5.4). The interesting fact is that many attractors, when sliced through, show a Cantor set like structure.

It may be difficult to grasp the idea of fractional dimensions when one is used to the usual use of the zero, one, two and three-dimensional way of interpreting the world, (i.e. a point, line, area and volume respectively, as depicted in figure 2-38b). One way to think of the fractal structure of the Cantor set is to recognise that the set cannot fit into a point, that is have zero dimension, as it is

specified over the unit interval. However, it can neither have a dimension of one, as it obviously has a length which tends to zero on the unit interval. It can be shown by applying mathematical descriptions of dimension, (see section 2.5.4), that the set does indeed have a fractional dimension of 0.6309..., i.e. it is a fractal. A graphical account of fractals is given by Peitgen and Richter [1986]. For a more comprehensive account of fractals and their role in natural phenomena the reader is referred to Mandelbrot [1977].

Ruelle [1980] describes strange attractors as 'relatively abstract mathematical objects', however, he goes on to say that computers may aid in their understanding, by giving them 'some life' by drawing pictures of them. The observation of strange attractors in real systems – hydrodynamic, chemical, electrical, biological etc., (see for example Swinney [1983]) – has provided the impetus for the development of non-linear dynamical systems theory. A few of the more important systems, both mathematical and real, are outlined in the next two sections.

#### 2.4.5 Examples of Mathematical Systems Exhibiting Chaotic Motion

As mentioned above, there are many examples of mathematical dynamical systems which exhibit chaotic motion. An overview of many of these are given by Holden and Muhamad [1986]. In addition, recent experimental work has also found that real systems (i.e. systems in nature), can exhibit such motion. In this section, and the next, a few of the very common systems that have appeared in the literature are outlined.

1 – The Logistic Map: This simple map, given by the difference equation

$$X_{n+1} = A.X_n.(1 - X_n) \quad (2.34)$$

where  $A$  is the control parameter. The map has been shown to produce varied behaviour for  $A$  in the range,  $1 < A < 4$ , see figure 2–39a. For values of the  $A$  less than 3, the system evolves to a stable state, or fixed point. After this limiting value, the system will oscillate between two values of  $X$ , when  $A$  is in the range

$3 < A < 3.449$ . As  $A$  increases beyond 3.449, the solution oscillates between four points, for the range  $3.449 < A < 3.544$ . This process, known as period doubling, continues as the control parameter,  $A$  is increased. The point at which the solution changes from one period to the next is known as a bifurcation point. If the first bifurcation occurs at  $A_1$ , the second at  $A_2$  and so on then as the control parameter is increased a universal number,  $\delta_\mu$ , is formed:

$$\delta_\mu = \lim_{k \rightarrow \infty} \frac{A_k - A_{k-1}}{A_{k+1} - A_k} = 4.669 \quad (2.35)$$

This number is universal for a large class of non-linear systems, [Feigenbaum, 1980], and is known as the Feigenbaum number. Figure 2-39b shows the bifurcation diagram of the logistic equation, where the resulting values of  $X$ , that the steady state oscillations occur on, is plotted against the control parameter  $A$ . However, the period doubling increases to an infinite period for a finite value of the control parameter, ( $A = 3.569944$ ). This finite value of  $A$  is known as the accumulation point, after which the system behaves chaotically.

There is not room in this text to cover the intricacies of such mappings, and for more information the reader is referred to Infeld and Rowlands [1982, Chapter 10] and Baker and Gollub [1990, Chapter 4].

2 - The Henon Map: Before moving on to non-linear systems described by differential equations, it will be useful to briefly look at the Henon mapping, (see Infeld and Rowlands [1990]), described as follows,

$$X_{n+1} = 1 - a \cdot X_n^2 + b \cdot Y_n \quad (2.36a)$$

$$Y_{n+1} = X_n \quad (2.36b)$$

The phase portrait obtained by plotting  $Y_n$  against  $X_n$ , is shown in figure 2-40a, where  $a = 1.4$  and  $b = 0.3$ , this is the Henon attractor. The initial values of  $X$  and  $Y$  were 0.631 and 0.189 respectively. The strangeness of the attractor is

revealed by enlarging a region of it, such as the small box in figure 2-40a. The enlargement is shown in figure 2-40b. Once enlarged we see detail that was not apparent at the previous level of magnification. Enlarging again, figure 2-40c, more detail may be observed. This process may be carried on *ad infinitum*. This self similar, fractal nature of the attractor's structure is a common feature of strange attractors.

3 - The Lorenz Equations: In 1967 Lorenz published his now famous paper entitled 'Deterministic, Nonperiodic Flow', in which he set out the basic underlying principles of chaotic motion. To do so he numerically integrated a stripped down version of the equations of motion for the atmosphere, now called the Lorenz equations. They are defined thus,

$$\dot{X} = -\sigma (X - Y) \quad (2.37a)$$

$$\dot{Y} = -XZ + rX - Y \quad (2.37b)$$

$$\dot{Z} = XY - bZ \quad (2.37c)$$

where  $\dot{X}$  is the first time derivative of the displacement  $X$ .

The equations may be integrated with a suitable numerical scheme, with the parameters  $\sigma = 10.00$ ,  $r = 28.00$  and  $b = 2.67$  giving chaotic motion. The chaotic time series and resulting attractor is shown in figure 2-41. Since Lorenz's article, much work has been done on these equations by many researchers. In addition, many other equations have been devised, (and studied in detail), which highlight the phenomena of chaotic motion. Some of which are discussed in the following.

4 - The Rossler Equations: The Rossler equations, (see for instance Holden and Muhamad [1986]), are again a highly truncated set of equations which in this case model the quintessential dynamics of a chaotic chemical reaction. They are as

follows,

$$\dot{X} = -Y - Z \quad (2.38a)$$

$$\dot{Y} = X + aY \quad (2.38b)$$

$$\dot{Z} = b + XZ - cZ \quad (2.45c)$$

Chaotic motion in this case can be obtained by setting the parameters  $a$ ,  $b$  and  $c$  to 0.20, 0.20 and 5.70 respectively. The strange attractor for these parameters is shown in figure 2-42.

### 5 - The Rossler Hyperchaos Equations

Rather more interesting behaviour can be found in the hyperchaos equation of Rossler [1979],

$$\dot{X} = -Y - Z \quad (2.39a)$$

$$\dot{Y} = X + 0.25 Y + W \quad (2.39b)$$

$$\dot{Z} = 3.00 + XZ \quad (2.39c)$$

$$\dot{W} = -0.52 + 0.05 W \quad (2.39d)$$

The  $Z$ -variable serves as a check on the growth of the system, and in effect  $Z$  is 'turned on' (i.e. has a non-zero value) only for certain values of  $X$ ,  $Y$  and  $W$ , as shown in figure 2-43. This gives the attractor variable properties, depending on whether the  $Z$ -variable is activated or not.

## 6 - The Truncated Navier-Stokes Equations

Franceschini and Tebaldi [1979], and Boldrighini and Franceschini [1979], presented a system of non-linear ordinary differential equations that are a stripped down version of the Navier-Stokes equations of a two-dimensional incompressible fluid. The authors claim that the model may exhibit many of the important features of the equations.

The equations are,

$$\dot{X}_1 = -2.X_1 + 4.X_2.X_3 + 4.X_4.X_5 \quad (2.40a)$$

$$\dot{X}_2 = -9.X_2 + 3.X_1.X_3 \quad (2.40b)$$

$$\dot{X}_3 = -5.X_3 - 7.X_1.X_2 + r \quad (2.40c)$$

$$\dot{X}_4 = -5.X_4 - X_1.X_5 \quad (2.40d)$$

$$\dot{X}_5 = -X_5 - 3.X_1.X_4 \quad (2.40e)$$

In the above equations,  $r$  represents the Reynolds number. As the value of  $r$  is increased the system passes from a fixed point attractor to a periodic attractor, then, via period doubling bifurcations, to a strange attractor. A strange attractor first appears at a value of  $r$  of approximately 28.7. The strange attractor for the system, (computed by the author for  $r = 31$ ), is plotted in figure 2-44.

In addition to the examples outline above, chaotic behaviour has been found in a very wide variety of systems, from models of Physiological control systems [Mackey and Glass, 1977] to models of articulated offshore loading platforms, [Choi and Lou, 1991]. (The chaotic output of the logistic equation has even been used to produce music!, [Pressing, 1988].) Thus, we see that a knowledge of this behaviour is important for the investigator dealing with non-linear dynamical problems, and their associated phenomena.

The Rossler, Rossler Hyperchaos and the Lorenz systems were used by the author to test the Grassberger–Procaccia dimension and Lyapunov algorithms, prior to them being used in the analysis of the experimental results. (See Section 2.5 and Appendix 2.)

#### 2.4.6 Real Systems with Strange Attractors

The literature is now full of examples of chaotic motion found in nature. These examples cover many areas of research involving dynamical systems, such as fluid dynamics, chemical kinetics, electrical circuits and biological processes. The phenomena is truly of a multi–disciplinary nature. A brief account of some of the main experimental realisations of chaotic motion will be given in the following. (Those found in fluid dynamics will be dealt with in more detail in section 2.6.)

##### 2.4.6.1 – Fluid Dynamics

Chaotic fluid flow has now been observed in many fluid systems. Of these, two of the most extensively studied are Rayleigh–Benard convection, and Taylor–Couette flow.

Rayleigh–Benard convection may be generated by heating from below, a thin layer of fluid between two horizontal plates. As the temperature gradient across the flow is increased, various phenomena occur, [Giglio<sup>etal</sup>, 1981]. The control parameter in this fluid situation is the Rayleigh number, Ra, which is defined thus:

$$Ra = \left[ \frac{g \cdot \alpha \cdot d^3}{k \cdot \nu} \right] \Delta T \quad (2.41)$$

where  $g$  is gravitational acceleration,  $\alpha$  is the coefficient of thermal expansion,  $d$  is the distance between the plates,  $k$  is the thermal diffusivity,  $\nu$  is the kinematic viscosity and  $\Delta T$  is the temperature difference between the two plates.

Up to the critical Rayleigh number,  $Ra_{crit}$ , no motion exists, and the heat is

transferred solely by conduction through the fluid. Just above  $Ra_{crit}$  convective rolls appear in the fluid, (figure 2-45a). The critical Rayleigh number has been well predicted by stability analysis. As the Rayleigh number increases above  $Ra_{crit}$ , successive bifurcations occur as the fluid progresses to the turbulent, or chaotic, state. (See Giglio et al [1982] and also Sano and Sawada [1985]). In fact, a wide variety of behaviour has been found to exist for flows above  $Ra_{crit}$ , some of which will be outlined in the next section.

The other well documented flow system which exhibits regular and chaotic flow is the Taylor–Couette system. This system involves the flow of fluid in two concentric, rotating cylinders which rotate at rates independent of each other, (figure 2-45b). As the Reynolds number is increased the velocity field proceeds from a regular to a weakly chaotic state, whereby a strange attractor may be observed in phase space, [Mullin and Price, 1989].

The interesting thing about both the Rayleigh–Benard and Taylor–Couette systems is that they have, in principle, an infinite number of degrees of freedom. However, it seems likely that, at the onset of chaos, only a few degrees of freedom are excited, [Swinney, 1983].

Both the systems discussed above are closed fluid systems, however, work has recently been done on open fluid systems, such as transitional flow in pipes, (see for example Sreenivasan and Ramshankar [1986] and, Huang and Huang [1989]) and the breakdown of vortex flows produced at an airfoil [Williams–Stuber and Gharib, 1990]. These flows are more difficult to control precisely, as they tend to have higher levels of background noise associated with them. This noise may tend to mask, or alter, the dynamics under investigation, [Swinney and Gollub, 1981]. More will be said on these systems in section 2.6.

#### 2.4.6.2 Other Areas

One system to feature prominently in the literature on experimental non-linear dynamics is the Belousov–Zhabotinski chemical reaction, [Hudson et al, 1981], whereby chemical reactants are continuously stirred in a chemical reactor. This reaction has been found to exhibit both periodic and chaotic behaviour, [Swinney et

al 1983], depending on the conditions present in the reacting vessel. The general method of looking at the system is to measure the concentration of one of the chemicals in the system, (usually the Bromide ion), and plot these against time. A strange attractor has been found for such flows by Roux et al [1981]. (See also Ruelle [1981].) The Belousof–Zhabotinskii strange attractor is shown in figure 2–46.

The most prominent example of a biological chaotic flow is that of the behaviour of electrically stimulated chick heart cells. Guevara et al [1981], forced specially prepared aggregates of chick heart cells with pulses of electrical current. Regular and irregular dynamics were exhibited by the system and a bifurcation chart, similar in many ways to that of the logistic equation, was produced. This work is especially important, as many researchers believe that certain types of heart fibrillation may be a chaotic response of the dynamics of the heart itself, [Glass et al, 1986]. Conrad [1986] gives an overview of the role of chaotic dynamics in many biological settings.

Chaotic responses have also been found in many electrical circuits, [Tomita, 1986], from simple circuits containing only a resistor, inductor and diode, [Smith, 1992], to systems which involve the parallel pumping of ferromagnets, [Waldner et al, 1985].

In this section only a few brief examples have been given of the experimental verification of chaotic flows, and other phenomena associated with non-linear dynamical systems. Many more areas have not been touched upon, such as the chaotic output of lasers, or the role of chaos in statistical and quantum mechanics, [Baker and Gollub, 1990, pp133–144]. However, it is hoped that this section has served to make the reader aware of the universal nature of this type of behaviour.

#### 2.4.7 Mathematical Routes to Turbulence

The work done on non-linear dynamical systems has shown that relatively simple systems may, as the control parameter is increased, evolve from a steady state via some route, to a chaotic (or turbulent) state. Much theoretical interest has been centred on the routes taken by such systems, and whether these routes may

be realised in the experimental situation.

There are currently four mathematical descriptions of the route taken from laminar flow through transition to fully developed turbulence, [Miles, 1983]. All of them begin with a Hopf bifurcation. A Hopf bifurcation occurs when a steady state bifurcates into a periodic solution, which generates a limit cycle in phase space, as shown in figure 2-47.

The four main theoretical routes to turbulence are as follows:

1 - Landau Model: Landau [1944] was the first to suggest a mathematical route to turbulence, whereby, as the control parameter, the Reynolds number,  $Re$ , is increased above a critical value,  $Re_{crit}$ . In this scenario, incommensurate frequencies would appear via a succession of Hopf bifurcations, as the control parameter was increased above the critical value. This would result in a quasi-periodic motion of increasing complexity. The final fully developed turbulence according to Landau is a quasi-periodic motion of great complexity.

2 - Feigenbaum Period Doubling Scenario: This consisted of a Hopf bifurcation of the initial stable state and then successive period doublings of the initial disturbance until an accumulation point is reached at a finite value of the control parameter. This scenario has already been outlined for the case of the logistic map in section 2.4.5.

3 - Reulle-Takens Route to Turbulence: Reulle and Takens have conjectured that a strange attractor will appear at the third bifurcation of the Landau sequence.

4 - Intermittent Scenario of Manneville and Pomeau: In this case the solution of the system alternates between a singly periodic limit cycle and a strange attractor.

The Landau model is now not regarded as a realistic route to turbulence as it has not been observed in any experiment to date. For a more complete description of the routes to turbulence see Miles [1983].

The initial stages of the period doubling route to turbulence, (route 2), has been observed in Taylor-Couette and Rayleigh-Benard flow, as well as the

Belousov–Zhabotinskii reaction and other systems. Routes 2, 3 and 4 have all been observed by Gollub and Benson [1980] in the Rayleigh–Benard system. Furthermore, they also found another route to turbulent flow, involving quasi–periodic locking at incommensurate frequencies. They concluded that the route taken by the system depends on the aspect ratio of the apparatus that they used.

Arneodo et al [1983] have observed another route followed by the Rayleigh–Benard system, which is a variation of the period doubling route. This alternative route, and others, have been observed in numerical simulations of such flows by Kida et al [1989]. These simulations have the advantage of being much more flexible, for instance the viscosity parameter is easily varied and its effect monitored, whereas, in the experimental situation this may be more difficult to do. Kida et al found that as the viscosity was reduced more complex patterns appeared in the flow.

Other deviations from the theoretical routes to chaos, (as described above), have been found in the pumping of ferromagnets by Waldner et al [1985] and also by Kaolin et al [1981] in an annular, free–surface fluid system, known as the Faraday experiment. The results of Kaolin et al are particularly interesting because instead of obtaining the usual period doubling subharmonic sequence of 1,2,4,8,16,32..., they observed sequences of 1,2,4,12,14,16... and 1,2,3,4,6,12.... These anomalous results serve to remind us that perhaps a full theoretical picture has not been yet been formulated.

Kaolin et al also observed hysteresis in some of their results. That is, the routes followed by the system, as the control parameter was increased then reduced, were not identical. On reduction of the control parameter, jumps appeared in the sequence. The phenomena of hysteresis has also been found by Mercader et al [1990] modelling the route to chaos of a mathematical model of the Rayleigh–Benard system, providing another link between experiment and theory.

#### **2.4.8 Modelling Non-linear Dynamical Systems**

Before concluding this section, it is appropriate to mention two cases where real non-linear dynamical systems have been found to produce non-linear phenomena, including chaotic motion, and have been successfully modelled numerically to produce qualitatively similar effects.

##### **The Dripping Faucet**

Robert Shaw [1984] investigated the behaviour of the dripping tap (faucet) with varying flow rate. At low flow rates, the drips initially fell with a regular period. As the flow rate was increased, period doubling ensued, which led finally to a chaotic falling of the drops. The drips were detected by interrupting the light beam that intersected with a photodetector, which in turn relays the signal to a computer for data acquisition and analysis. Shaw decided to use a 'naive' model to simulate the experiment, whereby the dripping tap was simulated as a non-linear oscillator, (see Shaw [1984]). Without going into great detail, similar behaviour was obtained between both the real system and the naive model, as is shown in the phase space portraits of figure 2-48.

##### **Fluid Elastic Vibrations of a Flexible Pipe**

The fluid elastic vibration dynamics of a flexible cantilevered pipe conveying fluid were investigated, both theoretically and experimentally, by Paidoussis and Moon [1988], figure 2-49. Once the pipe lost stability, bifurcations were observed leading to a chaotic response in both the experimental and analytical models. As with the dripping faucet model, remarkable qualitative agreement was found between the experimental and theoretical results, despite the great simplicity of the theoretical model.

## 2.5 THE TESTING OF NON-LINEAR DYNAMICAL SYSTEMS

### 2.5.1 Characterisation of Attractors

Many properties can be found for chaotic flows using various techniques, the problem is to find one which can differentiate between purely random (or noisy) flows and those which are chaotic. Fourier transforms, the autocorrelation function and Poincare maps will give a general indication of the change from the periodic to nonperiodic state, [Schuster, 1984], but these methods are unable to distinguish between chaotic and random flows. (That is between the seemingly unpredictable properties of chaotic flow and the actual unpredictable properties of noisy flow.) Thus, other types of measure or characterisation are required.

The dimension, the spectrum of Lyapunov exponents and the Kolmogorov entropy are all measures giving an indication of how chaotic a flow is, and they can, in theory, distinguish between chaotic and random flows.

Before using a sophisticated technique to analyse a time series, one should first visually inspect the series to see if any apparent features are present. Visual inspection of a velocity time trace from a fluid flow can distinguish whether a flow is laminar or turbulent, (see sections 2.2.2 and 2.2.3). Other types of simple motion may be identified from the velocity-time trace, such as periodic motion, and also a qualitative feel may be obtained of the complexity of the flow.

### 2.5.2 The Fast Fourier Transform

The fast Fourier transform (F.F.T.) is a numerical algorithm by which the discrete Fourier transform of a signal may be calculated with exceptional speed, [Cooley et al, 1969]. The discrete Fourier transform, (D.F.T.),  $F(x_j)$ , of a variable  $x_j$ , ( $j=1,2,3,4,\dots,N$ ) is defined thus:

$$F(x_j) = \frac{1}{N} \sum_{j=0}^{N-1} x_j \cdot e^{(-1(2 \cdot \pi \cdot k \cdot j/N))} \quad (2.42)$$

here,  $i$  is the imaginary number  $(-1)^{\frac{1}{2}}$ .

The F.F.T. algorithm enables the number of calculations required to compute the Fourier transform of a set of  $N$  data points to be reduced by a factor of  $\log_2(N)/N$ , which is significant for large  $N$ , [Newland, 1975]. The algorithm requires that the number of points in the signal is a power of 2, e.g.  $2^{14}$  (=16384), which is the number of points typically sampled in the experimental investigation outlined in this thesis.

From the resulting F.F.T. plot of a time signal, periodic, multiply periodic, quasi-periodic and 'turbulent' signals may be differentiated, [Berge, Pomeau and Vidal, 1984, pp111–123]. However, from the F.F.T. itself 'turbulent' flow cannot be differentiated into either a random or chaotic phenomena, as both give broad band frequency spectra, see figure 2–50a and b.

Typical power spectra for flows *en route* to a chaotic signal, via period doubling, are outlined by Crutchfield et al [1980], whereby the period doubled peaks broaden as the chaotic signal is approached. Huberman and Zisook [1981] go on to describe this spectral broadening in detail. The peaks in the power spectrum broaden at their base as the chaotic state is approached, as depicted in figure 2–51. These broadened bases of the peaks are referred to as skirts by Farmer [1981]. The power spectrum of the chaotic state consists of instrumentally narrow peaks surrounded by a broad band noise background.

### 2.5.3 Experimental Attractor Construction

Before we can estimate the dimension, Lyapunov exponent or other properties to test for the presence of a chaotic flow, we must first construct an attractor. This can be done for a single experimental time series by the method of time delays, devised by Ruelle [Ruelle, 1989, pp28–32]. (See also Roux et al [1980], who used the method to construct the attractor for the Belousof–Zhabotinskii chemical reaction.) Such an experimental time series is depicted in figure 2–52a and consists of  $N$  sampled points, separated by a time interval,  $dt$ .

In the method, the ordinates of the attractor,  $X$ , are constructed for

n-dimensional space from the original time series,  $x_i$ , ( $i = 1, 2, 3, \dots, N$ ), as follows,

$$X = \{x_i, x_{i+\xi}, x_{i+2\xi}, \dots, x_{i+(n-1)\xi}\} \quad (2.43)$$

where  $X$  is the n-dimensional attractor vector produced from the discretely sampled time series,  $x_i$ , and  $\xi$  is the delay. The time delay between reconstruction variables is thus  $T = \xi \cdot dt$ . The resulting attractor is shown in figure 2-52b.

The choice of  $\xi$  is non-trivial as we want the dynamical properties of the reconstructed attractor to resemble those of the actual attractor of the system under observation. Three common methods for the choice of  $\xi$  will now be outlined.

**Method 1** - For low dimensional attractors occurring in a system with periodic forcing, it is recommended, [Guckenheimer, 1986], that the most favourable value of ' $\xi$ ' is one quarter of the forcing period. (This has been demonstrated by the author when constructing an attractor for a journal bearing model in a chaotic mode, see Appendix 5.) This is a quick and easy method for such systems, however, many fluid systems do not possess such a forcing function and so another method to calculate the time delay is required.

**Method 2** - The autocorrelation function,  $C_\xi$ , is a frequently used method for finding a suitable time delay for attractor construction. Redefining the autocorrelation function, (section 2.2.3.2) for any fluctuating component,  $x_i'$ , of a variable  $x_i$ , where,

$$x_i' = x_i - \bar{x}_i \quad (2.44)$$

the superscripted bar above the variable denotes the time averaged value. The correlation integral, for a discretely sampled time series, is then,

$$C_{\xi} = \frac{(\dot{x}_i) \cdot (\dot{x}_{i+\xi})}{[\dot{x}_i]^2} \quad (2.45)$$

It is recommended, [Huang and Huang, 1989], that the time delay for the attractor construction,  $\xi$ , should be taken as the value which first gives  $C_{\xi} = 0.5$ .

**Method 3** – The minimum mutual information criterion is another method by which to determine a suitable time delay ' $\gamma$ '. It is argued, [Fraser and Swinney, 1986 and Fraser, 1989], that, whereas the autocorrelation function measures a linear dependence of two variables, the minimum mutual information measures the general dependence of two variables.

The minimum mutual information of two variables  $x$  and  $y$  is defined as,

$$I(x, y) = \sum_{i, j = 1}^N P_{x, y}(i, j) \log \left[ \frac{P_{x, y}(i, j)}{P_x(i) P_y(j)} \right] \quad (2.46)$$

where  $P_x(i)$  is the probability of a variable  $x(i)$  occurring, and  $P_{x, y}(i, j)$  is the joint probability of occurrence of variables  $x(i)$  and  $y(j)$ . A suitable choice of time delay requires  $I$  to be a minimum, when this is the case the attractor is as 'spread out' as possible, see figure 2-53.

When considering time delays we let  $x = x_t$ , and  $y = x_{t+\xi}$ . An obvious result is that when  $I(x_i, x_{i+\xi})$  is a minimum, this implies that  $I(x_{i+\xi}, x_{i+2\xi})$  is a minimum also, and so on. The value of the delay,  $\xi$ , to use in the attractor construction is that which gives the first minimum in mutual information,  $I(x_i, x_{i+\xi})$ .

Roux et al [1983] have actually used delays,  $\xi$ , obtained by visually inspecting phase portrait plots of the reconstructed attractors at various values of  $\xi$ . The value of time delay they subsequently chose to use, was the one that produced an attractor which appeared to be most spread out. However, the minimum mutual

information in effect does this numerically. Therefore, it is this method which the author recommends for time series which do not possess an obvious periodic fluctuation, and it is this method that was used for all attractor construction in the experimental investigation reported within this thesis in subsequent chapters.

#### 2.5.4 The Dimension of an Attracting Set

Once a strange attractor has been obtained from an experimental time series the next step is to characterise it. Of all the properties used to characterise strange attractors in chaotic flows, the two most commonly used are the dimension and the Lyapunov exponents of the system. Both these methods will be outlined in the following sections. First we will deal with the dimension as a means by which to characterise a dynamical system.

The dimension of an attracting set has been described by Farmer et al [1983] as 'the most basic property of an attractor', however, many definitions of dimension exist. The dimension is basically a measure of the scaling properties (fractalness) of a structure. The simplest and most easily understood definition is the Capacity (or Kolmogorov) dimension ' $D_c$ ', which is defined as :

$$D_c = - \lim_{\epsilon \rightarrow 0} \frac{\log_2 N(\epsilon)}{\log_2 (\epsilon)} \quad (2.47)$$

where  $N(\epsilon)$  is the number of  $n$ -dimensional boxes of side ' $\epsilon$ ' required to cover the attractor.

Another frequently cited dimension is the information dimension ' $D_i$ '. This measure seeks to account for the differences in distribution density of the points covering the attractor as follows,

$$D_i = - \lim_{\epsilon \rightarrow 0} \frac{I(\epsilon)}{\log_2 (\epsilon)} \quad (2.48)$$

$$\text{where } I(\epsilon) = - \sum_{i=1}^{N(\epsilon)} P_i \log_2 P_i \quad (2.49)$$

$I(\epsilon)$  is known as Shannon's formula, [Shannon and Weaver, 1949]. A more informative guide to the concepts of Information Theory and its role in statistical mechanics can be found in the literature, see for example Renyi [1970].

It is easily seen that, for an attractor with an even distribution of points,  $D_c = D_i$ . However the calculation of either of these two interpretations of dimension require a prohibitive amount of computing time.

The most widely used description of dimension used for experimental investigation is based on the correlation dimension, as defined by Grassberger and Procaccia [1983a and 1983c], and is denoted by  $D_{gp}$ . The reason for its popularity is its relative computational speed when implemented as an algorithm for dimension estimation.

To define  $D_{gp}$  we firstly need to define the correlation integral,

$$C_r = \frac{1}{N^2} \sum_{\substack{i, j=1 \\ i \neq j}}^N \Theta ( r - |X_i - X_j| ) \quad (2.50)$$

where  $\Theta$  is the Heaviside function.  $r$  is the radius of an  $n$ -dimensional hyper-sphere, centred on each of the points defining the attractor trajectory, (figure 2-54a). The correlation integral scales with the radius ' $r$ ' as,

$$C_r \sim r^{D_{gp}} \quad (2.51)$$

hence,  $D_{gp}$  can be found from the slope of the ' $\log(C_r) - \log(r)$ ' plot, (figure 2-54b).

$D_{gp}$  forms a lower bound to the capacity dimension and asymptotically approaches the value of  $D_c$  as the attracting set becomes more uniformly distributed in phase-space. In general,

$$D_i < D_{gp} < D_c. \quad (2.52)$$

It is appropriate to mention here that there are many other definitions of dimension such as the Hausdorff, Lyapunov and generalised Renyi dimensions to name but a few, see for example Farmer [1982], Farmer et al [1983], Froehling et al [1981] and Grassberger[1983].

There is still much that needs to be done on the dimension as a characterisation of chaotic flows, [Mayer-Kress, 1987]. Farmer [1982a] states that many questions remain to be answered, such as – 'How quickly does the dimension of a chaotic attractor change as the control parameter, (e.g. the Reynolds number), of a system is varied?', 'How steady is this change?', and, 'Are the attractors of an infinite-dimensional dynamical system qualitatively similar to those of low dimensional systems?'. (A point which is extremely valid for the endorsement of the use of such methods in real fluid systems, which possess in theory an infinite number of degrees of freedom.) Subsequent investigations by Farmer of an approximated infinite dimensional system, [Mackey and Glass, 1977], led him to conclude that the transition to 'turbulent' behaviour begins with a chaotic attractor, followed by attractors of increasingly higher dimension appearing as the control parameter is increased.

According to Whitney's embedding theorem, (see Gershenfeld [1992]), it can be guaranteed that an  $n$ -dimensional attractor may be embedded in a  $(2n+1)$ -dimensional embedding space, (phase space). However, this is a maximum, and in general an  $n$ -dimensional space, (or next nearest integer value of phase space), should be sufficient. Gershenfeld has also shown that, under certain circumstances it is possible to reliably measure the correlation dimension of attractors with dimension greater than 10.

## 2.5.5 The Grassberger–Procaccia Dimension Estimate and its Implementation.

When using the Grassberger–Procaccia technique to estimate the dimension of an attractor, the investigator must be aware of scale, and other, effects and how they relate to the results obtained. There are four main regions of behaviour of an attractor [Smith, 1988], these are outlined in the next section, beginning with the smallest length scales.

### 2.5.5.1 Regions of Behaviour on the Attractor

1 – At very small length scales the Grassberger–Procaccia dimension algorithm tends to a dimension estimate of zero. This occurs when the algorithm is testing the attractor at scales too small to pick up other points on the attractor, i.e. when the radius of the  $n$ -dimensional hypersphere used in the Grassberger–Procaccia algorithm is less than the inter-point distances on the attractor trajectories. See figure 2–55a.

2 – The next region depends very much on whether one is considering an experimental, and hence noisy, attractor, or if the attractor is a mathematical construction, (noise free), such as the Lorenz attractor or Rossler attractor.

If the attractor is noisy, then for length scales of the order of the characteristic noise level, (see figure 2–55b),  $D_{gp}$  will scale with the noise, (assuming white noise, see Section 2.5.5.2). That is, it will increase with, and should be approximately equal to, the value of the embedding dimension, [Ben–Mizrachi et al, 1984].

However, if the attractor is noise free and the length scales being probed are of the order of the distance between consecutive points on the trajectory, then for limited data sets the algorithm will only detect points immediately nearby on the trajectory. This region of the attractor will show up as essentially 'linear', and the value of  $D_{gp}$  will tend to one, see figure 2–55c.

3 – Once the hyper-sphere radius overcomes the effects of small length scales

of regions 1 and 2, values of  $D_{gp}$  will approach those of the actual fractal dimension  $D_c$ , assuming that a suitable time delay has been chosen. (Figure 2-55d).

4 - Once the length scales of the sphere are of the order of the attractor radius, edge effects become dominant, where large parts of the hyper-sphere are outside of the attractor and hence empty, thus reducing the value of  $D_{gp}$ . (figure 2.55e). As the radius becomes very large, the attractor tends to a point within the sphere and  $D_{gp}$  tends, once again, to zero. Edge effects are discussed by Smith [1988] and a modification to the Grassberger-Proccaccia dimension algorithm is proposed by Dvorak and Klaschka [1990] based on Smith's results. Whereby, they plot  $\log(C_r)$  against  $\log(r(2-r))$  instead of the usual ' $\log(C_r) - \log(r)$ ' plot, and suggest that the slope of this line gives the correct estimate of the dimension. However, as far as the author can see, this method is only applicable in the ideal case of an evenly distributed attractor in an  $n$ -dimensional hypersphere of unit radius.

#### 2.5.5.2 Attractors and Noise

Noise, as already mentioned, can have a detrimental effect on the value of the apparent dimension of the attracting set, and in some cases may be severe enough to render the estimation of dimension impossible. A novel method of reducing noise in the reconstructed attractor has been proposed in a paper by Kostelich and Yorke [1990], where they approximate the average dynamics of various regions of the attractor. They do this by a method known as Eckman-Ruelle linearization. These average approximations to the dynamics are then used to reduce the noise in individual trajectories as they pass through each region of the attractor.

A signal composed of purely white, (or Gaussian), noise will scale with the value of the embedding dimension due to its phase-space filling behaviour. However, stochastic systems with power-law frequency spectra have been shown, [Higuchi, 1990, and, Osborne and Provenzale, 1989], to give finite correlation dimensions. In this case, a finite value of  $D_{gp}$  will not necessarily indicate that the dynamics of the system can be described by a few degrees of freedom. In such cases, care must, therefore, be taken in the interpretation of dimension calculations

in such cases. It is therefore recommended that the dimension estimate is interpreted in conjunction with other analysis techniques, such as the frequency spectrum, autocorrelation function and the Lyapunov exponent spectrum.

### 2.5.5.3 Other Factors Affecting the Estimation of Attractor Dimension

The lacunarity of the set has a bearing on the estimation of the dimension. If the set has a high degree of lacunarity then the value of  $D_{gp}$  will fluctuate markedly as various parts of the attractor are visited.

Sparse or limited data sets tend to produce errors in the calculations, which increase as the embedding dimension is increased. According to Smith [1988] the number of points required to estimate the correlation exponent of a nonlacunar set to within 5% of its true value increases at least as fast as

$$N_{min} > 42^M \quad (2.53)$$

where 'M' is the greatest integer less than the actual dimension of the set.

However, results have been presented by Abraham et al [1986] which indicate that acceptable results can be derived with data sets much smaller than those required by the above condition. For example, they obtained dimension results for an attractor with a dimension just over 2 from a time series containing 3000 points. They claim that adequate dimension results may be obtained for time series segments containing only 500 points. These results suggest that chaotic attractors may be characterised by their dimension, using small data sets, which do not then strain the data acquisition apparatus, nor the computer resources for analysis.

### 2.5.6 The Lyapunov Exponent

We have seen in the previous section how the fractal dimension may be used

to categorise chaotic attractors. Another measure commonly used to quantify such motion is the Lyapunov exponent, [Wolf, 1986]. In section 2.6.3, it was shown that one of the properties of a chaotic signal is the rapid divergence of close points on the attractor. It is this stretching process, together with the folding at large scales on the attractor, which causes the rapid decorrelation of the signal and apparently random time series.

### 2.5.6.1 The Lyapunov Exponent as a Dynamical Measure

The Lyapunov exponent, denoted  $L$ , is a measure of the divergence of extremely close points on the attractor. Referring to figure 2-56,  $\epsilon_0$  is the separation of two close points on the attractor at time zero. After a time,  $t$ , the separation of the points has evolved to  $\epsilon_t$ . Assuming this divergence to be exponential in time, we may write

$$\epsilon_t = \epsilon_0 \cdot e^{Lt} \quad (2.54)$$

where  $L$  is the Lyapunov exponent. Thus,

$$L = \frac{1}{t} \cdot \ln \left[ \frac{\epsilon_t}{\epsilon_0} \right] \quad (2.55)$$

However, it is usual to redefine  $L$  as

$$L = \frac{1}{t} \cdot \log_2 \left[ \frac{\epsilon_t}{\epsilon_0} \right] \quad (2.56)$$

which is a measure of the information loss of the system in bits per second.

Chaotic flows have Lyapunov exponents which are finite, positive real numbers. On the other hand, a random flow, where no correlation exists between one point on the trajectory and the next, has an infinite Lyapunov exponent. Stable flows have negative Lyapunov exponents. Thus, the Lyapunov exponent is a measure of

whether a flow is chaotic or not. If we calculate the Lyapunov exponent for orthogonal directions of maximum divergence in phase space, we obtain a set of Lyapunov exponents,  $(L_1, L_2, L_3, \dots, L_n)$ , where  $n$  is the embedding dimension of phase space. This set of Lyapunov exponents is known as the Lyapunov spectrum, [Sano and Sawada, 1985].

The Lyapunov spectrum is normally ordered from the largest positive exponent down to the largest negative one. One of the exponents in the spectrum is normally zero and corresponds to the direction in phase space aligned with the trajectory, which neither expands nor contracts. Often it is enough to denote the Lyapunov spectrum symbolically in terms of negative or positive exponents. Thus  $(+, +, 0, -)$  would denote a system with two positive, one zero and one negative exponent. Lyapunov spectrums with as many as twenty positive exponents have been found by Farmer [1982] for a high dimensional system of equations. In practice, however, it is sufficient to check whether  $L_1$  is positive, if it is, then this signifies that the flow is chaotic.

The behaviour of the Lyapunov spectrum as a system becomes chaotic via a period doubling route is outlined by Huberman and Rudnick [1980]. Lyapunov exponents and dimension estimates are given for a model of Rayleigh–Benard convection by Velarde and Antoranz [1981]. In their article they show the dramatic change from negative to positive of the principle Lyapunov exponent as the system evolves from a steady state to a chaotic attractor.

#### 2.5.6.2 The Kaplan–Yorke Conjecture

It is conjectured, [Kaplan and Yorke, 1979], that the spectrum of Lyapunov exponents may be used to find an estimate of the fractal dimension of an attractor, denoted  $D_{KY}$ . This is done as follows,

$$D_{KY} = j + \frac{\sum_{i=1}^j L_i}{L_{j+1}} \quad (2.57a)$$

where

$$\sum_{i=1}^j L_i > 0 \quad \text{and} \quad \sum_{i=1}^{j+1} L_i < 0 \quad (2.57b)$$

This conjecture has been shown to produce quite accurate estimates of dimension for many mathematical dynamical systems by Wolf et al [1985], and also by Russel et al [1980]. It therefore remains a tool for the analysis of chaotic phenomena. The author notes that it has not yet been used in the analysis of the experimental results, probably due to the difficulty of accurately calculating all the Lyapunov exponents from an experimental time series.

### 2.5.7 Alternative Methods of Analysis

The experimental study presented in this thesis has concentrated on six main areas to characterise the fluid flows under investigation. These are the frequency spectra, autocorrelation function, minimum mutual information criterion, dimension estimate and the Lyapunov exponent of the time series. In addition, return maps and probability histograms have been used to elucidate time series and attractor behaviour. However, other methods do exist for the analysis of time series, some of which will be outlined in this section.

The Kolmogorov entropy,  $K$ , is another measure of chaotic signals. It may be seen that,

$$K < \sum_{i=1}^j L_i \quad (2.58)$$

where  $j$  is the index of the smallest positive Lyapunov exponent. In general, the equality holds, in which case the Kolmogorov entropy is equal to the sum of the positive Lyapunov exponents. Grassberger and Procaccia [1983] provide a method by which an estimate of the Kolmogorov entropy may be obtained as a by-product of the correlation plot required for their dimension algorithm. (That is the

' $\log(C_r) - \log(r)$ ' plot used to obtain the Grassberger–Procaccia dimension estimate, section 2.5.4). This estimate is known as  $K_2$  entropy. Due to the difficulties of implementation, this measure was not used in the experimental study presented herein.

Recently, there has been much in the literature about a new method of probing fractal structures, known as the wavelet transform, [Arneodo et al, 1988]. The method, which has been described as a mathematical microscope by Argoul et al [1989], works by applying a variable transformation to the fractal object under investigation. The method has been applied to elucidate many fractal objects. These include, the fractal nature of turbulent flow time series, [Argoul et al, 1989], the spatial structure of turbulent jets, [Everson et al, 1990] and many other types of turbulence and Brownian motion [Everson and Sirovich [1989], even speech and sound signals, [Grossmann et al, 1987, and, Kronland–Martinet, 1988]. The reader requiring more information on the subject of wavelet transforms is referred to the above references.

The author briefly looked at the wavelet transform method with a view to employing it as a tool in the experimental investigation. However, after some preliminary tests, it was decided that the method, which is still very much in its infancy, would not reveal much in the way of useful additional information. Thus, the method was not employed herein.

Many other methods have been introduced to analyse the features of complex non-linear flows, such as the conditional probability distribution function of Packard [1980], or using bispectral analysis [Elgar et al, 1989]. However, all the methods presented in this section are outside the scope of the work presented here.

## 2.6 NON-LINEAR DYNAMICS AND FLUIDS

### 2.6.1 Introduction

Fluid flows are non-linear dynamical systems governed by the Navier–Stokes equations. Recent interest has centred on the application of techniques from the

field of non-linear dynamics to the problem of fluid turbulence. This interest has ranged from closed flow systems (i.e. Rayleigh-Benard and Taylor-Couette) to open flows such as vortex shedding systems, pipe transition, ocean surface waves and so on.

### 2.6.2 The Fractal Nature of Fluids

Brandstater et al [1983] have investigated the Taylor-Couette system using Lyapunov exponent and dimension estimates to characterise the flow. They found that both increased with increasing Reynolds numbers above that required to give chaotic flow,  $Re_{chao}$ . This showed that, although the fluid could contain a relatively large number of degrees of freedom, only a few relevant degrees of freedom were excited, certainly less than five in their case, this for a Reynolds number 30% above  $Re_{chao}$ . Figure 2-57 shows their findings for dimension versus the Reynolds number normalised to the critical value at the onset of time dependency,  $Re_{crit}$ . (Note, not  $Re_{chao}$ .)

Dimension estimates have been used by Guckenheimer and Buzyna [1983] to elucidate the turbulent transition process of a rotated, differentially heated annulus of fluid. This being a laboratory model for the large scale, mid-latitude circulation of the earth's atmosphere. They found that the dimension increased from approximately 1.6 to 11 as the rotation rate increased and the fluid became fully turbulent.

Elgar and Mayer-Kress [1989] have estimated the dimension of ocean surface waves. They concluded from their investigation that even though the geometrical shape of these waves may be expressed as a fractal object with a dimension between 2 and 3, the attractor generating the time series behaviour of the waves is greater than 20. That is to say, the waves are not generated by a low dimensional attractor.

Aref et al [1989] have analysed the fractal structure of turbulent jets. They have found that the dimension of the jet boundary increases as the jet evolves, and the laminar-turbulent interface breaks down. Figure 2-58a shows cross sections of the jet at various evolution times, and figure 2-58b plots the fractal

dimension of the boundary versus the evolution time.

The fractal structure strange attractors, generated using time series obtained from real fluid systems, has been very much under investigation in recent years. However, many natural objects may be described as fractals. The branching of trees [Grey and Kjems] to the surfaces of clouds [Voss, 1989] may be described in such terms. Recently Sreenivasan [1991] has pointed out that time traces of highly turbulent flows have self-similar scaling properties. In fact, such traces belong to a special subset of fractal objects known as self affine fractals. Self affine fractals are self-similar under a scaling which varies for each of the variables used to construct the object, [Voss, 1989]. Sreenivasan describes a loose definition of a fractal object as one 'whose parts relate to the whole in *some way*'. He goes on to describe turbulence itself as a fractal object, i.e. it has self similar properties.

Goldburg et al [1989] have found experimental evidence to suggest that the energy containing eddies in a turbulent flow occupy a fractal region, whose dimension increases with the Reynolds number as it exceeds a threshold value. A simple model by Bak and Chen [1989] has been used to show how a uniform input of spatial energy may be dissipated on a fractal structure. This highly simplistic model, known as the forest fire model, gives an important insight into how it could be possible for energy to be dissipated on a fractal object in fully turbulent flows, [Bak and Chen, 1990].

Thus, we see that the concept of fractals is having an ever increasing role in the understanding of fluid dynamic phenomena, especially that of turbulence.

### 2.6.3 Chaotic Behaviour of Vortex Systems

Recent interest in vortex flows has centred on interpreting them as non-linear systems. Theoretical and experimental work has been done within this context.

Numerical studies on the interaction of three inviscid point vortices above a flat wall by Conlisk et al [1989] has shown that both regular, (periodic), and chaotic motion of the vortices may occur. The type of motion depending upon the initial conditions of the system. The chaotic motion in this case was detected when the

largest Lyapunov Exponent became 'markedly' positive. Novikov [1991] shows that it is sufficient for certain geometries of flow body configurations to have only one vortex to obtain chaotic motion.

Experimental work by Tabeling et al [1990] has demonstrated that a closed-system, linear array of co-rotating vortices behaves as a chain of non-linearly coupled oscillators. These vortices were generated in an electrolytic solution by electromagnetic forces. At large values of the driving current, chaotic motion was observed. The physical origin of the oscillations caused by the co-rotating vortices is attributed to the shear instabilities which develop in the region of high shearing of the fluid between each vortex.

In closed system flows, each particle of fluid remains in the system indefinitely and retains a history of its location in the system over all cycles of motion, examples of such include Taylor-Couette flow between rotating cylinders, Rayleigh-Benard convection in heated fluids and cavity driven flows. Open system flows, on the other hand, have a constant replenishment of fluid to the system and are more likely to be met in reality, such flows include pipe flows, channel flows and wake flows. In general, closed system flows contain significantly less background noise than open systems.

Williams-Stuber and Gharib [1990] reported on a forced open-system flow, that of a forced wake of an airfoil, as shown in figure 2.59a, (see also Gharib and Williams-Stuber [1989]). They perturbed the wake of an airfoil at various forcing frequencies and found behaviour characteristic of non-linear systems, such as quasi-periodic beating, frequency locking and chaotic motion. In their analysis they used power spectra, Poincare sections and Lyapunov exponents. They found chaotic responses caused by the interaction of three incommensurate frequencies in the wake system. The phase space reconstruction for the natural wake, locked wake and the chaotic wake are given in figure 2-59b. It is evident that the locked case appears much less noisy than the natural wake, this is due to random noise being suppressed by the forcing frequency.

Williams-Stuber and Gharib calculated the Lyapunov exponents across the flow. They found high values of Lyapunov exponent for the chaotic case. The locked and quasi-periodic cases displayed much lower values of Lyapunov exponent, as

shown in figure 2-60, (about one third of the chaotic case values). The authors note that the locked and quasi-periodic exponents are much larger than the near zero values expected. They suggest that the velocity dependent Lyapunovs of Diessler and Kaneko [1987] may be better. However, this system requires the Lyapunov exponents to be measured in a moving frame of reference, which is not practicable in real experimental situations.

Ordered and chaotic shedding of vortices from a cylinder have been observed by Elgar et al [1989]. Ordered vortex shedding was characterised by a power spectrum dominated by a narrow primary peak together with subharmonics, (figure 2-61a). On the other hand, chaotic vortex shedding was associated with relatively broad peaks near the shedding frequency and at very low frequencies, (figure 2-61b). Rockwell et al [1991] have observed period doubling of the spatial structure of vortices shed from a three dimensional cylinder. In this case, the vortex shed repeated its form every cycle, every second cycle and then every fourth cycle as the control parameter was turned up.

#### 2.6.4 Pipe Flows at Transition

Huang and Huang [1989] have investigated the laminar-turbulent transitional flow in pipes using techniques to estimate the dimension and  $K_2$  entropy and also plot the resulting frequency spectra. They found that for flows above  $Re_{crit}$  the dimension increases with the Reynolds number, (figure 2-62a). Compare this with the intermittency factor plot of figure 2-62b. Note that for low values of  $(Re - Re_{crit})/Re_{crit}$  the dimension is one. This reflects the periodic behaviour of the turbulent puffs which occur at flows just above  $Re_{crit}$ .

Huang and Huang also found evidence, (using frequency spectra plots), of a period doubling route to full turbulence, taken by the puffs, as the Reynolds number was increased above  $Re_{crit}$ . They also calculated the  $K_2$  entropy of the flow, for a dimension of 3.8. Figure 2-62c shows the calculated value of  $K_2$  as the embedding dimension,  $n$ , is increased. From the figure, it can be seen that the  $K_2$  entropy is levelling off to a finite positive value, which indicates that the attractor has divergence properties, and the flow is indeed chaotic.

The intermittent transition to turbulence in pipe flow has also been investigated, in the context of the intermittent route to chaotic flow of a dynamical system, by Sreenivasan and Ramshankar [1986]. They found a Grassberger–Procaccia dimension as high as 18 for the flow in the turbulent patches of the intermittent regime. This dimension calculation was performed with only 3000 points, far fewer than perhaps necessary. However, the authors state that this value was quite stable and at least underlines the fact that the dimension is not small.

Sreenivasan and Ramshankar go on to note that, as pipe flow is believed to be stable for all Reynolds numbers, noise is required to initiate transition. It is not clear to what extent the transition phenomena reflects the statistical properties of the noise.

The transition region of fluid flow in a pipe flow is obvious by the discrete patches of distinctly laminar and distinctly turbulent flow, separated by quite clearly defined interfaces. It has been proposed by Pomeau [1986] that these transition interfaces between laminar and turbulent flows may be modelled as sets of coupled oscillators, jumping from regular to intermittent behaviour, as they are excited by their neighbours.

## 2.7 SUMMARY

In this chapter the basic concepts of fluid flow in a pipe have been set out. Laminar flows, turbulent flows and transition flows have been outlined from a traditional fluid dynamic viewpoint. This has included the role of stability theories to predict transition, the use of experimentally derived empirical formulae used to obtain the energy losses in pipes, (and at orifice plates), and also a brief description of turbulence phenomena. In addition, the phenomena of vortex flows and orifice flows have been dealt with.

In the latter sections of this chapter, the emergent analytical techniques from the field of non-linear dynamics have been examined in detail. The role of such techniques in fluid dynamics, as a possible way forward in the elucidation of transitional and turbulent flows, has been outlined. Recent mathematical and

experimental results in this area suggest that simple dynamical systems may produce complex, irregular behaviour and conversely that complex flows may, at heart, be controlled by rather simple dynamics. Methods to characterise such systems have been described, and these methods will subsequently be used in the investigation reported in this thesis.

It is hoped that the literature review presented above has served two purposes. Firstly, to give a brief, but wide ranging description of the subject area being dealt with in the thesis. Secondly, to explain some of the analysis techniques used subsequently to investigate the properties of the breakdown of a forced vortex flow at an orifice at a pipe, the subject of this thesis.

**CHAPTER 2**  
**FIGURES**

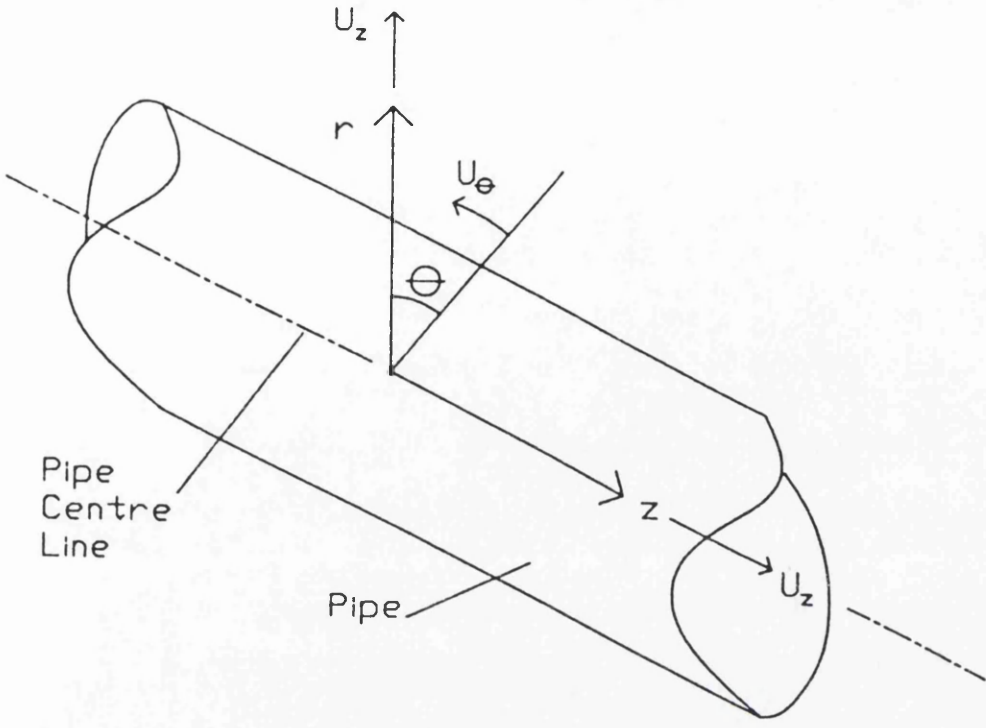


Figure 2-1: Typical Pipe Section Detail Showing the Cylindrical Coordinate System

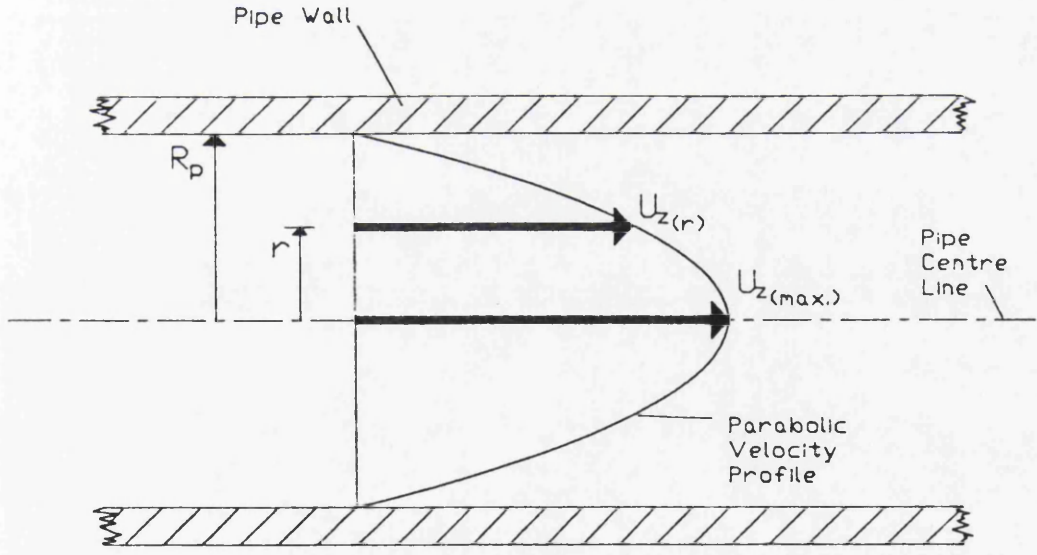
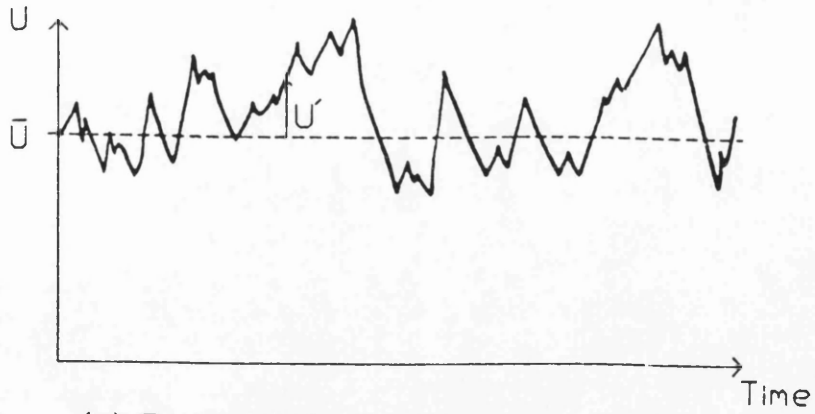
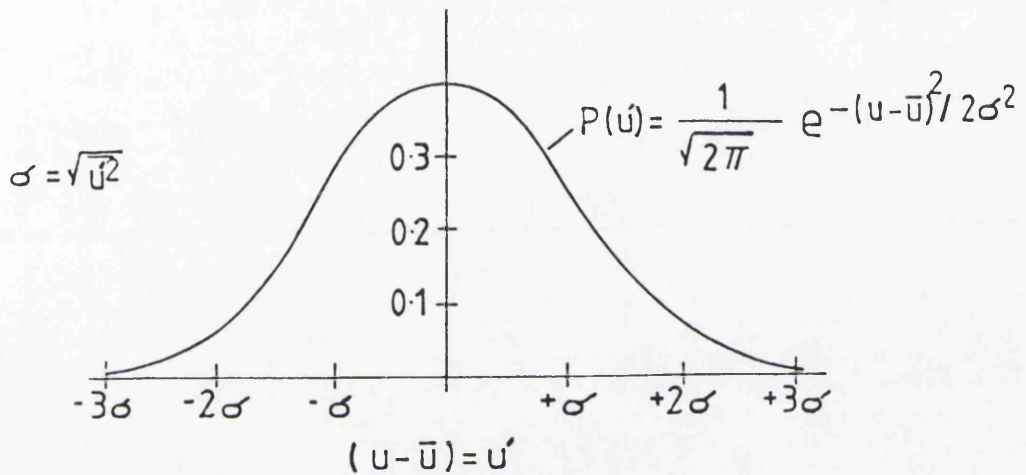


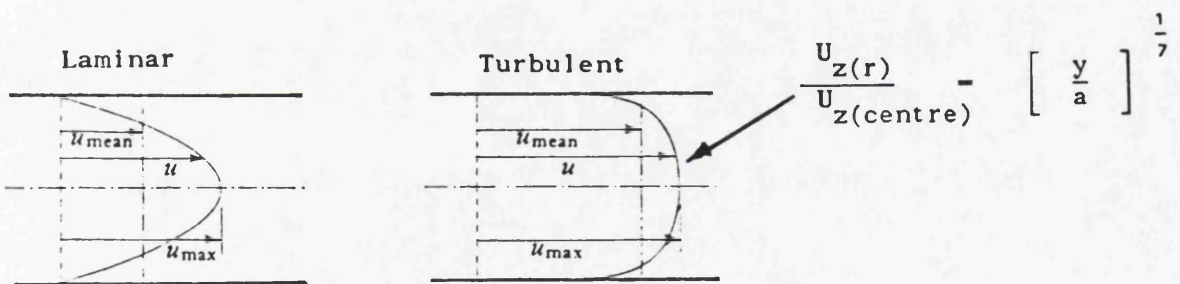
Figure 2-2: Parabolic Velocity Profile of Laminar Newtonian Pipe Flow



(a) Typical Velocity-Time Trace



(b) Typical Gaussian Probability Distribution Function



(c) A Comparison of Laminar and Turbulent Velocity Profiles

Figure 2-3: Elements of Turbulent Flow

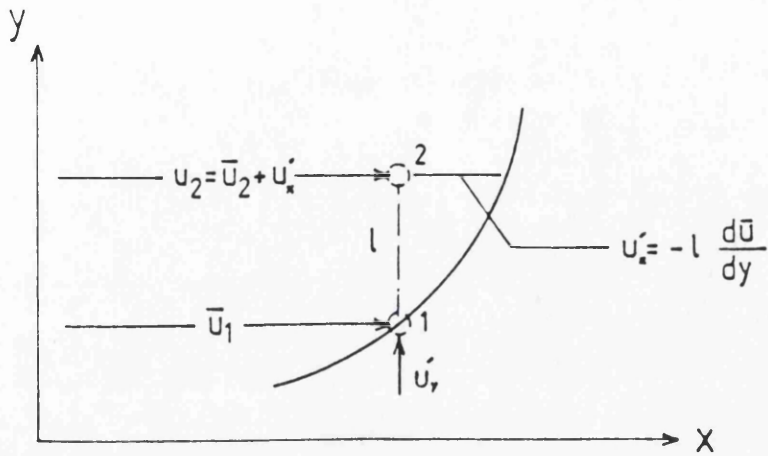


**Figure 2-4: Turbulent Mixing Length and Velocity Fluctuations**

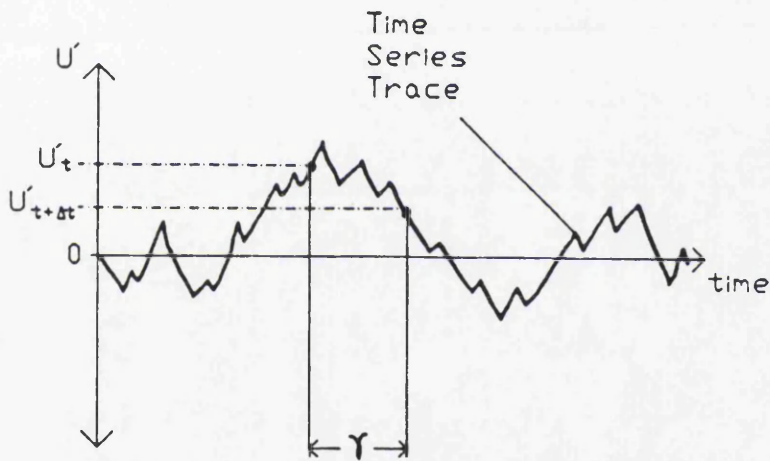


**Figure 2-5: The Autocorrelation Function**

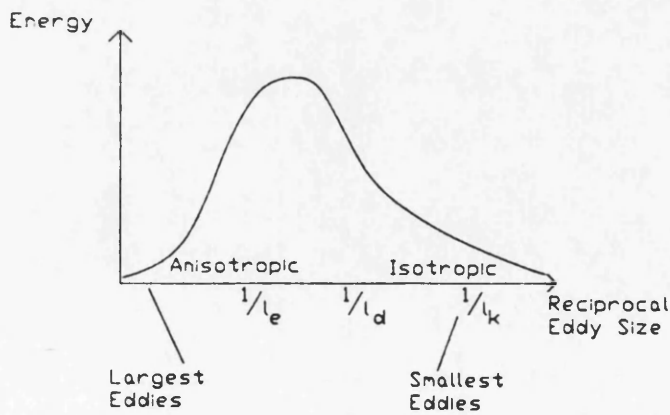
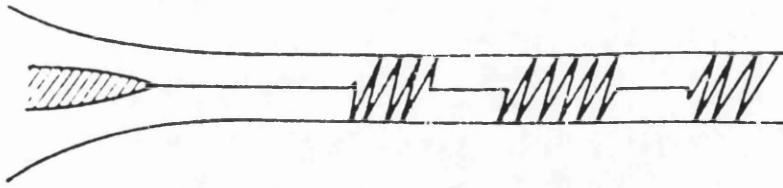
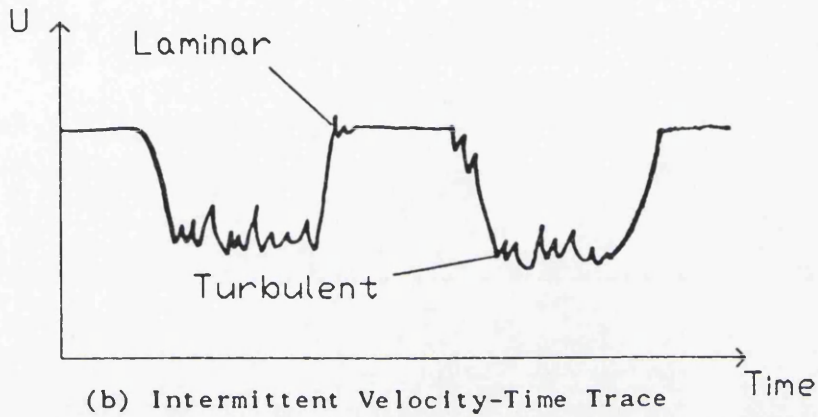


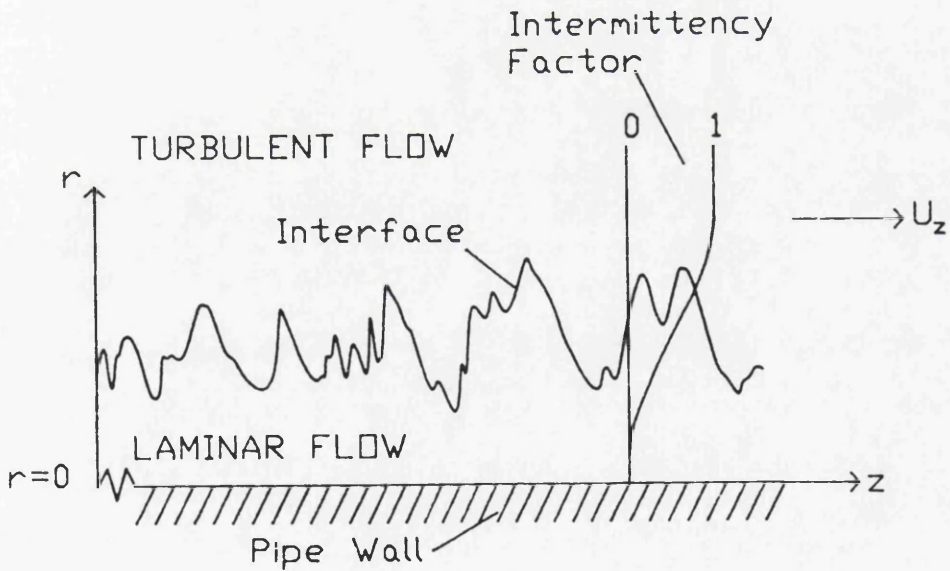
**Figure 2-6: Spectrum of Eddy Lengths Associated with Turbulent Flow**



(a) Schematic Diagram of Intermittency occurring in Pipe Flow  
(After Reynolds 1883)



(b) Intermittent Velocity-Time Trace



(c) Intermittency at the Laminar Turbulent Interface Close to the Wall

Figure 2-7: Intermittency

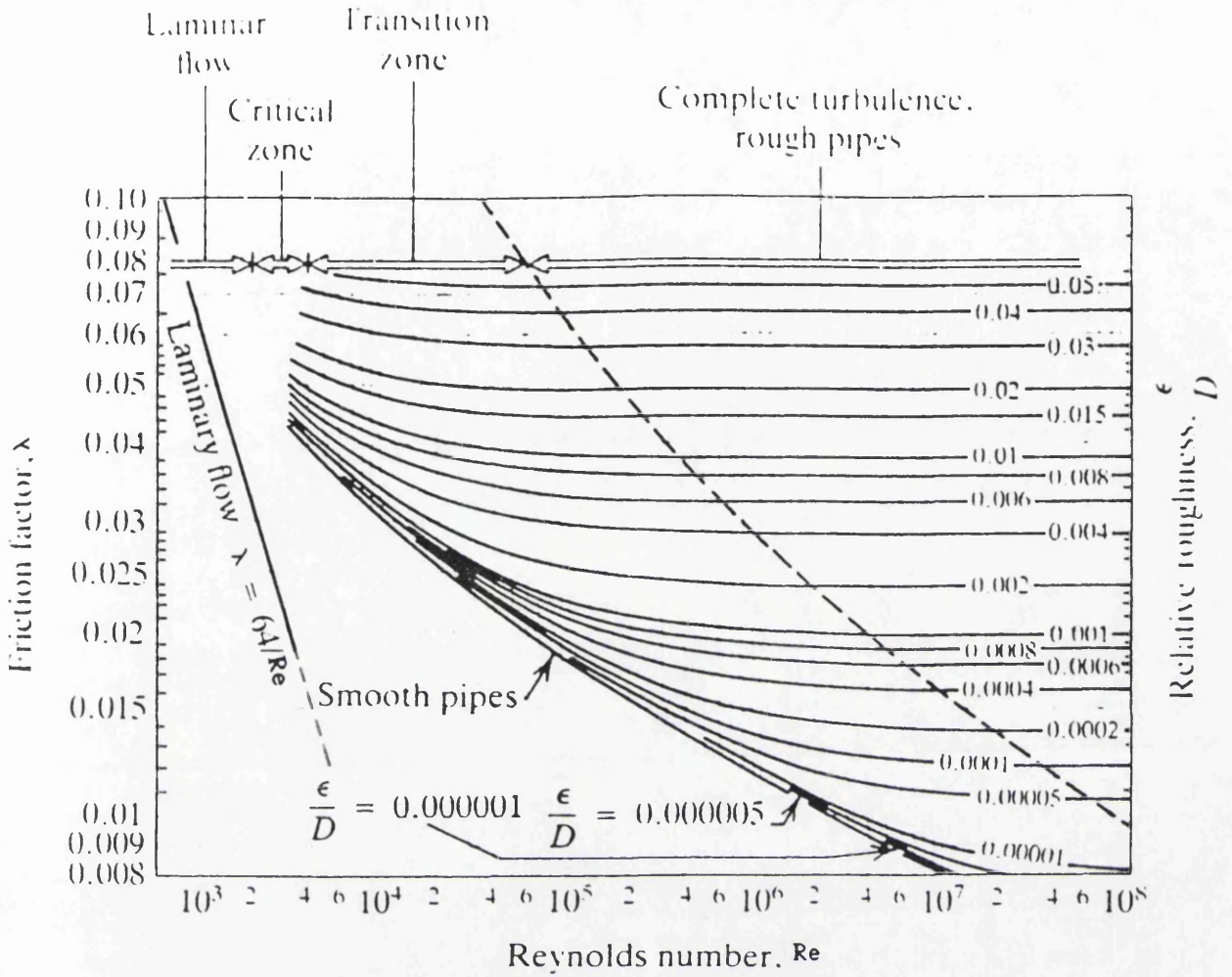


Figure 2-8: The Moody Diagram

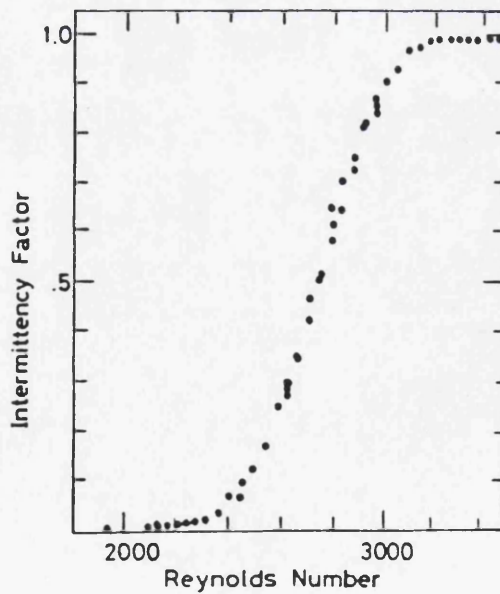


Figure 2-9: Intermittency Factor Versus Pipe Reynolds Number  
(After Fukuda)

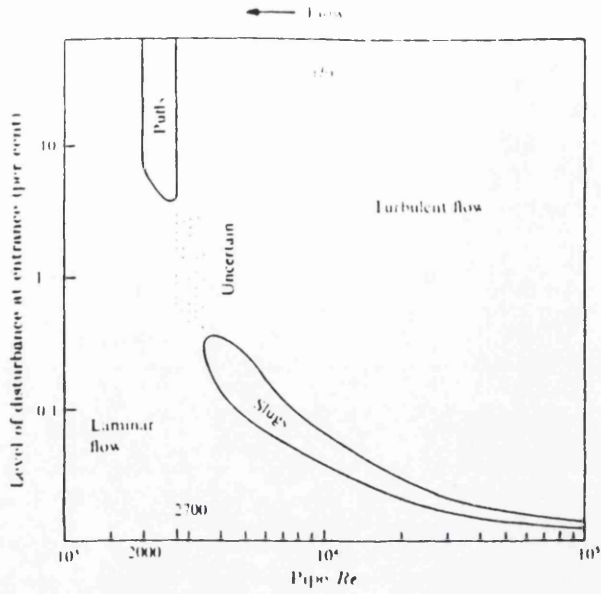


Figure 2-10: The Occurrence of Puffs and Slugs in a Pipe  
(After Wagnanski and Champagne)

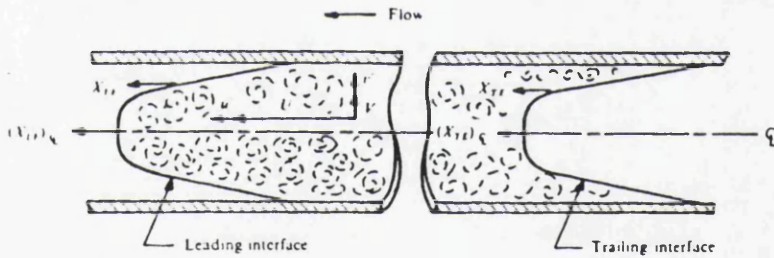


Figure 2-11: Leading and Trailing Edges of a Turbulent Slug  
(After Wagnanski and Champagne)

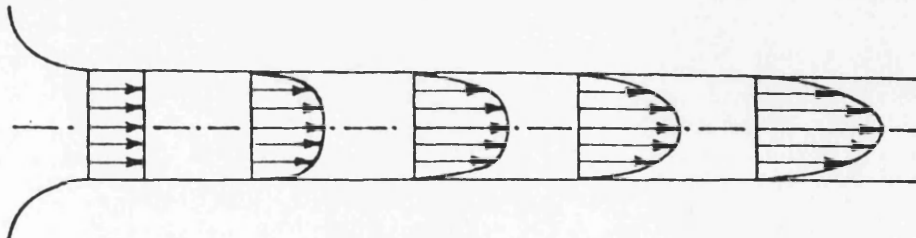


Figure 2-12: The Development of the Velocity Profile  
at a Pipe Entrance for Laminar Flow

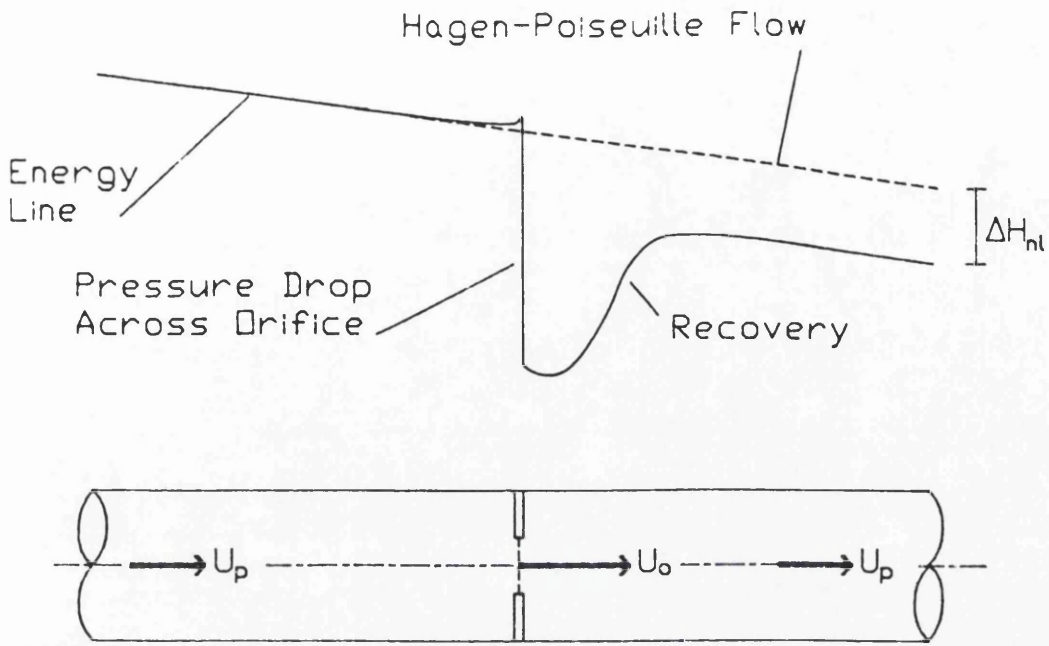


Figure 2-13: Pressure Drop in a Pipe Due to the Presence of an Orifice Plate

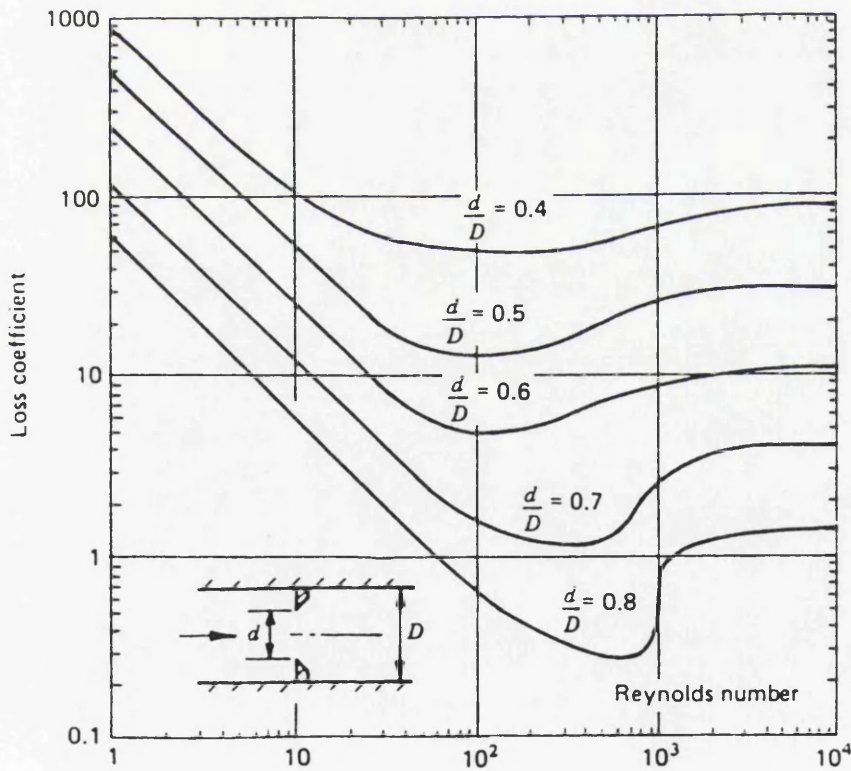
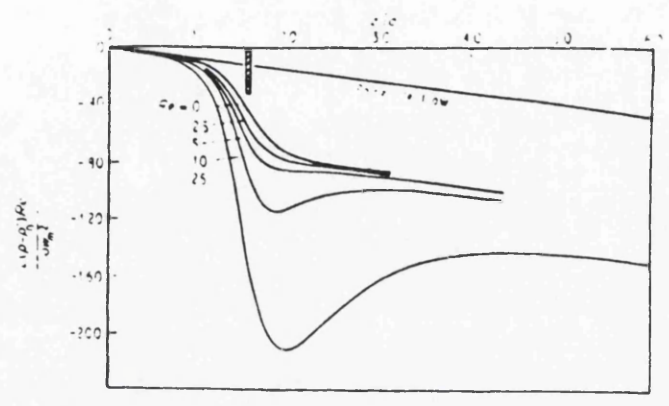
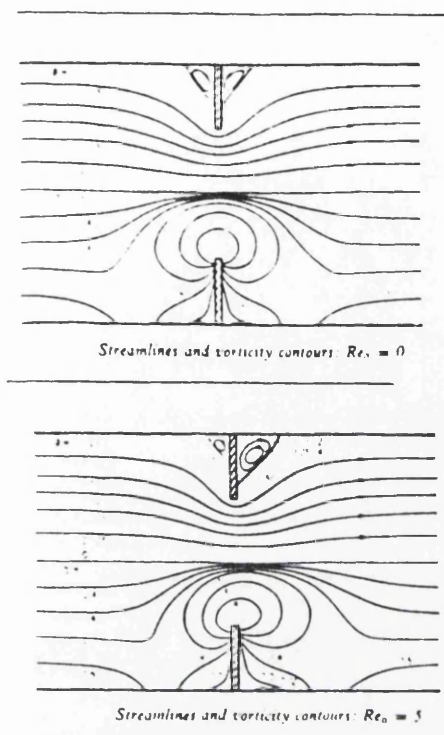


Figure 2-14: Pressure Loss Coefficients for Various Orifice Diameters (After Miller)



(a) Stream and Vorticity Lines

Figure 2-15: Numerical Solution of Low Reynolds Number Orifice Flows (After Mills)

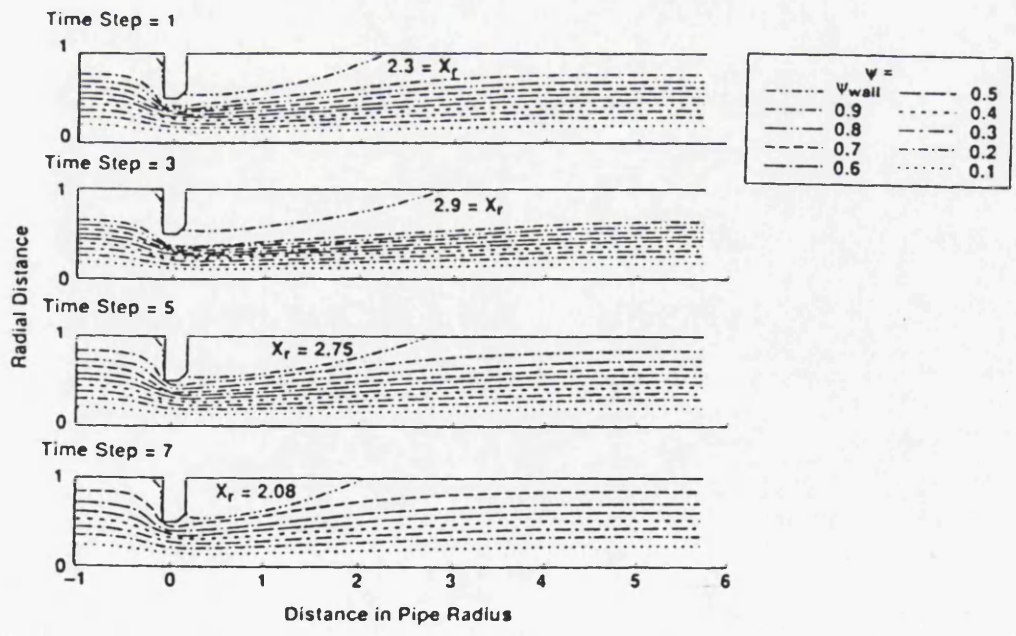


Figure 2-16: Flow Streamlines at an Orifice as a Function of the Forcing Cycle (After Jones and Bajura)

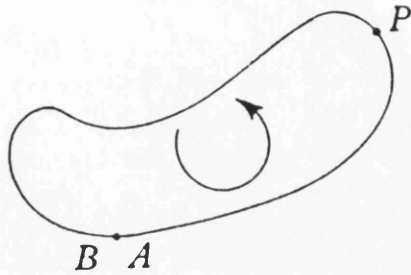


Figure 2-17: Closed Curve APB in a Fluid

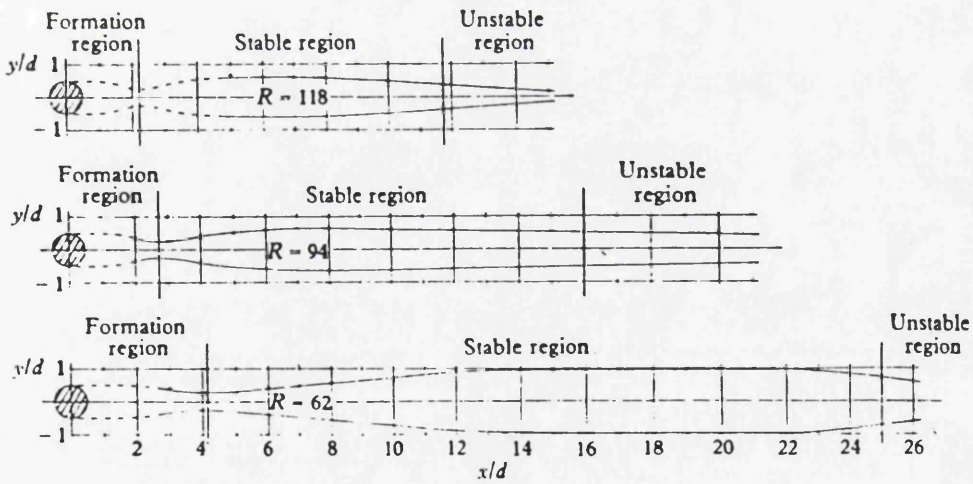
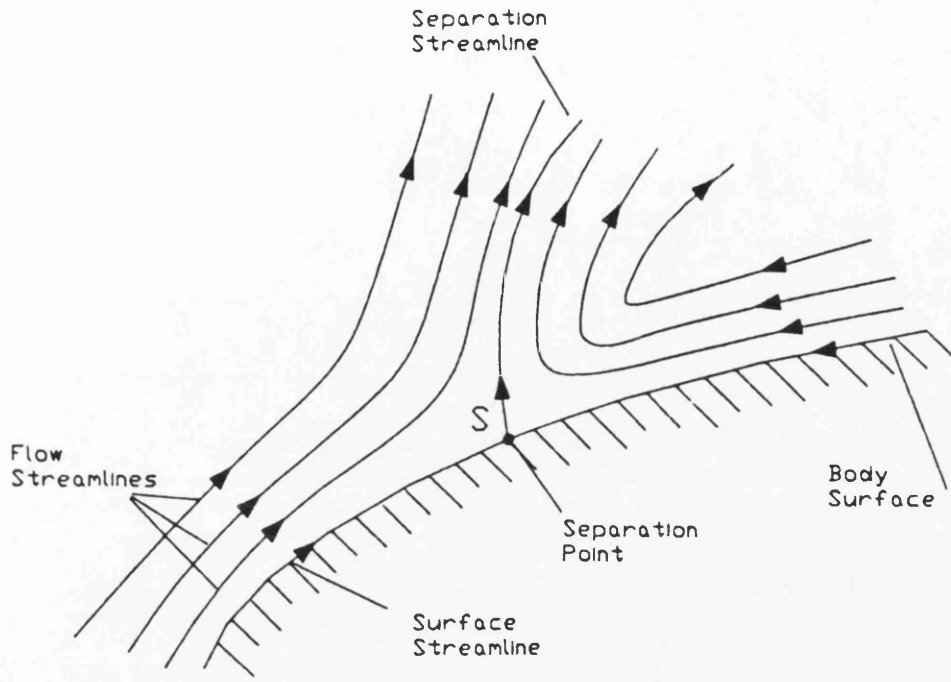
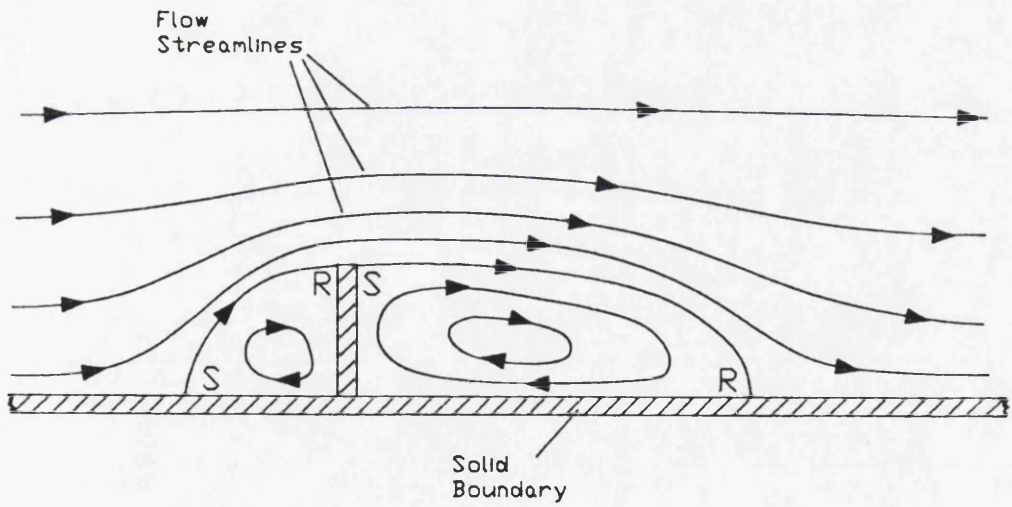


Figure 2-18: Regions of Formation, Stability and Instability in the Wake of a Cylinder, for Three Reynolds Numbers  
(After Schaefer and Eskmazi)

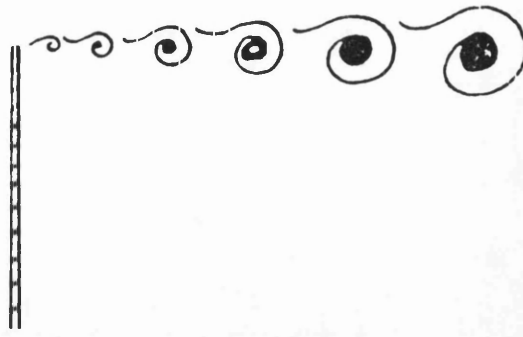


(a) At a Body Surface

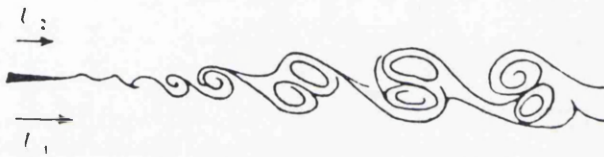


(b) At a Bluff Body

**Figure 2-19: Flow Separation**



(a) Generated at the Tip of a Bluff Body



(b) The Merging Process

Figure 2-20: Vortex Flows

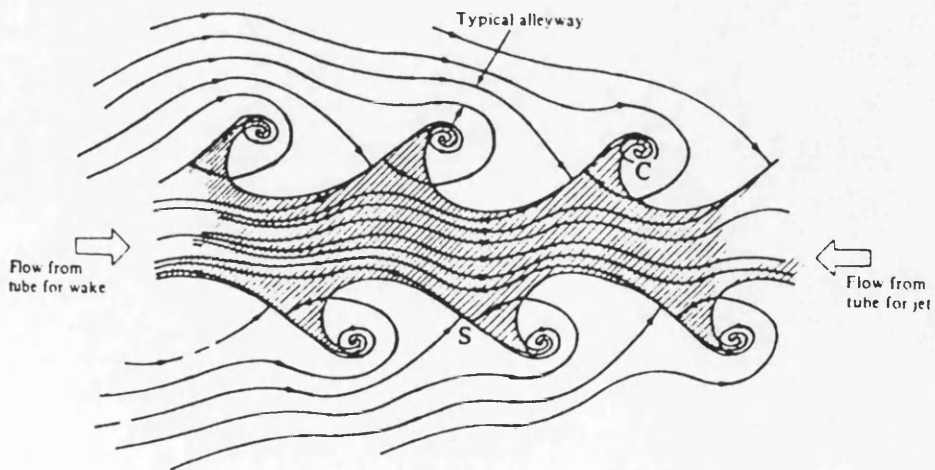
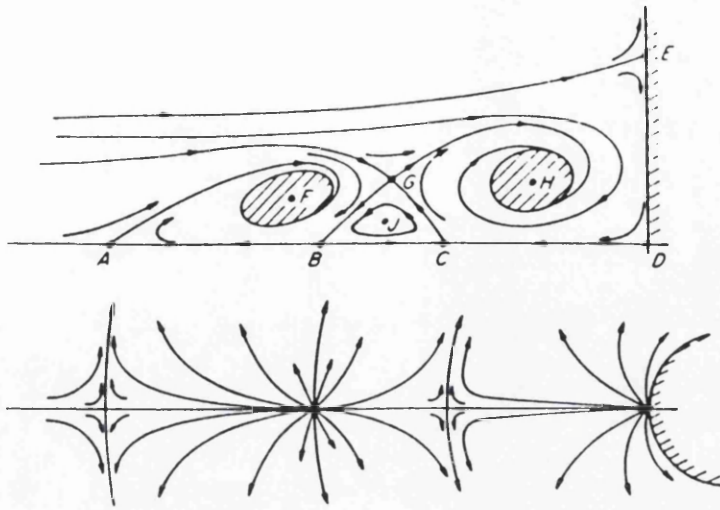
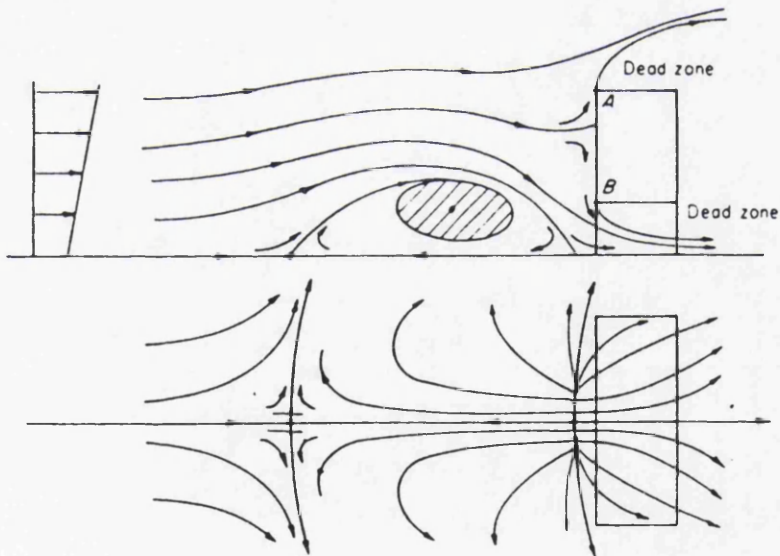


Figure 2-21: Vortices Generated at the Edge of a Jet Flow  
(After Perry et al)



(a) Laminar Separation in Front of a Cylindrical Object



(b) Flow Separation in Front of a Building with a Causeway Underneath

Figure 2-22: Viscous Flow Separation at Obstacles  
(After Perry et al)

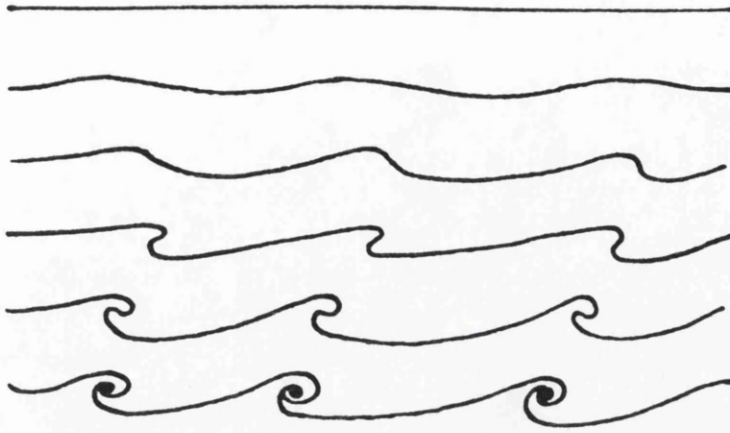


Figure 2-23: The Roll-up Process in Kelvin-Helmholtz Instability

(The Rolling up of the streamline may be Observed from the Top of the Figure Down)



Figure 2-24: The Karman Vortex Street Generated in the Wake of a Cylinder

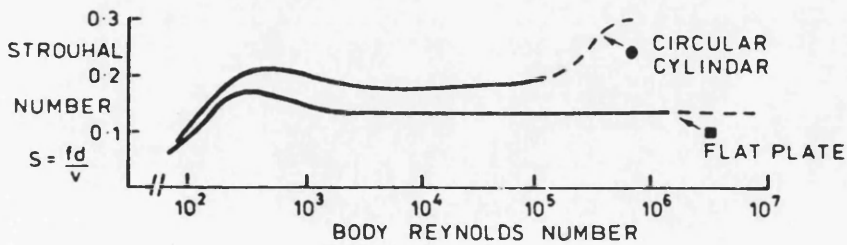


Figure 2-25: The Strouhal Number Versus the Reynolds Number for a Circular Cylinder and a Flat Plate  
(After Blevins)

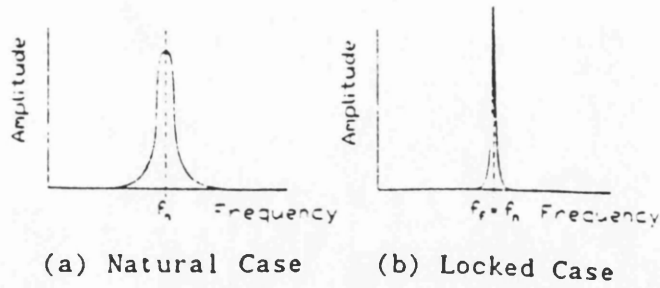


Figure 2-26: Frequency Spectra of Natural and Locked Vortex Flow

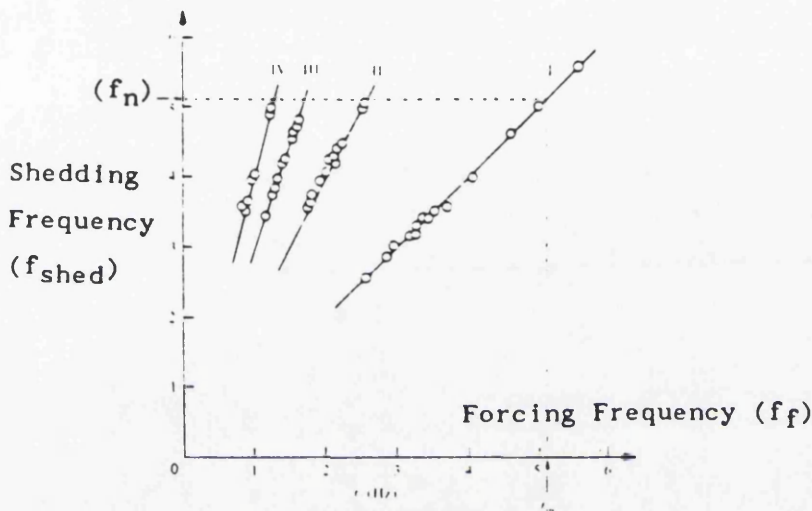


Figure 2-27: Frequency Locking Phenomena as Observed by Ho and Huang  
(See Text for Details)

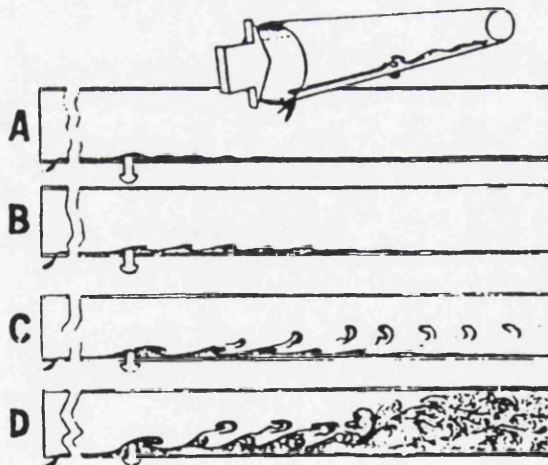


Figure 2-28: Schematic Diagram of a Trip-Induced Transition Pattern in a Pipe Showing the Effect of Increasing Disturbance Height  
(After Webb and Harrington)

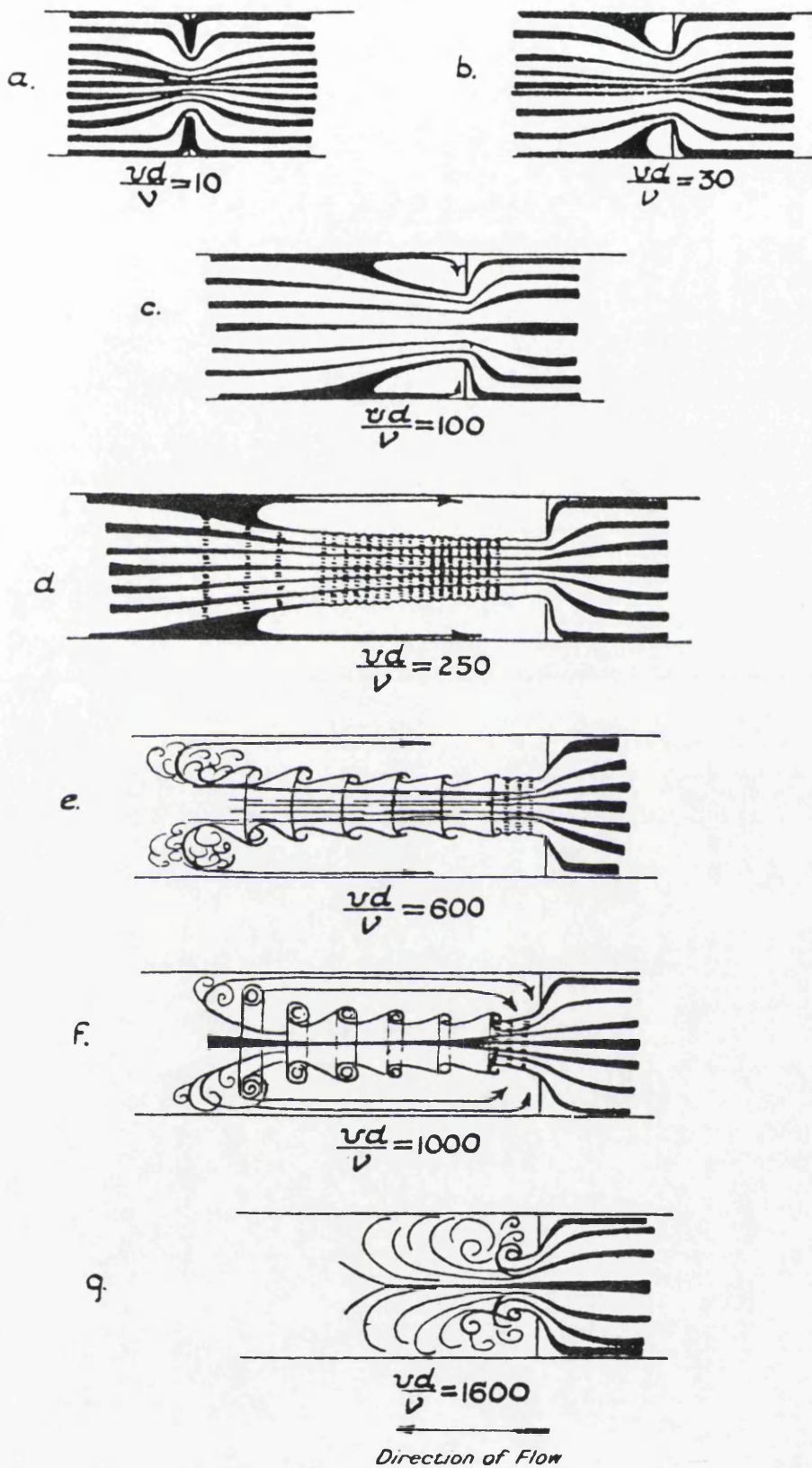


Figure 2-29: Flows at a Pipe Orifice as the Reynolds  
Number is Increased

(After Johansen)

(See Text for Details)

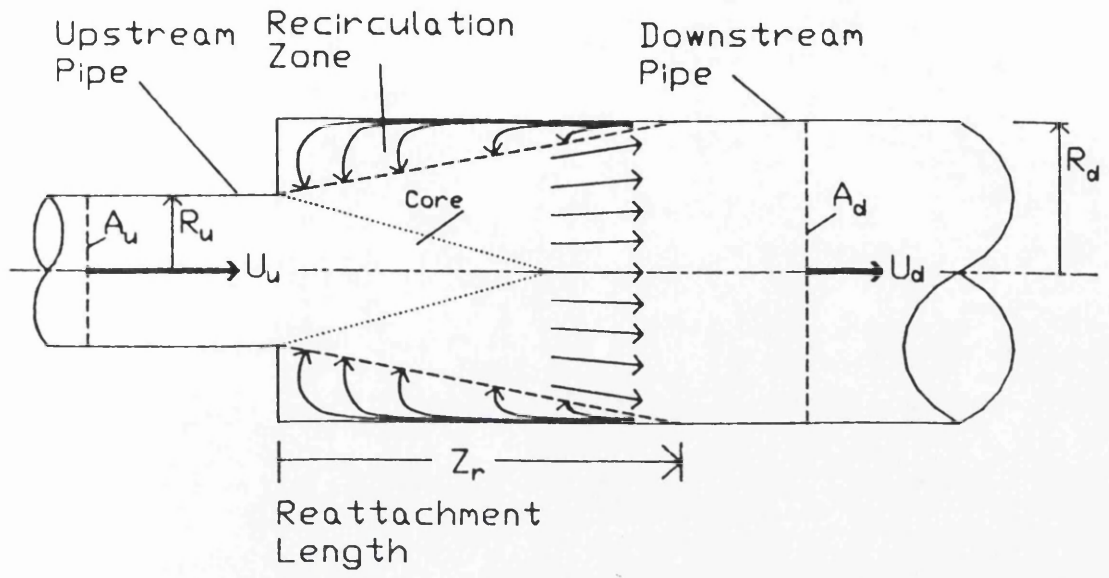


Figure 2-30: Flow at a Sudden Expansion within a Pipe

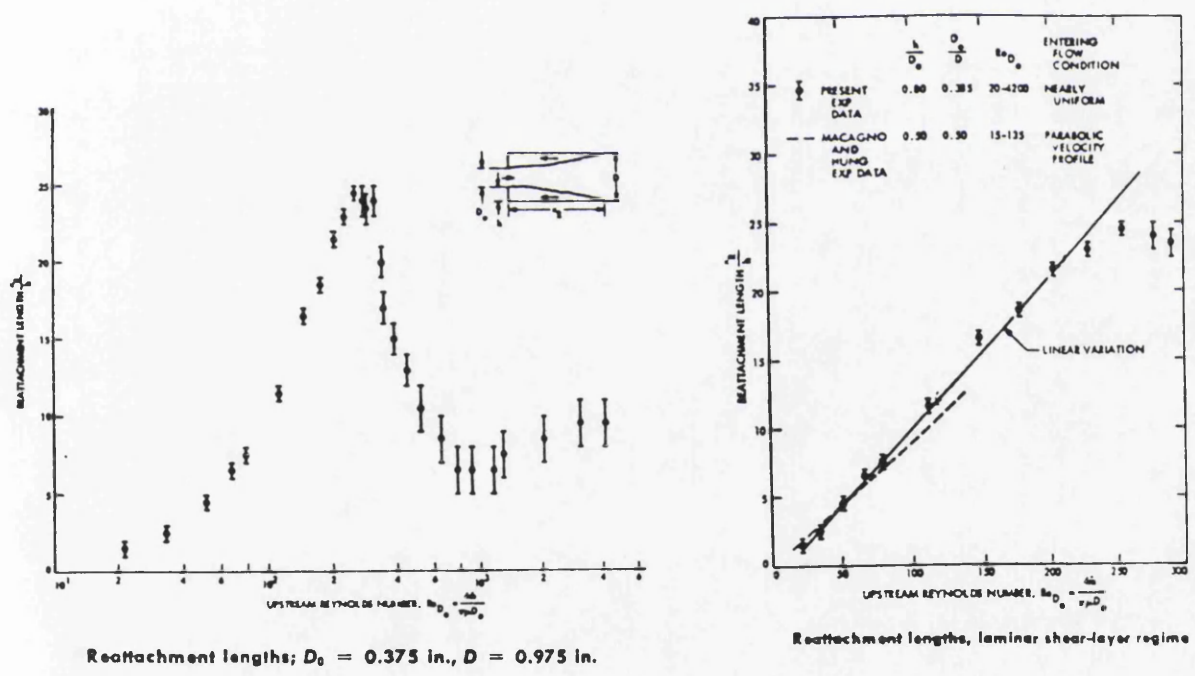


Figure 2-31: Reattachment Length Versus Upstream Pipe Reynolds Number for Sudden Expansion Flow in a Pipe  
 (After Back & Roshke)  
 (See Text for Details)

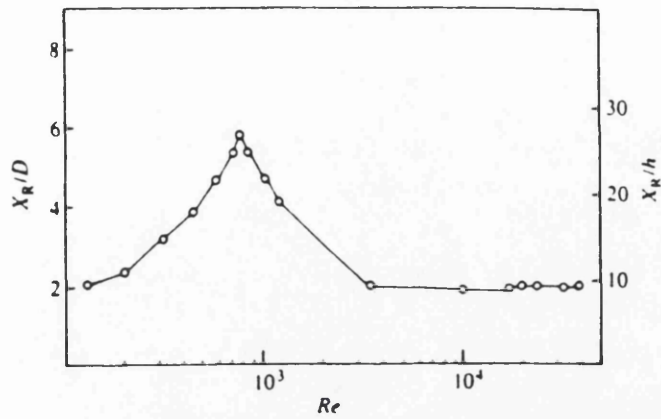


Figure 2-32: Reattachment Length Versus Upstream Pipe Reynolds Number for Sudden Expansion Flow in a Pipe  
(After Khezzar et al)

Results of Khezzar et al [1986]

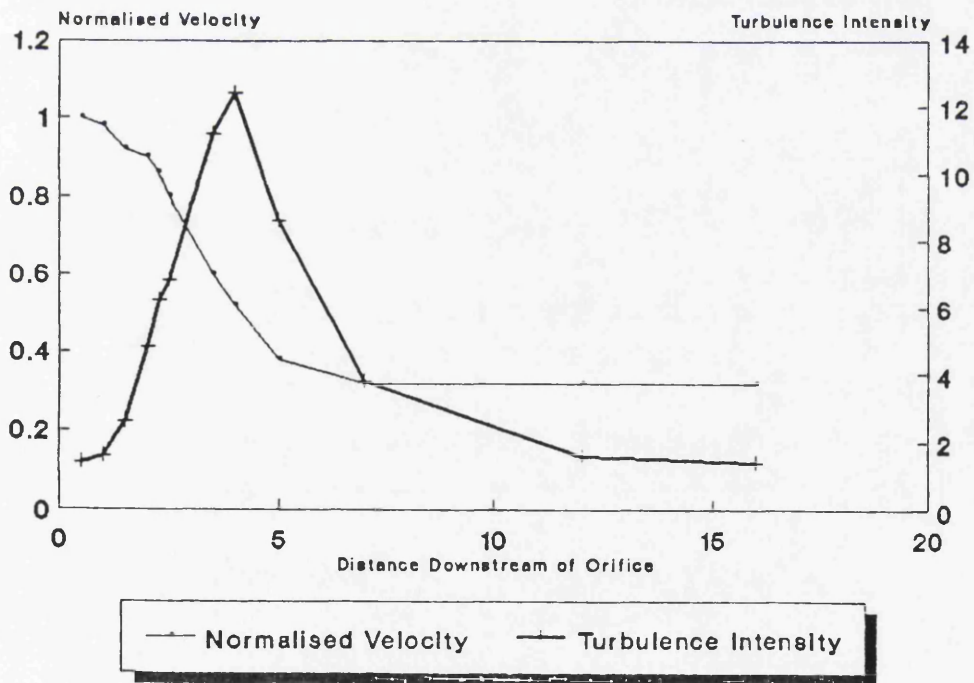
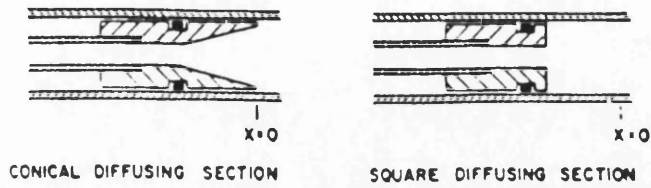
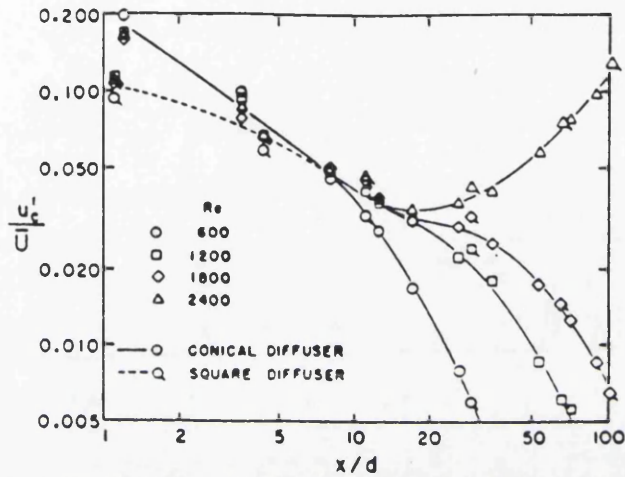


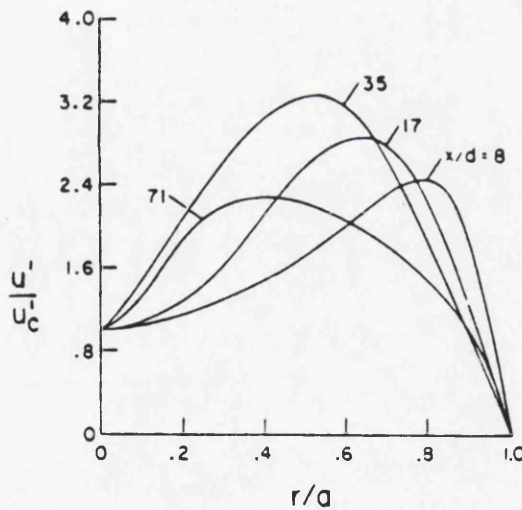
Figure 2-33: Centre-line Velocity and Turbulence Intensity Results of Khezzar, Replotted by the Author



(a) The Conical and Square Diffusing Sections

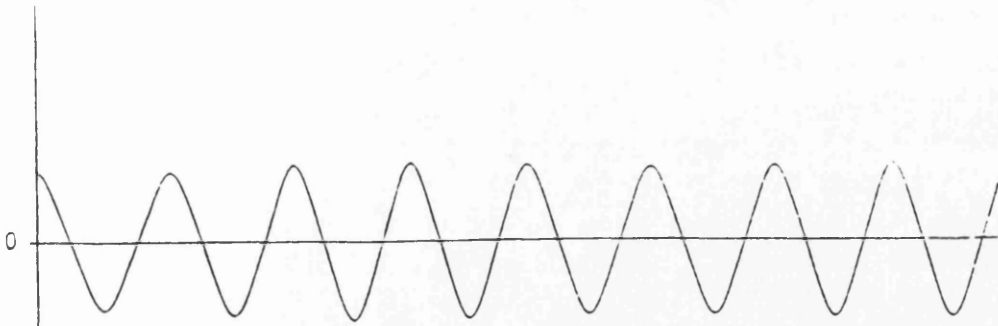


(b) Variation of the Centreline Turbulence Level with Axial Position for Several Reynolds Numbers

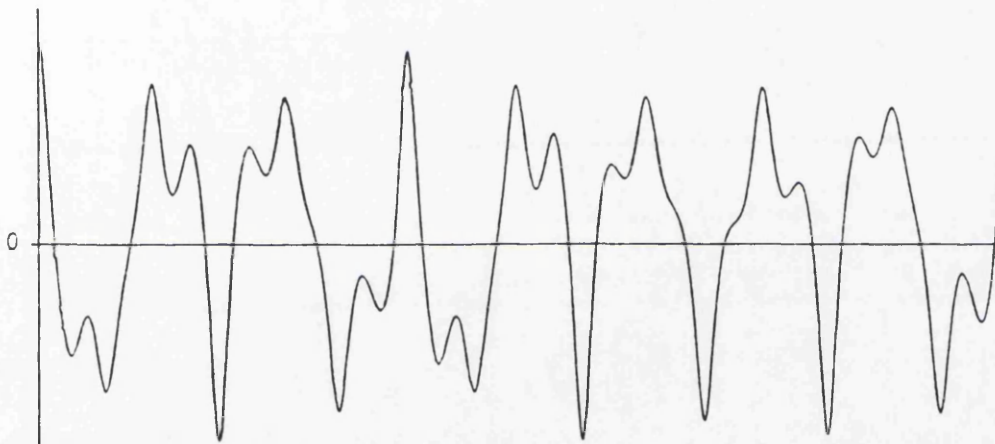


(c) Turbulence Intensity Profiles across the Flow taken at Several Cross Sections Downstream of the Diffuser

**Figure 2-34: Relaminarizing of Sudden Expansion Flow in a Pipe**  
(After Sibulkin)



(a) Periodic Solution

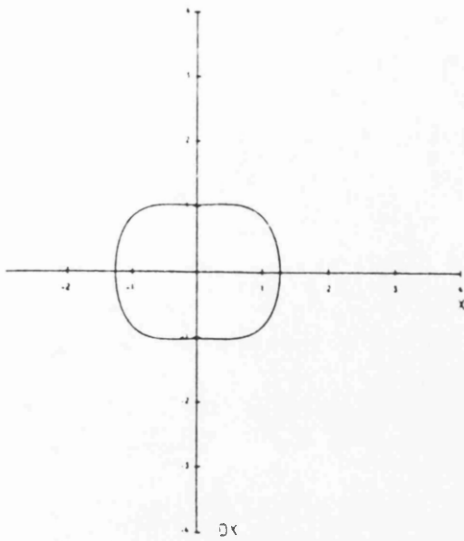


(b) Nonperiodic (Chaotic) Solution

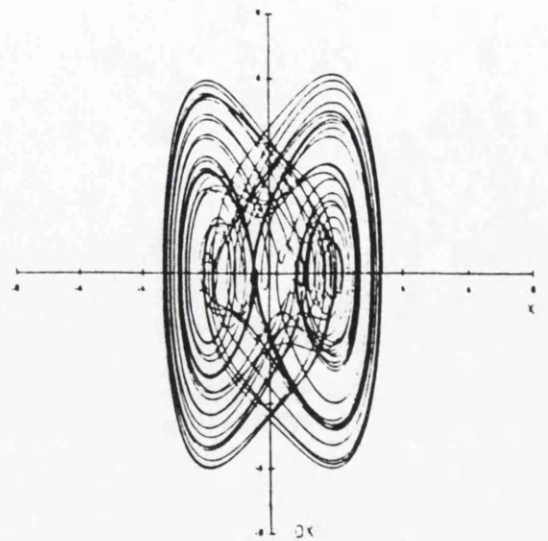


(c) The Effect of Different Initial  
Conditions on the Resulting Solution

Figure 2-35: 'x-t' Time Trace Solutions for  
the Duffing Oscillator

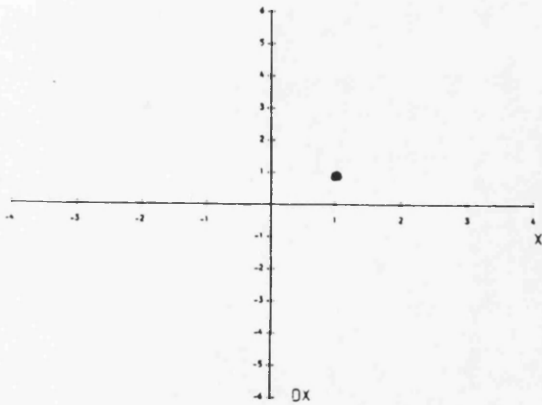


(a) Periodic Solution

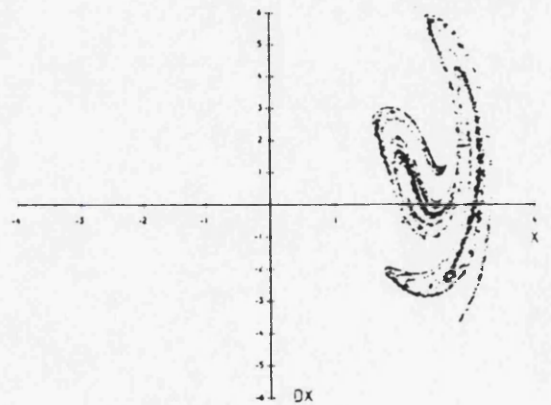


(b) Chaotic Solution

Figure 2-36: Phase Space Portraits of Solutions to the Duffing Oscillator

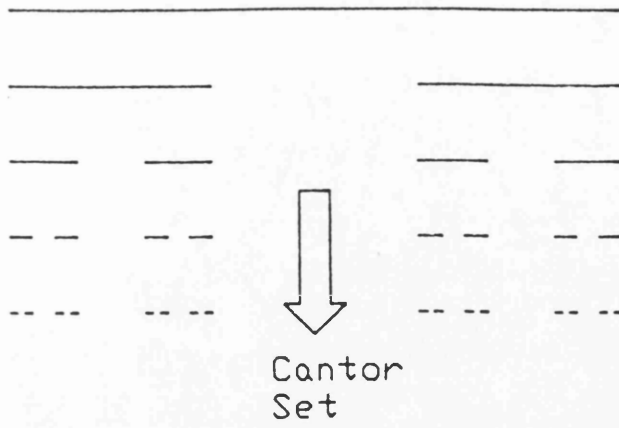


(a) Periodic Solution

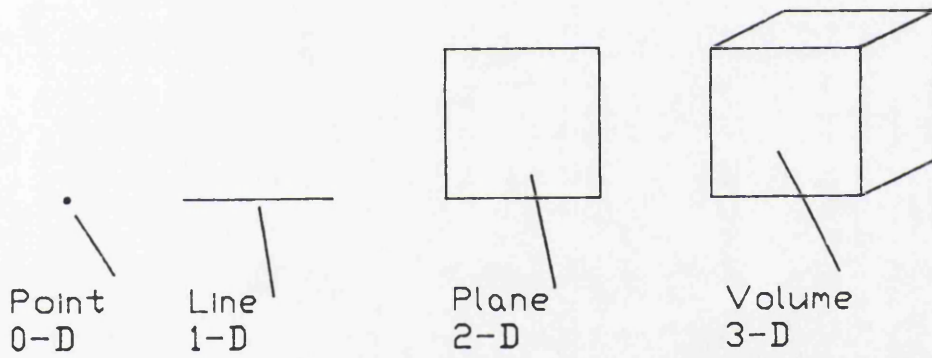


(b) Nonperiodic (Chaotic) Solution

Figure 2-37: Poincaré Sections of the Duffing Oscillator Solutions of Figure 2-35

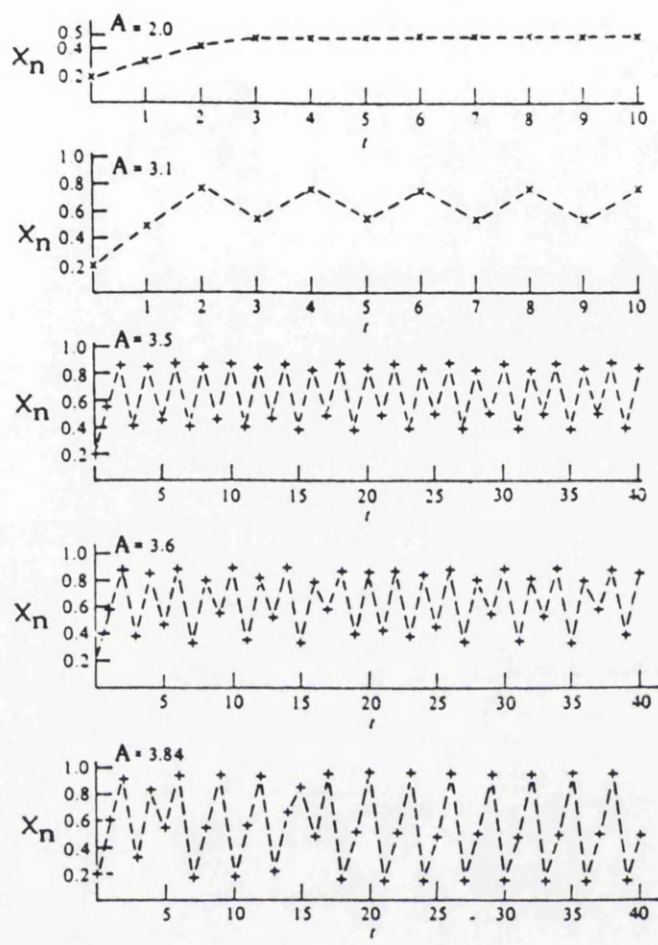


(a) The Cantor Set

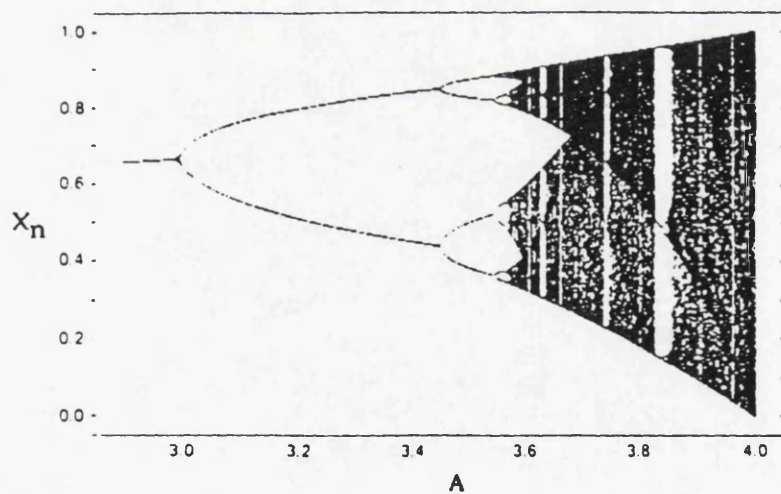


(b) Typical Dimensions

Figure 2-38: The Cantor Set, Fractals and Dimension

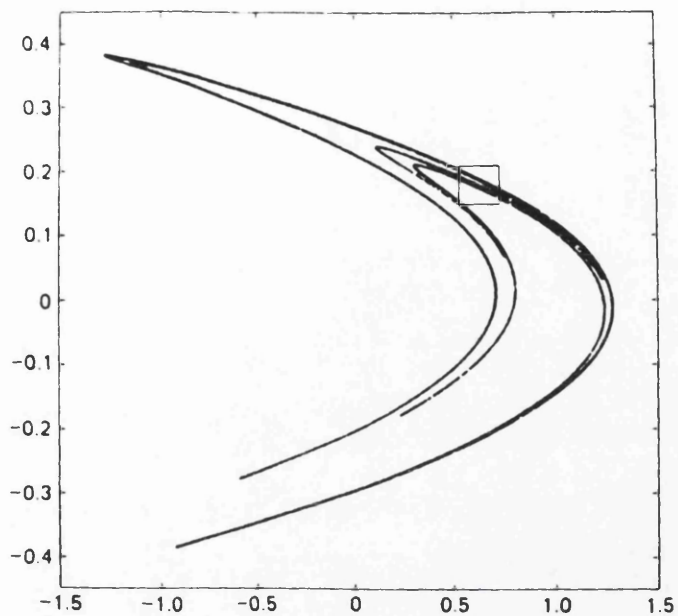


(a) Typical Solutions to the Mapping

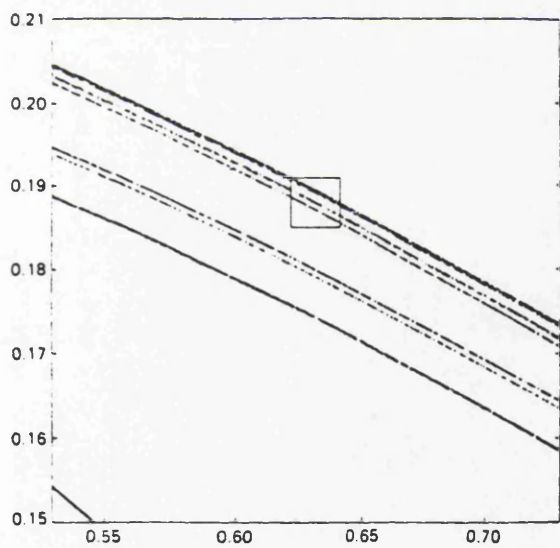


(b) The Bifurcation Diagram

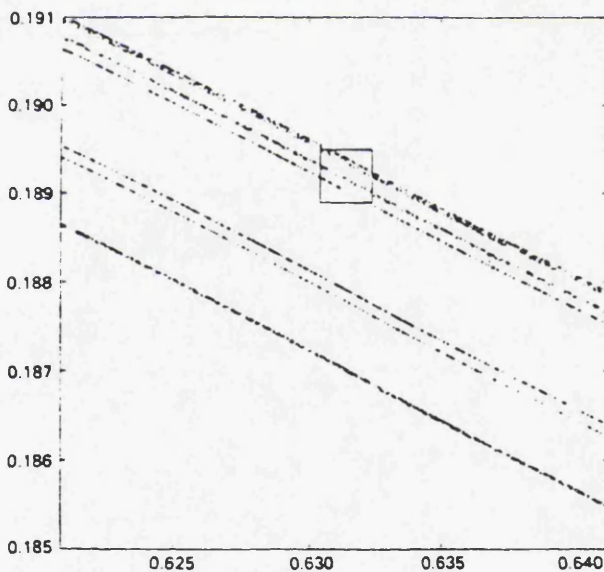
Figure 2-39: The Logistic Map



(a) The Henon Attractor

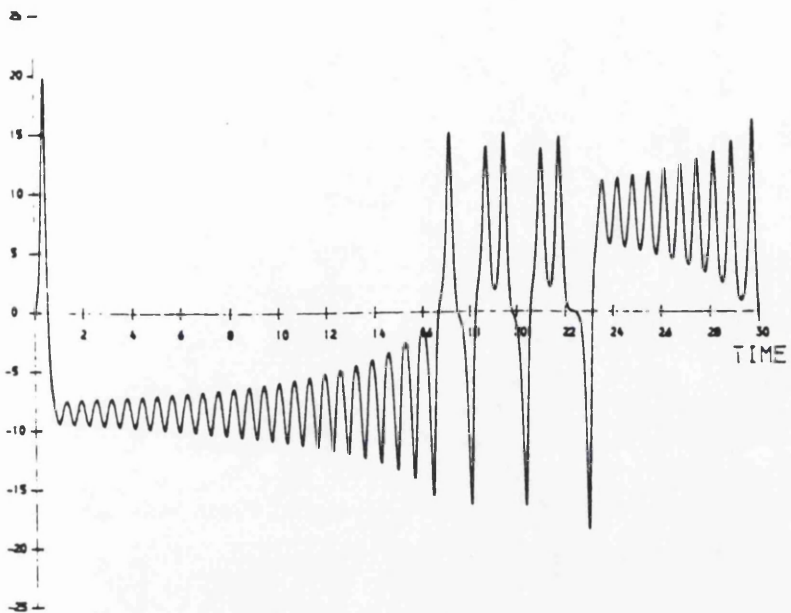


(b) Zoomed in Picture of (a)

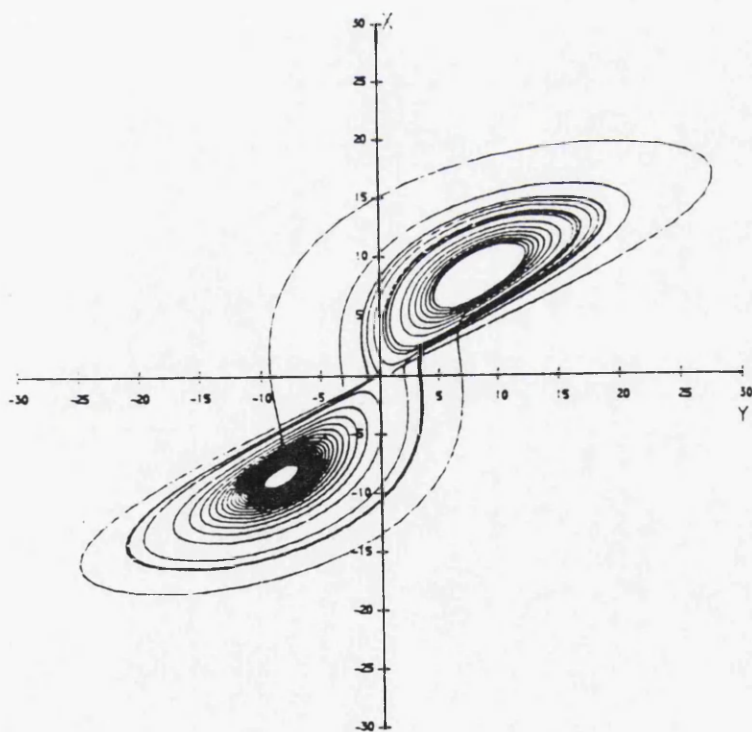


(c) Zoomed in Picture of (b)

Figure 2-40: The Henon Attractor

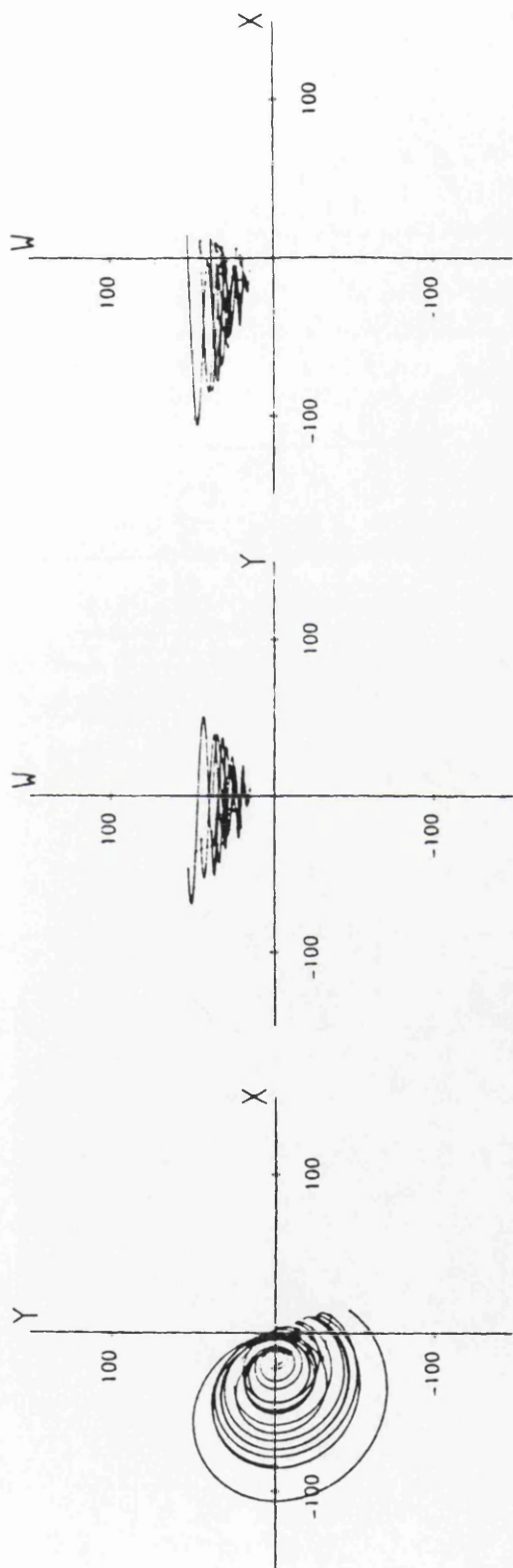


(a) The Chaotic Time Series



(b) The Chaotic Attractor

Figure 2-41: The Lorenz Equations



SIX VIEWS OF THE ROSSLER HYPERCHAOS ATTRACTOR

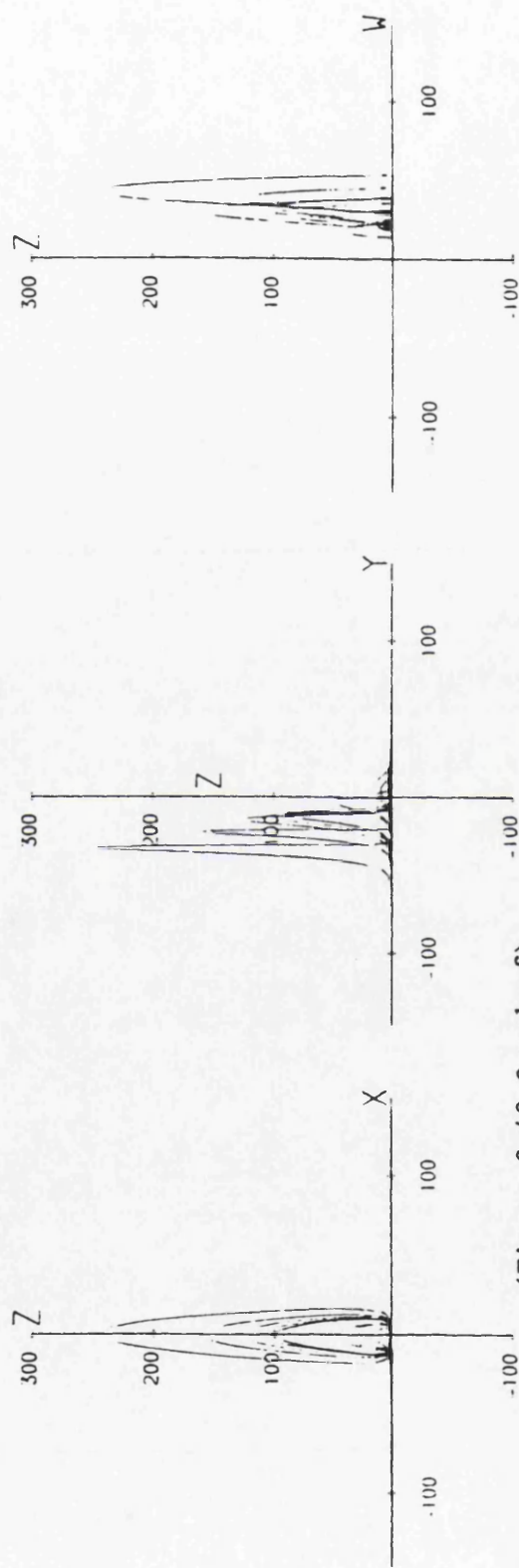


(Figure 2-42 Overleaf)  
 Figure 2-43: The Attractor of the Rossler Hyper-Chaos Equations

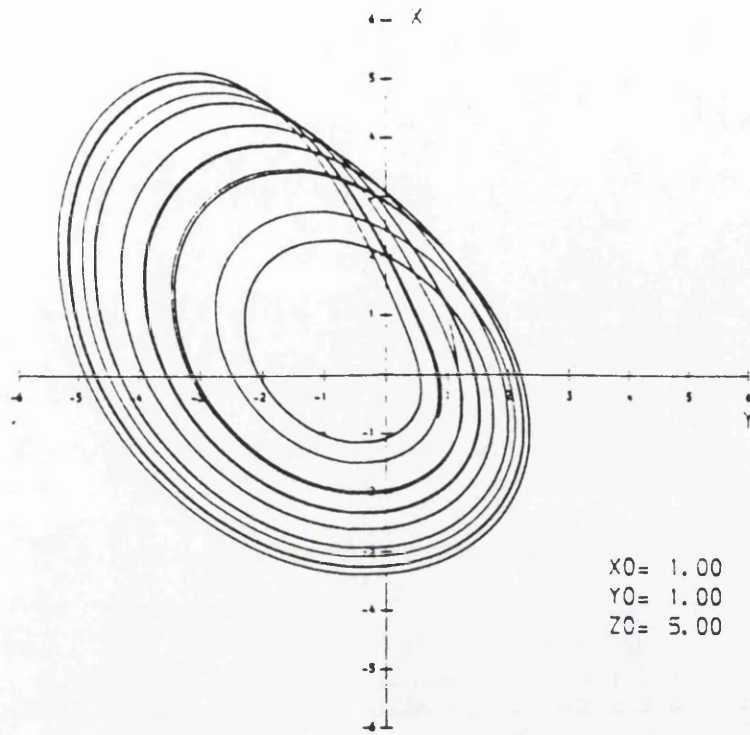


Figure 2-42: The Attractor of the Rossler Equations

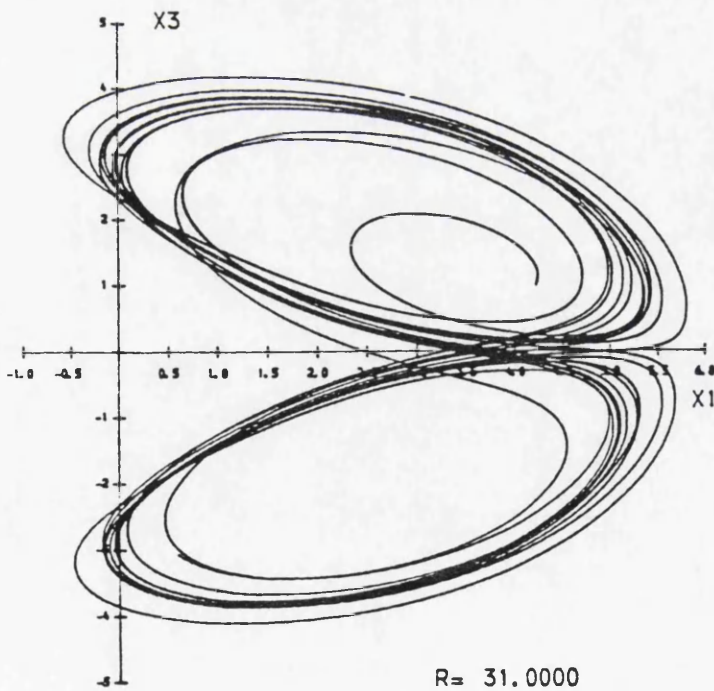
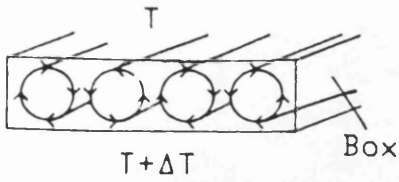
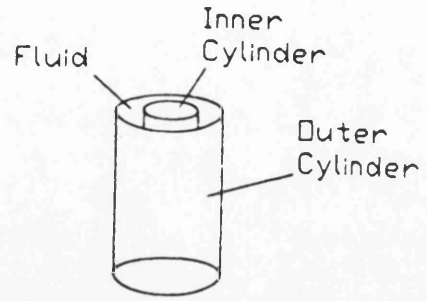


Figure 2-44: The Attractor of the Truncated Navier-Stokes Equations

(Figure 2-43 on Previous Page)



(a) The Rayleigh-Benard System



(b) The Taylor-Couette System

Figure 2-45: Schematic Diagrams of the Rayleigh-Benard and Taylor-Couette Experiments

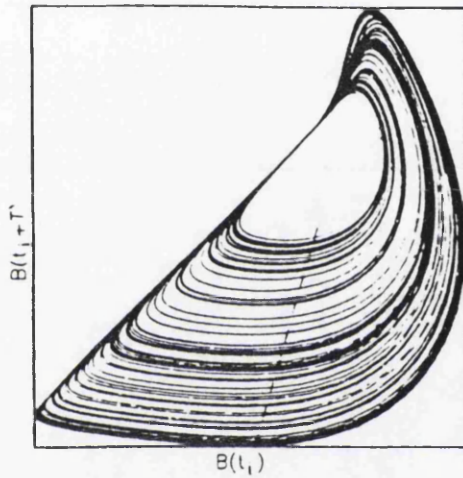


Figure 2-46: The Belousov-Zhabotinski Attractor  
(After Roux & Swinney)

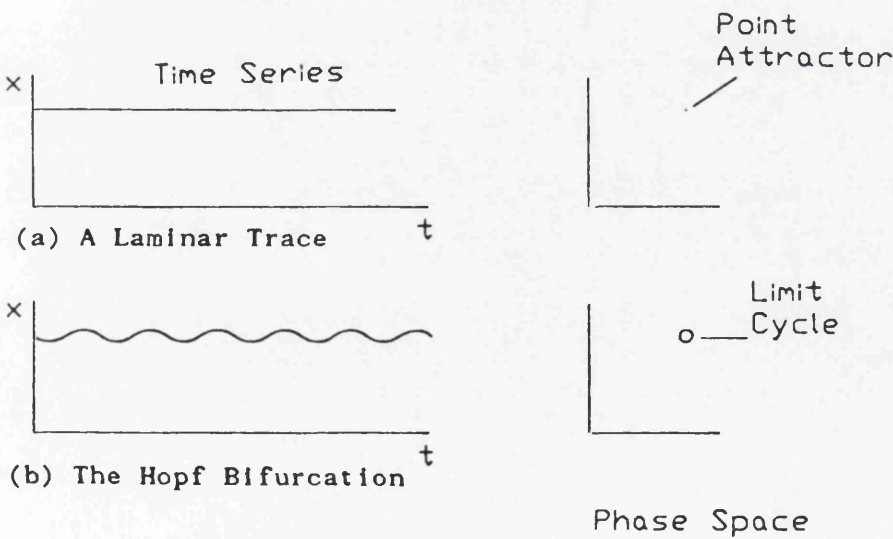


Figure 2-47: The Hopf Bifurcation

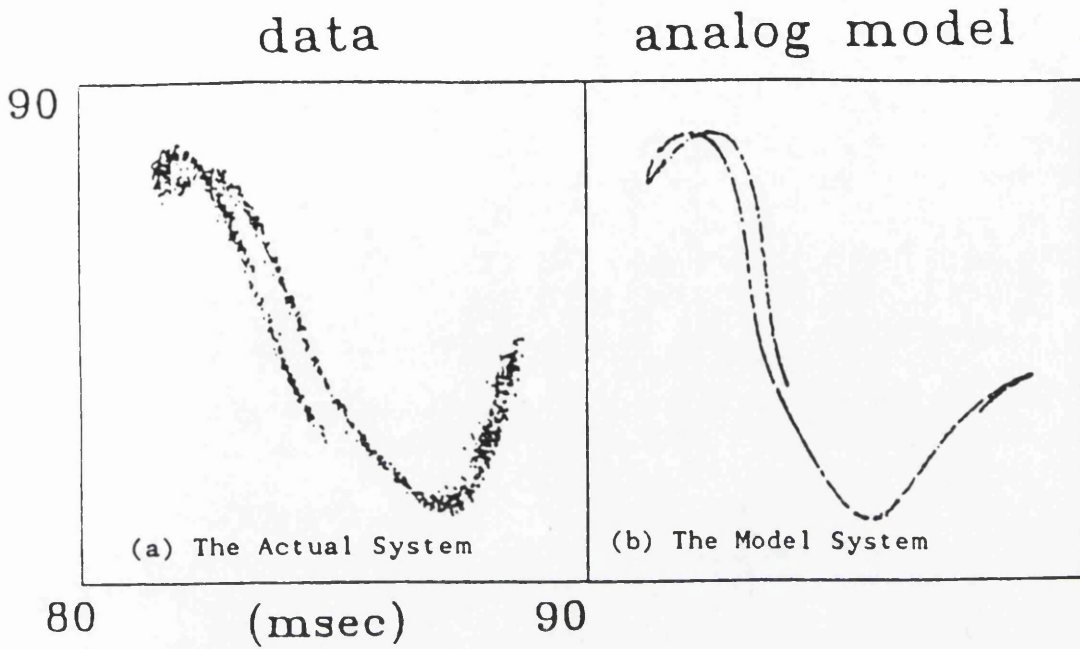


Figure 2-48: A Comparison of the Phase Portraits of the Actual and Modelled Dripping Faucet System (After Shaw)

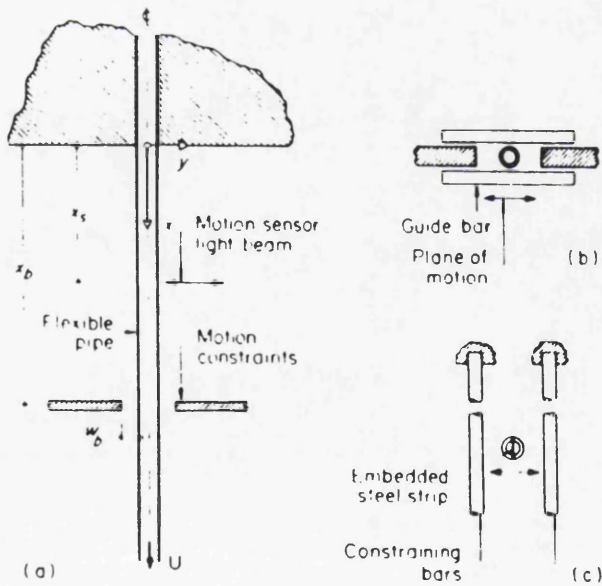
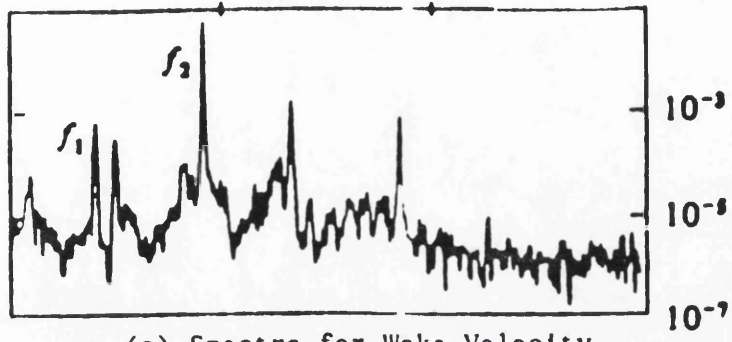
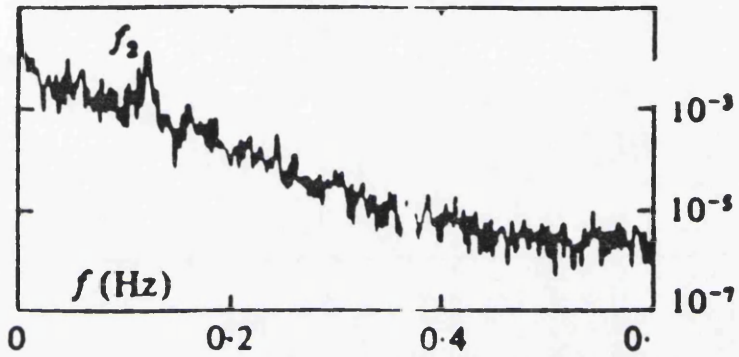


Figure 2-49: The Fluid Elastic Vibration System (After Paidoussis & Moon)



(a) Spectra for Wake Velocity  
During Ordered Shedding



(b) Spectra for Wake Velocity  
During Chaotic Shedding

Figure 2-50: Power Spectra Associated with Vortex Shedding at a Cylinder  
(After Elgar et al)

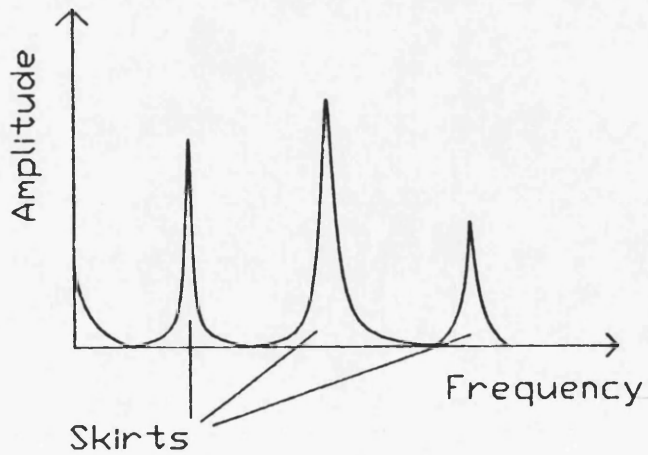
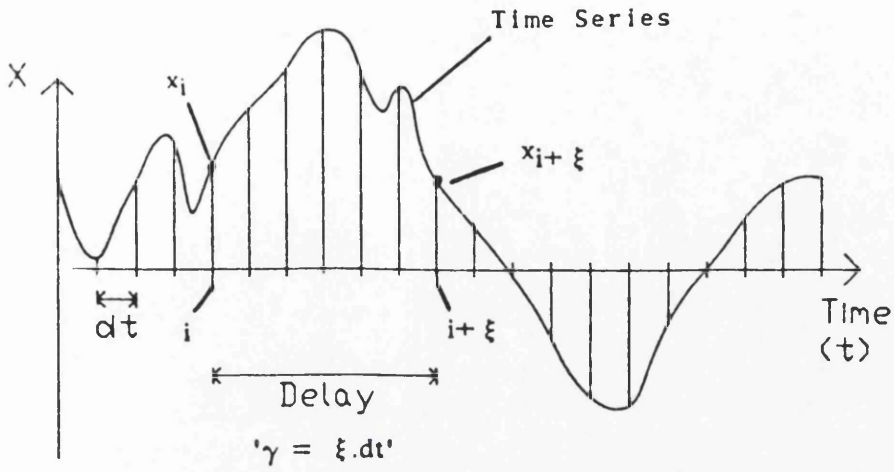
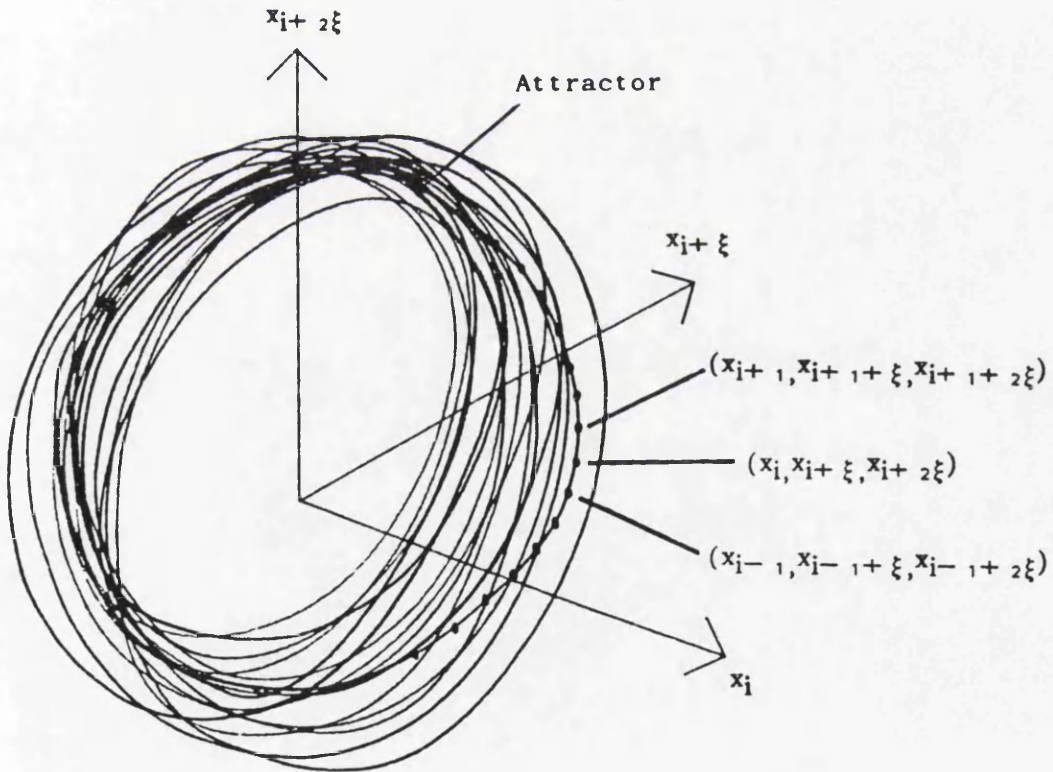


Figure 2-51: Broadening of Power Spectra Bases as the Chaotic State is Approached



(a) The Discretised Time Series



(b) The Resulting Attractor

Figure 2-52: The Method of Time Delays in Attractor Construction

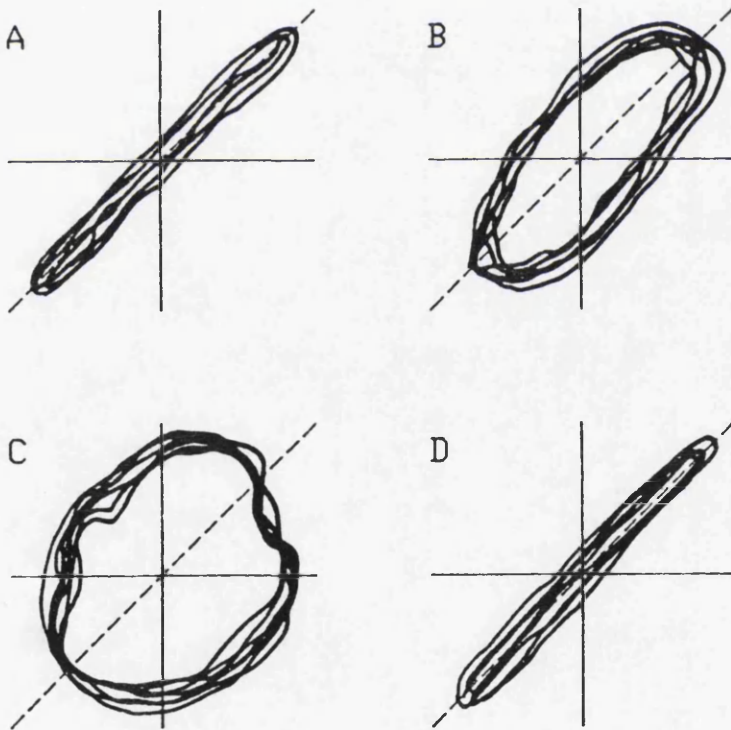
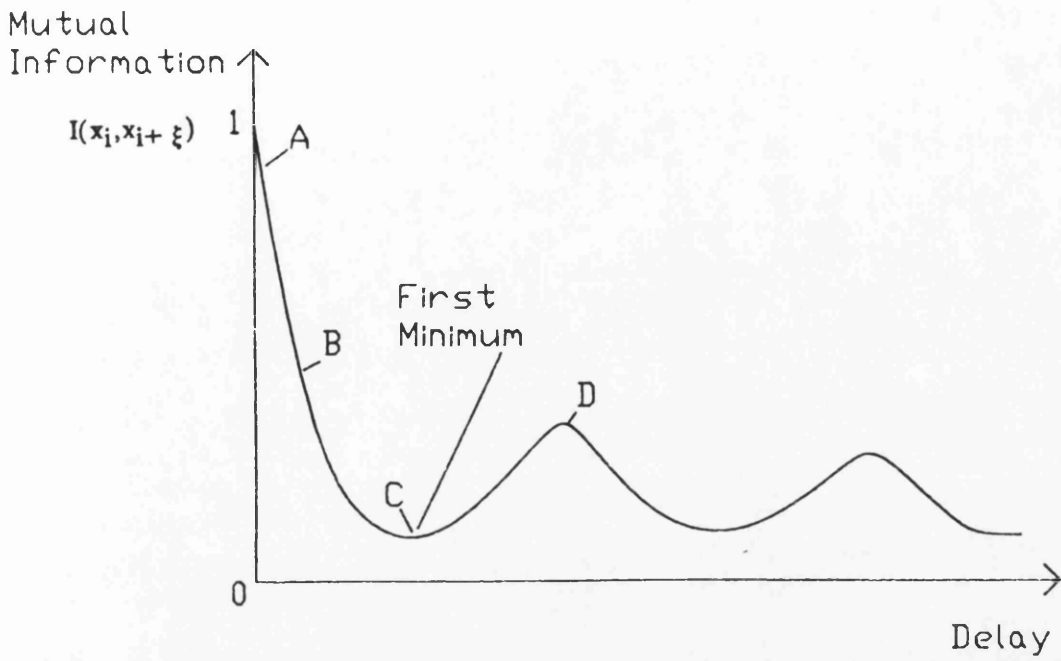
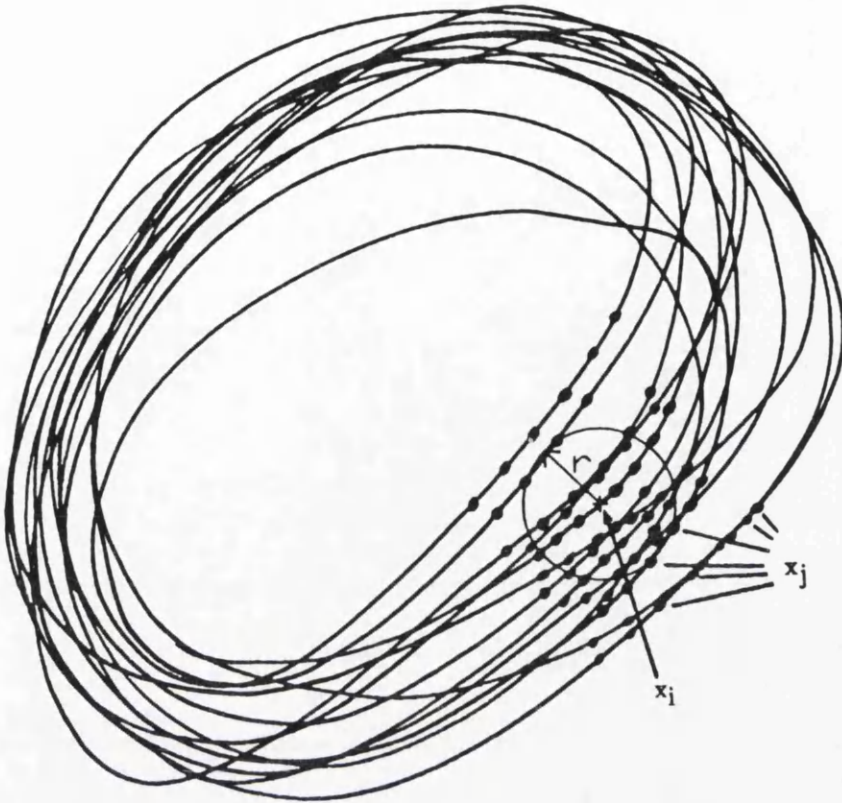
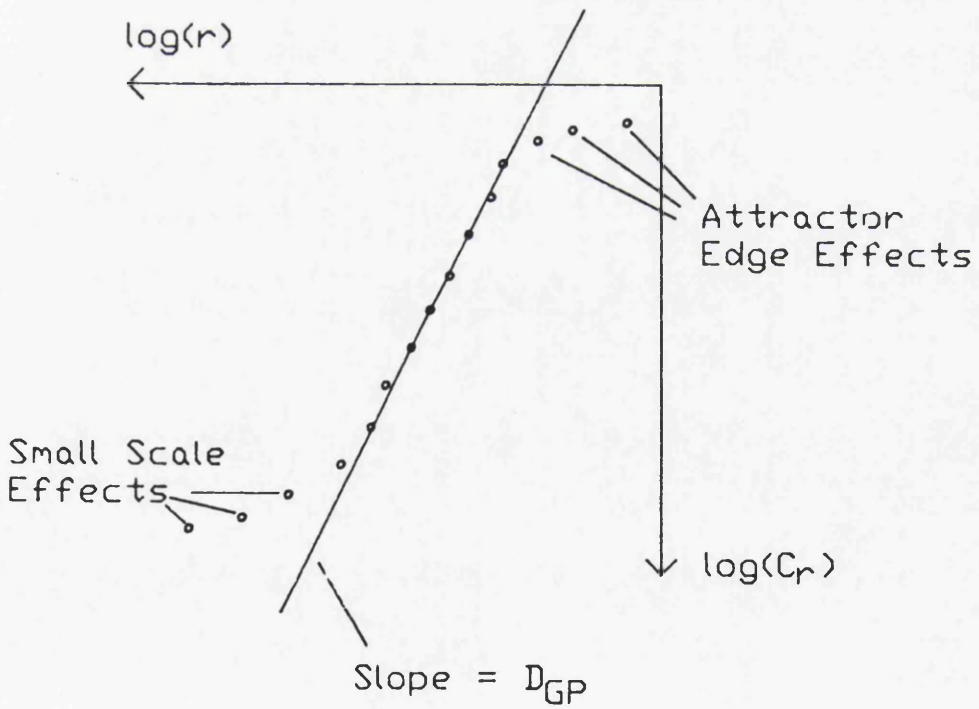


Figure 2-53: The Mutual Information and its Effect on the Reconstructed Attractor

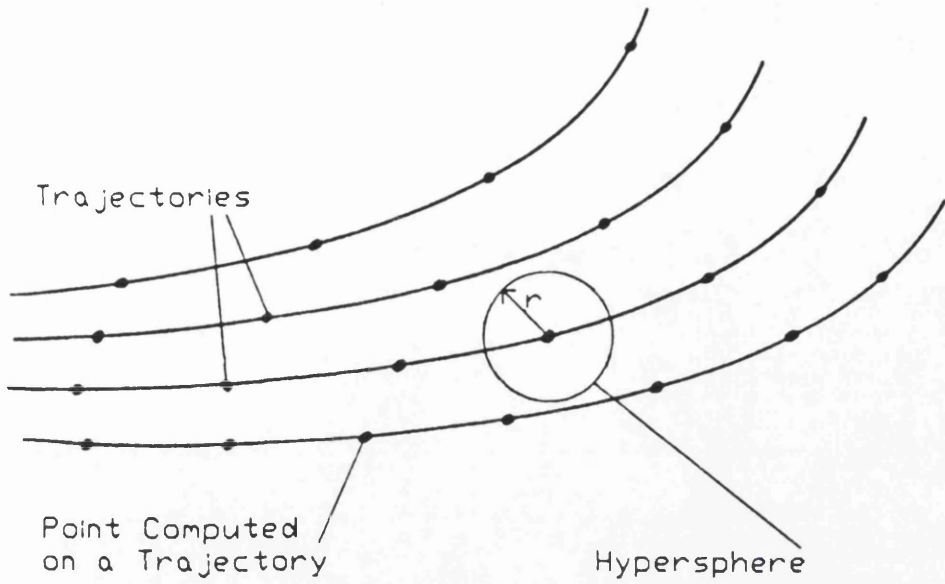


(a) The Attractor being Probed with Hypersphere



(b) The ' $\log(r)-\log(C_r)$ ' plot

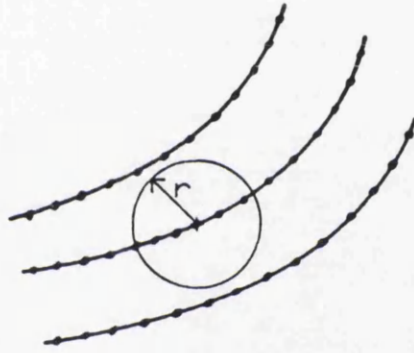
Figure 2-54: The Grassberger-Proccacia Dimension Estimate



(a) Length Scales Comparable with the Inter Point Distances of the Attractor Trajectories



(b) Short Length Scales on a Noisy Attractor



(c) Short Length Scales on a Noise Free Attractor



(d) Length Scales giving Estimates Approaching the Actual Dimension



(e) Length Scales Comparable with the Attractor Radius

**Figure 2-55: Regions of Behaviour on the Attractor**

(Full Details in Text)

Phase Space Trajectories

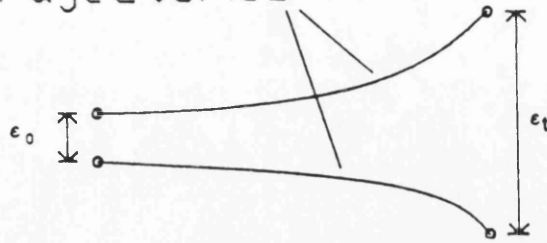


Figure 2-56: Definition Sketch of Trajectory Separation for the Lyapunov Exponent Calculation

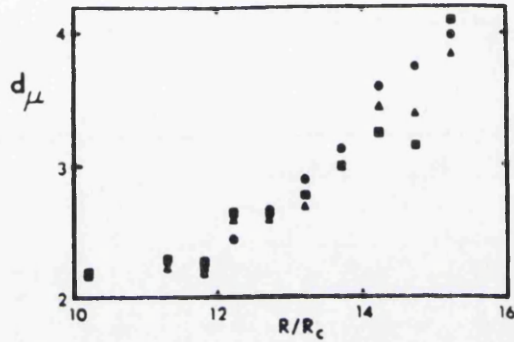
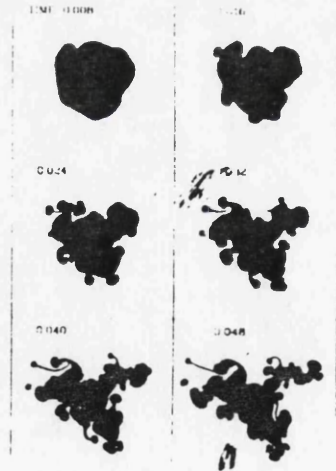
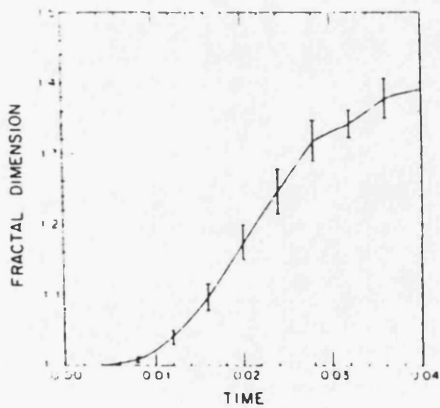
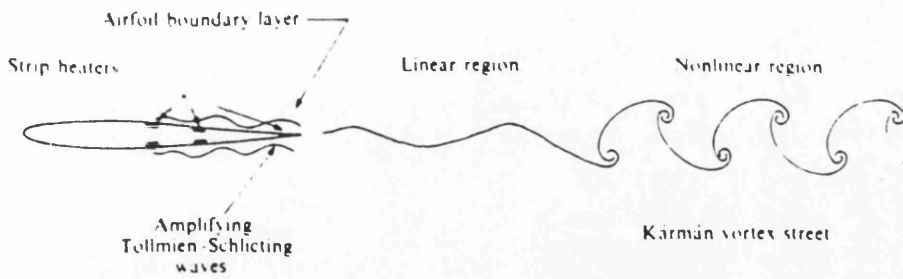


Figure 2-57: The Effect of Reynolds Number Increase on the Dimension of the Taylor-Couette System (After Brandstätter et al)

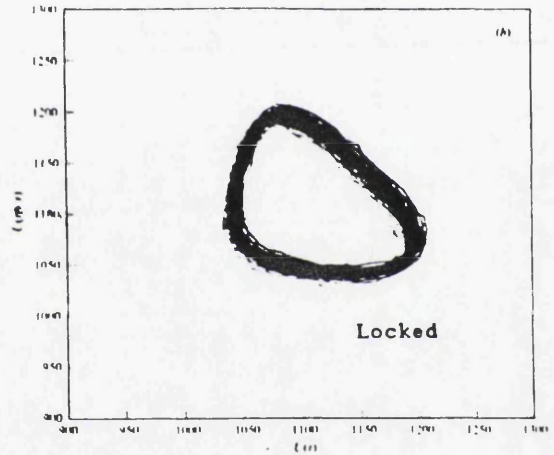
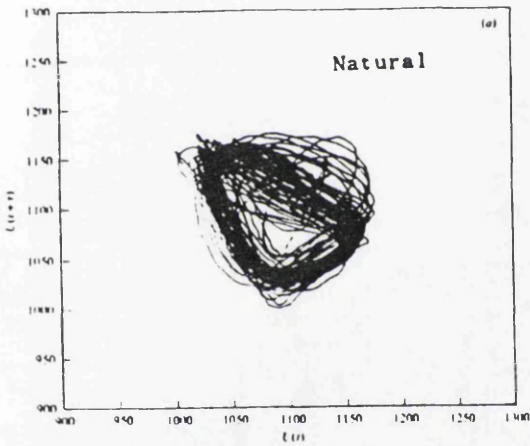


(a) Cross section of Jet at Various Evolution Times (b) Fractal Dimension of Jet Boundary as a Function of Evolution Time

Figure 2-58: The Fractal Nature of a Turbulent Jet (After Aref et al)



(a) A Schematic Diagram of the System



(b) Phase Space Reconstructions of the Natural, Locked and Chaotic Case

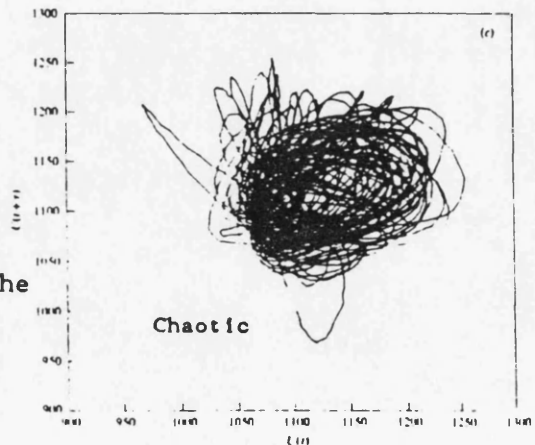


**Figure 2-59: Vortex Shedding Results from an Airfoil**  
(After Williams-Stuber & Gharib)

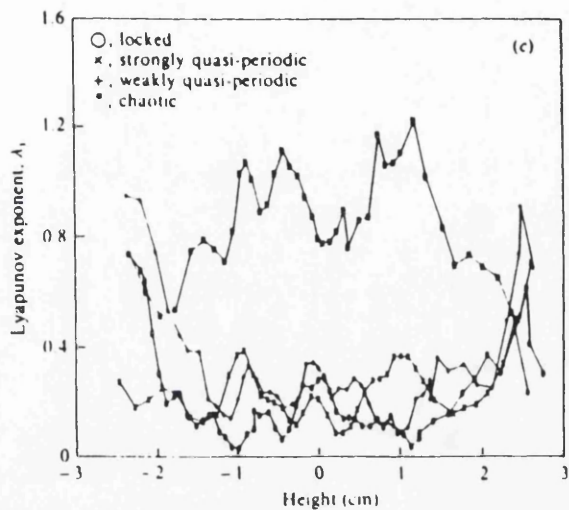
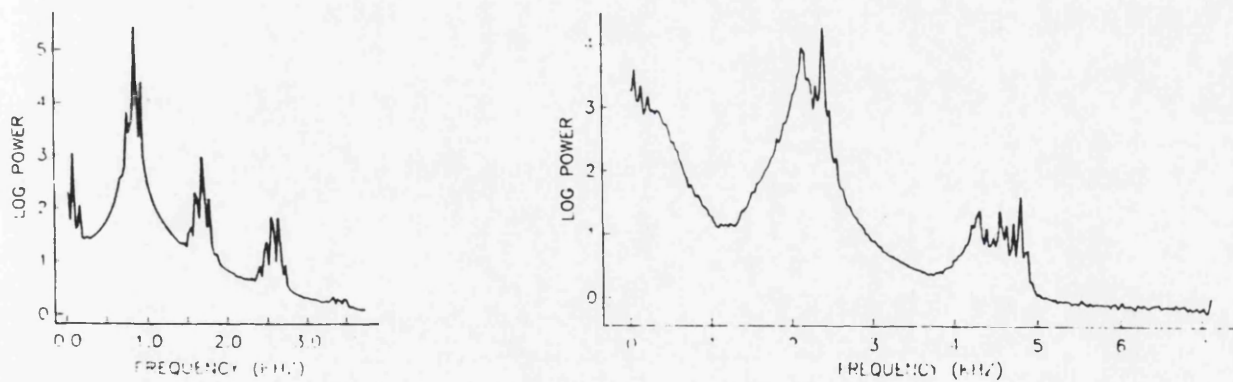


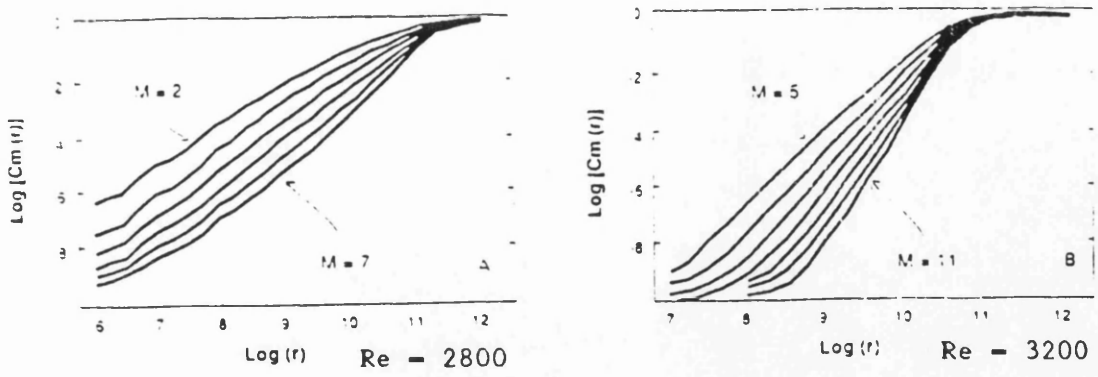
**Figure 2-60; Lyapunov Exponents Taken Across the Flow  
for Vortex Shedding at an Airfoil**



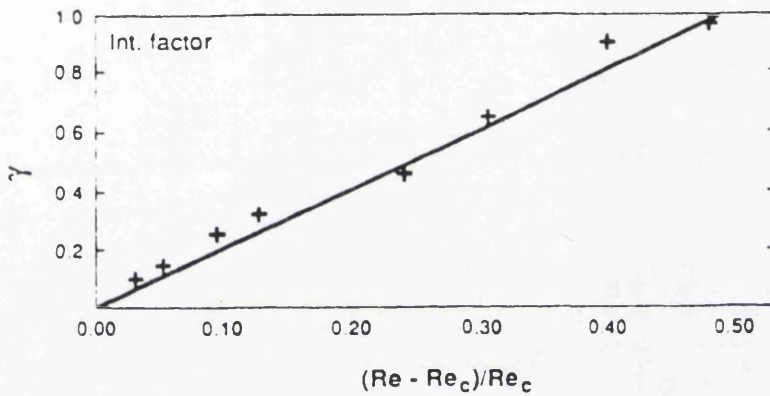
**(a) Spectra for Wake Velocity  
During Ordered Shedding**

**(b) Spectra for Wake Velocity  
During Chaotic Shedding**

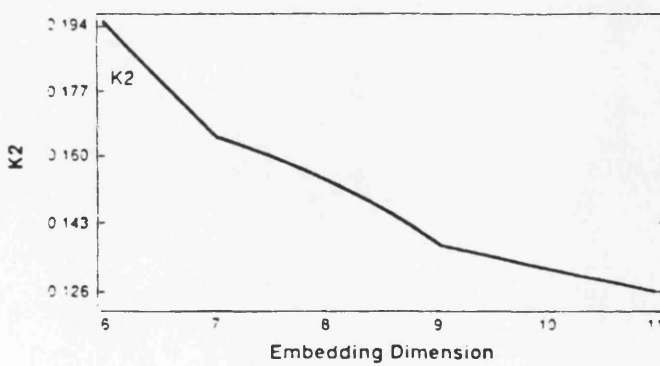
**Figure 2-61; Power Spectra Associated with Vortex  
Shedding at a Cylinder  
(After Elgar et al)**



(a) Correlation Dimension as a Function of Pipe Reynolds Number



(b) Intermittency Factor as a Function of Pipe Reynolds Number



(c) Kolmogorov Entropy Versus Embedding Dimension

Figure 2-62: Intermittent Pipe Flow Results  
(After Huang & Huang)

## CHAPTER 3

## CHAPTER 3

### EXPERIMENTAL APPARATUS

#### 3.1 GENERAL INTRODUCTION

#### 3.2 EXPERIMENTAL APPARATUS

- 3.2.1 General Layout of the Apparatus
- 3.2.2 Design of the Test Rig
- 3.2.3 Water Temperature and Viscosity
- 3.2.4 Laser Table Design
- 3.2.5 Piston Design
- 3.2.6 Entrance Piece Design
- 3.2.7 Pipe Specifications
- 3.2.8 The Orifice Plate
- 3.2.9 Pipe Alignment
- 3.2.10 Pipe Deflection and Expansion
- 3.2.11 Water Tank Specifications
- 3.2.12 Test Procedure

#### 3.3 MOTOR CONTROL

- 3.3.1 Introduction
- 3.3.2 Original Motor-Gearbox Arrangement
- 3.3.3 Modified Motor-Gearbox Arrangement
- 3.3.4 Reduction of Background Noise by  
Physical Means

- 3.3.5 Generation of a Pulsatile Fluid Flow
- 3.3.6 The A.C. Inverter and Function Generator
- 3.3.7 The Drive Shaft Limit Switches

### 3.4 INSTRUMENTATION - THE L.D.A. SYSTEM

- 3.4.1 Introduction
- 3.4.2 Components of the L.D.A. System
- 3.4.3 Principles of the L.D.A. System
- 3.4.4 Experimental Practice

### 3.5 DATA ACQUISITION

- 3.5.1 Introduction
- 3.5.2 Acquisition Hardware
- 3.5.3 Analog to Digital Conversion
- 3.5.4 Computer Specifications
- 3.5.5 Software
- 3.5.6 Sampling and Manipulation of the Data

### 3.6 FLOW VISUALISATION APPARATUS

- 3.6.1 Introduction
- 3.6.2 Light Box Design
- 3.6.3 Experimental Practice

### 3.7 SUMMARY

### 3.1 GENERAL INTRODUCTION

The experimental programme was designed to investigate low Reynolds number flow behaviour in a pipe where an orifice was used to generate coherent vortex structures and turbulence. The regime of flow was pulsatile in order to have optimum control over the experimental flow, vortex shedding downstream at the orifice, and also because of its range of practical applications.

The order of the experimental programme was:

- (a) to use flow visualisation in the elucidation of the phenomena present within the flow, and
- (b) to use the technique of laser Doppler anemometry, (L.D.A.), to pick up the velocity fluctuations in the flow at various points within the pipe, this data being used in subsequent analysis, outlined in Chapter 6.

With these aims in view, a sophisticated experimental test rig was constructed to produce constant average Reynolds number, pulsatile flows in a small diameter pipe, whereby the frequency and amplitude of the pulsating component could be controlled independently of the mean velocity component. Facilities were also provided on the rig to allow both for ease of use of a purpose built light box for the flow visualisation, and the L.D.A. system components. Two micro-computers were used, one for data acquisition and analysis and a second for the control and monitoring of the piston drive motor.

The experimental rig was designed by the author and built from scratch during a period of fourteen months, (from April 1990 to June 1991), during which time many obstacles and difficulties were met, and overcome.

### 3.2 EXPERIMENTAL APPARATUS

#### 3.2.1 General Layout of the Apparatus

The experimental apparatus was constructed within the Civil Engineering department of the University of Glasgow and located in the basement of the

Rankine building. A general view of the complete test rig is shown in figure 3-1. The Laser itself is omitted for clarity and is situated directly opposite side of the pipe from the photomultiplier, (P.M.), tube. A plan view of the apparatus is given in figure 3-2.

The room in which the experimental rig was set up is a purpose built cold room, which is thermally insulated from the rest of the building so that the temperature can be dropped to below 0°C. The room's thermal properties made it ideal for the experiment, as the temperature within the room, and hence the viscosity of the liquid, can be kept constant. The walls of the room were painted mat black, purposely done to minimise the risk of reflections of the laser beams.

### 3.2.2 Design of the Test Rig

It is seen from figure 3-1 and figure 3-2 that the experimental rig consists of a header tank, an accurately machined entrance transition to the pipe, a glass pipe with high tolerance and containing an orifice plate approximately half way its length. The laser equipment is located just downstream of the orifice and has the ability to move very precisely over a two dimensional plane, across and downstream of the flow. The downstream end of the pipe connected with a piston and motor which was specifically designed to draw flow from the header tank at completely uniform rates even though the head in the header tank varied.

An accurately controlled piston was used to drive the flow to and from the tank. Results are taken only when the liquid is flowing from the tank to the piston, as the smooth entrance transition piece inhibits disturbances being propagated, and entering into the flow. The reason for adopting a piston system was twofold. Firstly, it provided means by which repeatable and accurate, constant flow Reynolds numbers could be produced, and, secondly it allowed for pulsations of various frequencies and amplitudes to be superimposed on the mean flow rate. It was felt that a valve system could not satisfy either of these criteria. Flow control using a needle valve arrangement downstream would have been extremely difficult due to the intermittent nature of the flow around the laminar-turbulent transition zone in the pipe. This would have the effect of producing a varying friction factor within the pipe (depending on what proportion of the flow in the

pipe was in a laminar or turbulent state) and hence a varying flow rate. In addition the drop in head at the tank would have diminished the flow rate at the valve, and it was felt that a constant head tank would not be able to contain water still enough for the experiment. It would, therefore, be very difficult to envisage a valve system which could produce a controllable Reynolds number and a pulsating component on the mean flow. Thus, a driven piston was considered to be the only practical method to produce such flows.

The whole experimental apparatus was raised up to a suitable working height on a subframe fabricated from 50×50×5mm steel, square hollow section. Due to its large size and weight the subframe was welded together in five sections in the civil engineering workshop and then these sections were bolted together in situ in the experimental laboratory.

The whole rig rests at a slope of approximately 2.5° during operation. This is done by setting the adjustable feet to the appropriate heights along the length of the test rig. This arbitrarily chosen slope enables air bubbles, which have come out of solution to escape from the pipe during the experimentation.

An attempt was made to insulate the apparatus from vibrations in the floor from other parts of the building. This was done by sitting the top frame of the rig on a 110mm concrete base which itself sits on a 150mm medium density foam cushion, as shown in detail in figure 3-3. Approximate calculations using an experimentally obtained stiffness for the foam indicated that the natural frequency of the rig in the vertical direction was roughly 4.6 Hz. This is well away from the 50 Hz expected from machinery elsewhere in the building. The foam rests upon a 20mm thick plywood base which is attached to the subframe.

The concrete layer was constructed from two interleaved layers of unreinforced concrete slabs. These measured 900×600×55mm and were cut to suit where appropriate. The slabs were connected to the top steel frame by holding down bolts, with a thin layer of rubber sandwiched in between. This arrangement resulted in a rigid top structure onto which the main components of the experimental apparatus were attached.

### 3.2.3 Water Temperature and Viscosity

During the course of the investigation every effort was made to keep the water at a constant temperature of 11°C. This was done to keep the liquid viscosity constant. It was found that the mains supply, from which the water used in the experiment was taken, supplied water at a temperature between 10°C and 11°C. Water at less than 11°C was brought up to the required temperature by adding warm water to it in the tank.

The absolute viscosity,  $\mu(T)$ , of water at a temperature,  $T$ , may be obtained from the following expression of Kashin et al [1978],

$$\log_{10} \left[ \frac{\mu(T)}{\mu(20^\circ\text{C})} \right] = \frac{20 - T}{T + 96} \left[ 1.2364 - 1.37 \times 10^{-3}(20-T) + 5.7 \times 10^{-6}(20 - T)^2 \right] \quad (3.1a)$$

where

$$\mu(20^\circ\text{C}) = 1.002 \times 10^{-3} \text{ kg/ms} \quad (3.1b)$$

This expression is valid within the temperature range,

$$0^\circ\text{C} < T < 40^\circ\text{C}. \quad (3.2)$$

The expression gives the absolute viscosity of water at a temperature of 11°C to be

$$\mu(11^\circ\text{C}) = 1.2699 \times 10^{-3} \text{ kg/ms} \quad (3.3)$$

At this temperature the density of the water,  $\rho_w$ , is 999.6082 kg/m<sup>3</sup>, (according to Kashin et al), thus the kinematic viscosity,  $\nu$ , at 11°C is

$$\nu(11^{\circ}\text{C}) = \frac{\mu(11^{\circ}\text{C})}{\rho_w} = 1.2708 \times 10^{-6} \text{ m}^2/\text{s} \quad (3.4)$$

This is the value of kinematic viscosity used in all subsequent calculations requiring its use, although temperature was controlled and measured on a hourly basis while tests were being conducted.

### 3.2.4 Laser Table Design

A laser table was constructed to allow the laser and photomultiplier tube to be moved easily in the two dimensions of the horizontal plane, i.e. both across the flow and in the direction of the flow. Micrometric movement was achieved with the carriage laterally across the pipe, by which the laser intersection point could be placed nominally to an accuracy of  $0.01\text{mm} \pm 0.005\text{mm}$  in air. Taking refraction of the beam into account, as it passes into the water within the pipe, this corresponds to an accuracy of  $0.013\text{mm} \pm 0.0067$  in the water within the pipe. In the axial direction the intersection point may be located to  $1.0\text{mm} \pm 0.5\text{mm}$ . The table was constructed out of aluminium section for lightness and strength, and the movement in either direction was facilitated by linear bearings. Locking screws in the linear bearings allowed the carriage to be fixed in position if required. This set up allowed longitudinal measurements to be taken from 100mm upstream to 1150mm downstream of the orifice, and laterally across the diameter of the pipe on the horizontal axis.

### 3.2.5 Piston Design

The piston and piston casing dimensions were designed as follows. The maximum required pipe Reynolds number,  $Re_p$ , was assumed to be 2000. (This, for instance, corresponds to an orifice Reynolds number,  $Re_o$ , of 4000 for the 13mm diameter orifice.) This value of  $Re_p$  gives an average velocity in the pipe of 97.75 mm/s. Many variations of the piston casing dimensions were considered. Those eventually chosen were of a stroke length of 360mm and an internal

diameter of 203.2mm, (= 8 inches, so chosen because the piston seals came only in Imperial sizes). The pipe internal diameter being 26mm, gives a ratio of piston to pipe diameter of 7.815, and an area ratio of

$$\frac{A_{\text{piston}}}{A_{\text{pipe}}} = 61.174 \quad (3.5)$$

Using this area ratio, and invoking the continuity condition, results in a piston velocity of 1.60 mm/s, for an  $Re_p$  of 2000. This gives a run time of approximately 225 seconds assuming the piston stroke to be 360mm. This time is long enough for the flow conditions to stabilise and data to be captured. (A data capture run of 16384 points, sampled at 100 Hertz, takes 164 seconds.) As the experiment progressed it became apparent that the maximum pipe Reynolds number required was 640, which gives a run time of 703 seconds. This allowed more time for flow conditions to stabilise and allowed for a few data capture runs to be taken on each stroke, if required. Figure 3-4 gives an overall picture of the piston, piston casing and mountings.

The piston casing was manufactured from a single ingot of external diameter 228.6mm, the internal diameter was bored then honed to a fine finish. This work was done external to the department. The final internal diameter of the piston casing being of  $203.2 \pm 0.023$ mm. The bearing which drives the drive shaft is made from brass and its housing from steel. The piston drive shaft is a brass screwed rod, manufactured in the department for the purpose, and has a pitch of  $3.23 \pm 0.005$ mm. The large sprocket which drives the bearing directly has 80 teeth and is connected to a smaller 40-tooth sprocket, located on the motor drive shaft, by a flexible belt. This gives a 2/1 reduction of the motor output shaft speed to the bearing speed. The piston drive shaft is connected to the rear of the piston.

The piston was fabricated from aluminium in two parts, this allows for the main piston seal to be fitted. The seal selected for use with the piston was a JAMES WALKER- "HYPAK" Type PW 63-800, synthetic rubber seal with nylon end rings. Sealing is achieved by the deformation of the rubber under hydraulic loading, which squeezes the seal against the piston casing internal wall.

Air which has come out of solution is bled from the piston casing by the air bleed valve shown in the figure 3-4. The casing may be drained by a similar valve at the base of the front end wall, from which flexible plastic hose leads to the main drain situated directly under the experimental rig. The pipe is secured to the front of the casing by a water tight rubber O-ring seal which is squeezed tight onto the end flange by the pipe connection flange. The seal was designed to allow for any movement of the pipe due to thermal expansion/contraction and also movement of the tank wall when the tank was filled. These effects are discussed in more detail in sections 3.2.8 and 3.2.9.

The piston casing end walls were fabricated from 10mm thick aluminium plate. They are circular with a diameter of 300mm. The walls are secured to the front and rear of the casing shell by 8x10mm screwed rods running external to the casing. They are secured by bolt fasteners at each end and act, in effect, by squeezing the end walls onto the piston casing. A rubber seal between the walls and the casing ensures a watertight seal. The piston casing is mounted, via the end walls, onto a 20mm thick aluminium plate which also serves to secure the motor to the top frame of the rig.

### 3.2.6 Entrance Piece Design

An entrance piece was required to give a smooth transition from the still water in the tank to the flowing water in the pipe. The transition shape had to be tangential with the walls of the pipe and the tank, and so an ellipse was chosen as shape of the transition piece. The entrance piece design can be seen in figure 3-5. The major axis length is 156mm and the minor axis length is 52mm, this giving a ratio of 3:1.

A computer controlled lathe was used to bore out the entrance piece profile. However, due to the difficulty of having an elliptic shape machined, the shape was approximated by four arcs of circles of different radii which all met each other and the walls tangentially. It was felt that this pseudo-elliptic shape was an accurate enough approximation for the purposes of the investigation. The entrance piece is fixed to the tank by sixteen 5mm threaded screws, and is secured to the

pipe, in a similar manner as with the pipe–piston connection. That is a watertight rubber O–ring seal is squeezed tight onto the pipe by an end flange connected to the entrance piece.

### 3.2.7 Pipe Specifications

The pipe used in the main experiment was constructed from four 1.00m lengths of high precision piping manufactured by Pilkington, with a nominal internal diameter of 26.00mm and a nominal external diameter of 30.00mm, i.e. a wall thickness of 2.00mm. Accurate measurements of the glass pipe by the author found the average internal diameter of the glass pipe to be  $25.98\text{mm} \pm 0.01\text{mm}$ . The average external diameter of the pipe was found to be  $30.15\text{mm} \pm 0.08\text{mm}$ . The diameters were measured at four equi–angular positions around the pipe to check for ovality of the pipe. For a specific location along the pipe, the maximum variation in measured internal diameter was found to be less than 0.01mm and for the external diameter it was found to be 0.04mm.

The 1.00m lengths of glass piping were joined together at the necessary positions by pipe coupling connections, as illustrated in figure 3–6. The pipe was supported on six, specially made aluminium pipe supports which allowed fine movement both in the horizontal and vertical plane. A locking mechanism was also incorporated into their design which allowed the setting of each one to be permanently fixed. Their design is illustrated in figure 3–7.

### 3.2.8 The Orifice Plate

The orifice under investigation was placed at the mid point of the pipe, i.e. 2.00m from the entrance piece and the piston. This distance of 2.00m was sufficient to allow a fully developed laminar flow profile (Hagen–Poiseuille flow) to establish itself within the pipe. According to the theory of Freidmann et al [1968], the entrance length  $Z_e$ , (defined in chapter 2, section 2.2.9), is given by the simple relationship,

$$Z_e = 0.056 D_p \cdot Re_p \quad (3.6)$$

Thus the maximum pipe Reynolds number of 640, used in the investigation, results in an entrance length of 930mm. In addition, the theory assumes a flat velocity profile at the pipe entrance, whereas in the experiment outlined here the profile will already be distorted by the entrance piece before it enters the pipe. This should cause the development of Hagen–Poiseuille flow to occur nearer to the pipe entrance than predicted by theory.

Six different sizes of orifices were used during the investigations, and these were made from brass. The orifice diameters were, in ascending order: 6.50mm, 9.75mm, 13.00mm, 16.25mm, 19.50mm and 22.75mm, or to put them in terms of the pipe diameter 'D': 2/8D, 3/8D, 4/8D, 5/8D, 6/8D and 7/8D, (i.e. integer multiples of an eighth of the pipe internal diameter). All orifices were 0.5mm thick and were of a flat edge type. The orifices comply to the design criteria of B.S. 1042 : 1989, Sections 1.1 and 1.2, which deals with the measurement of fluid flow in closed conduits using pressure differential devices. However, the slow flows being investigated herein are quite different from those covered by the standard which deals solely with fully turbulent flows at pipe Reynolds numbers in excess of 5000. The standard was used merely as a guide for the manufacture of the orifice plates.

The pipe slots into the orifice plate lip and thus locates itself concentrically with the orifice. The orifice is held in position by two end plates, figure 3–8. One of the end plates has a long flange to ensure that the plane of the orifice aperture is perpendicular to the pipe central axis, (i.e. to allow the pipe central axis and the orifice plate central axis to correspond). One drawback of the long flange is that it denies access to that part of the pipe it covers, both from the laser and from flow visualisation methods. The flange was positioned in the upstream direction as the main emphasis of the work was to elucidate the resulting downstream phenomena due to the presence of the orifice plate.

Each orifice plate has a small hole drilled in it which allows for the bleeding of air, which is trapped downstream of the orifice plate. This air hole is capped by a rubber seal which is held in position by a screw and washer. During the

course of the experimentation, however, a much quicker and more effective method was found for expunging the air trapped downstream of the orifice plate. This was done by simply blowing air sharply into the piston chamber via the front air bleed valve on the piston casing front wall. This causes a small volume of water to be accelerated quickly in the pipe in the upstream direction and through the orifice. It was found that this was of sufficient strength to force the trapped air through the orifice with it.

### 3.2.9 Pipe Alignment

Great care was taken during the alignment of the four, one-metre sections of glass pipe to ensure that they followed a true line, both in the horizontal and vertical planes.

The vertical alignment of the pipe was ensured by the use of a level. Levels were taken at each end of the pipe sections as they initially lay in the pipe supports prior to adjustment as shown in figure 3-9. The rise in level between A and E ( $\Delta H$ ) was determined, and knowing the value of the horizontal distance from A to E, namely ' $X_e$ ', the required gradient could be found. Using this value and knowing the distances to the points B, C and D, the heights of these intermediate points required for a true linear alignment could be calculated. The difference between these calculated values and the actual values observed is the error in alignment.

The errors at sections B, C and D, (see figure 3.9), were calculated from the levelling data, then the pipe supports were then adjusted to correct for the discrepancies between the true alignment and the actual alignment. The levels of the pipe ends were then checked and the process of adjustment repeated at each end until the levels at B,C and D were equal to those required to within 0.25mm.

The horizontal alignment of the pipe was also performed with the aid of the level, together with three short sighting-rods. These straight sighting-rods were attached to heavy, copper half-collars with which they could be made to sit upon the pipe. The procedure for the horizontal alignment of the pipe sections was then conducted as follows.

One of the sighting-rods was placed at each end of the pipe. The level was then set up so that the vertical cross wire was aligned with the edges of both rods. This ensured that both rods were truly vertical, and it gave a straight site line between them on which the rest of the pipe was aligned. The method is shown pictorially in figure 3-10.

The third sighting rod was then placed at successive intermediate positions on the pipe next to the pipe supports. The supports were then adjusted in the horizontal direction until the intermediate rod came into alignment with the other two. This was repeated at each pipe support until all sections of the pipe came into alignment.

### 3.2.10 Pipe Deflection and Expansion

The theoretical deflection of the pipe between supports was checked. This was done for a glass walled pipe containing water, and using an estimated Young's modulus for the glass,  $E_g$ , of  $71 \times 10^9$ , [Haward, 1949]. Taking the density of the glass,  $\rho_g$ , and the density of the water,  $\rho_w$ , respectively to be  $2600 \text{ kg m}^{-3}$  [Tennent, 1986] and  $999.61 \text{ kg m}^{-3}$  [Kashin et al, 1978]. The mass per unit length of glass pipe filled with water is then

$$W = g \rho_g A_g + g \rho_w A_w \quad (3.7)$$

Where  $g$  is the constant of gravitational acceleration and is equal to  $9.81 \text{ m s}^{-2}$ . The cross sectional areas of the glass,  $A_g$ , and the water,  $A_w$ , may be easily calculated, knowing the external radius of the pipe,  $R_1$ , to be 15mm and the internal radius,  $R_2$ , to be 13mm, (see figure 3-11). Thus the mass per unit length,  $W$ , is  $9.695 \text{ N m}^{-1}$ .

To give an indication of the magnitude of expected deflections that may occur due to this loading, calculations were performed for a worst case situation, which was that of each pipe section supported at its ends only and the end conditions assumed to be pin jointed. (This worst case does not occur in reality on the rig as the pipe supports are closer together than the pipe section lengths of 1.00m).

The deflection,  $\delta$ , at the mid span of a pin jointed beam element may be calculated from the following expression,

$$\delta = \frac{5 W L^3}{384 E_g I_{xx}} \quad (3.8)$$

where  $I_{xx}$  is the second moment of area of the section and may be calculated for the glass pipe wall thus,

$$I_{xx} = \frac{\pi}{4} [R_1^4 - R_2^4] = 1.7329 \times 10^{-8} \text{ m}^4 \quad (3.9)$$

The deflection at the midpoint between supports was calculated, using expression 3.8, to be 0.103mm. This value was taken to be well within the acceptable tolerances of the pipe line. However, this figure serves only to give a feel for the magnitude of the deflections that may occur. Since the pipe sections are not supported at each end, may not behave as pin jointed elements and the weight of the pipe couplings and orifice plate has been ignored.

As the pipe is filled with water at the beginning prior to an experimental test, the pipe wall changes in temperature from the ambient room temperature to that of the cold fluid within it. Therefore, it seemed prudent to attempt to estimate the thermal expansion of the pipeline during the filling process.

The maximum room temperature recorded was 27° Centigrade and considering the water temperature to be 11°C, this gives a maximum difference in temperature experienced by the pipe,  $\Delta T$ , of 16°C. The coefficient of thermal expansion of glass,  $C_t$ , was taken to be  $9 \times 10^{-6} \text{ } ^\circ\text{C}^{-1}$ , [Tennent, 1986]. Thus the strain experienced by the material,  $\alpha$ , may be calculated from the following relationship,

$$\alpha = \Delta T \cdot C_t \quad (3.10a)$$

by substituting the above values we find obtain,

$$\alpha = 0.000144 \quad (3.10b)$$

thus for a 4.00m length of pipe,  $L$ , the expected change in length,  $\Delta L$ , is

$$\Delta L = L \cdot \alpha = 0.000576m \quad (3.11)$$

Thus the maximum probable change in length experienced by the pipe during filling is 0.576mm. Note, however, that this is a contraction, since it is a temperature drop. This should serve to accommodate somewhat the movement in the pipe caused by the tank walls expanding outwards when filled, as discussed in the next section.

The glass pipe was at its most vulnerable when it had been reassembled after cleaning and great care was taken to ensure that all the pipe joints (i.e. at the entrance piece, at the piston, at the pipe connections and at the orifice) were slackened off during filling at this initial stage. All pipe breakages, of which there were five in number, were incurred at this stage. The ends of the pipe sections were susceptible to chipping at the slightest knock, and care had to be taken during the reassembling process to avoid this.

Pipes were replaced due to either breakages or excessive chipping of the ends, as described above. New pipe sections were placed in position downstream of the orifice, thus the section of pipe where most of the results were taken always had the newest section of pipe. The next best section of pipe being placed just upstream of the orifice where the remaining results were taken.

### 3.2.11 Water Tank Specifications

The header tank which contains the water for the experiment measures 700×700×700mm internally and has a capacity of 343 litres. The two side walls are made from 10mm thick perspex allowing the inside of the tank to be visible. This serves three purposes. Firstly, the inner walls of the tank can be inspected daily for bacterial and algal growth. Regular, weekly cleaning of the tank (and pipe) eliminated the build up of these undesirable deposits. Secondly, the water inside

the tank can be visually inspected to see that it is still enough to start an experimental run. Finally the water inside the tank can be inspected to ensure that the flow visualisation chemical is homogeneously mixed prior to a run. The front and rear tank walls and the base are manufactured from 10mm thick aluminium, to ensure rigidity of the structure during the filling of the tank. The top of the tank has a large lid allowing access to the tank for cleaning and adding the flow visualisation agent into the water.

Originally the tank was to be filled from the top, a valve and piping was fitted for this purpose. However, it was quickly realised that this method of filling entrained a substantial quantity of air into the liquid, some of which came out in the pipe during the experimental runs. To this effect, the tank is slowly filled from a hole in the bottom corner next to the front wall, this procedure results in a minimum of air entrained in the solution. The tank is drained by a hole at the other corner adjacent to the front wall. The maximum difference in head at the tank for an experimental run, where the piston takes a full stroke, is 23.8mm.

Some time was spent measuring the deflections of the tank walls while the tank was filled with liquid. A knowledge of wall behaviour, particularly the front wall, was critical as any wall movement would have to be accommodated within the pipe joint at the piston. This joint would have to be flexible enough to ensure ease of movement of the fragile glass pipe and also be secure enough to effectively seal the pipe at the piston. Deflections were measured at the centre of each wall as the tank was filled in 100mm increments. The results showed that the aluminium walls deflected much less than those made of perspex, as one would expect. The results of the tests are shown in table 3.1. (Note that these tests were performed on the tank prior to the hole for the entrance piece being formed at the centre of one of the aluminium walls.)

The aluminium walls initially deflected inwards up to 0.031mm, this for a water depth of 300mm. When the tank was full, i.e. at a depth of 700mm, the aluminium walls deflected outwards by a maximum of 0.233mm. This gives an overall possible movement of the aluminium wall of 0.264mm. The perspex walls initially deflected inwards to a maximum of 0.078mm, for a water depth of 100mm. When the tank was full the perspex walls had deflected outwards by maximum value of 5.450mm, giving an overall possible deflection for the perspex

walls of 5.528mm. This knowledge of wall behaviour, particularly the front wall, was critical, as any wall movement would have to be accommodated within the pipe joint at the piston.

Once the rig was constructed and operational the deflections experienced at the front wall entrance piece were measured. The overall deflection experienced by the pipe, when the tank is filled with water, was found to be 0.210mm. This is approximately 20% less than the value obtained during the test (0.264mm). However, this is a reasonable result as the initial tests were performed on the aluminium wall centre without the entrance piece in place.

WATER DEPTH (mm)	Perspex Wall Deflection (mm)	Aluminium Wall Deflection (mm)
0	0.000	0.000
100	-0.078	-0.007
200	-0.073	-0.023
300	0.573	-0.031
400	1.503	0.007
500	2.833	0.097
600	4.285	0.160
700	5.450	0.233

**Table 3.1 – Tank Deflection Test Results**

### **3.2.12 Test Procedure**

The investigation set out to shed light upon the breakdown of forced vortex flows at a pipe orifice. For the purposes of this investigation the pulsating component of the flow, at which frequency the vortices are forced, was always set to the natural frequency of the orifice plate at the specific Reynolds number being investigated. Thus, the actual parameters varied in the investigation were:

- 1 – The orifice diameter.
- 2 – The Reynolds number of flow in the pipe.

3 – The forcing amplitude of the fluctuating flow component.

Although the option remains, for subsequent research work to be performed with forcing frequency set to values other than the natural frequency of the orifice, in the work outlined in this thesis only the natural frequency of the orifice plate was used.

Two methods were used to elucidate the flow phenomena present within the pipe. These were qualitatively by flow visualisation and quantitatively by Laser Doppler Anemometry.

The flow field at various positions of the pipe was initially observed visually using flow visualisation techniques. (See section 3.6) This gave a qualitative insight into the flow processes involved at, or near, the orifice plate. This was done for the same system parameters as used in the L.D.A. study.

After the flow visualisation had taken place the velocity values of the flow were taken at various positions upstream and downstream of the orifice plate. After much initial testing both in terms of the L.D.A. system, and with the aid of flow visualisation, it was decided to take the L.D.A. readings at fixed distances from the orifice plate for all values of flow parameters. These distances are:

- 1 – upstream of the orifice plate, 90mm, 75mm, 50mm and 35mm. (90mm being the maximum distance that the laser carriage may traverse up the pipe, and 35mm being the nearest upstream distance to the orifice that may be located by the Laser beams due to the presence of the of the orifice end plate flange.)
- 2 – downstream of the orifice plate, 10mm, 20mm, 30mm, 40mm, 50mm, 60mm, 75mm, 100mm, 150mm, 200mm, 250mm, 500mm and 950mm. The majority of the readings were taken close to the orifice plate, i.e. less than 100mm, where most of the flow processes take place.

Thus seventeen readings were taken for each set of flow parameters, these readings were taken on the pipe centre-line. The time taken to take one such set of seventeen readings took on average two full working days. The time required depended very much upon the flow parameters under investigation, as the tracker system was very sensitive to large abrupt fluctuations in flow velocity and the presence of these could cause dropouts in the signal. In such circumstances many runs would be required to get an acceptable set of flow data for that L.D.A.

position.

Although most of the L.D.A. readings were taken at the pipe centre—line, towards the end of the experimental programme a few tests were taken at various L.D.A. positions across the flow. These details of which are discussed in more detail in chapter 6.

### 3.3 MOTOR CONTROL

#### 3.3.1 Introduction

During each experimental run it is essential that both the time averaged flow Reynolds number and the amplitude and frequency of the pulsating component of the flow be controlled with some degree of precision. This requires that the motor speed, including the fluctuating component, is controlled accurately for the duration of each specific run. It is also necessary that the motor output can be altered from run to run. The speed of the motor used to drive the piston was controlled using an A.C. inverter and a function generator. A three phase, 340 volt, 50 Hz supply enters the inverter and outputted is a three phase, 340 volt, variable frequency supply. The inverter allows the load on the motor to be continually monitored and the input frequency to the motor to be set to within  $\pm 0.05$  Hz. It was found during the experimentation that, once set, the motor output remained constant for that particular setting, from run to run.

Preliminary results taken during the spring and summer of 1991 indicated that the motor, which drives the piston, introduced stray frequencies into the flow. This was first discovered with the pipe set up without an orifice. However once an orifice was introduced into the system, it soon became apparent that the frequencies of the vortex shedding from the orifice were being influenced by these stray motor frequencies. The following sections give details of these effects and the measures taken to solve the problem.

### 3.3.2 Original Motor–Gearbox Arrangement

In the original experimental set up, an inherited A.C. motor and gear box unit was used. Previous to it being utilised for the work outlined here, it was employed as part of a wave generating device on an open channel flow flume. Within the housing of the unit, the electric motor is connected to a variable speed or Kop gear box, this is in turn connected to a fixed gear box, having a reduction ratio 30/1. A schematic diagram of the overall arrangement used to drive the flow is given in figure 3–12. The output shaft from the second gear box could be driven at speeds in the range 15 to 90 R.P.M. for an input frequency of 50 Hz to the motor. With a proportional reduction in speed for input frequencies from the controller of less than 50 Hz. Thus this arrangement had two means of output speed control through the Kop gearbox and through the controller.

However, it soon became apparent that this arrangement introduced stray frequencies into the flow. The main rogue frequencies were found to be related to both the output shaft rotational speed and the electric motor rotational speed. Other lesser frequencies appeared in the flow and their possible cause remained unclear. The rate of one of the cyclic variations was 30 times the output shaft frequency. After much investigation, (which included stripping down the gearbox several times), it was reasoned that this was probably due to an eccentricity of the shaft connecting the Kop gear to the fixed gear. The other main rogue frequency was either equal to, or half of, (or both), the motor rotational speed, depending on the driven flow rate. The overall effect of these ripples in the motor output speed, was to cause a variation in the mass flux of the flow as the piston was withdrawn. Thus a many frequency, pulsatile flow was being produced that could not be controlled independently of the motor output speed and hence the Reynolds number of the flow.

These stray frequencies were picked up in the preliminary investigations of Hagen–Poiseuille flow, in the pipe without an orifice. Whereas the actual laminar flow should have no frequencies. If the flow was driven without a superimposed fluctuating component then the rogue frequencies, in certain circumstances, controlled the vortex shedding at the pipe orifice. More details on this phenomena are contained in the 2nd Year Progress Report by the author, [Addison, 1991].

Some considerable effort was expended trying to eliminate the effect of these stray frequencies by physical means, (or at least reduce them to a point where they no longer interfered with the results). The problem was to find where exactly they came from and what could be done to solve the problem.

Many means were used to try and find out their cause and reduce their effect. These include:

- 1 — The use of a various thick, highly viscous oils in the Kop gearbox to smooth out fluctuations in displacements.
- 2 — Stripping down and extensively cleaning the moving parts of the motor gearbox arrangement, to remove foreign bodies which may be causing variations in internal clearances.
- 3 — Fitting of flexible motor mountings between the motor and the base plate, see figure 3-14b.
- 4 — Varying the tension on the belt drive between the motor output drive shaft sprocket and the piston drive shaft sprocket.

All these measures showed no real improvement whatsoever and thus it was eventually decided to obtain a new motor for the rig.

### 3.3.3 Modified Motor—Gearbox Arrangement

A new motor was purchased for the experimental rig, (a FENNER gearmotor, model 981-1806.) This unit has no variable gearbox, with the electric motor connected directly to a fixed gearbox which gave a nominal output shaft speed of 37 R.P.M. The arrangement is shown schematically in figure 3-13. As there is no variable gearbox, the only means of control in this arrangement is through the inverter—signal generator set-up. This arrangement gave a much smoother performance. However, stray frequencies were still to be found in the flow, although, their effect was much smaller than those from the original motor—gearbox arrangement. The stray frequencies were completely drowned out by the fluctuating flow component generated by the signal generator and therefore did not affect the main experimental results. Stray frequencies, it seems, must therefore be expected in flows driven by such mechanical means, and the experimentalist's task is to try and limit their effect as far as possible.

### **3.3.4 Reduction of Background Noise by Physical Means**

Various methods were employed in an effort to reduce, by physical means, the general background noise level of the results. These included:

- 1 - Increasing the mass of the piston casing by placing heavy weights upon it to alter its frequency response characteristics.
- 2 - Dampening the pipe along its length, with sponge placed between it and the drip tray.
- 3 - Leaving an airpocket within the piston casing when running the experiment to dampen vibrations.
- 4 - Using flexible mountings for the connection of the motor to the rig, as used in an attempt to reduce the amplitude of the stray frequencies of the original motor set-up. Best results were obtained from mountings made from a sandwich of rubber and dense foam, see figure 3-14b.
- 5 - Inserting approximately 40mm of sponge at the end of the pipe just before the piston, see figure 3-14a.
- 6 - Placing rubber strips between the piston casing and the screwed rods, which hold the end plates in position, to stop the screwed rod vibrating.
- 7 - Stiffening up the piston casing support by the addition of angle brackets.

Methods 1, 2 and 3 had no noticeable effect on the background noise level. However, the other methods had varying degrees of success in lowering the background noise level. Most noticeable of which was the placing of sponge within the pipe at the entrance to the piston, (method 5). This seemed to inhibit noise, being propagated from within the piston casing, travelling up the pipe.

### **3.3.5 Generation of a Pulsatile Fluid Flow**

Four options were considered to put a dominant frequency into the flow and trip the vortex shedding at the orifice. They are as follows.

- 1 - Sinusoidal variation of the input signal to the motor. This could be done by putting a signal generator into the system, which could vary the motor speed at the required frequencies. This in turn would impose a variation in mass flux of the flow in the pipe.
- 2 - Sinusoidal forcing of the water in and out of the piston casing. As with the

above system this would impose a mass flux variation on the flow coming down the pipe. The exact variation would be easy to calculate using the continuity condition. Practical considerations would tend to suggest that this would be a very difficult system to manufacture.

3 - Vibration of the orifice. Some mechanism could be employed to vibrate the orifice. However, the mass flux rate would not be affected and it would be difficult to achieve a symmetric vibration of the plate. Also during flow visualisation it was noticed that tapping the orifice quite stiffly did not effect the vortex shedding frequency.

4 - The use of existing motor vibrations. The existing rogue motor frequencies,  $f_{m1}$  and  $f_{m2}$  could be employed. The value of the rogue frequencies could be changed for a specific Reynolds number by changing the gear sprocket between the motor and the drive shaft. Thus with a few sprockets of different diameters, various frequencies could be introduced into the flow, and the effect thereof could be monitored. A major problem with this method is that although the rogue frequencies may be well defined, their amplitudes cannot be controlled.

Method one was employed as it provided a simple and controllable way to generate the pulsation components within the flow. A minor modification to the A.C. Inverter's control circuit was required.

### 3.3.6 The A.C. Inverter and Function Generator

A JAGUAR variable frequency inverter, type 400 was employed to drive the motor. A software package (C.C.D.) was supplied with the inverter which allows for both monitoring and controlling its output using the OPUS-V personal computer. However, the C.C.D. software is unable to add a fluctuating component to the motor speed. Therefore, the inverter was adapted to facilitate its control by a signal generator, set manually for the duration of each run.

The signal generator used for the task of driving the inverter was a BLACK STAR - JUPITER 500 FUNCTION GENERATOR, (see figure 3-15a). The D.C. offset controls the average motor speed, and hence the average pipe Reynolds number. The fluctuating flow component is set using the frequency and amplitude controls of the generator.

The output frequency of the function generator was checked by running the apparatus, taking Laser measurements of the flow in the pipe, then plotting out the frequency spectrum. If the frequency was in error, the fine adjustment dial of the function generator was adjusted and another frequency spectrum was produced. This process was repeated until the frequency was that required by the flow conditions. The amplitude of the function generator signal was set by monitoring the signal generator output using a SCHLUMBERGER – 7151 COMPUTING MULTIMETER, (figure 3–15b).

### 3.3.7 The Drive Shaft Limit Switches

The procedure for changing the direction of the piston at the end of each stroke is as follows:

- 1 – At the end of each piston stroke the drive shaft trips a limit-switch, located within the drive shaft cover, which switches off the current from the inverter.
- 2 – The operator then manually switches the direction of the motor on the inverter front control panel and over-rides the limit switches, setting the piston in motion in the opposite direction.

There are a further set of limit switches which the shaft will trip if it accidentally continues moving in its previous direction, these switches activate the external trip in the controller and cut off the power. This mechanism acts as a fail-safe and prevents the piston from running into one of the casing end walls and possibly causing damage to either the piston or the motor. An emergency stop button is located on top of the drive shaft cover, this activates the external trip within the controller when depressed. The drive shaft cover is situated behind the piston rear wall and above the motor.

## 3.4 INSTRUMENTATION – THE L.D.A. SYSTEM

### 3.4.1 Introduction

The technique of Laser Doppler Anemometry (L.D.A.), (also known as Laser Doppler Velocimetry), has been used in experimental flow situations since the mid 1960's. The technique is now commonplace in experimental flow set ups.

The prime advantage of the L.D.A. system is that there is no flow interference from the procedure, i.e. it is a purely optical process. This is not the case with the traditional hot-wire anemometry method, used for finding velocities of flows. This method interferes with the flow, due to its physical presence within the fluid, and thus changes slightly the flow conditions. See for example the comparison between the two methods by Lau et al [1981]. Another advantage of the laser system is that the output information of the velocities is given as a linear function of the actual velocities. The L.D.A. system also enables high spatial and temporal resolution of the flow phenomena.

### 3.4.2 Components of the L.D.A. System

The components of the L.D.A. system are shown in figure 3-16, and are as follows:

- 1 – A DISA LDA 03 He-Ne Laser unit which produces two laser beams with a wavelength of 632.8 nm. These beams intersect in air at a distance of 300mm from the front lens of the laser unit, at an angle,  $\theta$ , of 11.42°.
- 2 – A DISA Photomultiplier unit, which picks up the scattered laser light from particles in the flow and converts this into a detector current which is in turn picked up by the frequency tracker.
- 3 – A DISA 55N20 Doppler Frequency Tracker, this demodulates the detector current and converts it into an analog output voltage which is directly proportional to the velocities in the control volume. This analog output is then sent, via an analog to digital converter, to the IBM personal computer for analysis.

### 3.4.3 Principles of the L.D.A System

L.D.A. basically measures the rate of change of phase (= frequency) of lightwaves after scattering from particles in the fluid, known as seeding particles. These particles must be small enough to track the flow accurately, yet large enough to scatter sufficient light for the proper operation of the photodetector, [Durst and Ruck, 1987]. It was found that the natural particles occurring in the mains water, used for the experimental investigation, were of sufficient size and concentration for the L.D.A. system. A fact which has been previously found to be true by Lewis et al [1968], who investigated flows in pipes at the transition between laminar and turbulent flow.

The intersection of the laser beams occurs at the point of minimum beam waist thickness (i.e. the beam diameter) and forms a region known as the probe volume. In the probe volume fringes are formed due to the intersection of the plane wave fronts of the monochromatic laser beams, see figure 3-17a. The distance between fringes  $\delta_f$ , may be calculated from a knowledge of the wavelength of the laser light,  $\lambda$ , and the half angle between the two beams,  $\Theta/2$ , as follows,

$$\delta_f = \frac{\lambda}{2 \sin \left[ \frac{\Theta}{2} \right]} \quad (\text{m}) \quad (3.12)$$

Particles in the flow entering this volume with a velocity  $U_z$ , scatter the laser light. This scattering is picked up by the P.M. tube at a Doppler frequency  $f_D$  which is proportional to the flow velocity  $U_z$ . ( $f_D = (f_{s1} - f_{s2})$ , and  $f_{s1}$  and  $f_{s2}$  are scattering frequencies in the directions of the two beams.) Figure 3-17b gives a diagrammatic view of the process. The Doppler frequency is related to the flow velocity by the following relationship,

$$f_D = \frac{U_z}{\delta_f} = \frac{2U_z}{\lambda} \sin \left[ \frac{\theta}{2} \right] \quad (\text{Hz}) \quad (3.13)$$

$f_D$  is picked up by the tracker from the P.M. tube signal. Note that the Doppler frequency  $f_D$  does not differentiate the flow direction. Thus  $U_x$  and  $-U_x$  give the same result. This may be remedied by the addition of a Bragg cell module within the laser optics. A Bragg cell acts by introducing a fixed frequency shift  $f_{(\text{fixed})}$  between the two laser beams. The resultant Doppler shift  $f_D$  will add to or subtract from the fixed frequency shift, this enables the signal processor to distinguish between negative and positive flow directions.

The information about the flow velocity is picked up by the photomultiplier and sent to the tracker unit as a frequency modulation of the detector current. The tracker must be set to a suitable frequency range for the flow velocities under investigation. This is done using a switch on the front control panel of the tracker unit. The relevant frequency range is found by determining the maximum likely flow velocity to be encountered, and using the above expression to calculate the maximum expected Doppler frequency. The frequency range set on the tracker unit is then the lowest range which encompasses the maximum expected Doppler frequency. The output voltage from the tracker,  $V_o$ , is simply the ratio of the two frequencies multiplied by 10.0 volts. If we denote the maximum of the frequency range by  $f_R$  then the output voltage corresponding to a Doppler frequency  $f_D$  is,

$$V_o = \frac{f_D}{f_R} \times 10.0 \quad (3.14)$$

An obvious result is that the frequency range,  $f_R$ , set on the controller, is that which utilises to the full the output voltage range of 0.00 to 10.00 volts.

A knowledge  $V_o$  (output from the tracker),  $f_R$  (set by the operator)  $\lambda$  (632.8nm) and  $\theta$  (11.42°), enables  $U_z$  to be calculated as follows,

$$U_z = \frac{f_R V_o}{10.0} \times \frac{\lambda}{2.0} \times \frac{1}{\sin \left[ \frac{\theta}{2} \right]} \quad (3.15a)$$

$$U_z = 3.18 \times 10^{-7} \times f_R \times V_o \quad (3.15b)$$

This calculation is performed by the IBM personal computer on the digitised input of the tracker output voltage as described in section 3.5. Thus a time series of the flow velocities is obtained.

#### 3.4.4 Experimental Practice

The L.D.A. system requires a substantial amount of fine tuning during data sampling runs. The tracker must be locked on to the photomultiplier signal throughout the run, this is indicated by a green L.E.D. on the tracker control panel. The input current must be held at a constant 5.0  $\mu$ A. for the duration of each run, and the voltage across the P.M. tube must be held at a constant 1.00 K.V.

The beam intersection point was located at the pipe centre line by the following procedure.

- 1 - The laser table was set up so that the beams intersected at the outer wall face of the pipe.
- 2 - Then the micrometer was used to move the laser by the amount necessary to locate the beams at the centre of the pipe. The amount of movement can be calculated from a knowledge of Snell's law, as follows

$$\frac{\sin (\theta_i)}{\sin (\theta_r)} = \frac{N_r}{N_i} \quad (3.16)$$

Where i and r refers to the incident and refracted beams,  $\theta_i$  and  $\theta_r$  are the

angles of incidence or refraction respectively, and  $N$  is the refractive index of the medium that the beams are passing through. The refractive indices used in the experiment were:

- Air -  $N_a = 1.000$  (Tennent, 1986)
- Water -  $N_w = 1.333$  (Tennent, 1986)
- Glass -  $N_g = 1.473$  (Supplied by the manufacturer)

This method was checked by running the experiment without an orifice. The velocity profile in this case is parabolic corresponding to axisymmetric Hagen–Poiseuille flow. At the centre of the pipe one would expect to find the velocity maximum. Readings were taken at the centre as found by the method outlined above then the point of beam intersection was moved in either direction across the pipe to ensure that the velocity found at the centre–line was a maximum. Results showed consistently that the velocities obtained were a maximum at these points and it would indicate that this method is indeed satisfactory in locating the pipe centre line and placing the laser probe volume upon it.

An alternative method to locate the centre–line is to intersect the beams on the outer pipe wall at both sides of the pipe, noting the micrometer position. Then the centre of the pipe may simply be found by finding the mid position of the two readings. However, this method was not used as the micrometer only measured to 30mm which is the nominal diameter of the pipe. This leaves no room for manoeuvre when taking the measurements.

It had been hoped, prior to building the apparatus, that once set in position, the laser carriage would be able to keep the intersection point of the beams on the centreline, as the carriage was moved in the upstream and downstream directions. However, this was not achieved in practice. The reason for this was twofold. Firstly, the main runner bars, on which the carriage traversed in the axial direction of the pipe, were subject to slight bending. This bending depended on the position of the carriage, and thus varied as the carriage was moved up and down the pipe. Secondly, the process of regularly cleaning the pipe caused the pipe alignment to change slightly with respect to the carriage rails. As it involved taking the pipe sections out of position to clean them, reassembling the sections and then realigning the pipe. It was, therefore, easier to find the pipe centre–line

for the position of each L.D.A. reading and make a note of these, then adjust the carriage accordingly at each point.

The laser was set at the correct angle with respect to the pipe by a simpler method. In theory, when the system is set up properly, the beams from the laser should be on a line coincident with the diameter of the pipe, that is the plane of the beams passes through the pipe centreline. On leaving the front optics of the laser, the beams pass through the pipe wall for the first time, then through the liquid, and then through the pipe wall again on the way to the photomultiplier, as shown in figures 3-18a and 3-18b. However, if the laser is displaced slightly it is very easy for the plane of the beams not to be coincident with the pipe diameter, figure 3-18c. A substantial amount of the beams is reflected as they pass from the liquid to the glass in the pipe, figure 3-18d. Thus two sets of beams were apparent in the fluid, the original pair and this, less distinct, reflected pair. Looking at the pipe wall at the laser side four dots are visible corresponding to the two main beams entering the pipe wall and the two reflected beams exiting from the pipe, figure 3-18e. By altering the angle of the laser, using its adjustable feet, these four dots could be made to align themselves. Once aligned, this ensured that the laser beam was in fact travelling through a diameter of the pipe.

A detailed description of the calculations involved in the lateral positioning of the laser beams within the pipe is given in Appendix 3.

### 3.5 DATA ACQUISITION

#### 3.5.1 Introduction

The components of the data acquisition system are shown schematically in figure 3-16, and are as follows. (Components 1,2 and 3 have been outlined already in section 3.4.1.)

- 1 - DISA LDA 03 Helium-Neon Laser unit.
- 2 - DISA Photomultiplier (P.M.) unit.
- 3 - DISA 55N20 Doppler Frequency Tracker.

4 – Burr Brown Intelligent Interface Board. This board is located within the IBM P.C. and a carrier card located on the board carries out the function of receiving the analog input signal then transmitting it to the A.D. converter on the card and finally sending the returned digital signal to the IBM P.C in a form which the ASYST software can read.

5 – A.D. Converter Module. This is located on the Burr Brown card and converts the analog output signal from the frequency tracker into a digital form which is readable by the computer.

6 – IBM Personal Computer XT. This microcomputer is used in conjunction with the Burr Brown carrier card and the ASYST software package to analyse the signal from the frequency tracker. Output from the ASYST package can be displayed graphically to the screen or printer, or to either hard disk, for storage, or floppy disk to be transferred to another machine.

7 – ASYST software package. Programs in the ASYST language were written to read in the time signal data from the Burr Brown card and perform certain data analysis techniques on it.

### 3.5.2 Data Aquisition Hardware

As mentioned above, the hardware employed to interface the tracker output signal with the IBM P.C. was in the form of a Burr Brown PCI 20000 Intelligent Interface System. The board consists of a termination panel, a carrier card and an analog input module.

The termination panel provides screw terminal connections for the input signal wires. The analog module accepts the analog input signal from an external source, in this case the DISA 55N20 Frequency Tracker. It then performs the analog to digital (A/D) conversion of the signal to change the data into a form readable by the digital computer. The digitised output signal from the module has a 12 bit resolution.

The carrier card is the main printed circuit board on the PCI 20000 system. It is designed to interface directly with the internal bus of the IBM P.C. through an available expansion slot. The carrier card receives the analog input signal, sends it to the analog module and then sends the returned digitised signal to the P.C.

### 3.5.3 Analog to Digital Conversion

A 12 bit resolution is attained on the Burr Brown A/D converter. This means that the continuously varying analog signal from the frequency tracker is represented digitally over the voltage range by 4096 ( =  $2^{12}$  ) binary integers, (or bits). The PCI 20000 card is set for voltages within  $\pm 10$  volts, i.e. a 20 volt range. Therefore each bit of resolution represents,

$$\frac{20.0 \text{ V}}{4096 \text{ bits}} = 4.88 \quad (\text{milliVolts per bit}) \quad (3.17)$$

Thus a digital reading,  $R$ , corresponds to a voltage from the tracker,  $V_f$ , of

$$V_f = ( 0.00488 \times R ) - 10.0 \quad (3.18)$$

### 3.5.4 Computer Specifications

The specifications of the two micro-computers and the mainframe used in the study are as follows.

#### IBM Personal Computer X.T.

This now slightly dated machine with its 80086 processor and 8087 co-processor, was used for collecting and storing the data, and performing preliminary analyses to find the Turbulence Intensity and mean velocity of the flow. It was also used to produce frequency spectra using an F.F.T. analysis tool in the ASYST software package. The frequency spectra was plotted for each flow result taken. This was done using an Epson LX-80 printer connected to the computer.

### OPUS Personal Computer P.C.V

This is a faster machine than the somewhat older IBM P.C., with its 80286 processor and 80287 co-processor. When not in use for controlling and monitoring the motor, it was used to edit the experimental data files obtained from the IBM X.T. machine. In addition, it was used to calculate the mutual information of each of the time series obtained. In some cases it was used to compute the Lyapunov exponent of the output signal.

### IBM CMS Main Frame

The mainframe used was an IBM 3090 VF 150 and the FORTRAN compiler was 'VM FORTRAN Version 4.3' also supplied by IBM. The mainframe was used for all the main computationally intensive work including the calculation of the Grassberger-Procaccia dimension of the time series. The main reasons for using the mainframe for this task was its ability to process up to five batch files at a time, and also the availability of graphical output with the results. The time series data was downloaded to disc from the IBM P.C. and then uploaded to the mainframe from a remote terminal. These terminals were situated elsewhere in the Civil Engineering department.

With the exception of the Lyapunov exponent calculation, the mainframe was used for all of the computational work involved with the project. This includes the writing and testing of all programs written by the author.

#### 3.5.5 Software

The purpose of this section is to give a brief outline of the software used in the experimental study, some of which have already been mentioned in the text. Programming was performed in the **ASYST** language and also in **FORTRAN 77**.

**ASYST** is an integrated software design system designed exclusively for scientific and engineering applications. The **ASYST** language was used to write the data acquisition program, and contained some specific Burr Brown call routines which were compatible with the **ASYST** system. These routines operated the **PCI 20000**

board and received the digital input data into an array within the ASYST program. The program then calculates the mean velocity component,  $\bar{U}_z$ , the turbulence intensity (T.I.) and the frequency spectrum of the results.  $\bar{U}_z$  and the T.I. are displayed on the screen and the frequency spectrum is outputted to the screen in graph form. The results are then sent to the printer for plotting.

All the programs written to perform the dynamical analyses, (i.e. Grassberger–Procaccia dimension, Lyapunov exponent, autocorrelation function, mutual information etc.), as well as basic plotting programs were written in FORTRAN, on the mainframe. The graphics routines in the FORTRAN programs were provided by GHOST–80. This is a graphics package resident on the mainframe, whereby graphical instructions from the GHOST–80 package are called from within the program code. In certain circumstances, complete routines were imported from the NAG library for use in certain programs. The NAG library contains many statistical and numerical method algorithms. It is resident on the mainframe and its routines are called from within the main program, in much the same way as the GHOST–80 graphics package.

The main ASYST and FORTRAN programs are given in Appendix 2.

### 3.5.6 Sampling and Manipulation of the Data

Up to 16384 digitised data points of the flow velocity may be collected with the set up outlined above. The points are stored in the array named 'POSITIONA' in the program 'LASERP4', see appendix 2. Due to memory limitations only the first 4096 points are converted into velocities using equation 3.19. These points are stored in the array 'POSITION0'. It is these points on which the first preliminary analyses are performed to find the T.I.,  $\bar{U}_z$ , and plot the F.F.T. graph.

The larger array, POSITIONA, is saved to disk, and it is this array on which subsequent dynamical analyses are performed. Before doing so each array is cleaned up by editing out the additional characters at the beginning and end of the data set left by the ASYST software.

## 3.6 FLOW VISUALISATION APPARATUS

### 3.6.1 Introduction

Initial test trials were performed with aluminium powder as the flow visualisation agent. However, it soon became apparent that the settling out rate was far too rapid for the slow flow rates being investigated here. It was therefore decided to use natural guanine crystals as the flow visualisation agent. A quantity was obtained (trade name – Mearlmaid Pearlessence AA) and tested. This proved to be adequate for the required task, with a much lower settling out rate than the aluminium particles and they are highly visible in the flow. (In fact the crystals are in wide use in the cosmetic industry and give a pearly or opalescence look to shampoos, soaps, lipsticks and eye make up.) The crystals come in a concentrated, water soluble paste form and require to be diluted with water before use.

Results, reported elsewhere, (see Matisse and Gorman [1984]), for the type of particles used herein suggest a sedimentation velocity  $V_s$  of around 0.1 cm/hour, or  $2.78 \times 10^{-7}$  m/s. It soon became apparent that this was a rather hopeful figure and some of the particles settled out quite rapidly. This was discovered to be partly due to incomplete mixing of the guanine paste into a solution with water. This mixing was originally done by hand stirring in a beaker, subsequently, the mixing of the flow visualisation agent was performed with a mechanical stirrer. (A TECHNE ELE stirrer, model F968D.) This provided a much more suitable flow mixture.

### 3.6.2 Light Box Design

A suitable light source for the flow visualisation was provided by a purpose built light box, figure 3-19. This was designed to direct a sheet of light through the diameter of the pipe. The light box basically consisted of a 500 Watt light unit, fitted to a fabricated aluminium box with a slit aperture in its floor leading to a light guide which channels the light onto the pipe. At a later stage a flash unit was fabricated which was interchangeable with the light unit, thus providing two methods of illumination.

The light box was initially designed to direct a 168mm long by 1mm wide 'slice' of light through the vertical diameter of the pipe. The box being supported on the pipe drip tray by four adjustable legs. This allows parts of the pipe, remote from the orifice, to be illuminated for study. The box is cooled by a blower fan, which is connected to the box by flexible hosing, and circulates air through the box while the light is on.

The flow field illuminated by the light box tended to have a higher concentration of tracer particles at the bottom of the pipe. This was due to some the particles settling out, as described above, before reaching the orifice plate. This often resulted in the photographs showing clear, well defined vortices being shed from the bottom of the orifice lip, whereas little or no structure was visible at the top of the pipe. This effect is clearly shown in Chapter 5. Thus it was decided to illuminate the flow with the light sheet along the horizontal diameter of the flow, as it was reasoned that the flow concentration should be much more consistent across the flow. To do this the light box was modified slightly by removing its legs and placing it on its side against the pipe. A much better representation of the flow field was thus obtained.

### 3.6.3 Experimental Practice

Various Reynolds number flows were passed through each of the orifices in turn. The flows were inspected visually to give a clear picture of the vortex shedding at the orifice. Photographs were taken for many flow-orifice configurations. A video was taken of the main experimental runs. This has the benefit of being able to re-run, and slow down the sequence of events to see more clearly the actions of the flow. It also enables the vortex shedding phenomena to be elucidated much more clearly for higher Reynolds numbers flows.

All flow visualisation photographs were taken by the author using a PENTAX 'SPOTMATIC-F' single lens reflex camera, with a 'standard' 50mm, f1.4 lens. The choice of film was important. After a few trials the film eventually chosen was KODAK T-MAX 400 ASA PROFESSIONAL FILM, a fast, black and white film with a wide latitude, (that is, it is much less susceptible to over- and under-exposure). This film proved suitable for taking high quality pictures in the

low lighting conditions. This was due to its exceptionally fine grained structure, which provided a higher definition than obtainable with a conventional 400 ASA film.

The video photography was performed with a PANASONIC CCD sVHS 625 video camera. Although capable of using the higher definition super VHS video tape, for reasons of compatibility, the video was taken using conventional VHS tape. This was found to be adequate for the purpose of this investigation. The video was edited down to a more presentable form, from over one hour to approximately 20 minutes using the editing facilities provided by the Audio Visual Unit of Glasgow University.

Photographs using the lamp as the light source were taken with the camera aperture set at fully open, i.e. f1.4, with the shutter speed used to control the exposure. Three photographs were taken at different shutter speeds, (1/60, 1/125 and 1/250 of a second), for each required flow set-up. The shutter speed giving the best result tended to depend upon the concentration of flow visualisation chemical. When the flash was used as the light source the procedure was different. This time the shutter speed was held constant at a sixtieth of a second and the aperture was varied to control the exposure of light onto the film. Again three photographs were taken for each flow set-up, with the aperture set at f5.6, f8 and f11 respectively.

Of the two methods, it was easier to obtain good results with the lamp as the source of illumination. This is because the flow field was illuminated at all times and could be seen prior to taking the photograph. It was more difficult to obtain good results with the flash photographs, as the flow field was only illuminated by the flash during the taking of the photograph. For this reason the lamp light photographs were taken first so that a general picture of the flow conditions would at least be known.

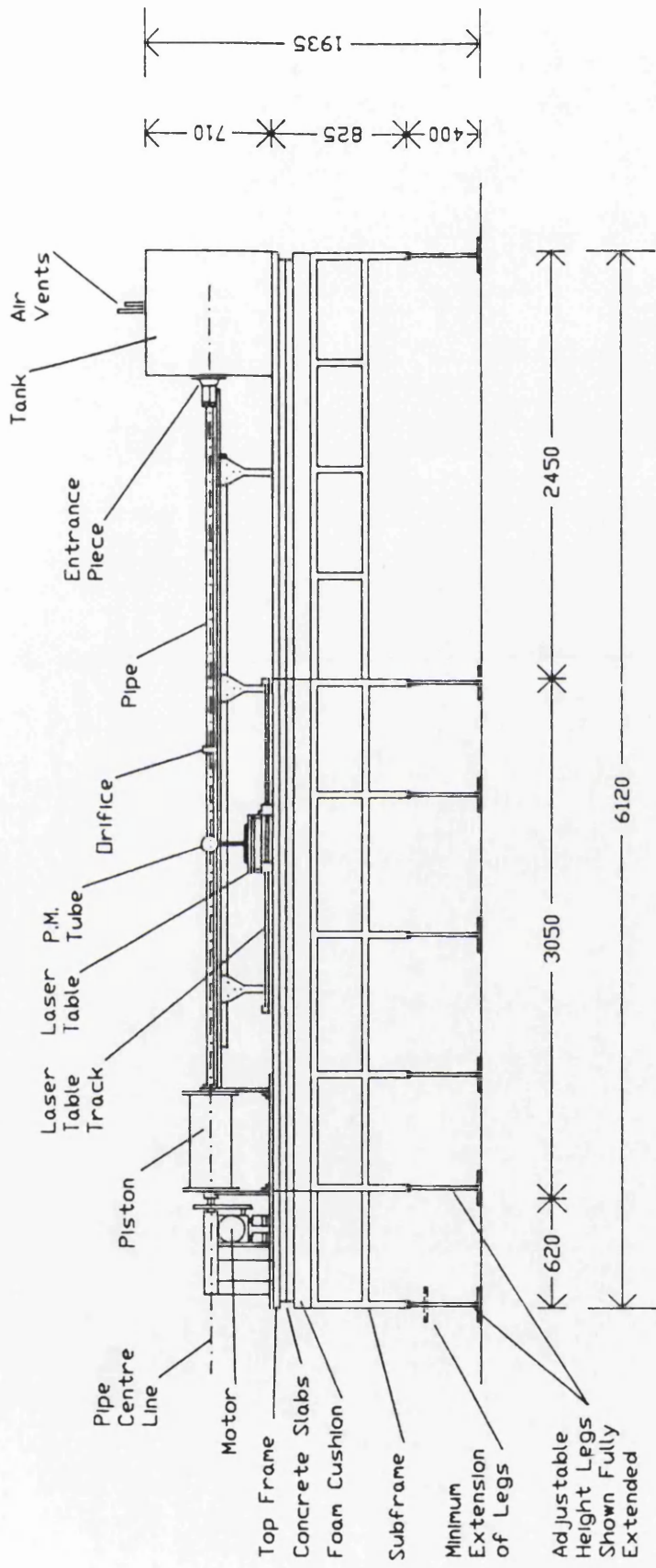
### 3.7 SUMMARY

The apparatus described above in Chapter 3 was designed in detail and built

from scratch, and represents a large input of time from the author. The construction alone took approximately fourteen months to complete. The author has no previous experience in the design and fabrication of experimental apparatus and the expertise attained from this work will prove invaluable in future research work.

Much time was also spent on setting up the L.D.A. apparatus together with the associated computing hardware and software. Also the generation of a pulsatile flow required considerable attention. After fine tuning of the apparatus, and a range of preliminary tests, (outlined in Chapter 4), the equipment performed well during the course of the experimental programme.

**CHAPTER 3**  
**FIGURES**



Scale 40:1

Note - All Dimensions in mm.

Figure 3-1: General Layout of the Experimental Apparatus

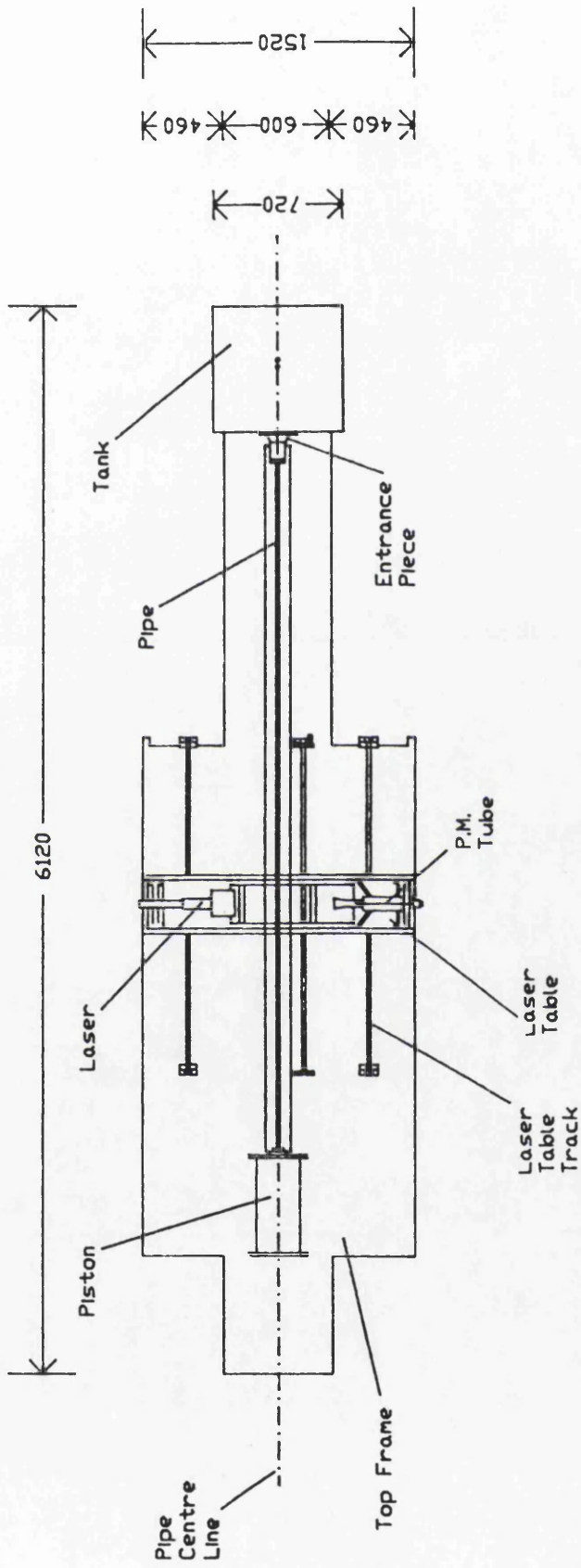


Figure 3-2: Plan View of the Experimental Apparatus

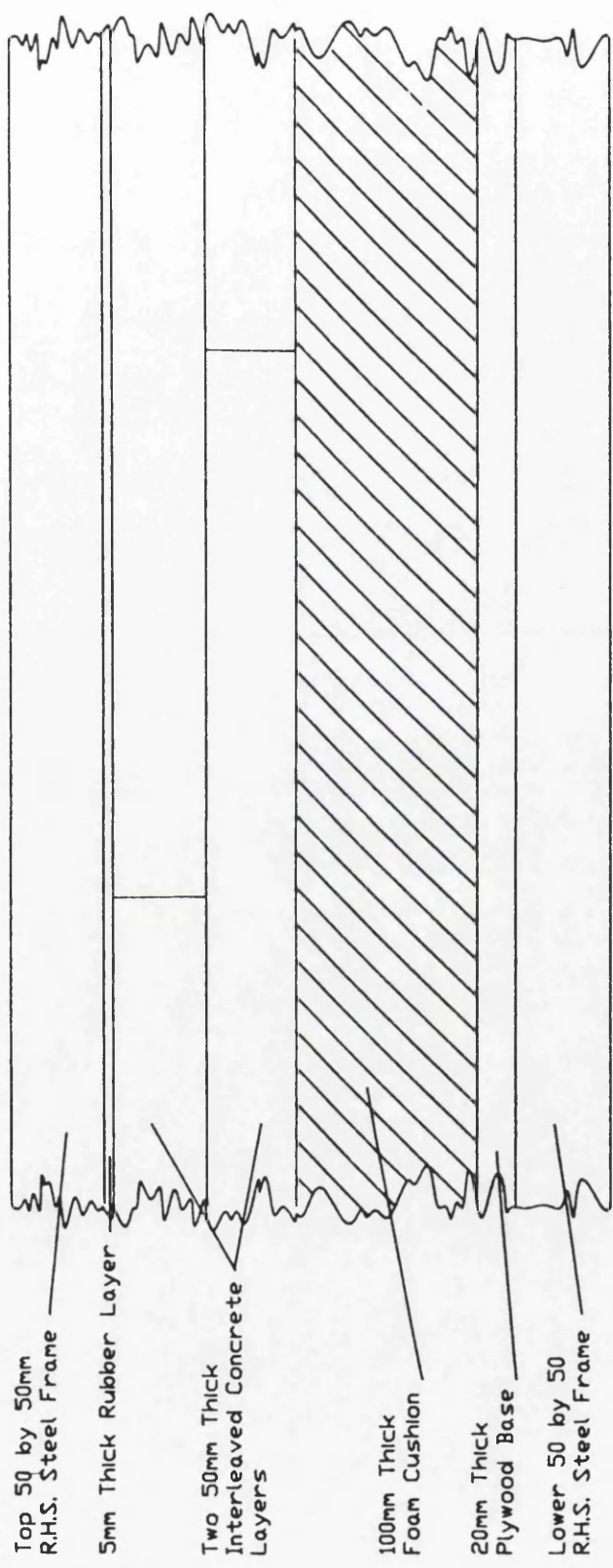


Figure 3-3: Sketch of the Layered Structure of the Experimental Rig to Eliminate Vibrations from the Surroundings

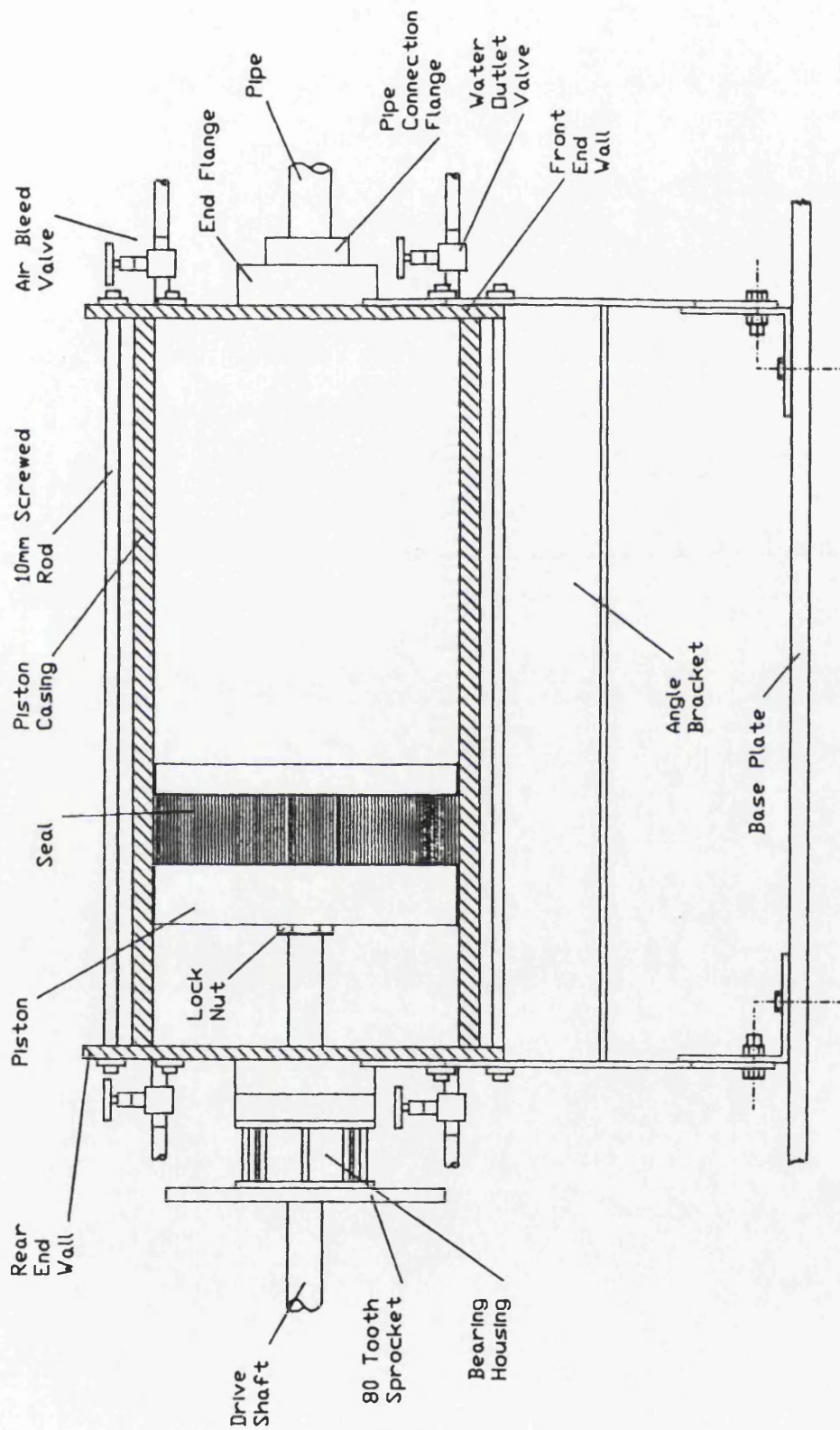
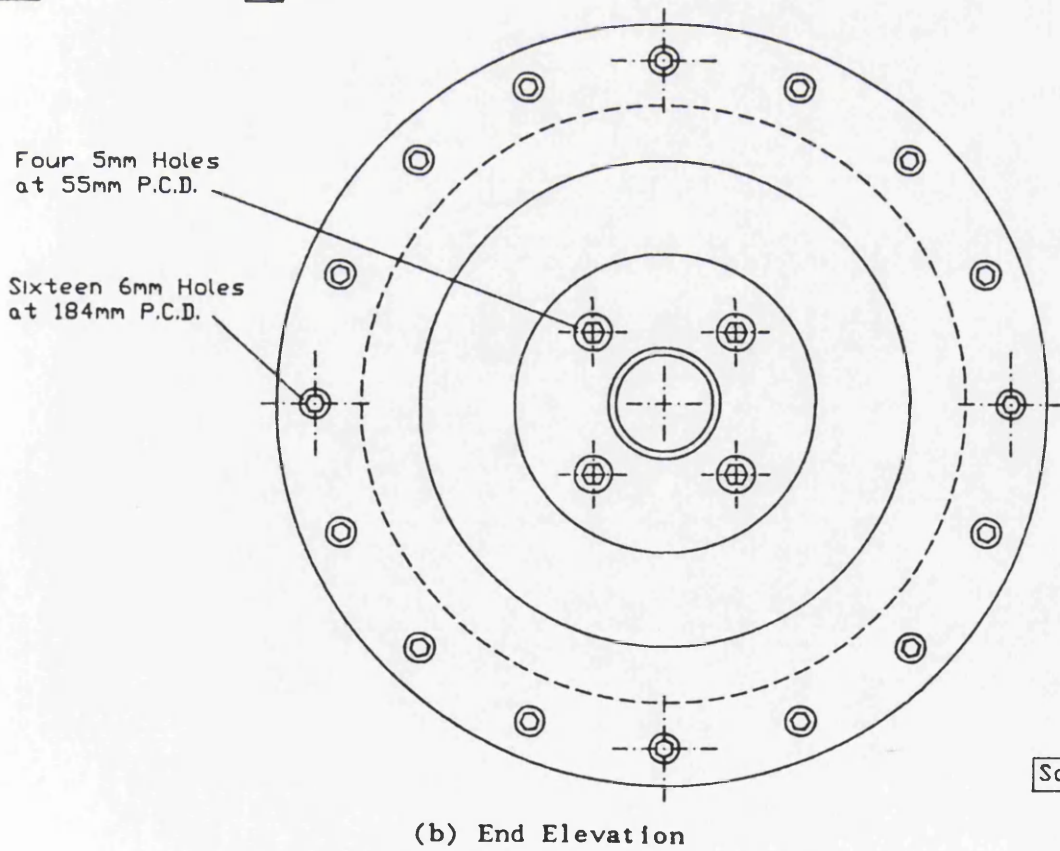
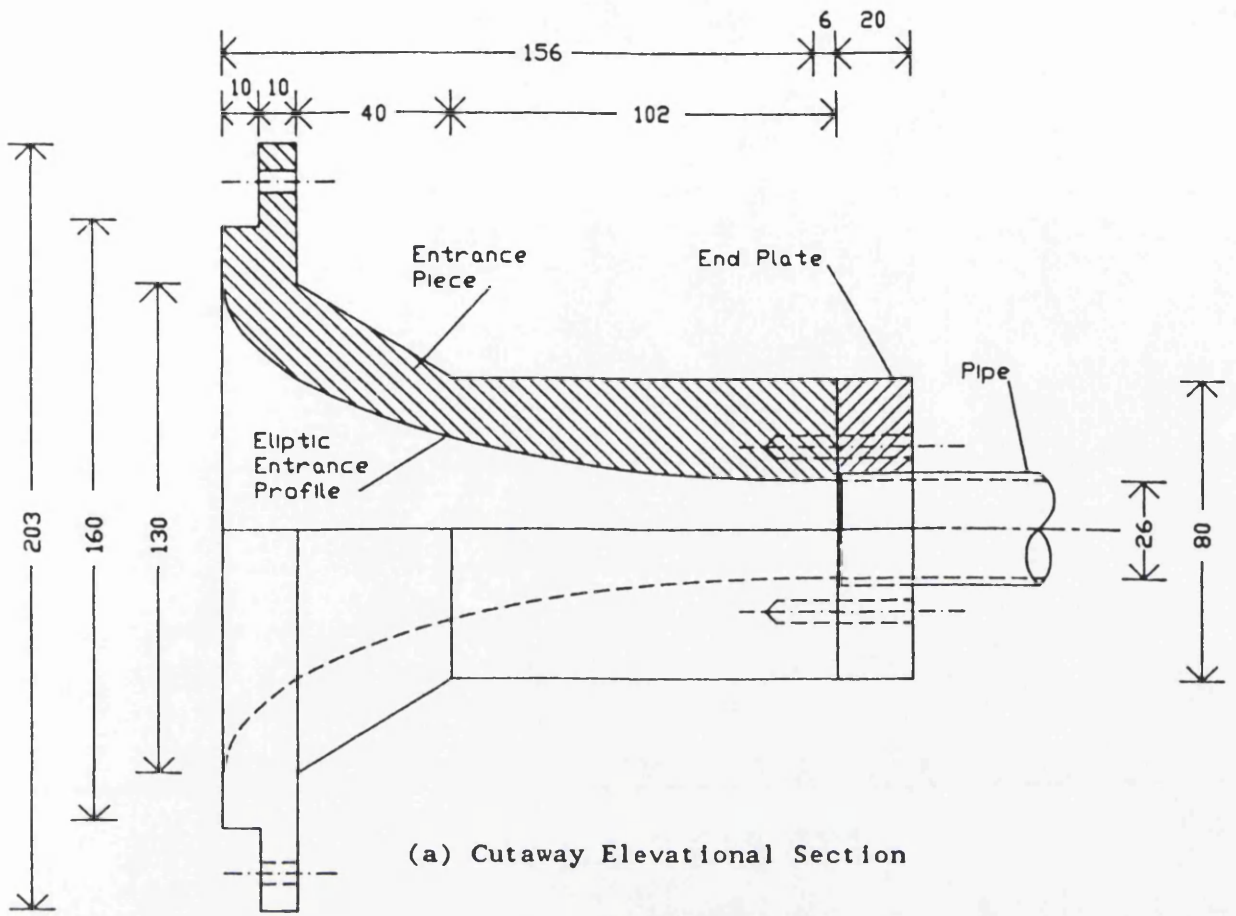
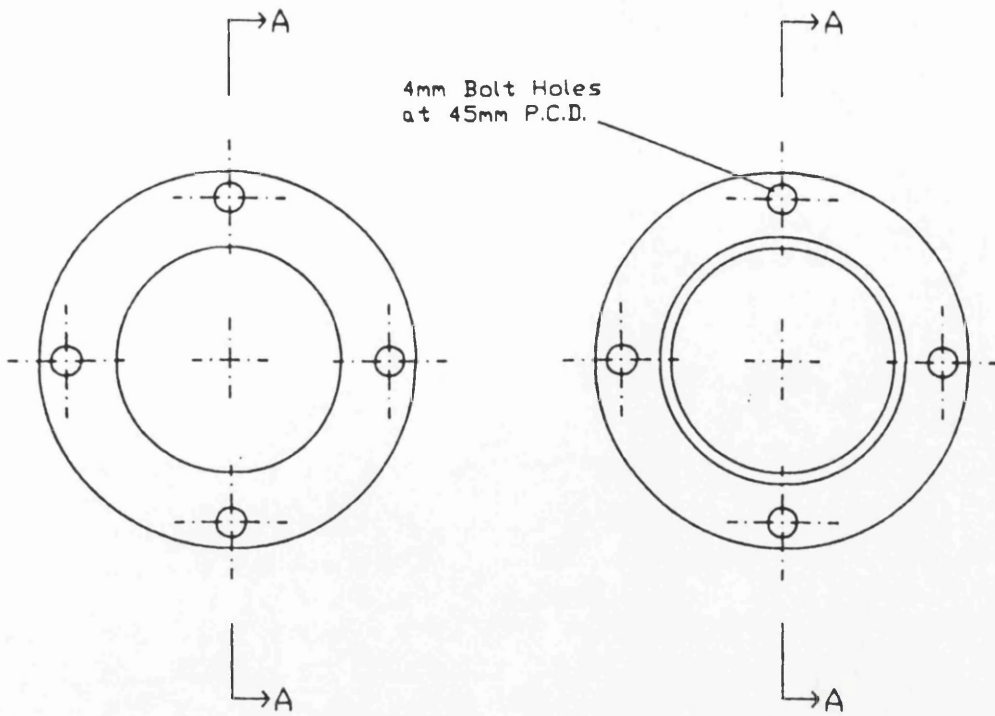


Figure 3-4: Cutaway Section of Piston Casing Showing Piston

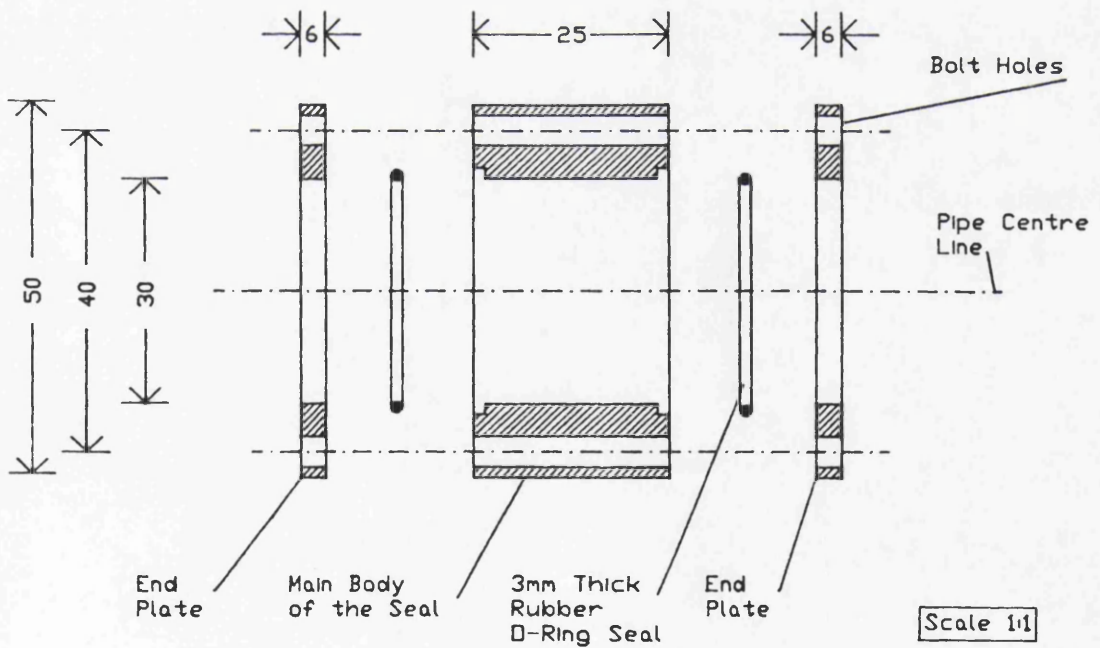


Scale 2:1

Figure 3-5: Pipe Entrance Piece



(a) End View of Coupling End Plate (b) End View of Coupling Main Body



(c) Section AA Through the Coupling

Figure 3-6: Pipe Coupling Detail

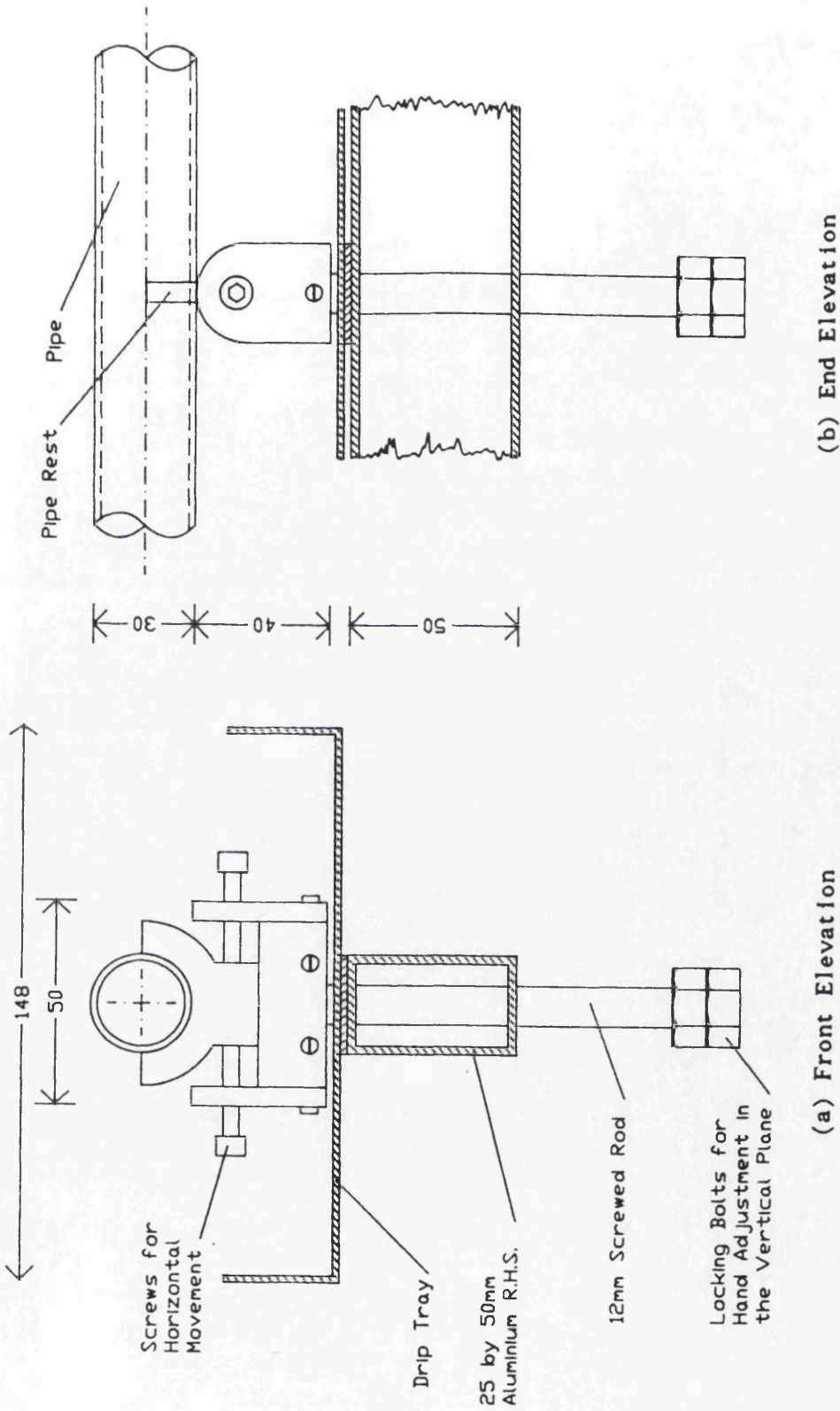
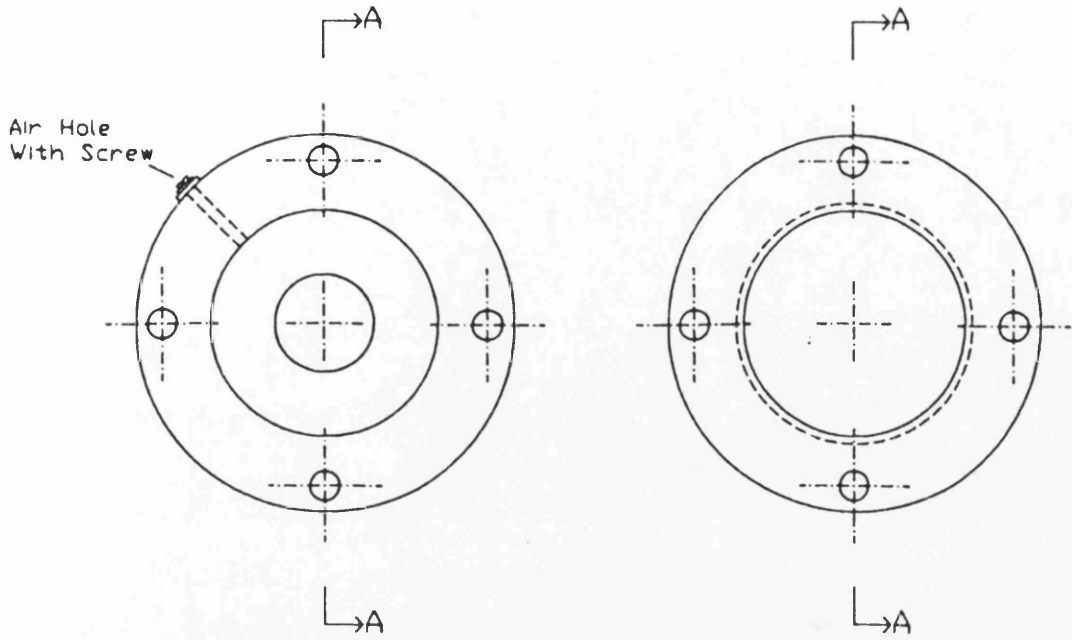
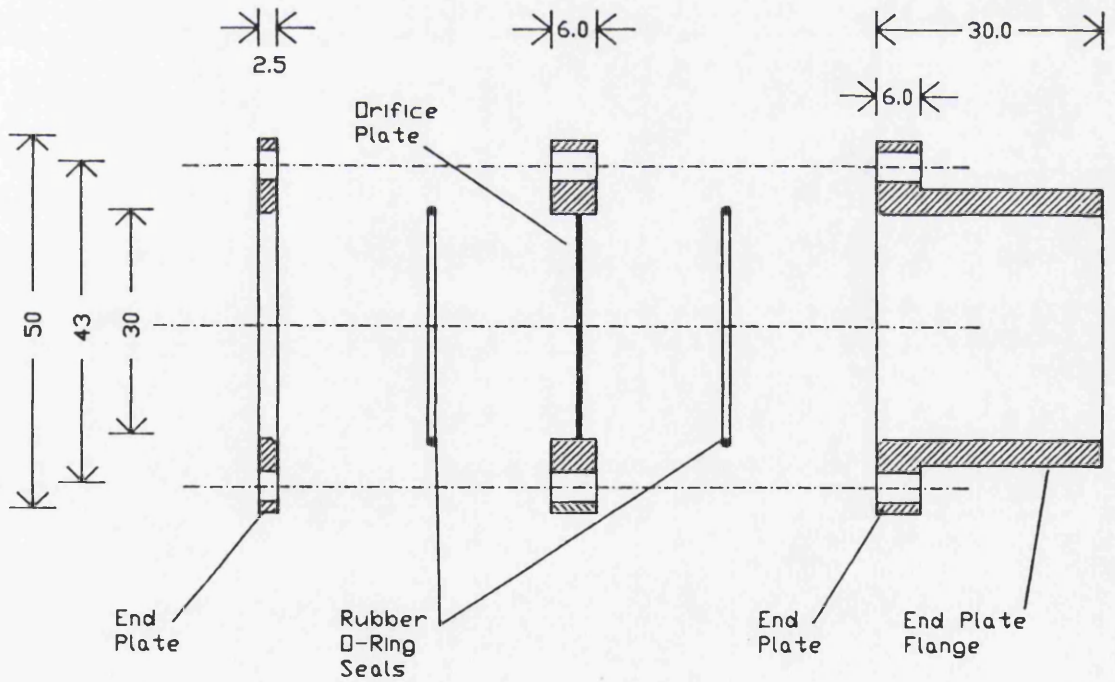


Figure 3-7: Two Views of a Typical Pipe Support



(a) Orifice Plate

(b) End Plate



(c) Section AA Through Orifice and End Plates

Figure 3-8: Orifice and End Plate Detail

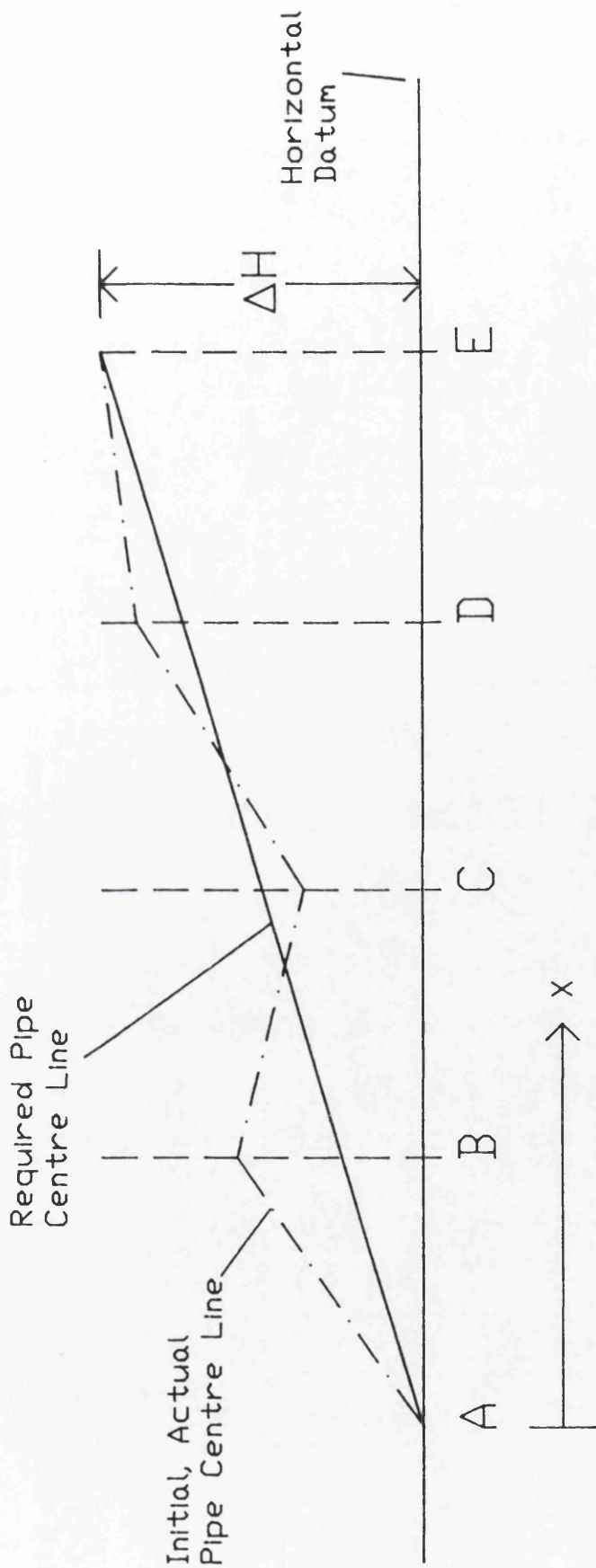
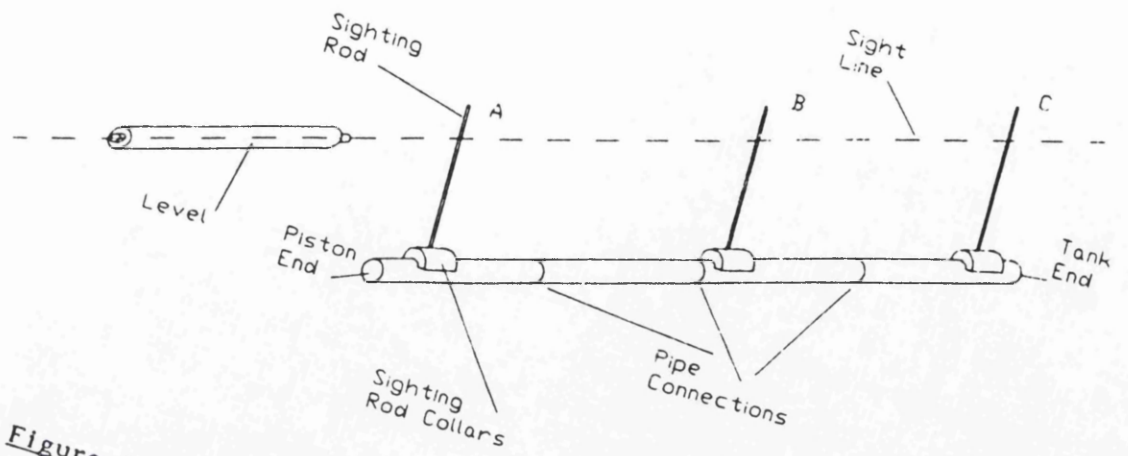
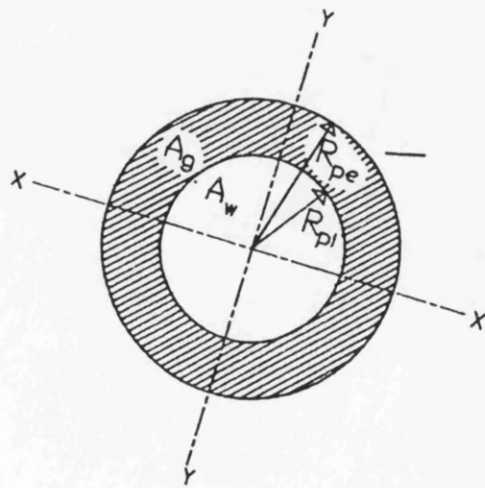


Figure 3-9: Method of Aligning the Pipe in the Vertical Plane



**Figure 3-10: Schematic Diagram of the Horizontal Alignment of the Pipe**



**Figure 3-11: Pipe Cross Section Details**

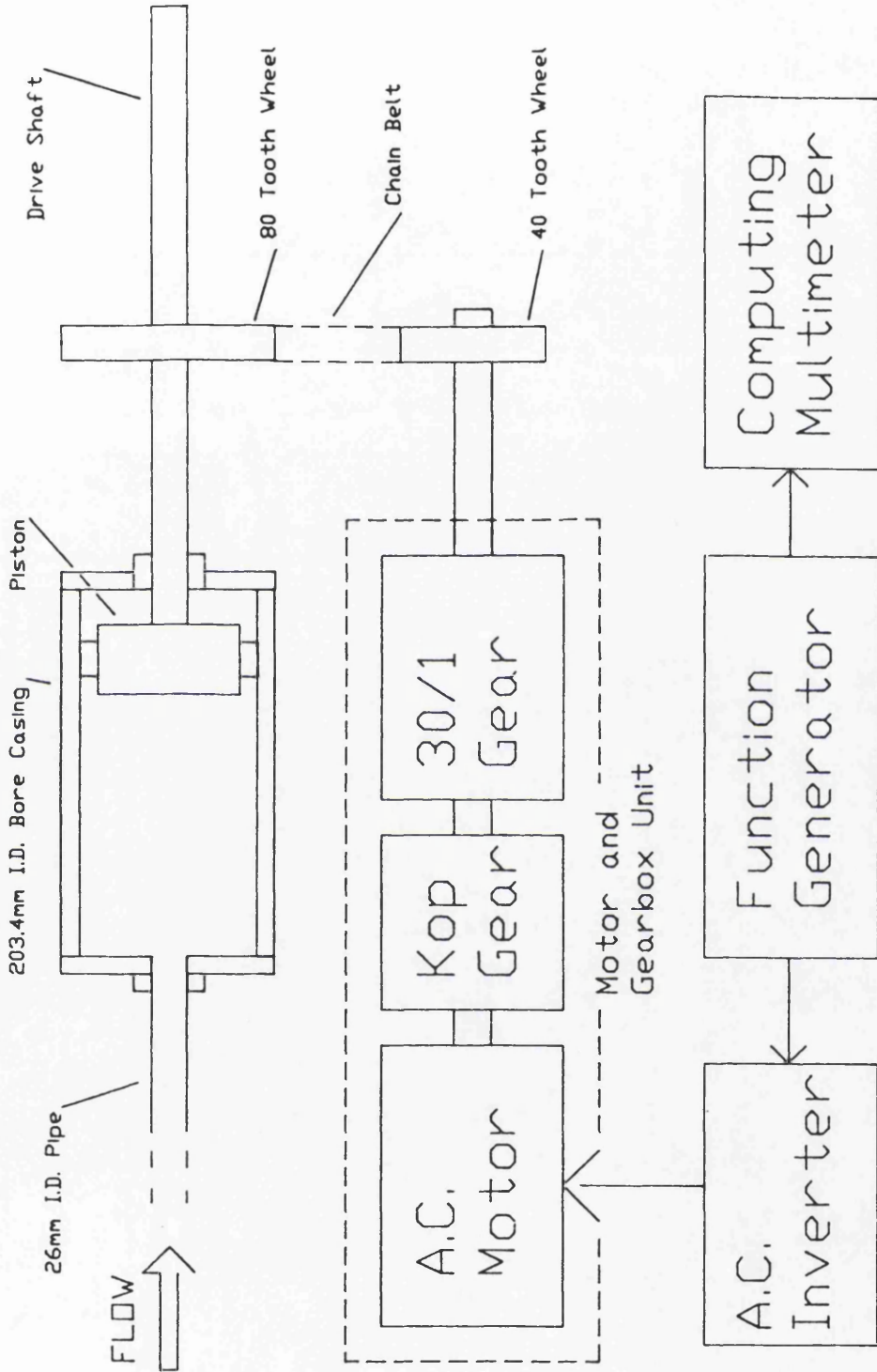


Figure 3-12: Schematic Diagram of the Original Piston-Motor Control Arrangement

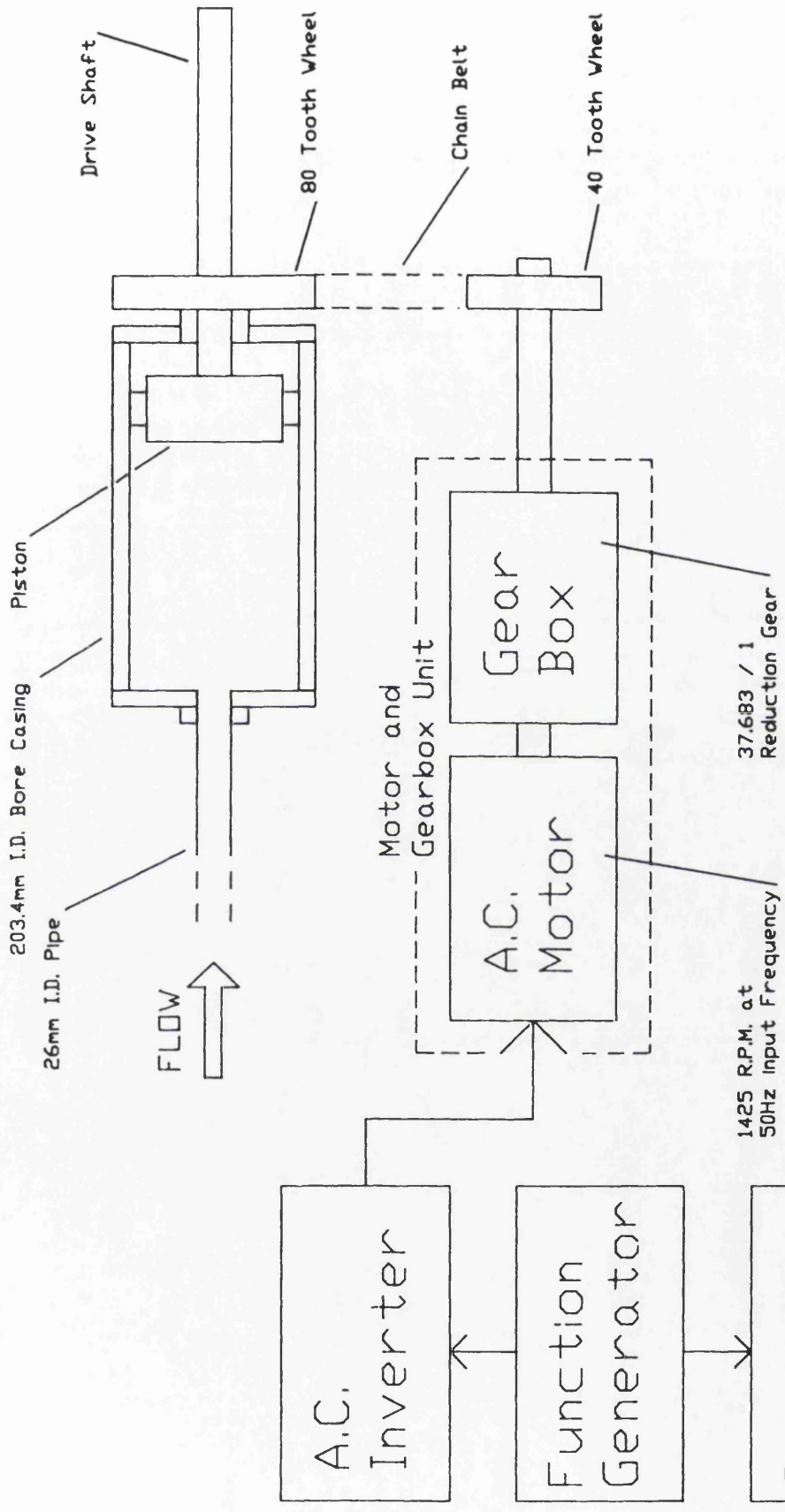
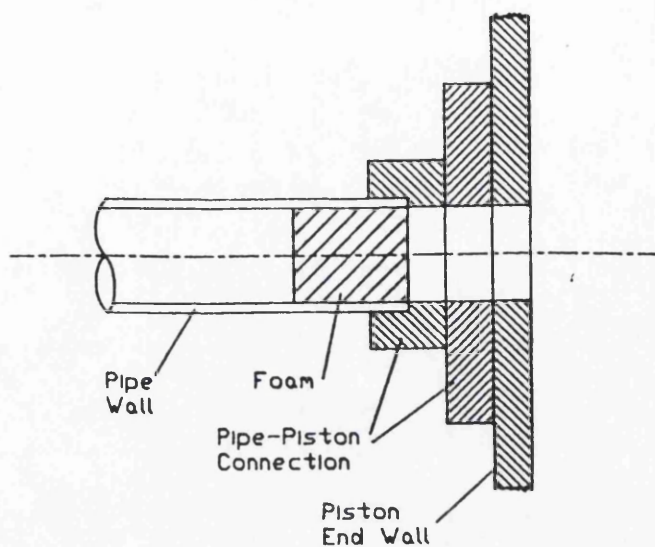
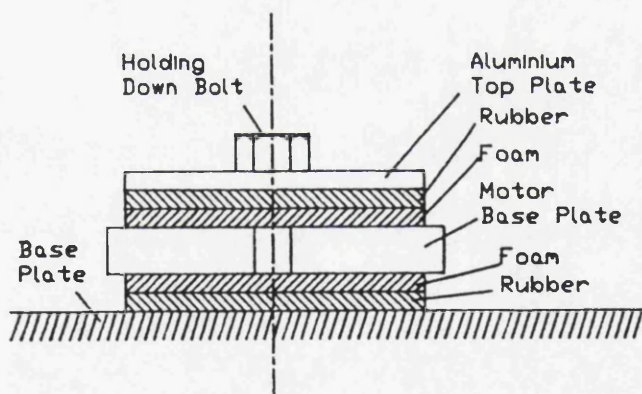


Figure 3-13: Schematic Diagram of the Modified Piston-Motor Arrangement

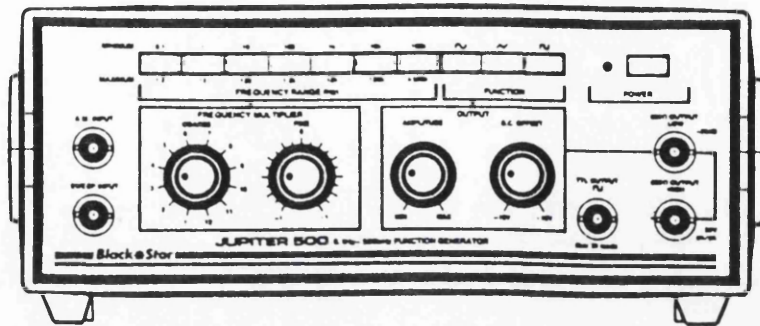


(a) Foam Placed Within the Pipe at the Piston End

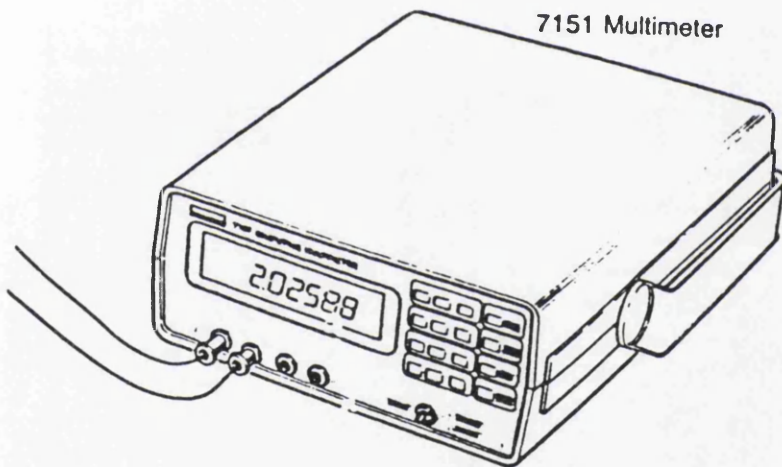


(b) Foam-Rubber Sandwich Motor Mounting

Figure 3-14: Physical Methods of Noise Reduction on the Rig



(a) Signal Generator



(b) Multimeter

Figure 3-15: Signal Generator and Multimeter

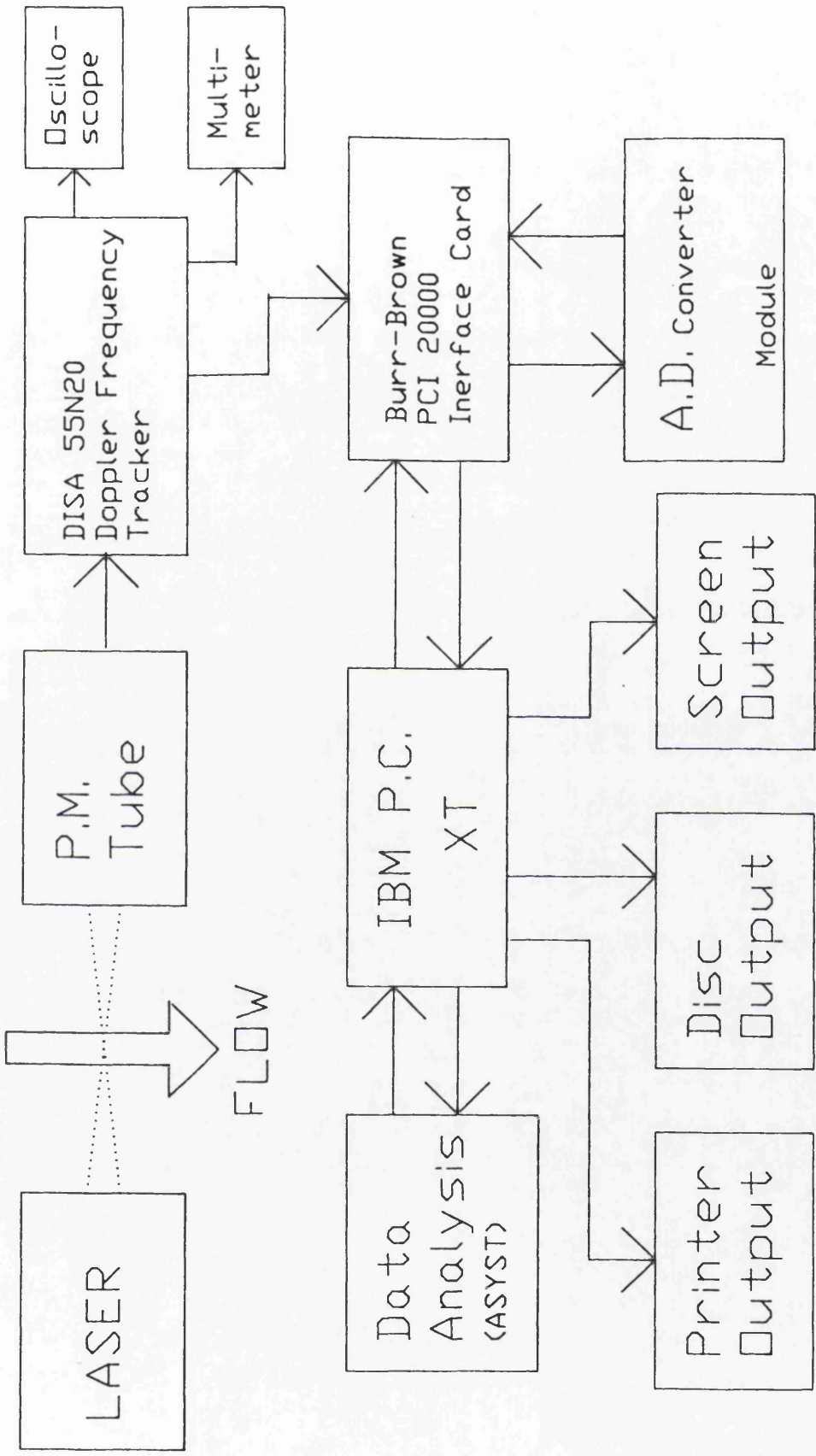
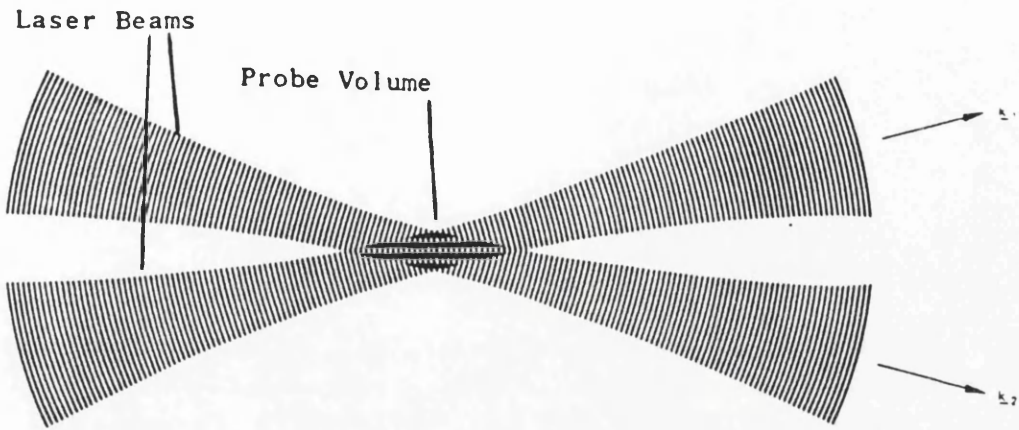
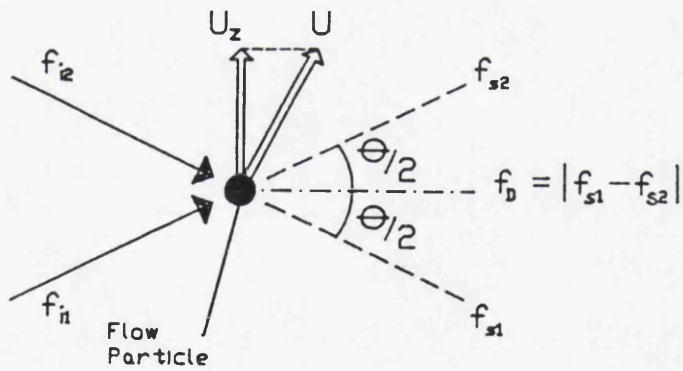


Figure 3-16: Data Acquisition and Flow Chart



(a) Formation of the Probe Volume  
by Intersecting Beams



(b) Diagrammatic View of the L.D.A. Operation

Figure 3-17: L.D.A. Operation

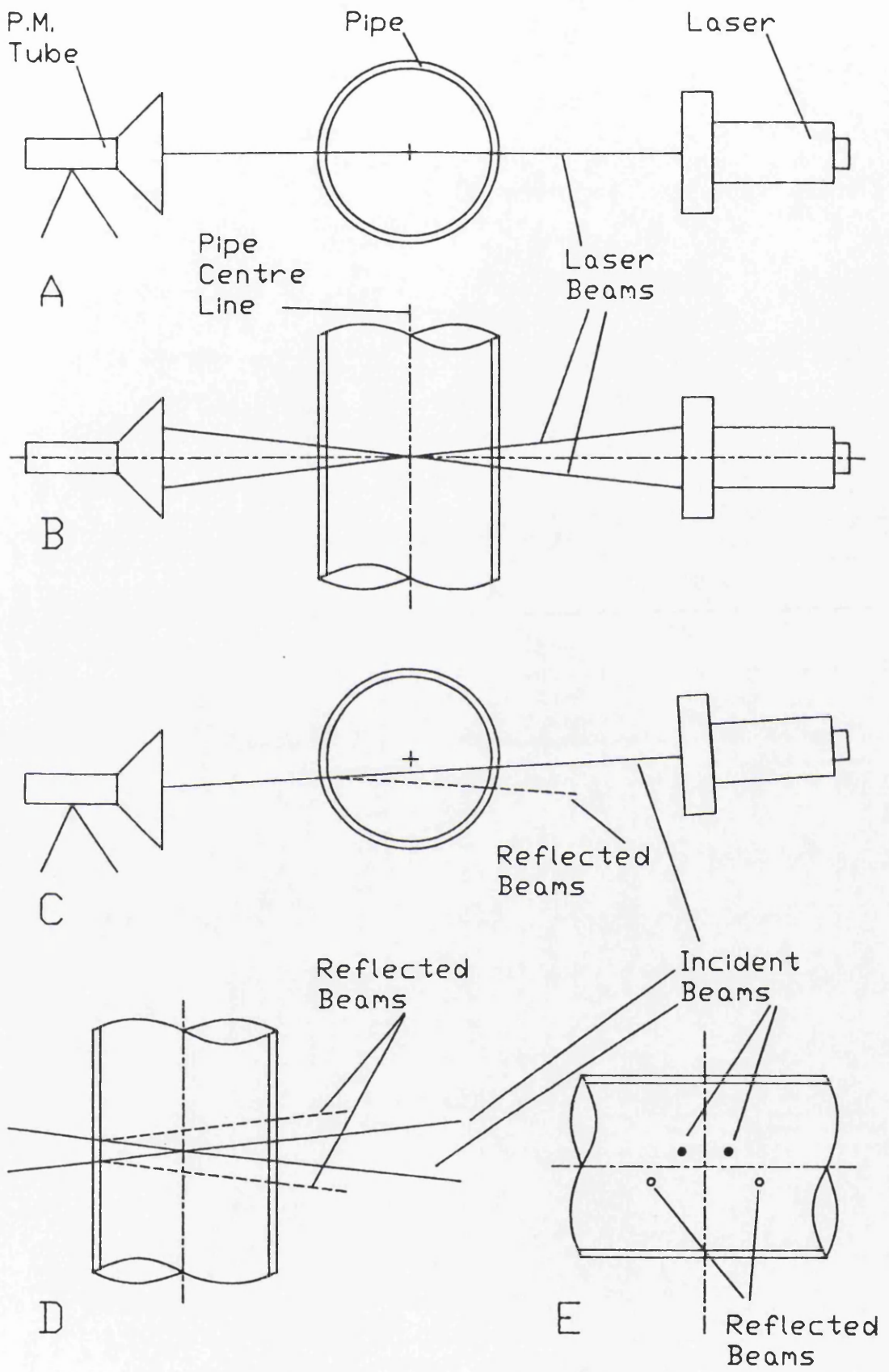


**Figure 3-18: Laser Intersection with the Pipe**  
 (See Text for Details)

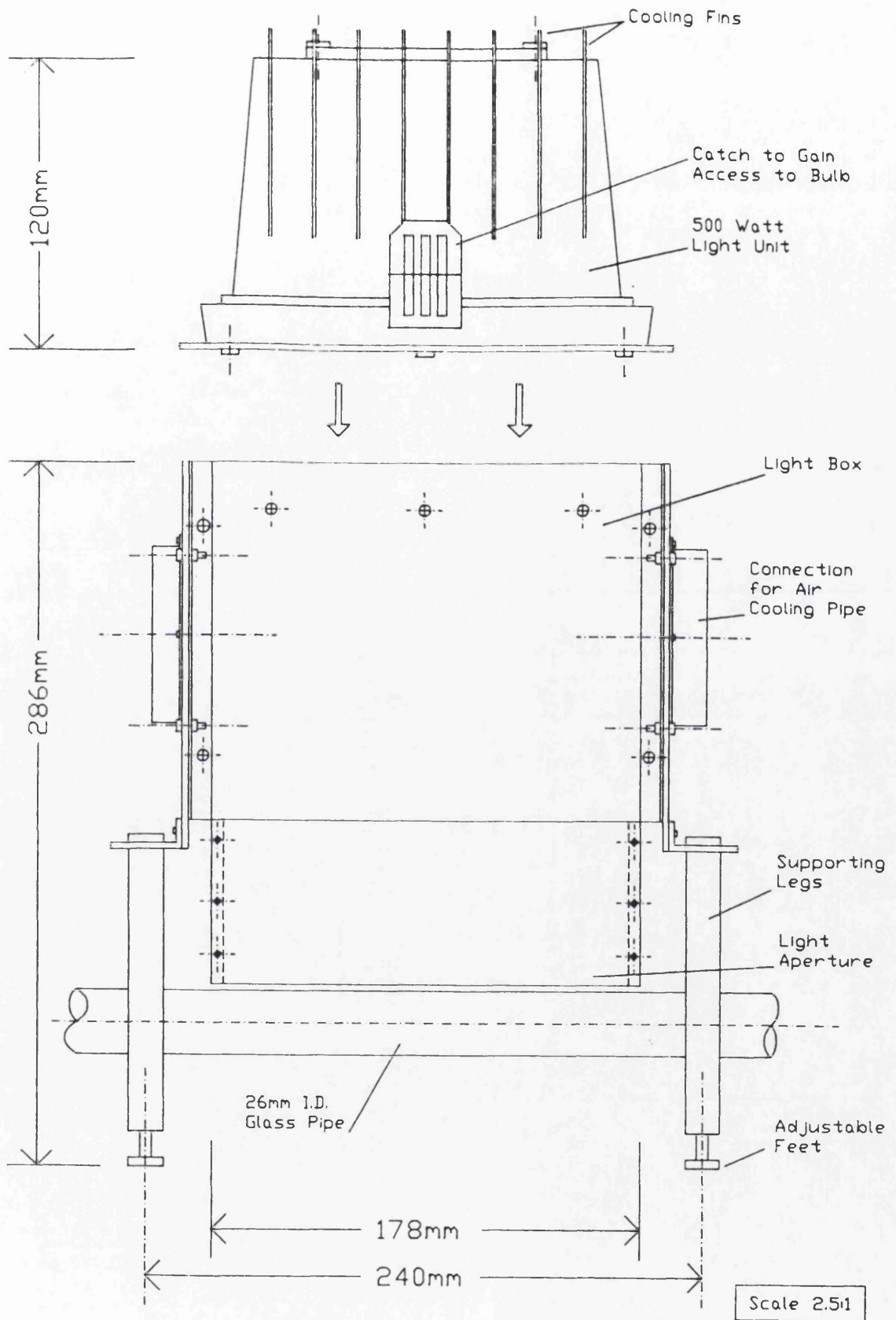


Figure 3-19: Light Box used in the Flow Visualisation

## CHAPTER 4

## CHAPTER 4

### PRELIMINARY RESULTS AND CALIBRATION

#### 4.1 INTRODUCTION

#### 4.2 CALIBRATION OF APPARATUS AND PRELIMINARY RESULTS

4.2.1 The Inverter Frequency - Pipe  
Reynolds Number Relationship

4.2.2 Centre-line Velocity Results

4.2.3 Parabolic Hagen-Poiseuille Flow

4.2.4 Selection of Forcing Frequency and Amplitude

4.2.5 Pulsatile Laminar Flow

4.2.6 Natural Frequency Results and  
the Strouhal Number

#### 4.3 CALIBRATION OF THE COMPUTER ALGORITHMS

#### 4.4 DERIVED RELATIONSHIPS

4.4.1 Pipe, Orifice and Reynolds  
Number Relationships

4.4.2 The Wake Reynolds Number

4.4.3 The Forcing Frequency - Pipe Reynolds  
Number Relationship

4.4.4 Vortex Shedding Velocity and Wavelength

4.4.5 Forcing Amplitude Relationship

#### 4.5 OUTLINE OF THE EXPERIMENTAL WORK

## 4.1 INTRODUCTION

The contents of this chapter represent neither a description of the apparatus as in chapter 3, nor systematic experiments as in chapters 5 and 6, but rather preliminaries in leading to systematic experimentation. Thus chapter 4 encompasses calibration and sensitivity tests on the apparatus, interrelationships used in the experiments, as well as a description of the range of parameters varied in the experiments.

## 4.2 CALIBRATION OF APPARATUS AND PRELIMINARY RESULTS

### 4.2.1 The Inverter – Pipe Reynolds Number Relationship

The A.C. Inverter is a device which controls the motor and piston speeds, (as described in chapter 3), and may be set from 0 to 37.5Hz, in 0.1 Hz units. The motor controls the average pipe flow velocity, via the piston. The inverter, therefore, directly controls the pipe Reynolds number. Tests were performed to find the relationship between the Inverter A.C. setting and the resultant pipe Reynolds number. These are described below.

The Inverter was set to values from 0 to 35Hz in 5Hz increments, and the piston velocity was measured at each stage. This was converted into an average pipe flow velocity,  $U_p$ , using the continuity condition and a knowledge of the internal diameters of the pipe and piston casing,  $D_p$  and  $D_{pis}$  respectively, where,

$$U_p = \frac{U_{pis} \cdot A_{pis}}{A_p} \quad (4.1)$$

Using the pipe and piston dimensions quoted in chapter 3, the relationship for pipe and flow velocity is obtained,

$$U_p = 61.174 U_{pis} \quad (4.2)$$

The pipe velocities, calculated from the piston velocities, were checked against L.D.A. readings of the pipe centreline velocities. (Since for the case of laminar pipe flow the maximum velocity occurring at the centre-line is twice the average flow velocity.) The L.D.A. velocity readings were found to be in good agreement with the calculated velocities, as shown in figure 4.2 and discussed in section 4.2.2 below.

The pipe velocities were converted into Reynolds numbers using equation 2.5, and a plot of the inverter frequency  $f_i$  versus the Pipe Reynolds,  $Re_p$ , was produced. This plot is shown in figure 4-1. In the figure, the measured points are shown by crosses. A best fit line, using the least squares method, was calculated and is shown in the figure. The equation of the best fit line is

$$Re_p = 25.597 f_i - 0.17143 \quad (4.3)$$

This relationship was used in all subsequent calculations of the pipe Reynolds number involved in the main results.

#### 4.2.2 Centre-line Velocity Results

The relationship between the average piston velocity and the average pipe velocity should be linear. This was checked by measuring the average piston velocity and calculating the pipe centre-line velocity from it, (i.e. twice the average pipe velocity). This value was then compared to the L.D.A. velocities obtained at the centre-line. Figure 4-2 shows the L.D.A. velocities plotted against those calculated from the piston rate. These points are plotted '+' in the figure. (The points correspond to pipe Reynolds numbers of 128 to 896 in increments of 128.)

It is noticeable that for higher flow rates the L.D.A. velocities fall short of the piston rate values. However, after some investigation it was noticed that this error could be much reduced by switching up the Doppler frequency range of the tracker to a higher range, (section 3.4.3). The point marked '\*' in the figure was taken at

$f_D = 100,000$  Hz whereas the other points were taken at 33,000 Hz. Thus by using a higher tracker frequency, a much more accurate L.D.A. velocity is obtained. The reason for this behaviour is not apparent.

#### 4.2.3 Parabolic Hagen–Poiseuille Flow

The velocities across the pipe were checked for pipe Reynolds numbers of 128, 256, 512 and 768. At these Reynolds numbers the flow was laminar, thus the resultant velocity profile should be parabolic, (see the expression for Hagen–Poiseuille flow, equation 2–16b). Figures 4.3a to d show the L.D.A. results, (plotted with an 'x'). Superimposed on the diagram is the parabolic Hagen–Poiseuille profile. It can be clearly seen from the figures that the L.D.A. results are very accurate at, and near to, the centre of the pipe. However, as one departs from the centre–line the results become much less accurate.

The general picture is the same for each plot. The plots suggest that the L.D.A. results are accurate up to approximately 6mm from the centre–line, beyond which they tend to drop off until they are near to the pipe wall, (radial distance = 13mm), at which point they level off. Apart from one set of measurements, all the main flow measurements, of the investigation reported in this thesis, were taken at the centre line. The one set of L.D.A. readings taken across the flow were only taken from the pipe centre to a maximum radial distance of 6mm. Thus ensuring accurate measurements within the pipe. (See chapter 6 for more details.)

Five possible reasons for the error in the velocity measurement, as the pipe wall is approached by the laser probe volume, are as follows:

- 1 – The finite length of the probe volume itself, which means that at positions within the flow, where there are steep velocity gradients, velocities over a wide range may be picked up by the L.D.A. system. Such steep velocity gradients occur at the pipe wall in pipe flow.
- 2 – Excessive flare occurring at the pipe wall. Flare as a possible cause of the error in the velocity results close to the wall was suggested during consultations with the manufacturer DISA.
- 3 – The absolute velocity near to the wall being very small, possibly out of the

range of the L.D.A. system.

4 – A lack of seeding particles near to the wall, due to the relatively low volume flow rate.

5 – Wrong designation of the location of the laser beams in the pipe, due refractive effects on a slightly ovaloid pipe wall.

#### 4.2.4 Selection of Forcing Frequency and Amplitude

In pulsatile flow in pipes, especially in the presence of an orifice plate to generate turbulence, it is important to chose suitable amplitude and frequency pulses, with which to force the vortices from the orifice plate.

A method for selecting both a forcing amplitude and forcing frequency had to be found, which allowed for the pulsation amplitude and frequency to be varied independently of each other. These criteria were satisfied by varying the Inverter input signal sinusoidally using the signal generator, (function generator outlined in section 3.3.7). The flow forcing frequency was controlled by the input frequency of the signal generator. The forcing amplitude was controlled by varying the input peak to peak voltage of the signal generator. The peak to peak voltage of the oscillation could be accurately controlled and monitored using an oscilloscope and a computing multimeter. An outline sketch of the forcing frequency and amplitude is given in figure 4.4a. Once this method had been devised to introduce the forcing amplitude at the required frequency, tests were then performed to see how the amplitude affected the L.D.A. results.

The forcing amplitude had to satisfy two criteria. Firstly, the amplitude must be large enough to produce a dominant frequency in the flow, as seen from the frequency spectra. This dominant frequency must 'drown out' the stray motor frequency,  $f_m$ , which is always present in the flow, (just visible in the frequency spectra plot), and which, if allowed, may influence the vortex shedding frequency when an orifice plate is fitted. Secondly, the amplitude must not be so large that it produces undesirable effects in the flow, such as turbulence, flow reversal etc.

Five tests were carried out to observe the flow behaviour due to the amplitude variation. Thus five tests were conducted keeping the Reynolds number and the

forcing frequency,  $f_f$ , constant while varying the peak to peak voltage of the forcing amplitude,  $A_v$ . These are as follows:

Test-1 -  $Re_p = 256, f_f = 3.3\text{Hz}$

Test-2 -  $Re_p = 256, f_f = 6.6\text{Hz}$

Test-3 -  $Re_p = 256, f_f = 9.9\text{Hz}$

Test-4 -  $Re_p = 512, f_f = 6.6\text{Hz}$

Test-5 -  $Re_p = 768, f_f = 9.9\text{Hz}$

The results of the tests are summarised in figure 4-4b to f. In the figures the Fourier amplitudes of each frequency spike, in each respective frequency spectrum, are plotted against the forcing amplitude, (peak to peak), of the frequency generator. This forcing amplitude is in volts. A voltage of 10 volts from the signal generator gives a pipe Reynolds number of 960, thus to convert from a voltage to a pipe Reynolds number the voltage is multiplied by 96. More details of the forcing amplitude relationship is given in section 4.4.5.

From the figure 4.4b to f the following is apparent.

- 1 - In all cases the stray motor frequency,  $f_m$ , is apparent.
- 2 - In tests 1 and 2 a secondary peak is observed at a frequency of twice that of the forcing frequency.
- 3 - For low values of forcing amplitude, ( $A_v < 0.2$  Volts), the forcing frequency amplitude is comparable with the stray motor frequency.
- 4 - At mid range values of forcing frequency, ( $0.2 < A_v < 1.0$  Volts), the variation of frequency spectrum amplitude with forcing frequency amplitude is roughly linear.
- 5 - At high values of forcing amplitude, ( $A_v > 1.0$  Volts), the frequency spectra amplitude no longer follows the linear relationship, tends to level off, and the secondary frequency becomes markedly dominant. This represents a non-linear, unstable phase of the pulsations.

Thus for the experimental investigation reported herein, and with the exception of one set of test results, the forcing frequency amplitude was maintained at a value of 0.6 Volts, which corresponds to a peak to peak variation in the pipe Reynolds number,  $Re_p$ , of 57.60, or equivalently an R.M.S. fluctuation of the pipe Reynolds

number of 20.36. 0.6 Volts was chosen as it is a large enough amplitude to drown out the rogue motor frequencies while at the same time being less than the non-linear, unstable range which exists from approximately 1.0 Volts peak to peak amplitude.

The set of test results that aimed to look at the effect of forcing amplitude on the flow processes, used three amplitudes, namely 0.2, 0.6 and 1.0 Volts, (R.M.S. fluctuations in  $Re_p$  of 6.79, 20.36 and 33.93). All these lying within the linear range.

#### 4.2.5 Pulsatile Laminar Flow

Prior to the introduction of an orifice plate it was decided to take some preliminary results for various pulsatile pipe flows. The Reynolds number, forcing frequency and forcing amplitude were varied independently of each other. This was done to test the method by which the data was to be abstracted and analysed for the main results. It also served as a test of the various analysis algorithms, such as the dimension algorithm, autocorrelation function, F.F.T. and the algorithm to find the first minimum in mutual information. Furthermore, plotting routines to produce time series and attractor plots, (section 2.4.3), could be refined.

The results for one such test are given in figure 4-5. This test was performed for a pipe Reynolds number of 256, a forcing frequency of 3.3Hz and a forcing amplitude of 0.6 Volts, (an R.M.S. fluctuation of 7.95%). In the figure one may see the time series, attractor plot and dimension plot for the velocity-time series at the centre-line of the pipe.

The time series is plotted in figure 4-5a. The time series looks periodic. However, a closer inspection reveals that most of the peaks and troughs are not smooth. This is due to two effects:

- 1 - The time series is not generated from a continuous signal, but a digitised signal. Thus the resultant time series is made up of a series of points connected by straight lines. This accounts in part for the general lack of smoothness of the time series.

2 – The time signal also contains a small amount of noise, which tends to distort the form of the time series.

The attractor plotted in figure 4–5b, is obviously periodic at large scales, as it displays a simple closed loop of a simple periodic wave function. However, a thickening of the attractor due to noise is also apparent. This noise is at smaller scales, too small to mask the overall periodic structure of the attractor.

The fractal dimension of the attractor is obtained from the ' $\log(r) - \log(Cr)$ ' plot shown in figure 4–5c, (see section 2.5.5). The plot has been performed for an embedding dimension,  $n$ , from 2 to 30. It can be seen from the plot that, at large length scales on the attractor, the slope of the lines tends to a value of 1. (Actually a value of 1.05 was measured by the author, denoted by the heavy line in the diagram.) This confirms the fact that the attractor is periodic, with one degree of freedom at these length scales. However, also evident from the figure is that for smaller length scales the slopes of the lines increase as  $n$  is increased. This is the typical behaviour of noisy flows. Thus it may be concluded that the attractor is indeed noisy at smaller length scales. This picture fits in with those derived by both visual observation of the time series and attractor plot.

The tests performed on pulsatile flows in the pipe without the orifice present, and reported in this section, will serve as a benchmark, (or perhaps a starting position), by which to interpret the main results.

#### **4.2.6 Natural Frequency Results and the Strouhal Number**

Tests were conducted to find the natural frequency of vortex shedding from each of the orifice plates used in the experimental investigation. The tests were performed with unpulsed flows by opening the drain valve at the piston. This was done over a wide range, thereby causing flows in the pipe at various Reynolds numbers. These Reynolds numbers were calculated by measuring the volume of water passing through the valve over a specific period of time.

The natural vortex shedding frequencies were measured using the L.D.A. system at various points downstream of each orifice plate. Flow visualisation was used to

check the L.D.A. readings by counting the number of vortices shed in a specified time period.

The Strouhal number was then calculated for each of these observations using equation 2.77, as follows,

$$S = \frac{f_{shed} \cdot L}{\bar{U}}$$

The results of these tests are summarised in figures 4-6 and 4-7.

Figure 4-6 gives the results obtained by the author for the 13mm orifice plate at Reynolds numbers from 282 to 1983. The results tend to suggest that the Strouhal number remains fairly constant up to a pipe Reynolds number of approximately 1500, from which point it increases. The average value of the Strouhal number over the 'flat' range is 0.668. Such a flat range, whereby the Strouhal number remains constant over a large Reynolds number range is typical of vortex shedding flows. (This type of behaviour has been illustrated in section 2.4.5, and figure 2.33.)

After a long search in the literature, the only source of data that could be found regarding Strouhal numbers of orifice flows at a Pipe orifice were those of Johansen [1929]. These results are for a pipe internal diameter of 27mm and water as a fluid. The results are also plotted in figure 4-6, and were obtained using flow visualisation only. (Unfortunately Johansen quoted neither the viscosity nor the temperature of the fluid, thus the Reynolds numbers he quotes may be for a different flow rate than equivalent Reynolds numbers for the author's results, this is a minor point which should only be noted.)

The Strouhal numbers were obtained for various Reynolds numbers for all the orifice plates used in the study. The results of these tests are shown in figure 4-7. Reliable results could not be obtained for the 22.75mm orifice plate, as the resulting frequency spectra was very broad band, i.e. no distinct peak could be seen. In figure 4-7 the best fit line of the data is shown dashed, together with the error bars of the Strouhal number points. The best fit line is obtained using a

least squares fit and the error bars represent 95% confidence limits using Students t- test, [Snedecor and Cochran, 1967].

The equation of the best fit line is,

$$S = 0.70643 - 0.13292 \cdot (D_o/D_p) \quad (4.4)$$

this equation was used to calculate the natural frequency,  $f_n$ , of the orifice plates at various Reynolds numbers in the study. The forcing frequency of the vortex shedding,  $f_f$ , was then set equal to this derived natural frequency. The Strouhal numbers for each orifice diameter used in the investigation are listed in table 4.1.

### 4.3 CALIBRATION OF THE COMPUTER ALGORITHMS

Prior to their use in the experimental investigation, the main computer programs, (the Grassberger-Procaccia dimension algorithm and Lyapunov exponent algorithm), were run using test data with known characteristics. The testing of the algorithms was rather extensive and to aid continuity in this chapter full details of these tests, and the results thereof, are given in appendix 2. Furthermore, appendix 2 contains a description of all computer programs used in the study, and listings of the main programs are given.

### 4.4 DERIVED RELATIONSHIPS

In what follows in this section an attempt will be made to clarify the many relationships and interrelationships between the parameters and variables in use in the experiments, prior to their use in subsequent chapters.

#### 4.4.1 Pipe, Orifice and Reynolds Number Relationships

First it is important to state two geometrical relationships of the pipe and

orifice plate – the diameter ratio,  $B$ , and the area ratio, or porosity,  $\alpha$ .  $B$  is the ratio of the orifice diameter to pipe internal diameter,

$$B = \frac{D_o}{D_p} \quad (4.5)$$

The porosity, which is the ratio of the orifice area,  $A_o$ , to the pipe internal area,  $A_p$ , is thus

$$\alpha = \frac{A_o}{A_p} = B^2 \quad (4.6)$$

Table 4.1 gives the ratios  $\alpha$  and  $\beta$  for the six orifice plates used in the study. The pipe and orifice Reynolds numbers are defined as,

$$Re_p = \frac{U_p \cdot D_p}{\nu}, \quad Re_o = \frac{U_o \cdot D_o}{\nu} \quad (4.7a \& b)$$

where  $U_p$  and  $U_o$  are the average velocities of the flow through the pipe and orifice plate respectively.

Now using the continuity condition one arrives at a simple expression relating the average pipe velocity to the average orifice velocity

$$U_p = B^2 \cdot U_o = \alpha \cdot U_o \quad (4.8)$$

Also from the above one can derive a simple relationship between the pipe Reynolds number and the orifice Reynolds number,

$$Re_p = B \cdot Re_o \quad (4.9)$$

#### 4.4.2 The Wake Reynolds Number

The Reynolds number may be defined using any arbitrary velocity and length scale deemed to suit the flow situation. For orifice diameters of the same order as that of the pipe, the flow may behave in a similar way to boundary layer flows encountering a bluff body, figure 4-8a. Whereas flows through orifice plates of diameters much smaller than the pipe diameter may behave more in the fashion of submerged jet flows as depicted in figure 4-8b. It thus may be argued that a more suitable definition of the Reynolds number for orifice plates with diameters comparable to the pipe internal diameter may be that of the wake Reynolds number, [Bandyopadhyay, 1986 and 1989] defined thus,

$$Re_w = \frac{U_h \cdot h}{\nu} \quad (4.10)$$

Where the length scale,  $h$ , is the height to which the orifice lip protrudes into the flow, and the velocity,  $U_h$ , is the velocity which would occur at a distance  $h$  from the pipe wall in the absence of the orifice plate.  $U_h$  is obtained by rearranging the Poiseuille pipe flow law into the following form,

$$U_h = \frac{8 \cdot \bar{U} \cdot h}{D_p} \left[ 1 - \frac{h}{D_p} \right] \quad (4.11)$$

Thus the wake Reynolds number in terms of the pipe Reynolds number is

$$Re_w = \frac{8 \cdot h^2}{D_p^2} \left[ 1 - \frac{h}{D_p} \right] \cdot Re_p \quad (4.12)$$

Now the lip height  $h$  is simply half the difference between the orifice diameter and the pipe diameter, i.e.

$$h = \frac{D_p - D_o}{2} = \frac{D_p}{2} \cdot (1 - B) \quad (4.13)$$

Thus equation 4.12 becomes

$$Re_w = (1 - B)^2 \cdot (1 + B) \cdot Re_p \quad (4.14)$$

Table 4.1 gives the lip height,  $h$ , and the ratio of  $Re_w$  to  $Re_p$  for all the orifice plates involved in this study. Substituting equation 4.10 into the above, the equivalent expression for the wake Reynolds number in terms of the orifice Reynolds number becomes,

$$Re_w = (1 - B)^2 \cdot (1 + B) \cdot B \cdot Re_o \quad (4.15)$$

$D_o$ (mm)	$S$	$\beta$	$\alpha$	$h$ (mm)	$\frac{Re_w}{Re_p}$
6.50	0.684	0.250	0.0625	9.750	0.703
9.75	0.673	0.375	0.1406	8.125	0.537
13.00	0.661	0.500	0.2500	6.500	0.375
16.25	0.650	0.625	0.3906	4.875	0.229
19.50	0.639	0.750	0.5625	3.250	0.109
22.75	0.628	0.875	0.7656	1.625	0.029

Table 4.1: Pipe-Orifice Relationships

4.4.3 The Forcing Frequency – Pipe Reynolds Number Relationship

The Strouhal number has been previously defined in sections 2.4.5 and 4.2.6 as

$$S = \frac{f_{shed} \cdot D_o}{U_o}$$

where  $f_n$  is the natural frequency of an orifice plate, orifice diameter  $D_o$ , with an average flow velocity through the orifice plate of  $U_o$ . All flows in the experiment reported herein, were forced at a frequency,  $f_f$ , equal to the natural frequency,  $f_n$ , (see section 4.5.). Therefore, the frequency of forcing of the flow in terms of the orifice and pipe Reynolds numbers is

$$f_f = \frac{S \cdot \nu}{D_o^2} \cdot Re_o = \frac{S \cdot \nu}{B^3 \cdot D_p^2} \cdot Re_p \quad (4.16)$$

4.4.4 Vortex Shedding Velocity and Wavelength

The vortices shed in a shear flow generally travel with a certain average velocity  $U_v$  and have a wavelength  $l_v$  and shedding frequency  $f_v$ , where,

$$U_v = f_v \cdot l_v \quad (4.17)$$

The vortex shedding frequency in the experimentation herein was controlled by setting the pulsation, or forcing frequency,  $f_f$ , at the natural frequency,  $f_n$ . Using the above definition of the Strouhal number, the vortex shedding velocity  $U_v$  may be obtained from the following relationship,

$$U_v = \frac{U_o \cdot l_v \cdot S}{D_o} = f_n \cdot l_v = f_f \cdot l_v \quad (4.18)$$

This is another useful relationship, since the vortex shedding wavelength,  $l_v$ , may be obtained by scaling from the flow visualisation photographs, and so the mean velocity of the vortices,  $U_v$ , could be estimated.

#### 4.4.5 Forcing Amplitude Relationship

In all cases, with the exception of one set of results, the forcing amplitudes were kept constant as the pipe Reynolds number was varied, this resulted in a different percentage forcing amplitude for each different value of  $Re_p$ . Lower values of  $Re_p$  therefore have a higher percentage of forcing. This was found to be advantageous since for higher Reynolds numbers lower disturbance levels are required to produce discrete vortices.

Thus for a value of  $Re_p$  of 256, a forcing voltage of 0.6 volts represents an R.M.S. fluctuation value of 7.95%. The general formula for finding an R.M.S. fluctuation value is:

$$\text{R.M.S (fluct)} = \frac{\text{Voltage} \times 96}{Re_p} \cdot \frac{1}{2 \cdot (2)^{\frac{1}{2}}} \quad (4.19)$$

#### 4.5 OUTLINE OF THE EXPERIMENTAL WORK

The results from the experimental work undertaken are reported in chapters 5 and 6. Chapter 5 deals with the flow visualisation both from photographs and video film. Whereas chapter 6 deals with the main L.D.A. results and subsequent data analysis.

The flow visualisation results (Chapter 5) are primarily to present an overall visual description of the flow processes at the orifice plate, and thus give a qualitative insight into the various phenomena prior to the L.D.A. readings. Quantitative results are also derived from the flow visualisation by scaling wavelengths from photographic and video film, from which vortex velocities may be found. Vortex trajectories may also be obtained. Vortex velocities, and the timing

of other events, may be obtained by using the video film of events with a time code superimposed upon it. The video may be paused from frame to frame and distance travelled by certain flow areas measured. More will be said about these methods in chapter 5.

The L.D.A. results of chapter 6 deal with the quantitative analysis of certain regions of the flow. The parameters could varied independently during the course of the study were:

- 1 - The Pipe Reynolds Number ( $Re_p$ )
- 2 - The Orifice Diameter ( $D_o$ )
- 3 - The Forcing Amplitude ( $A_v$ ). (Varied in only one set of tests.)
- 4 - The Forcing Frequency ( $f_f$ ).
- 5 - The Measuring Position along the Pipe ( $z$ )
- 6 - The Measuring Position across the Pipe ( $r$ )

The orifice Reynolds number ( $Re_o$ ), is dictated solely by (1) and (2) thus is not an independent variable. During the investigation the pipe used was of the same internal and external diameter. Also kept constant was the temperature of the water, and thus the kinematic viscosity. (See Chapter 3, section 3.2.3 and 3.2.7).

The number of independent experimental parameters which may be varied is therefore six. This was considered still too large a number to effectively study within the time constraints of the work, thus it was decided to force the vortex shedding at the natural frequency only, (i.e.  $f_f = f_n$ ). This reduces the number of independent parameters to five. Therefore,  $f_f$  is a function of the Reynolds number linked to it via the Strouhal number as outlined in equation 4.16. A comprehensive investigation of the effect of forcing frequency is therefore outside the scope of this investigation.

Strictly speaking parameters (5) and (6) are not really experimental variables. Since by varying either, and hence moving the observation point of the L.D.A. system, the flow processes do not change. They are only parameters in the sense, that by varying the position of the laser probe volume in the flow, various time traces with different properties may be obtained. This is because the time dependent flow properties vary spatially within the flow.

The tests performed varied these parameters in a controlled manner and the effect they had on the flow processes monitored. The tests performed are outlined in table 4.2. A standard set of results which is common to both set-A and set-B and with which most of the other sets of results may be compared to is as follows:

$$\begin{aligned} Re_p &= 256, D_o = 13\text{mm}, Re_o = 512, \\ f_f &= 2.52\text{Hz}, A_f = 0.6\text{V} (= 7.95\% \text{ R.M.S. fluctuation}) \end{aligned}$$

these parameters were observed along the pipe axis, ( $r = 0$ ), at the seventeen longitudinal positions, ( $z$ ), outlined in chapter 3 section 3.2.12.

Set-A could be described as the main set of results. This set monitors the effect on flow behaviour of varying the pipe Reynolds number. Set-B looks at the effect of varying the forcing amplitude while keeping the pipe Reynolds number constant. Set-C and set-D look in detail at the flow processes occurring for various values of  $Re_p$ , at orifice plates of diameters of 9.75mm and 16.25mm respectively. Set-E briefly looks at the remaining orifice diameters of 6.5mm, 19.5mm and 22.75mm. Only the frequency spectra, average velocity and the turbulence intensities are measured for these orifice plates. Whereas, the above sets of results are taken at the centre-line of the longitudinal axis of the pipe, set-F, aims to investigate the flow properties across the flow in the immediate vicinity downstream of the orifice plate. Lastly set-G is another set of results taken for the parameters of the standard set and used as a check on the repeatability of the experiment.

Parameter	Test						
	A	B	C	D	E	F	G
$D_o$ (mm)	13	13	9.75	16.75	Range	13	13
$Re_p$	Range	256	Range	Range	256	256	256
$Re_o$	$\beta.Re_p$						
$f_f$	$f_n$						
$A_f$ (Volts)	0.6	Range	0.6	0.6	0.6	0.6	0.6
$A_f$ (Re)	57.6	Range	57.6	57.6	57.6	57.6	57.6
'z' No. of Longit'nal Positions	17	17	17	17	17	5	17
'r' No. of Radial Positions	C.L.	C.L.	C.L.	C.L.	C.L.	10	C.L.
TOTAL NUMBER OF TESTS	5	3	3	3	3	1	1

Table 4.2: Outline of the Experimental Tests

Legend: C.L. - Result Taken at the Centre Line Only

**CHAPTER 4**  
**FIGURES**

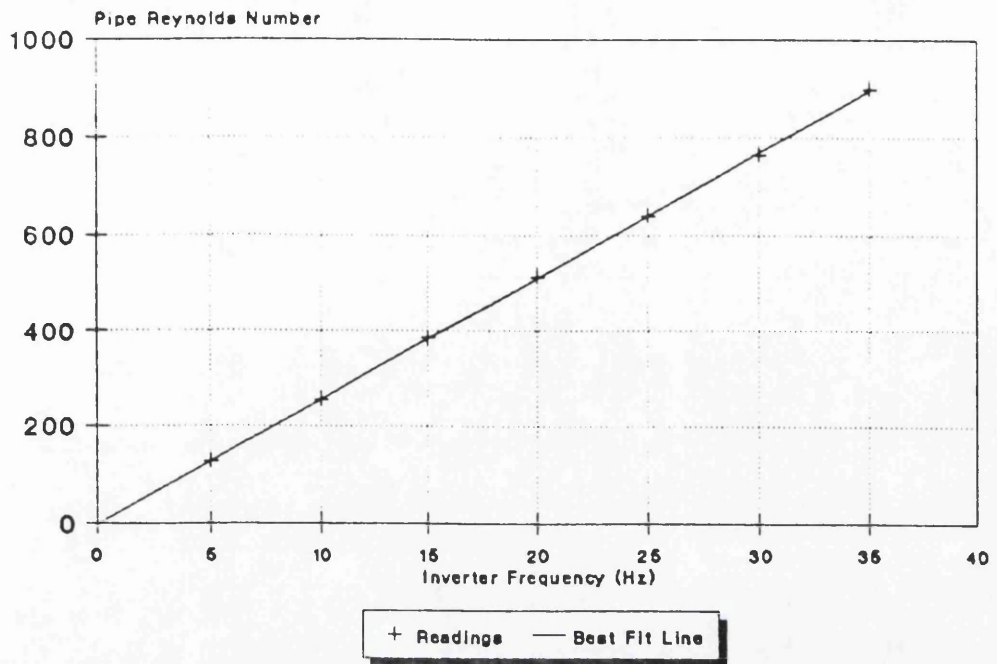
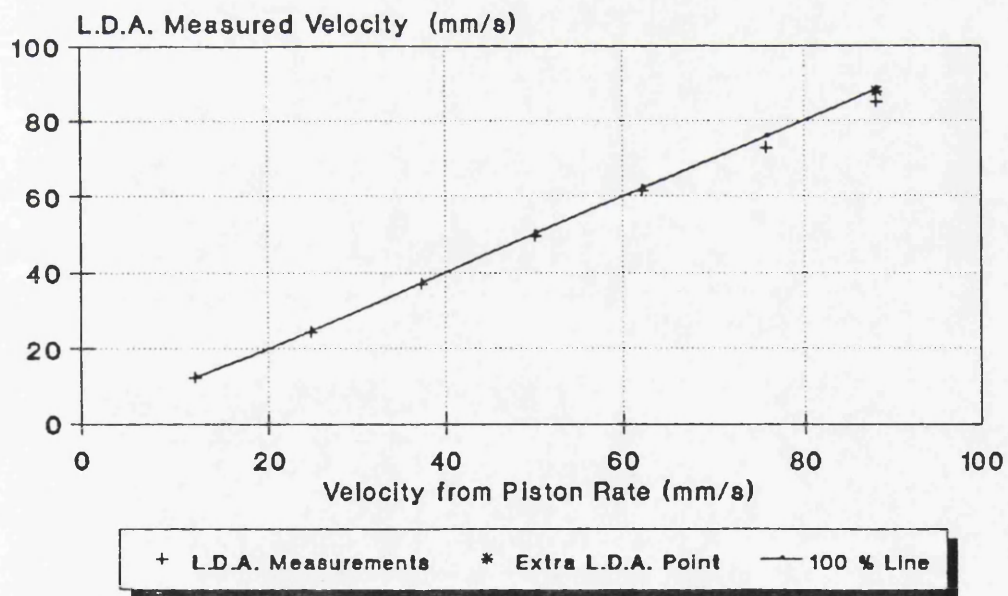
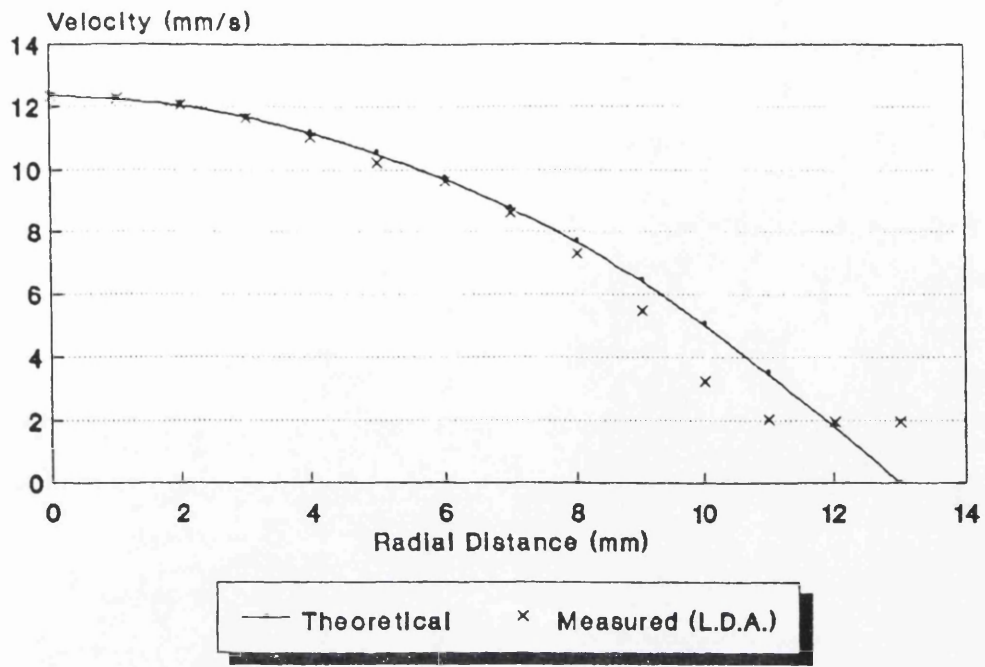


Figure 4-1: Inverter Frequency - Pipe Reynolds Number Relationship

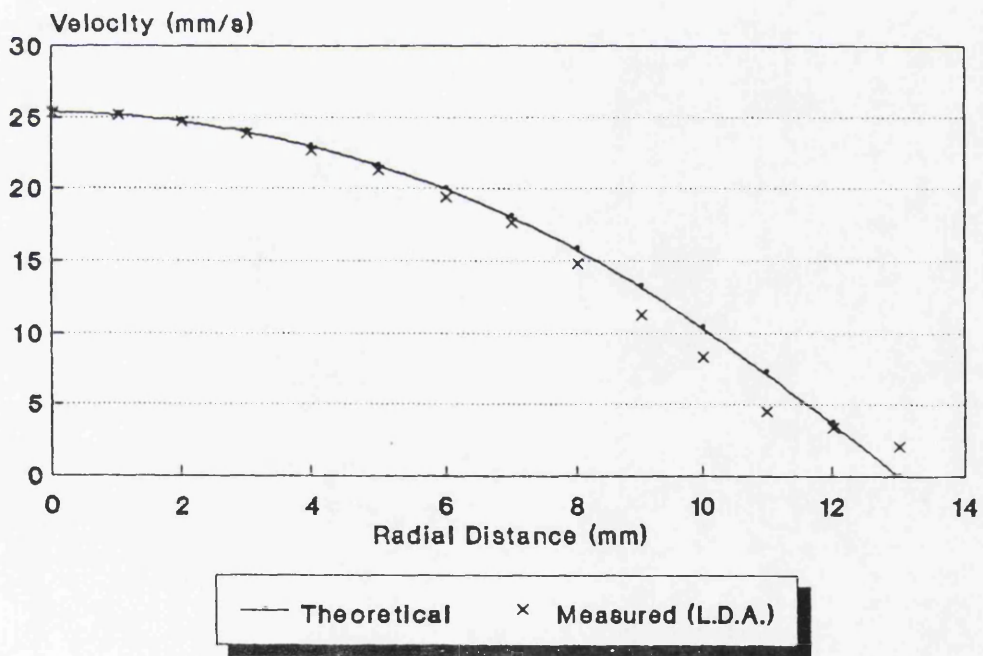


L.D.A. Points Taken at  $F_d=33000$   
 Extra L.D.A. Point Taken at  $F_d=100000$

Figure 4-2: Centre-line Velocity Comparison

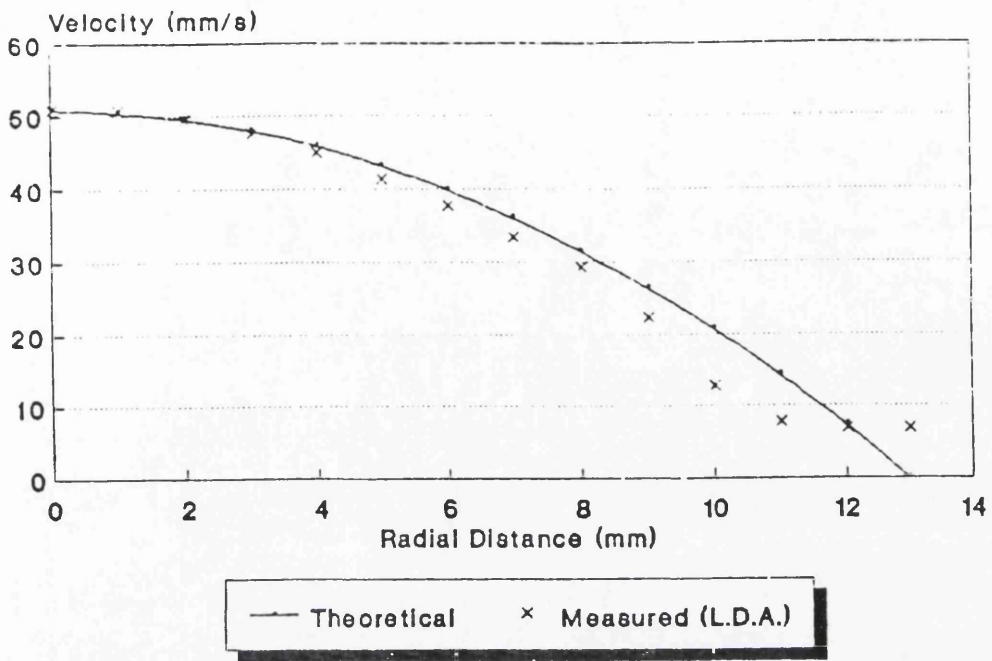


(a)  $Re_p = 128$

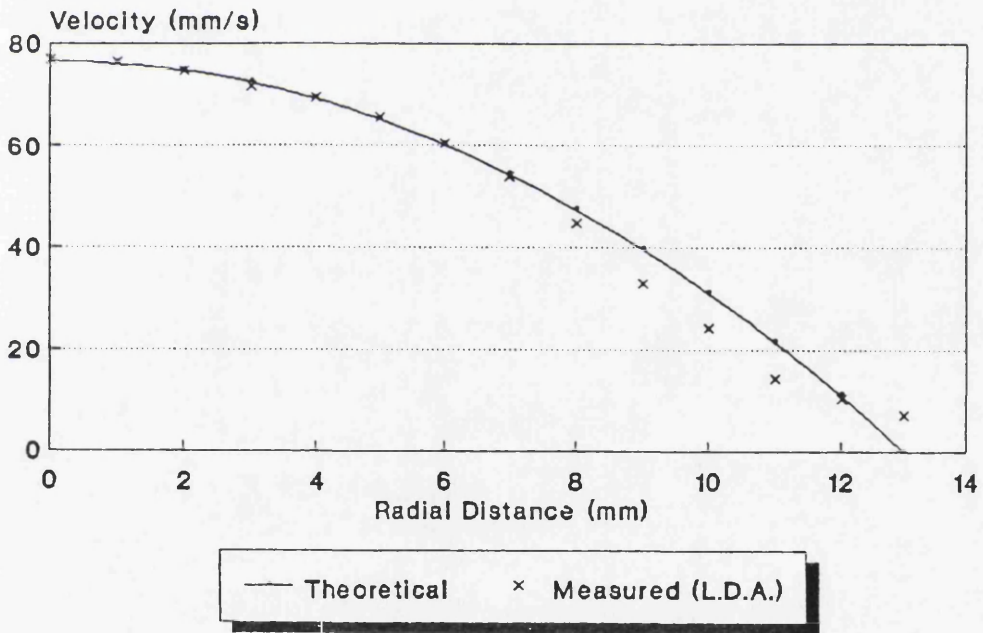


(b)  $Re_p = 256$

Figure 4-3: L.D.A. Velocity Profiles

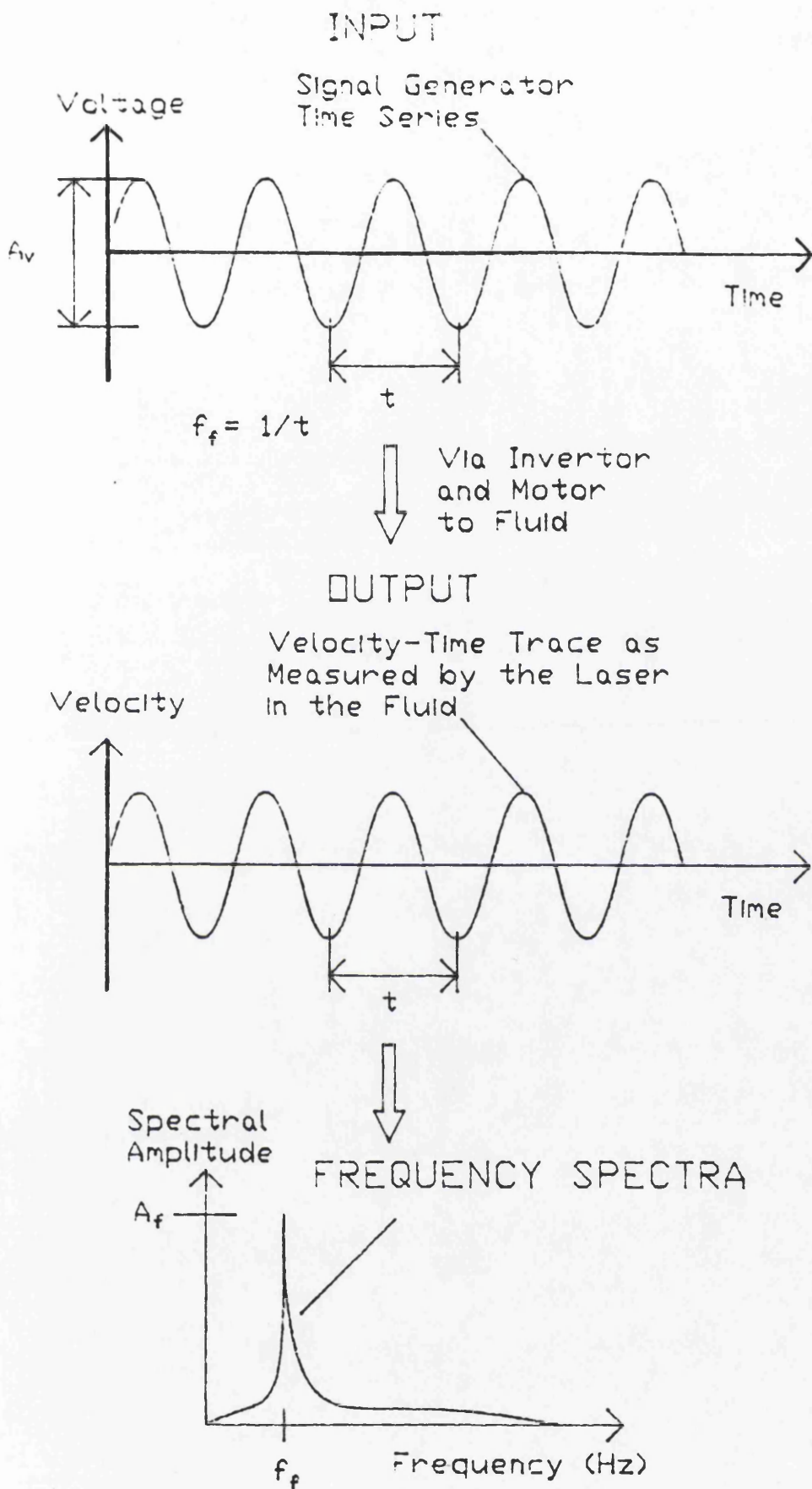


(c)  $Re_p = 512$



(d)  $Re_p = 768$

Figure 4-3: L.D.A. Velocity Profiles



(a) Definition Sketch of the Relative Amplitude Test  
**Figure 4-4: Relative Amplitude Tests**

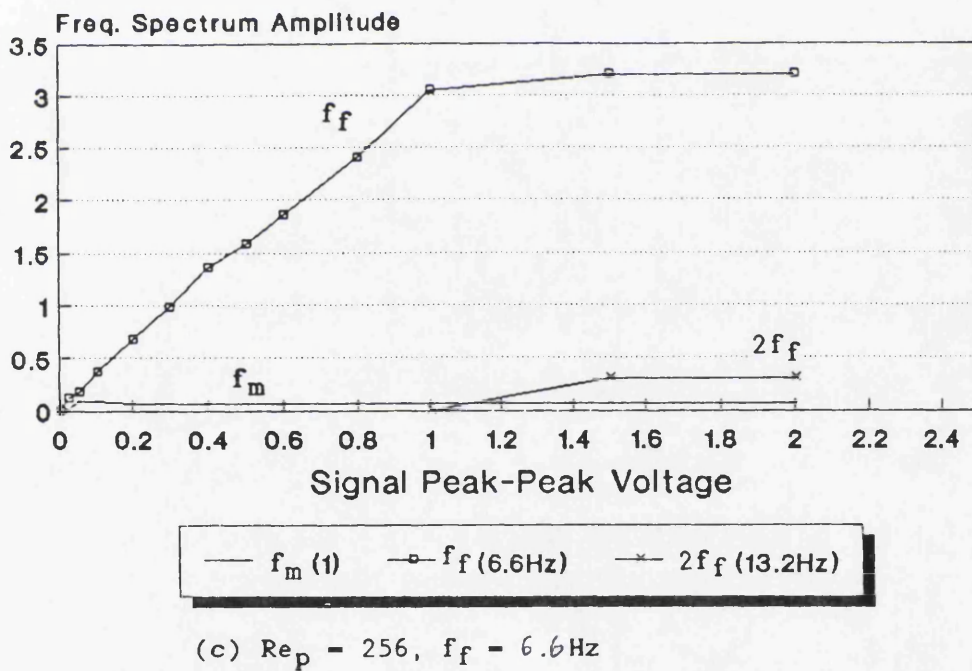
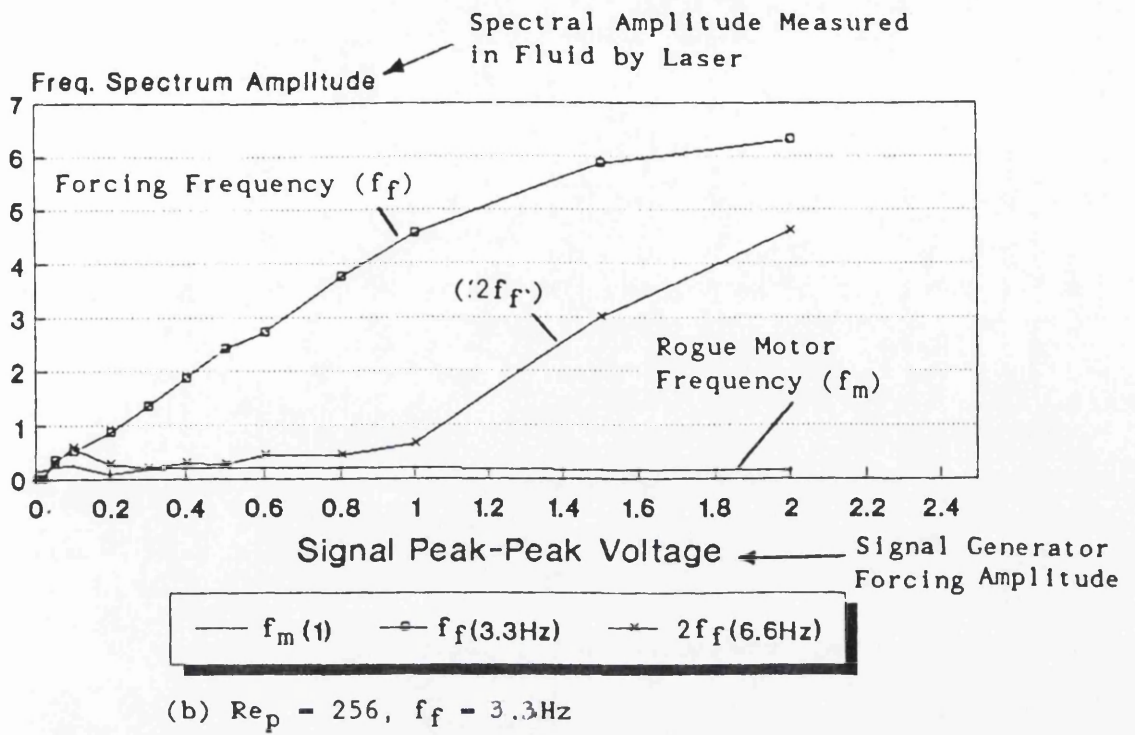
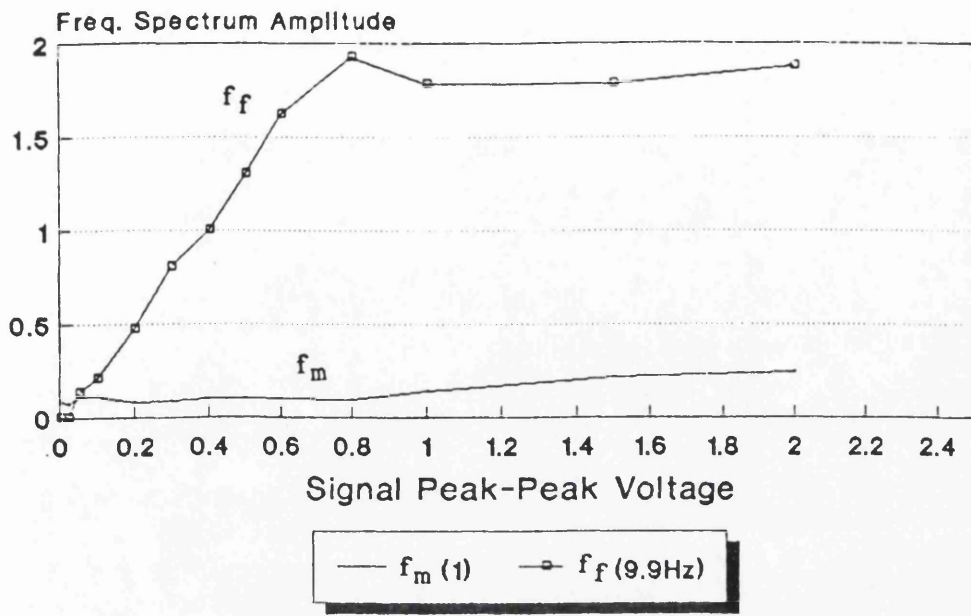
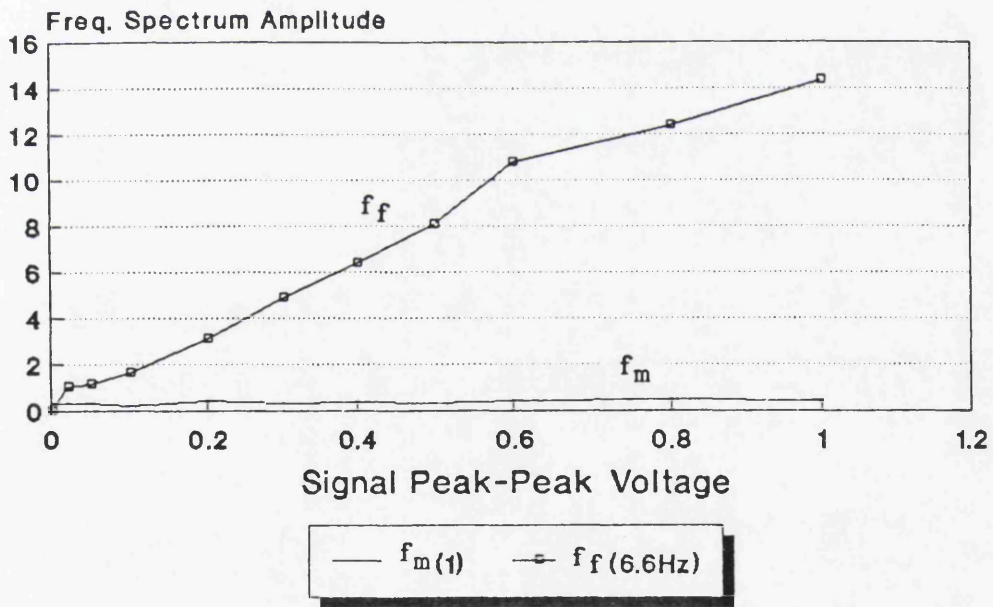


Figure 4-4: Relative Amplitude Tests



(d)  $Re_p = 256$ ,  $f_f = 9.9\text{Hz}$



(e)  $Re_p = 512$ ,  $f_f = 6.6\text{Hz}$

Figure 4-4: Relative Amplitude Tests

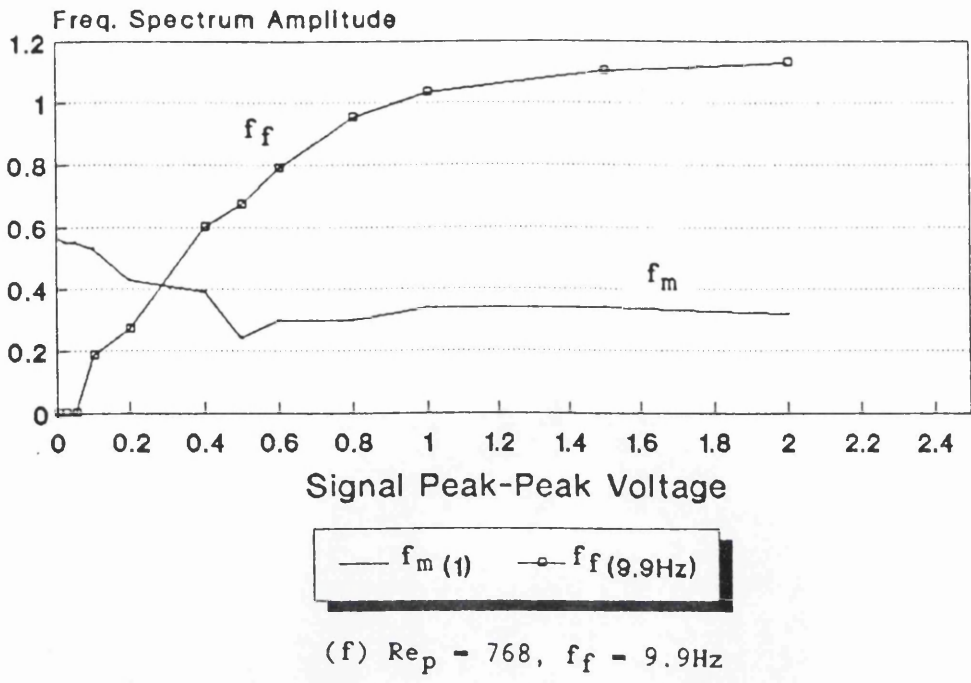
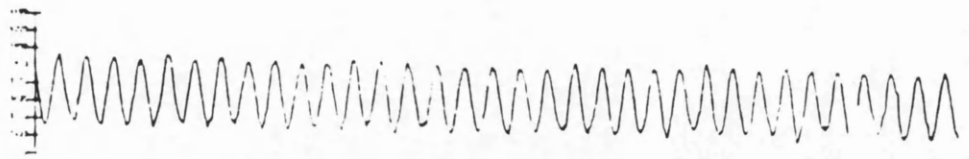
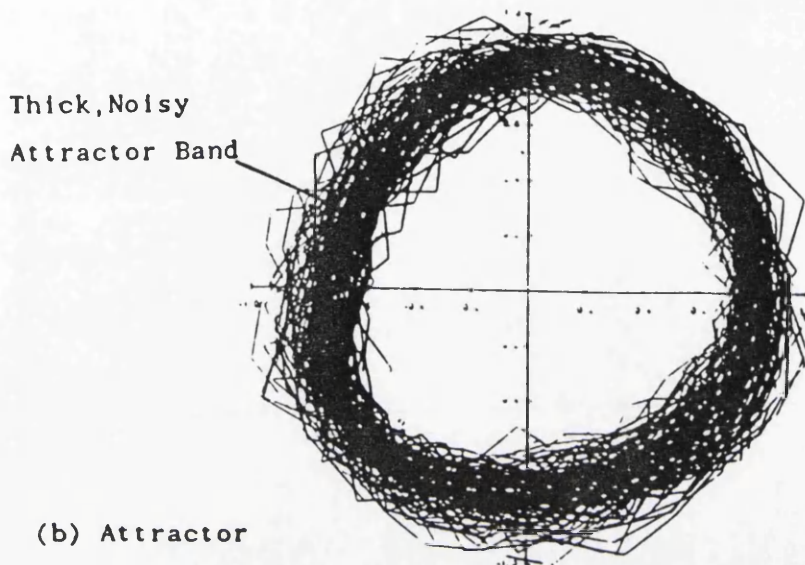


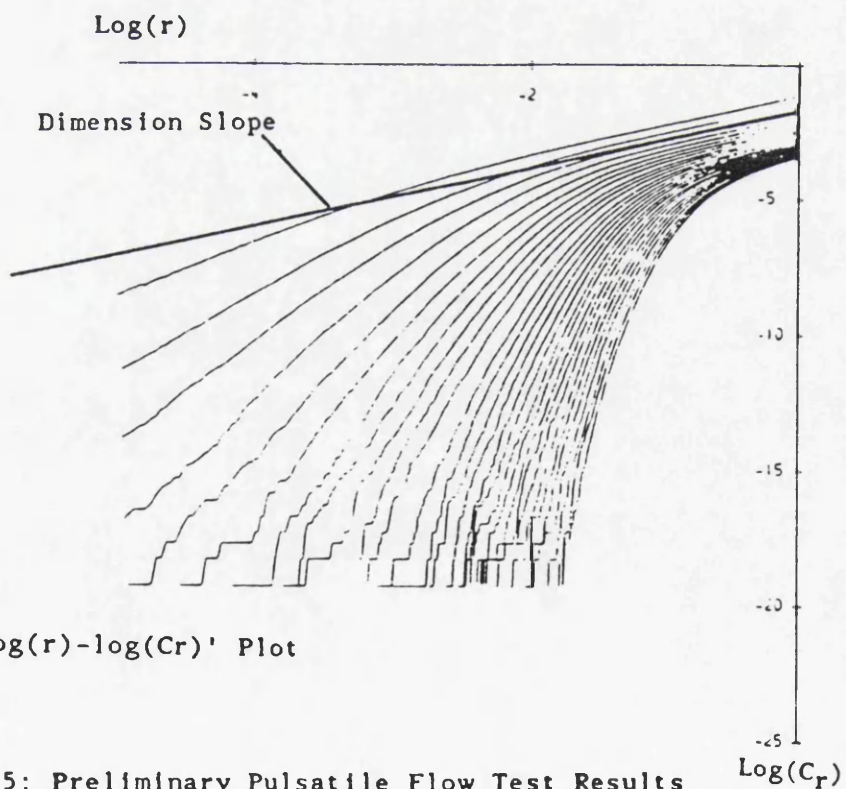
Figure 4-4: Relative Amplitude Tests



(a) Time Series



(b) Attractor



(c) ' $\log(r)$ - $\log(Cr)$ ' Plot

Figure 4-5: Preliminary Pulsatile Flow Test Results

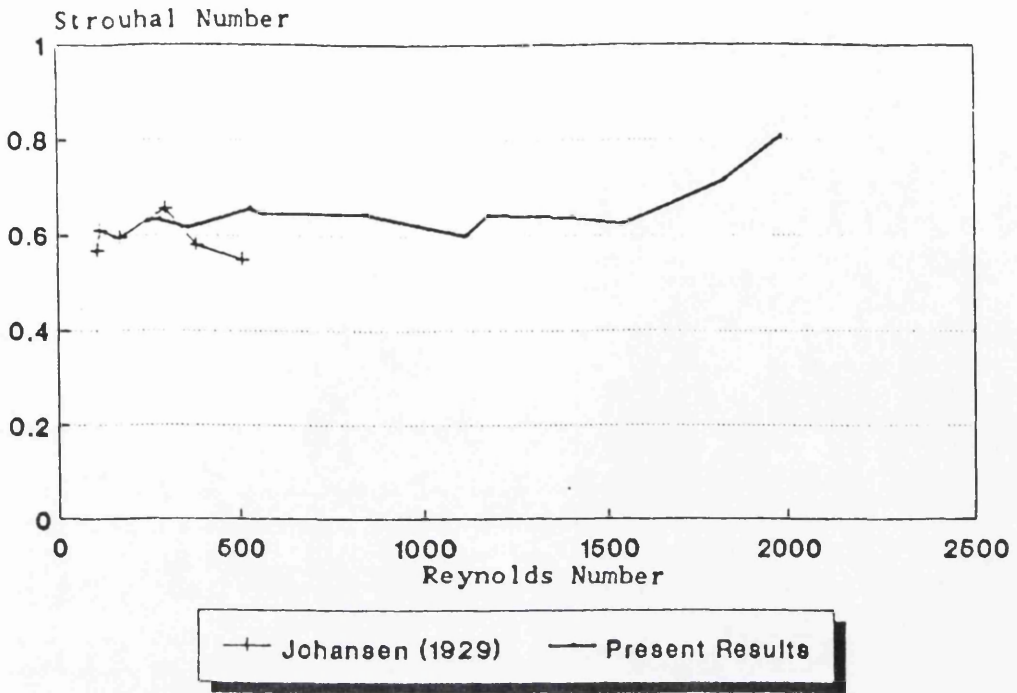


Figure 4-6: Strouhal Number Results - 13.00mm Orifice Plate

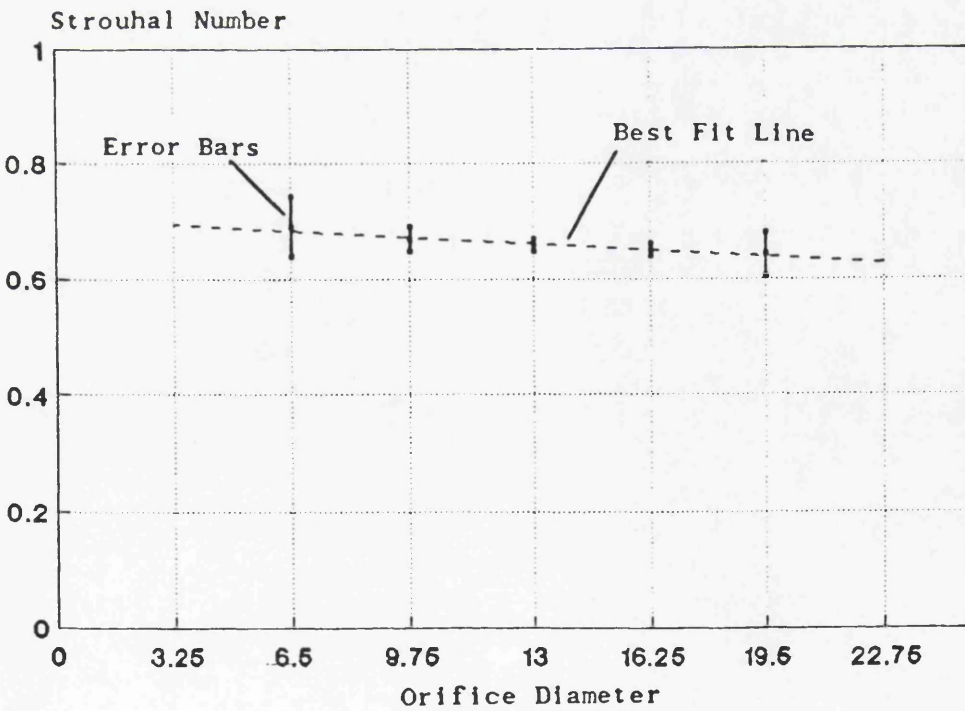
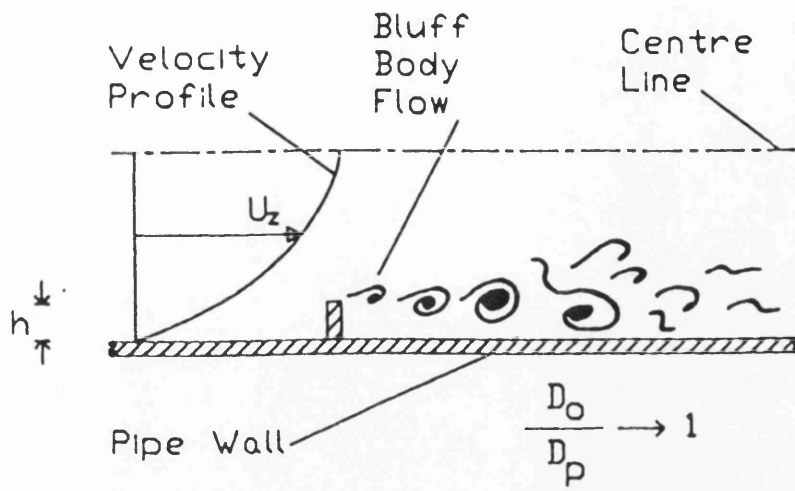
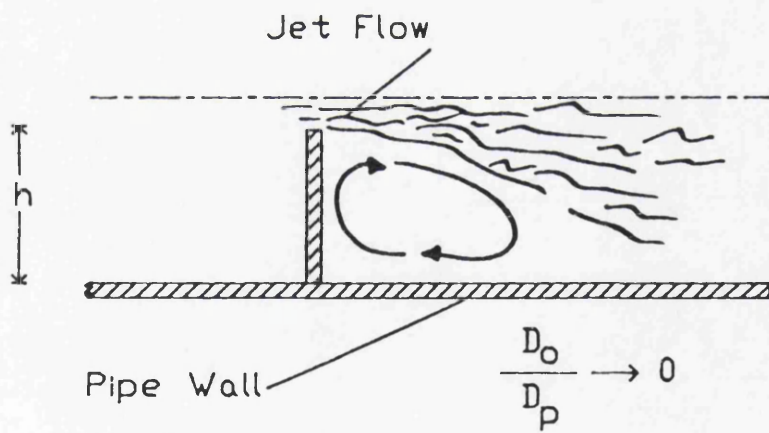


Figure 4-7: Strouhal Number Results - All Orifice Plates



(a) Wake Flow



(b) Jet Flow

**Figure 4.8; Wake and Jet Flows at an Orifice Plate**

## CHAPTER 5

## CHAPTER 5

### FLOW VISUALISATION RESULTS

#### 5.1 INTRODUCTION

#### 5.2 BACKGROUND TO FLOW VISUALISATION

5.2.1 The Technique of Flow Visualisation

5.2.2 Interpretation of the Flow Phenomena

5.2.3 Illumination of the Flow

5.2.4 Information from Film

5.2.5 Geometrical and Refractive Properties  
of the Pipe

5.2.6 Flow Visualisation at a Pipe Orifice

#### 5.3 PRELIMINARY TESTS

#### 5.4 NATURAL, UNFORCED FLOW RESULTS AT THE 13.00mm ORIFICE PLATE

#### 5.5 FORCED FLOW RESULTS: THE 13mm ORIFICE

5.5.1 Flows at the Orifice Plate

5.5.2 Downstream Dissipation of the Disturbances

#### 5.6 FORCED FLOW RESULTS: THE 9.75 AND 16.25mm ORIFICE PLATES

5.6.1 The 9.75mm Orifice

5.6.2 The 16.25mm Orifice

## **5.7 VIDEO RESULTS**

### **5.7.1 Introduction**

### **5.7.2 Contents of the Video Film**

### **5.7.3 Overall Picture of the Flow Processes**

### **5.7.4 Categorisation of the Flow Visualisation Results**

## **5.8 VORTEX WAVELENGTH AND VELOCITY RESULTS**

## **5.9 SUMMARY**

## 5.1 INTRODUCTION

The purpose of this chapter is to introduce the reader to the concept of flow visualisation in Fluid Mechanics, to report on photographs and a video taken for a range of orifice diameters, Reynolds Numbers in the pipe and forcing frequencies covering an area in the immediate vicinity of the orifice plate. The chapter concludes with experimental measurements of vortex wavelengths taken from the flow visualisation tests.

## 5.2 BACKGROUND TO FLOW VISUALISATION

### 5.2.1 The Technique of Flow Visualisation

Flow visualisation has for many years played an important role in the understanding of flow phenomena. The technique provides the experimentalist with both spatial and temporal information about the flow, whereas more quantitative methods such as laser Doppler anemometry or hot wire techniques may be limited to a few spatial positions. Various flow visualisation techniques have been developed to elucidate the properties of gas and liquid flows with the intention of giving an insight into the processes involved. Flow visualisation achieves this aim by rendering visible the actions of the flow, aiding visual perception of the processes. In the study presented herein, flow visualisation was undertaken to aid the physical interpretation of the L.D.A. data.

The technique of flow visualisation works by releasing an agent into the flow which is distinctly visible within the fluid, and, under certain illumination serves to highlight the processes in certain areas of the flow field. There are many agents that are suitable for such studies, and they may be split into two broad categories — dyes and tracer particles. Many substances may be used as dyes in the flow, these include, food colouring, ink, potassium permanganate, methanol blue dye, fluoresceine, even milk. Spherical and non-spherical tracer particles are used in flow visualisation studies. The choice of particles is also wide including, helium bubbles, oil droplets, smoke particles, talcum powder, guanine crystals, hollow glass

spheres, polystyrene and so on. The choice of both dyes and particles really depends on the flow process being observed and the working fluid being used. A much more complete list of these substances and the role they play can be found in Merzkirch [1987].

The most famous example of the use of flow visualisation to elucidate a flow phenomenon is certainly the classic experiment by Osborne Reynolds [1883] who, in the latter part of the last century studied the laminar to turbulent transition processes within a pipe. Reynolds used a dye to produce a streakline in water running through a pipe. The streakline remained as an ordered linear element when the flow was laminar. At the laminar–turbulent transition point the streakline would become unstable, breaking down and mixing rapidly in the turbulent state. This work enabled Reynolds to conclude that the transition point depended on a non–dimensional flow parameter, now known as the Reynolds number in his honour.

### 5.2.2 Interpretation of the Flow Phenomena

Depending on the agent used and the mode of observation different conclusions may be reached. It is therefore necessary to define the various observable flow patterns.

**Streakline** – (Also known as filament lines.) This is the instantaneous locus of all fluid particles which have passed through a particular, fixed spatial location in the flow. If one requires to observe these flow lines then a dye would be used. Injecting the dye at a particular spatial position in the flow and taking a photograph of the instantaneous flow field will show the streakline. A good example of the use of streaklines in obtaining flow information can be found in the paper by Zdravkovich [1969]. In the article smoke streaklines were observed in the wake of laminar flow past a circular cylinder, giving an insight into the regions of high vorticity production in the flow field which led to vortex roll up. The downstream development of the resulting vortex streets could be seen leading to an overall picture of the flow processes involved.

**Particle Path** – This is the curve that a fluid particle traverses in the flow field

over a finite time period. Particle paths may be obtained by observing single tracer particles (or a low concentration which allows for individual particles to be easily distinguished) and using a long exposure time. The image of each particle on the resulting photograph will be drawn out as a locus of points known as the particle path.

**Streamlines** – These are curves tangential to the instantaneous direction of the flow velocity vector, at all points within the flow. Streamlines may be obtained with a low concentration of tracer particles within the fluid. An intermediate exposure time should be used that is long enough to allow the tracer particles to produce very short particle paths at each position in the fluid. From these short paths the fluid velocities may be obtained, (by the method outlined below in section 2.4.3), and the fluid streamlines may be inferred.

For the case of steady flow, in which the flow field is independent of time, these three curves coincide with each other. Whereas in unsteady, time dependent flows, these curves are not coincident and one must be careful in the interpretation of flow photographs. This is especially true for unsteady shear flows, [Gursul et al, 1990, Hama, 1962, and Gursul and Rockwell, 1991].

One of the most popular tracer particles for use with low to moderate Reynolds number flows is natural guanine crystals, [Matisse and Gorman, 1984]. It was decided to use these particles for the study reported here. These crystals occur naturally in fish and are in fact responsible for the pearly, lustrous appearance of their scales. The crystals have a plate-like structure, their approximate dimensions being 30.0  $\mu\text{m}$  long by 6.0  $\mu\text{m}$  wide and 0.1  $\mu\text{m}$  thick. This shape enables the particles to align themselves with the shear in the flow, [Rhee et al, 1984]. This property, combined with their relatively high refractive index of 1.85, allows them to render flow structures visible when illuminated by a suitable light source.

A basic requirement of a flow visualisation agent is that it stays in suspension for as long as possible, that is, it has a slow settling out rate. It is particularly important that this rate is on a much larger time scale than the flow phenomena under investigation. The settling out rate of a sphere can be found using Stokes theory, [Massey, 1983]. Unfortunately, there is no such simple theory for non-spherical particles.

Another requirement of the flow visualisation agent is that its mere presence does not interfere with the flow processes being studied. For the purposes of most investigations it is assumed that the particle size and concentration is so low that the characteristics of the flow field are not altered by the presence of the particles. The two main sources of deviation of a particle's velocity vector from that of the fluid are:

- 1 – a velocity lag due to the inertia of the particle, and,
- 2 – a deviation in the particle direction due to a lift force caused by velocity gradients acting over the particle.

Both these errors are explained in detail in Merzkirch [1987].

### 5.2.3 Illumination of the Flow

The most common method of illumination in flow visualisation studies is the light sheet. Light sheets may be generated in a variety of ways, the most common of which are lamps (or flashguns) with appropriate light guides and lenses. They may also be generated by expanding laser beams in one plane by a suitable lens, Schlien [1987].

With the light sheet one may visualise the two velocity components in the plane of the sheet for many points or particles, [Emrich, 1983]. The sheet can be moved from region to region of the flow field under investigation and a complete picture built up of the flow processes involved, see for example Prenel et al [1989]. A suitable light sheet for the flow visualisation undertaken in the study reported herein was provided by a purpose built light box, more details of which will be given in the experimental chapter, section 3.6.

When using a lamp for illumination, precision and control of the exposure time,  $t_e$ , is very important. The higher the flow velocity, the faster the exposure time required to eliminate excessive blurring of the image. However, where there is a flow field containing a wide range of velocities one is required to compromise with the exposure time.

#### 5.2.4 Information from Film

In photographs taken with lamplight the amount of light falling on the photographic film is determined by both the exposure time (shutter speed) and lens aperture. Streaks on the film corresponding to the faster particles will naturally appear more faint than those generated by the slower ones, this is due to the shorter residence time that light from the particle spends at a certain location on the photographic film.

A flashgun may also be used as the source of illumination in flow visualisation studies. The pulse of light emanating from a flashgun typically lasts approximately  $1/10,000$  of a second. The shutter speed is set to a nominal value, typically  $1/60$ th or  $1/250$ th of a second. The flashgun is synchronised to go off within the time the shutter opens and closes. Therefore, the only variable the photographer is able to use, to control the amount of light falling on the photographic film, is the aperture. (This is the case for all standard flash photography. Although some advanced flash systems for professional use do allow for the flash pulse time to be varied.) The extremely short duration of the flash pulse essentially causes the particles of the flow to appear frozen, as there is no time for streaks to appear on the film.

Moving film, such as cine or video, to capture the results of flow visualisation investigations, is useful for time dependent flows. It can provide an overall description of the flow processes as they evolve through time by giving a frame by frame account of the events, each frame is separated by a constant time interval. The film may then be slowed down so that rapidly occurring events can be made to unfold at a more comprehensible speed. The film may even be stopped and each frame analysed individually to shed light on complex flow interactions as they develop with time. There are many good examples of the use of such techniques in the literature. Hernan and Jiminez [1982] analysed cine film of plane turbulent mixing layers to look at the process of vortex merging, pairing, tripling and tearing. Willert and Gharib [1989], made use of the instant playback facility of video to analyse visualised flows quickly.

### 5.2.5 Geometrical and Refractive Properties of the Pipe

When visualising flows in a pipe the observer must bear in mind that the flow field, made visible by the light sheet, is not the true picture of the phenomena. This is due to the geometry of the pipe and the different refractive properties of the air, glass and water, [Gardarvsk/ et al, 1989]. Thus photographs of the apparent, observed flow field are slightly in error from the actual flow field. Appendix 3 deals in detail with the geometric and refractive considerations involved in the study.

### 5.2.6 Flow Visualisation at a Pipe Orifice

There are a great number of flow visualisation experiments cited in the literature which deal with all manner of flow phenomena. Most of which are documented in the comprehensive text on the subject by Merzkirch [1987]. A confirmation of the importance attached to the use of flow visualisation is the fact that many of the experimental papers cited elsewhere in this thesis contain flow visualisation pictures as an aid to the understanding of the main text. See for example Bandyopadhyay [1986], Durst et al [1989], Lindgren [1957], Wygnanski and Champagne [1973], Hanco [1967], Lugt [1962], Baumann et al [1992], Gharib and Stuber [1989], Stuber and Gharib [1990], Novikov [1991], Hunt et al [1978], and Perry et al [1980]. Flows at a pipe orifice, however, seem to have escaped the attention of researchers. Two experimental studies of pipe orifice flow, one at low Reynolds numbers the other at relatively higher Reynolds numbers will be discussed briefly in the following paragraphs.

Johansen [1929 ], investigated the pressure drop caused by low Reynolds number flows at a pipe orifice. In conjunction with the main pressure readings he successfully used flow visualisation to present an overall picture of the flow details at the orifice. Water was the liquid in the pipe and streaklines formed from a 0.2% solution of methylene blue in distilled water were produced. The pipe diameter was 27mm, and the majority of the experiments were made with an orifice to pipe diameter ratio of approximately a half, (0.502). From the resulting observable flow patterns Johansen [1933], was able to show the sequence of events at the orifice plate as the orifice Reynolds number was increased from rest to 1600. A full explanation is given in section 2.3.7.

A flow visualisation study at much higher orifice Reynolds numbers was performed by Kowalke [1938], where the orifice diameter was typically about an eighth of the pipe diameter. Thus, even for relatively low pipe Reynolds numbers, jet flows were produced at the orifice plate. (Since the ratio of the orifice to pipe Reynolds number scales inversely with the ratio of the orifice to pipe diameter). These jet flows were well above the flow conditions required for coherent vortices to be formed. Kowalke used aluminium powder as the flow visualisation agent, with the liquid being a glycerol-water mixture. The high settling out rate of aluminium powder was not a problem with such fast flows.

### 5.3 PRELIMINARY TESTS

Photographs were taken of the main tests using a flow visualisation chemical. (Details of the photographic equipment and the flow visualisation chemical are given in chapter 3.) It was hoped to elucidate visually, from the photographs, some of the pertinent mechanisms involved in the flow processes at the orifice plate. In the flow visualisation photographs presented in this chapter the orifice plate is at the right hand of the picture, (unless otherwise stated), with the fluid flowing from right to left.

Figure 5-1 gives an overall view of the apparatus, as seen through the camera lens, when the camera is in position for taking the flow visualisation photographs. The light guide of the light box is seen entering from the top of the picture and has a scale attached to its bottom edge. (The smaller scale in the figure, above the pipe.) The glass pipe runs across the centre of the photograph. At the right hand edge, the orifice plate and end flanges are visible. On the glass pipe itself, two markers may be seen, these are placed at intervals of 100mm from the orifice plate. These markers, which extend further downstream, were used in photographs taken of the dissipation of the disturbances downstream of the orifice plate.

The lower scale in the photograph, beneath the pipe, is attached to the drip tray and was used to position the laser carriage in the axial direction, upstream and downstream of the orifice plate.

In the photograph of figure 5-1 the flow within the pipe is illuminated by flash. It can be seen that the flow detailing is quite poor due to the fact that the room lights are on. It was decided therefore to take all the main photographs of flow phenomena with the room lights switched off. (In some circumstances the upper scale was illuminated by a suitably placed table lamp.)

Figures 5-2a and 5-2b highlight both the difference obtained by flash and lamp light illumination, and the tendency for the flow visualisation chemical to settle out. As is evident from the two figures, the flash photograph (figure 5-2b) gives a sharper image. This is a result one would expect due to the exceptionally short duration of the flash pulse. However, most photographs were taken with lamplight, as the phenomena could be viewed prior to taking the picture, whereas all flash photographs had to be taken in the dark. (See chapter 3, section 3.6.)

The settling out of the flow visualisation chemical was a problem which was solved, after some thought, by simply turning the light box on its side, thus illuminating the flow in the horizontal plane rather than the vertical plane. It was reasoned that this would give an axisymmetric variation of the chemical across the flow, showing both halves of the vortex ring sections. The stand mechanism of the light box was modified for this purpose.

In the next three sections, (5.2, 5.3 and 5.4), some of the photographic results obtained are presented and discussed. In section 5.5 details are given of the filming of the flow processes using video film. Note that in all instances, (i.e. in both photographic and video film), the flow is from right to left. Section 5.6 presents the results of vortex wavelength and velocity measurements taken directly from photographic and video film.

#### 5.4 NATURAL, UNFORCED FLOW RESULTS AT THE 13.00mm ORIFICE PLATE

Preliminary results were taken of the unforced flows at the 13.00mm orifice plate, to find the natural vortex shedding frequency of the orifice plate for various

Reynolds numbers. Unforced flows, that is flows without an imposed forcing frequency, were produced without the piston by opening the lower drain valve on the front face of the piston casing and thereby controlling the flow rate. Figures 5-3a to 5-3e give a few natural vortex shedding results for the 13mm orifice plate. The figures cover a wide range of orifice flows, from slow divergent flows, through vortex shedding flows to jet flows.

Figure 5-3a shows the flow through the orifice for a pipe Reynolds number of 194. The detachment of the flow as it passes through the orifice is clearly evident. No discrete vortices may be seen. The main flow streaming through the orifice expands in a smooth conical fashion until it reattaches at the pipe wall.

The smooth, orderly manner of the flow in figure 5-3a should be compared with the flow in figures 5-3b and c, both for a pipe Reynolds number of 373, (different exposures). In these cases, discrete vortices may be seen at the edges of the main flow jet, streaming through the orifice. These vortices increase in size and a breakdown to turbulence occurs at approximately 70mm, or 5.39 orifice diameters, downstream of the orifice plate.

Figure 5-3d gives details of the flow breakdown for a pipe Reynolds number of 437. The flow breaks down at approximately 55mm, ( $4.33 \times D_o$ ), from the orifice plate, an earlier point than for  $Re_p = 373$ .

Finally, figure 5-3e shows the flow through the orifice plate for a pipe Reynolds number of 2432. A confined jet flow may be clearly seen emanating from the orifice plate. The conical, central core of the jet extending into the highly turbulent region up to 40mm, or three orifice diameters, into the flow.

## 5.5 FORCED FLOW RESULTS: THE 13mm ORIFICE

### 5.5.1 Flows at the Orifice Plate

The main forced flow regimes are given in figures 5-4a to g, for pipe Reynolds numbers from 128 to 640. This corresponds to test set A, (see chapter 4,

section 4.5). In figures 5-4a and 5-4b, two views are given for a vortex flow at a pipe Reynolds number of 128 and a forcing frequency,  $f_f$ , of 1.27Hz.

In figure 5-4a the light box has been placed over the orifice and end plates. The laminar flow upstream of the orifice plate is clearly visible as well as the regular shedding of vortices downstream. Figure 5-4b shows the dissipation of the vortices as they proceed downstream and die out.

Figure 5-4c is for a pipe Reynolds number of 256 and a forcing frequency of 2.54Hz. It is evident that in this case the flow develops into a turbulent state downstream of the orifice plate, in contrast to the flows of figures 5-4a and 5-4b. It is difficult to see from the figure whether discrete vortices are being shed from the orifice plate. However, a flash photograph of the same flow characteristics is given in figure 5-4d. From figure 5-4d two discrete vortices are clearly visible being shed from the lower orifice plate lip.

Figure 5-4c was taken with lamp illumination at a shutter speed of one sixtieth of a second. The average velocity of the fluid streaming through the orifice plate is  $50.0\text{mm s}^{-1}$ . Thus, the average displacement of the flow visualisation particles is 0.8mm. This could cause enough blurring of the image to mask the presence of discrete vortices in the flow, as seen in figure 5-4d.

The flow through the orifice plate for a pipe Reynolds numbers of 384 ( $f_f = 3.82\text{Hz}$ ), 512 ( $f_f = 5.09\text{Hz}$ ) and 640 ( $f_f = 6.37\text{Hz}$ ) are given in figures 5-4e, 5-4f and 5-4g respectively. The qualitative increase in the intensity and complexity of the turbulence may be visually observed from the figures.

### 5.5.2 Downstream Dissipation of the Disturbances

In general, the vortex flows generated at the orifice plate appear to follow one of two routes depending on the relative values of the flow Reynolds number, the orifice diameter, the forcing frequency and the forcing amplitude. That is, the vortices generated either increase in size to a maximum then die out, or, the vortices increase in size until they interact both with each other and the main flow, and then breakdown to a turbulent state, (see section 5.5.4). The turbulent

state generated by the latter of the two routes begins to degenerate, and as the flow proceeds downstream, the disturbances dissipate out, returning to the laminar pipe flow regime which exists upstream of the orifice plate.

This process by which the flow breaks down into a weakly turbulent state and then dissipates back out into a laminar flow is outlined in figures 5-5 and 5-6, for pipe Reynolds numbers of 256 and 384 respectively. In the figures intervals of 100mm are marked on the pipe wall using adhesive tape.

Figure 5-5a shows the flow from the orifice plate (right hand side) to approximately 180mm downstream of the orifice. In figure 5-5b, the flow from before the 100mm mark to beyond the 200 mm mark is shown, (i.e. from 100- mm to 200+ mm). Figure 5-5c shows the flow from 200- mm to 300+ mm, also noticeable in this figure is the silhouette of the pipe support between the two marks.

The downstream flow regime for a pipe Reynolds number of 384 and a forcing frequency of 3.82Hz is given in figure 5-6. Figure 5-6a contains the image of the flow from the orifice plate to about 180mm downstream of the plate. Figure 5-6b is from 200- to 300+ mm, (in contrast to figure 5-5b from 100- to 200+ mm). Figure 5-6c is from 300- to 400+ mm.

Evident from the photographs in figures 5-5 and 5-6 is the qualitative decrease in the complexity of the flow as it proceeds downstream after the breakdown point. From figure 5-6c it may be seen that the flow is beginning to accelerate in the central region of the pipe as the flatter velocity profile of the turbulent flow readjusts to the sharper laminar velocity profile. This is shown by the curved streaklines at the pipe centre. Compare with the turbulent flow of figure 5-6a.

## **5.6 FORCED FLOW RESULTS: THE 9.75mm AND 16.25mm ORIFICE PLATES**

Flow visualisation photographs were also taken for the 9.75mm and 16.25mm

orifice plates, for various values of the pipe Reynolds number. In this section some of the photographs will be presented and discussed.

### 5.6.1 The 9.75mm Orifice Plate

The flow phenomena for a pipe Reynolds number of 128 and a forcing frequency of 3.07Hz is shown in figure 5-7a. As can be seen in the figure, discrete vortices are formed at the edge of the jet issuing from the orifice aperture. The jet edge remaining coherent for some distance downstream. The flow breakdown seems to consist of the jet as a whole losing stability and a weakly fluctuating flow filling the whole pipe at a distance of approximately 100mm ( $= 10.26 \times D_o$  or  $3.85 \times D_p$ ) downstream of the orifice plate.

Figure 5-7b shows the flow for a pipe Reynolds number of 256, ( $f_f = 6.14\text{Hz}$ ). The flow breaks down rapidly into a turbulent state. A close inspection of the photograph near to the orifice plate reveals discrete vortices being shed into the flow, however, breakdown of these vortices is rapid. The general picture of the flow behaviour remains the same for a pipe Reynolds number of 384 ( $f_f = 9.21\text{Hz}$ ), as shown in figure 5-7c. However, a qualitative increase in the flow complexity may be discerned.

### 5.6.2 The 16.25mm Orifice Plate

The sequence of events for a pipe Reynolds number of 128, 256 and 384 are given in figure 5-8, and again in figure 5-9. The photographs of figure 5-8 were taken with the light box illuminating the flow in the vertical plane, whereby, only the lower vortices are shown. However, these photographs show great detail of the vortices and for this reason it was decided by the author to include them in this thesis. The photographs of figure 5-9 were taken with the light sheet in the horizontal plane, which gives a better insight into the axisymmetry of the phenomena.

In figure 5-8a, the shedding of vortices from the 16.25mm orifice at a pipe Reynolds number of 128 ( $f_f = 0.64\text{Hz}$ ) is shown. Once shed, the vortices almost

immediately become oval in shape as they flatten and die out. (Compare with figure 5.9a).

The vortices in figure 5-8b, ( $Re_p = 256$ ,  $f_f = 1.28\text{Hz}$ ), immediately after production at the orifice lip begin to spread out into the flow and entrain fluid from the main flow. However, this process reaches a cut-off point as the vortices proceed downstream from the orifice plate, after which the vortices tend to die out, becoming flatter and moving back towards the pipe wall. The maximum penetration into the flow by the vortices takes place at a distance of approximately 110mm downstream of the orifice plate, (or approximately  $6.77 \times D_o$  or  $4.23 \times D_p$ ). (The same flow conditions are also shown in figure 5-9b).

The photograph of figure 5-8c was taken just as the first traces of flow visualisation chemical passed through the 16.25mm orifice plate at a pipe Reynolds number of 384, ( $f_f = 1.92\text{Hz}$ ). The vortices increase in size as they proceed downstream of the orifice plate, however, unlike those of figure 5-8b, they continue to increase in size until they breakdown into a more complex flow pattern. The chemical at the left hand side of the photograph is just entering the region of flow breakdown. A better illustration of the overall breakdown pattern is given in figures 5-9c and 5-9d.

The flow patterns depicted in figures 5-8a to c are again given in figures 5-9a to c, this time the flow is illuminated in the horizontal plane. The flow upstream and downstream of the orifice plate for a pipe Reynolds number of 384 is shown in figure 5-9d. The laminar flow upstream of the orifice plate is clearly visible in the figure.

## 5.7 VIDEO RESULTS

### 5.7.1 Introduction

Following on from the process of still photography, it was decided to investigate the possibility of capturing the flow processes on video film. A video recorder, close up lenses and other accessories were borrowed from the Department

of Media Studies, within the University. The author filmed the various flow regimes investigated using the L.D.A. system, and in total approximately 1hr 20mins of film was shot. This was edited down to a 20 minute film, with titles superimposed on the film, which made it more suitable for presentation purposes. It was decided not to submit this edited version as part of this thesis, but rather present sketches of the underlying phenomena obtained from the film, (section 5.5.3). The film is available in the Department of Civil Engineering for viewing.

A copy of the original film, as shot, was rerecorded with a time code superimposed on top of the film, whereby, the time in hours, minutes, seconds and frames (1/25 sec) were visible at the top of the screen. This film was used for subsequent analysis of the flow processes. The edited video includes shots of all the flow processes, (without the time code), and is in effect a shortened, cleaned-up version of the time coded film. The contents of the 20 minute presentation film, which contains samples of all the shots used in the video analysis, are outlined in the next section.

### 5.7.2 Contents of the Video Film

The video film comprises the following 27 shots and 10 title pages, denoted S and T respectively. The forcing amplitude is 0.6V unless otherwise stated.

---

T : The Breakdown to Turbulence of a Forced Vortex System  
at a Pipe Orifice

---

T : An Overview of the Apparatus

S1 : Overview of the Apparatus (Zoom in and out)

---

T : The 13mm Orifice - Various Reynolds Numbers

S2 :  $Re_p = 128$ ,  $D_o = 13\text{mm}$ ,  $f_f = 1.27\text{Hz}$

S3 :  $Re_p = 128$ ,  $D_o = 13\text{mm}$ ,  $f_f = 1.27\text{Hz}$  (Close-Up)

S4 :  $Re_p = 256$ ,  $D_o = 13\text{mm}$ ,  $f_f = 2.54\text{Hz}$

S5 :  $Re_p = 256$ ,  $D_o = 13\text{mm}$ ,  $f_f = 2.54\text{Hz}$  (Close-Up)

S6 :  $Re_p = 384$ ,  $D_o = 13\text{mm}$ ,  $f_f = 3.82\text{Hz}$   
S7 :  $Re_p = 512$ ,  $D_o = 13\text{mm}$ ,  $f_f = 5.09\text{Hz}$   
S8 :  $Re_p = 640$ ,  $D_o = 13\text{mm}$ ,  $f_f = 6.37\text{Hz}$

---

T : The 13mm Orifice - Various Forcing Amplitudes

S9 :  $Re_p = 256$ ,  $D_o = 13\text{mm}$ ,  $f_f = 2.54\text{Hz}$ ,  $A_f = 0.2\text{V}$   
S10:  $Re_p = 256$ ,  $D_o = 13\text{mm}$ ,  $f_f = 2.54\text{Hz}$ ,  $A_f = 0.6\text{V}$   
S11:  $Re_p = 256$ ,  $D_o = 13\text{mm}$ ,  $f_f = 2.54\text{Hz}$ ,  $A_f = 1.0\text{V}$

---

T : Downstream Dissipation of the Disturbances

S12:  $Re_p = 128$ ,  $D_o = 13\text{mm}$ ,  $f_f = 2.54\text{Hz}$ , 0 - 150mm  
S13:  $Re_p = 128$ ,  $D_o = 13\text{mm}$ ,  $f_f = 2.54\text{Hz}$ , 150 - 300mm  
S14:  $Re_p = 128$ ,  $D_o = 13\text{mm}$ ,  $f_f = 2.54\text{Hz}$ , 300 - 450mm

---

T : The 9.75mm Orifice - Various Reynolds Numbers

S15:  $Re_p = 128$ ,  $D_o = 9.75\text{mm}$ ,  $f_f = 3.07\text{Hz}$   
S16:  $Re_p = 128$ ,  $D_o = 9.75\text{mm}$ ,  $f_f = 3.07\text{Hz}$  (Close-Up)  
S17:  $Re_p = 256$ ,  $D_o = 9.75\text{mm}$ ,  $f_f = 6.14\text{Hz}$   
S18:  $Re_p = 384$ ,  $D_o = 9.75\text{mm}$ ,  $f_f = 9.21\text{Hz}$

---

T : The 16.25mm Orifice - Various Reynolds Numbers

S19:  $Re_p = 128$ ,  $D_o = 16.25\text{mm}$ ,  $f_f = 0.64\text{Hz}$   
S20:  $Re_p = 128$ ,  $D_o = 16.25\text{mm}$ ,  $f_f = 0.64\text{Hz}$  (Close-Up)  
S21:  $Re_p = 256$ ,  $D_o = 16.25\text{mm}$ ,  $f_f = 1.28\text{Hz}$   
S22:  $Re_p = 256$ ,  $D_o = 16.25\text{mm}$ ,  $f_f = 1.28\text{Hz}$  (Close-Up)  
S23:  $Re_p = 384$ ,  $D_o = 16.25\text{mm}$ ,  $f_f = 1.92\text{Hz}$   
S24:  $Re_p = 384$ ,  $D_o = 16.25\text{mm}$ ,  $f_f = 1.92\text{Hz}$  (Close-Up)

---

T : The 6.5, 19.5 and 22.75mm Orifices -  $Re = 256$

S25:  $Re_p = 256$ ,  $D_o = 6.5\text{mm}$ ,  $f_f = 21.05\text{Hz}$   
S26:  $Re_p = 256$ ,  $D_o = 19.5\text{mm}$ ,  $f_f = 0.73\text{Hz}$

S27:  $Re_p = 256$ ,  $D_o = 22.75\text{mm}$ ,  $f_f = 0.45\text{Hz}$

---

T : Final Credits Title

---

T : Copyright Declaration

---

### 5.7.3 Overall Picture of the Flow Processes

From the video film taken of the flow phenomena, an overall picture of the flow regimes for the various tests could be discerned. Sketches were produced by the author of the various flow phenomena in an attempt to understand more fully the events taking place at the orifice plate. These sketches were produced by inspecting the video recording and at times freezing the picture so that the processes could be better interpreted.

The process of sketching the flow phenomena from the video film aided greatly in the understanding of the overall picture of the phenomena. These drawings are presented and discussed in this section, and should be viewed in conjunction with the photographs, where appropriate. The sketches show only half of the pipe cross section, as the phenomena is axisymmetric in nature.

The results of test set-A are shown in figures 5-10a to e. Figure 5-10a shows details of the flow at a pipe Reynolds number of 128 passing through the orifice. (Compare with figure 5-4a). As the flow passes through the orifice, vortices are formed at the forcing frequency of the flow, these, however, die out as they proceed downstream, flattening out as they do so.

At a pipe Reynolds number of 256 the vortices formed grow as they proceed downstream, become unstable and breakdown into a weakly turbulent state. In the video film of the phenomena, two, sometimes three, discrete vortices are visible being shed from the orifice plate before breakdown occurs and the flow pattern becomes complex. These events are shown in figure 5-10b.

As the Reynolds number is increased to 384, (figure 5-10c), the breakdown of

the vortices, generated at the orifice plate, proceeds more rapidly. This trend is repeated as the pipe Reynolds number is increased to 512 and 640 in turn, as depicted in figures 5-10d and e.

The effect of the various forcing amplitudes, (test set B), is depicted in figures 5-11a to c. These are for a pipe Reynolds number of 256. The forcing amplitudes used were 0.2, 0.6 and 1.0 Volts, these correspond to R.M.S. fluctuation values of 2.65%, 7.95% and 13.26%. For the lowest forcing amplitude of 2.65% R.M.S., (0.2 volts), the vortices remain fairly coherent up to a distance downstream of the orifice plate of approximately  $4.0 \times D_0$ . After this point they lose their stability and degenerate into a weakly turbulent state. At a forcing amplitude of 7.95% R.M.S. (0.6 volts), the vortices degenerate more quickly into a turbulent state and only two, (on some occasions three), vortices are formed. At a forcing amplitude of 13.24% R.M.S., (1.0 volts), the vortices grow rapidly. The diameter of the vortices reach a size comparable with the pipe radius at approximately  $1.5 \times D_0$  downstream of the orifice plate, at which point they breakdown rapidly into a weakly turbulent state. From these observations, it would seem that the forcing amplitude directly controls the rate of vortex growth, and this influences the downstream pattern of flow disturbances in turn.

The 9.75mm orifice plate results are shown in figure 5-12. At a pipe Reynolds number of 128, (corresponding to an orifice Reynolds number of 341), discrete vortices are shed from the orifice plate, which die out as they proceed downstream, (figure 5-12a). However, a more interesting phenomena is observed in this type of flow. The slow jet flow that emanates from the orifice, upon which the ring vortices are formed and subsequently die out, does not degenerate in an axisymmetric pattern. Rather, the jet becomes unstable and fluctuates as a whole filling the pipe with a very weakly perturbed flow. At a pipe Reynolds number of 256, (figure 5-12b), the vortices formed at the orifice plate breakdown quickly after detaching from it. The turbulent region in this case appears to be quite energetic. At a pipe Reynolds number of 384 the process is qualitatively the same as for  $Re_p = 256$ , but breakdown is even more rapid, (see figure 5-12c).

The 16.25mm orifice plate results are shown in figure 5-13a to c. At a pipe Reynolds number of 128, (figure 5-13a), discrete vortices are shed close to the pipe wall. These dissipate out immediately after their production. At a Reynolds

number of 256, (figure 5-13b), the vortices grow initially after their detachment from the orifice lip due to entrainment of fluid. However, this process halts further downstream of the orifice plate, and the vortices eventually succumb to viscosity, dying out close to the wall. At a pipe Reynolds number of 384 the vortices created at the orifice plate grow in size as they proceed downstream, interact with each other and degenerate into a weakly turbulent flow, as depicted in figure 5-13c. Some of the fluid from the degenerated vortices returns into the recirculation zone, this is depicted in the figure by the wavy arrows pointing in the upstream direction close to the wall.

The last set of sketches, shown in figures 5-14a to c, are for orifice sizes  $D_o = 6.5, 19.5, 22.75\text{mm}$ , all at a pipe Reynolds number of 256. (Test set E). Figure 5-14a is a sketch of the flow through the 6.5mm orifice plate, ( $Re_o = 1024$ ). The flow at this rate behaves as a confined jet flow, with rapid mixing of the fluid streaming through the orifice plate. Figure 5-14b is a sketch of the 19.5mm orifice plate, ( $Re_o = 341$ ), the vortices generated at the orifice plate are quickly dissipated out as they proceed downstream, dying out close to the wall. Figure 5-14c contains the sketch for the 22.75mm orifice plate ( $Re_o = 293$ ), the 'vortices' roll up briefly just downstream of the orifice plate. The rotational motion of the vortices is almost immediately damped out and the flow visualisation chemical shows a series of regularly spaced undulations close to the wall.

#### 5.7.4 Categorisation of the Flow Visualisation Results

An attempt was made to put into context the visual information obtained from the video and photographic film of the events at the orifice plate. The behaviour may initially be split up into two categories. The first, whereby the vortex flow produced at the orifice plate dissipates out and the flow streamlines remain axisymmetric. This type of flow, labelled **DIRECTLY DISSIPATING** flow, remains simple, i.e. the most complex structures in the flow are the axisymmetric vortex rings. The second type of flow, which has been labelled **INITIALLY INTERACTING** flow by the author, includes all the flows which upon leaving the orifice plate increase in complexity. (Note that the **INITIALLY INTERACTING** flow eventually dissipates out after the breakdown to the weakly turbulent state). These two types of flow are outlined in more detail in what follows.

## 1 - DIRECTLY DISSIPATING VORTEX FLOWS

This type of flow is typical of low Reynolds number flows, and is depicted in figure 5-15a. Discrete vortex rings are formed at the edges of the flow issuing from the orifice plate. These vortices die out as they proceed downstream. For the case of very low Reynolds number flows vortices are not fully formed and only a series of undulations are noticeable at the jet edge. At all points in the flow the flow field is axisymmetric. (Examples of flows which behave in the manner described above are:  $D_o = 13.00\text{mm}$ ,  $Re_p = 128$ ;  $D_o = 16.25\text{mm}$ ,  $Re_p = 128$  and  $256$ ;  $D_o = 19.50\text{mm}$ ,  $Re_p = 256$  and  $D_o = 22.75\text{mm}$ ,  $Re_p = 256$ .)

## 2 - INITIALLY INTERACTING VORTEX FLOWS

### 2.1 - UNSTABLE JET FLOW

In this case, depicted in figure 5-15b, vortices appear at the jet edge as it emanates from the orifice aperture. These vortices die out as they proceed downstream. However, the jet itself loses stability and causes a weakly fluctuating flow to appear further downstream of the orifice plate. This type of flow occurred for the 9.75mm orifice plate at a pipe Reynolds number,  $Re_p$ , of 128.

### 2.2 - INTERACTING VORTEX FLOW

As with the above flow, discrete vortices are formed at the orifice plate. However, as they proceed downstream they increase in size, until they reach a point at which they interact with each other and the weakly turbulent flow region further downstream. The vortices then breakdown into the weakly turbulent regime. (See figure 5-15c.) (Examples of flows which behave in the manner described above are:  $D_o = 9.75\text{mm}$ ,  $Re_p = 256, 384$ ;  $D_o = 13.00\text{mm}$ ,  $Re_p = 256, 384, 512$  and  $640$  and  $D_o = 16.25\text{mm}$ ,  $Re_p = 384$ .)

### 2.3 - CONFINED JET FLOW

This type of flow, typical of high orifice Reynolds numbers, exhibits high rates of

shearing between the flow streaming through the orifice plate and the slower moving flow in the recirculation zone just downstream of the orifice plate. (See figure 5-15d). The flow passing through the orifice plate almost immediately breaks down into a turbulent flow. Such flows are known as confined jet flows. This type of flow occurred for the 6.50mm orifice plate at a pipe Reynolds number,  $Re_p$ , of 256.

## 5.8 VORTEX WAVELENGTH AND VELOCITY RESULTS

Using both the video film and photographs the vortex velocities and wavelengths at certain parts of their development were measured. This was done in the case of the photographs by measuring directly from them and scaling these measurements up by the appropriate factors. Wavelength measurements were taken from the video by freezing the picture and measuring directly from the screen. The average velocity of the vortices could easily be calculated by multiplying the obtained wavelength by the shedding frequency.

In some instances the vortex velocities,  $U_v$ , were measured directly from the video film with the time code superimposed. This was done by freezing the film, noting the position of the vortex centre and the time, then running the film for a short duration, freezing the film again, and noting the new position and time. Thus the distance covered by the vortex could be calculated together with the time required for this distance to be traversed, and hence the vortex velocity could be calculated. Figures 5-16 and 5-17 give the results of the vortex wavelength and velocity measurements.

The vortex wavelength results are given for the 13.00mm orifice plate in figure 5-16a. The results in the figure are for a pipe Reynolds number of 256 and various forcing amplitudes. The results for  $Re_p = 128$  are also plotted for comparison. The flow at  $Re_p = 128$  is a DIRECTLY DISSIPATIVE flow, and it can be seen that the vortex wavelengths remain at a constant value as they proceed downstream from the orifice plate. In general, vortex flows which decay immediately after leaving the orifice plate reach a maximum wavelength just downstream of the orifice lip. This wavelength remains at this value as the vortex system decays.

All the flows at  $Re_p = 256$  breakdown to turbulence. The higher the forcing amplitude, the sooner the breakdown occurs. From figure 5-16a it is noticeable that the wavelengths increase in length sooner as the forcing amplitude is increased. The vortices may no longer be discerned after they interact with the weakly turbulent region. This fact accounts for the last plotted point occurring nearer to the orifice plate as the forcing amplitude increases, and hence the breakdown region is brought further upstream.

Figure 5-16b contains vortex wavelength results for all the orifice plates used in the study. The points plotted in figure 5-16a are plotted as single stars (\*) in figure 5-16b. From the figure it may be seen that the general trend is for the maximum vortex wavelength to increase, both with orifice diameter, and distance downstream of the orifice plate.

At higher Reynolds numbers, the flow breaks down soon after leaving the orifice plate, and it becomes very difficult to measure the vortex wavelengths. As a result, only those very close to the orifice may be taken. This accounts for the single wavelength results obtained for the 9.75mm orifice plate at pipe Reynolds numbers of 256 and 384, (these represent values of  $Re_o$  of 683 and 1024 respectively). These results are plotted in the lower left hand corner of figure 5-16b.

Figure 5-17a presents the same results as 5-16b, but with both axes nondimensionalised. Both axes are normalised by dividing the coordinates by the orifice aperture diameter  $D_o$ . After the initial growth of the vortex wavelengths just downstream of the orifice plate they tend to a constant value, (approximately  $1.2 \times D_o$ ).

The normalised vortex velocity results,  $U_v/U_o$ , are plotted against the normalised downstream distance,  $Z/D_o$ , in figures 5-17b. From the figure it is immediately obvious that vortex velocity increases proportionally with increasing orifice Reynolds number,  $Re_o$ , and thus decreasing orifice diameter,  $D_o$ , as one would expect. Also, from this plot it is evident that the vortex velocities increase as they leave the orifice lip, tending to a value of approximately  $0.8 \times U_o$ , downstream of the orifice plate.

The two plots 5-17a and 5-17b are qualitatively very similar, this is because the nondimensional numbers,  $l_v/D_o$  and  $U_v/U_o$ , are related to each other by the Strouhal number,  $S$ , as follows,

$$\frac{U_v}{U_o} = \frac{f_v \cdot l_v}{U_o} = \frac{f_v \cdot D_o}{U_o} \cdot \frac{l_v}{D_o} = S \cdot \frac{l_v}{D_o} \quad (5.1)$$

Thus the vortex and wavelength plots are linked through the Strouhal number. The value of  $S$  ranges from 0.684 for the 6.50mm orifice plate to 0.628 for the 22.75mm orifice plate. The average Strouhal number over the range is then 0.656. This is approximately the multiplicative factor between the downstream wavelength relationship of,  $l_v = 1.2 \times D_o$ , and the downstream vortex velocity relationship of,  $U_v = 0.8 \times U_o$ , a result one would expect for a constant Strouhal number.

## 5.9 SUMMARY

This chapter has provided a visual description of the flow processes encountered in the study. Two main flow types have been identified, these are:

- 1 - Directly Dissipating Flows, and,
- 2 - Interacting Vortex Flows.

The second flow type divides into three further identifiable sub-categories, which are:

- 2.1 - Unstable Slow Jet Flow
- 2.2 - Interacting Vortex Flow, and,
- 2.3 - Confined Jet Flow.

The presence of each flow depends upon the flow conditions at the orifice, with the four controlling parameters being the pipe Reynolds number, orifice diameter, forcing frequency and forcing amplitude.

Measurements have been made of the vortex wavelengths and velocities for each set of control parameters, from both still photographs and video film. The

results suggest that the vortex wavelength and velocity, normalised to the orifice diameter and average orifice velocity respectively, tend towards constant values.

Further analysis of the results presented in this chapter, together with the L.D.A. results of Chapter 6, is undertaken in chapter 7 with the aim of presenting an overall description of events leading to flow breakdown at the orifice plate.

**CHAPTER 5**  
**FIGURES**

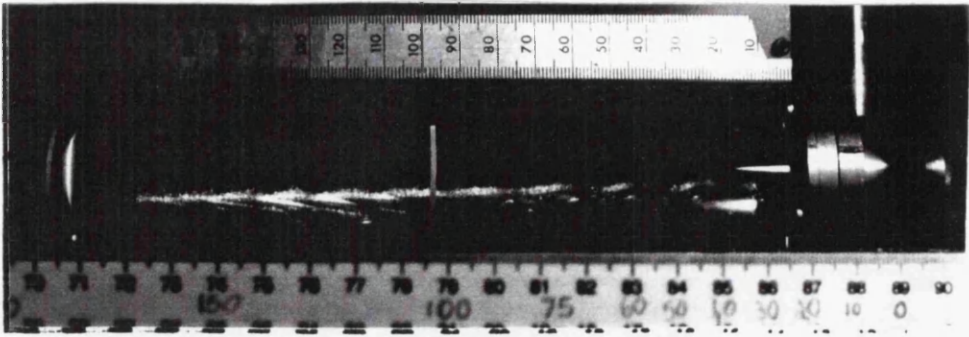
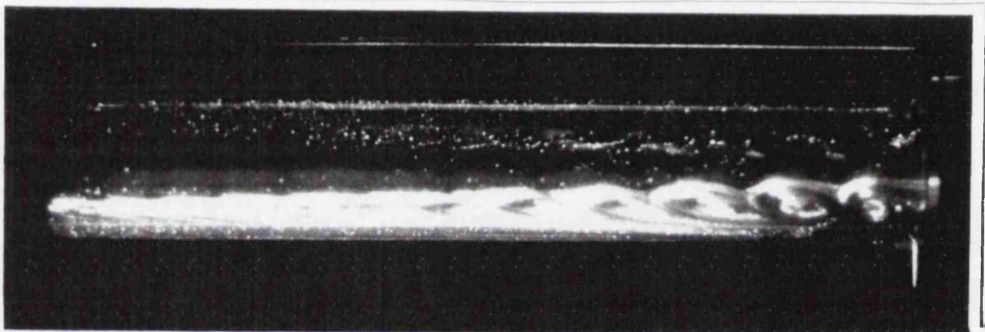
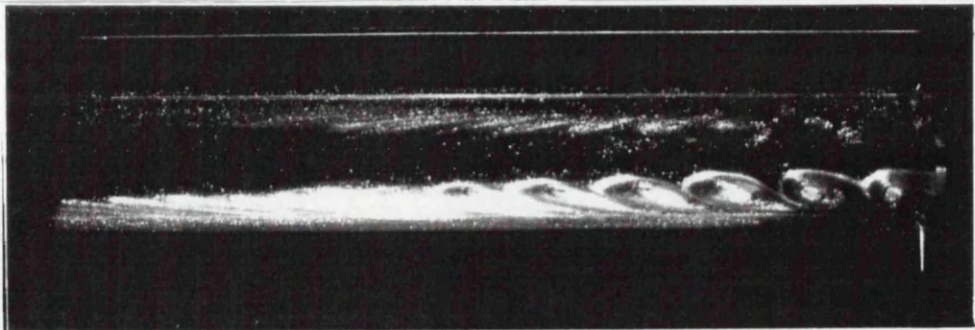


Figure 5-1: Flow Visualization Set-Up



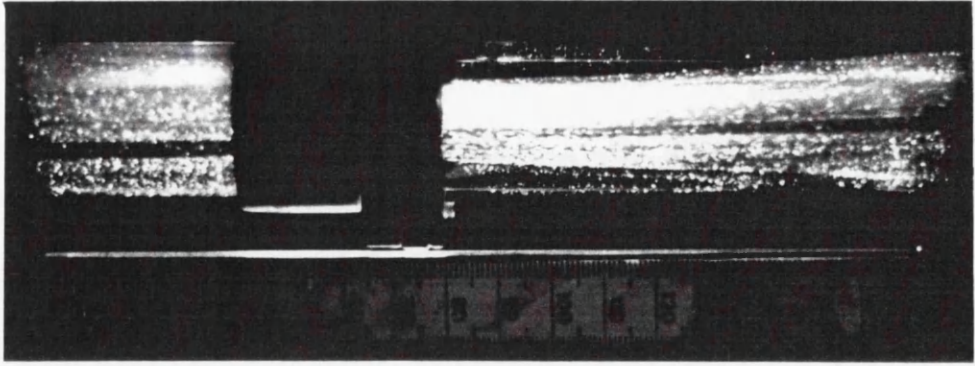
(a) Lamp Illumination (f1.4, 1/60sec.)



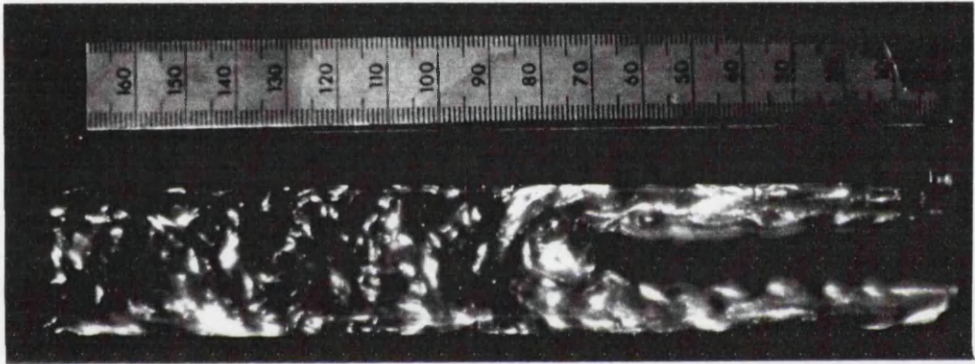
(b) Flash Illumination (f5.6, 1/60sec.)

Figure 5-2: Lamp versus Flash Illumination

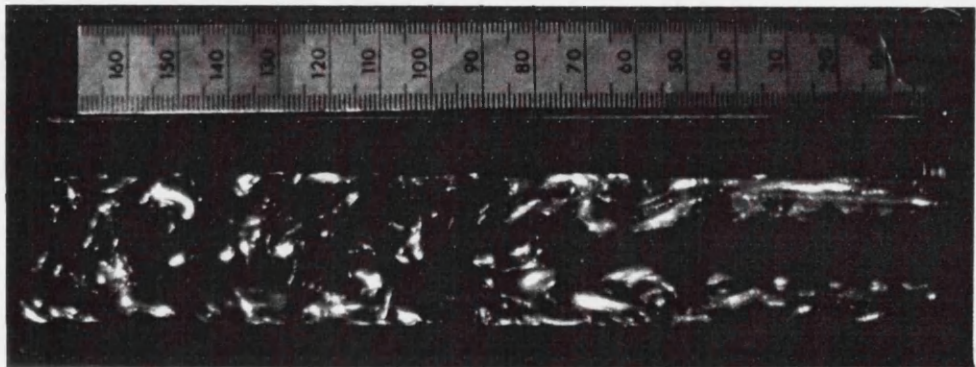
(13mm Orifice Plate,  $Re_p = 128$ ,  $Re_o = 256$ ,  $f_f = 1.27$ )



(a)  $Re_p = 194$ ,  $Re_o = 388$  (Lamp,  $f1.4$ ,  $1/60\text{sec.}$ )

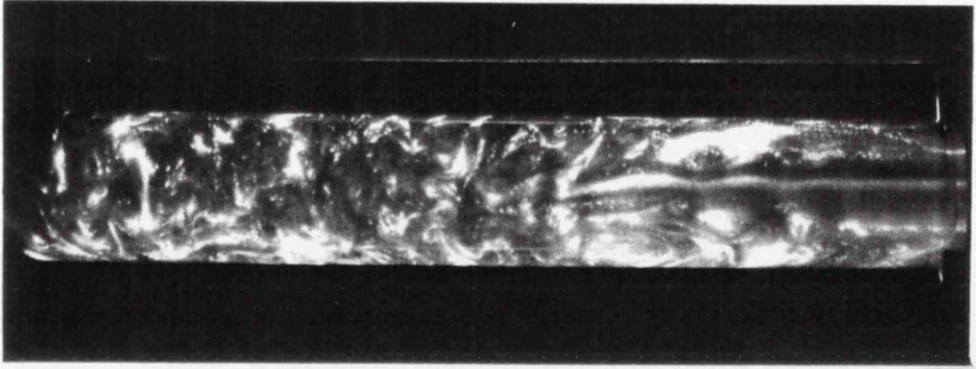


(b)  $Re_p = 373$ ,  $Re_o = 746$  (Lamp,  $f1.4$ ,  $1/125\text{sec.}$ )

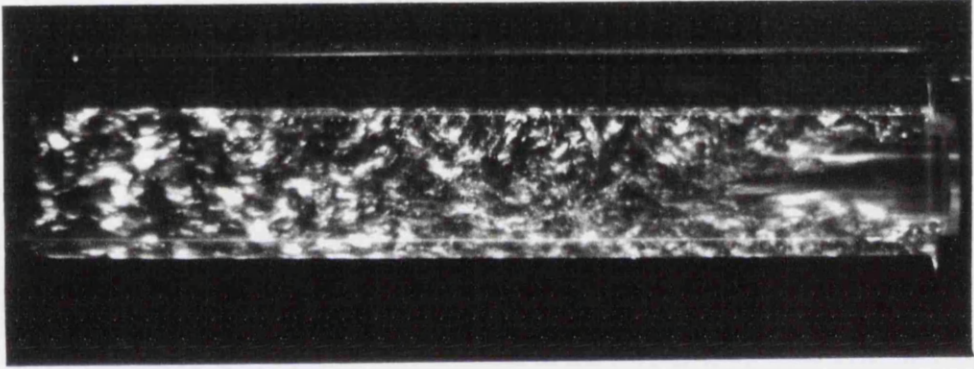


(c)  $Re_p = 373$ ,  $Re_o = 746$  (Lamp,  $f1.4$ ,  $1/250\text{sec.}$ )

Figure 5-3: Natural Unforced Vortex Flows at the 13mm Orifice Plate

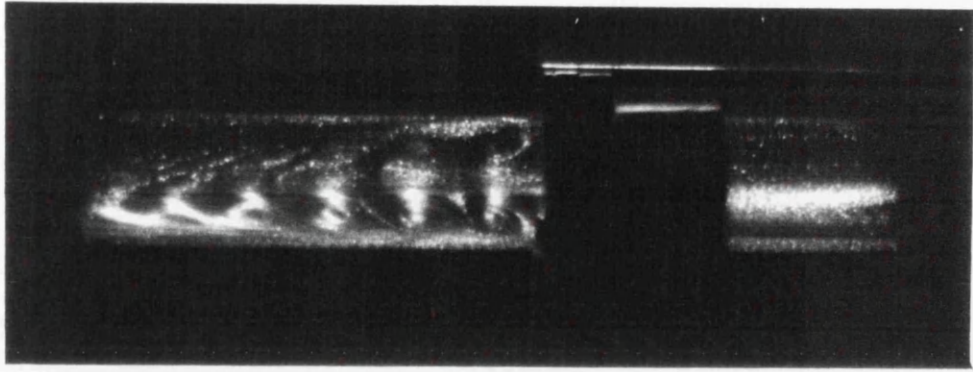


(d)  $Re_p = 437$ ,  $Re_o = 874$  (Lamp, f1.4, 1/60sec. )

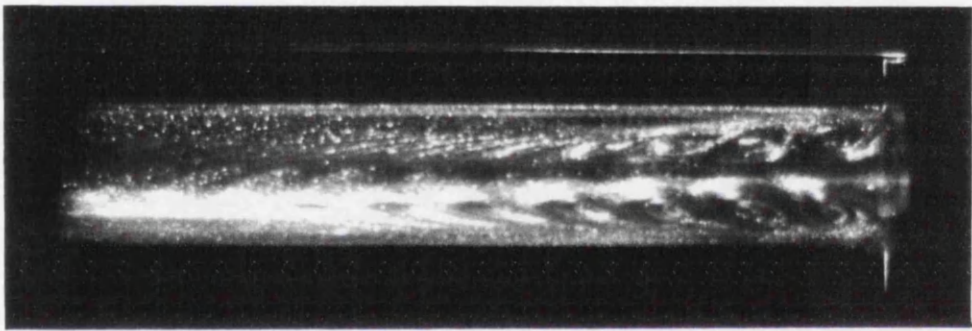


(e)  $Re_p = 2432$ ,  $Re_o = 4864$  (Lamp, f1.4, 1/60sec. )

Figure 5-3: Natural Unforced Vortex Flows at  
the 13mm Orifice Plate



(a)  $Re_p = 128$ ,  $Re_o = 256$ ,  $f_f = 1.27\text{Hz}$ , (Lamp,  $f_{1.4}$ ,  $1/125\text{sec.}$ )

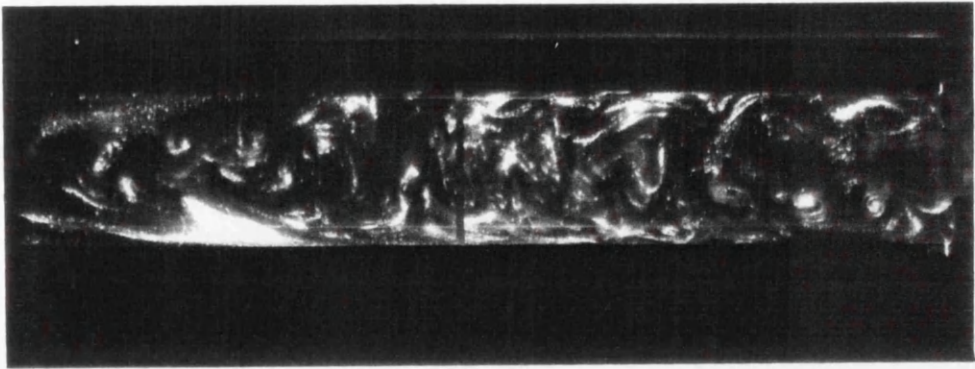


(b)  $Re_p = 128$ ,  $Re_o = 256$ ,  $f_f = 1.27\text{Hz}$ , (Lamp,  $f_{1.4}$ ,  $1/60\text{sec.}$ )

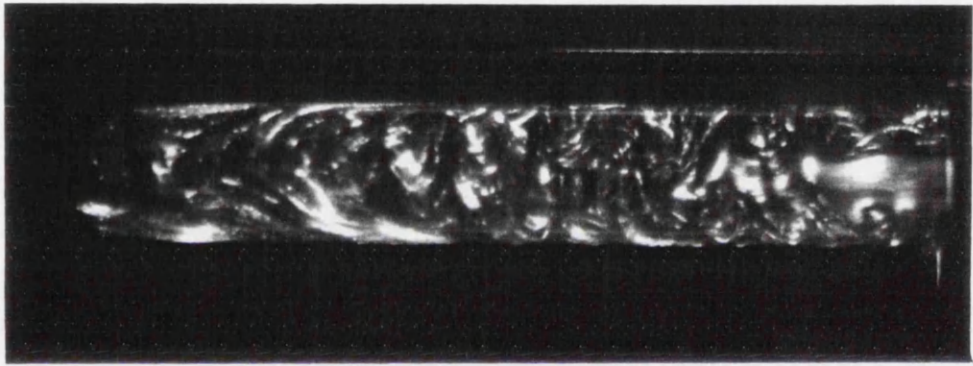


(c)  $Re_p = 256$ ,  $Re_o = 512$ ,  $f_f = 2.54\text{Hz}$ , (Lamp,  $f_{1.4}$ ,  $1/60\text{sec.}$ )

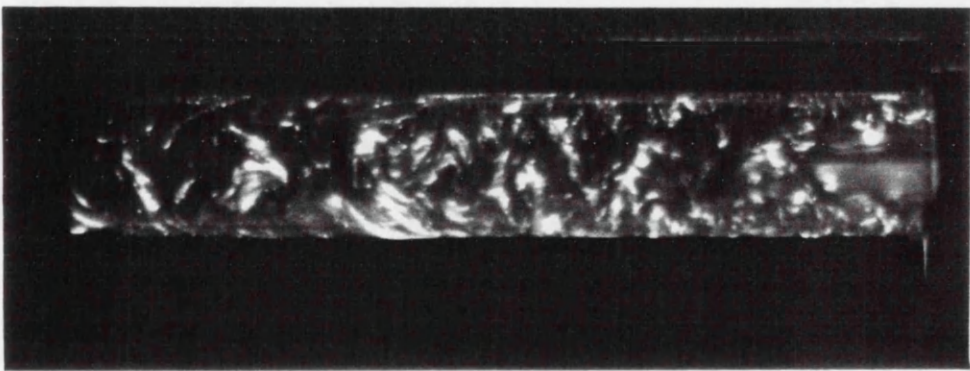
Figure 5-4: The 13mm Orifice Plate - Various Reynolds Numbers



(d)  $Re_p = 256$ ,  $Re_o = 512$ ,  $f_f = 2.54\text{Hz}$ , (Lamp,  $f_{1.4}$ ,  $1/60\text{sec.}$  )

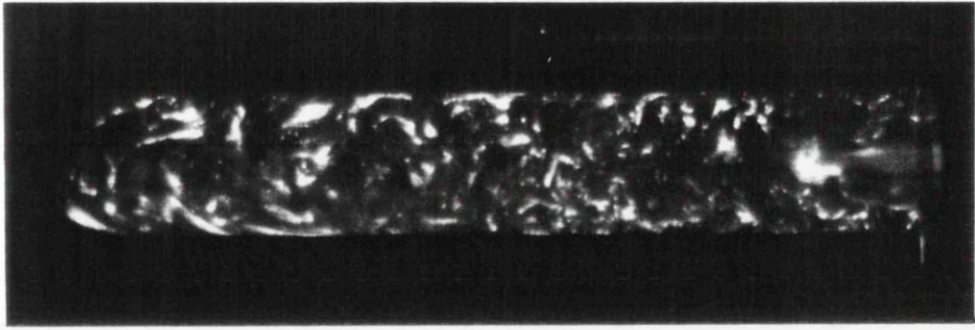


(e)  $Re_p = 384$ ,  $Re_o = 768$ ,  $f_f = 3.82\text{Hz}$ , (Lamp,  $f_{1.4}$ ,  $1/60\text{sec.}$  )



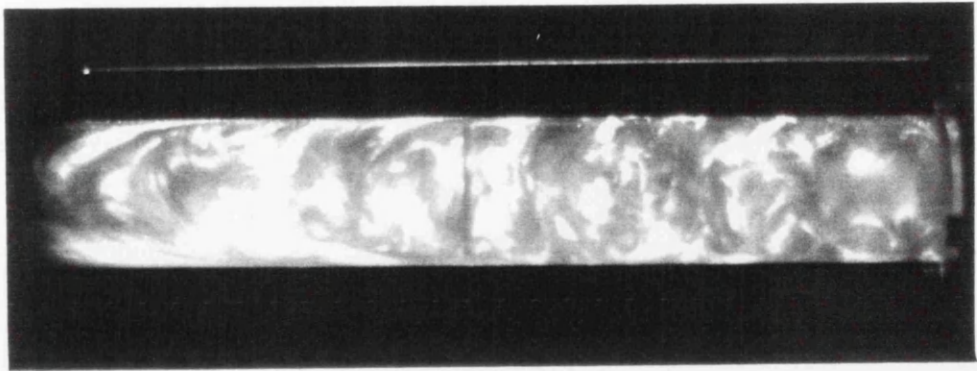
(f)  $Re_p = 512$ ,  $Re_o = 1024$ ,  $f_f = 5.09\text{Hz}$ , (Lamp,  $f_{1.4}$ ,  $1/60\text{sec.}$  )

Figure 5-4: The 13mm Orifice Plate - Various Reynolds Numbers

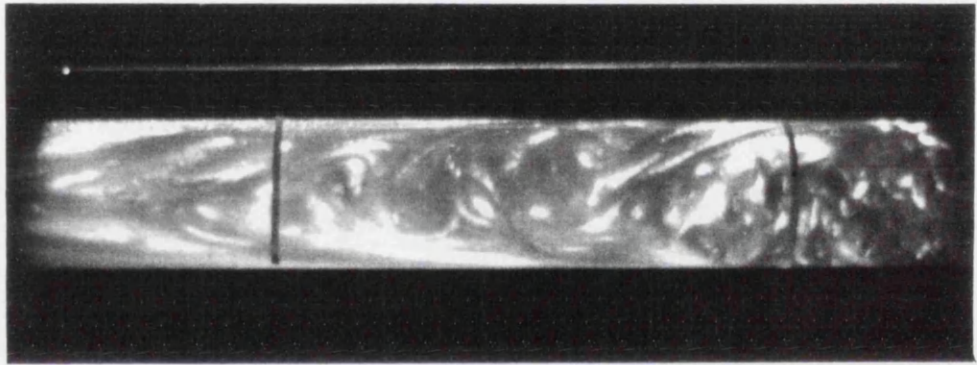


(g)  $Re_p = 640$ ,  $Re_o = 1280$ ,  $f_f = 6.37\text{Hz}$ , (Lamp,  $f_{1.4}$ ,  $1/125\text{sec.}$ )

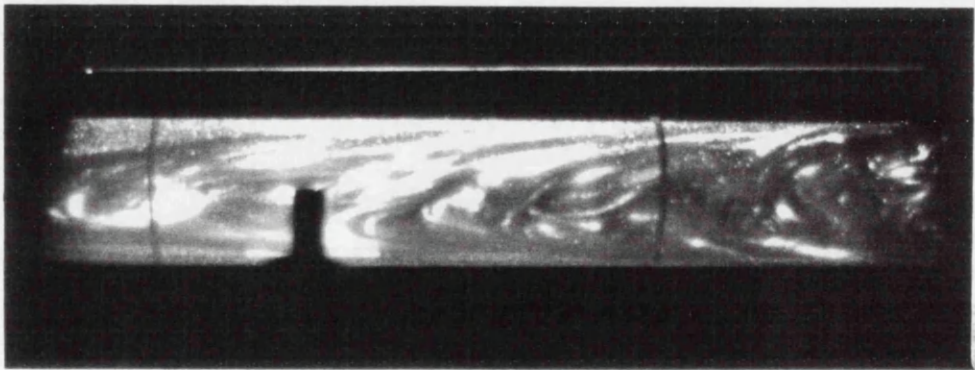
Figure 5-4; The 13mm Orifice Plate - Various Reynolds Numbers



(a) 0mm (Orifice Plate)  $\rightarrow$  100+mm



(b) 100-  $\rightarrow$  200+mm

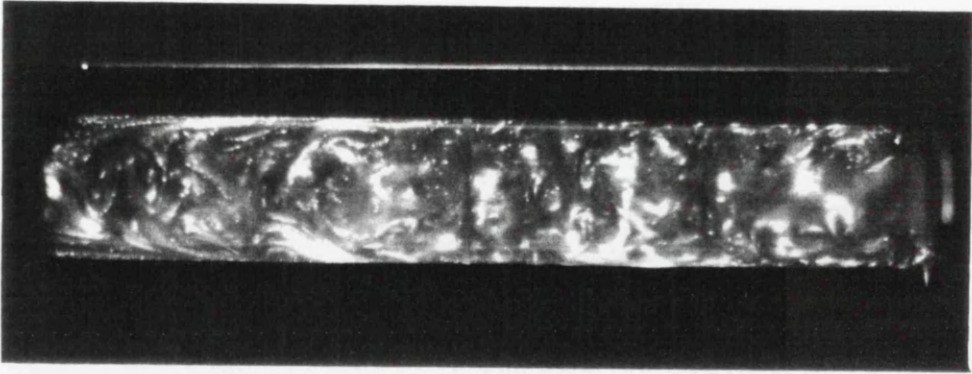


(c) 200-  $\rightarrow$  300+mm

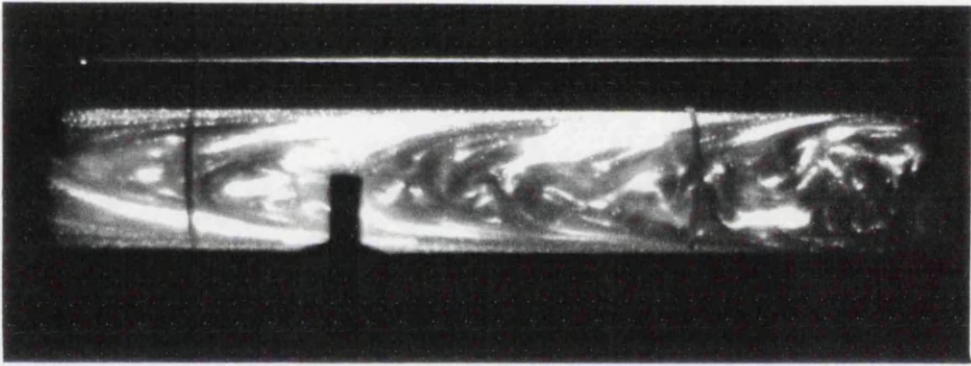
Figure 5-5: Downstream Dissipation of the Disturbances

$$Re_p = 256, Re_o = 512, f_f = 2.54\text{Hz.}$$

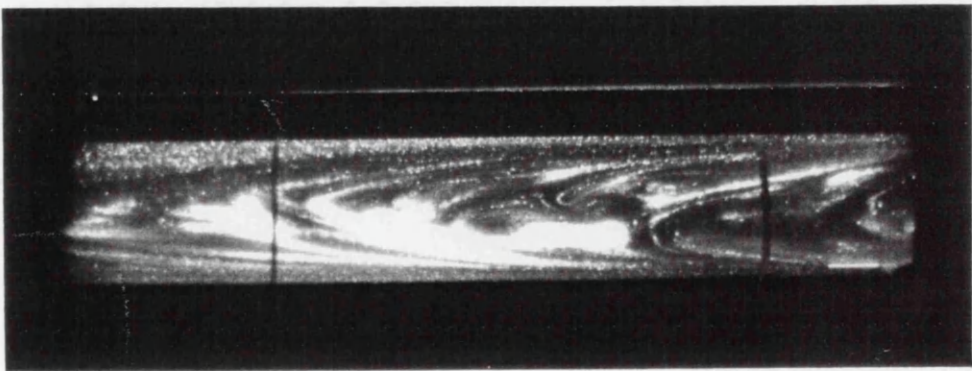
All Photo's - Lamp, f1.4, 1/125sec.



(a) 0mm (Orifice Plate)  $\rightarrow$  100+mm



(b) 200-  $\rightarrow$  300+mm

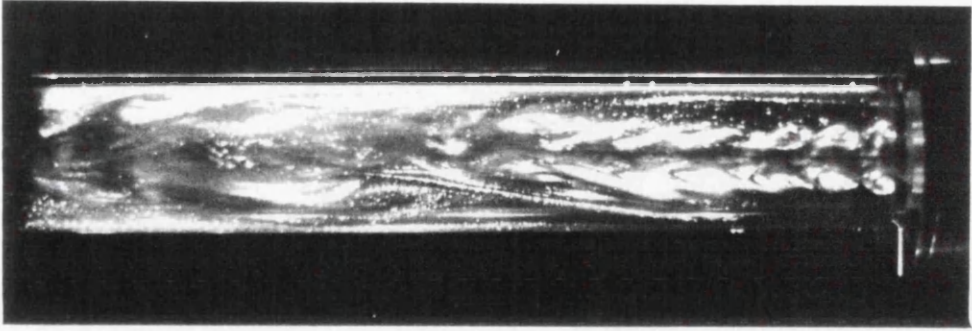


(c) 300-  $\rightarrow$  400+mm

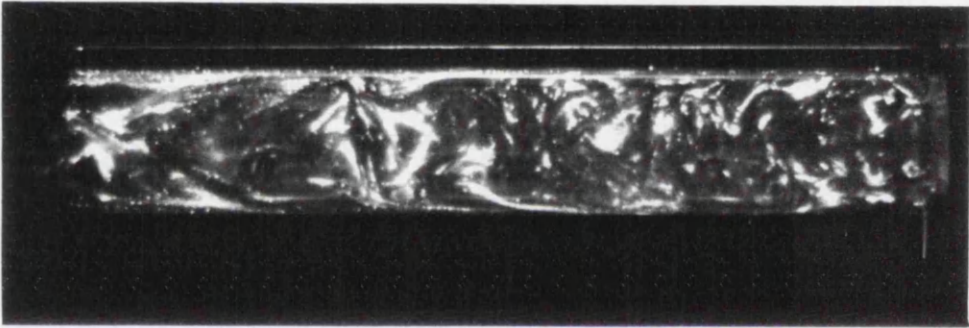
Figure 5-6: Downstream Dissipation of the Disturbances

$$Re_p = 384, Re_o = 768, f_f = 3.82\text{Hz.}$$

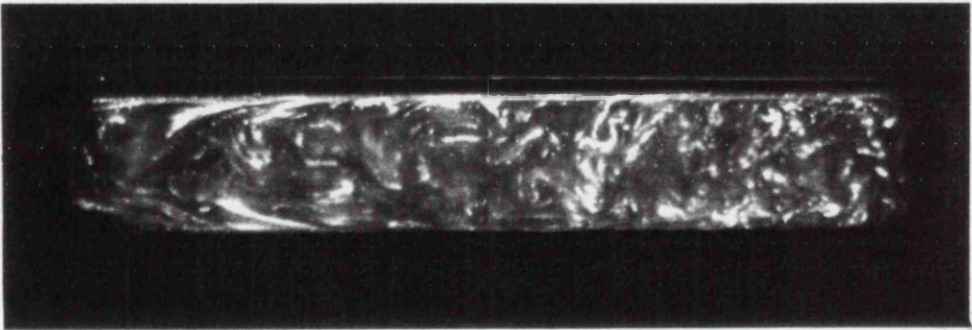
All Photo's - Lamp, f1.4, 1/125sec.



(a)  $Re_p = 128$ ,  $Re_o = 341$ ,  $f_f = 3.07\text{Hz}$ , (Lamp,  $f_{1.4}$ ,  $1/60\text{sec.}$ )

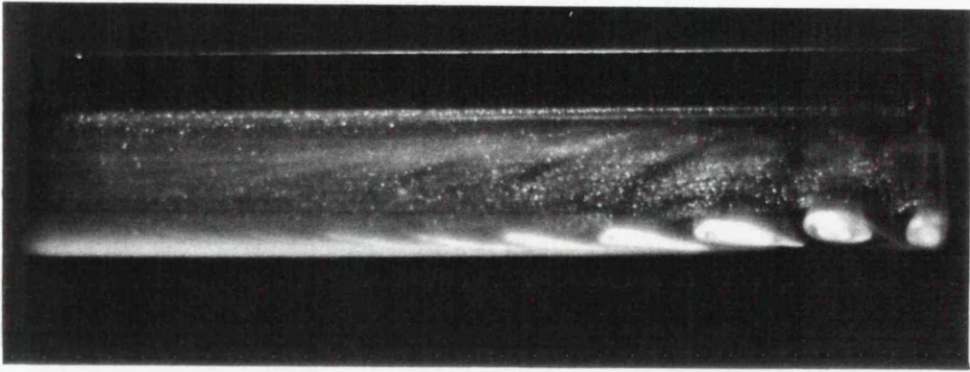


(b)  $Re_p = 256$ ,  $Re_o = 683$ ,  $f_f = 6.14\text{Hz}$ , (Lamp,  $f_{1.4}$ ,  $1/125\text{sec.}$ )

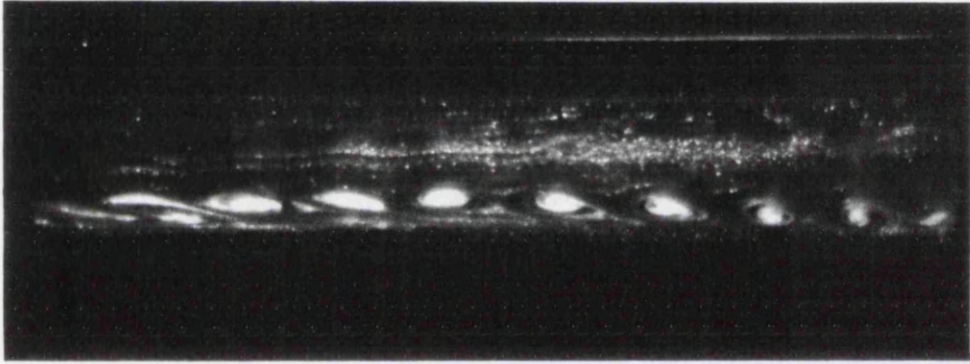


(c)  $Re_p = 384$ ,  $Re_o = 1024$ ,  $f_f = 9.21\text{Hz}$ , (Lamp,  $f_{1.4}$ ,  $1/125\text{sec.}$ )

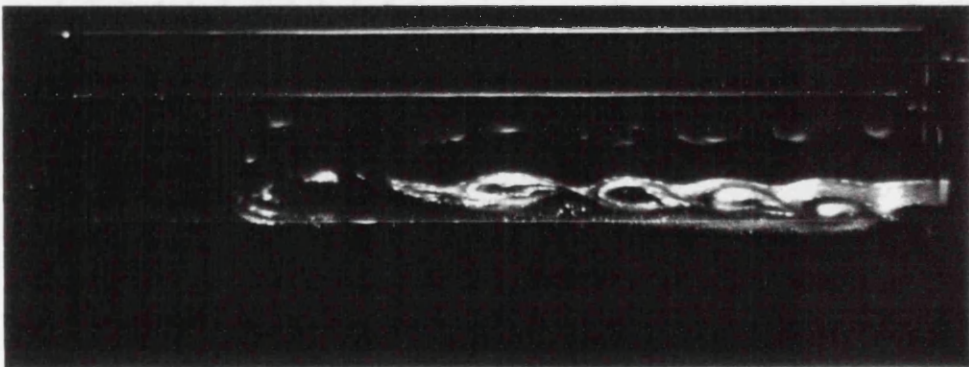
Figure 5-7: The 9.75mm Orifice - Various Reynolds Numbers



(a)  $Re_p = 128$ ,  $Re_o = 205$ ,  $f_f = 0.64\text{Hz}$ , (Lamp,  $f_{1.4}$ ,  $1/125\text{sec.}$ )

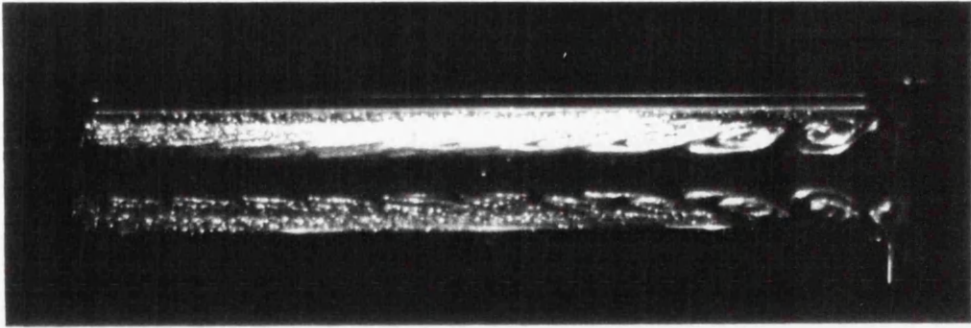


(b)  $Re_p = 256$ ,  $Re_o = 410$ ,  $f_f = 1.28\text{Hz}$ , (Lamp,  $f_{1.4}$ ,  $1/125\text{sec.}$ )

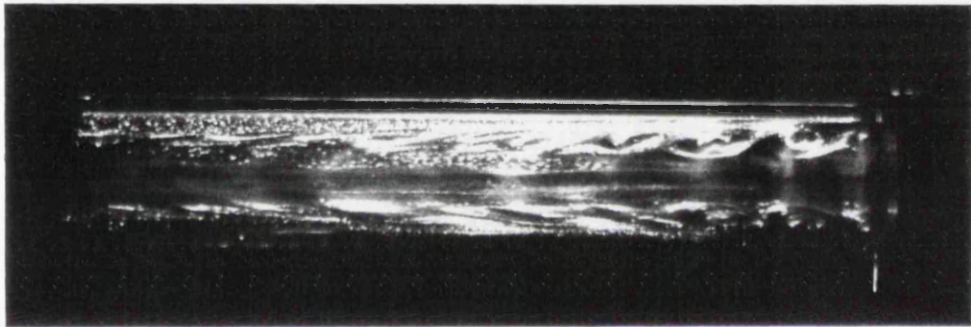


(c)  $Re_p = 384$ ,  $Re_o = 614$ ,  $f_f = 1.92\text{Hz}$ , (Lamp,  $f_{1.4}$ ,  $1/60\text{sec.}$ )

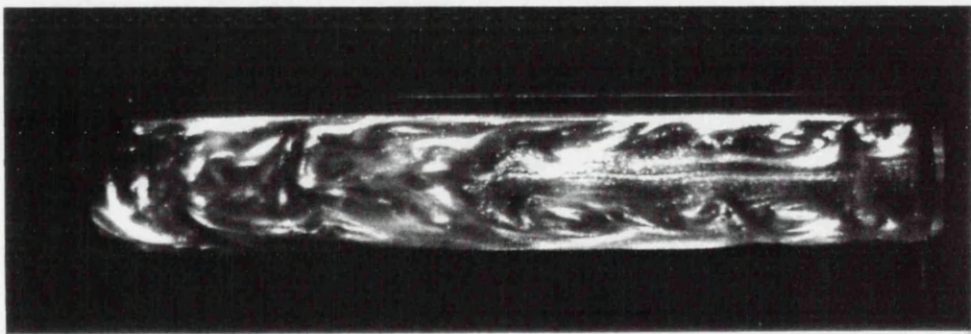
Figure 5-8: The 16.25mm Orifice - Various Reynolds Numbers  
- Illumination in the Vertical Plane



(a)  $Re_p = 128$ ,  $Re_o = 205$ ,  $f_f = 0.64\text{Hz}$ , (Lamp,  $f_{1.4}$ ,  $1/125\text{sec.}$ )

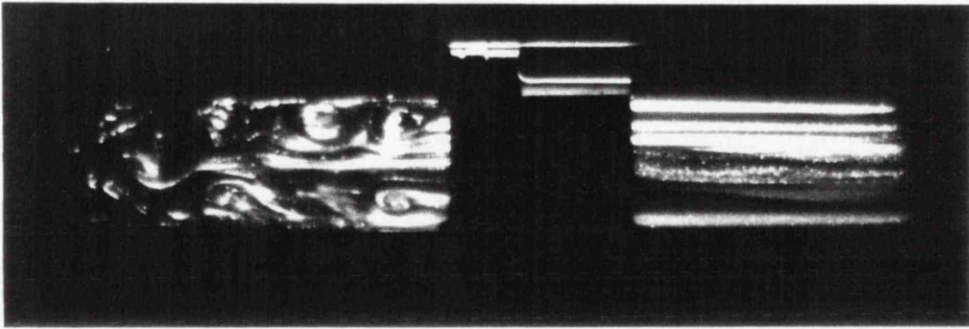


(b)  $Re_p = 256$ ,  $Re_o = 410$ ,  $f_f = 1.28\text{Hz}$ , (Lamp,  $f_{1.4}$ ,  $1/125\text{sec.}$ )



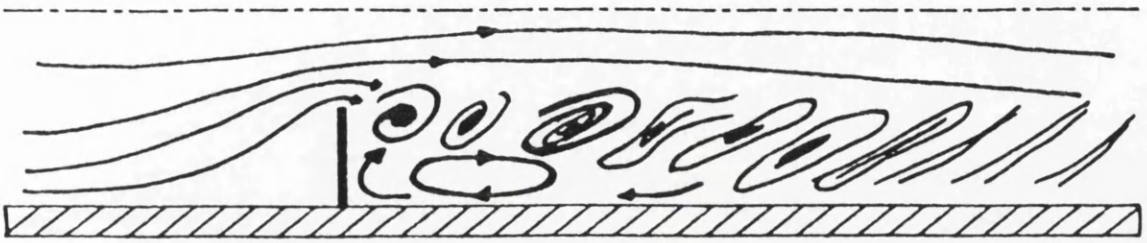
(c)  $Re_p = 384$ ,  $Re_o = 614$ ,  $f_f = 1.92\text{Hz}$ , (Lamp,  $f_{1.4}$ ,  $1/60\text{sec.}$ )

Figure 5-9: The 16.25mm Orifice - Various Reynolds Numbers  
- Illumination in the Horizontal Plane

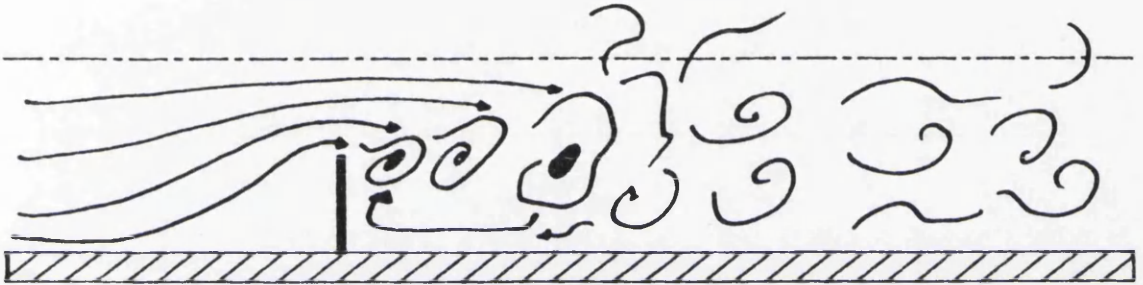


(d) As with (c) Showing Laminar Flow Upstream of  
the Orifice Plate

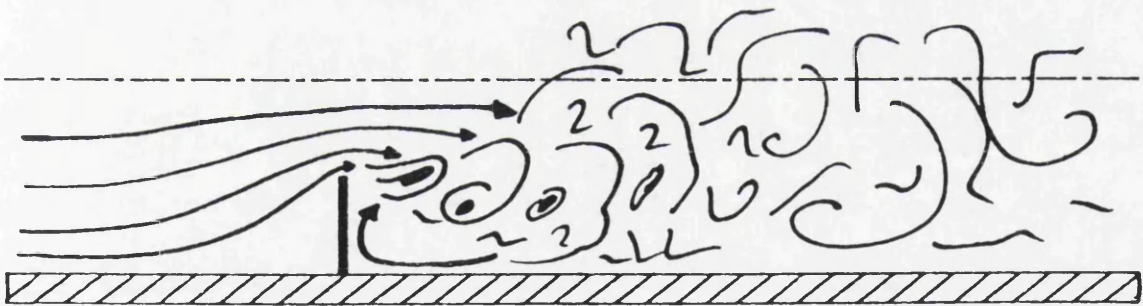
Figure 5-9: The 16.25mm Orifice - Various Reynolds Numbers  
- Illumination in the Horizontal Plane



(a)  $Re_p = 128$ ,  $Re_o = 256$ ,  $f_f = 1.27\text{Hz}$ .

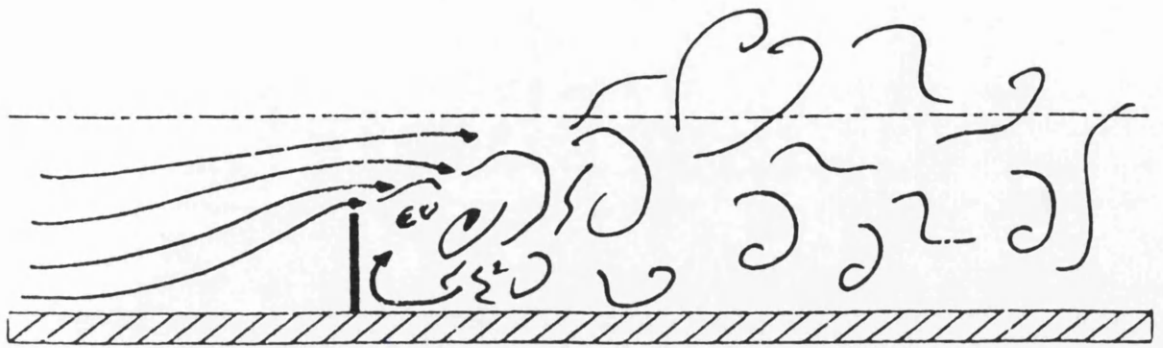


(b)  $Re_p = 256$ ,  $Re_o = 512$ ,  $f_f = 2.54\text{Hz}$ .

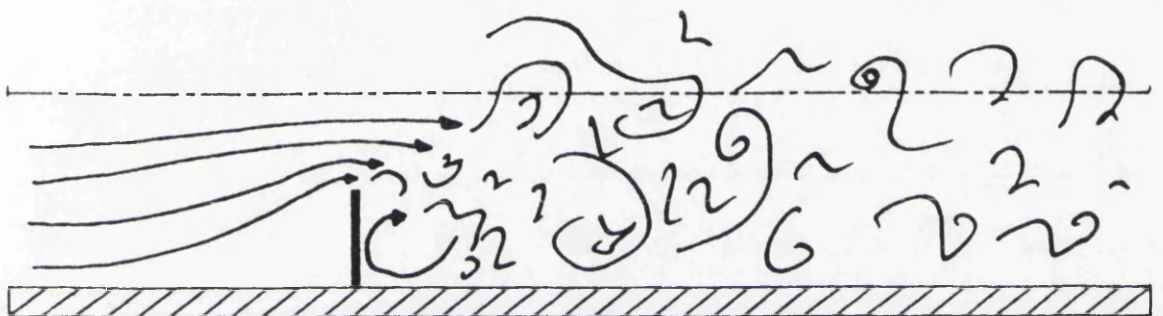


(c)  $Re_p = 384$ ,  $Re_o = 768$ ,  $f_f = 3.82\text{Hz}$ .

**Figure 5-10: Sketch of the Flow Processes at the 13.00mm Orifice Plate - Various Reynolds Numbers**

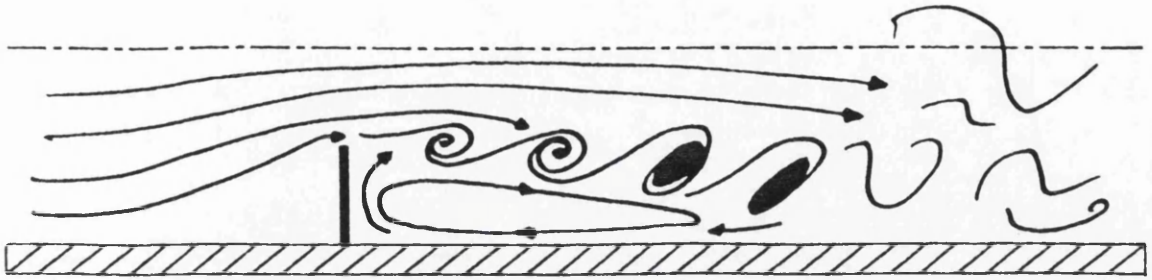


(d)  $Re_p = 512$ ,  $Re_o = 1024$ ,  $f_f = 5.09\text{Hz}$ .



(e)  $Re_p = 640$ ,  $Re_o = 1280$ ,  $f_f = 6.37\text{Hz}$ .

Figure 5-10: Sketch of the Flow Processes at the 13.00mm Orifice Plate - Various Reynolds Numbers



(a)  $Re_p = 256$ ,  $Re_o = 512$ ,  $f_f = 2.54\text{Hz}$ ,  $A = 0.2\text{V}$ .



(b)  $Re_p = 256$ ,  $Re_o = 512$ ,  $f_f = 2.54\text{Hz}$ ,  $A = 0.6\text{V}$ .

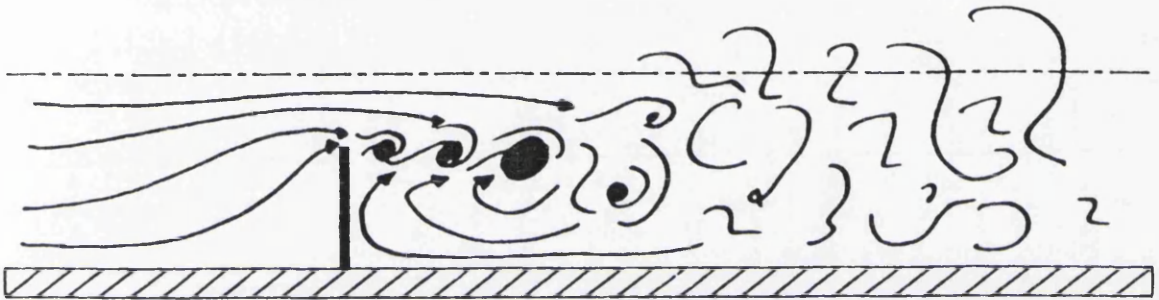


(c)  $Re_p = 256$ ,  $Re_o = 512$ ,  $f_f = 2.54\text{Hz}$ ,  $A = 1.0\text{V}$ .

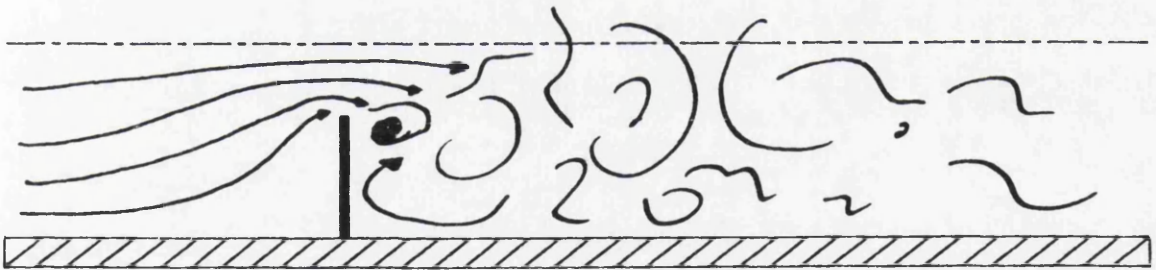
**Figure 5-11: Sketch of the Flow Processes at the 13.00mm Orifice Plate - Various Forcing Amplitudes**



(a)  $Re_p = 128$ ,  $Re_o = 341$ ,  $f_f = 3.07\text{Hz}$ .



(b)  $Re_p = 256$ ,  $Re_o = 683$ ,  $f_f = 6.14\text{Hz}$ .



(c)  $Re_p = 384$ ,  $Re_o = 1024$ ,  $f_f = 9.21\text{Hz}$ .

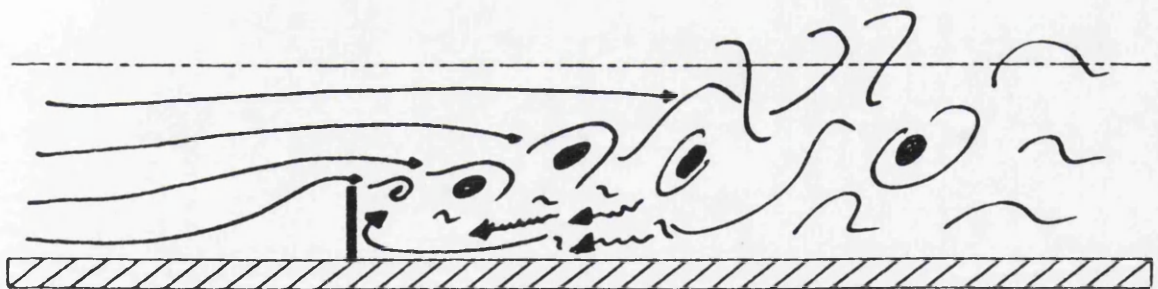
Figure 5-12: Sketch of the Flow Processes at the 9.75mm Orifice Plate - Various Reynolds Numbers



(a)  $Re_p = 128$ ,  $Re_o = 205$ ,  $f_f = 0.64\text{Hz}$ .



(b)  $Re_p = 256$ ,  $Re_o = 410$ ,  $f_f = 1.28\text{Hz}$ .

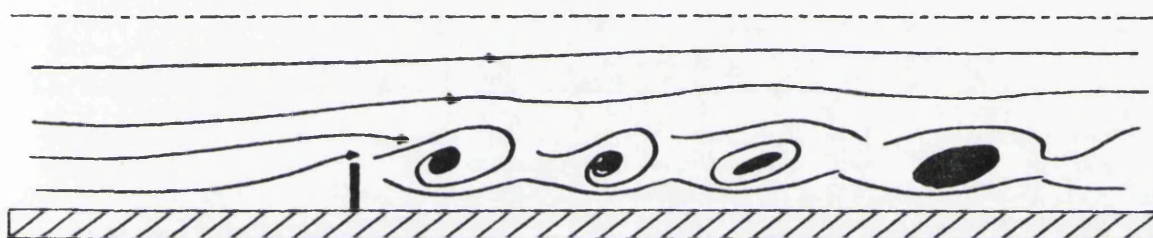


(c)  $Re_p = 384$ ,  $Re_o = 614$ ,  $f_f = 1.92\text{Hz}$ .

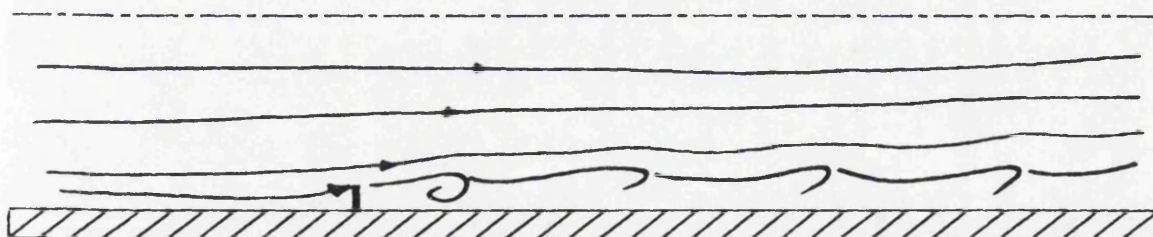
Figure 5-13: Sketch of the Flow Processes at the 16.25mm Orifice Plate - Various Reynolds Numbers



(a)  $D_o = 6.50\text{mm}$ ,  $Re_p = 256$ ,  $Re_o = 1024$ ,  $f_f = 21.05\text{Hz}$ .

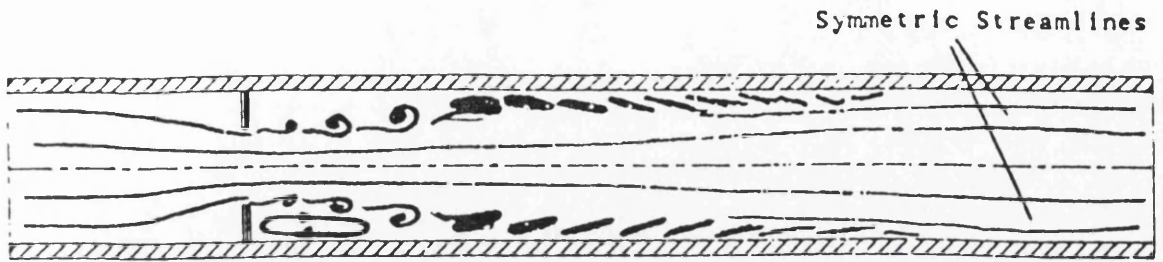


(b)  $D_o = 19.50\text{mm}$ ,  $Re_p = 256$ ,  $Re_o = 341$ ,  $f_f = 0.73\text{Hz}$ .

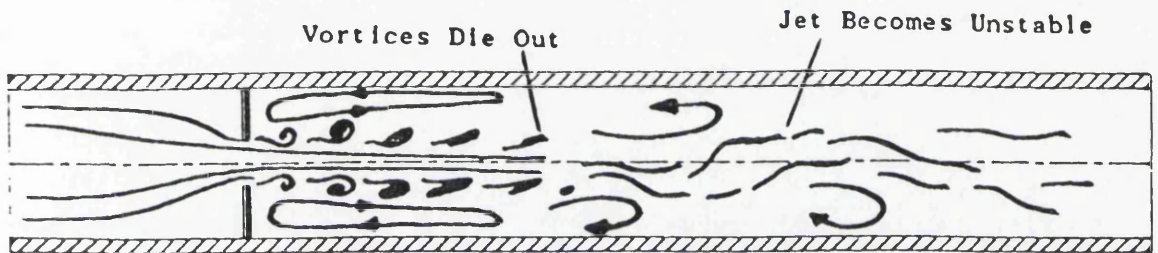


(c)  $D_o = 22.75\text{mm}$ ,  $Re_p = 256$ ,  $Re_o = 293$ ,  $f_f = 0.45\text{Hz}$ .

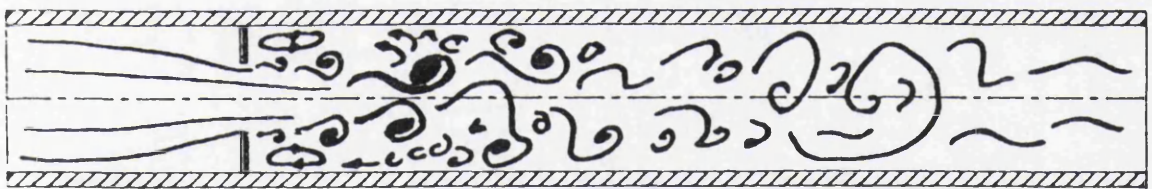
Figure 5-14: Sketch of the Flow Processes at the 6.50mm, 19.50mm and 22.75mm Orifice Plates



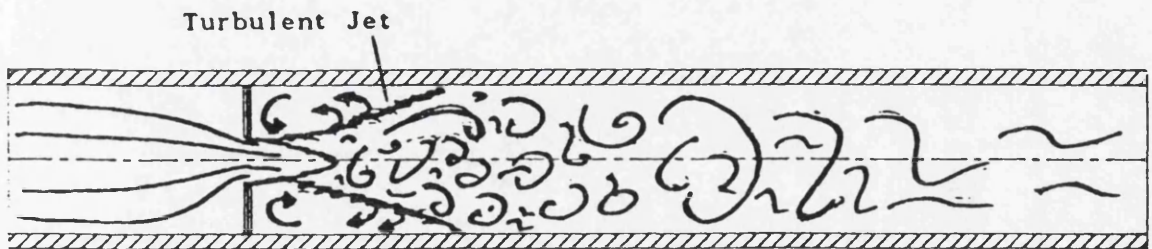
(a) DIRECTLY DISSIPATING FLOW



(b) INITIALLY INTERACTING FLOW: Unstable Jet Flow

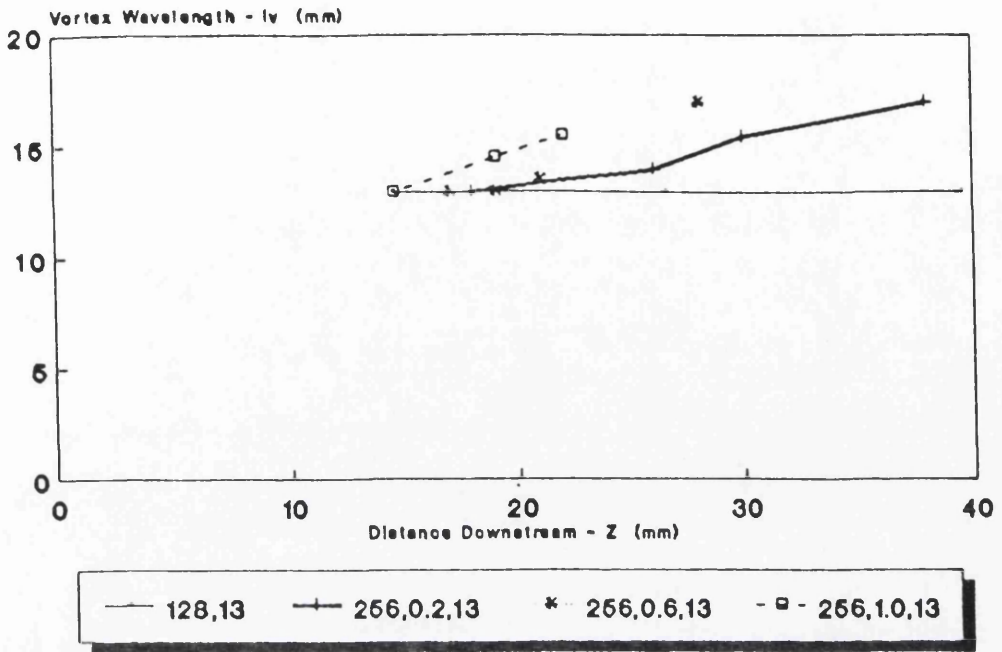


(c) INITIALLY INTERACTING FLOW: Interacting Vortex Flow

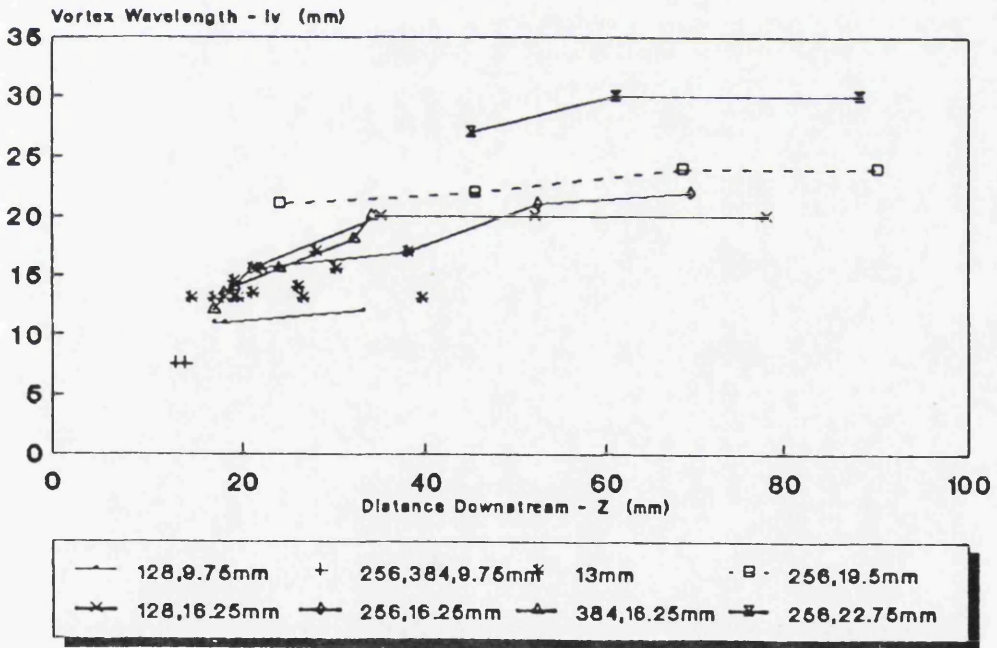


(d) INITIALLY INTERACTING FLOW: Confined Jet Flow

Figure 5-15: Catagorization of the Flow Processes

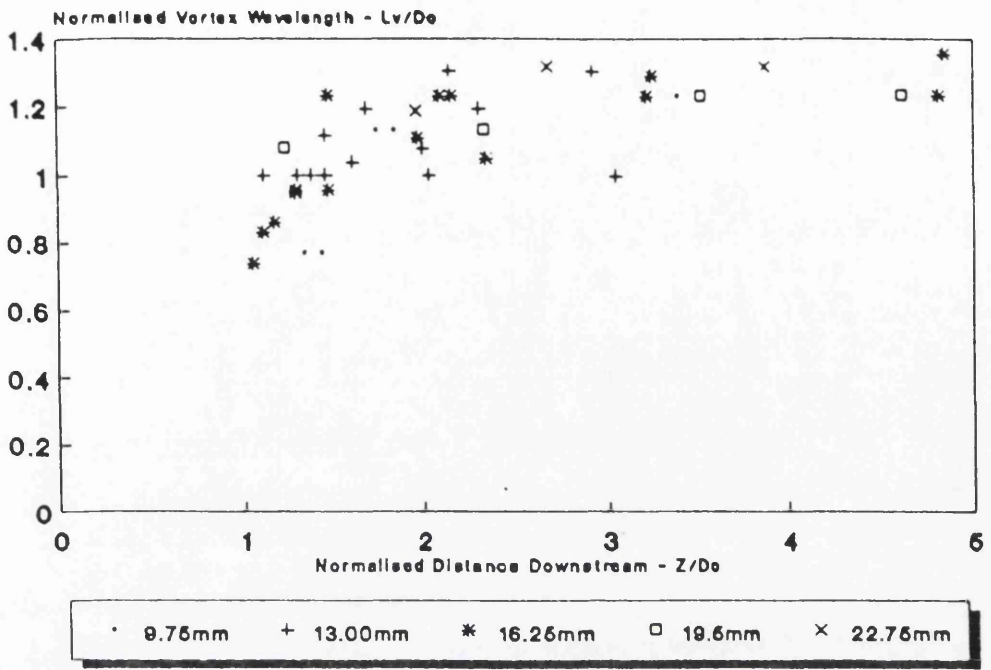


(a)  $D_o = 13.00\text{mm}$ ,  $Re_p = 256$ , Various Forcing Amplitudes.  
Also  $D_o = 13.00\text{mm}$ ,  $Re_p = 128$ .

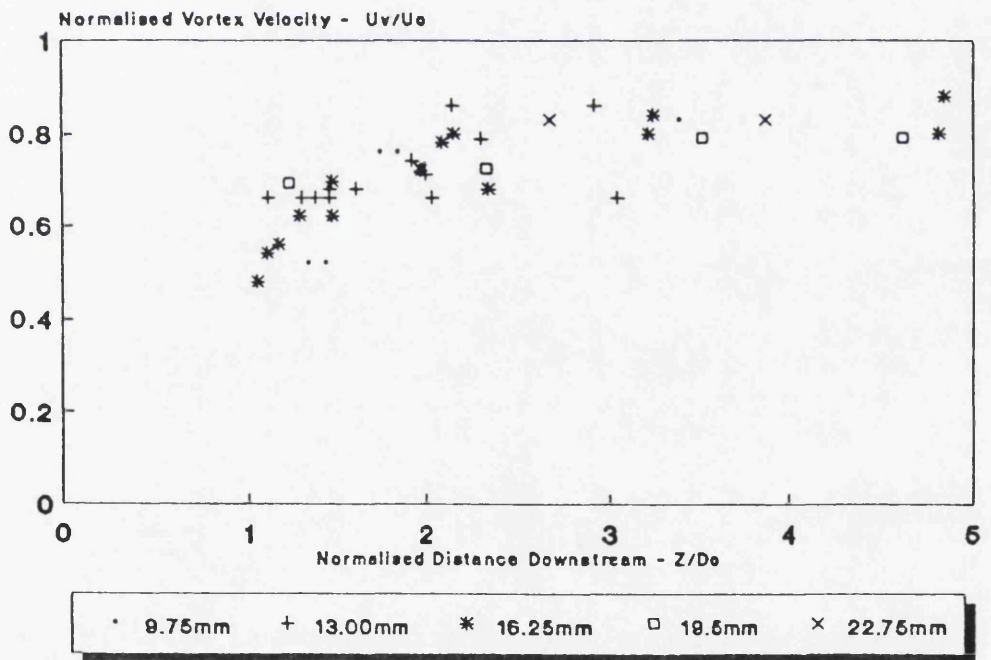


(b) Results for all Orifice Sizes and Pipe Reynolds Numbers

Figure 5-16: Downstream Wavelength Results



(a) Normalised Downstream Vortex Wavelength Results



(b) Normalised Downstream Vortex Velocity Results

Figure 5-17: Normalised Vortex Wavelength and Velocity Results

## CHAPTER 6

## CHAPTER 6

### MAIN L.D.A. RESULTS AND ANALYSES

#### 6.1 INTRODUCTION

#### 6.2 TEST SET A:

THE 13mm ORIFICE PLATE, VARIOUS REYNOLDS NUMBERS

6.2.1 Frequency Spectra, Centre-line Velocities  
and Turbulence Intensities

6.2.2 Minimum Mutual Information  
and Attractor Construction

6.2.3 Dimension and Lyapunov Exponent Results

#### 6.3 TEST SET B:

THE 13mm ORIFICE PLATE, VARIOUS FORCING AMPLITUDES

6.3.1 Frequency Spectra, Centre-line Velocities  
and Turbulence Intensities

6.3.2 Minimum Mutual Information  
and Attractor Construction

6.3.3 Dimension and Lyapunov Exponent Results

#### 6.4 TEST SET C:

THE 9.75mm ORIFICE PLATE, VARIOUS REYNOLDS NUMBERS

6.4.1 Frequency Spectra, Centre-line Velocities  
and Turbulence Intensities

6.4.2 Minimum Mutual Information  
and Attractor Construction

6.4.3 Dimension and Lyapunov Exponent Results

**6.5 TEST SET D:  
THE 16.25mm ORIFICE PLATE, VARIOUS REYNOLDS NUMBERS**

**6.5.1 Frequency Spectra, Centre-line Velocities  
and Turbulence Intensities**

**6.5.2 Minimum Mutual Information  
and Attractor Construction**

**6.5.3 Dimension and Lyapunov Exponent Results**

**6.6 TEST SET E:  
A COMPARISON OF THE VARIOUS ORIFICE PLATES  
AT A PIPE REYNOLDS NUMBER OF 256**

**6.6.1 A Comparison of the 9.75mm, 13.00mm  
and 16.25mm Orifice Plates:  
Frequency Spectra, Centre-line Velocities  
Turbulence Intensities, Minimum  
Mutual Information, Dimension  
and Lyapunov Exponent Results**

**6.6.2 A Comparison of all the Orifice Plates  
used in the Study:  
Frequency Spectra, Centre-line Velocities  
and Turbulence Intensities.**

**6.7 TEST SET F:  
ACROSS FLOW RESULTS FOR THE 13mm ORIFICE PLATE  
AT A PIPE REYNOLDS NUMBER OF 256**

**6.7.1 Frequency Spectra, Centre-line Velocities  
and Turbulence Intensities**

**6.7.2 Minimum Mutual Information  
and Attractor Construction**

**6.7.3 Dimension and Lyapunov Exponent Results**

**6.8 TEST SET G:  
A CHECK ON THE REPEATABILITY OF THE EXPERIMENT**

**6.9 OTHER ANALYSES**

**6.9.1 Autocorrelation Results**

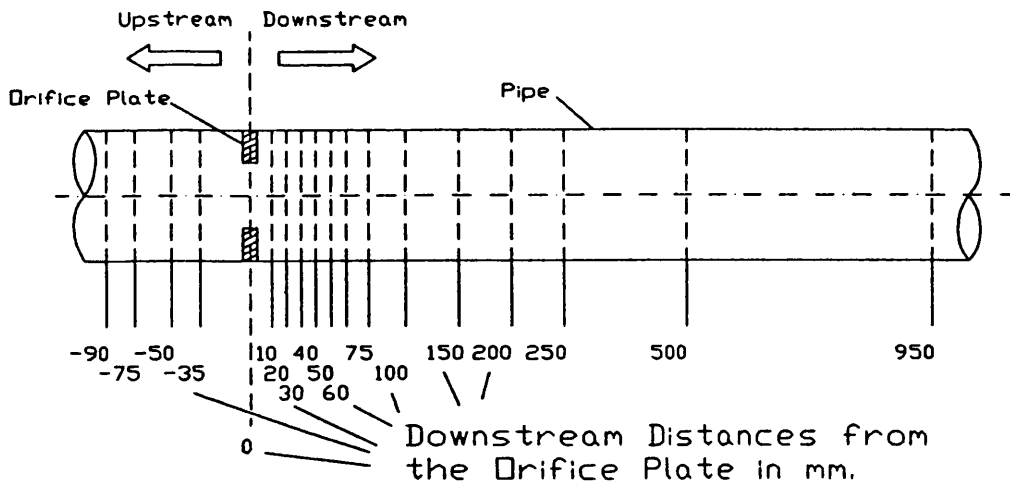
**6.9.2 Probability Distributions of  
Selected Attractor Slices**

**6.9.3 Return Map Results**

**6.10 SUMMARY**

## 6.1 INTRODUCTION

The purpose of this chapter is to report on the physical data resulting from Laser Doppler Anemometry (L.D.A.) measurements upstream and downstream of the orifice plate. Analysis of the results is left to chapter 7. A comprehensive outline of the experimental test programme is given in table 4.2, (chapter 4), and discussed in section 4.5. The tests fall into 7 categories, as defined in table 4.2, corresponding to test sets A to G. As discussed in chapter 4 results are presented for a range of Reynolds numbers from 128 to 640; a range of forcing amplitudes from 0.2 Volts to 1.0 Volts; a range of orifice diameters from 6.25mm to 22.75mm; a range of forcing frequencies from 0.45Hz to 21.05Hz, and for a range of cross sections, from 90mm upstream to 950mm downstream of the orifice plate, as defined in chapter 3, section 3.2.12, and sketched below.



The results from the Laser Doppler system are presented in various forms to assist in the interpretation of the physical flow behaviour when turbulence is tripped in a pipe at low Reynolds numbers. A typical range of information presented includes:—

- 1 - Velocity Measurements
- 2 - Frequency Spectra
- 3 - Turbulence Intensity Data

- 4 - Minimum Mutual Information Data
- 5 - Time Series
- 6 - Reconstructed Attractors
- 7 - Dimension Calculations
- 8 - Lyapunov Exponent Calculations
- 9 - First Return Maps
- 10- Trajectory Probability Histograms of Attractor Slices

Limited space does not allow for the above ten techniques to be applied to each test run, although techniques 1 to 8 are presented in most cases.

As a matter of interest there are two definitions of relative turbulence intensity, (T.I.). Turbulence intensity at a point is defined as the root mean squared value of the fluctuation velocity,  $u'$ , divided by the mean flow velocity at the point at which the measurement was taken,

$$\text{Point-T.I.} = \frac{u'_{\text{rms}}}{\bar{U}_{\text{pt}}} \quad (6.1)$$

The Point-T.I is therefore a measurement of the relative magnitudes of the velocity fluctuations compared to the mean flow velocity at each spatial location within the flow field.

The Hagen-Poiseuille turbulence intensity, H.P.-T.I., is defined as the root mean squared value of the velocity fluctuation divided by the centre-line pipe velocity for the case of Hagen-Poiseuille flow at the same mass flow rate as that of the experimental run. This centre-line value is equal to twice the average velocity within the pipe,  $\bar{U}$ , thus,

$$\text{H.P.-T.I.} = \frac{u'_{\text{rms}}}{2 \cdot \bar{U}} \quad (6.2)$$

The H.P.-T.I. is, therefore, a measure of the actual scale of the fluctuations

within the flow relative to the mean flow velocity.

It should also be noted that the data is plotted over a range of cross sections in the pipe as sketched above. There are four cross sections upstream of the orifice and thirteen downstream, with the distances between each cross section shown. In many cases, the distance downstream of the orifice is normalised by the internal pipe diameter  $D_p$ .

## 6.2 TEST SET A:

### THE 13mm ORIFICE PLATE AT VARIOUS REYNOLDS NUMBERS

#### 6.2.1 Frequency Spectra, Centre-line Velocities and Turbulence Intensities

The frequency spectra for the 13mm orifice plate for various pipe Reynolds number flows are shown in figures 6-1 to 6-5, for values of  $Re_p$  of 128, 256, 384, 512 and 640 respectively. In all cases the forcing amplitude was set to 0.6 Volts and the forcing frequency was set to the natural frequency of vortex shedding for the 13mm orifice plate at each flow Reynolds number. This was done using the Strouhal number test results outlined in chapter 4 and defined by equation 4.4.

The frequency spectra results for  $Re_p = 128$  are given in figure 6-1. In the figures the frequency spectra are given for all 17 cross sections, (4 upstream positions and 13 downstream positions), corresponding to section (a) to (d) upstream and (e) to (q) downstream.

As can be seen from figures 6-1a, b, c and d, the dominant frequency, ( $f_f = 1.27\text{Hz}$ ), is evident. At 10mm downstream of the orifice plate, (figure 6-1e), the  $f_f$  peak is still dominant, but now a smaller  $2.f_f$  harmonic has appeared. Also a peak at  $3.f_f$  is just visible. This situation remains the same for L.D.A. positions of 20, 30 and 40mm downstream. At 30mm downstream the harmonics reach a maximum amplitude. The harmonics disappear by the 60mm position, and the frequency spectra remain qualitatively the same, (i.e. a dominant single peak), from the 60mm, (figure 6-1j), position downstream to the last L.D.A. position at 950mm, (figure 6-1q).

The higher harmonics are probably generated within the motor-piston mechanism and amplified in the relatively faster moving flow emanating from the orifice aperture. Existence of a higher harmonic, at twice the forcing frequency, has also been found in results published by Gharib and Williams-Stuber [1989], in the forced oscillations of an airfoil wake. (See also chapter 2, section 2.6.3.)

The results for the  $Re_p = 256$  flow, downstream of the 13mm orifice plate, are given in figures 6-2a to m. (This flow is the standard flow regime as defined in chapter 4, section 4.5, and it also features in test sets B, E, F, and G.) The flow is an initially interacting flow, as compared to the directly dissipating flow of figure 6-1, (see section 5.7.4). As the flow proceeds downstream of the orifice plate the initial dominant frequency,  $f_f = 2.54\text{Hz}$ , gives way to the period doubling peak of  $f_f/2$ , which by 50mm downstream becomes dominant within the flow. This period doubled peak in turn gives way to a peak at roughly  $f_f/4$  at the 60mm and 75mm downstream position. By 100mm downstream, (figure 6-2h), the signal is composed of a low frequency broad band spectra and a small  $f_f$  peak as the forcing frequency begins to reassert itself within the flow. The low frequency components die out as the flow proceeds downstream, and by 500mm downstream, (figure 6-2l), the dominant  $f_f$  peak has reasserted itself within the flow and the low frequency noise has all but disappeared. Also noticeable from the first three figures is the  $2.f_f$  harmonic, which disappears, (or is swamped), by 40mm downstream, and does not reappear further downstream when the low frequency turbulent components die out.

The downstream frequency spectra results for the  $Re_p = 384$ , and forcing frequency,  $f_f = 3.82$ , flow are given in figures 6-3a to m. The situation is similar to the  $Re_p = 256$  flow, however, this time the period doubling,  $f_f/2$ , peak appears at 20mm downstream of the orifice, and completely degenerates into a noisy signal by the 30mm downstream position. Furthermore, the dominant forcing frequency spike does not disappear into the general noisy spectra until 50mm downstream. The forcing frequency spike reappears at approximately 100mm downstream, emerging from the dissipating, low frequency noisy spectra which corresponds to the weakly turbulent flow. The emergence of  $f_f$ , and the dissipation of the low frequency noise is clearly seen if one inspects the frequency spectra from the 100mm to 950mm L.D.A. position, (corresponding to figures 6-3h

to m).

Qualitatively similar results, as those obtained for the  $Re_p = 384$  flow, were obtained for the  $Re_p = 512$ ,  $f_f = 5.09\text{Hz}$  and  $Re_p = 640$ ,  $f_f = 6.37\text{Hz}$  flows. The frequency spectra from 10 to 100mm downstream for both flows are given in figures 6-4a to h, and 6-5a to h respectively. Both flows breakdown via a period doubling route, as with the  $Re_p = 256$  and  $Re_p = 384$ . Thus, all the initially interacting flows breakdown via a period doubling route. The period doubling peak is generated by vortex merging taking place as the vortices move downstream from the orifice plate, (as described in chapter 2, section 2.3.6.)

The results of the centre-line velocity measurements are shown in figure 6-6. From the figure it may be seen that there is a general trend for the velocities at, and above, a pipe Reynolds number of 256. Whereas, the slower flow ( $Re_p = 128$ ) follows a different decay pattern.

The  $Re_p = 128$  flow is a directly dissipating flow, (section 5.7.4), and thus this flow decays in a smooth axisymmetric manner back to the original upstream condition. The faster flows, ( $Re_p = 256, 384, 512$  and  $640$ ), are all initially interacting flows. These flows breakdown to a weakly turbulent state prior to dissipating out back to the upstream condition.

From figure 6-6a, it may be seen that the maximum centre-line velocity occurs just downstream of the orifice plate. There is then a region, between 25 and 100mm downstream of the orifice plate, within which the velocity decreases rapidly. A minimum velocity is reached at approximately 100mm downstream of the orifice plate. After which the downstream velocity profile begins to re-establish itself and rises back to the upstream condition.

The difference between the directly dissipating flow and the initially interacting flows is more apparent in figure 6-6b, in which the normalised velocity results are presented. The centre-line velocities are normalised by dividing them by the Hagen-Poiseuille centre-line velocity for an equivalent mass flux rate. (In the same manner as the Hagen-Poiseuille turbulence intensity, H.P.-T.I.) Thus, the downstream normalised velocities all tend to the same value, that of unity.

From figure 6-6b it can be seen that the normalised velocities of the initially interacting flows all appear to follow an identical route as they emanate from the orifice plate. The initially interacting flows decrease rapidly in centre-line velocity and dip below the normalised downstream (laminar) centre-line velocity. This is probably due to a flattening of the velocity profile caused by the turbulent zone downstream of the orifice plate. As the flow moves through the turbulent zone and the turbulent fluctuations die out, the velocity profile begins to revert back to the downstream laminar flow profile and the resulting centre-line velocity increases. (This effect will be discussed in more depth in chapter 7.)

The results of the centre-line turbulence intensity measurements are given in figures 6-7a and b. In figure 6-7a the point turbulence intensity, (Point-T.I.), is plotted versus the normalised downstream distance, (i.e. the downstream distance divided by the pipe Diameter,  $D_p$ ), and figure 6-7b plots the H-P T.I. versus the normalised downstream distance. As with the centre-line velocity results one may discern a general difference between the directly dissipating flow and the other initially interacting flows. From figure 6-7a it may be seen that the  $Re_p = 128$  flow peaks at a distance of approximately  $D_p$  from the orifice plate. The initially interacting flows peak in turbulence intensity much further downstream, at between  $2.5 \times D_p$  and  $3.0 \times D_p$  from the orifice plate, this is after the breakdown of the discrete vortices into the weakly turbulent region.

### 6.2.2 Minimum Mutual Information and Attractor Construction

Figures 6-8a and b contain the results of the minimum mutual information calculations for each of the time series. The minimum mutual information is required to determine a suitable time delay in the construction of an attractor from an experimental time series. (Mutual information is defined in detail in chapter 2, section 2.5.3 and equation 2.46.)

In figure 6-8a, the first minimum in the mutual information function, (in multiples of the time series time step, = 0.01secs), is plotted against downstream distance. The peak in the first minimum occurring for the initially interacting flows just downstream of the orifice plate. The  $Re_p = 128$ , (directly dissipating), flow remains fairly constant along the length of the pipe, its value remaining

approximately equal to a quarter of the pulsation time period as one would expect from a sinusoidal signal, (see section 2.5.3).

The individual minimum mutual information calculations for the  $Re_p = 256$ , (forcing frequency  $f_f = 2.54\text{Hz}$ ), flow, for L.D.A. positions from 10 to 50mm, and 950mm downstream are given in figures 6–9a to f. It can be seen from the figures that the coherent signals, with dominant  $f_f$  spikes, have fairly well defined minima and maxima in mutual information as the time delay is varied. However, the 40mm reading is beginning to appear less well defined and by 50mm downstream the mutual information function decays fairly rapidly with increasing time delay. The signal becomes more coherent further downstream, as shown by the 950mm plot, (figure 6–9f).

In the plots of mutual information in figures 6–9a to f the first minimum occurs at roughly 0.1 seconds (each unit of time delay on the horizontal axis is 0.01 seconds). Now the forcing frequency  $f_f$  is 2.54Hz, the cycle time is therefore  $1/f_f$ , or approximately 0.4 seconds. Thus, the first minimum in mutual information occurs at one quarter of the forcing cycle period. This indicates that the forcing frequency dominates the flow, (see section 2.5.3). Therefore, flows where the forcing frequency is dominant have more evident maxima and minima in the mutual information function, whereas, flows in which there are a multitude of frequencies, and the forcing frequency is not dominant, have no discernible mutual information maxima or minima. (See for example figure 6–9e and also its corresponding frequency spectrum given in figure 6–2e.)

The normalised minimum mutual information plot is given in figure 6–8b. In this case the value of the first minimum is normalised by dividing it by the value for one quarter of the forcing function time period. The reasoning behind this, is that for all time series where the forcing frequency is dominant, (i.e. upstream of the orifice, far downstream and just downstream where the shed vortices are still coherent), one should obtain a first minimum in the mutual information at one quarter of the forcing cycle time. Whereas, for more complex forms of the time series, (i.e. after the vortex breakdown), the first minimum in mutual information will tend to increase. From figure 6–8b it can be seen that the normalised values of the first minimum are approximately equal to unity at the positions expected, namely upstream, just downstream and far downstream. Also the peak values of the

first minimum tend to increase for increasing pipe Reynolds numbers.

The time series for the  $Re_p = 256$  flow, for all downstream positions, (except the 500mm position), are depicted in figures 6–10a to l. The first 1024 data points are plotted, equivalent to 10.24 seconds as the sampling rate was 100Hz. As can be seen from the figure, the initially periodic waveform remains stable until 40mm downstream, at which point a period doubling waveform is obvious. The first 4096 data points are plotted for the 40mm position to emphasise the varying complexity of the flow over the longer time period. This period doubled wave,  $f_f/2$ , switches intermittently with the original forcing frequency waveform,  $f_f$ . By 50mm the waveform has become quite complex, however, peaks are still visible at multiples of the forcing period, (i.e.  $1/f_f$ ). At the 75mm downstream position, large coherent structures are visible in the waveform, probably due to third or fourth generation vortex merging. By the 100mm position the flow appears quite random. Slowly the forcing frequency pulsation begins to reappear as one proceeds downstream towards the 950mm L.D.A. station.

The attractors for the  $Re_p = 256$  flow, for the first six L.D.A. positions, are shown in figure 6–11. The attractors are constructed from the first 4096 data points of the time series. The process by which the initially periodic attractor breaks down is clearly seen in these figures. At 10mm downstream, (figure 6–11a), a periodic attractor is clearly visible, with a thickened band due to the presence of experimental noise in the signal. At 20mm downstream, (figure 6–11b), the attractor is slightly unstable and by 30mm downstream, (figure 6–11c), the band is now quite thick. A distinct change in the attractor form occurs by the 40mm position, (figure 6–11d), whereby the attractor has changed shape dramatically, and is in fact reminiscent of a period doubled attractor with a high level of added noise. By 50mm downstream, (figure 6–11e), complete breakdown of the attractor form seems to have occurred. The attractor at 60mm downstream, (figure 6–11f), is of a similar complexity to the 50mm downstream attractor. The remaining attractors from 60mm to 950mm downstream all show similar complexity. Such complexity would suggest that the attractors are exhibiting high dimensional dynamics, and require high dimensional phase spaces to capture their complexity. By the 950mm position, an obvious move back toward a pulsatile flow may just be discerned, this is indicated by an exceptionally noisy periodic attractor, (not shown).

### 6.2.3 Dimension and Lyapunov Exponent Results

An estimate of the fractal dimension of the attractors constructed above was obtained using the Grassberger–Procaccia dimension estimate, as described in chapter 2, section 2.5.4. The slope of the ' $\log(r)$ – $\log(Cr)$ ' plot gives an estimate of the fractal dimension of the object, where  $r$  is the radius of the  $n$ –dimensional hyper–sphere probing the attractor constructed in increasing embedding dimensions, and  $Cr$  is the correlation integral as defined by equation 2.50, in chapter 2.

The ' $\log(r)$ – $\log(Cr)$ ' plots for the  $Re_p = 256$  flow are given in figure 6–12 for all the downstream L.D.A. positions. The slope at large length scales, and thus the dimension, for the 10 and 20mm positions is approximately equal to unity, (1.08 and 1.03 respectively). This supports the visual information obtained from the attractor plots, where the attractors are composed of noisy, periodic bands which are the dominant features on large length scales above the noise level. (See for example the results obtained with pulsatile laminar flow in section 4.2.5.)

At lower length scales the slopes become very steep due to the presence of noise. At 30mm downstream a more interesting picture is evident. There is a slope of 1.09 at large length scales and a slope of approximately 3.57 at intermediate length scales. This would tend to suggest that the attractor is periodic at large length scales, but more complex, or fractal, at lower length scales. This in turn may imply that this signal is from a low dimensional chaotic flow. At 40mm downstream the slope has increased to 4.96 and no periodic element is visible. At 50mm downstream the slope has increased to 12.71. The value of dimension remains fairly high, until at 200mm the dimension returns to approximately 4.38, then back to 2.05 by 950mm downstream. These dimension results, together with the other flow results, ( $Re_p = 128, 384, 512$  and  $640$ ), are presented in figure 6–13. In the figure the dimension is plotted against the normalised downstream distance,  $Z/D_p$ .

The dimension results, of figure 6–13, follow a similar pattern for all the initially interacting flows, which differ markedly from the directly dissipating flow. The dimension of the initially interacting flows increase rapidly immediately after issuing from the orifice aperture, and peak at values between 15.00 and 20.00.

This may in fact represent a limit in the computer application of the Grassberger–Procaccia dimension algorithm, and the flows may in fact have dimensions much higher than these values, (even infinite). All dimensions then decay as the flow proceeds downstream.

The Lyapunov exponent was calculated to measure the divergence properties of the attractors. A positive Lyapunov exponent indicates that initially close points on the attractor diverge rapidly, and indicates the presence of a chaotic flow, (see chapter 2, section 2.5.6.1).

The results of the Lyapunov exponent calculations are given in figure 6–14. The Lyapunov exponents were calculated for each time series embedded in 4–dimensional phase space, (see section 2.4.3). The time delay used in the attractor construction was that used in the dimension estimate, i.e. it was found using the minimum mutual information criteria. The evolution time for the separation calculations was taken as one quarter of the forcing cycle time.

The Lyapunov exponent results mirror the dimension results. Just downstream of the orifice, the Lyapunov exponents increase rapidly, reaching a peak between 40 and 50mm downstream for all initially interacting flows. The Lyapunov exponents seem to 'cut-off' at about the 40 to 50mm downstream position, after which they decay back to lower values as the flow proceeds further downstream. This cutting off of the initially, rapidly increasing exponents, is most probably due to the fact that the actual attractor dimension has exceeded the embedding dimension, ( $= 4$ ).

### **6.3 TEST SET B:**

#### **THE 13mm ORIFICE PLATE, VARIOUS FORCING AMPLITUDES**

##### **6.3.1 Frequency Spectra, Centre–line Velocities and Turbulence Intensities**

The downstream frequency spectra for the  $Re_p = 256$  flow and 13mm orifice plate forced at 0.6 Volts has already been presented above in figure 6–2. (When looking at various Reynolds numbers, all forced at 0.6 Volts forcing amplitude.)

The downstream frequency spectra for the  $Re_p = 256$  flow and 13mm orifice plate forced at 0.2 and 1.0 volts are given in figures 6-15 and 6-16. The forcing amplitudes of 0.2, 0.6 and 1.0 volts respectively, correspond to an R.M.S. variation in the mass flow rate of 2.65%, 7.95% and 13.26%. All three of these flows, considered in this section, are initially interacting flows.

The downstream frequency spectra for the 0.2 Volts forcing amplitude are given in figures 6-15a to m. As the flow passes through the orifice plate the dominant frequency at  $f_f = 2.54\text{Hz}$  is visible. A harmonic begins to grow at  $2.f_f$ . This harmonic reaches a maximum at approximately 30mm downstream, after which point it begins to decrease. A subharmonic at  $f_f/2$ , begins to appear in the spectrum at the 40mm position. At 50mm downstream this subharmonic peak is quite distinct. The  $f_f/2$  subharmonic grows and by 60mm downstream has started to decay into broad band spectra. The spectra remains fairly broad band from 75mm downstream to 250mm downstream, by which point the forcing frequency peak has re-emerged in the flow spectra. By the 950mm downstream position the low frequency broad band noise has decayed and the  $f_f$  spike dominates the frequency spectrum.

The frequency spectra for the 0.6 Volts forcing amplitude have already been discussed above for the  $Re_p = 256$  flow in section 6.2.1. Briefly the flow follows a similar pattern to the above 0.2 flow, as shown in figure 6-2. However, in this case the period doubling peak becomes dominant within the flow at the 50mm downstream position, whereas in the 0.2 Volts case the period doubling peak becomes dominant 75mm downstream of the orifice.

The frequency spectra for the 1.0 Volts forcing are given in figure 6-16. As the flow passes through the orifice plate the dominant frequency at  $f_f = 2.54\text{Hz}$  is again visible. The  $2.f_f$  harmonic is again evident as the flow issues from the orifice plate. The subharmonic at  $f_f/2$ , begins to appear in the spectrum at the 20mm position. At 30mm downstream this subharmonic peak is quite distinct. By 40mm downstream the  $f_f/2$  subharmonic has started to decay into broad band spectra, although it may be still discerned within the flow at the 50mm position. The frequency spectrum becomes broad band by 75mm downstream, and the re-emergence of the  $f_f$  peak is just visible. The re-emergence of the pulsation peak and the decay of the low frequency noise may be followed as one proceeds

from the 100mm downstream position to the 950mm position, (figures 6-16h to 6-16m).

The results of the centre-line velocity measurements are given in figures 6-17a and b, for all three forcing amplitudes at  $Re_p = 256$  and the 13mm orifice plate. All three flows are initially interacting flows and the two larger amplitude flows ( $A=0.6$  and 1.0 Volts) reach a velocity minimum at approximately  $3 \times D_p$  downstream. The flow with the lowest amplitude forcing, ( $A=0.2$  Volts), appears to flatten out and reaches the downstream centre-line velocity asymptotically, without first reaching a minimum at, or near to, the breakdown point.

The results of the turbulence intensity measurements are given in figures 6-18a and b, again for all three forcing amplitudes. All three flows reach similar maximum values of both Point-T.I. and H.P.-T.I. However, the 0.2 forcing flow peaks farther downstream than the other two flows and the turbulent fluctuations decay more slowly.

### 6.3.2 Minimum Mutual Information and Attractor Construction

The first minimum in mutual information plot is given in figure 6-19a, and the normalised plot in figure 6-19b, (for comparison with other normalised plots). The value of the first minimum increases rapidly as one proceeds downstream. Interestingly the low forcing amplitude, (0.2 Volts), peaks much further downstream than the two larger forcing amplitudes, (at approximately twice the distance.) From the normalised graph of figure 6-19b, it is clear that the forcing frequency dominates immediately downstream of the orifice plate, (where the normalised first minimum is unity), and again far downstream where the forcing frequency re-establishes itself within the flow.

The attractors for the 0.2 forcing, are shown in figure 6-20. These are constructed using the time series obtained from the first six downstream L.D.A. positions, (i.e. 10mm to 60mm downstream). The figures show quite clearly the breakdown of the attractor as the flow evolves downstream of the orifice plate, increasing in complexity as it does so. The attractor remains distinctly periodic,

with added noise, until at 50mm downstream, the attractor band begins to spread. The attractor departs from its singly periodic structure by 60mm downstream.

The attractors obtained for the intermediate, 0.6 Volts, forcing amplitude, have already been discussed in section 6.2.2, and are plotted in figure 6-11.

The attractors for the 1.0 Volts forcing amplitude are plotted in figure 6-21. Only the first five attractors are plotted, (from 10 to 50mm downstream). The breakdown of the initially noisy-periodic attractor is quite fast. The initially periodic attractor occurring at 10mm, thickens markedly by 20mm. Breakdown occurs at 30mm downstream, one may see from the associated time series, (not shown), that a period doubling has occurred, however, noise obscures the picture somewhat in the attractor plot. The attractor at 40mm is now quite complex, the time series showing intermittent large and small structures within it. The 50mm attractor also appears reasonably complex, however, the time series, (not plotted), is interesting in that a second period doubling may be discerned. That is, structures with a period of four times that of the flow pulsations are visible.

### 6.3.3 Dimension and Lyapunov Exponent Results

The dimension results for the three forcing amplitudes are given in figure 6-22. The dimension of all three flows increase rapidly, immediately after issuing from the orifice aperture, and peak at values between 13.00 and 20.00. The dimensions then reduce in value as the flow proceeds downstream.

It is noticeable from figure 6-22, that the dimension plot for the 0.2 Volt amplitude does not decrease markedly from its peak value as it proceeds downstream. No obvious reason for this is apparent, however, one possible explanation is that the noise present in the signal was sufficient to obscure the downstream pulsations in the flow and give an erroneous high value of dimension. However, just downstream of the orifice plate where the flow velocity is higher, the absolute magnitude of the velocity fluctuations is higher and able to dominate over the noise. In this case, the dimension algorithm is able to detect the attractor structure within the noise.

The results of the Lyapunov exponent calculations are given in figure 6-23. Once again the Lyapunov exponent results mirror the dimension results. Just downstream of the orifice, the Lyapunov exponents increase rapidly. The figure would tend to suggest that the larger the forcing amplitude the more rapid the increase in the Lyapunov exponent with downstream distance. The lowest amplitude, (0.2 Volts), peaks farthest downstream, at the 75mm position. Once again the Lyapunov exponents cut-off at a specific distance downstream, after which they decay back to lower values as the flow proceeds further downstream.

#### 6.4 TEST SET C:

##### THE 9.75mm ORIFICE PLATE, VARIOUS REYNOLDS NUMBERS

#### 6.4.1 Frequency Spectra, Centre-line Velocities and Turbulence Intensities

Frequency spectra for the 9.75mm orifice plate, for three Reynolds number flows, ( $Re_p = 128, 256$  and  $384$ ) and a forcing amplitude of 0.6 Volts are shown in figures 6-24 to 6-26.

The frequency spectra results for  $Re_p = 128$  are given in figure 6-24. As the flow emanates from the orifice, the dominant  $f_f = 3.07\text{Hz}$  peak, together with its harmonic at  $2.f_f$ , is visible at 10mm downstream, (figure 6-24a). At the 20mm position, (figure 6-24b), the period doubling subharmonic is evident, which increases in magnitude by the 30mm position. By 40mm downstream, the forcing frequency peak has diminished and the period doubled peak dominates the spectrum, together with some very low frequency components. The breakdown of the  $f_f/2$  peak occurs by the 75mm position, and the flow is composed of very low frequency components. (See figure 6-24g, where the spectrum from 0 to 50Hz is shown). At the 150mm position the forcing frequency begins to dominate the spectrum once more. The low frequency components completely disappear from the spectrum by the 950mm position.

The frequency spectra results for  $Re_p = 256$  are given in figure 6-25. Once again the forcing frequency,  $f_f = 6.14$ , is dominant at the 10mm position, a small 'hump' at  $f_f/2$  is also visible. At 20mm downstream, the  $f_f/2$  peak has

increased in magnitude. The  $f_f/2$  grows larger at the 30mm position. At the 40mm position, the  $f_f/2$  subharmonic is visible within what is otherwise a noise spectrum. The spectrum becomes quite indistinguishable by 50mm downstream. The forcing frequency peak begins to re-emerge from the broad band spectra by 100mm downstream. The forcing peak then increases as the low frequency broad band components dissipate out of the flow, as the L.D.A. position is moved downstream.

The frequency spectra results for the  $Re_p = 384$  flow are given in figure 6-26. The dominant frequency,  $f_f = 9.21\text{Hz}$ , breaks down via a period doubling route, as with the slower flows. The  $f_f/2$  subharmonic is just visible in the 10mm downstream plot. This subharmonic grows, and by 30mm is quite distinct within the spectrum, together with lower frequency, ( $< f_f/2$ ), broad band components. The overall picture is much the same as for the  $Re_p = 256$  flow, with the forcing frequency peak reappearing in the spectrum at 75mm downstream.

The centre-line velocity results are plotted in figures 6-27a and b. From the figures, it can be seen that both the  $Re_p = 256$  and 384 flows follow a similar route, reaching a velocity minimum at approximately three pipe diameters downstream of the orifice plate. However, the  $Re_p = 128$  flow velocity decreases much less rapidly on leaving the orifice plate and reaches the downstream centre-line velocity value asymptotically. All three flows are initially interacting flows, however, the  $Re_p = 128$  flow is an 'unstable slow jet flow' as defined in section 5.5.4, whereas the faster flows are 'interacting vortex flows'.

The Point-T.I.'s, given in figure 6-28a, show a marked difference between the  $Re_p = 128$  flow and the two faster flows. The slow flow shows a decrease in the Point-T.I. after issuing from the orifice plate to a minimum at approximately  $2.5$  to  $3.0 \times D_p$  downstream. The  $Re_p$  flow then increases to a maximum at about  $8.0 \times D_p$  downstream. The higher Reynolds number flows reach maxima at approximately  $4 \times D_p$  downstream after an initially rapid increase.

The H.P.-T.I. measurements reach maxima at positions earlier than the Point-T.I.'s for all three flows. The  $Re_p = 256$  and 384 flows peak at between  $2.0$  and  $2.5 \times D_p$  downstream. Whereas, the  $Re_p = 128$  flow first reaches a minimum at  $2.5$  to  $3.0 \times D_p$  downstream.

#### 6.4.2 Minimum Mutual Information and Attractor Construction

The first minimum in mutual information plots are given in figures 6-29a and b. From the figures, it may be seen that the  $Re_p = 128$  and  $256$  flows peak at the same position,  $4 \times D_p$  downstream, whereas, the  $Re_p = 384$  flow peaks earlier.

The attractors for the  $Re_p = 128$  flow at the 10, 20, 30, 40, 60 and 100mm position are plotted, in figure 6-30, to illustrate the downstream development in the attractor shape. The band of the initially circular, noisy-periodic shape at 10mm, thickens dramatically by 30mm and has completely changed by 60mm downstream. The 100mm attractor is also shown, this attractor is constructed from a waveform which contains intermittent large troughs, which probably correspond to large coherent structures passing the L.D.A. probe position.

The attractors, for the first four L.D.A. positions for the  $Re_p = 256$ ,  $f_f = 6.14\text{Hz}$  flow, are given in figure 6-31. The breakdown of the initially periodic attractor is clearly visible from the plots. The attractors at the 20 and 30mm positions seem to be essentially periodic, however, the loops of the attractor wander up and down the  $45^\circ$  line. This is perhaps due to another low frequency component superimposed on the flow. At the 40mm position, the attractor form is no longer simple.

The change in attractor complexity as the L.D.A. position is moved downstream for the  $Re_p = 384$  flow is shown in figure 6-32 for the first four L.D.A. positions. The initially noisy-periodic attractor at 10mm downstream quickly becomes unstable. By 20mm, the attractor band has become quite thick, and some of the trajectories have wandered from the main attractor loop. At 30mm, the attractor seems to have lost any clearly defined shape and the trajectories are now wandering quite markedly. By 40mm the attractor has lost any discernible form and has become quite complex.

### 6.4.3 Dimension and Lyapunov Exponent Results

The dimension results for the three pipe Reynolds numbers are given in figure 6–33. All three flows are initially interacting flows and correspondingly all dimensions increase rapidly with downstream distance immediately after the orifice plate. The dimensions reach peaks of between 15.00 and 22.00. The dimension then reduces in value as the flow proceeds downstream.

The results of the Lyapunov exponent calculations are given in figure 6–34. The Lyapunov exponent values for the all three flows increase rapidly as they proceed downstream from the orifice plate. The magnitude of the exponent maxima increases with increasing  $Re_p$ .

## 6.5 TEST SET D:

### THE 16.25mm ORIFICE PLATE, VARIOUS REYNOLDS NUMBERS

#### 6.5.1 Frequency Spectra, Centre–line Velocities and Turbulence Intensities

The downstream frequency spectra for the three pipe Reynolds number flows, using the 16.25mm orifice plate, are depicted in figures 6–35 to 6–37.

The frequency spectra results, for the first four downstream positions, for  $Re_p = 128$ ,  $f_f = 0.64\text{Hz}$  are given in figure 6–35. As the flow emanates from the orifice a harmonic at  $2.f_f$  is visible, (at 10 and 20mm downstream). At the 30mm position a third harmonic is visible within the flow at  $3.f_f$ . By 40mm downstream only the forcing frequency is visible within the spectrum, this remains the case for all subsequent downstream positions.

The frequency spectra results for  $Re_p = 256$ ,  $f_f = 1.28\text{Hz}$  are given in figure 6–36. Once again the forcing frequency,  $f_f$ , is dominant at the 10mm position, small peaks at  $2.f_f$  and  $f_f/2$  are also just visible. At 20mm downstream, the  $2.f_f$  peak has increased in magnitude and the  $f_f/2$  peak has disappeared. The  $f_f/2$  peak re–emerges by 30mm downstream. At the 40mm position the  $2.f_f$  peak has disappeared and the  $f_f/2$  subharmonic is starting to grow. The subharmonic

reaches a maximum by 75mm downstream of the orifice plate and has completely disappeared by 150mm downstream. The spectrum shape remains essentially the same at subsequent downstream positions.

The frequency spectra results for  $Re_p = 384$ ,  $f_f = 1.92\text{Hz}$  are given in figure 6-37. The forcing frequency,  $f_f$ , dominates at the positions immediately downstream of the orifice plate. By 30mm downstream, a subharmonic peak at  $f_f/2$  emerges, and also a smaller  $f_f$  peak becomes visible. The subharmonic peak then increases in amplitude and begins to widen by the 100mm downstream position. At the 150mm position the  $f_f$  peak is still visible, however, the spectrum is now composed of broad band components. The broad band part of the spectrum then begins to decay as the laser position is moved further downstream and the weakly turbulent flow begins to dissipate out.

The centre-line velocity results are given in figure 6-38a. Again the difference between directly dissipating and initially interacting flow patterns is visible. The two directly dissipating flows ( $Re_p = 128$  and  $256$ ) showing a smooth decay in the centre-line velocity, whereas the initially interacting flow ( $Re_p = 384$ ) has a much more dramatic velocity decrease immediately after issuing from the orifice plate, dropping to below the downstream level before gradually increasing back to it. These results are replotted in a nondimensional form in figure 6-38b.

The turbulence intensities are plotted in figures 6-39a and b. All three flows show quite erratic movement in the value of the turbulence intensity immediately downstream of the orifice plate, the reason for this is unclear. The turbulence intensity, (both H-G and T.I.), for the fastest flow ( $Re_p = 384$ ) increases to a maximum at approximately 100mm, or  $8 \times D_o$ , from the orifice plate. After which point it decays back to the upstream level.

### 6.5.2 Minimum Mutual Information and Attractor Construction

The first minimum in mutual information plot is given in figure 6-40a, and the normalised plot in figure 6-40b. From the normalised plot, it is obvious that only the initially interacting flow, ( $Re_p = 384$ ), departs from the near unity value

one expects from a periodic flow.

The attractors for the  $Re_p = 128$  flow at the 60, 75 and 100mm position are plotted, in figure 6-41, to illustrate an interesting development in the attractor shape. The initially circular, noisy-periodic shape at 60mm, becomes flattened by 75mm and returns to its original noisy, circular shape by 100mm. The reason for this flattening of the attractor is, as yet, unclear. It may, however, be the hallmark of the onset of a more complex flow, which did not proceed, as the 100mm position shows a noisy periodic attractor once again.

The change in attractor complexity as the L.D.A. position is moved downstream for the  $Re_p = 384$  flow is shown in figure 6-42 for the downstream positions of 20mm, 60mm and 75mm. The initially noisy-periodic attractor, at 20mm downstream, slowly becomes unstable and by 60mm the attractor band has become quite thick and the attractor has become more oval in shape. At 75mm the attractor has lost its clearly defined shape and is now of a complex construction.

### 6.5.3 Dimension and Lyapunov Exponent Results

The dimension results for the three pipe Reynolds numbers are given in figure 6-43. Only the dimension of the  $Re_p = 384$  flow increases after issuing from the orifice aperture, and peaks at a value of 16.58. This maximum value occurs at a distance of 150mm, or approximately 12 orifice diameters, downstream of the orifice plate. The dimension then reduces in value as the flow proceeds downstream.

The results of the Lyapunov exponent calculations are given in figure 6-44. The Lyapunov exponent values for the  $Re_p = 128$  flow remain low for all flows downstream of the orifice plate. The Lyapunov exponents for the  $Re_p = 256$  flow, increases quite slowly, peaking quite far downstream, at 200mm from the orifice plate. The Lyapunov exponents increase rapidly for the  $Re_p = 384$  flow, peaking at 150mm downstream, (as with the dimension).

## 6.6 TEST SET E:

### A COMPARISON OF THE VARIOUS ORIFICE DIAMETERS AT A PIPE REYNOLDS NUMBER OF 256

#### 6.6.1 A Comparison of the 9.75mm, 13.00mm and 16.26mm Orifice Plates; Frequency Spectra, Centre-line Velocities, Turbulence Intensities, Minimum Mutual Information, Dimension and Lyapunov Results

The frequency spectra for the 9.75, 13.00 and 16.25mm orifice plates have been given above in figures 6-2, 6-25 and 6-36 respectively.

The centre-line velocity results are given together in figure 6-45. As can be seen from the figure, the initial velocity of the flow leaving the orifice increases with decreasing orifice aperture diameter. A result one would expect from the continuity condition. The 9.75mm and 13.00mm flows are both initially interacting flows and have velocity profiles characteristic of such flows. On the other hand, the 16.25mm orifice flow, (a directly dissipating flow), has a smooth transition from its velocity at the orifice plate to those downstream.

The turbulence intensities are plotted in figures 6-46a and b. Figure 6-46a contains the Point-T.I. results. The two initially interacting flows show marked increases in Point-T.I. downstream of the orifice, the maximum value of Point-T.I. increases with decreasing orifice diameter.

In figure 6-46b, the H.P.-T.I. is plotted against downstream distance. The peak in turbulence intensity increases with increasing pipe Reynolds number. This turbulence measure is a direct measure of the actual r.m.s velocity fluctuations. Thus, the velocity fluctuations are increasing as the orifice aperture diameter decreases.

The minimum mutual information results are depicted in figures 6-47a and b. From the plot of 6-47b, it may be seen that the normalised first minimum increases with Pipe Reynolds number. The  $Re_p = 128$  flow remains at unity for all L.D.A. positions, probably due to the dominance of the pulsation frequency

throughout the flow.

The dimension results for the three pipe Reynolds numbers are given in figure 6-48. All three dimensions increase as they proceed from the orifice position. The maximum dimension increases with decreasing orifice diameter.

The results of the Lyapunov exponent calculations are given in figure 6-49. As with the dimension results, all three exponents increase upon proceeding downstream of the orifice plate, and, the maximum value of the exponents increases with decreasing orifice diameter.

#### 6.6.2 A Comparison of all the Orifice Diameters used in the Study: Frequency Spectra, Centre-line Velocities, and Turbulence Intensities

Tests were also conducted for three additional orifice plates of diameters,  $D_o$ , of 6.50mm, 19.50mm and 22.75mm. (Corresponding to  $1/4D_p$ ,  $3/4D_p$  and  $7/8D_p$ .) The tests were conducted solely for a Reynolds number of 256. The data obtained from the L.D.A. measurements were used to produce frequency spectra, centre-line velocities and turbulence intensities, with which to compare to the other three orifice diameters used in the study, (section 6.2.1). The frequency spectra for the 9.75, 13.00 and 16.25mm orifice plates have been given above in figures 6-2, 6-25 and 6-36.

The frequency spectra for the 6.50mm orifice plate is given in figure 6-50 and plots the development of the spectra downstream of the orifice plate, for the first four L.D.A. positions. At 10mm downstream, the dominant  $f_f = 21.05\text{Hz}$  peak is clearly visible. A period doubling peak is seen to enter the flow at the 20mm position, and has grown by the 30mm position. At 30mm low frequency, broad band components have also arisen within the spectrum. By 40mm downstream, these low frequency components have swamped the signal. The plots for subsequent downstream position show quite clearly the shift in the broad band components to lower frequencies. This is the general picture of the downstream frequency spectra, and the forcing peak only re-emerges by the 950mm position.

The frequency spectra for the 19.50mm orifice flow, ( $f_f = 0.73$ ), are given for the first four L.D.A. positions in figure 6-51. The dominant peak at 10mm downstream continues to dominate the spectrum for all downstream positions, the only deviation from the single peak in the spectrum occurs at the 30mm downstream position where a peak at the  $2.f_f$  harmonic appears. This peak then disappears by the 40mm L.D.A. position, and the spectrum remains essentially the same for all subsequent positions.

No plots are given for the 22.75mm orifice, ( $f_f = 0.45\text{Hz}$ ), as the spectra at all downstream positions are composed of a single  $f_f$  peak.

The centre-line velocities for all six orifice plates are given in figure 6-52. The difference between the three directly dissipating flows, (lower Reynolds numbers) and the three initially interacting flows may be seen. All flows eventually reach the same downstream centre-line velocity value by the 950mm L.D.A. position.

The turbulence intensities may be seen in figure 6-53a and b. The directly dissipating and initially interacting flows again showing different behaviour. The initially interacting flows all increase in Point-T.I. immediately after issuing from the orifice, reaching maxima at between 100 and 150mm downstream. The directly dissipating flows, on the other hand, remain fairly constant over the range of L.D.A. positions. The H.P.-T.I. results are plotted in figure 6-53b. It may be seen from the figure that the H.P.-turbulence intensities peak before the Point-T.I. results.

## 6.7 TEST SET F:

### ACROSS FLOW RESULTS FOR THE 13MM ORIFICE PLATE AT A PIPE REYNOLDS NUMBER OF 256

An attempt was made to measure the radial variation in the time series properties. Longitudinal velocity-time data was measured at radial positions from the centre-line to 5.33mm inclusive, in increments of 0.66mm. This was done for the first five downstream L.D.A. positions, namely the 10mm, 20mm, 30mm,

40mm and 50mm position. The results of these measurement are given below.

### 6.7.1 Centre-line Velocities and Turbulence Intensities

The velocities at each of the five downstream positions are plotted in figure 6-54a, and the normalised velocities in figure 6-54b. From the figure, it may be seen that the velocity decreases in the downstream direction, as outlined above, and also in the radial direction. The retarding of the edge of the jet may be seen by inspecting each velocity plot in turn. The velocity plot for the 10mm downstream section indicates that the velocity profile of the issuing jet is fairly flat until at 4.00mm from the centre-line the velocity drops off dramatically. This drop-off point occurs at 4.00mm for the 20mm downstream position also. By 30mm the drop-off point has progressed into the flow and occurs at the 2.66mm position. AT the 40mm position the drop-off point is less well defined and seems to occur at 2.00mm from the jet centre line. By 50mm downstream the retarding of the jet has reached the centre-line.

The Point-T.I. results are given in figure 6-55a. From the figure, it may be seen that the turbulent fluctuations increase dramatically towards the jet edge, as one would expect, due to the high shearing taking place between the jet flow passing through the orifice aperture and the slower moving flow in the recirculation region. The H.P.-T.I. results are given in figure 6-55b, the turbulence intensities in this case increase dramatically at the jet edge for the flows immediately downstream of the orifice plate, however, at greater distances downstream, the H.P.-T.I. values are more even across the flow. This would indicate that the jet has now fully broken down and that the turbulent fluctuations are fairly evenly spread across the flow by this stage.

### 6.7.2 Minimum Mutual Information

The first minimum in mutual information plot for each of the downstream positions is given in figure 6-56a, and the normalised plot in figure 6-56b. Both plots are identical as the same flow conditions are being investigated, however, both plots are given for comparison with other results. The plots show an increase

in the value of the first minimum downstream as the flow complexity increases. Across the flow the first minimum in mutual information increases for the near-orifice flows, (10, 20 and 30mm), as the jet edge is approached. The values of these flows, at the edge, reach those of the broken down flow at 50mm.

### 6.7.3 Dimension and Lyapunov Exponent Results

The dimension results for the across flow results are given in figure 6-57. The general trend for the dimension of the flows is to increase with downstream distance, only the 20mm position plot seems to increase with radial position. This would tend to suggest that the complexity of the flow is mainly a function of downstream distance.

The results of the Lyapunov exponent calculations are given in figure 6-58. The Lyapunov exponents increase with downstream position. However, unlike the dimension results, the exponent values do increase with radial position for the near orifice positions, (10, 20 and 30mm). This may in fact be an inherent property of the Lyapunov exponent itself, (or the computer algorithm), as the presence of noise at the jet edge may greatly effect the result.

## 6.8 TEST SET G:

### A CHECK ON THE REPEATABILITY OF THE EXPERIMENT

The repeatability of the experiment was checked by retaking the measurements for the standard set of results, i.e.  $Re_p = 256$ ,  $D_o = 13\text{mm}$ , (see section 4.5). The results for the centre-line velocities, turbulence intensities, (point T.I.), first minimum in mutual information and Lyapunov exponents are given in figures 6-59 to 6-62 respectively. As can be seen from the figures, the results are fairly consistent for both the original results, (TEST 1), and the remeasured results, (TEST 2).

## 6.9 OTHER ANALYSES

Other means of analysis were attempted. These are outlined as follows for the  $Re_p = 256$ ,  $D_o = 13.00\text{mm}$  flow. (Standard test, see section 4.5).

### 6.9.1 The Autocorrelation Function

The autocorrelation function is plotted for the downstream positions from 10mm to 100mm inclusive in figure 6-63. The autocorrelation function for the 10mm and 20mm position is typical of that for a periodic waveform. The autocorrelation of the time series taken at the 30mm positions shows a slight amplitude difference between each alternate peak, as a second period begins to enter the flow. At 40mm the effect of the period doubling is clearly seen in the autocorrelation plot, also a decrease in the average autocorrelation value. As the flow temporally decorrelates. By 50mm downstream the flow is decorrelating rapidly and the period doubled fluctuations are very much in evidence. The 60mm plot of the autocorrelation function shows the flow to be quite complex, rapid decorrelation is evident, however, small ripples in the plot at the forcing period may be discerned. The 75mm plot is similar in form to the 60mm plot, and by 100mm downstream, the forcing frequency ripples are coming back into the picture.

### 6.9.2 Probability Distribution of Selected Attractor Slices

It was decided to investigate the development of the attractor bands as the attractor lost stability from a noisy-periodic form. To do this the attractor was cut across its band, and the trajectories crossing the cut, or slice, were counted and a histogram was produced of the number of trajectory passes at each position.

The histograms obtained for the first four attractors of the  $Re_p = 256$ ,  $D_o = 13.00\text{mm}$  flow are given in figure 6-64. Their respective attractors are given in figure 6-11a to d. Each attractor histogram is plotted with an equivalent Gaussian distribution superimposed over it for comparison. The trajectory histogram at the 10mm downstream position would suggest that the trajectories are bundled in a Gaussian structure, due to the presence of random noise in the signal. By 20mm

downstream the histogram appears to be skewed slightly, with the peak displaced outward from the attractor centre. The 30mm histogram has now departed completely from the Gaussian distribution and a secondary peak is clearly evident appearing closer to the centre of the attractor. (A third peak is also just visible.) The 40mm attractor has now broken down into a dense complex structure and the corresponding trajectory histogram appears to be Gaussian once again, after this point the use of the trajectory histogram is limited as a means of probing the attractor structure.

### 6.9.3 Return Map Results

The use of return maps to elucidate the dynamics of the vortex shedding phenomena was also investigated. However, the results were rather vague due to the presence of noise in the signal. To try and increase the effectiveness of the return map as a tool for determining period doubling, each alternate point on the mapping was denoted by a circle and a cross respectively. The results of the mapping for the first four downstream positions are given in figure 6-65.

At the 10mm downstream position, the distribution of crosses and circles is fairly even. This situation is again true for the 20mm position. In both figures, a slight tendency for the crosses to land above the  $45^\circ$  line and the circles to land below the  $45^\circ$  line may be observed on close examination. However, by 30mm downstream, there is a marked tendency for every second point to land either side of the  $45^\circ$  line. This would indicate that the flow is noisy and consists of a period doubled waveform. (A period doubled flow in the absence of noise would consist of two points, one either side of the  $45^\circ$  line, which the mapping would visit alternately.) The return map for the 40mm data shows a more random distribution of points once again as the attractor has broken down into a more complex form.

## 6.10 SUMMARY

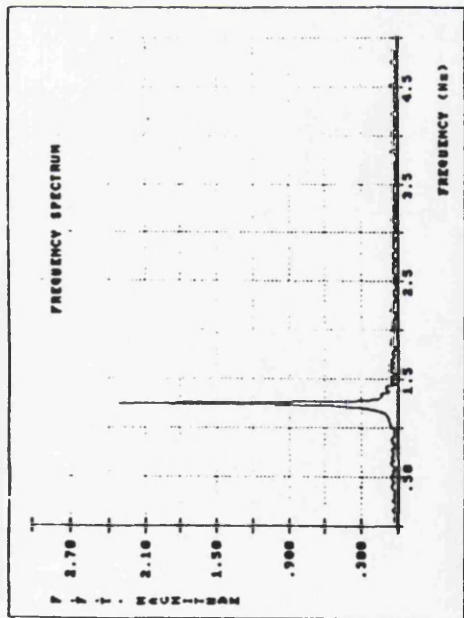
This chapter has presented the physical data resulting from the Laser Doppler Anemometry measurements. The information was presented in various forms to aid in the comprehension of the physical flow phenomena at the orifice plate for low

Reynolds number pulsed flows.

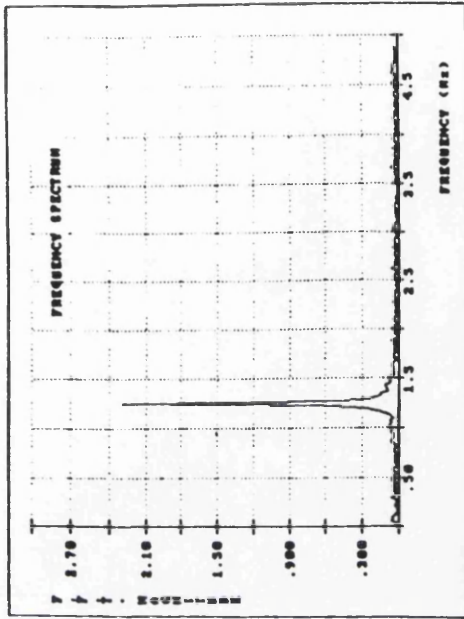
The tests were divided into six discrete, but inter-related tests, (test A to F), in which the effect of the Reynolds number, pulsation frequency (a function of the Reynolds number), pulsation amplitude were monitored at various positions downstream and across the flow. With a check on the repeatability of the experiment also undertaken, (test set G).

Analysis of the data as presented in this chapter has been undertaken and is presented in chapter 7.

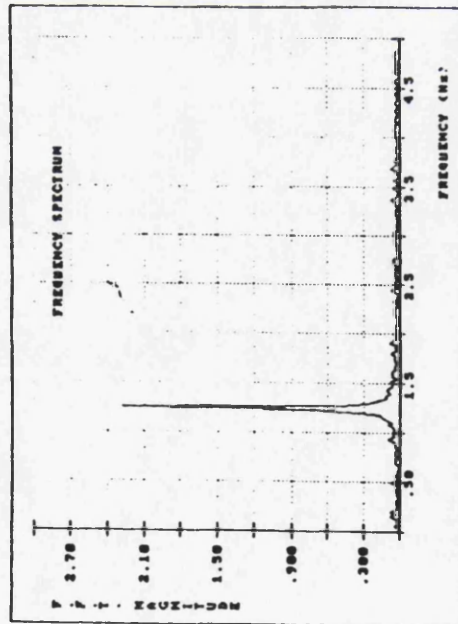
**CHAPTER 6**  
**FIGURES**



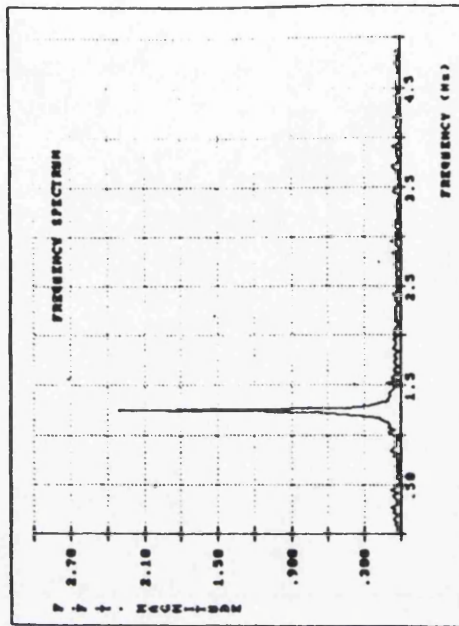
(a) 90mm Upstream



(b) 75mm Upstream

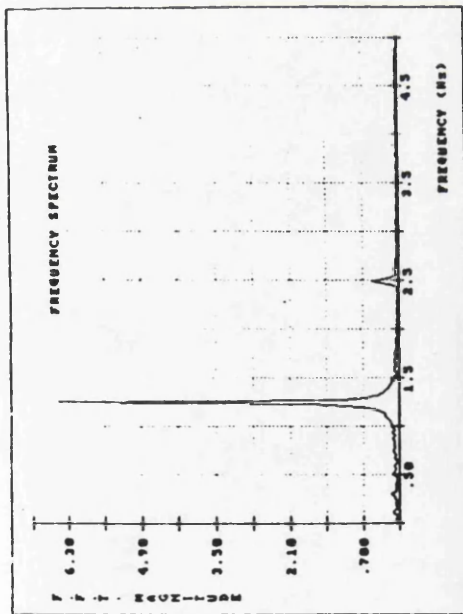


(c) 50mm Upstream

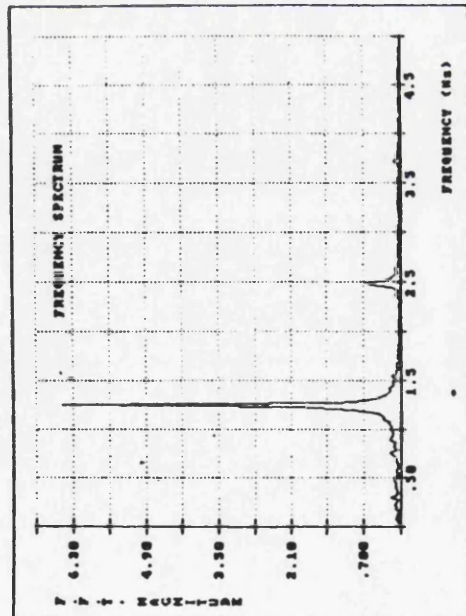


(d) 35mm Upstream

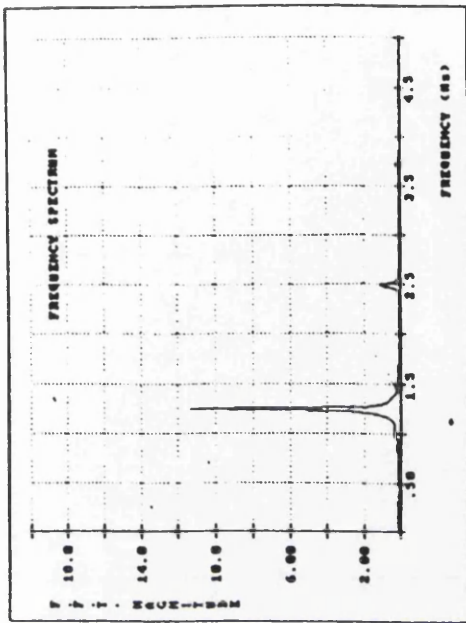
Figure 6-1: Frequency Spectra - 13.00mm Orifice - Rep - 128



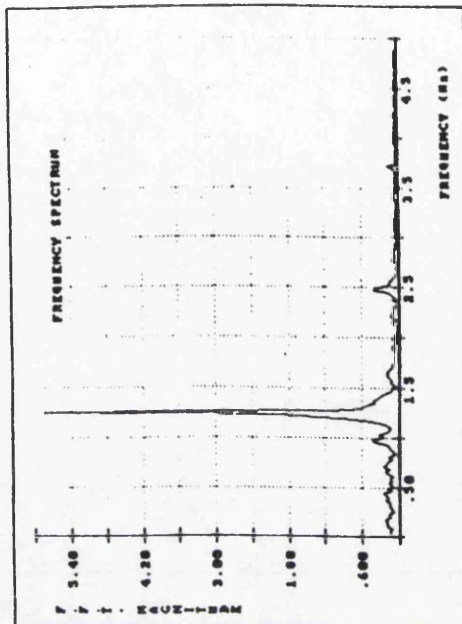
(e) 10mm Downstream



(g) 30mm Downstream

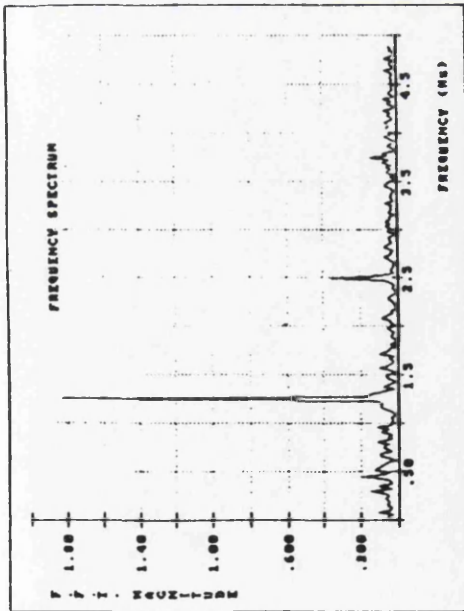


(f) 20mm Downstream

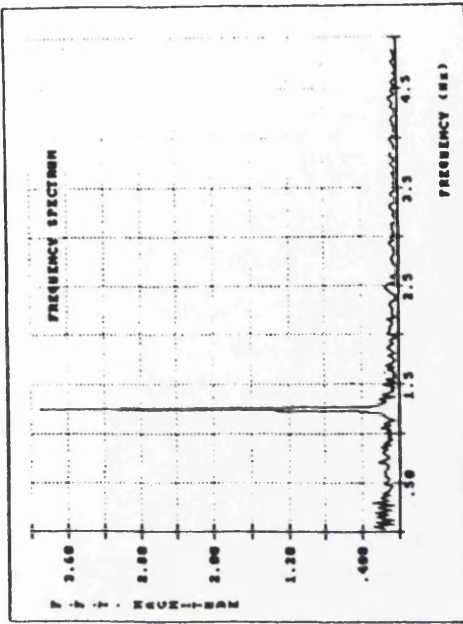


(h) 40mm Downstream

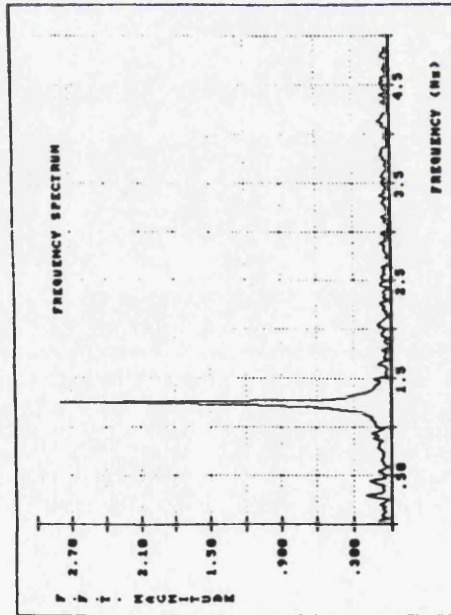
Figure 6-1: Frequency Spectra - 13.00mm Orifice - Rep - 128



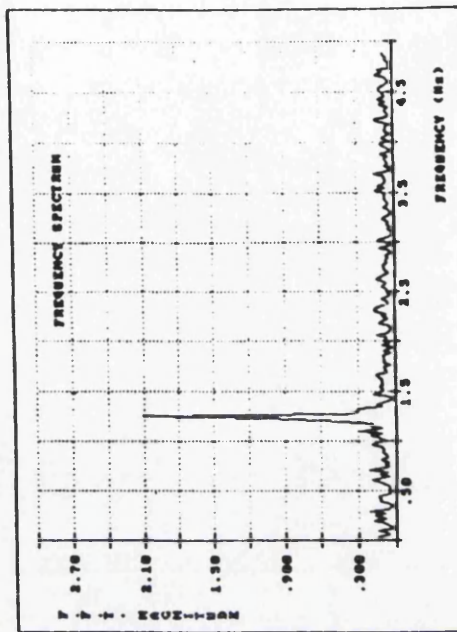
(i) 50mm Downstream



(j) 60mm Downstream

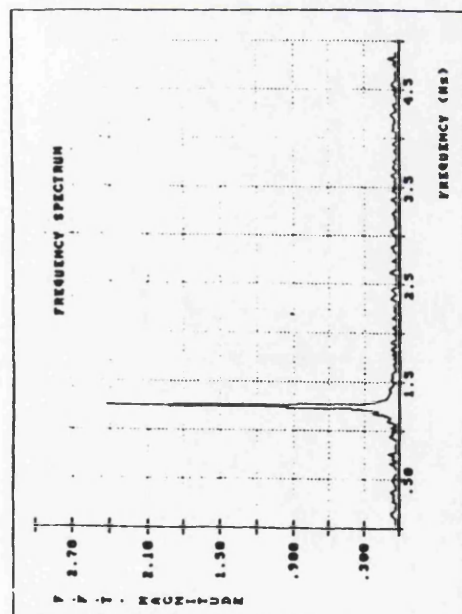


(k) 75mm Downstream

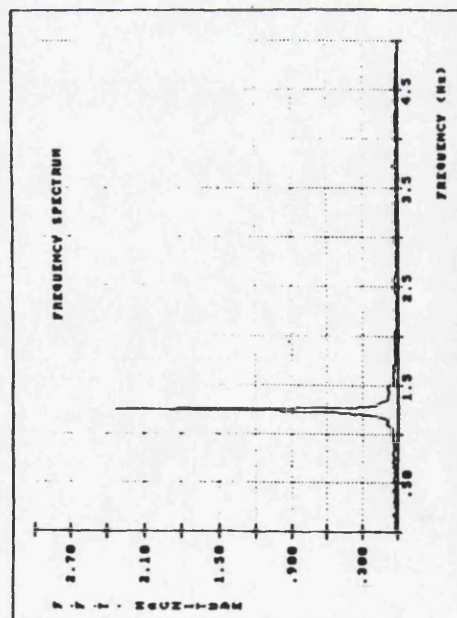


(l) 100mm Downstream

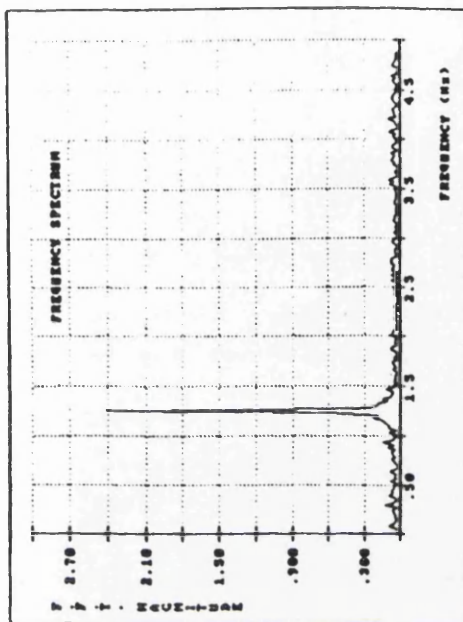
Figure 6-1: Frequency Spectra - 13.00mm Orifice - Rep - 128



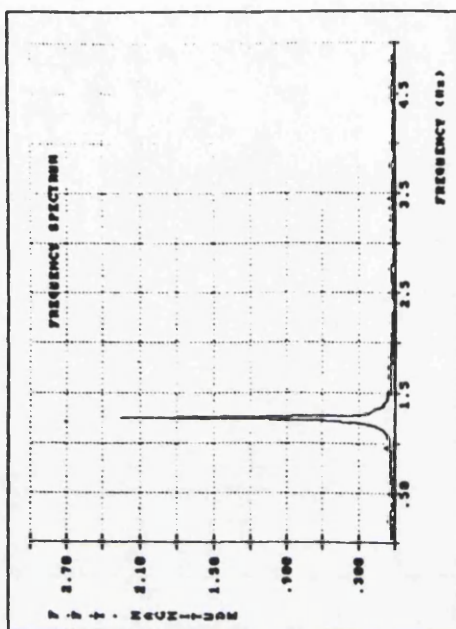
(m) 150mm Downstream



(o) 250mm Downstream

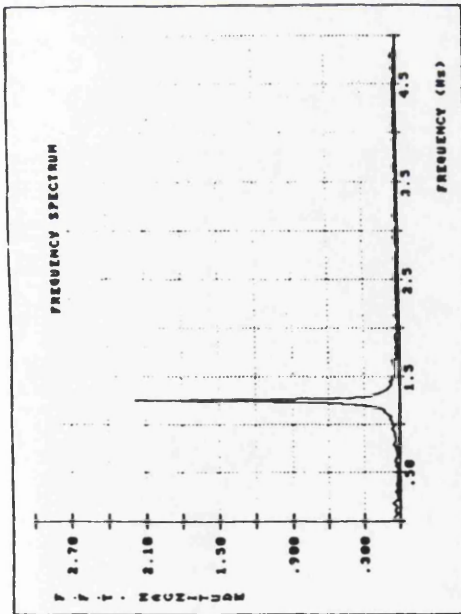


(n) 200mm Downstream



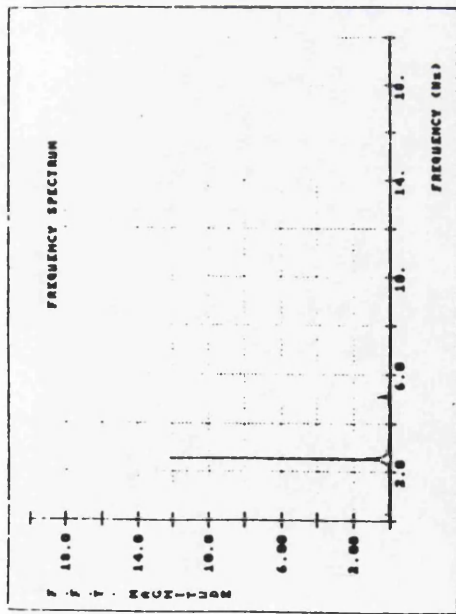
(p) 500mm Downstream

Figure 6-1: Frequency Spectra - 13.00mm Orifice - Rep - 128

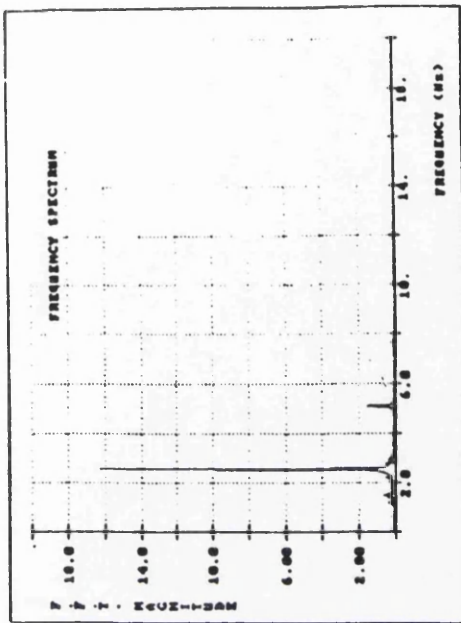


(q) 950mm Downstream

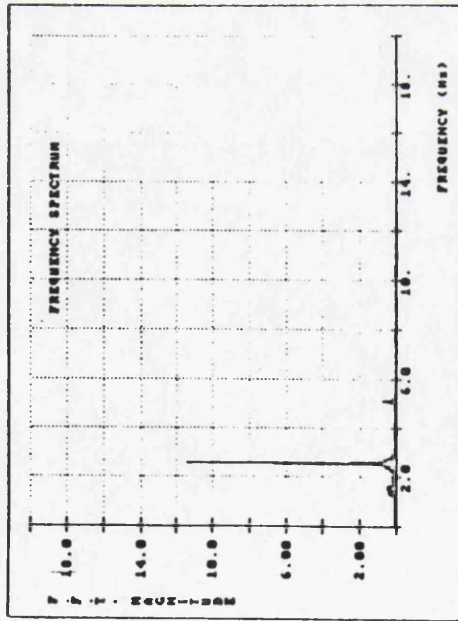
Figure 6-1: Frequency Spectra - 13.00mm Orifice - Rep - 128



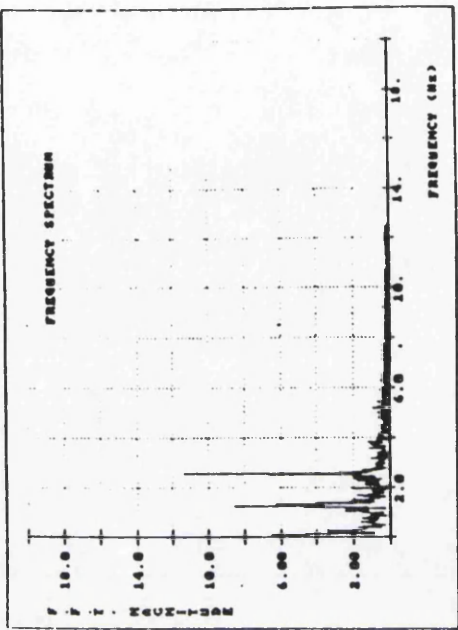
(a) 10mm Downstream



(b) 20mm Downstream

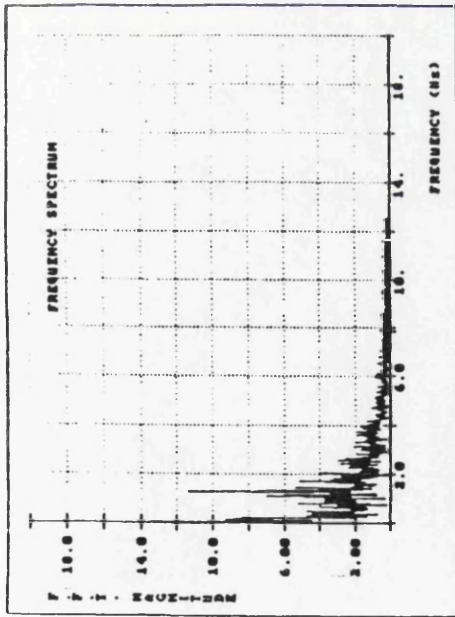


(c) 30mm Downstream

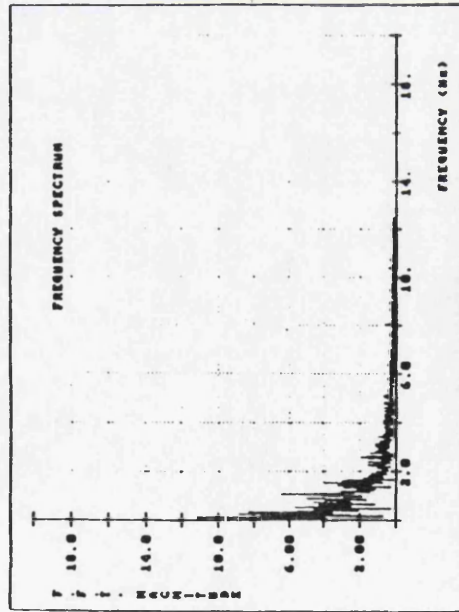


(d) 40mm Downstream

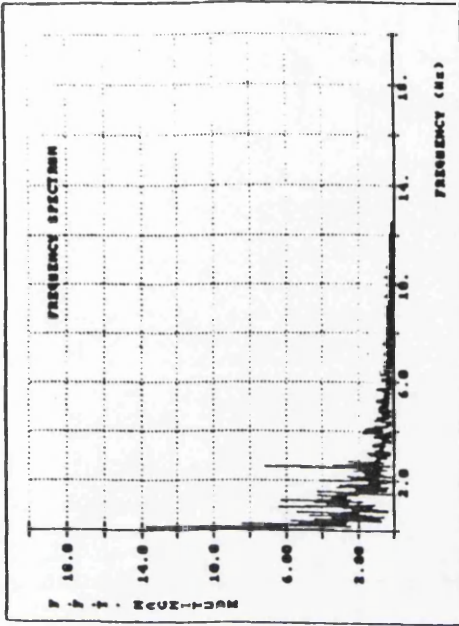
Figure 6-2: Frequency Spectra - 13.00mm Orifice - Rep - 256



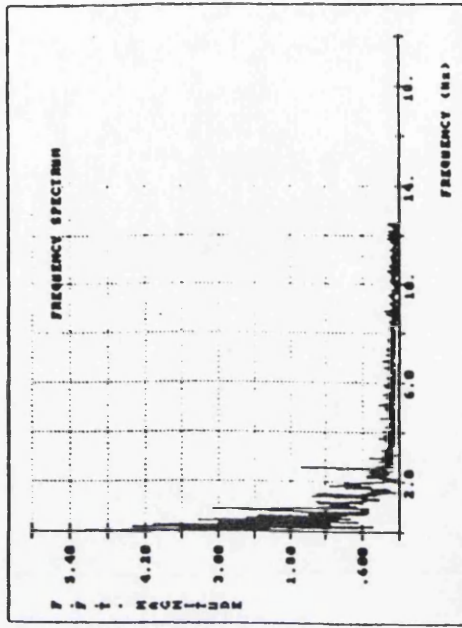
(e) 50mm Downstream



(g) 75mm Downstream

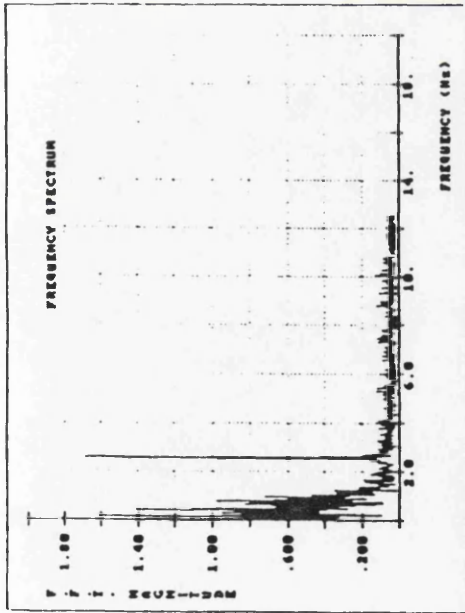


(f) 60mm Downstream

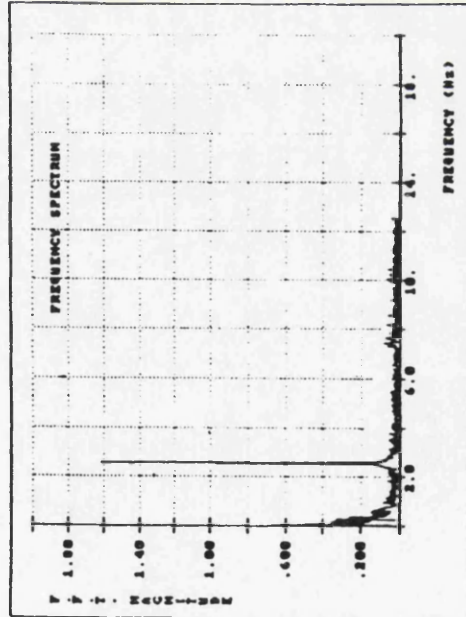


(h) 100mm Downstream

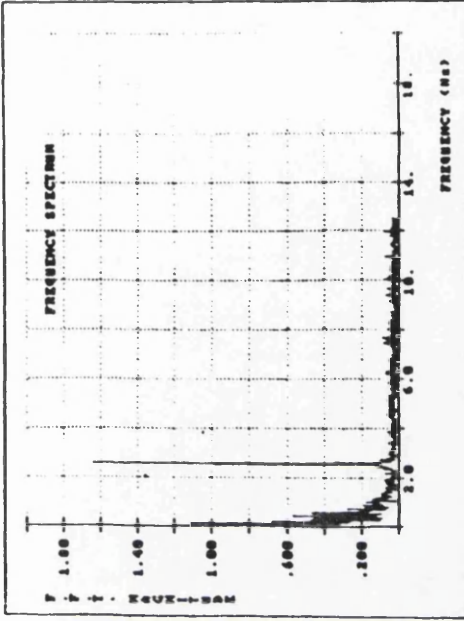
Figure 6-2: Frequency Spectra - 13.00mm Orifice - Rep - 256



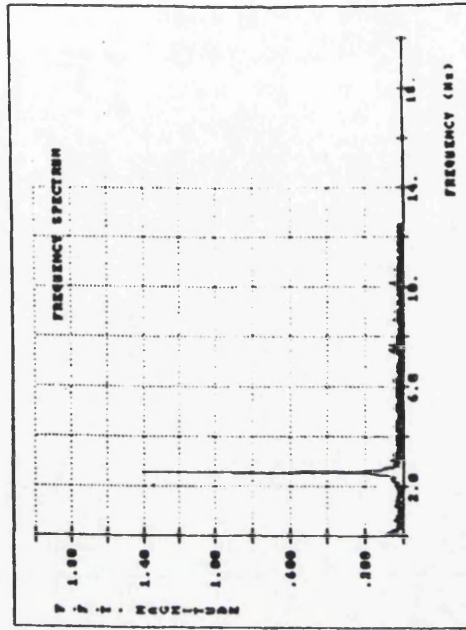
(i) 150mm Downstream



(k) 250mm Downstream

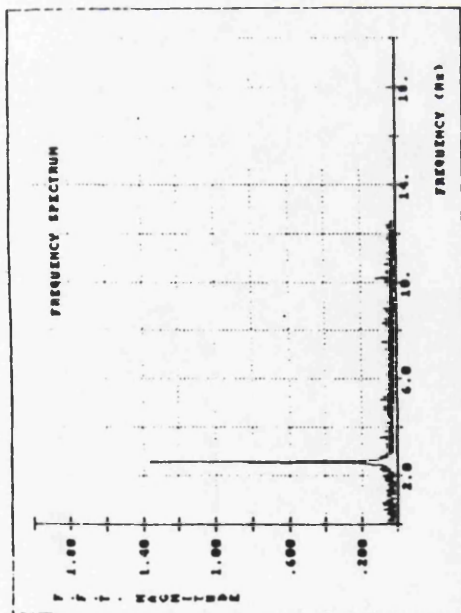


(j) 200mm Downstream



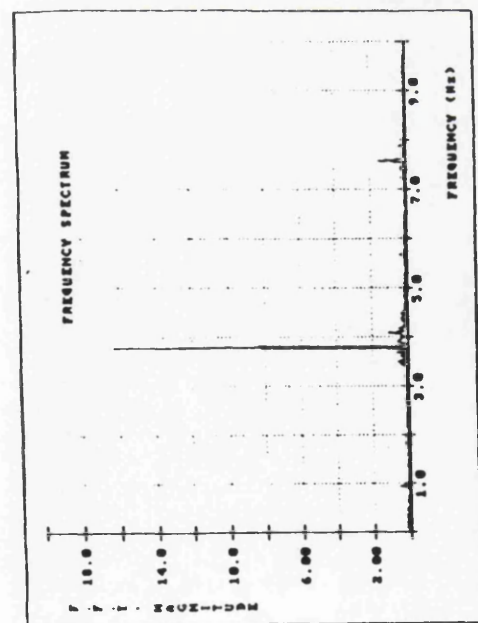
(l) 500mm Downstream

Figure 6-2: Frequency Spectra - 13.00mm Orifice - Rep - 256

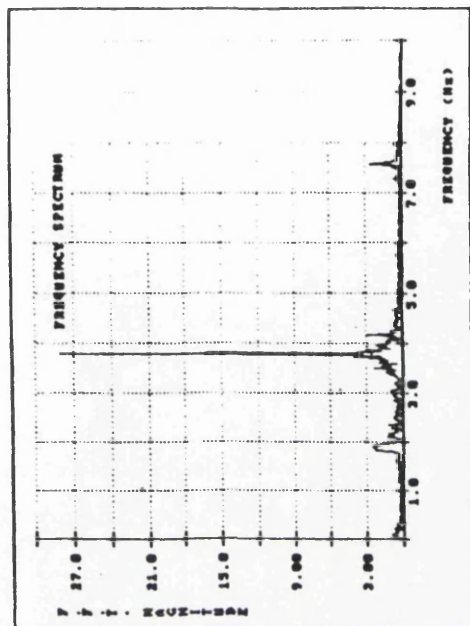


(m) 950mm Downstream

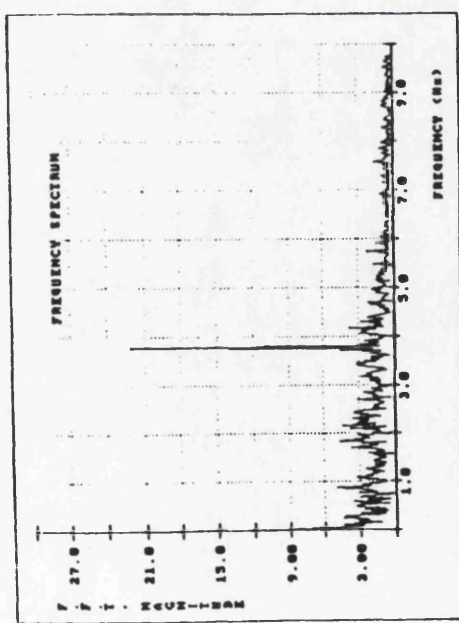
Figure 6-2: Frequency Spectra - 13.00mm Orifice - Rep - 256



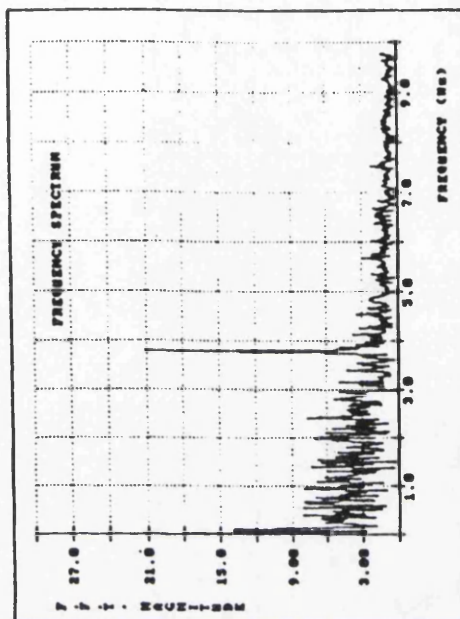
(a) 10mm Downstream



(b) 20mm Downstream

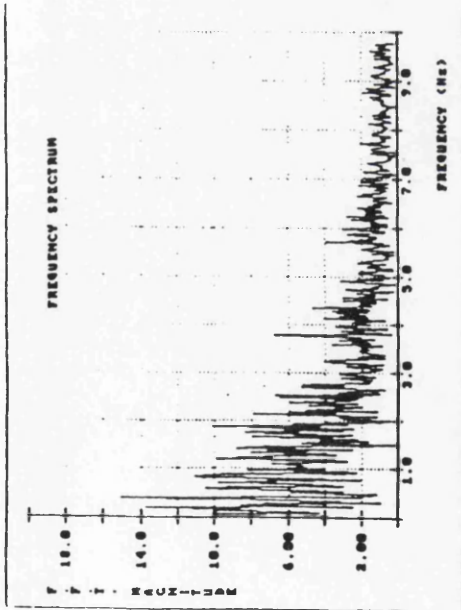


(c) 30mm Downstream

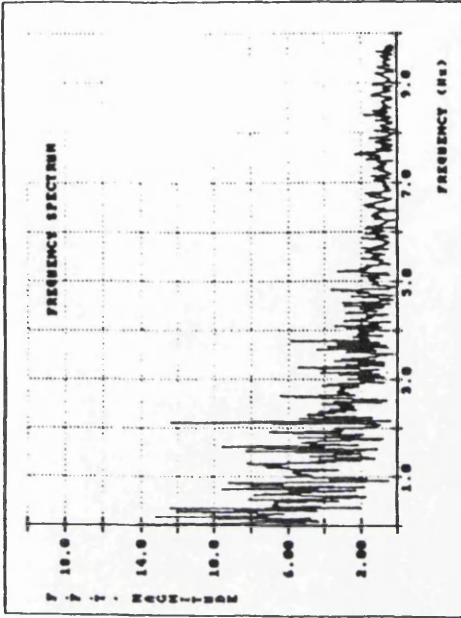


(d) 40mm Downstream

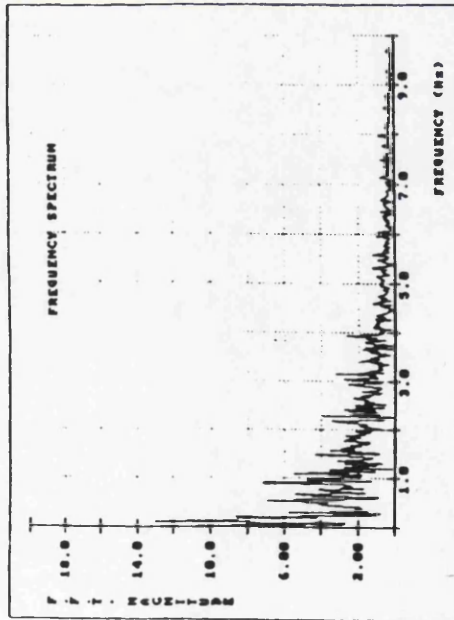
Figure 6-3: Frequency Spectra - 13.00mm Orifice - Rep - 384



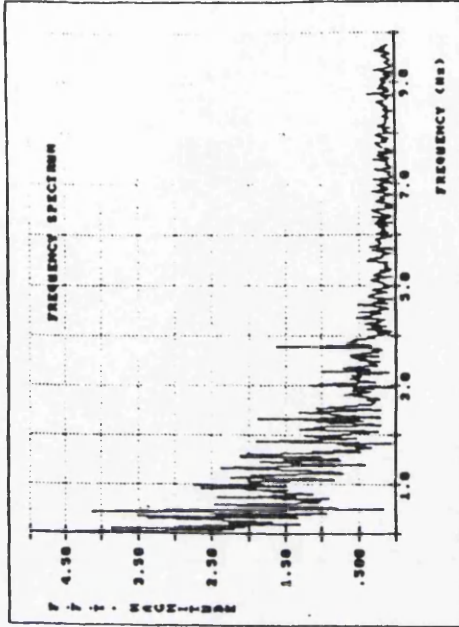
(e) 50mm Downstream



(f) 60mm Downstream

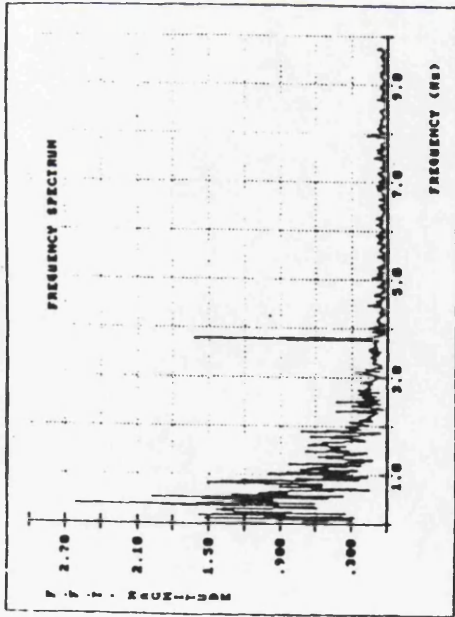


(g) 75mm Downstream

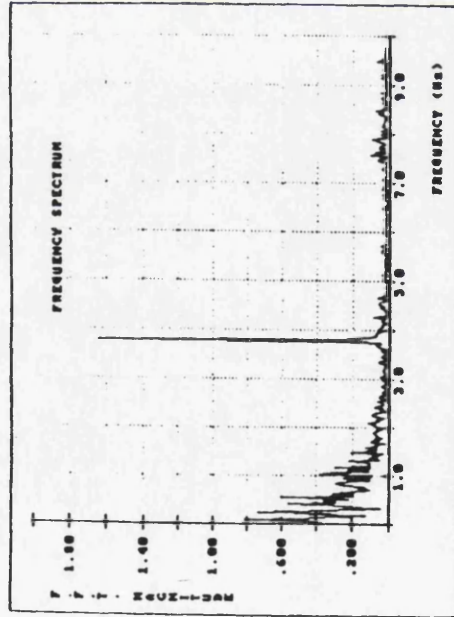


(h) 100mm Downstream

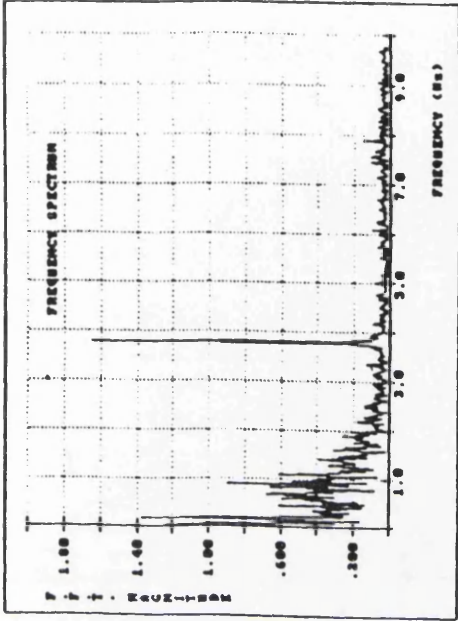
Figure 6-3: Frequency Spectra - 13.00mm Orifice - Rep - 384



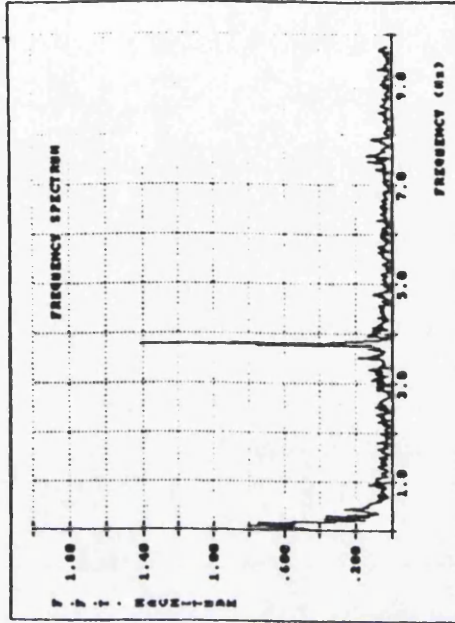
(i) 150mm Downstream



(k) 250mm Downstream

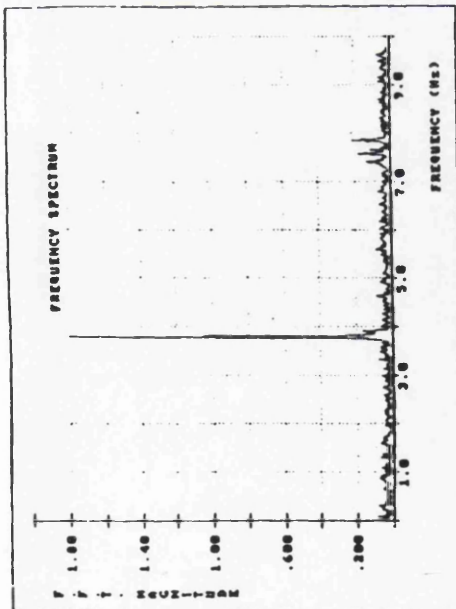


(j) 200mm Downstream



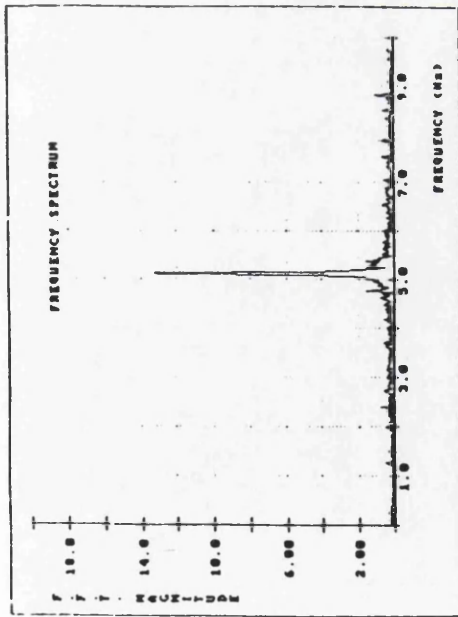
(l) 500mm Downstream

Figure 6-3: Frequency Spectra - 13.00mm Orifice - Rep - 384

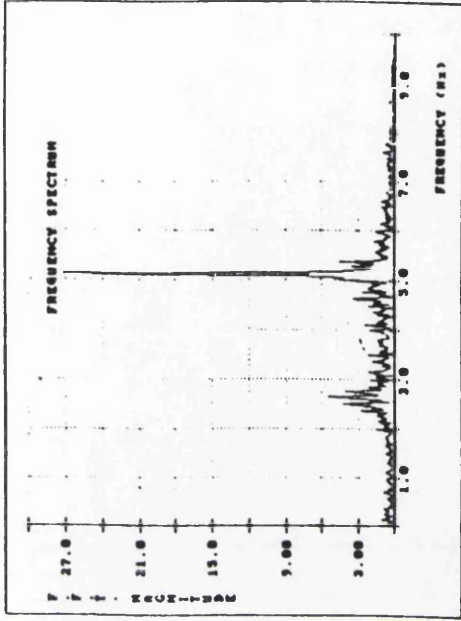


(m) 950mm Downstream

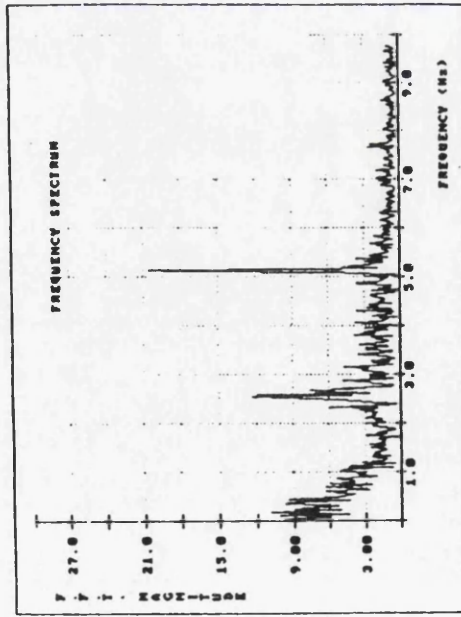
Figure 6-3: Frequency Spectra - 13.00mm Orifice - Rep. - 384



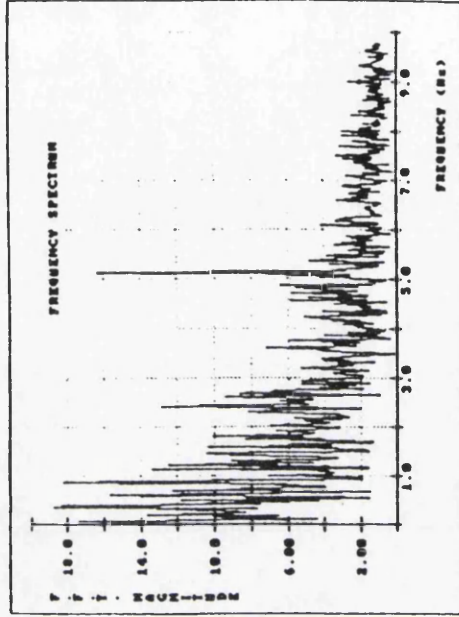
(a) 10mm Downstream



(b) 20mm Downstream

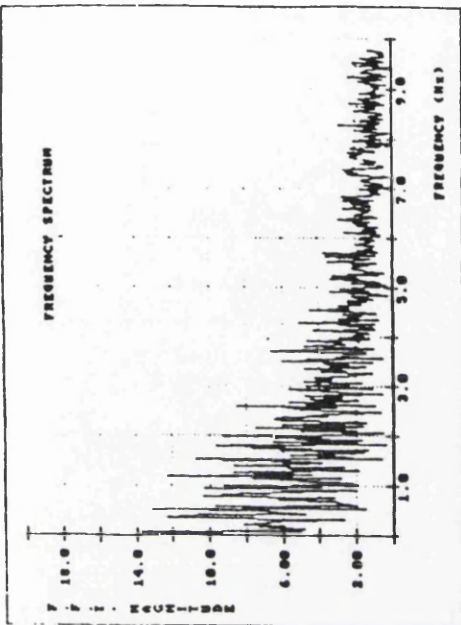


(c) 30mm Downstream

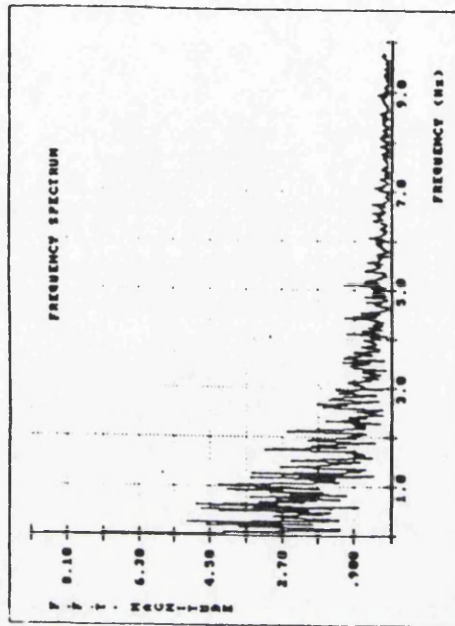


(d) 40mm Downstream

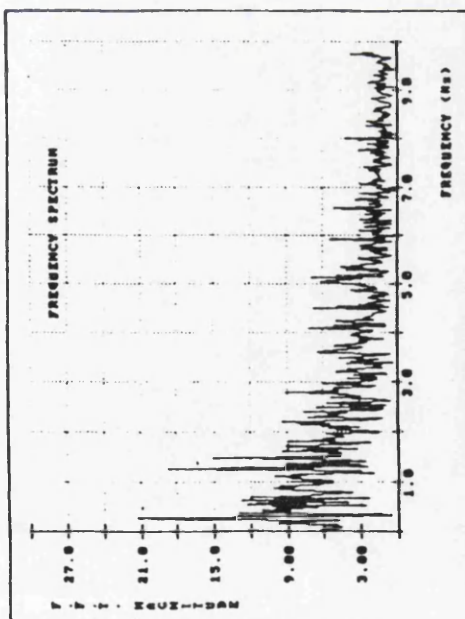
Figure 6-4: Frequency Spectra - 13.00mm Orifice - Rep - 256



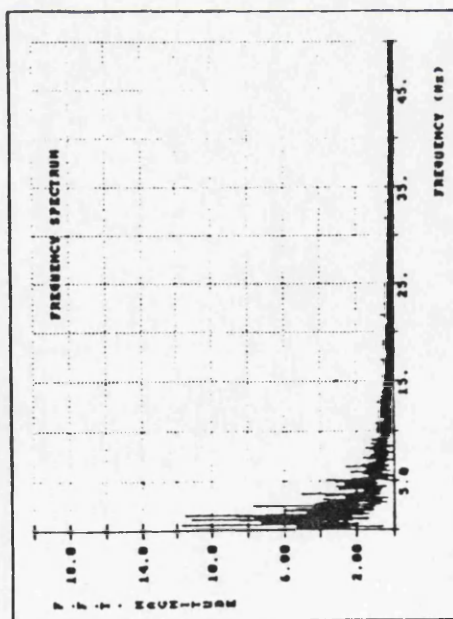
(f) 60mm Downstream



(h) 100mm Downstream

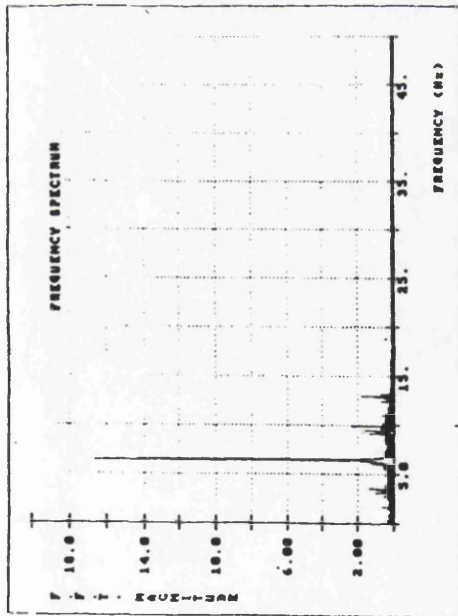


(e) 50mm Downstream

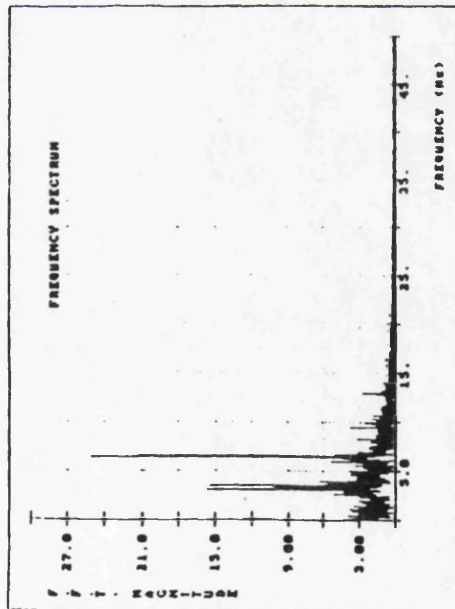


(g) 75mm Downstream

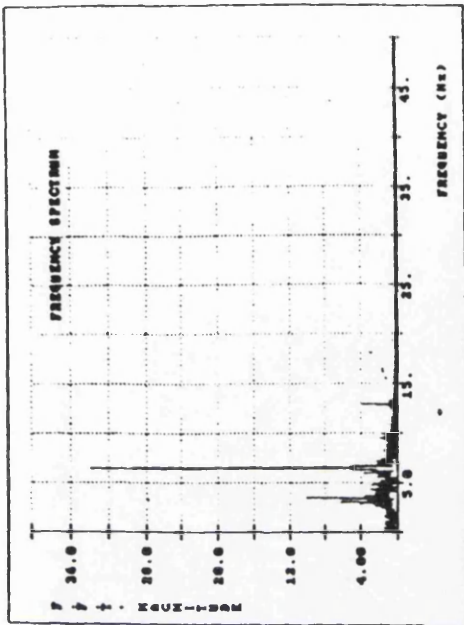
Figure 6-4: Frequency Spectra - 13.00mm Orifice - Rep = 256



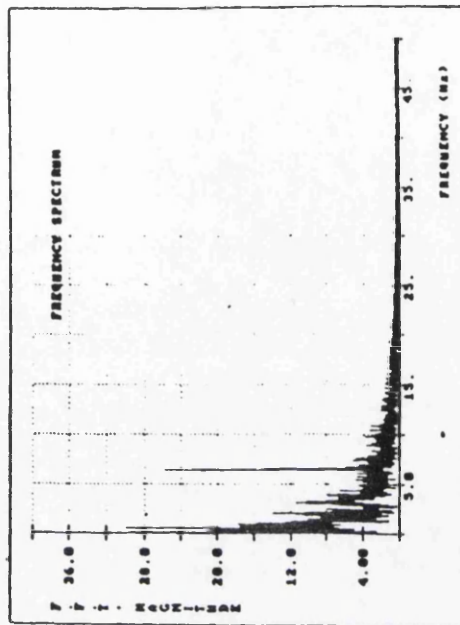
(a) 10mm Downstream



(c) 30mm Downstream

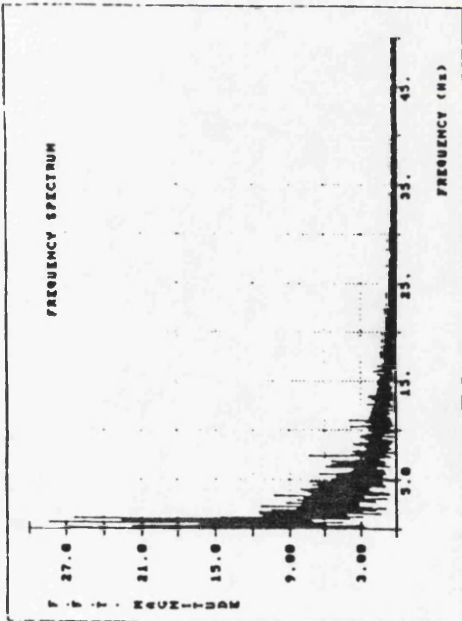


(b) 20mm Downstream

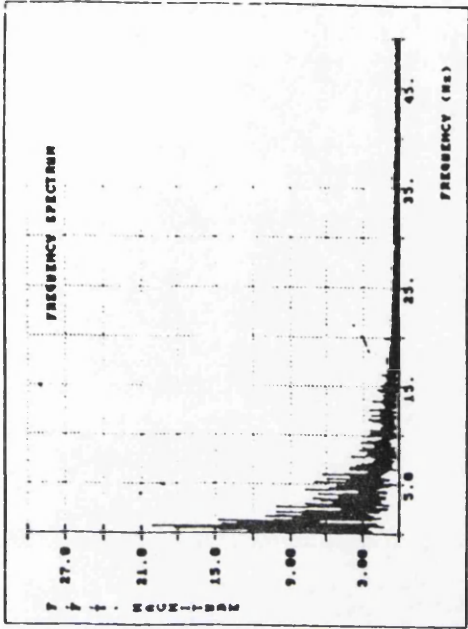


(d) 40mm Downstream

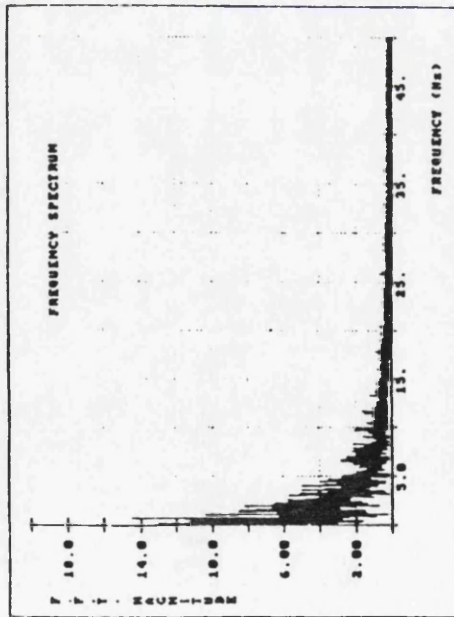
Figure 6-5: Frequency Spectra - 13.00mm Orifice - Rep - 256



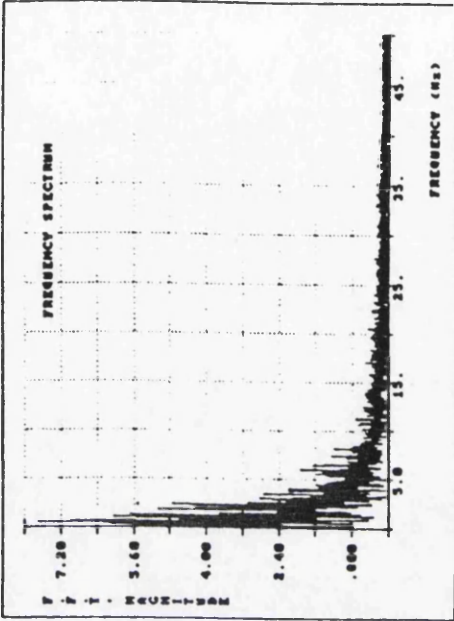
(e) 50mm Downstream



(f) 60mm Downstream



(g) 75mm Downstream



(h) 100mm Downstream

Figure 6-5: Frequency Spectra - 13.00mm Orifice -  $Re_D = 256$

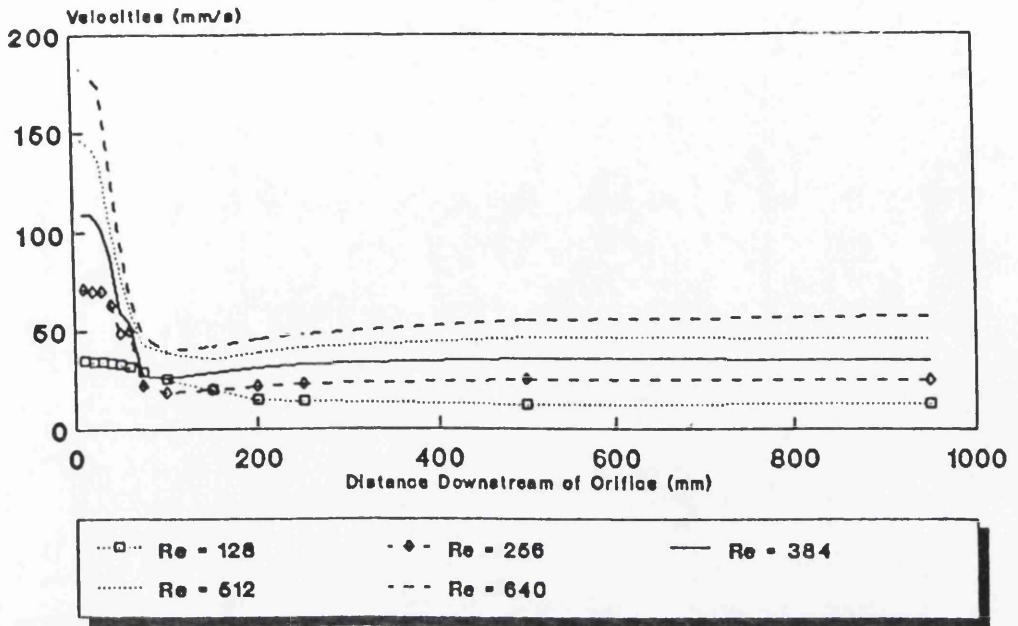


Figure 6-6a: Centreline Velocities - 13.00mm Orifice  
Various Reynolds Numbers

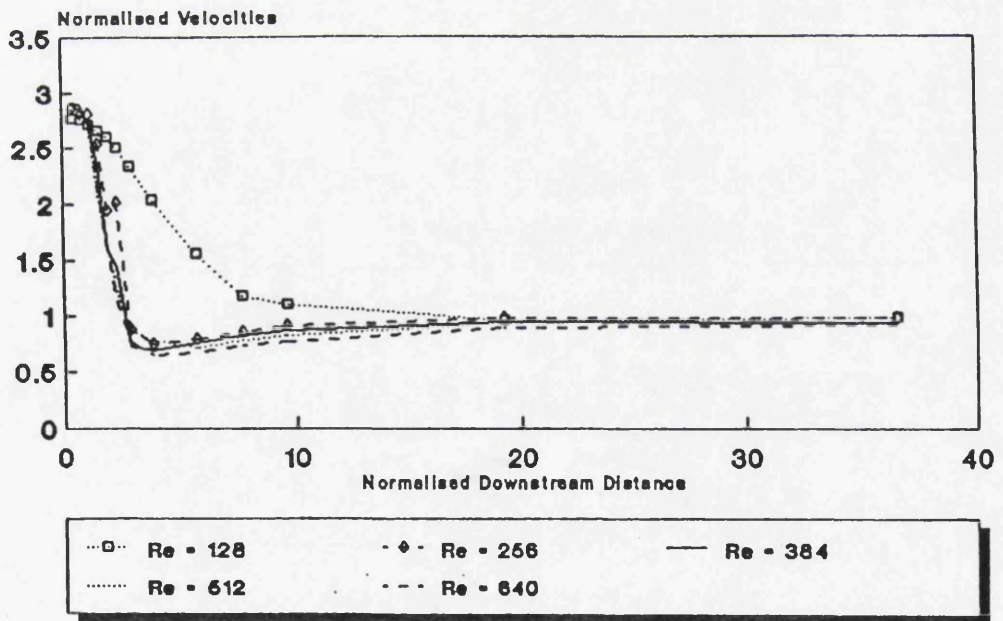


Figure 6-6b: Normalised Centreline Velocities - 13.00mm Orifice  
Various Reynolds Numbers

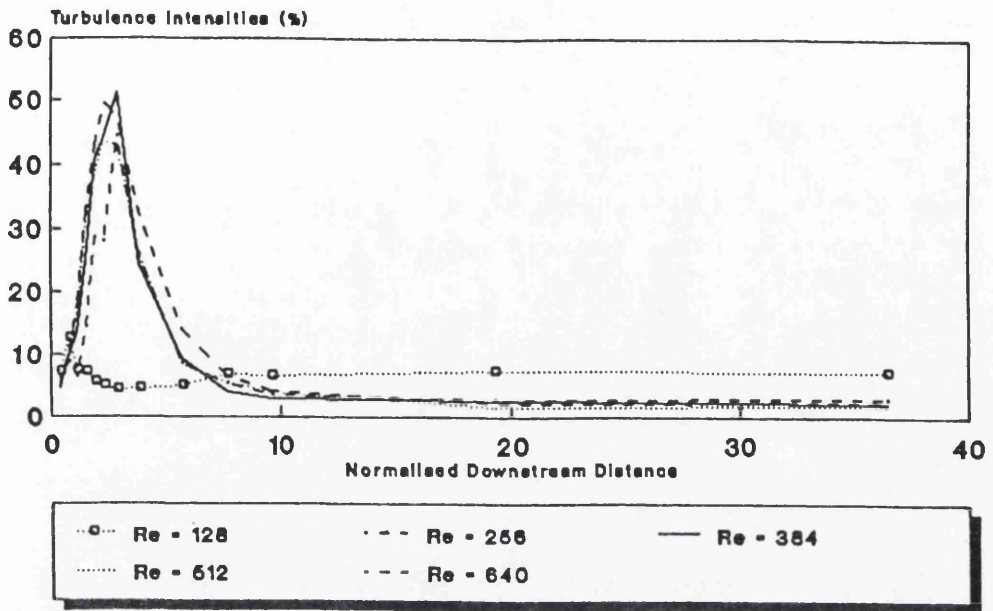


Figure 6-7a: Point-Turbulence Intensities- 13.00mm Orifice  
Various Reynolds Numbers

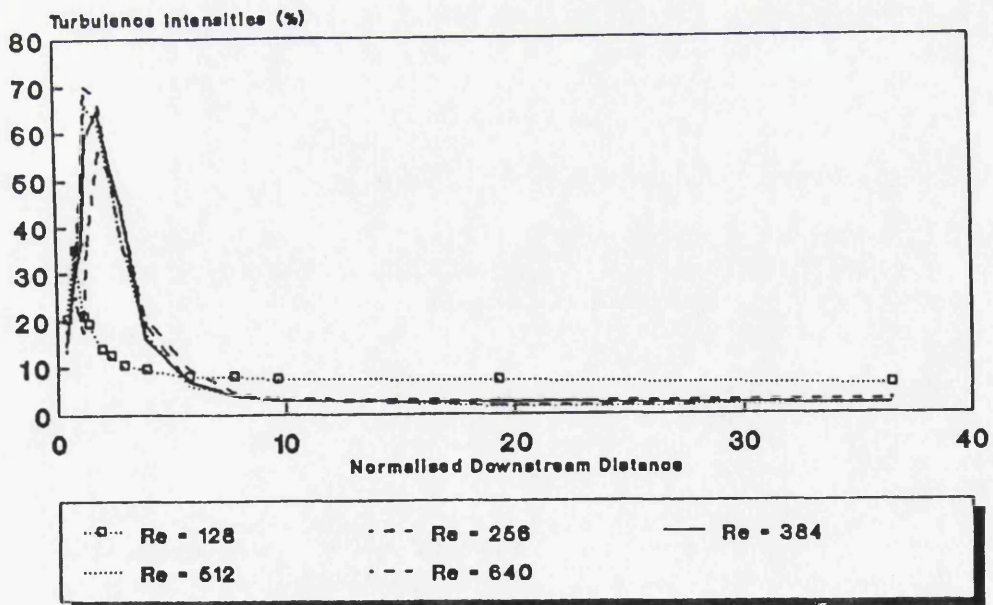


Figure 6-7b: H.G.-Turbulence Intensities - 13.00mm Orifice  
Various Reynolds Numbers

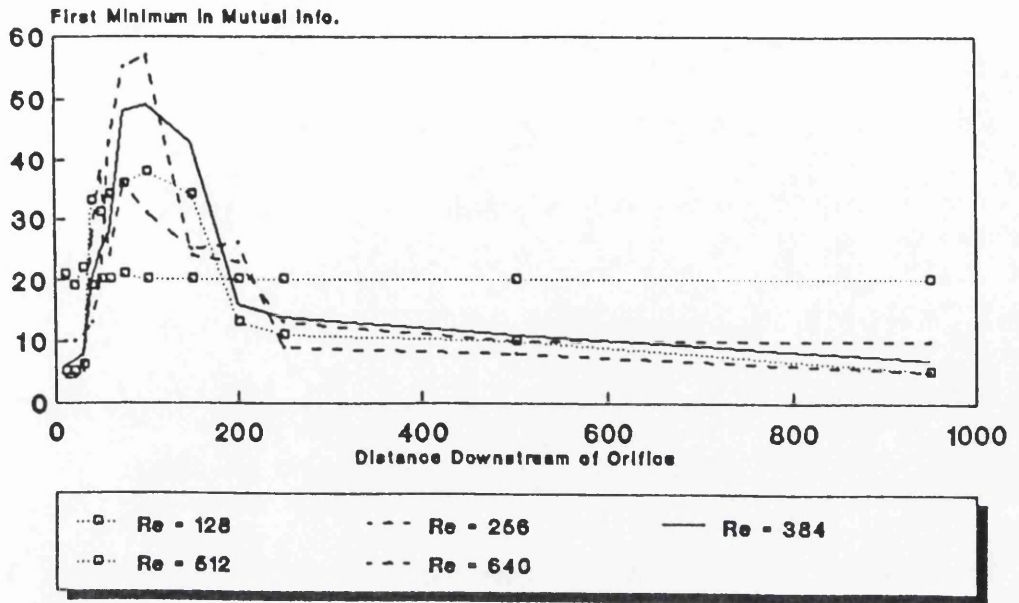


Figure 6-8a: Minimum Mutual Information - 13.00mm Orifice  
Various Reynolds Numbers

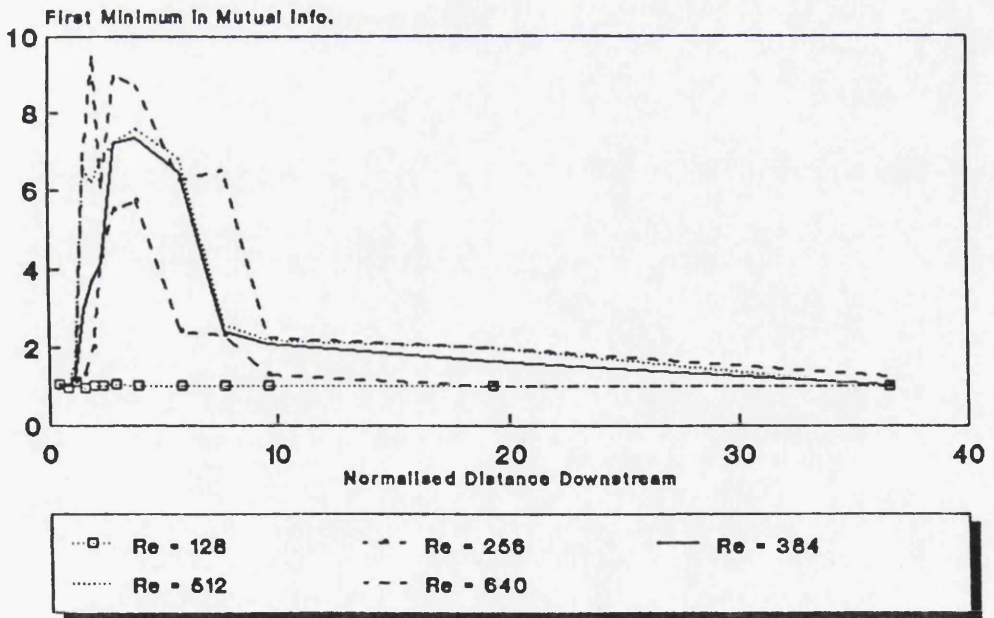
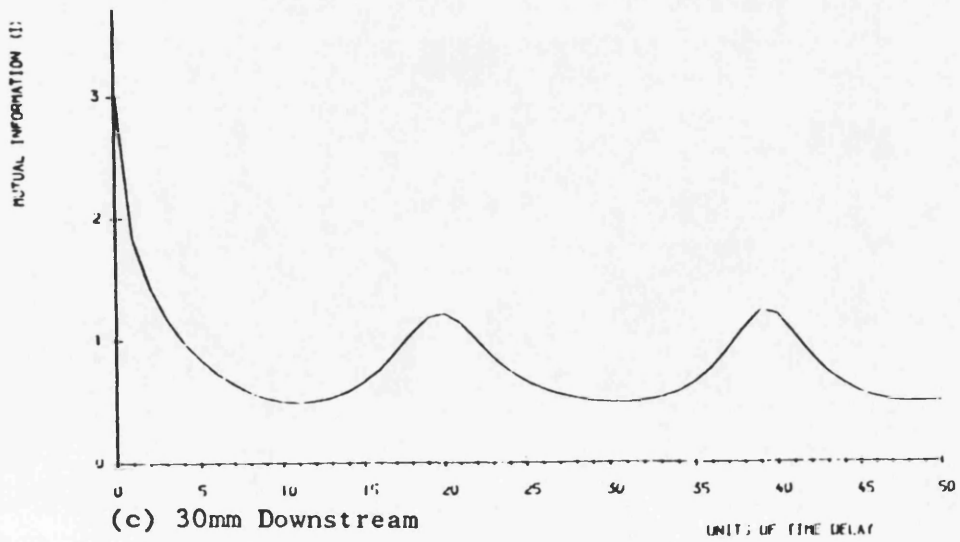
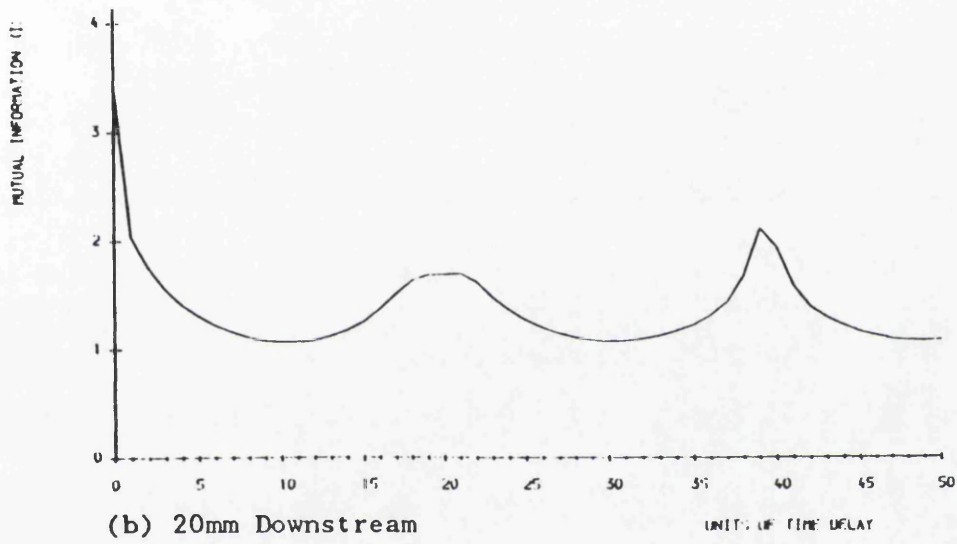
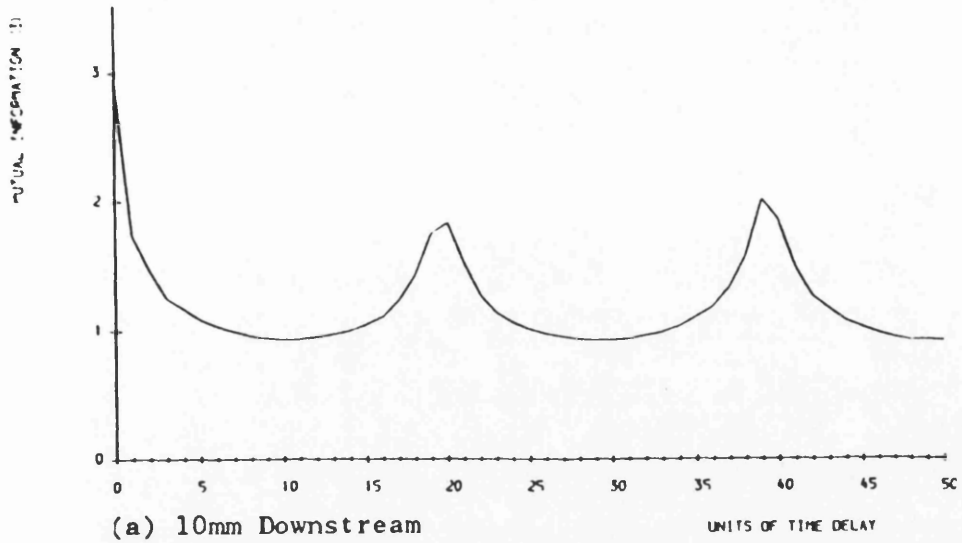


Figure 6-8b: Normalised Minimum Mutual Info. - 13.00mm Orifice  
Various Reynolds Numbers



**Figure 6-9: Individual Minimum Mutual Information Plots**  
13.00mm Orifice -  $Re_p = 256$

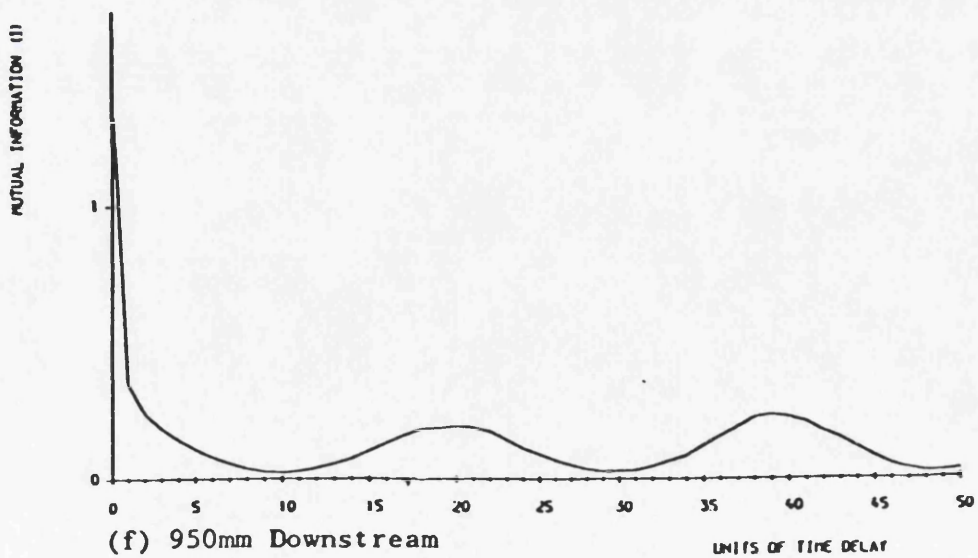
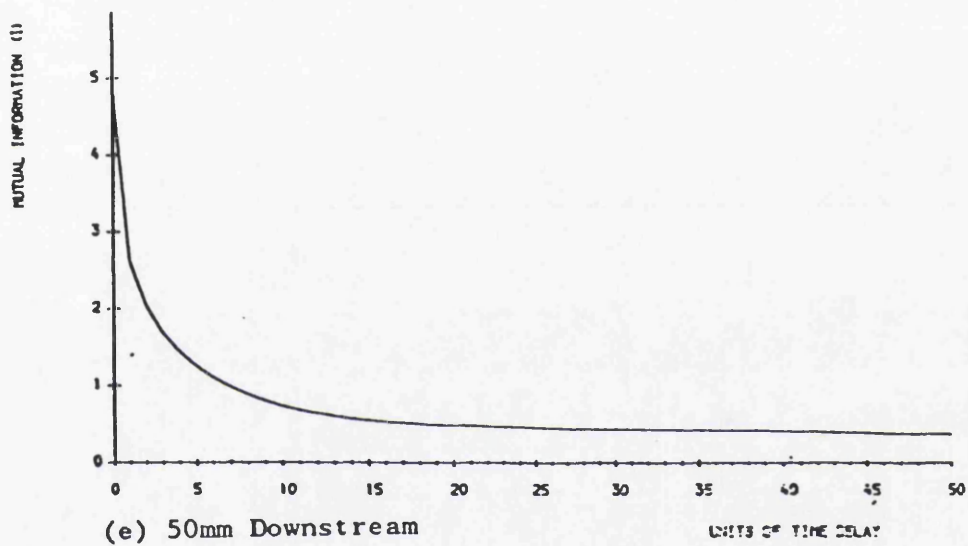
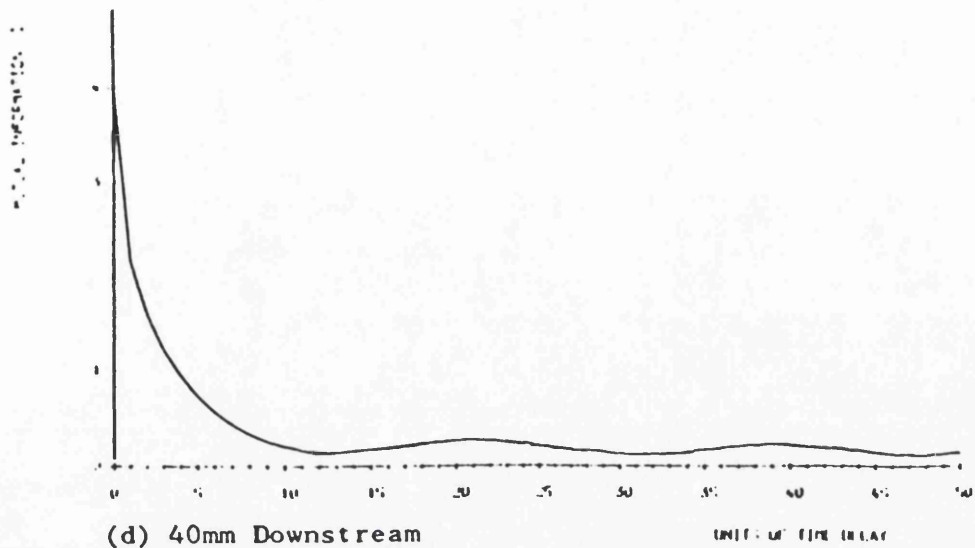
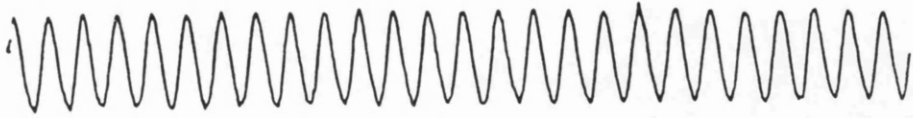
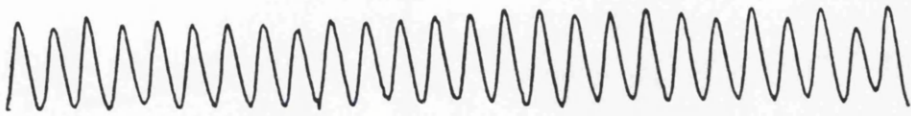


Figure 6-9: Individual Minimum Mutual Information Plots  
13.00mm Orifice -  $Re_p = 256$



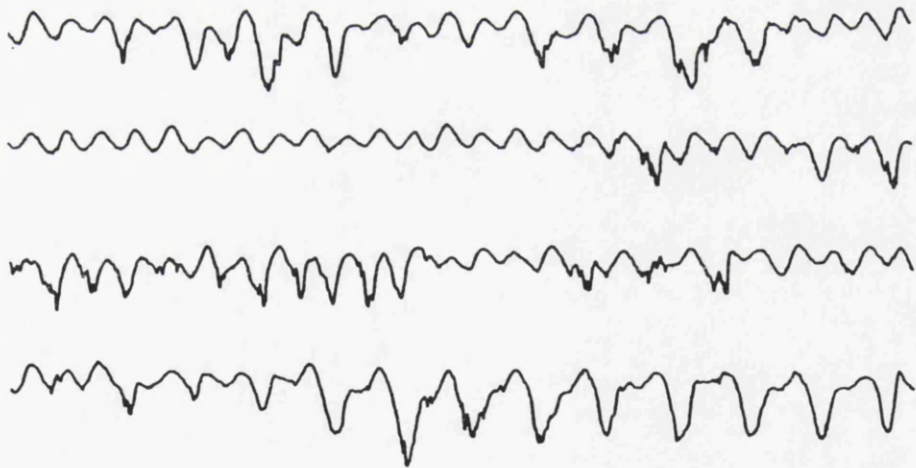
(a) 10mm Downstream



(b) 20mm Downstream



(c) 30mm Downstream

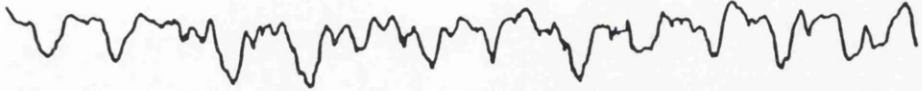


(d) 40mm Downstream

Figure 6-10: Time Series Plots - 13.00mm Orifice -  $Re_p = 256$



(e) 50mm Downstream



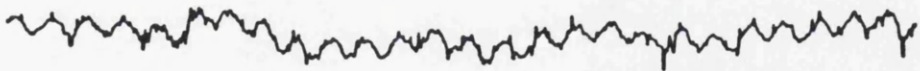
(f) 60mm Downstream



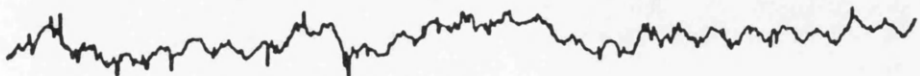
(g) 75mm Downstream



(h) 100mm Downstream



(i) 150mm Downstream



(j) 200mm Downstream

Figure 6-10: Time Series Plots - 13.00mm Orifice -  $Re_p = 256$

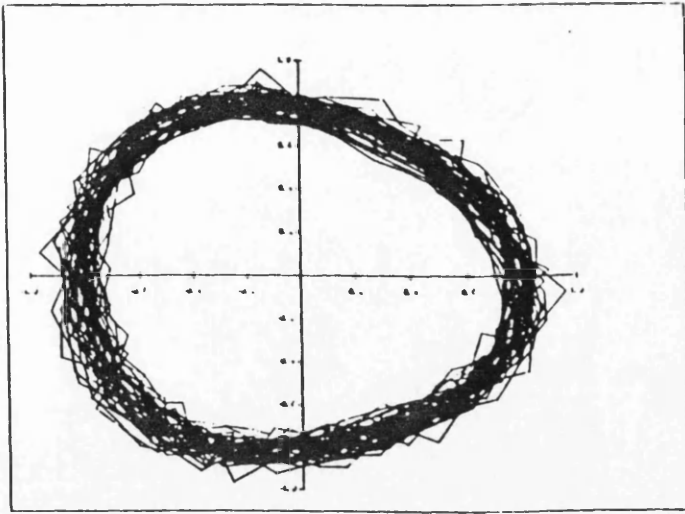


(k) 250mm Downstream

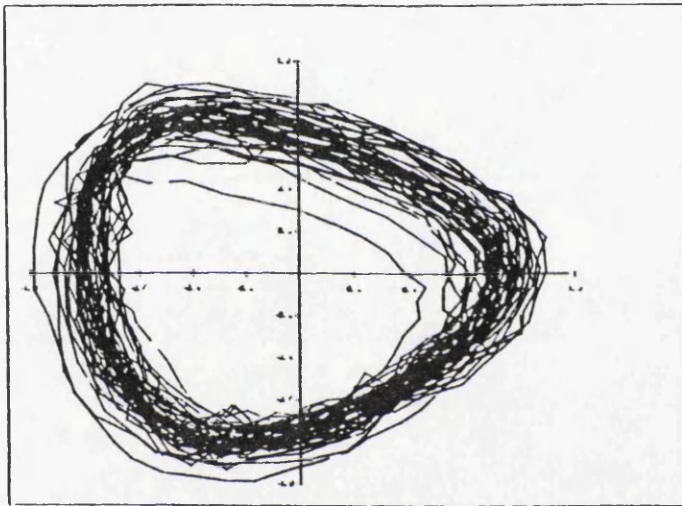


(l) 950mm Downstream

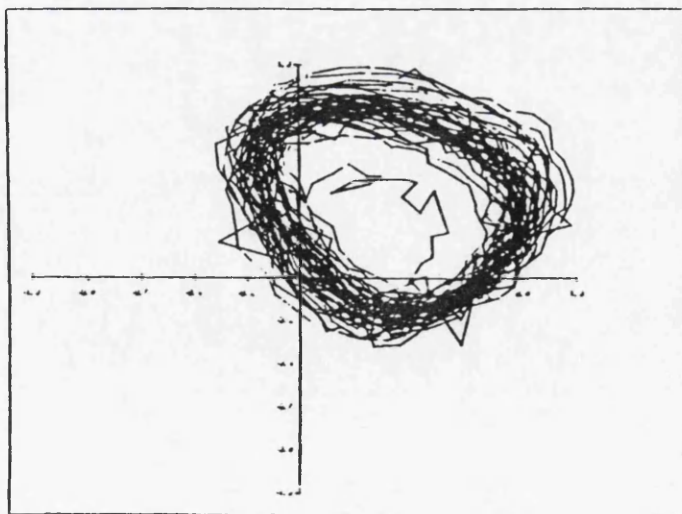
Figure 6-10: Time Series Plots - 13.00mm Orifice - Re<sub>p</sub> - 256



(a) 10mm Downstream

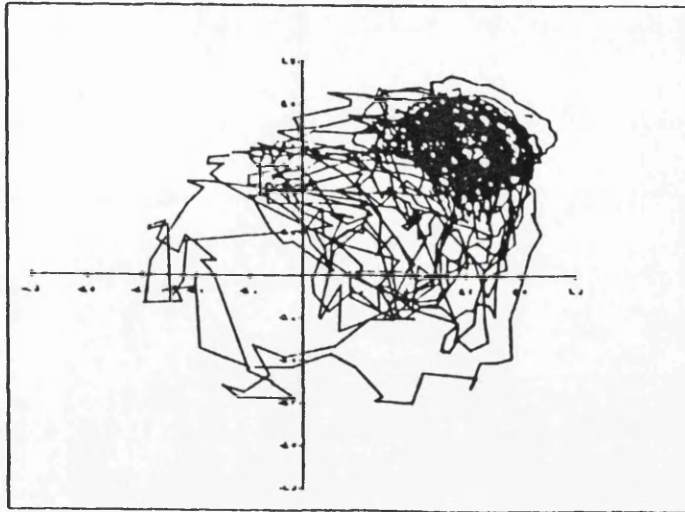


(b) 20mm Downstream

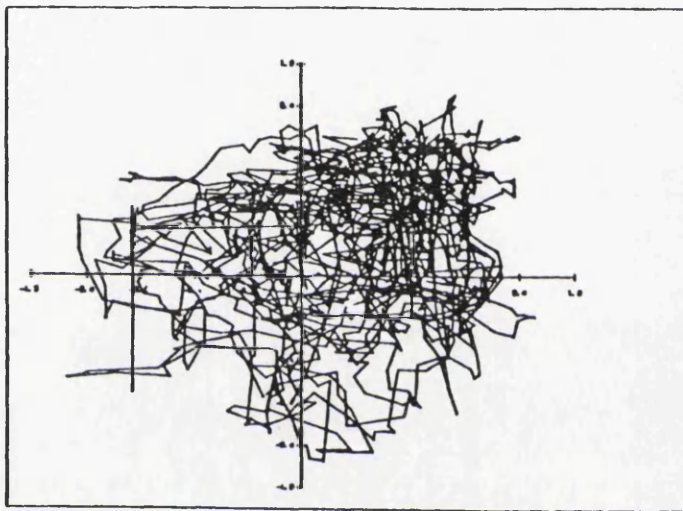


(c) 30mm Downstream

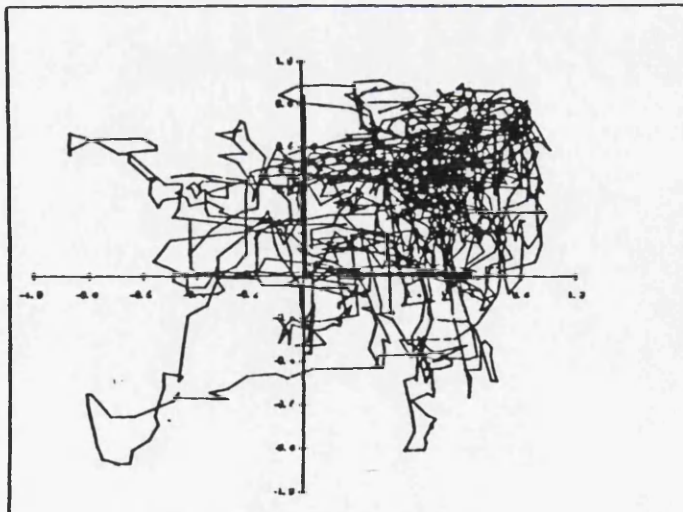
Figure 6-11: Attractor Plots - 13mm Orifice -  $Re_p = 256$



(d) 40mm Downstream

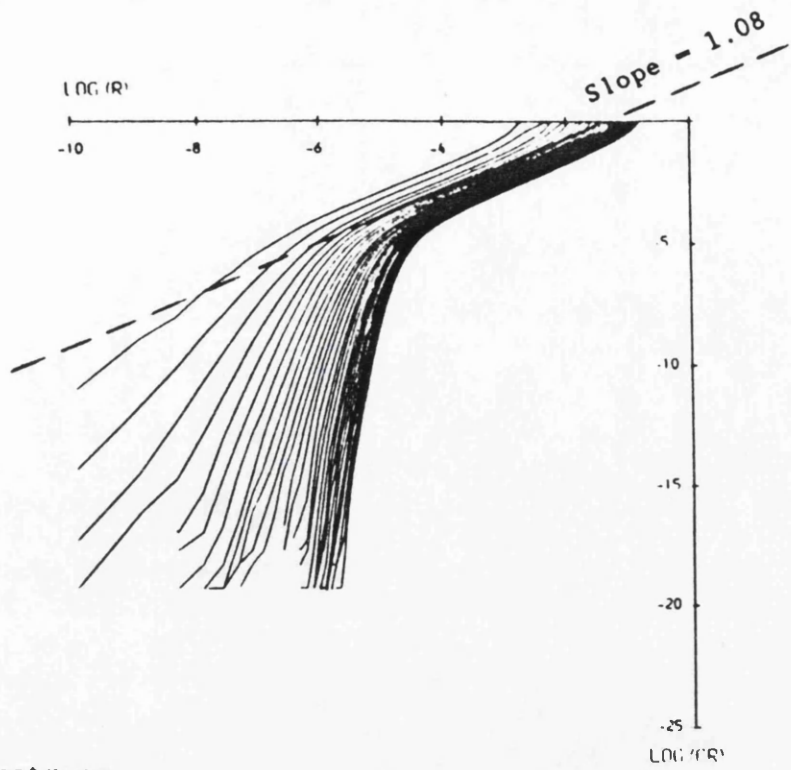


(e) 50mm Downstream

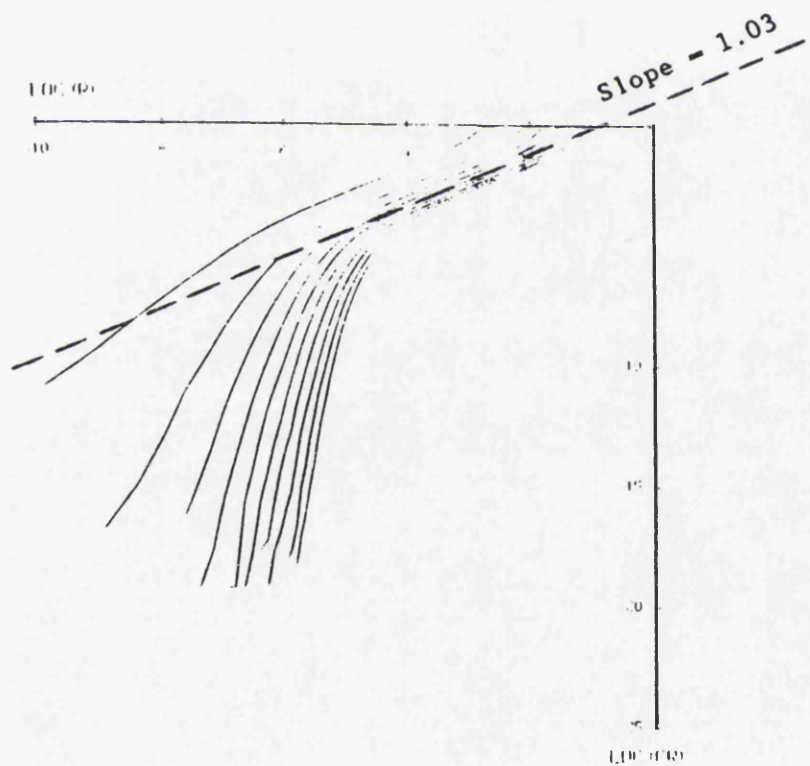


(f) 60mm Downstream

Figure 6-11: Attractor Plots - 13mm Orifice -  $Re_p = 256$

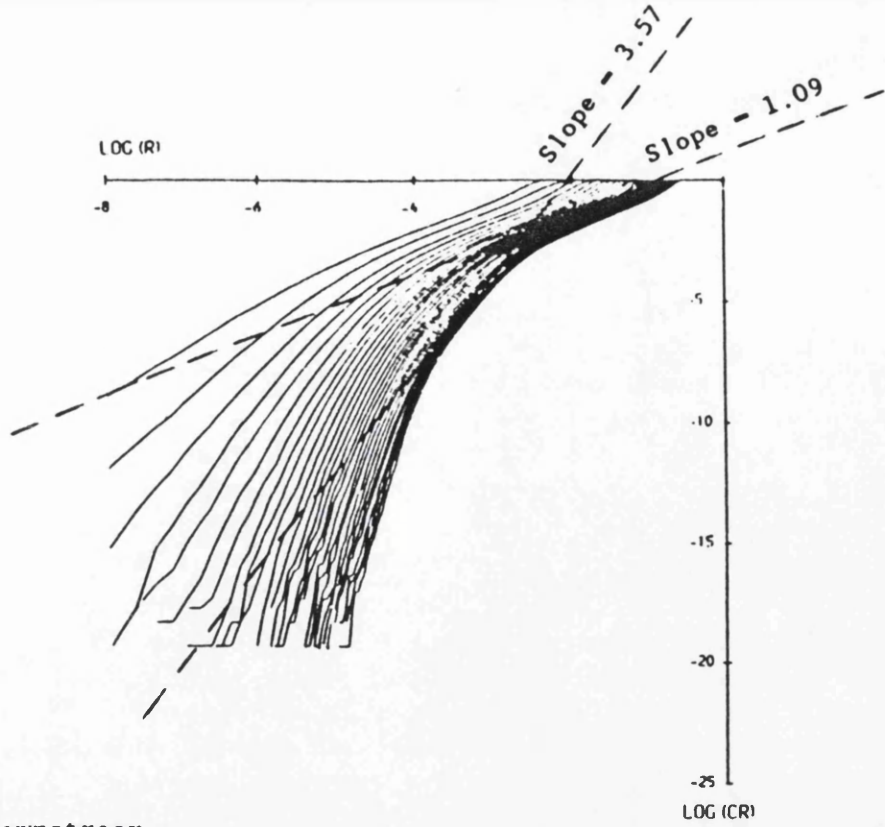


(a) 10mm Downstream

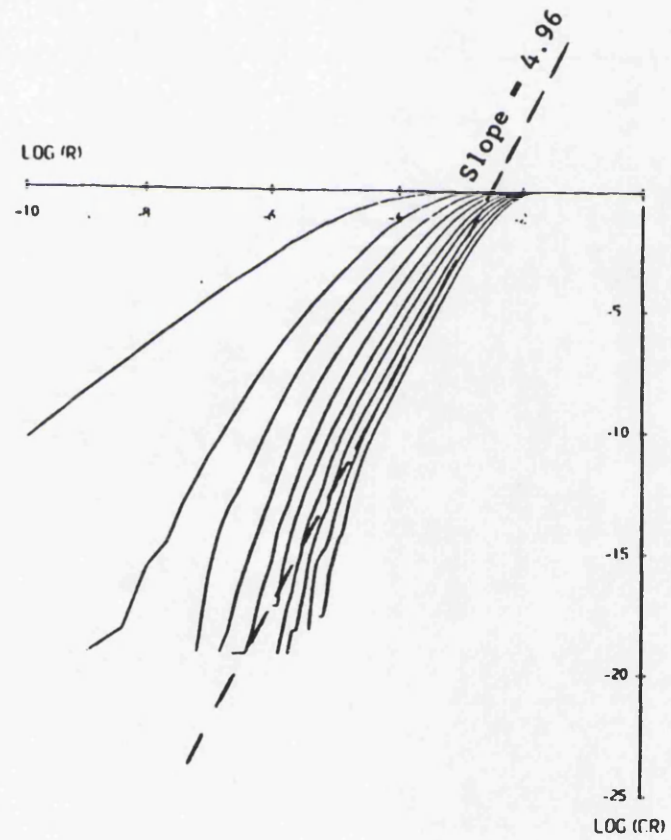


(b) 20mm Downstream

Figure 6-12: 'log(r) - log(Cr)' Plots  
13mm Orifice -  $Re_p = 256$

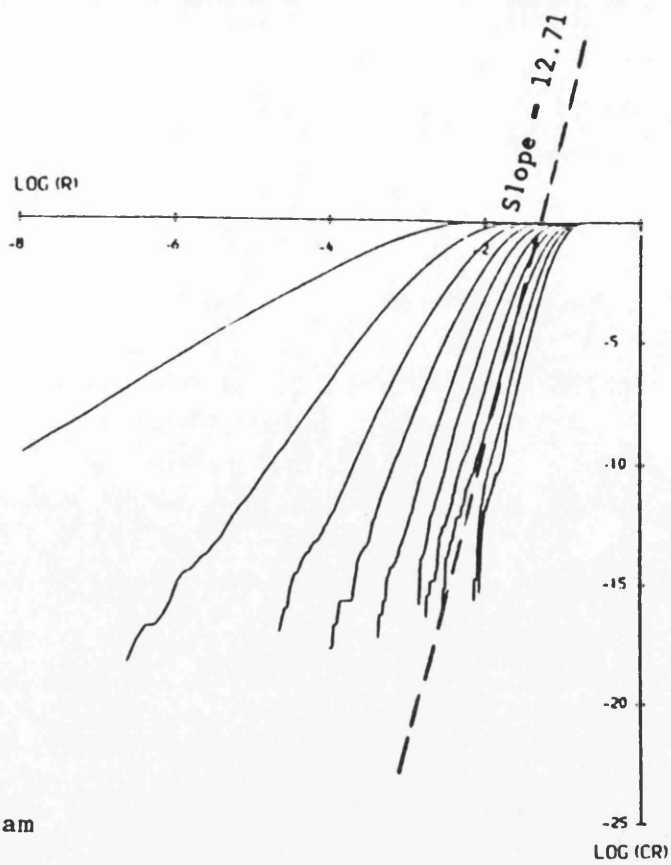


(c) 30mm Downstream

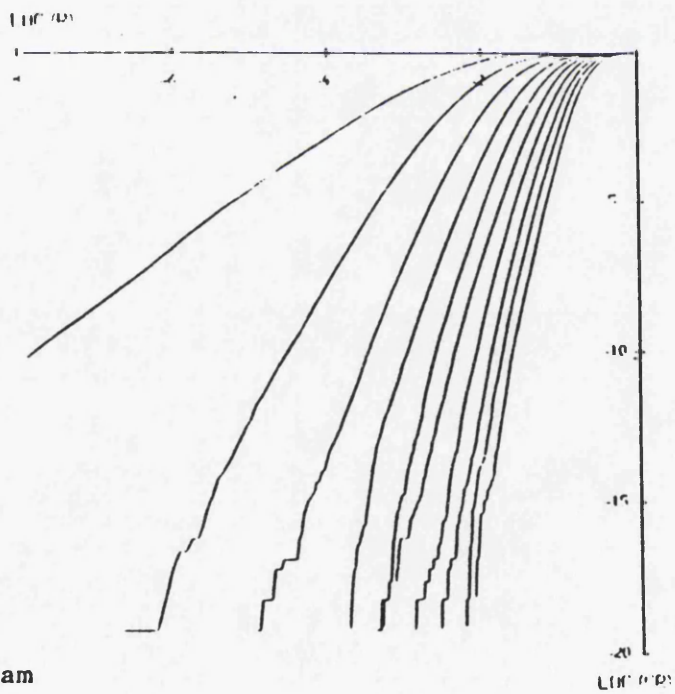


(d) 40mm Downstream

Figure 6-12: 'log(r) - log(Cr)' Plots  
13mm Orifice -  $Re_p = 256$

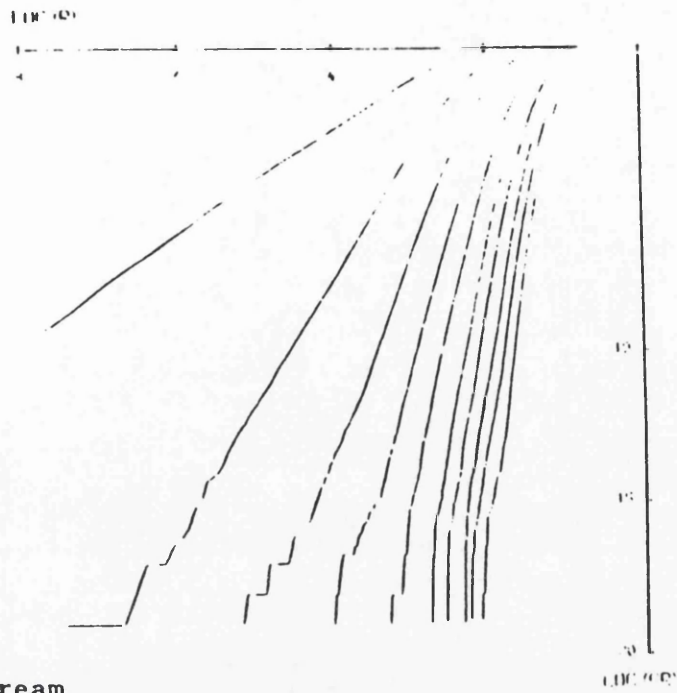


(e) 50mm Downstream

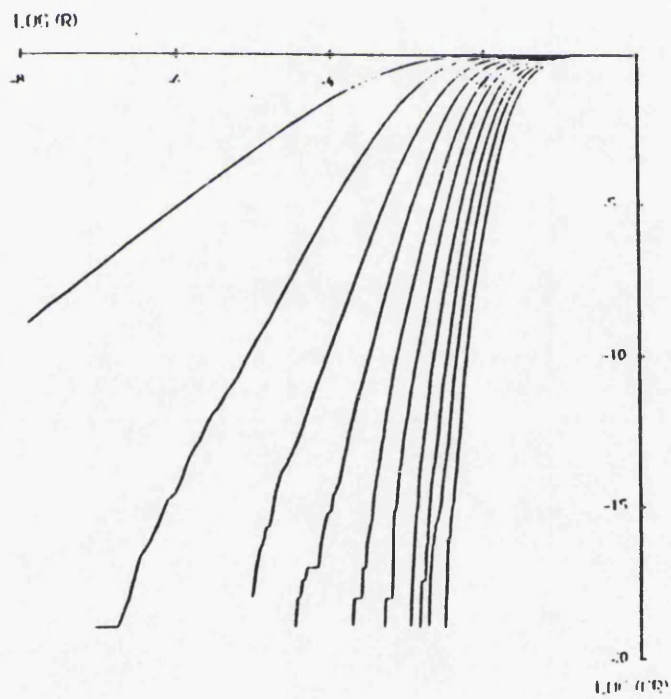


(f) 60mm Downstream

Figure 6-12: 'log(r) - log(Cr)' Plots  
13mm Orifice -  $Re_p = 256$

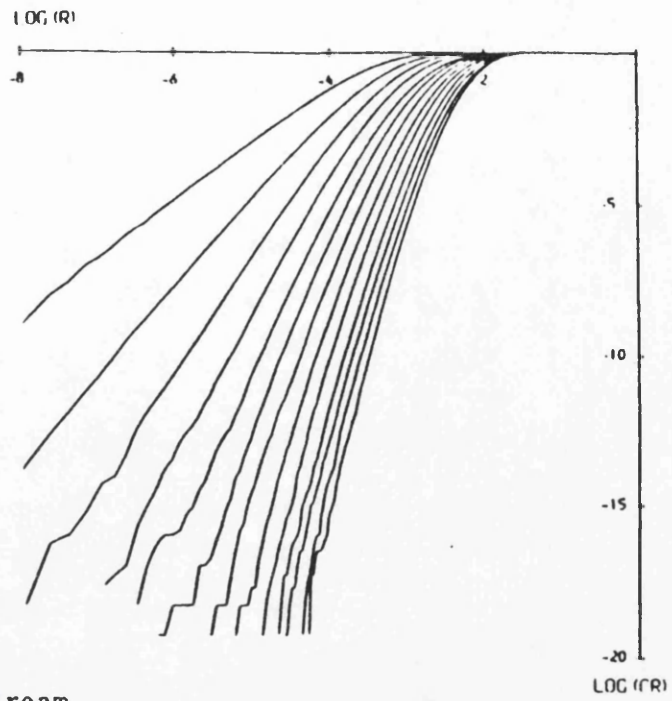


(g) 75mm Downstream

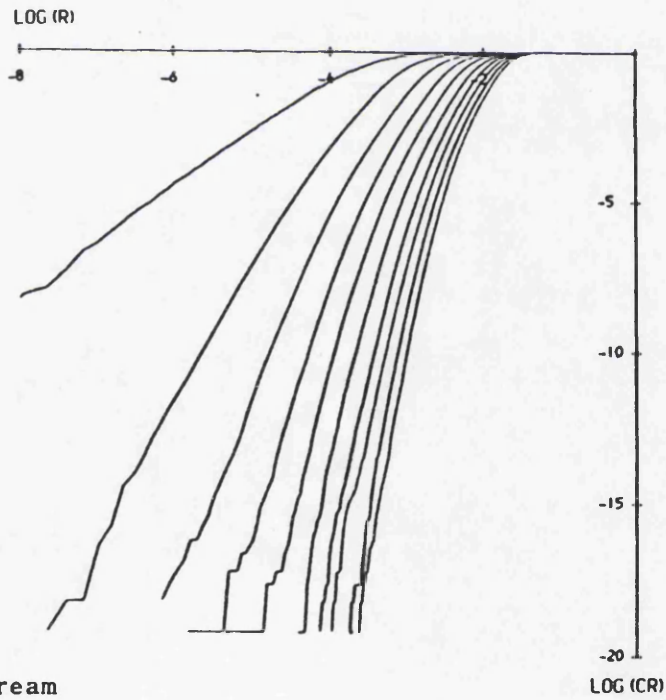


(h) 100mm Downstream

Figure 6-12: 'log(r) - log(Cr)' Plots  
13mm Orifice -  $Re_p = 256$

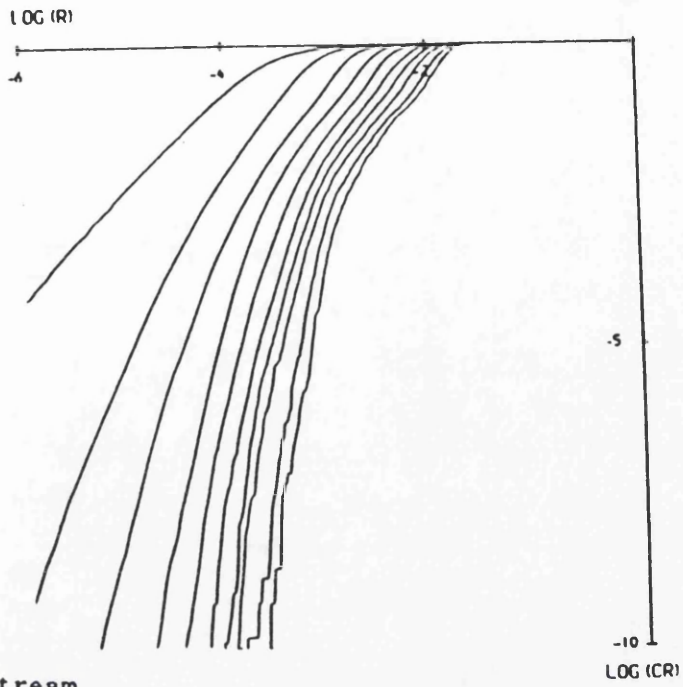


(i) 150mm Downstream

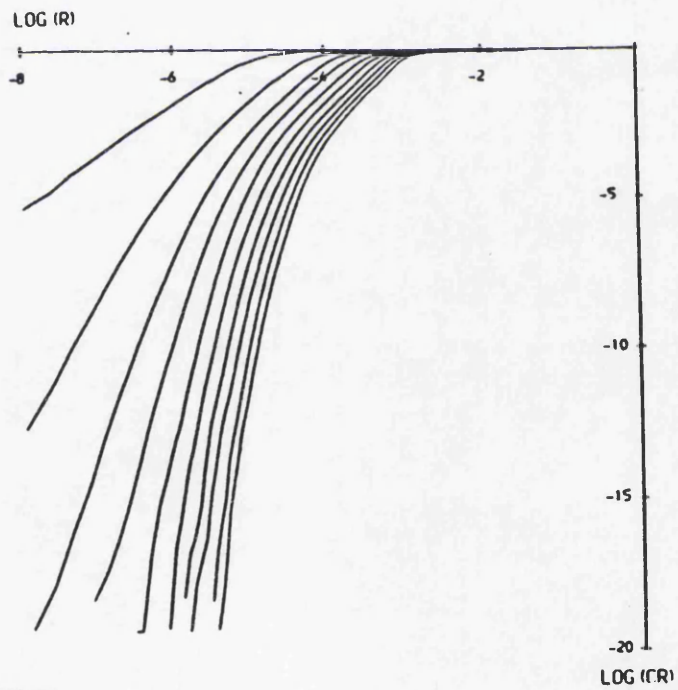


(j) 200mm Downstream

Figure 6-12: 'log(r) - log(Cr)' Plots  
13mm Orifice -  $Re_p = 256$



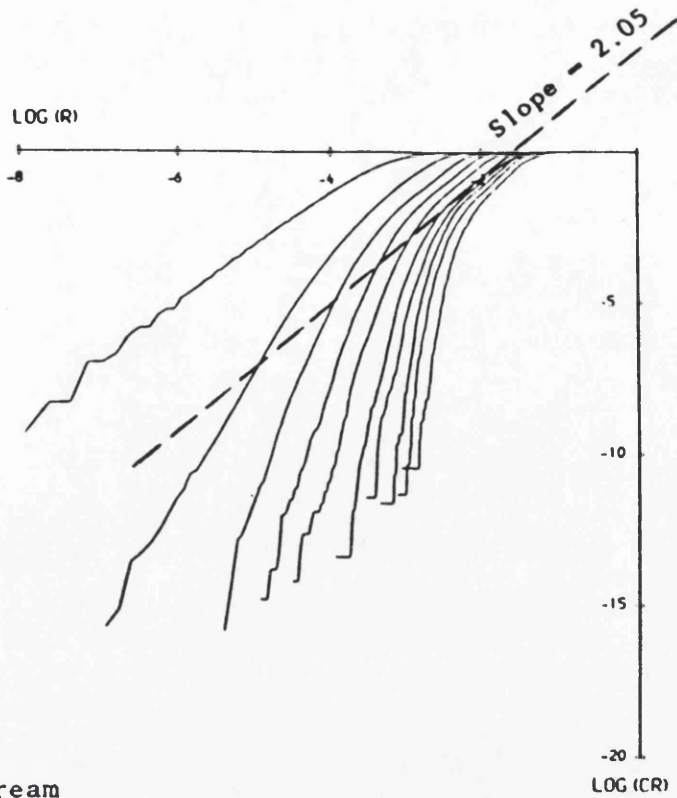
(k) 250mm Downstream



(l) 500mm Downstream

Figure 6-12; 'log(r) - log(Cr)' Plots

13mm Orifice -  $Re_p = 256$



(m) 950mm Downstream

Figure 6-12: 'log(r) - log(Cr)' Plots  
13mm Orifice -  $Re_p = 256$

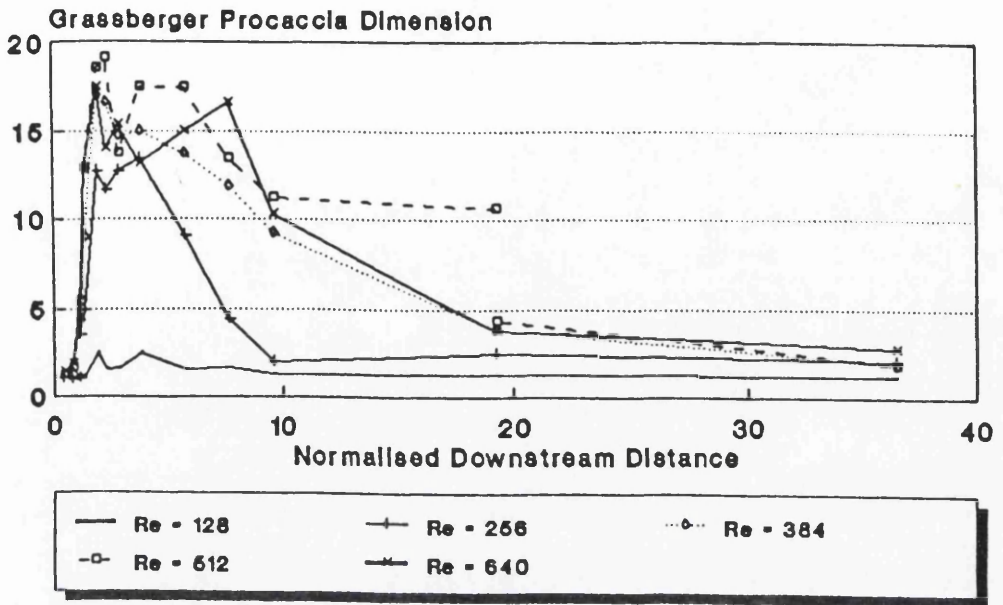


Figure 6-13: Dimension Results - 13.00mm Orifice  
Various Reynolds Numbers

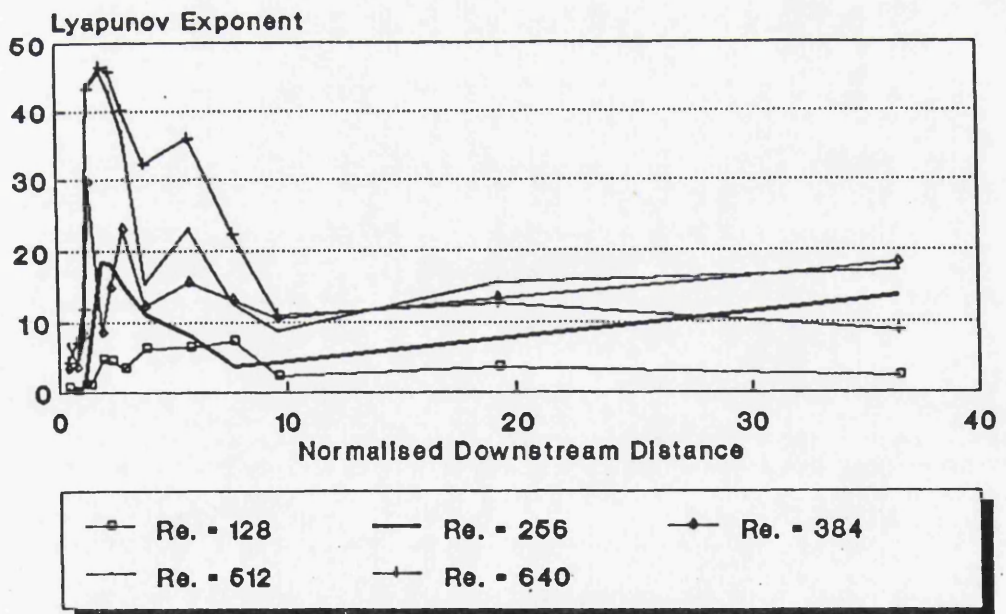
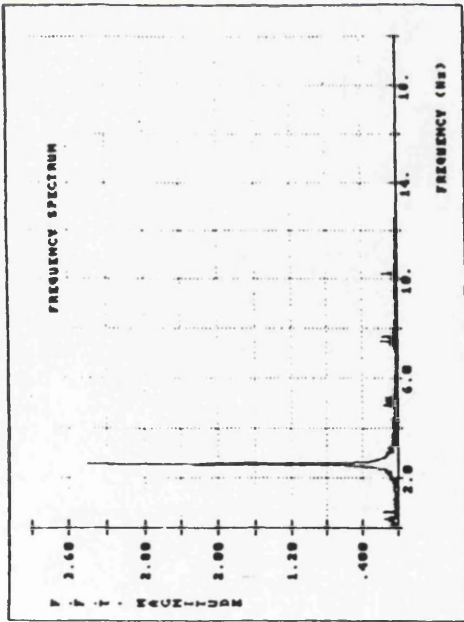
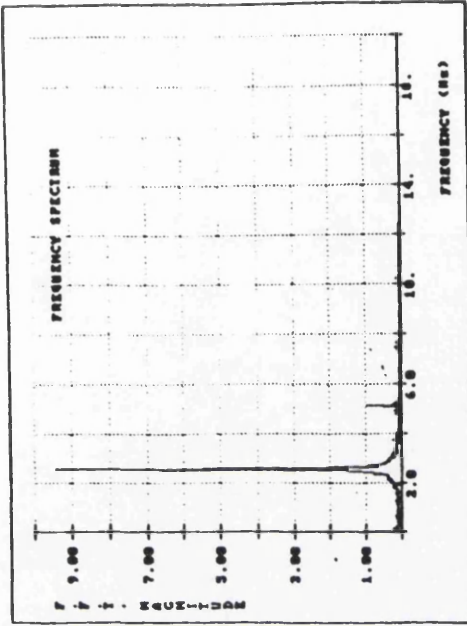


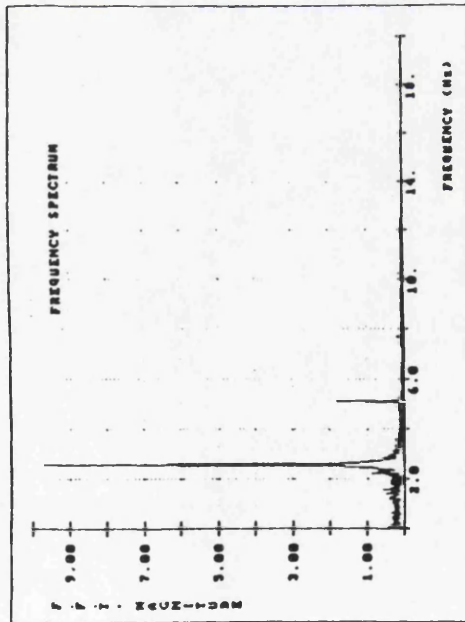
Figure 6-14: Lyapunov Exponent Results - 13.00mm Orifice  
Various Reynolds Numbers



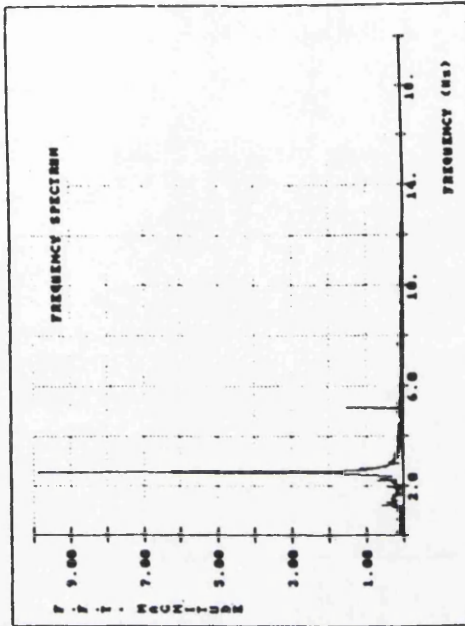
(a) 10mm Downstream



(b) 20mm Downstream



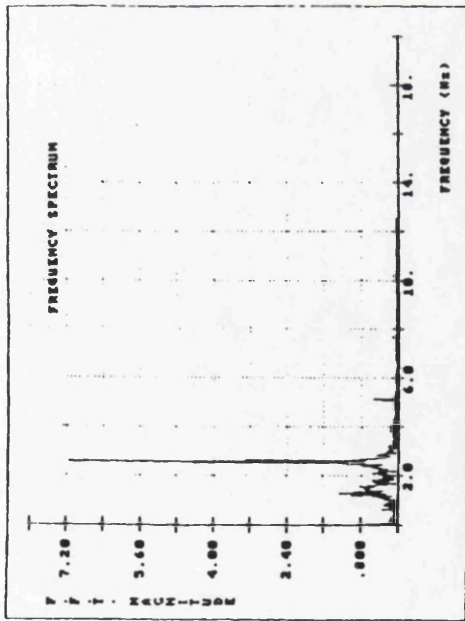
(c) 30mm Downstream



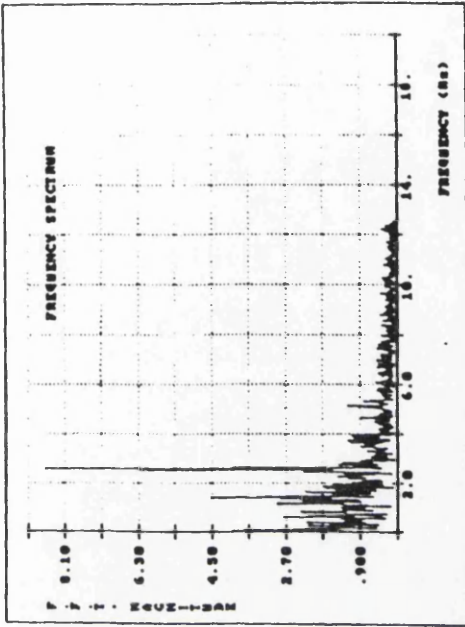
(d) 40mm Downstream

Figure 6-15: Frequency Spectra - 13.00mm Orifice - Rep - 256

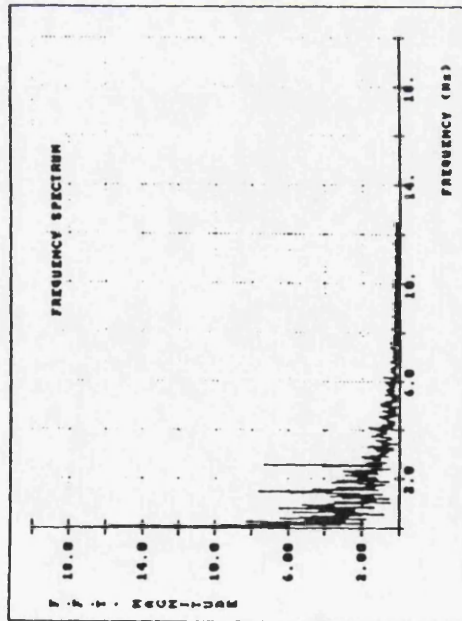
0.2 Volts Forcing



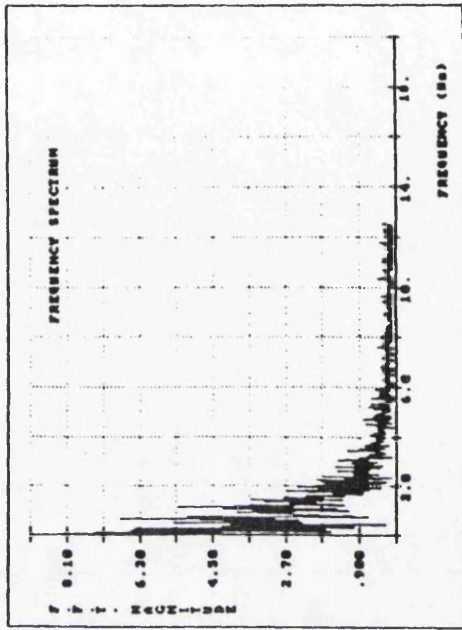
(e) 50mm Downstream



(f) 60mm Downstream



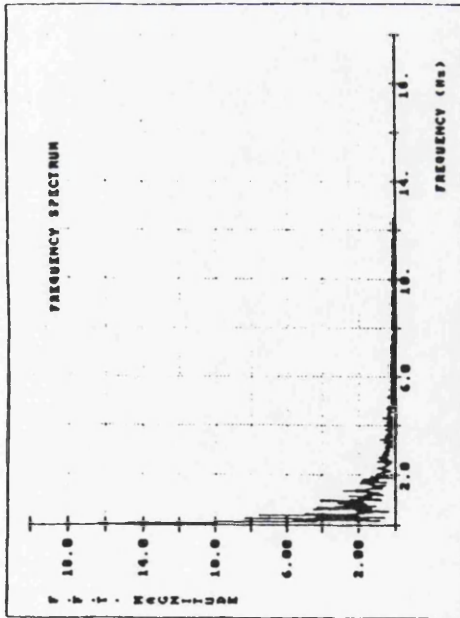
(g) 75mm Downstream



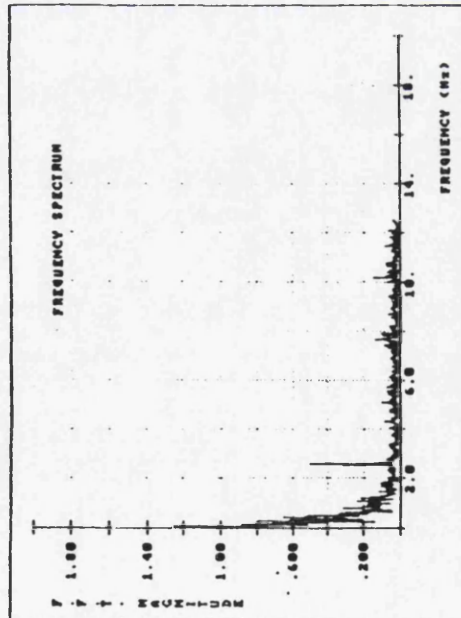
(h) 100mm Downstream

Figure 6-15: Frequency Spectra - 13.00mm Orifice - Rep - 256

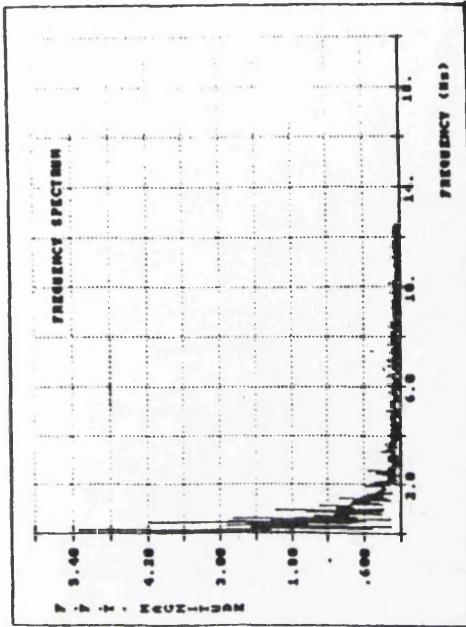
0.2 Volts Forcing



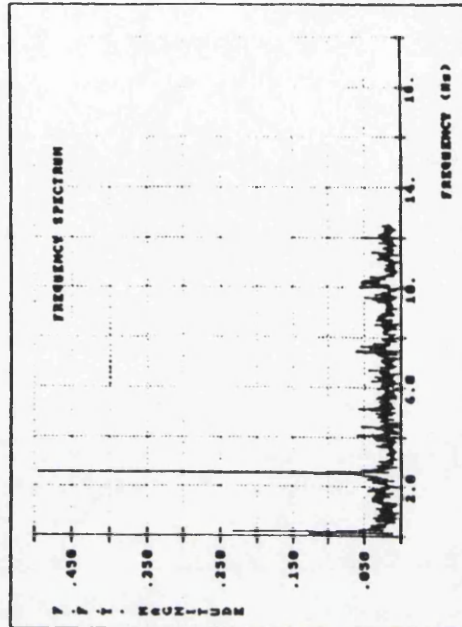
(i) 150mm Downstream



(k) 250mm Downstream



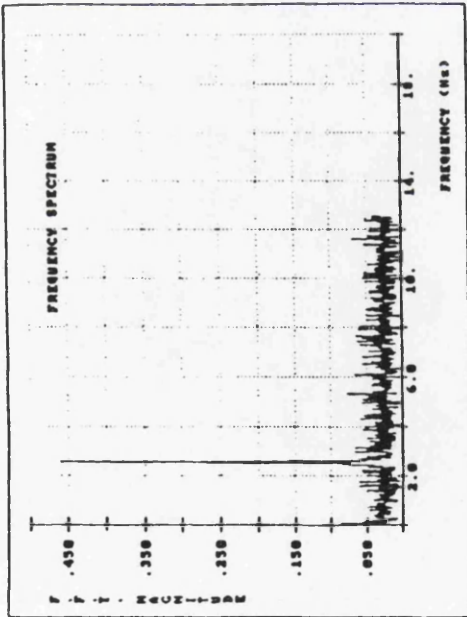
(j) 200mm Downstream



(l) 500mm Downstream

Figure 6-15: Frequency Spectra - 13.00mm Orifice - Rep - 256

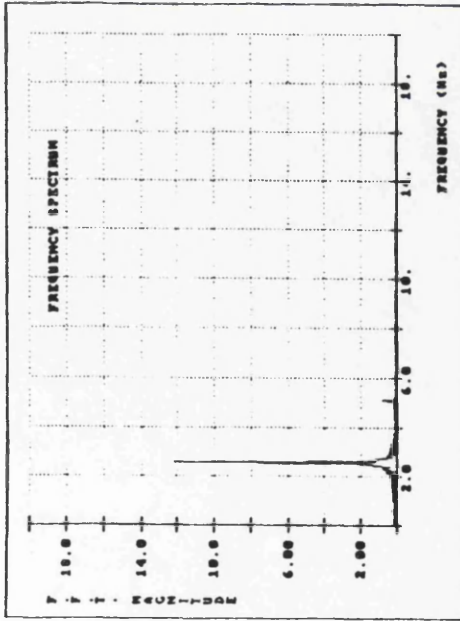
0.2 Volts Forcing



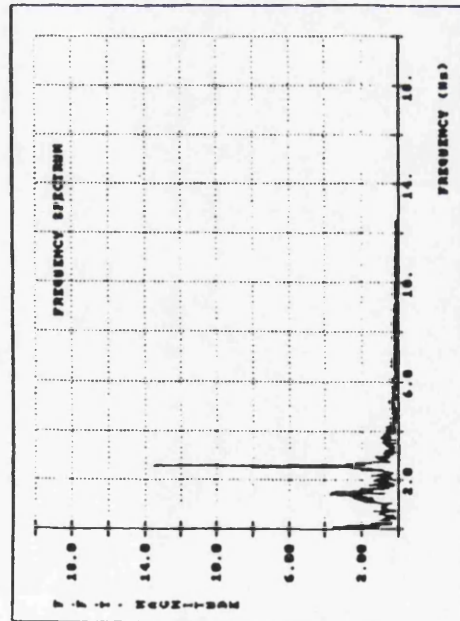
(m) 950mm Downstream

Figure 6-15: Frequency Spectra - 13.00mm Orifice - Rep - 256

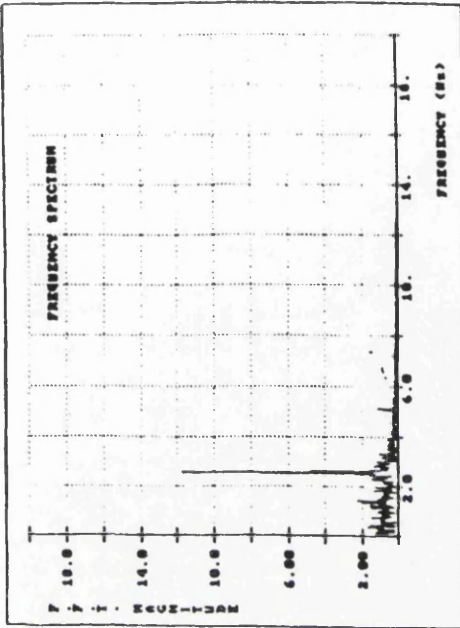
0.2 Volts Forcing



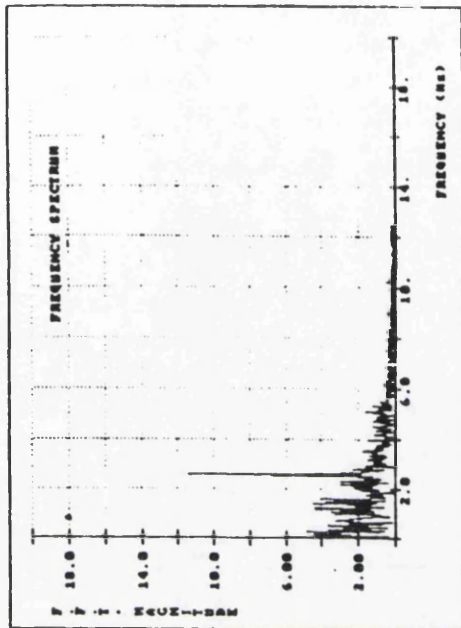
(a) 10mm Downstream



(c) 30mm Downstream

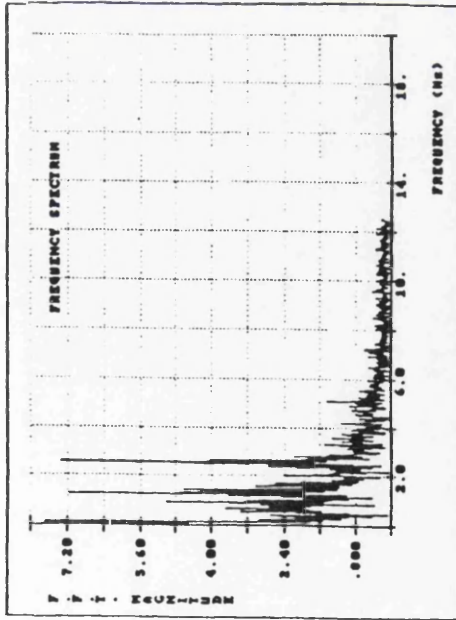


(b) 20mm Downstream

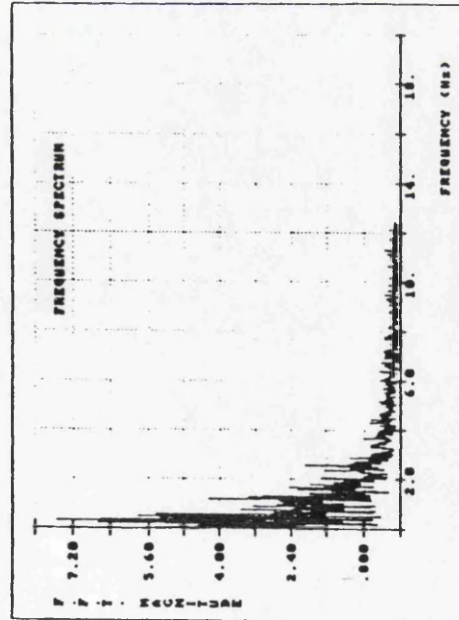


(d) 40mm Downstream

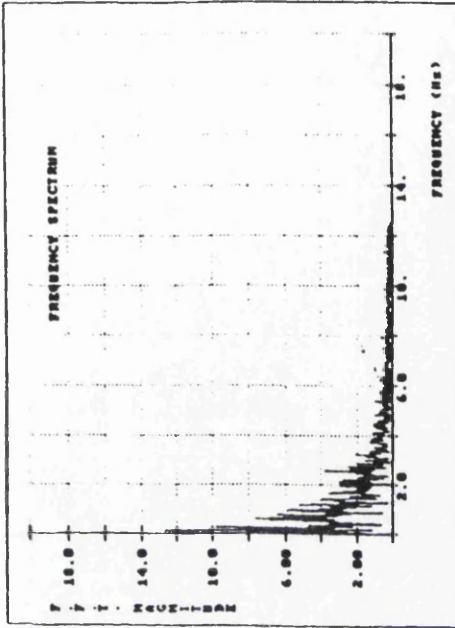
Figure 6-16: Frequency Spectra - 13.00mm Orifice - Rep - 256  
1.0 Volts Forcing



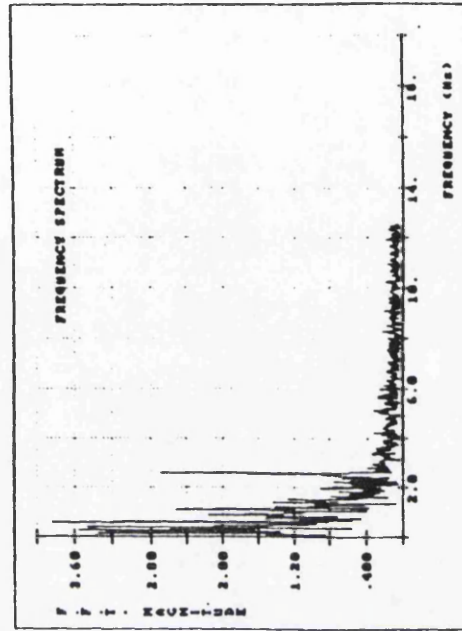
(e) 50mm Downstream



(g) 75mm Downstream

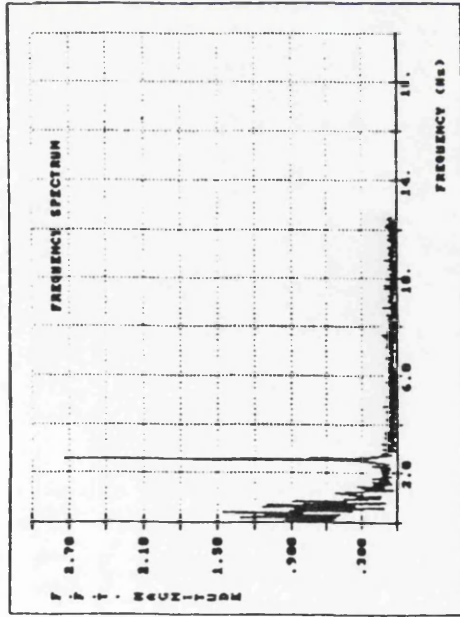


(f) 60mm Downstream

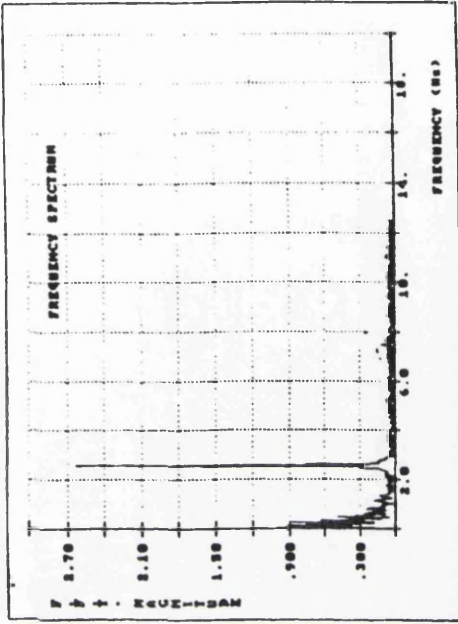


(h) 100mm Downstream

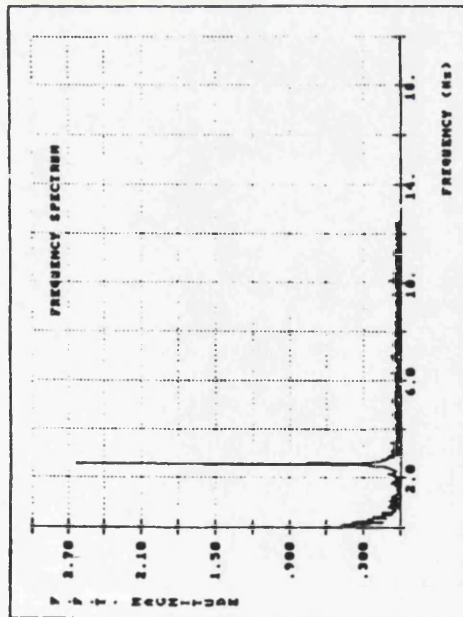
Figure 6-16: Frequency Spectra - 13.00mm Orifice -  $Re_p = 256$   
1.0 Volts Forcing



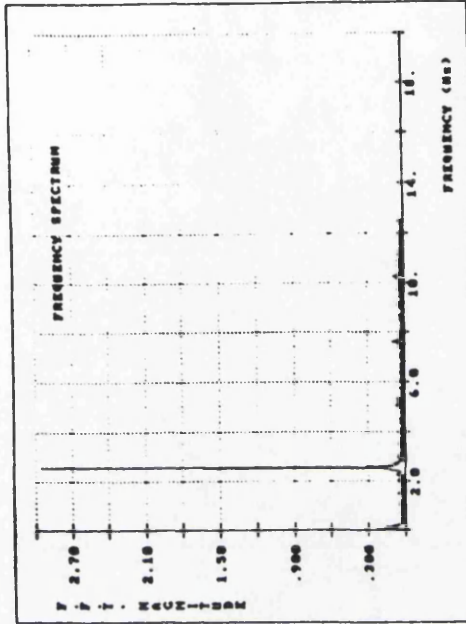
(i) 150mm Downstream



(j) 200mm Downstream

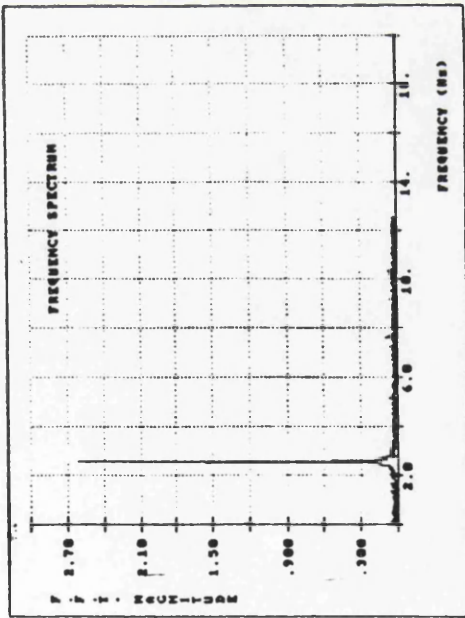


(k) 250mm Downstream



(l) 500mm Downstream

Figure 6-16: Frequency Spectra - 13.00mm Orifice - Rep - 256  
1.0 Volts Forcing



(m) 950mm Downstream

Figure 6-16: Frequency Spectra - 13.00mm Orifice - Rep - 256  
1.0 Volts Forcing

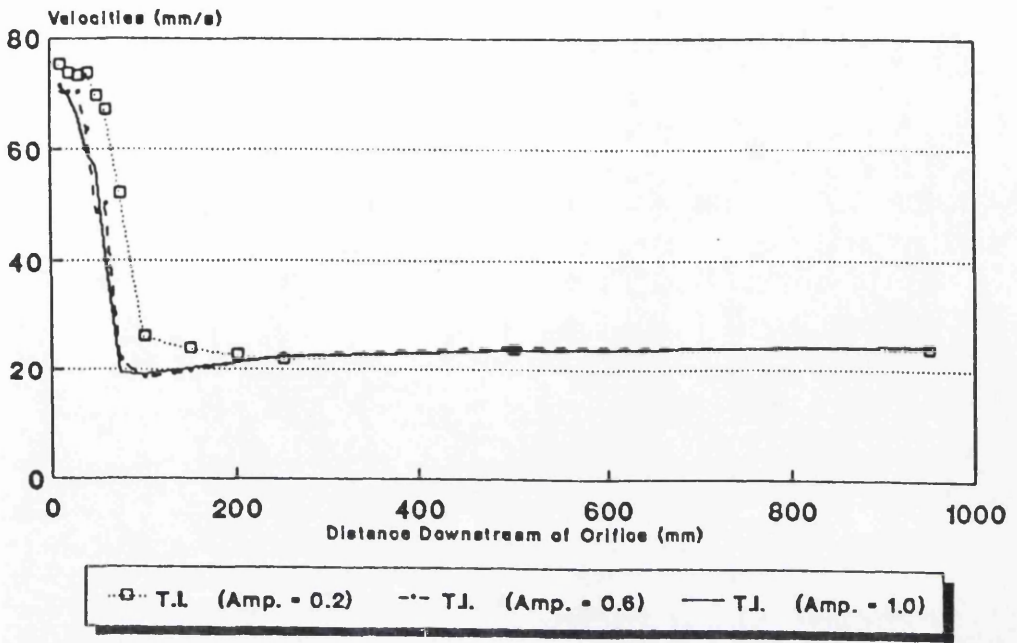


Figure 6-17a: Centreline Velocities - 13.00mm Orifice  
Various Forcing Amplitudes

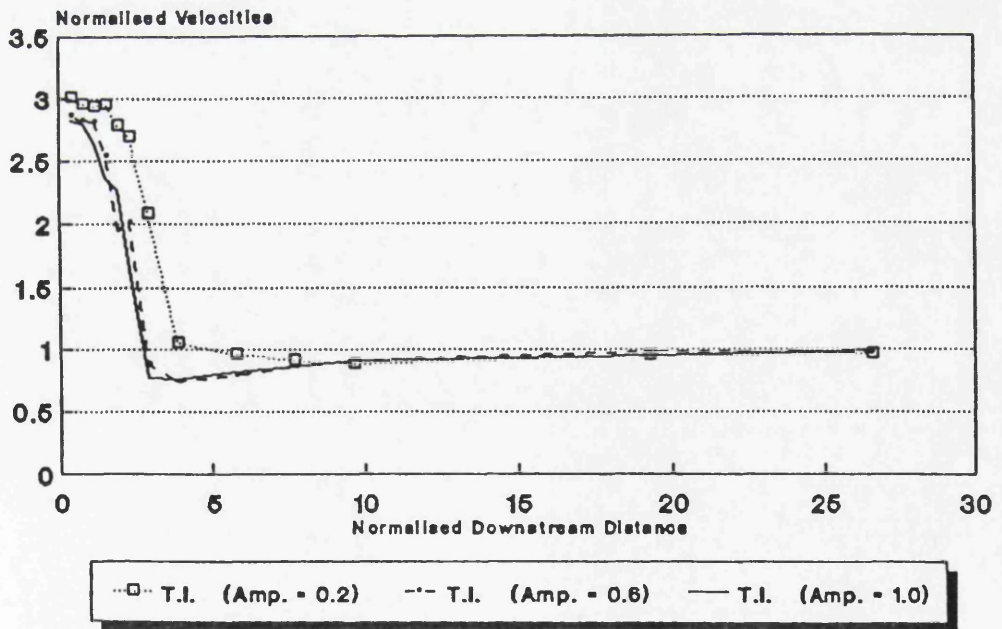


Figure 6-17b: Normalised Centreline Velocities - 13.00mm Orifice  
Various Forcing Amplitudes

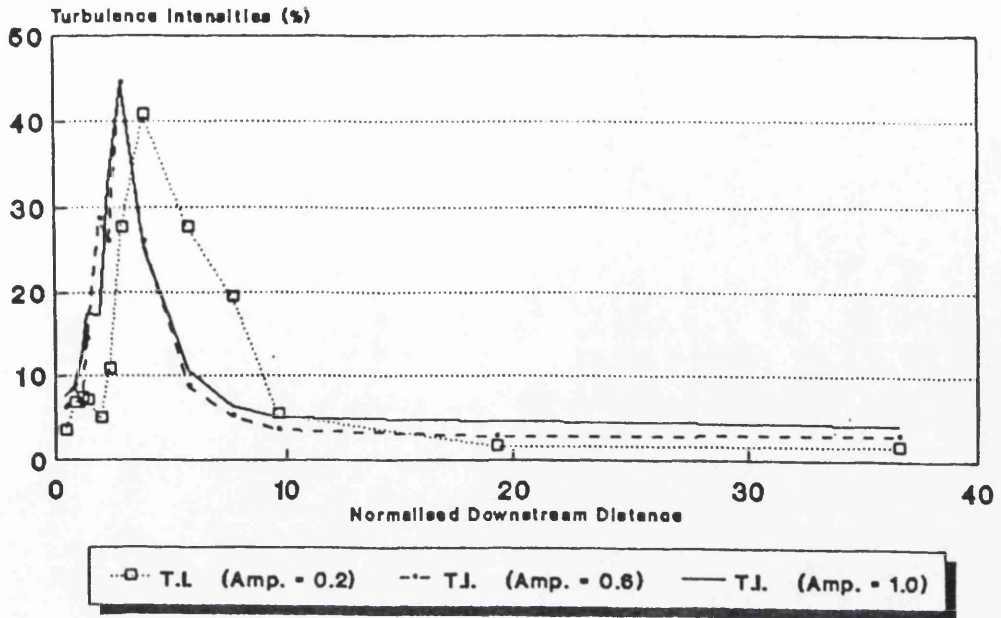


Figure 6-18a: Point-Turbulence Intensities- 13.00mm Orifice  
Various Forcing Amplitudes

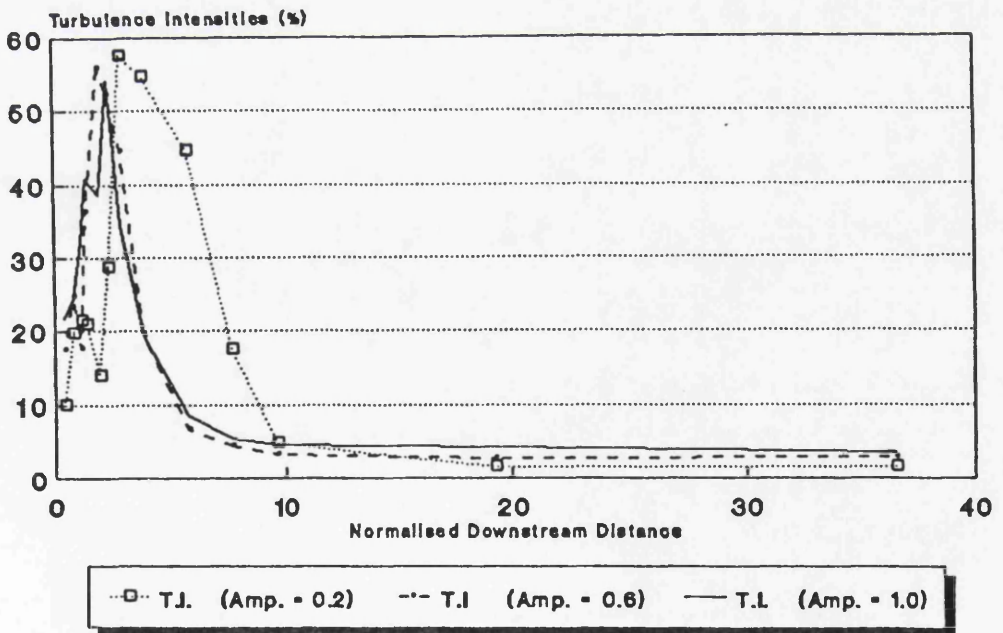


Figure 6-18b: H.G.-Turbulence Intensities - 13.00mm Orifice  
Various Forcing Amplitudes

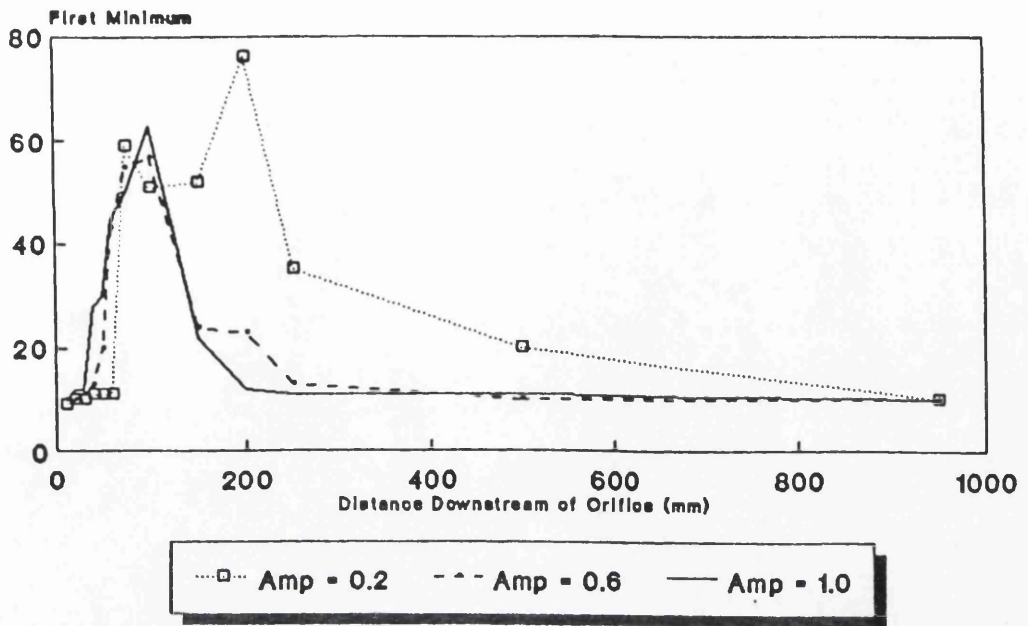


Figure 6-19a: Minimum Mutual Information - 13.00mm Orifice  
Various Forcing Amplitudes

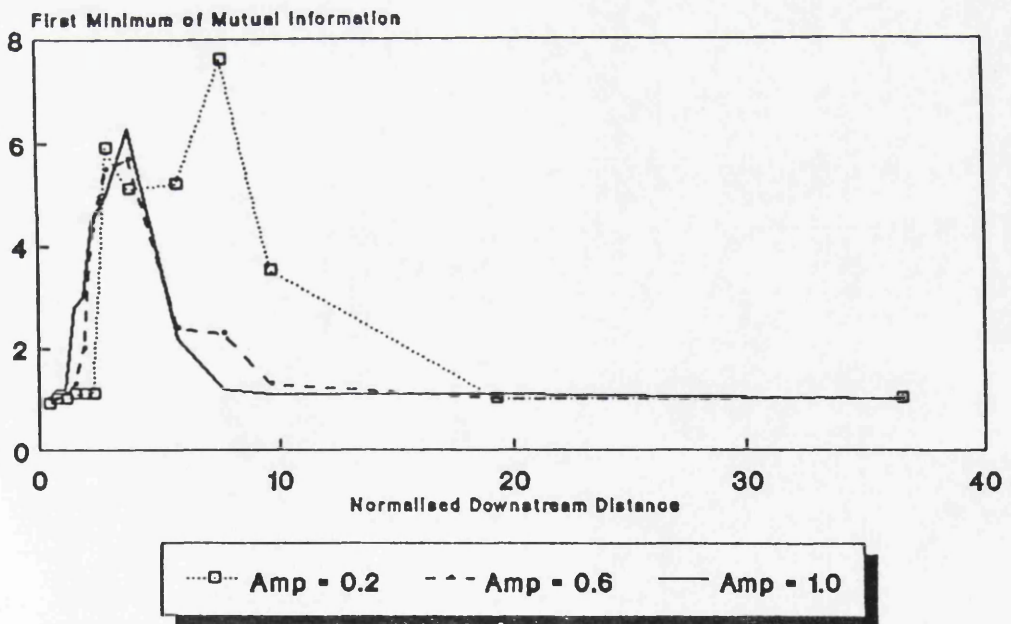
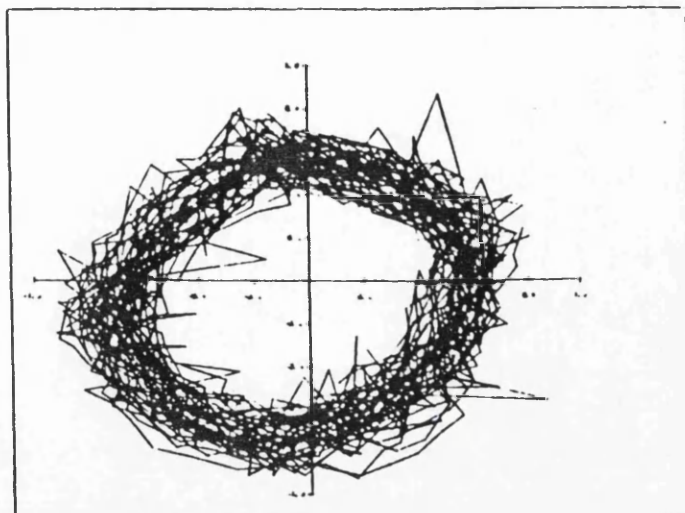
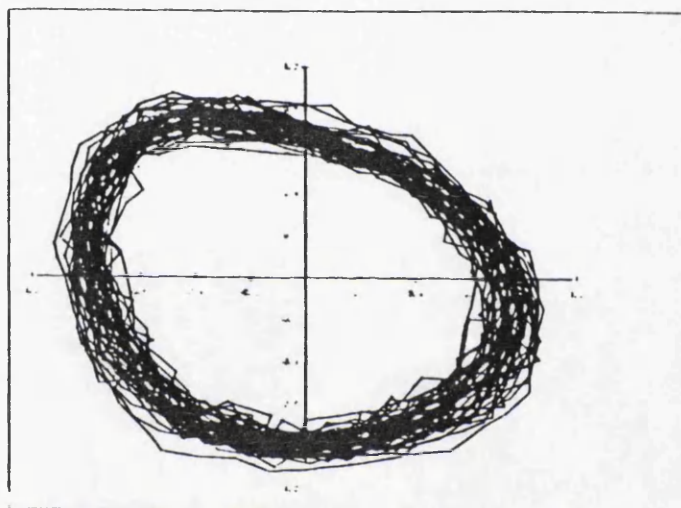


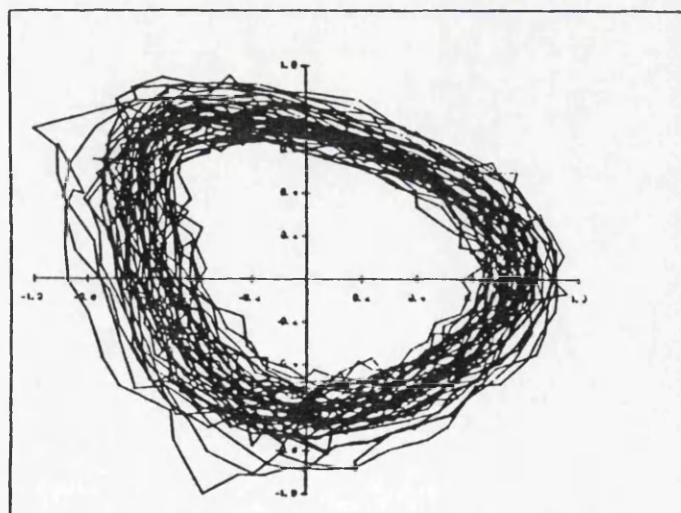
Figure 6-19b: Normalised Minimum Mutual Info. - 13.00mm Orifice  
Various Forcing Amplitudes



(a) 10mm Downstream

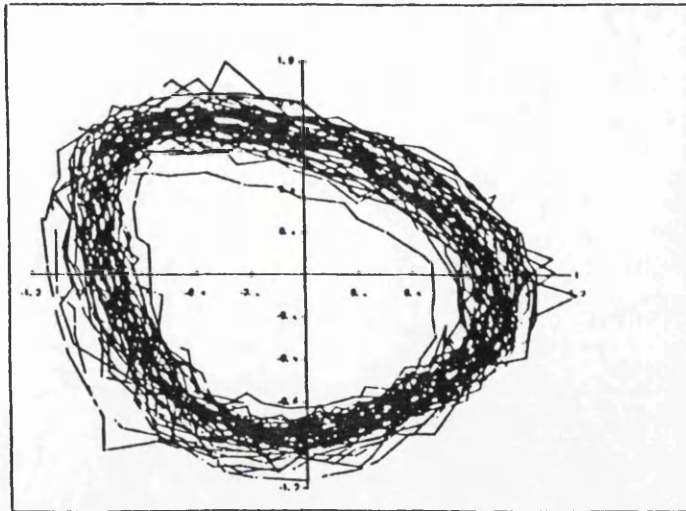


(b) 20mm Downstream

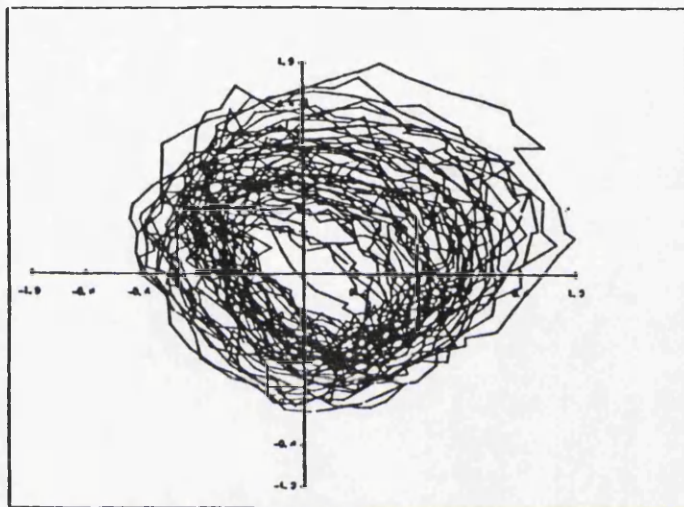


(c) 30mm Downstream

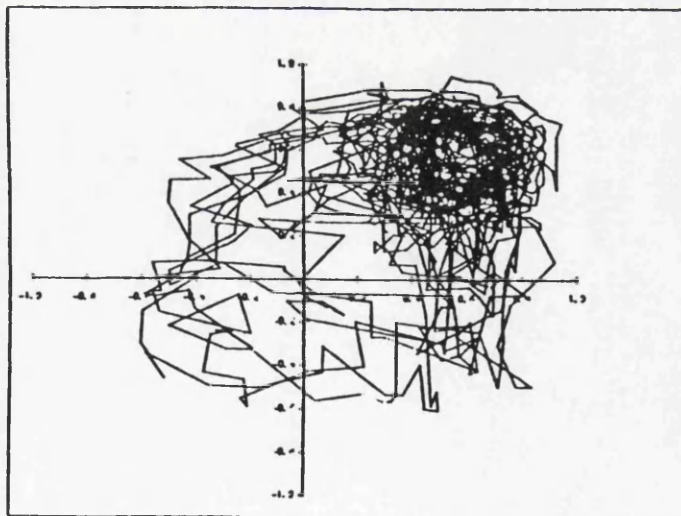
**Figure 6-20: Attractor Plots - 13mm Orifice**  
**0.2 Volts Forcing**



(d) 40mm Downstream

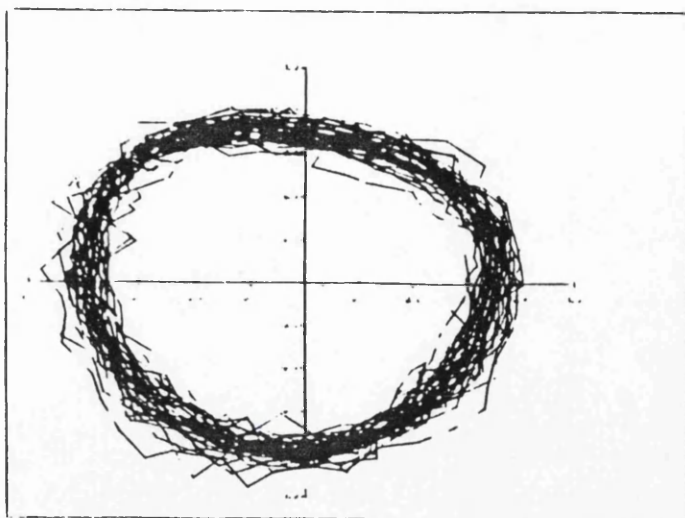


(e) 50mm Downstream

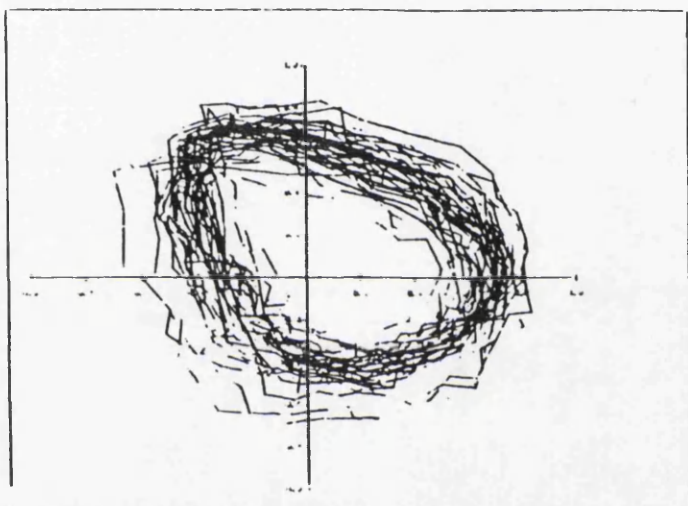


(f) 60mm Downstream

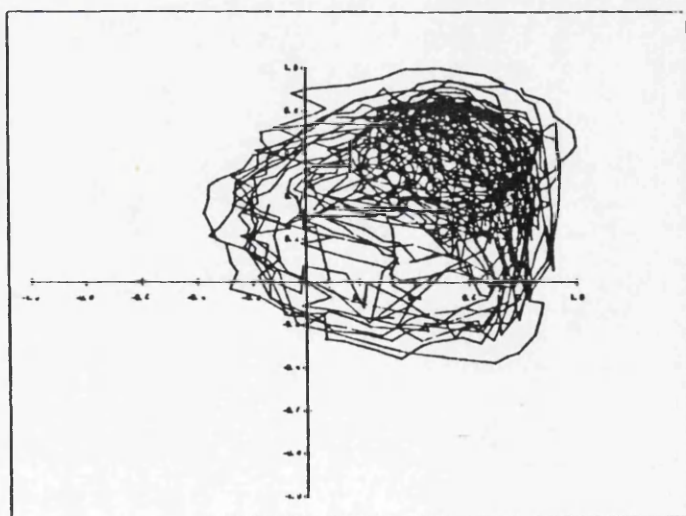
**Figure 6-20: Attractor Plots - 13mm Orifice  
0.2 Volts Forcing**



(a) 10mm Downstream

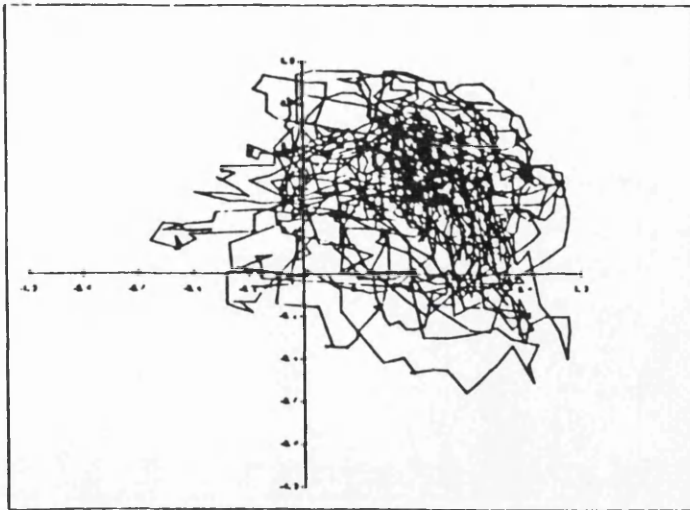


(b) 20mm Downstream

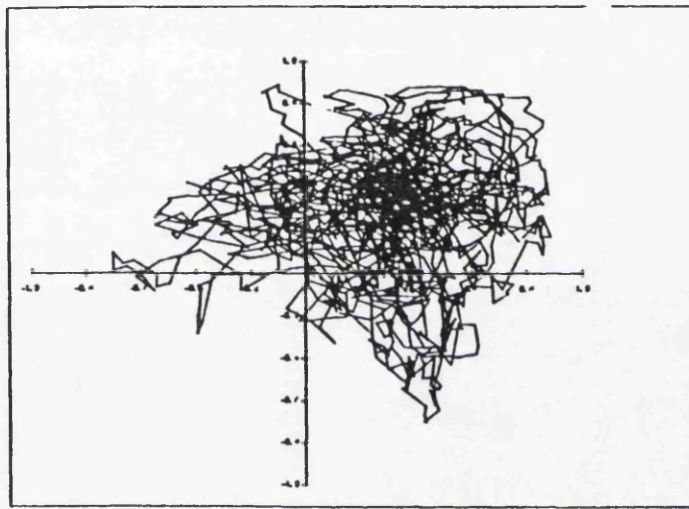


(c) 30mm Downstream

**Figure 6-21; Attractor Plots - 13mm Orifice  
1.0 Volts Forcing**



(d) 40mm Downstream



(e) 50mm Downstream

**Figure 6-21: Attractor Plots - 13mm Orifice**  
**1.0 Volts Forcing**

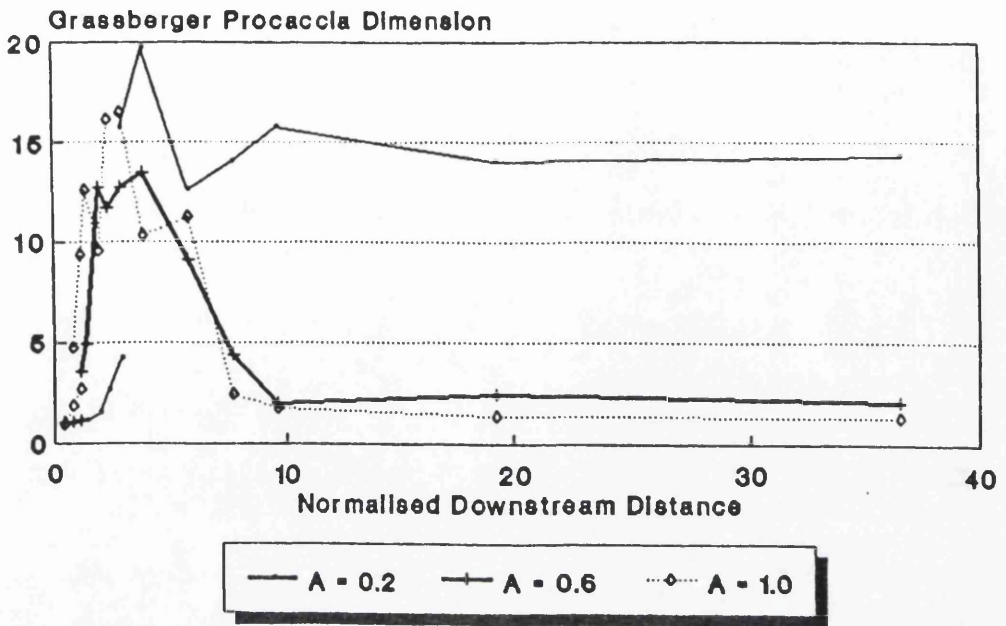


Figure 6-22: Dimension Results - 13.00mm Orifice  
Various Forcing Amplitudes

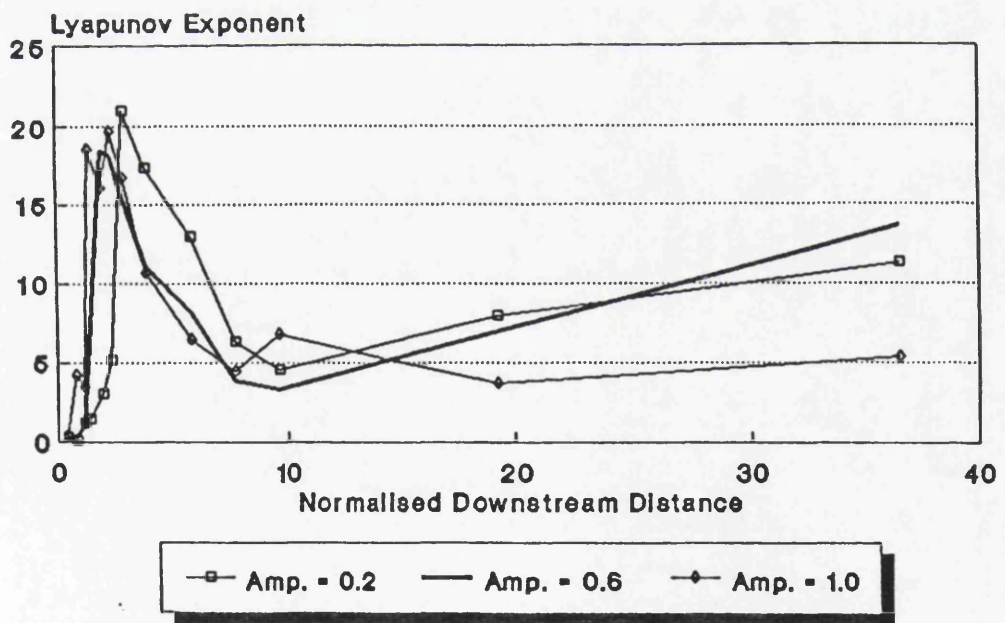


Figure 6-23: Lyapunov Exponent Results - 13.00mm Orifice  
Various Forcing Amplitudes

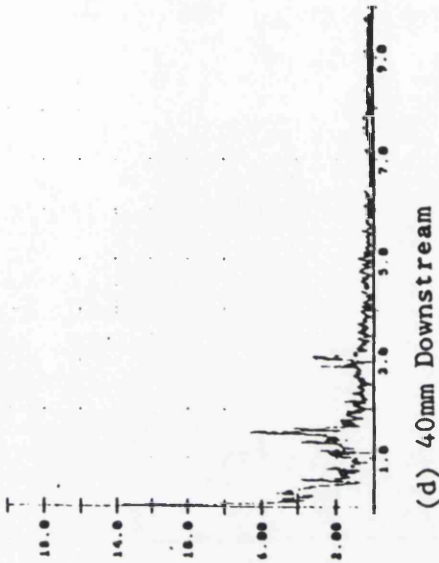
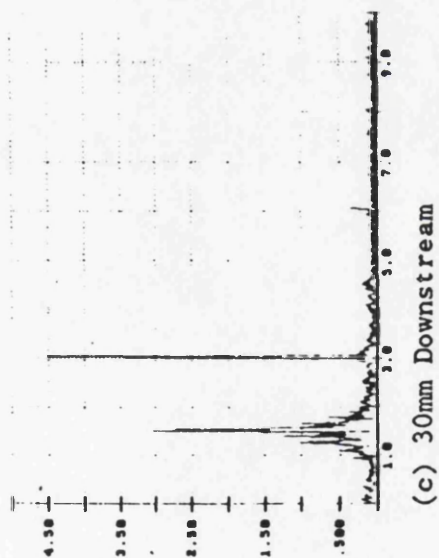
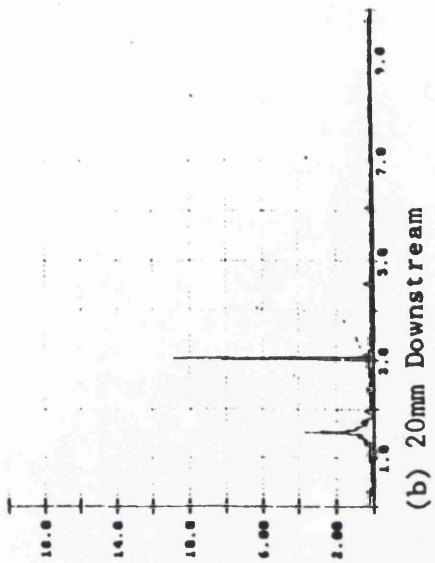
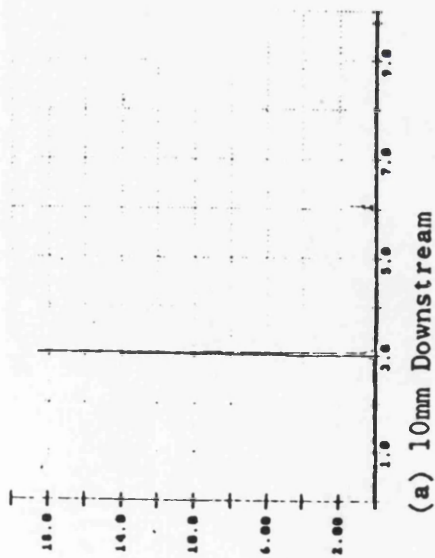


Figure 6-24: Frequency Spectra - 9.75mm Orifice - Rep - 128

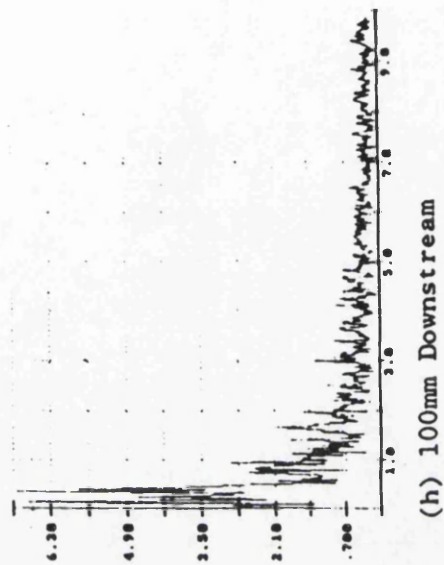
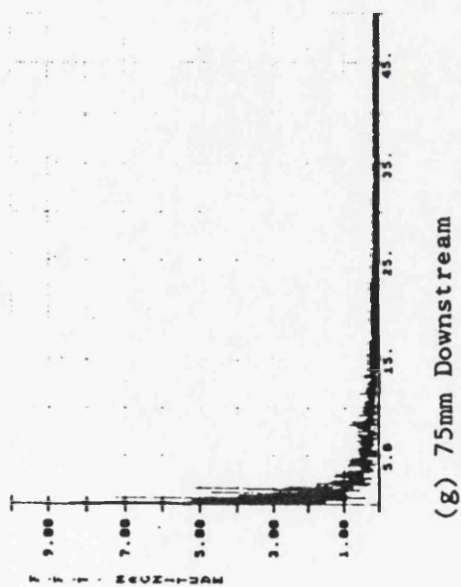
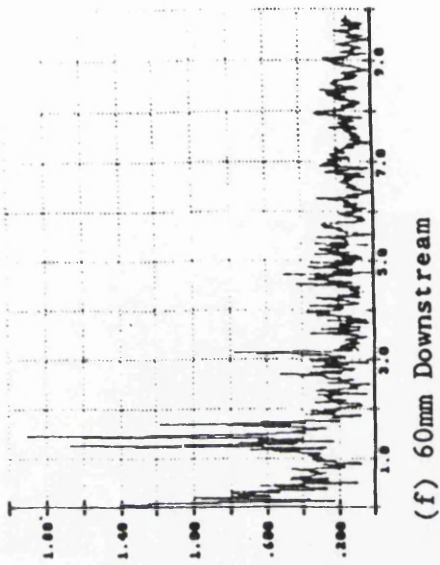
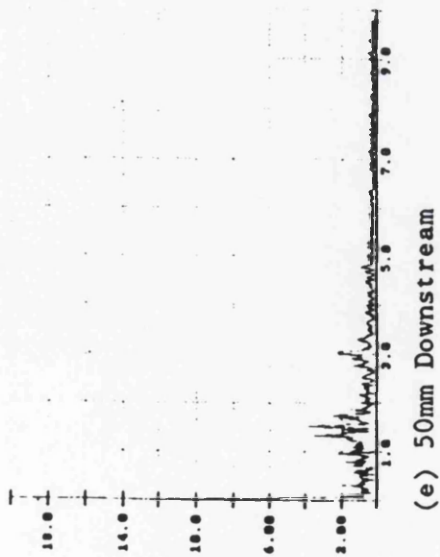


Figure 6-24: Frequency Spectra - 9.75mm Orifice - Rep - 128

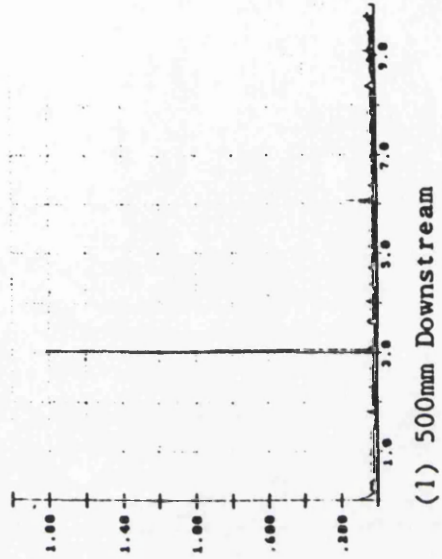
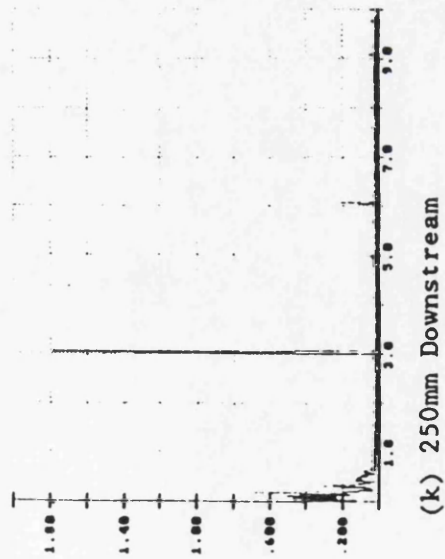
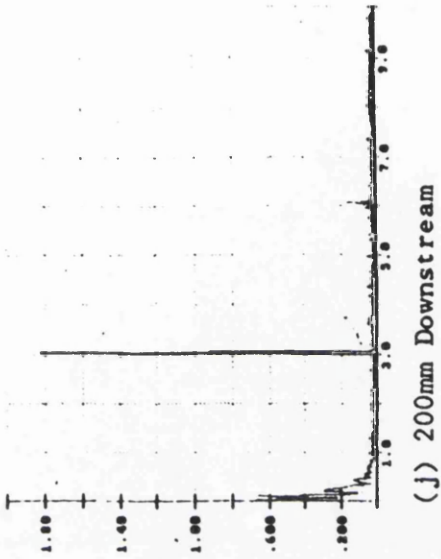
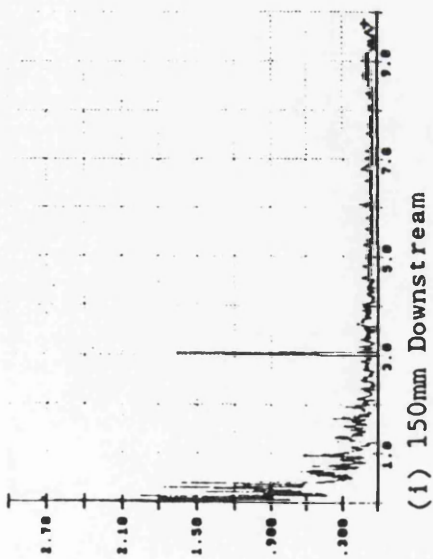
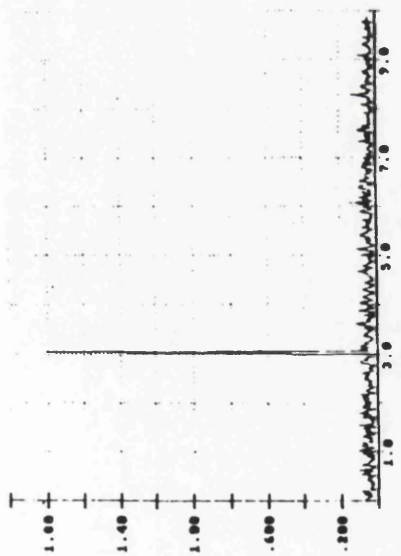


Figure 6-24: Frequency Spectra - 9.75mm Orifice - Rep - 128



(m) 950mm Downstream

Figure 6-24: Frequency Spectra - 9.75mm Orifice - Rep - 12B

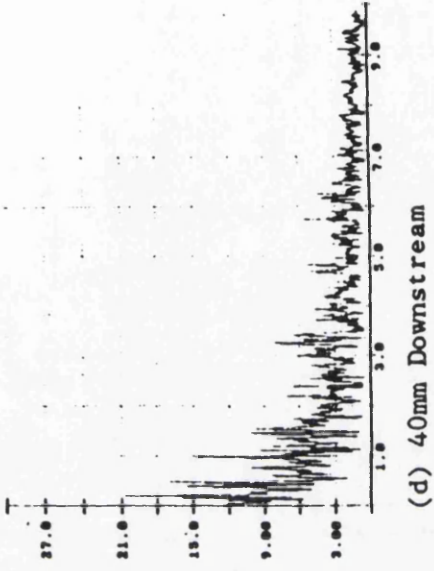
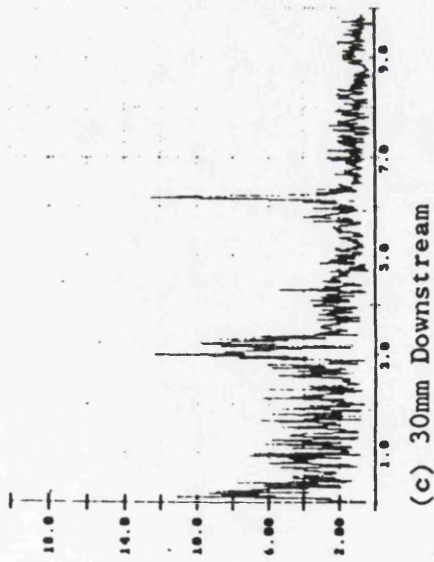
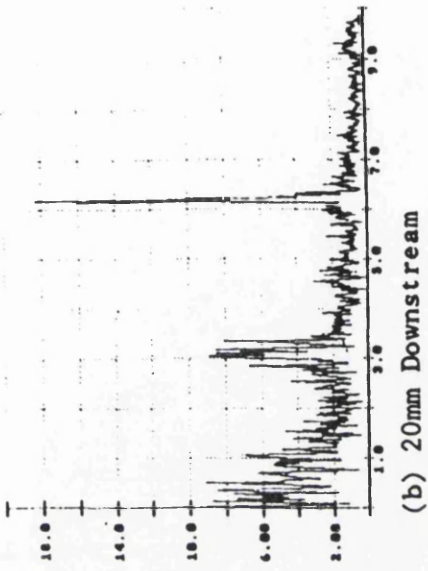
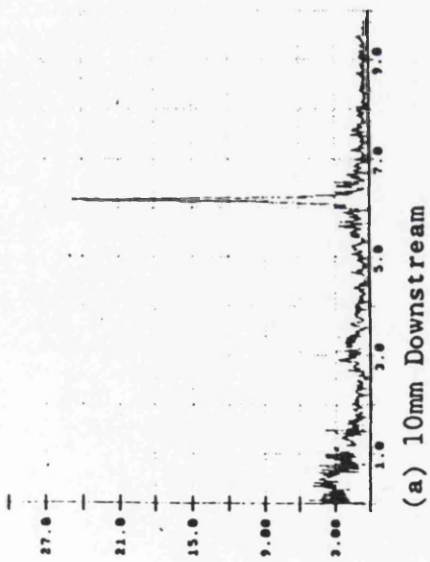


Figure 6-25: Frequency Spectra - 9.75mm Orifice - Rep - 256

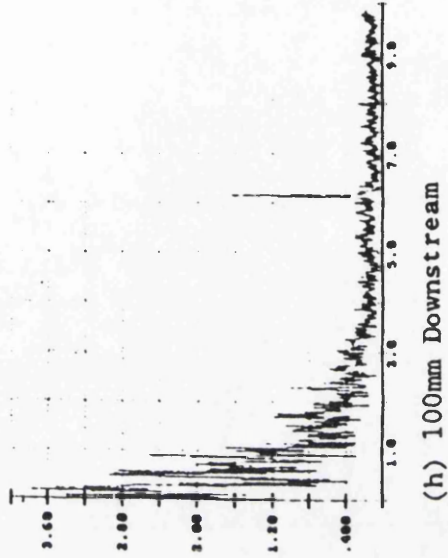
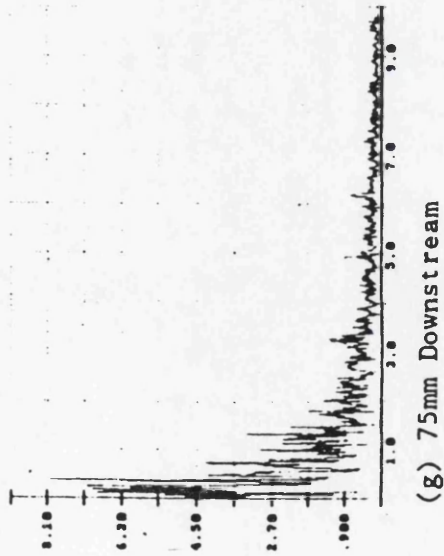
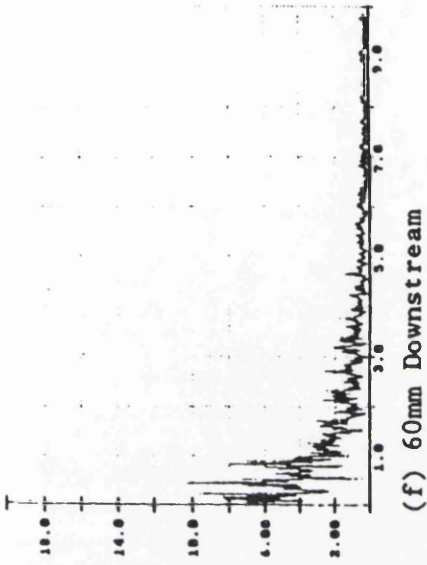
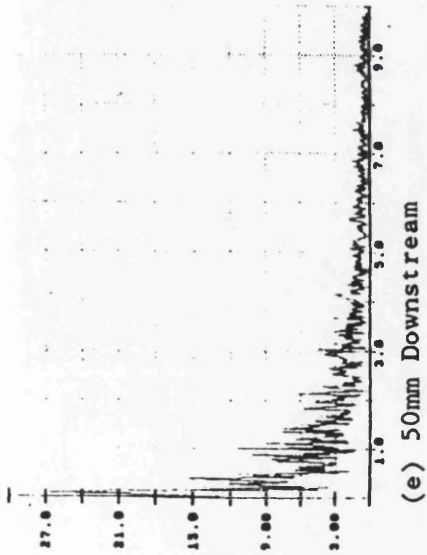


Figure 6-25: Frequency Spectra - 9.75mm Orifice - Rep - 256

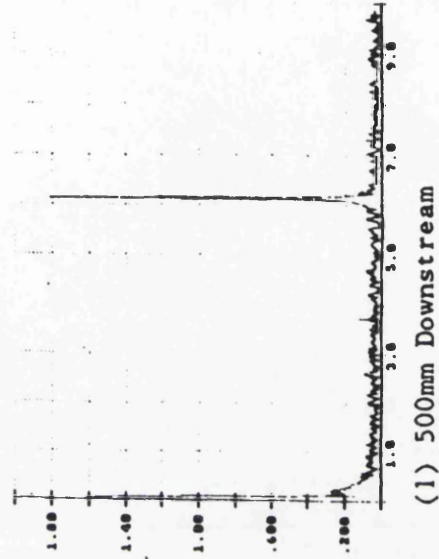
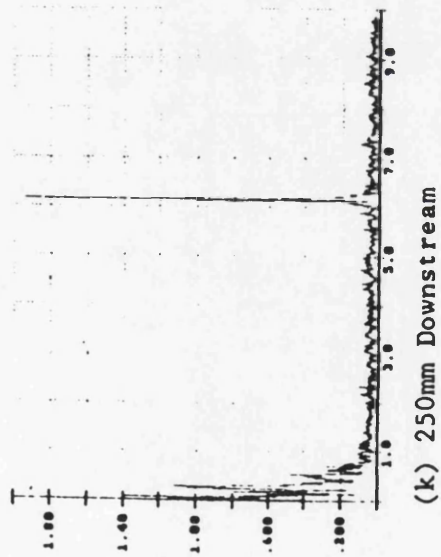
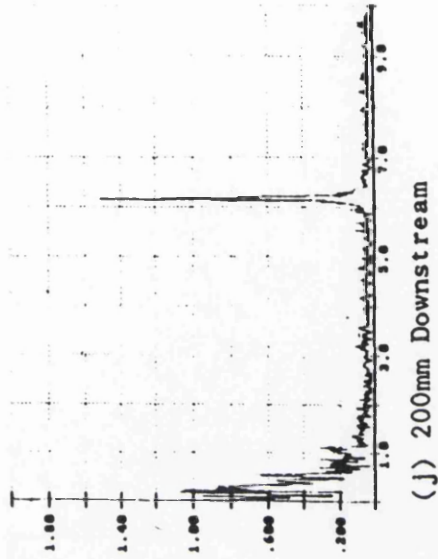
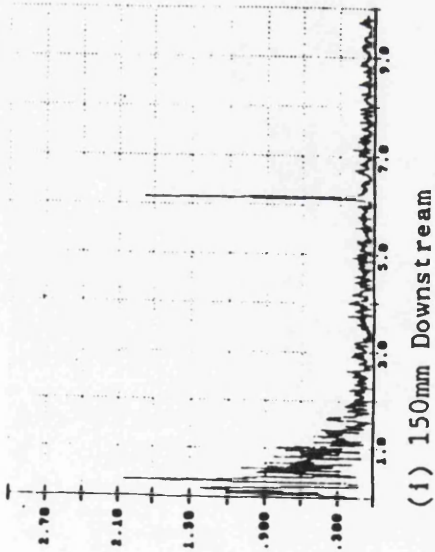
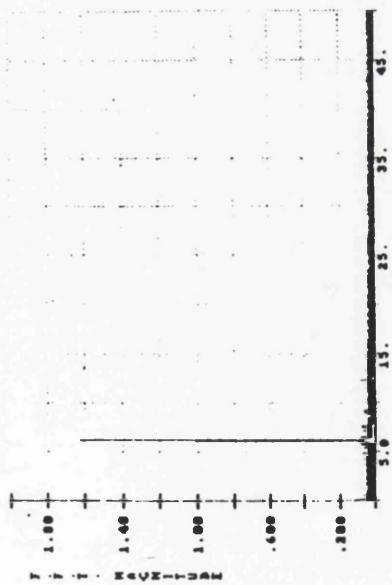
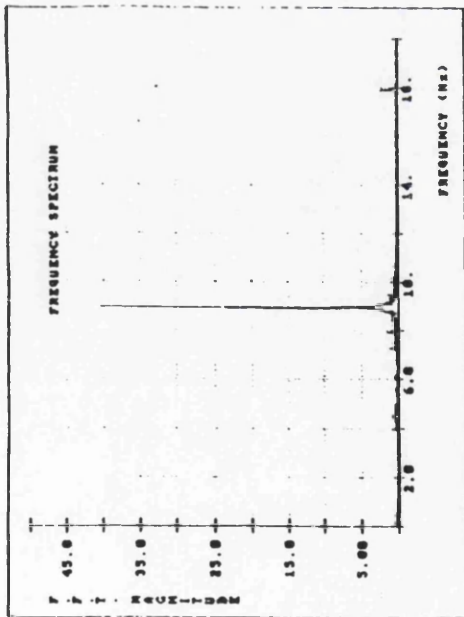


Figure 6-25: Frequency Spectra - 9.75mm Orifice - Rep - 256

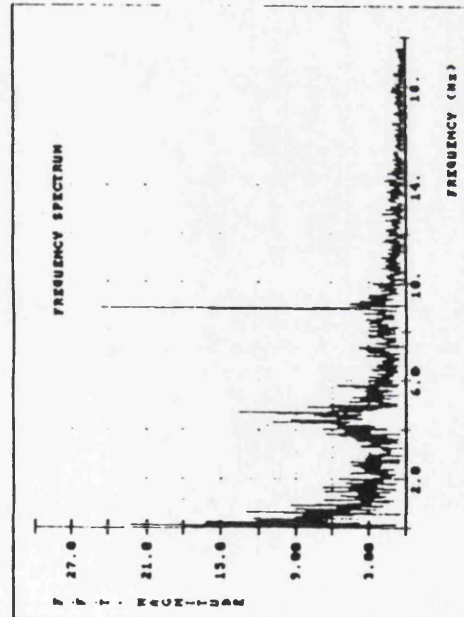


(m) 950mm Downstream

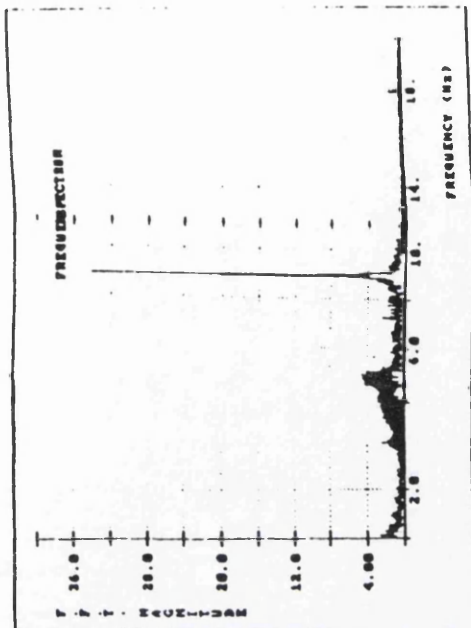
Figure 6-25: Frequency Spectra - 9.75mm Orifice - Rep - 256



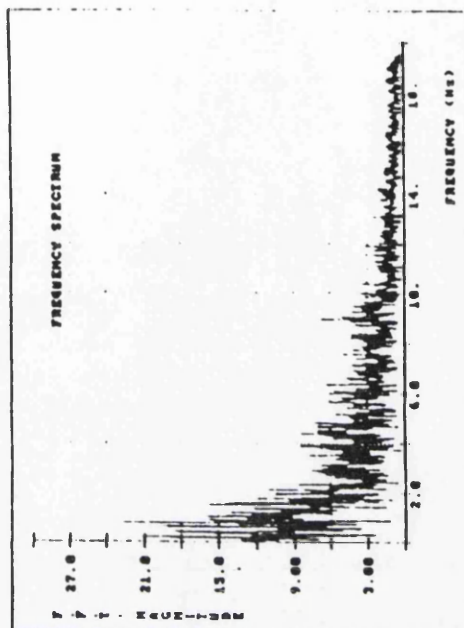
(a) 10mm Downstream



(c) 30mm Downstream

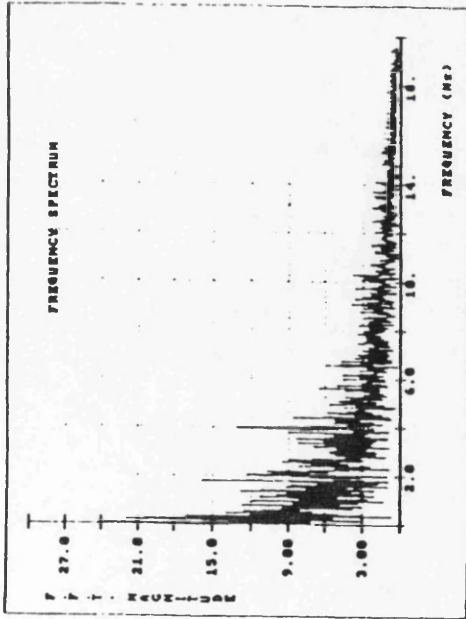


(b) 20mm Downstream

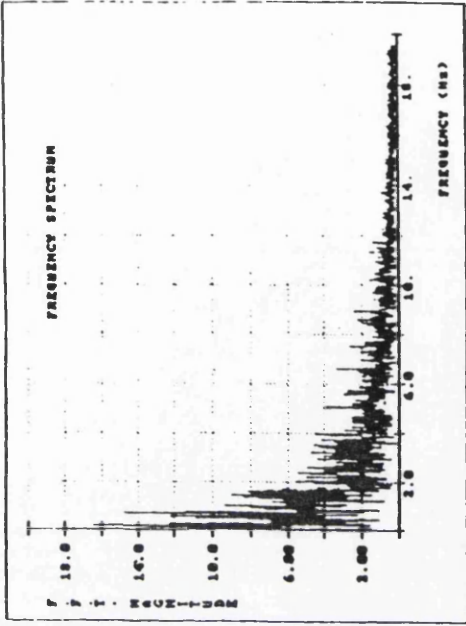


(d) 40mm Downstream

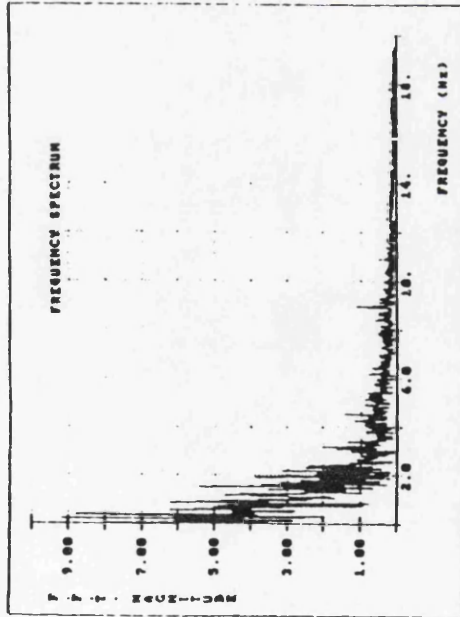
Figure 6-26: Frequency Spectra - 9.75mm Orifice - Rep - 384



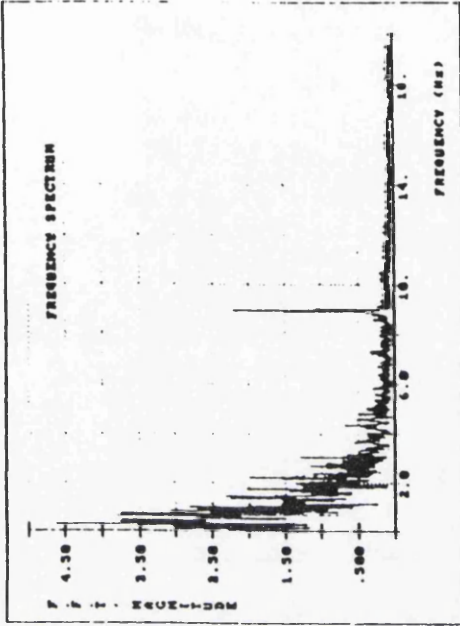
(e) 50mm Downstream



(f) 60mm Downstream

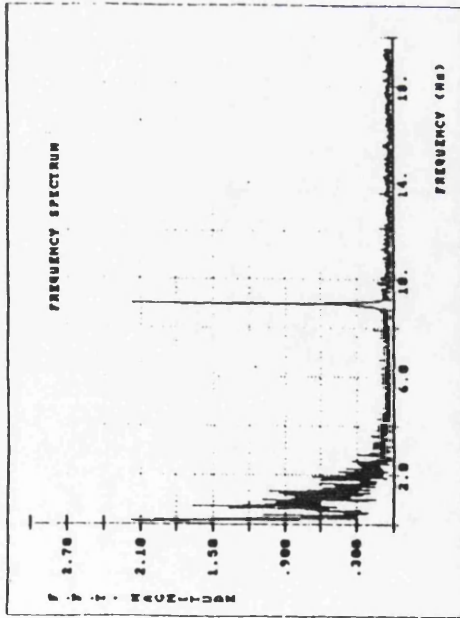


(g) 75mm Downstream

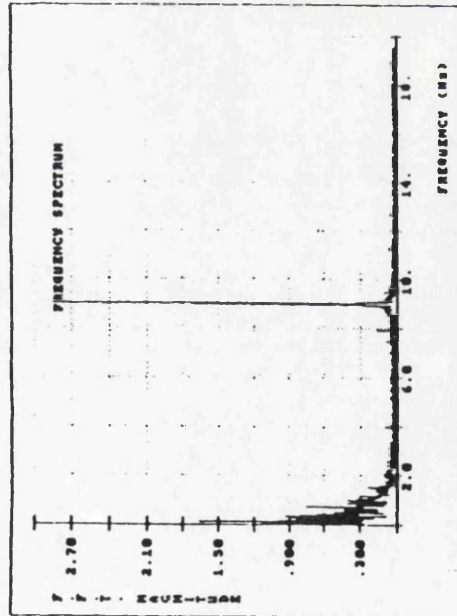


(h) 100mm Downstream

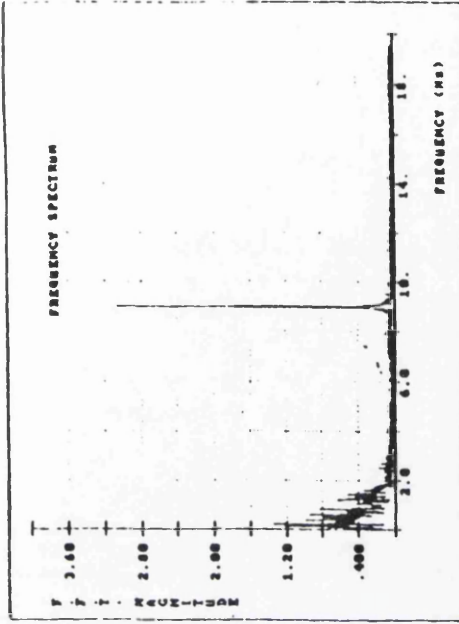
Figure 6-26: Frequency Spectra - 9.75mm Orifice - Rep = 384



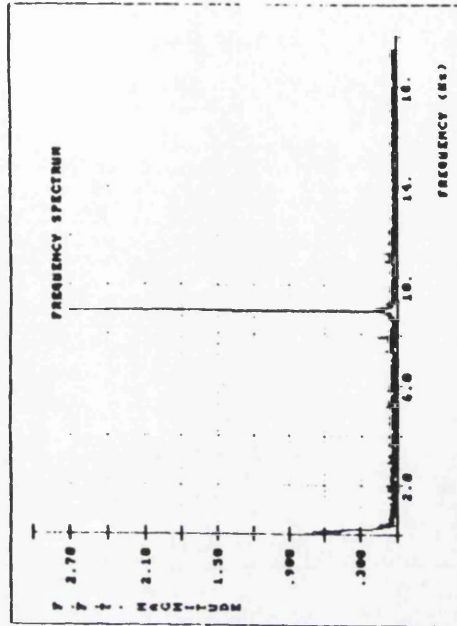
(i) 150mm Downstream



(k) 250mm Downstream

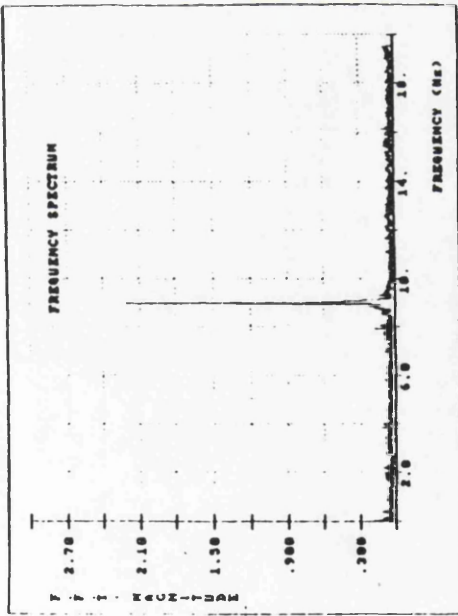


(j) 200mm Downstream



(l) 500mm Downstream

Figure 6-26: Frequency Spectra - 9.75mm Orifice - Rep - 384



(m) 950mm Downstream

Figure 6-26: Frequency Spectra - 9.75mm Orifice - Rep - 384

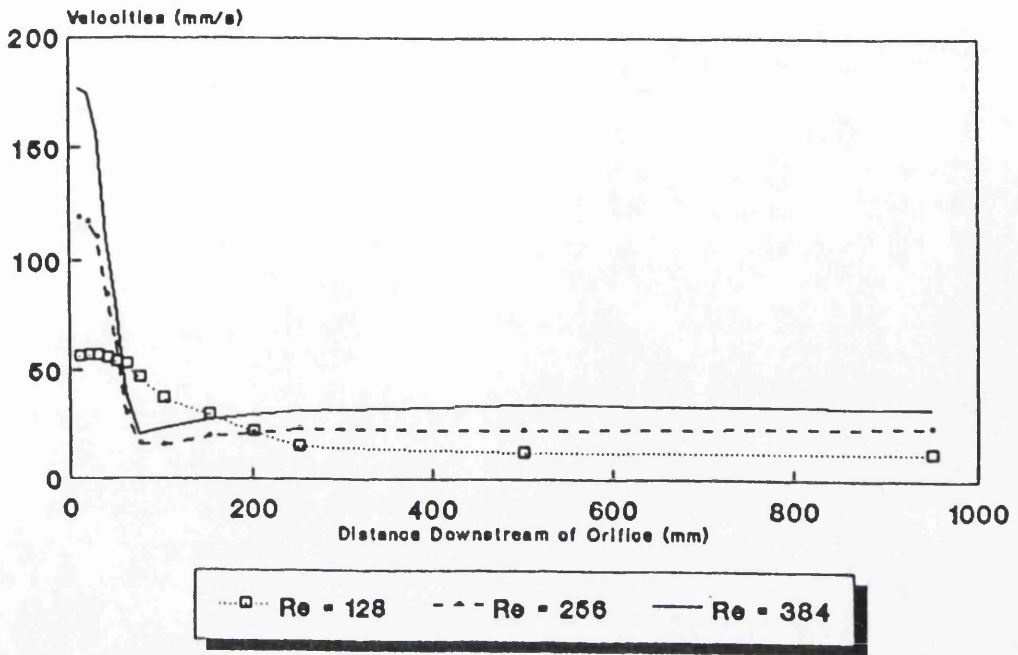


Figure 6-27a: Centreline Velocities - 9.75mm Orifice  
Various Reynolds Numbers

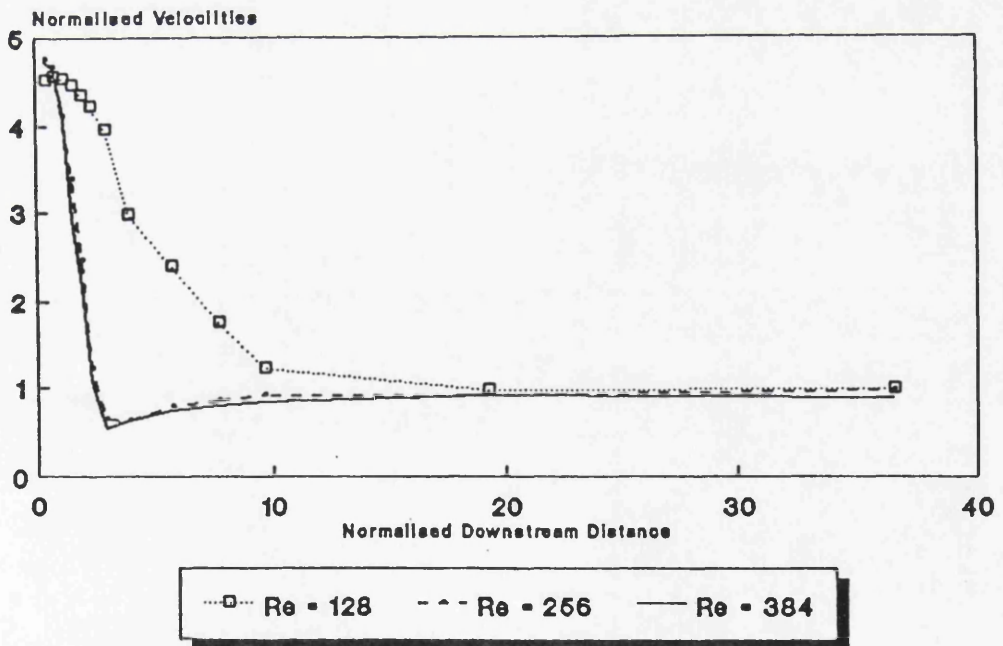


Figure 6-27b: Normalised Centreline Velocities - 9.75mm Orifice  
Various Reynolds Numbers

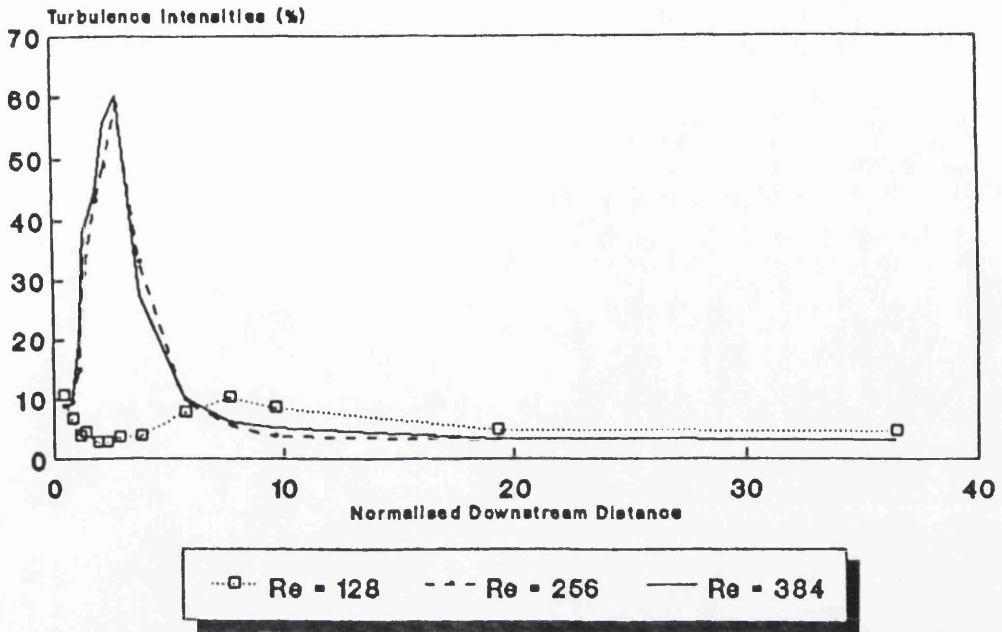


Figure 6-28a: Point-Turbulence Intensities- 9.75mm Orifice  
Various Reynolds Numbers

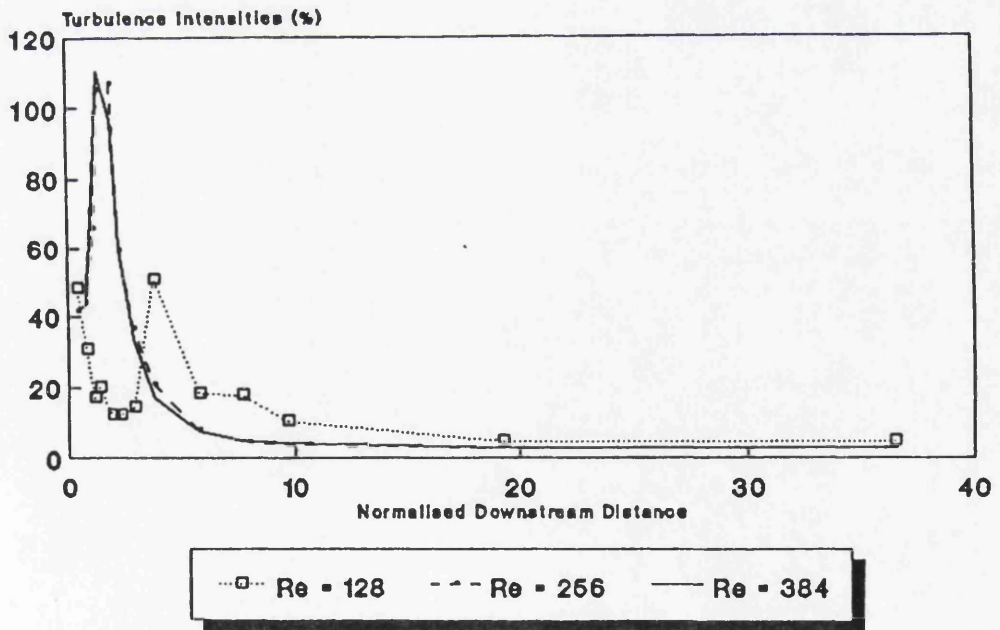


Figure 6-28b: H.G.-Turbulence Intensities - 9.75mm Orifice  
Various Reynolds Numbers

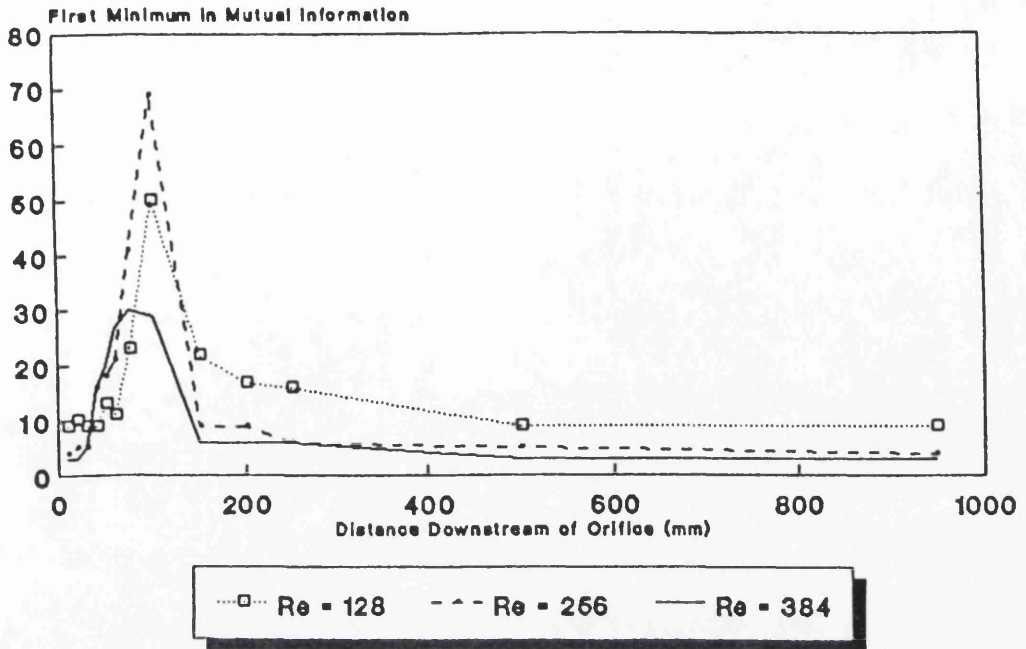


Figure 6-29a: Minimum Mutual Information - 9.75mm Orifice  
Various Reynolds Numbers

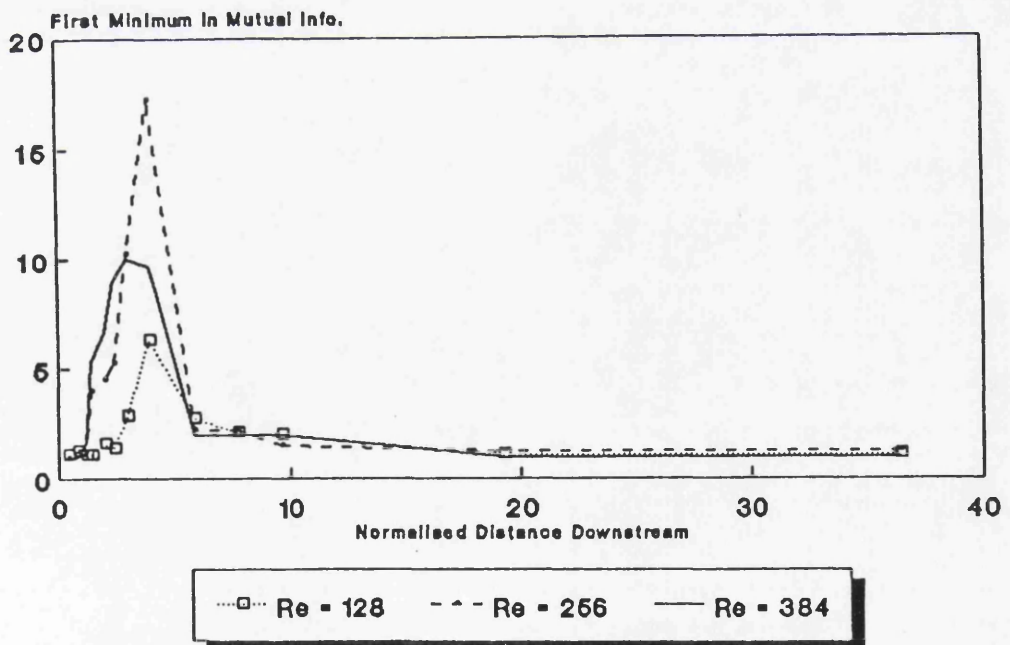
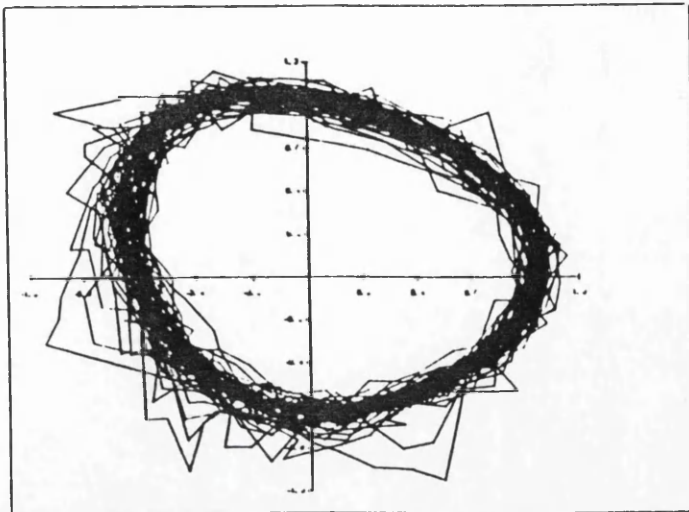
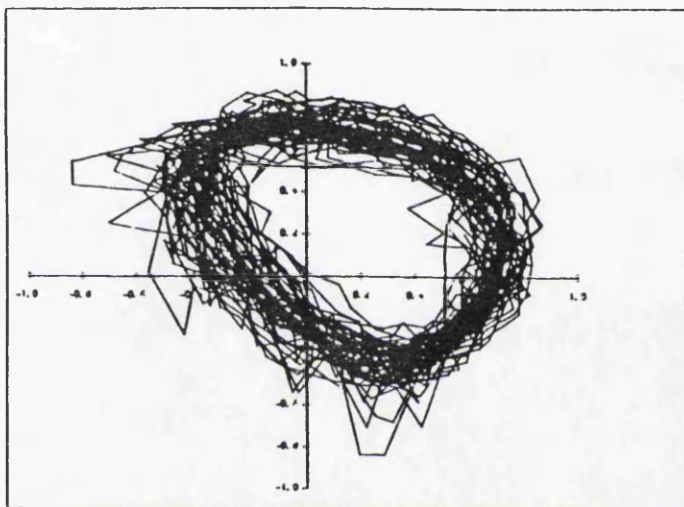


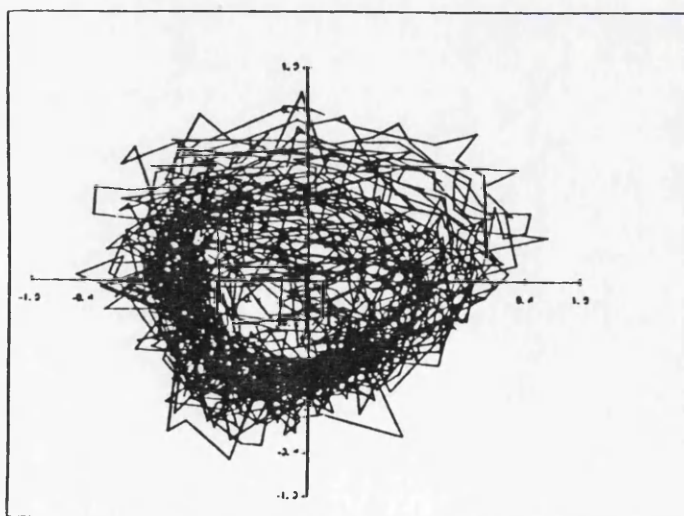
Figure 6-29b: Normalised Minimum Mutual Info.- 9.75mm Orifice  
Various Reynolds Numbers



(a) 10mm Downstream

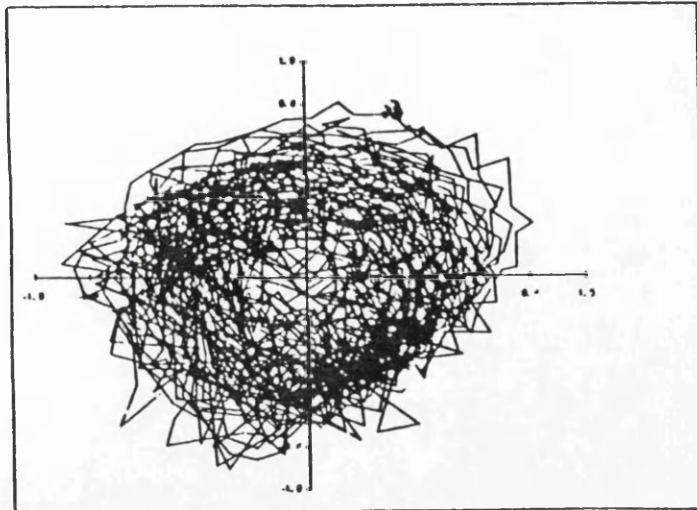


(b) 20mm Downstream

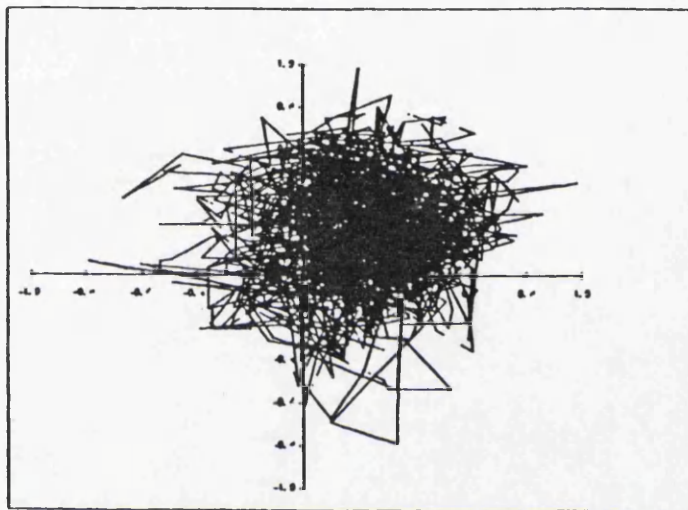


(c) 30mm Downstream

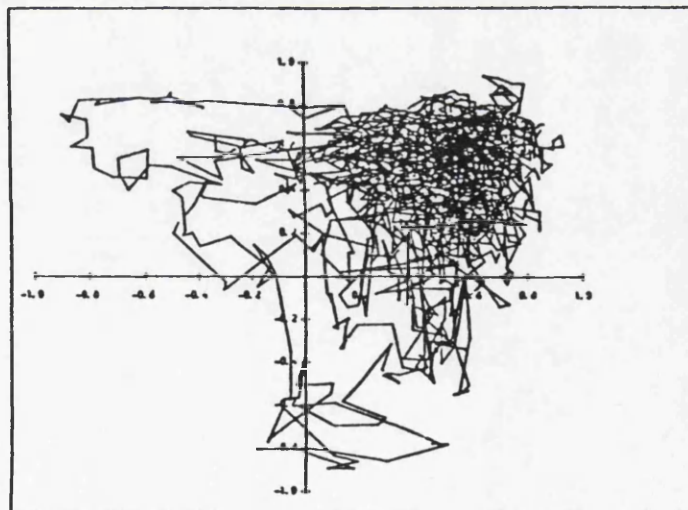
Figure 6-30: Attractor Plots - 9.75mm Orifice -  $Re_p = 128$



(d) 40mm Downstream

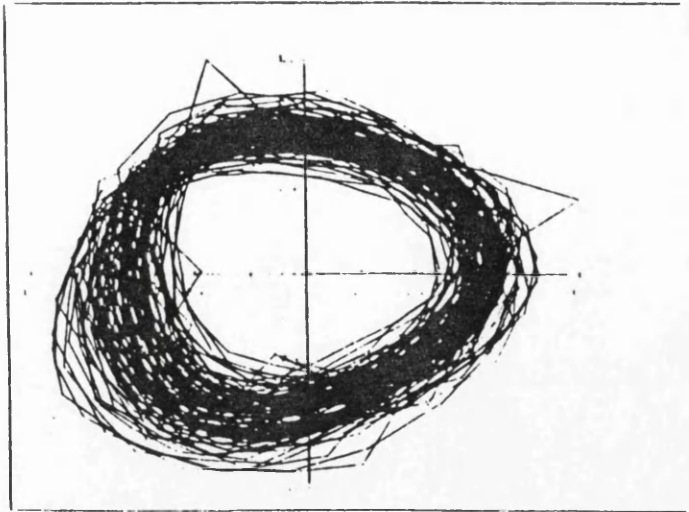


(e) 60mm Downstream

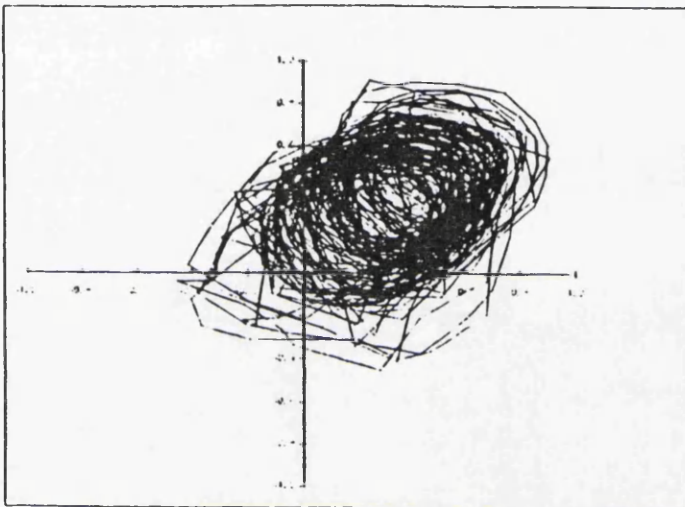


(f) 100mm Downstream

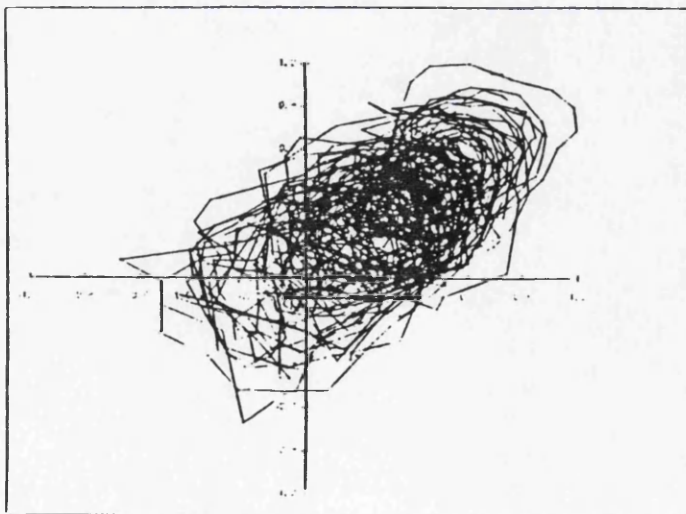
Figure 6-30: Attractor Plots - 9.75mm Orifice -  $Re_p = 128$



(a) 10mm Downstream

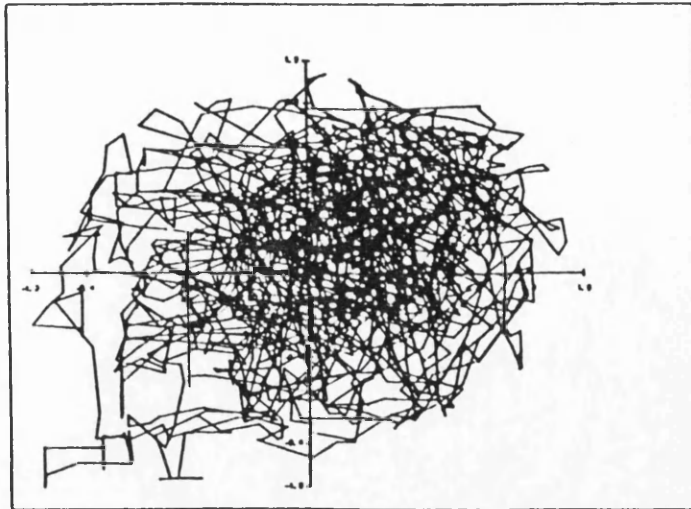


(b) 20mm Downstream



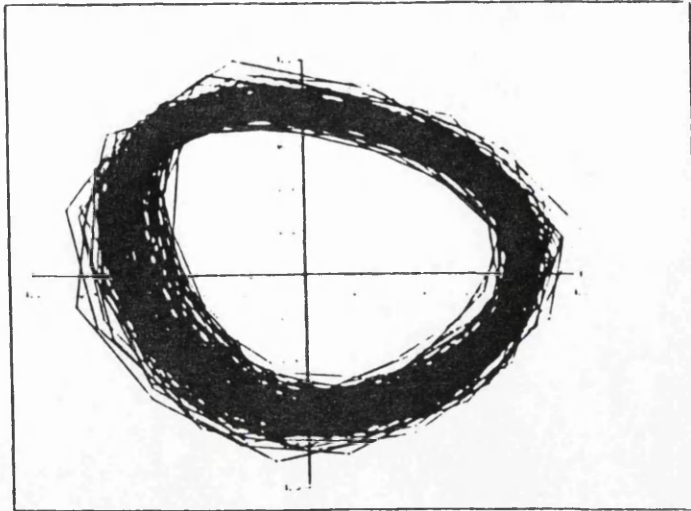
(c) 30mm Downstream

**Figure 6-31: Attractor Plots - 9.75mm Orifice -  $Re_p = 256$**

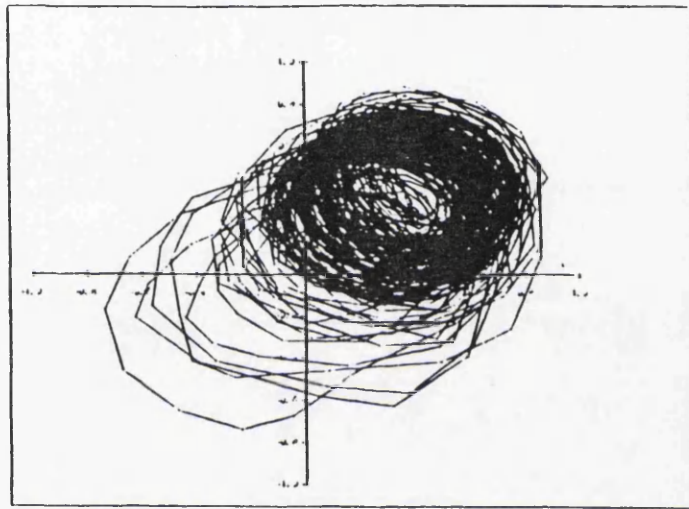


(d) 40mm Downstream

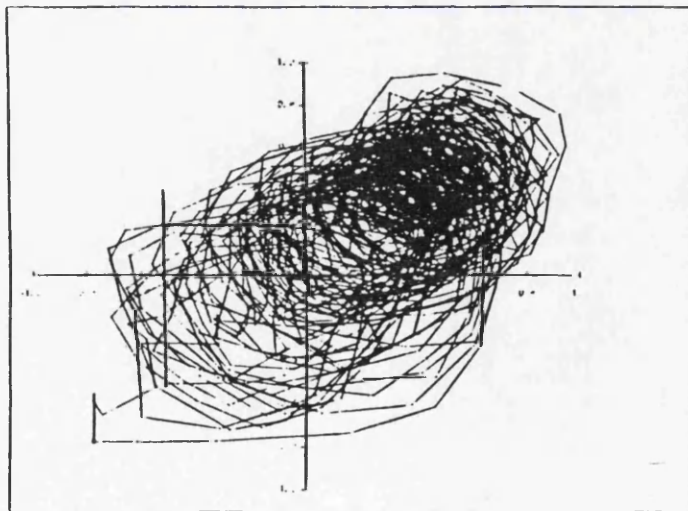
Figure 6-31: Attractor Plots - 9.75mm Orifice -  $Re_p = 256$



(a) 10mm Downstream

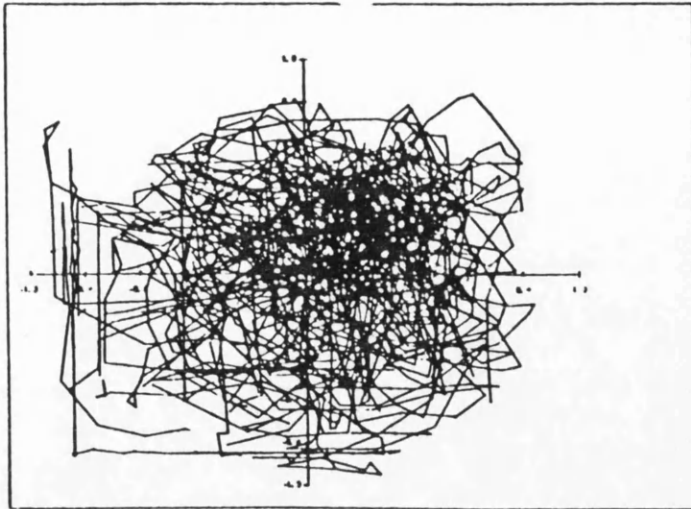


(b) 20mm Downstream



(c) 30mm Downstream

Figure 6-32: Attractor Plots - 9.75mm Orifice -  $Re_p = 384$



(d) 40mm Downstream

Figure 6-32: Attractor Plots - 9.75mm Orifice -  $Re_p = 384$

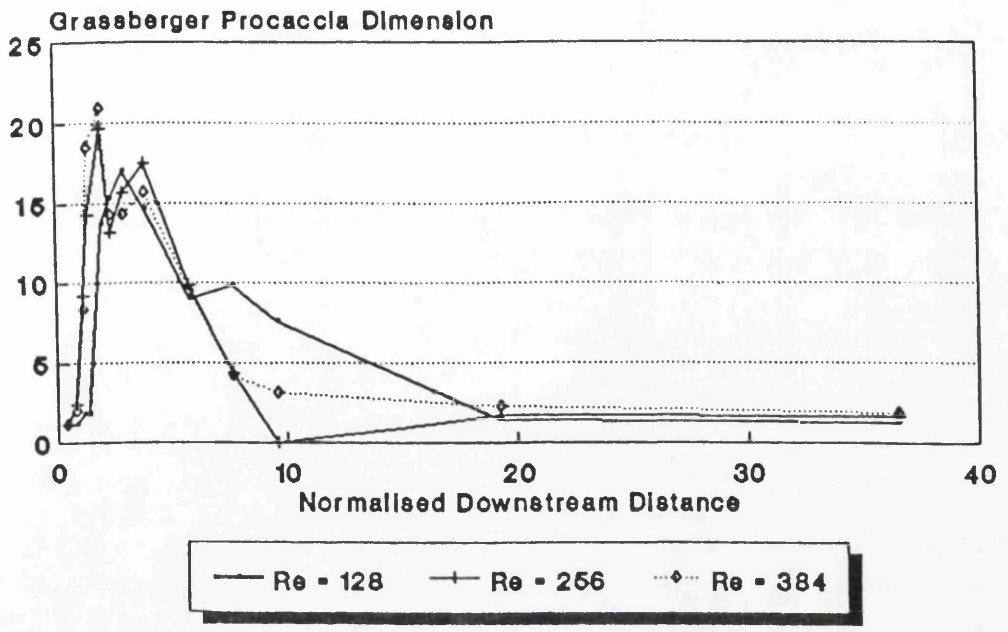


Figure 6-33: Dimension Results - 9.75mm Orifice  
Various Reynolds Numbers

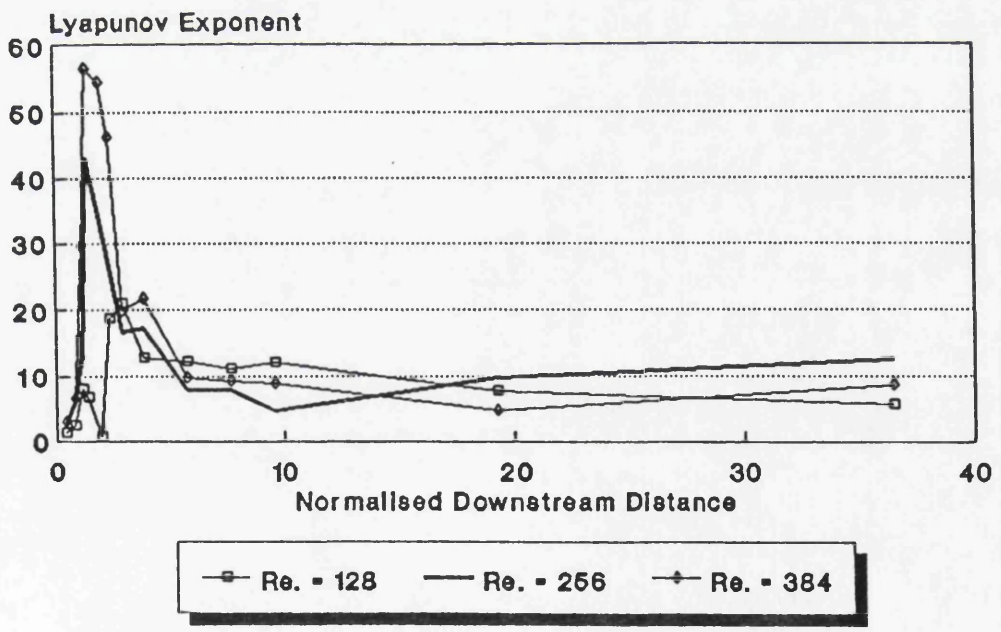
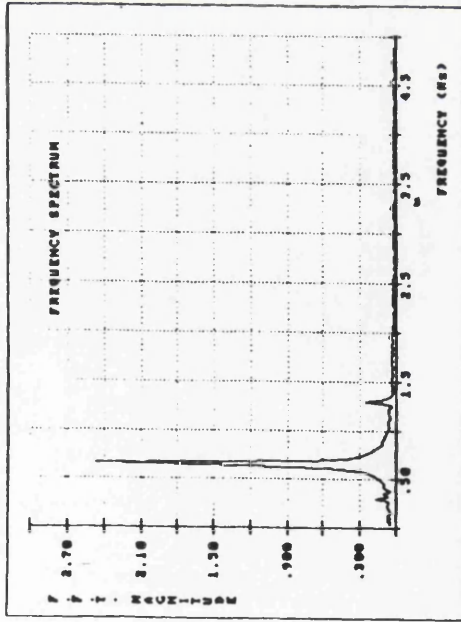
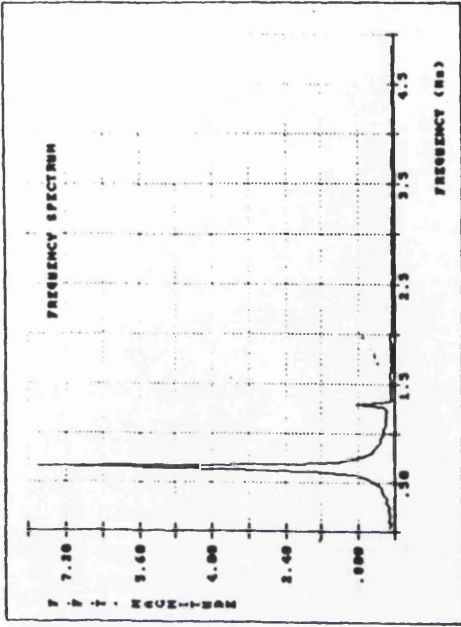


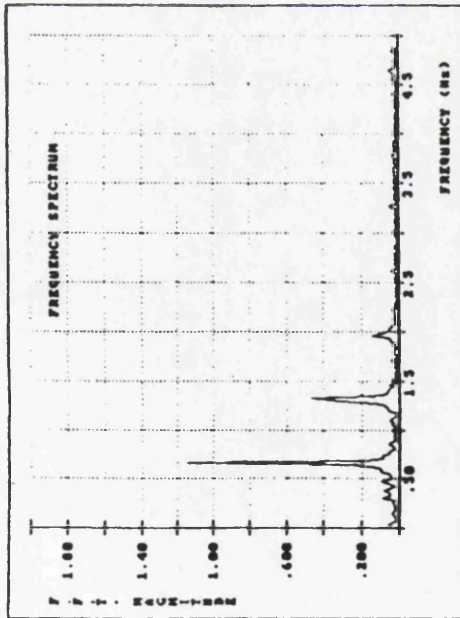
Figure 6-34: Lyapunov Exponent Results - 9.75mm Orifice  
Various Reynolds Numbers



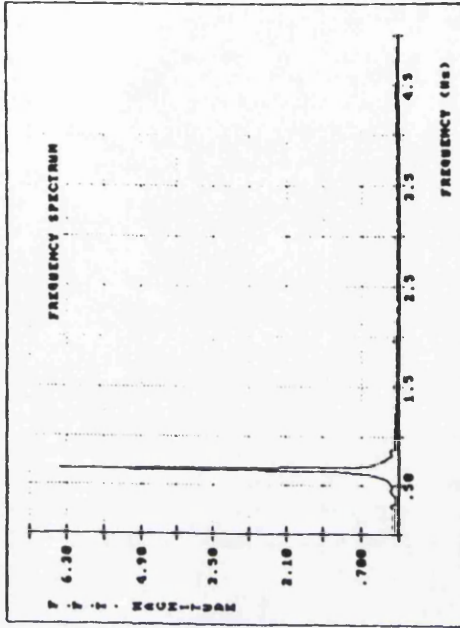
(a) 10mm Downstream



(b) 20mm Downstream

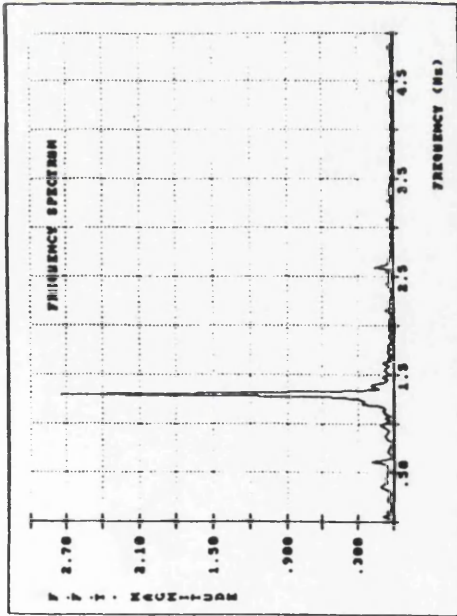


(c) 30mm Downstream

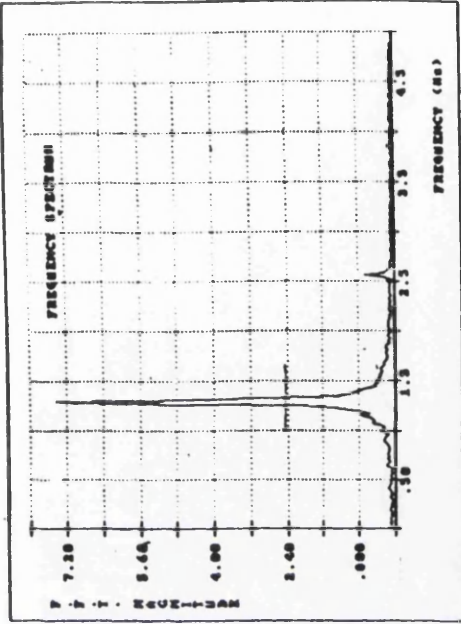


(d) 40mm Downstream

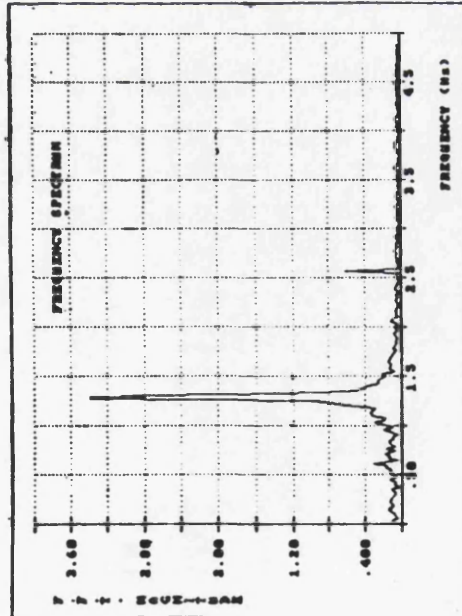
Figure 6-35: Frequency Spectra - 16.25mm Orifice - Rep - 128



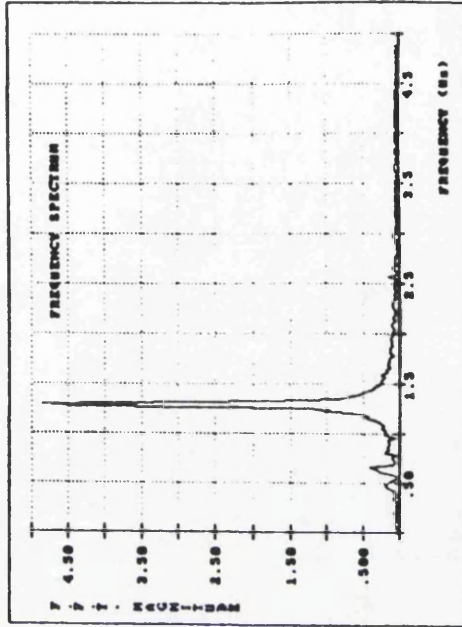
(a) 10mm Downstream



(b) 20mm Downstream

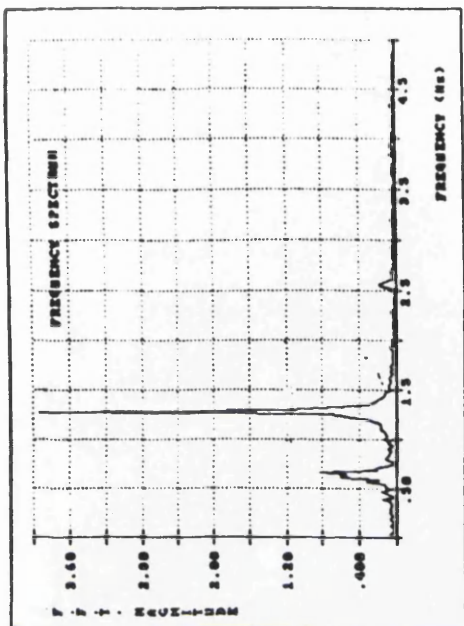


(c) 30mm Downstream

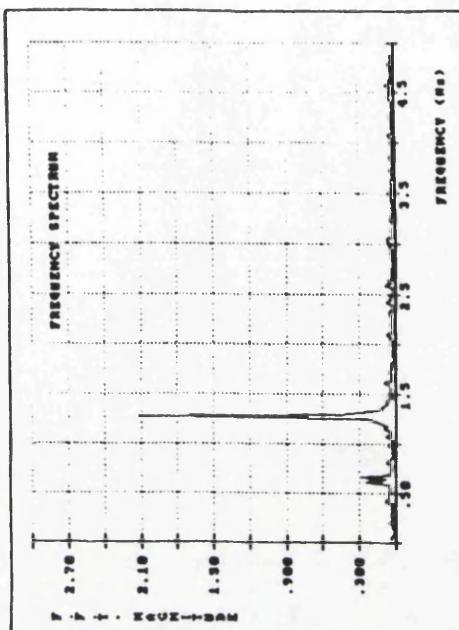


(d) 40mm Downstream

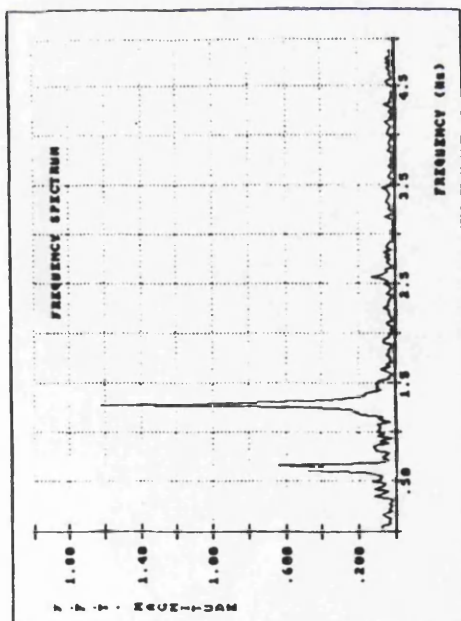
Figure 6-36: Frequency Spectra - 16.25mm Orifice - Rep - 256



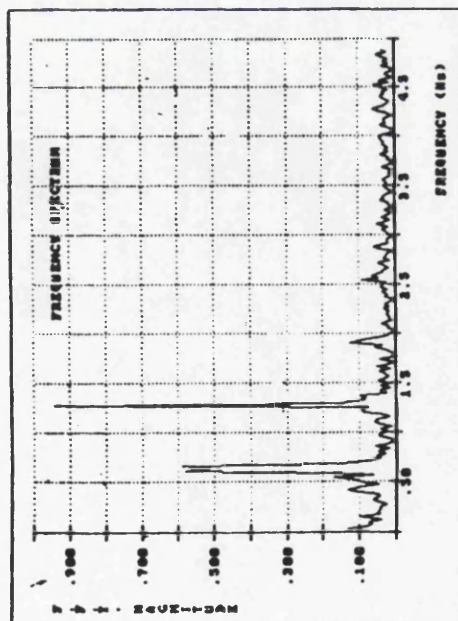
(f) 60mm Downstream



(h) 100mm Downstream

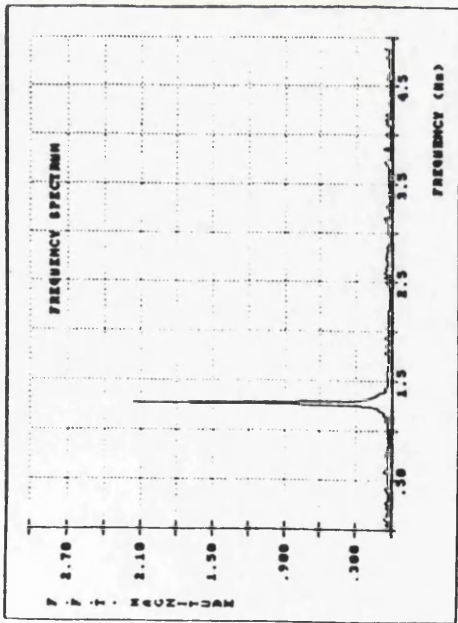


(e) 50mm Downstream

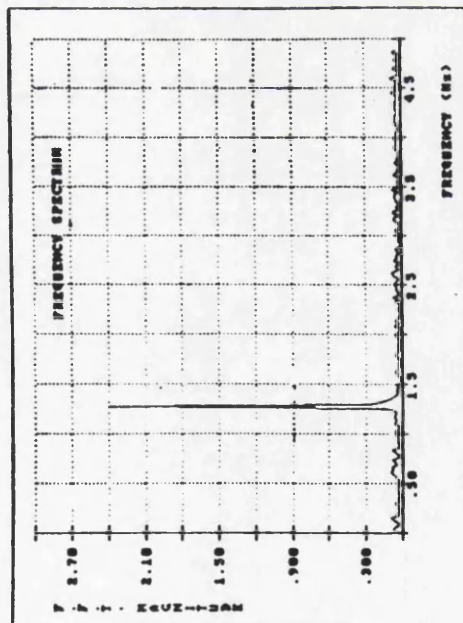


(g) 75mm Downstream

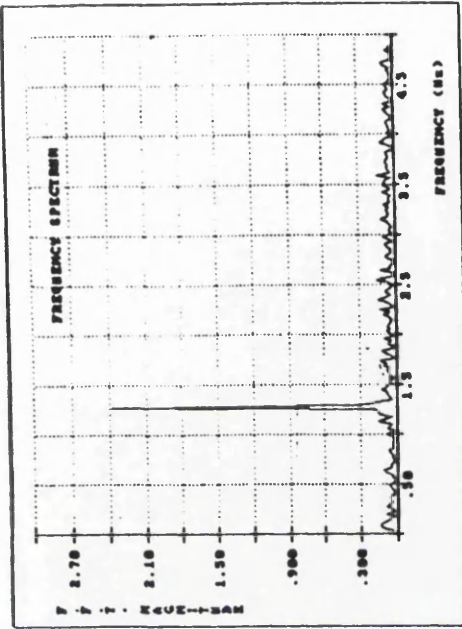
Figure 6-36: Frequency Spectra - 16.25mm Orifice - Rep - 256



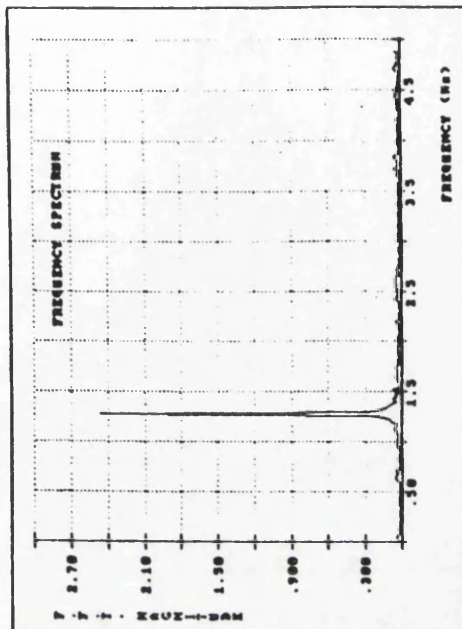
(i) 150mm Downstream



(k) 250mm Downstream

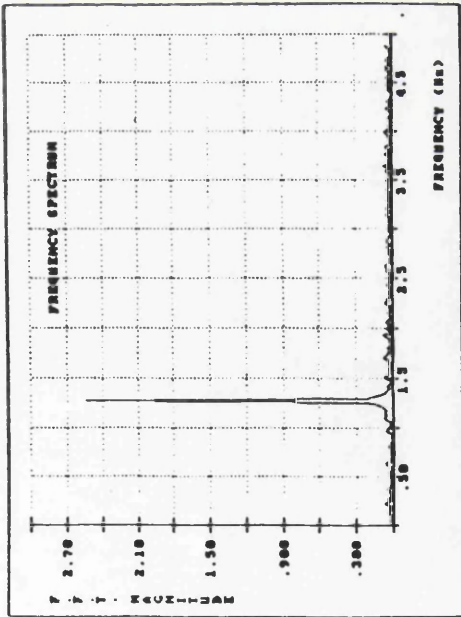


(j) 200mm Downstream



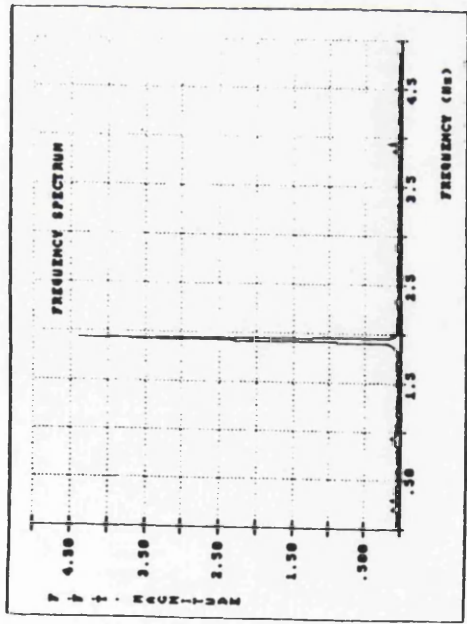
(l) 500mm Downstream

Figure 6-36: Frequency Spectra - 16.25mm Orifice -  $Re_p = 256$

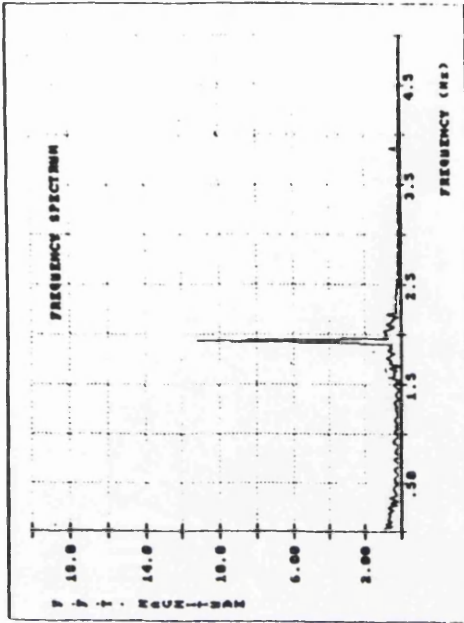


(m) 950mm Downstream

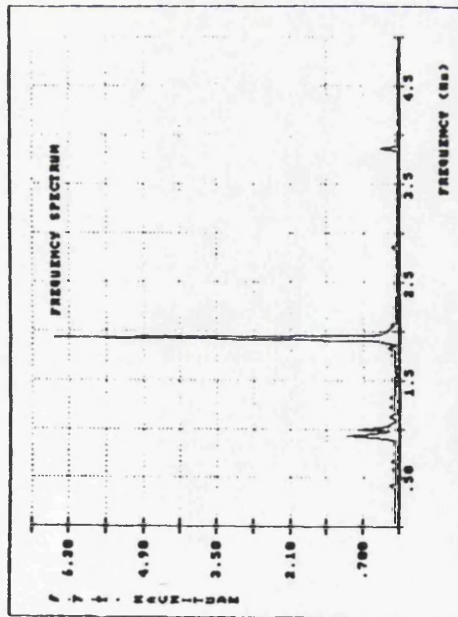
Figure 6-36: Frequency Spectra - 16.25mm Orifice - Rep - 256



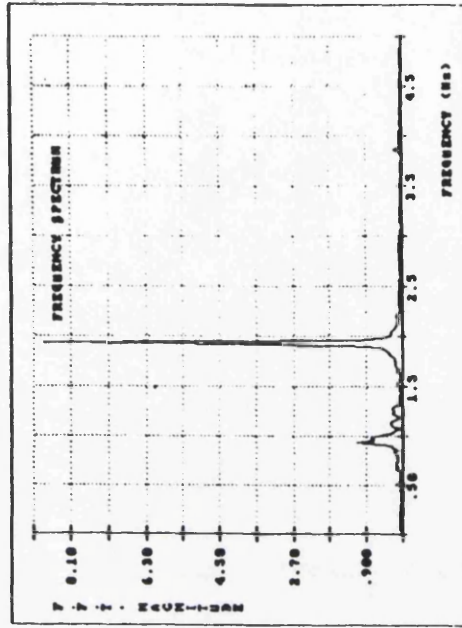
(a) 10mm Downstream



(b) 20mm Downstream

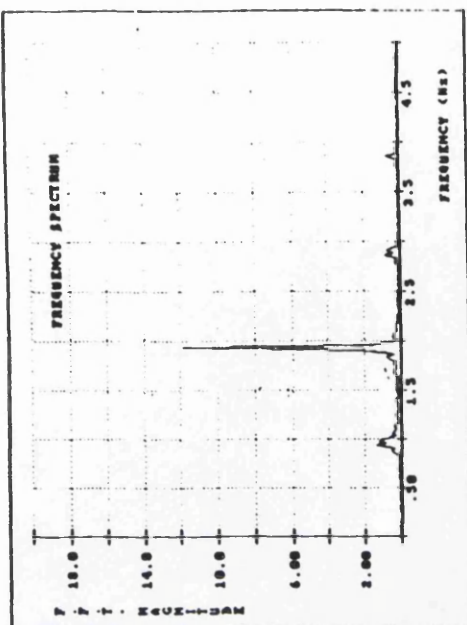


(c) 30mm Downstream

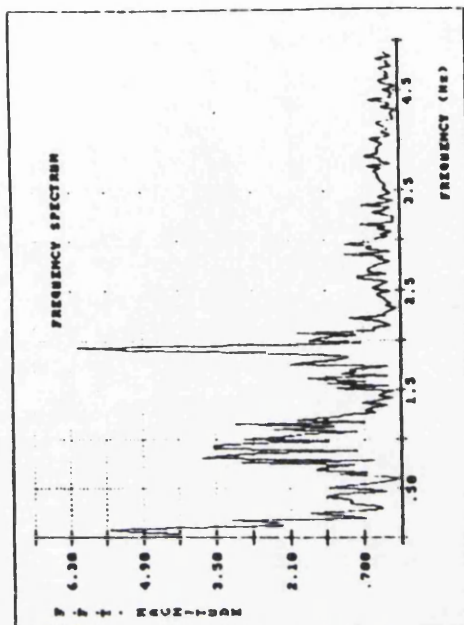


(d) 40mm Downstream

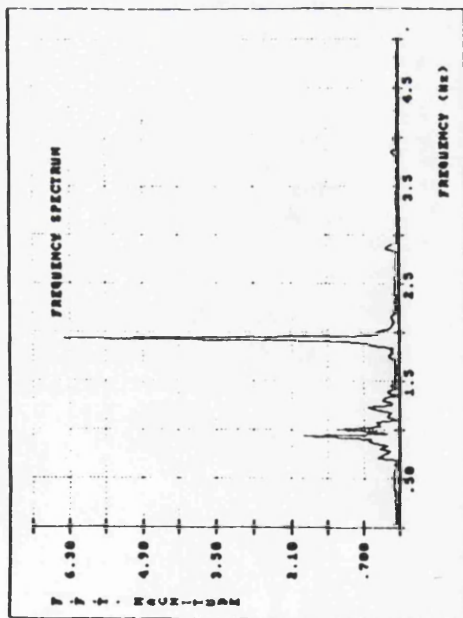
Figure 6-37: Frequency Spectra - 16.25mm Orifice - Re<sub>p</sub> = 384



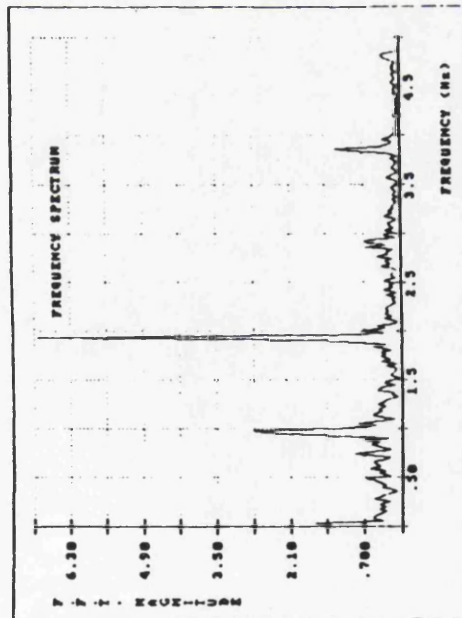
(f) 60mm Downstream



(h) 100mm Downstream

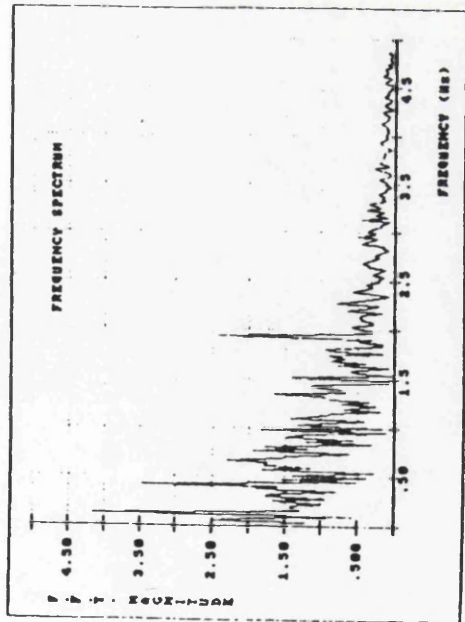


(e) 50mm Downstream

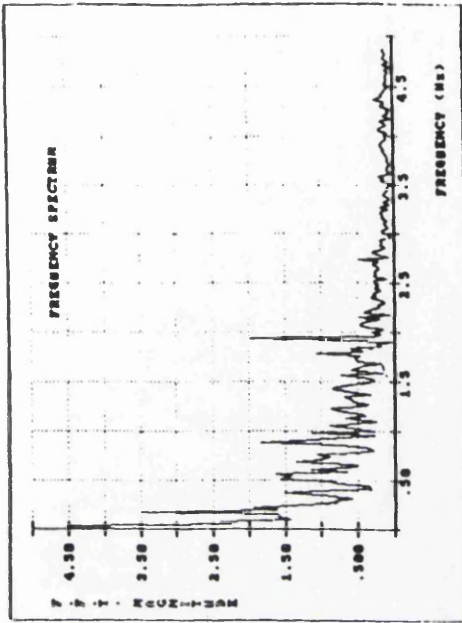


(g) 75mm Downstream

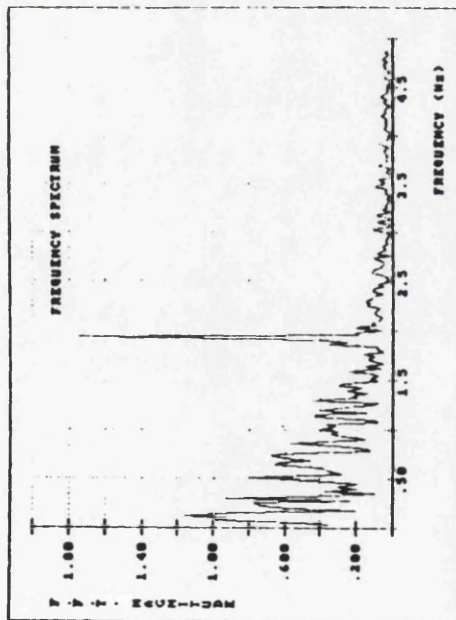
Figure 6-37: Frequency Spectra - 16.25mm Orifice -  $Re_p = 384$



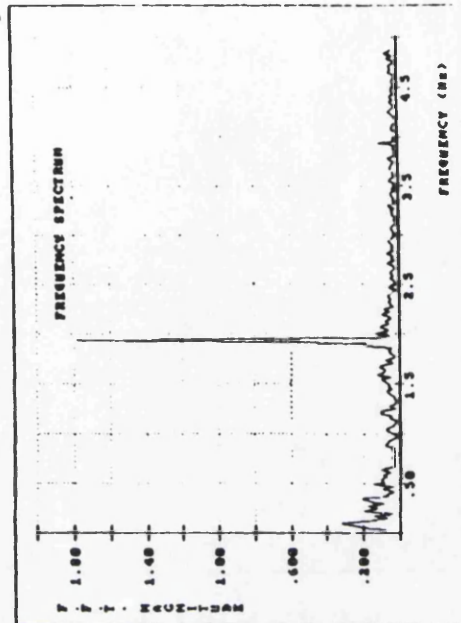
(i) 150mm Downstream



(j) 200mm Downstream

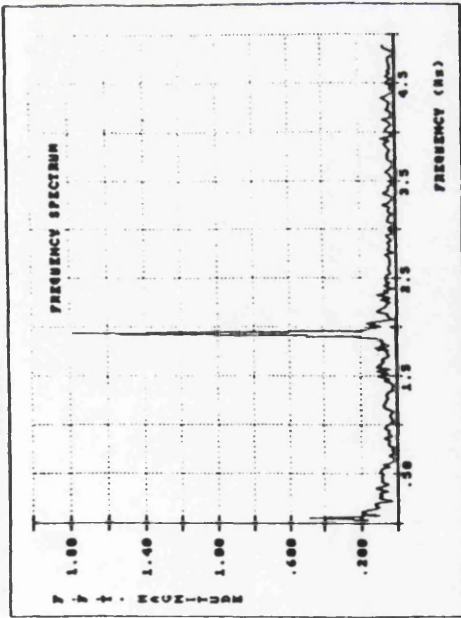


(k) 250mm Downstream



(l) 500mm Downstream

Figure 6-37: Frequency Spectra - 16.25mm Orifice - Rep - 384



(m) 950mm Downstream

Figure 6-37: Frequency Spectra - 16.25mm Orifice - Rep - 384

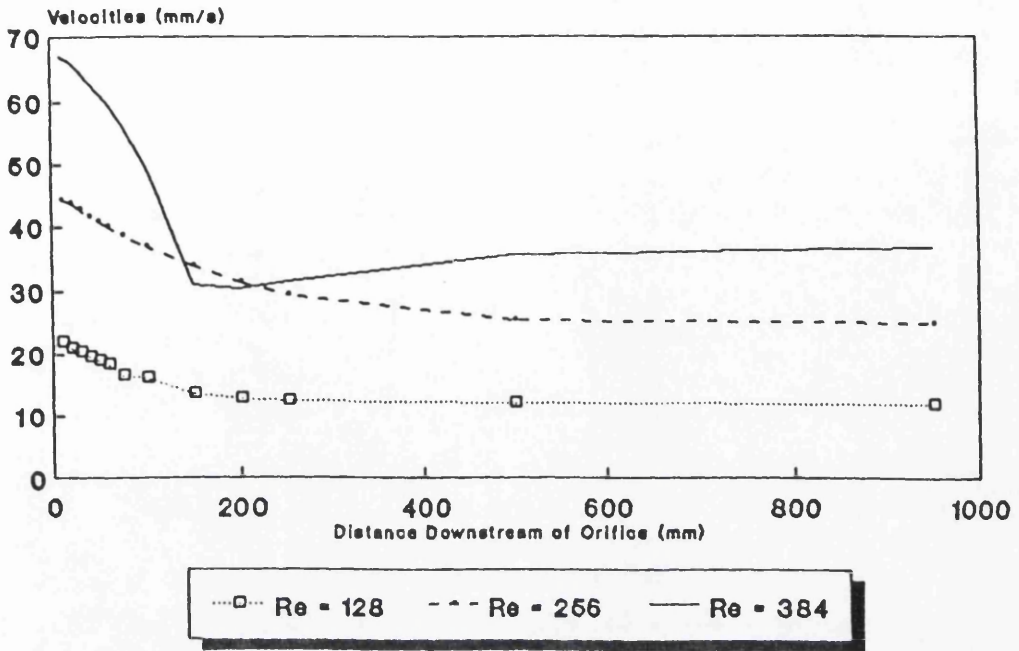


Figure 6-38a: Centreline Velocities - 16.25mm Orifice  
Various Reynolds Numbers

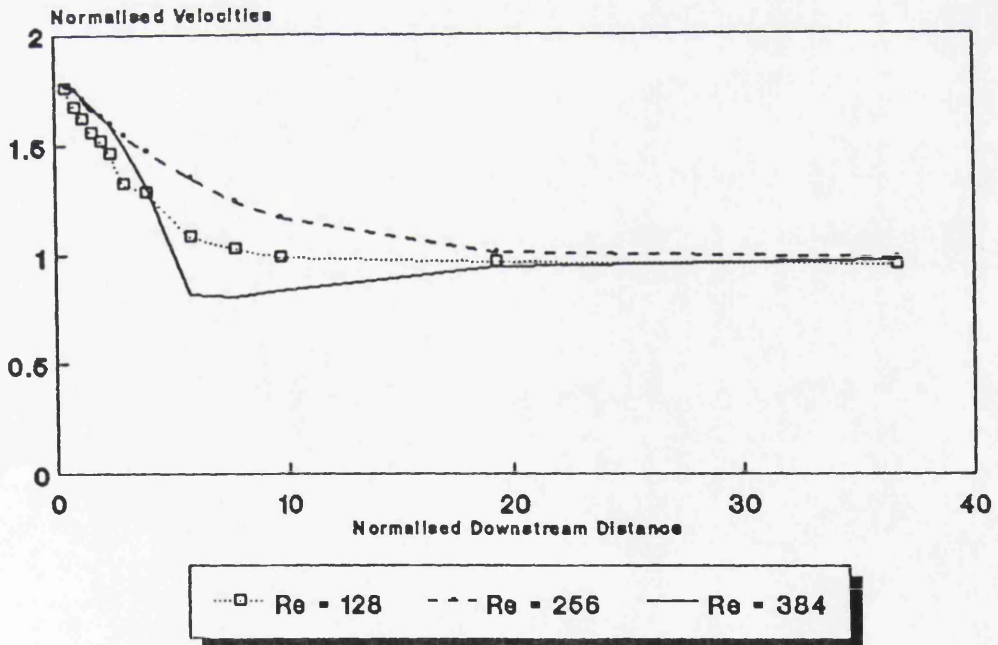


Figure 6-38b: Normalised Centreline Velocities -16.25mm Orifice  
Various Reynolds Numbers

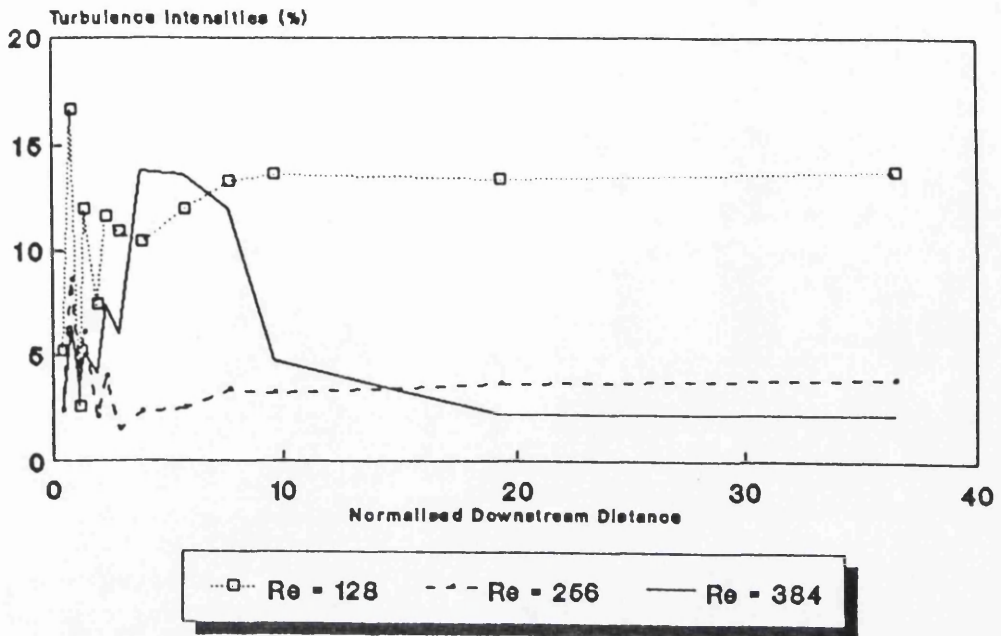


Figure 6-39a: Point-Turbulence Intensities- 16.25mm Orifice  
Various Reynolds Numbers

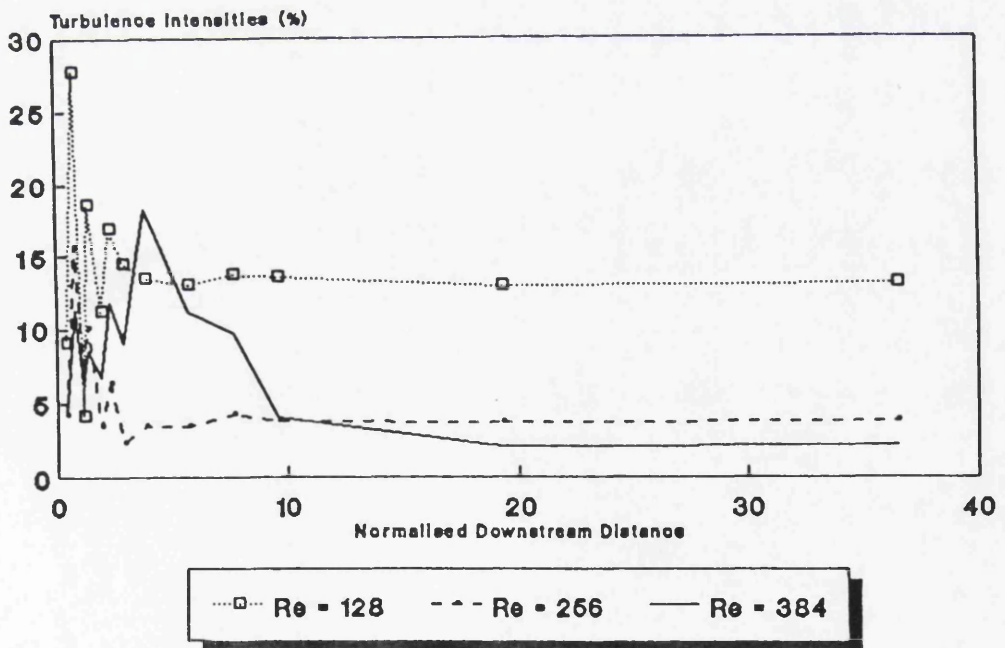


Figure 6-39b: H.C.-Turbulence Intensities - 16.25mm Orifice  
Various Reynolds Numbers

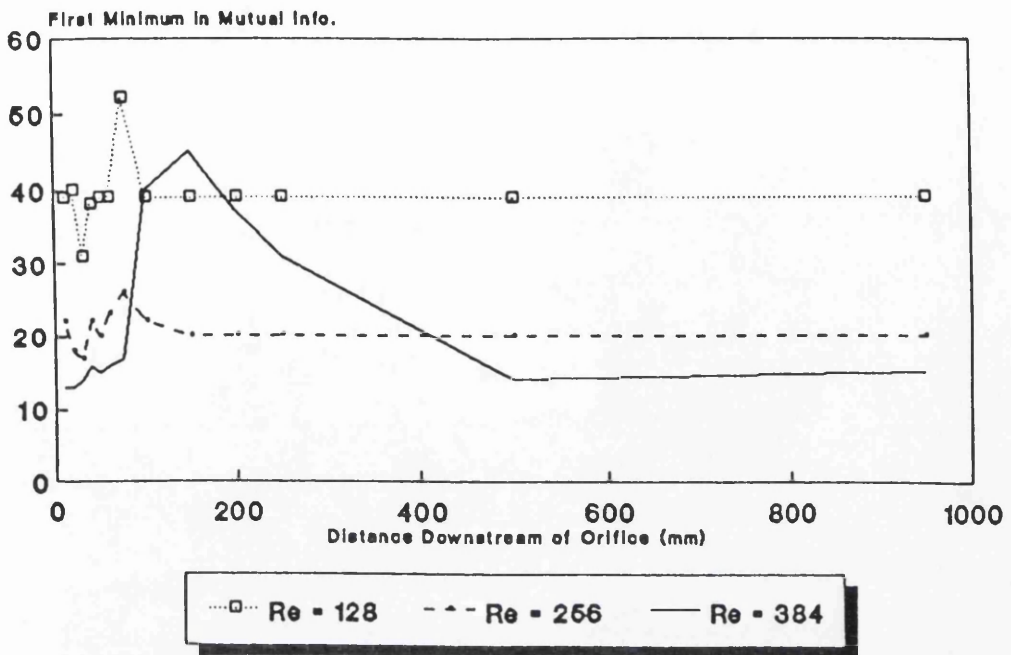


Figure 6-40a: Minimum Mutual Information - 16.25mm Orifice  
Various Reynolds Numbers

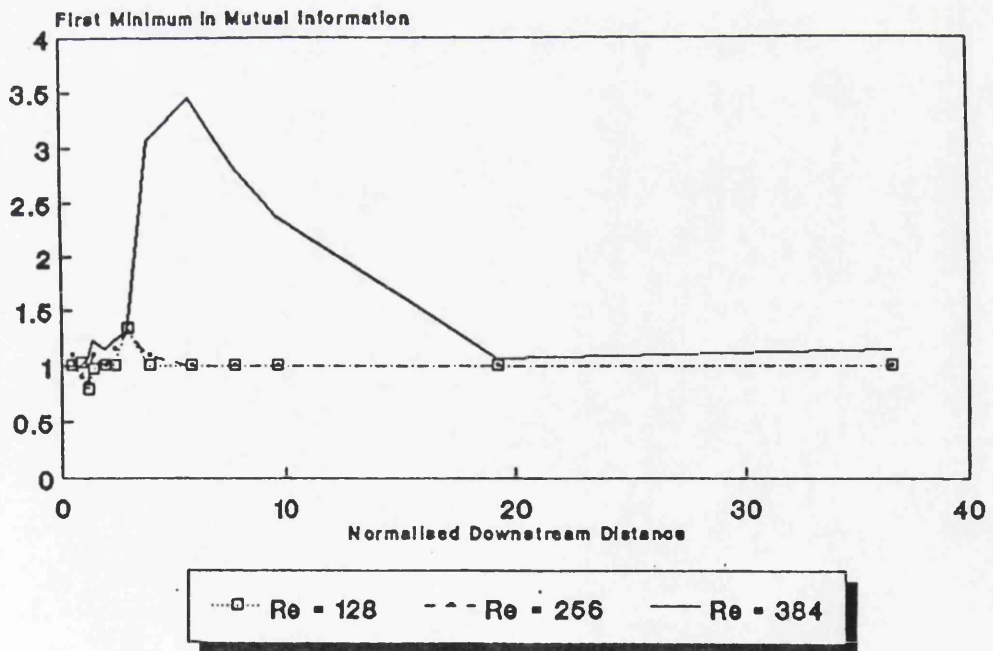
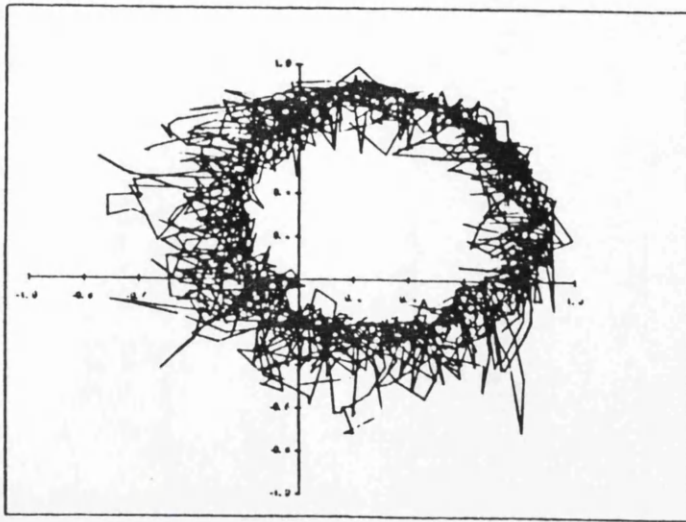
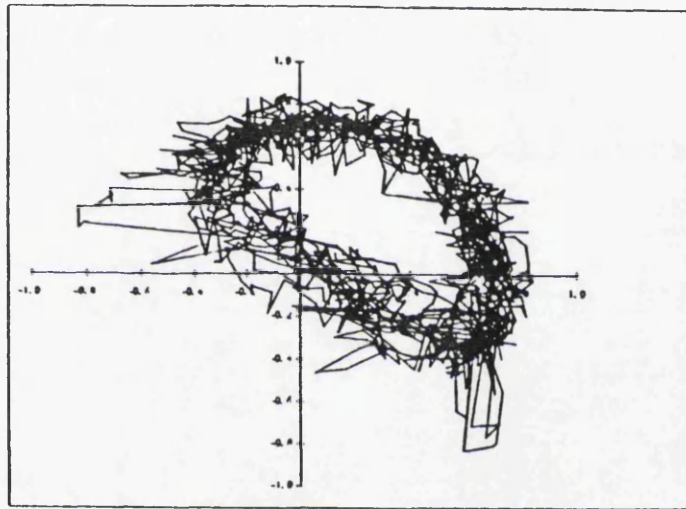


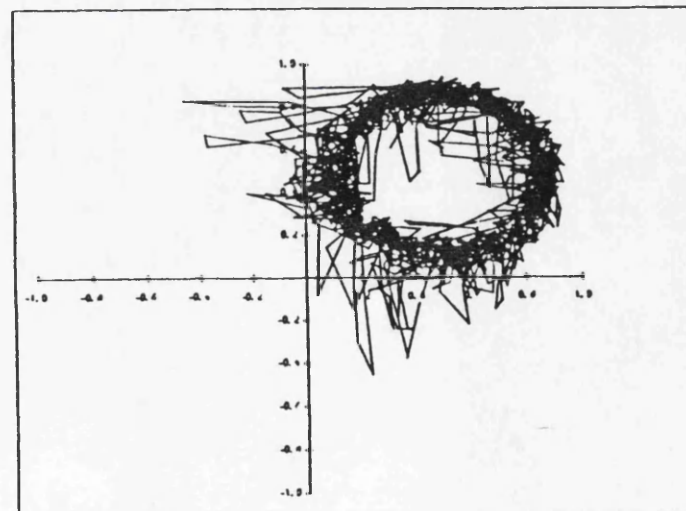
Figure 6-40b: Normalised Minimum Mutual Info.- 16.25mm Orifice  
Various Reynolds Numbers



(a) 60mm Downstream

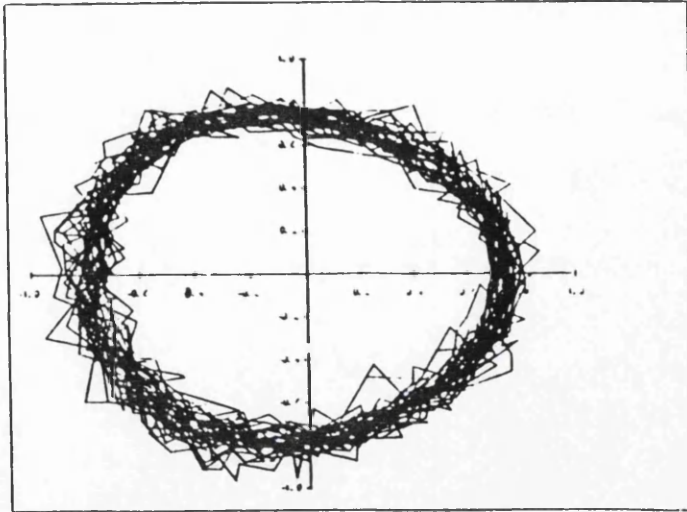


(b) 75mm Downstream

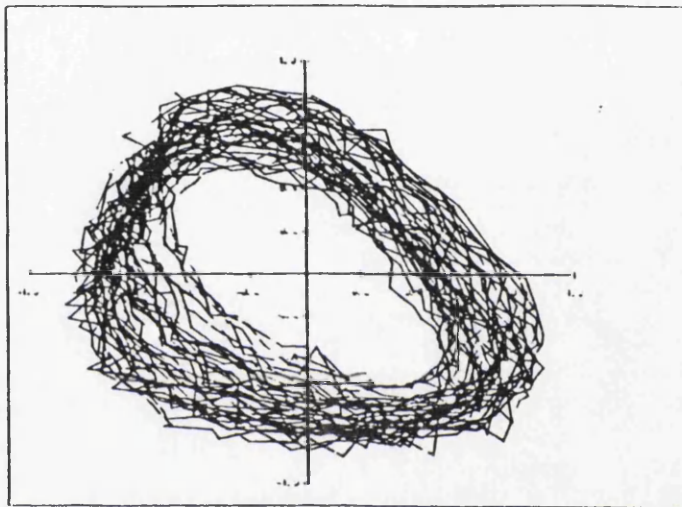


(c) 100mm Downstream

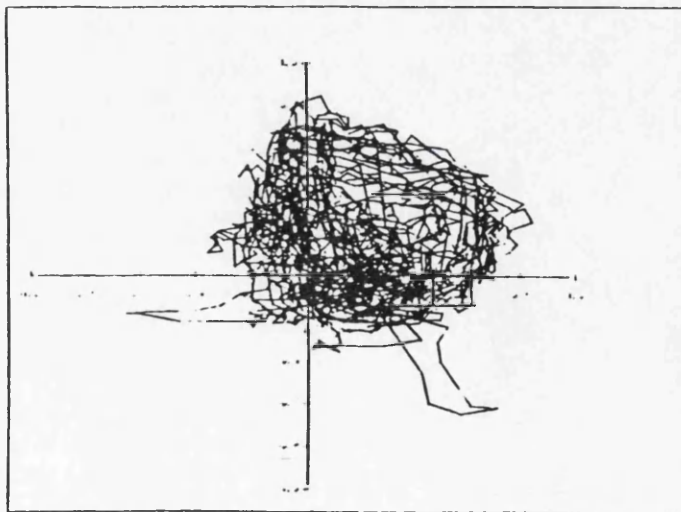
Figure 6-41: Attractor Plots - 16.25mm Orifice -  $Re_p = 128$



(a) 20mm Downstream



(b) 60mm Downstream



(c) 75mm Downstream

Figure 6-42: Attractor Plots - 16.25mm Orifice -  $Re_p = 384$

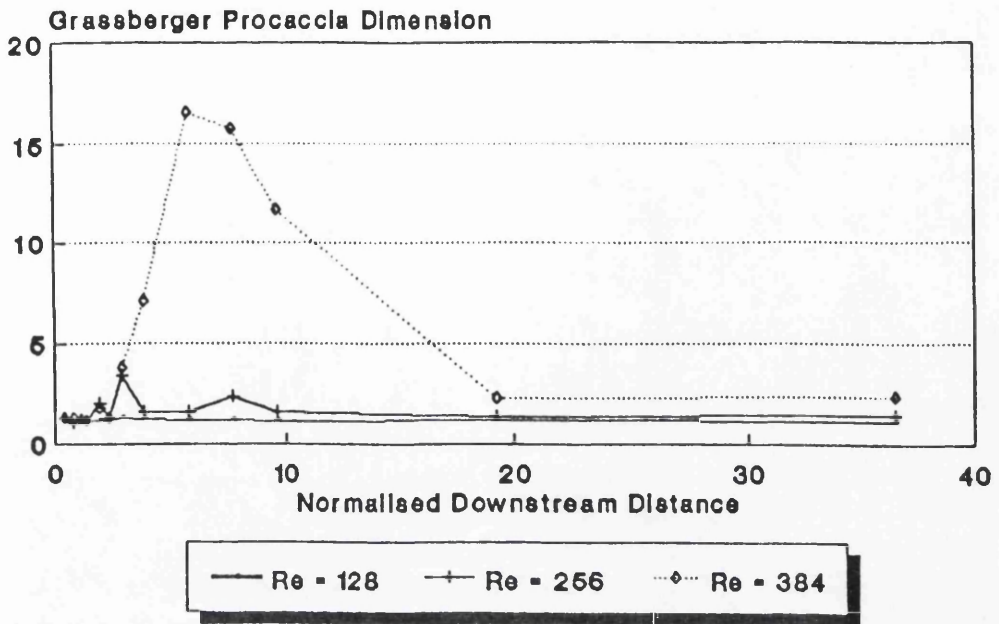


Figure 6-43: Dimension Results - 16.25mm Orifice  
Various Reynolds Numbers

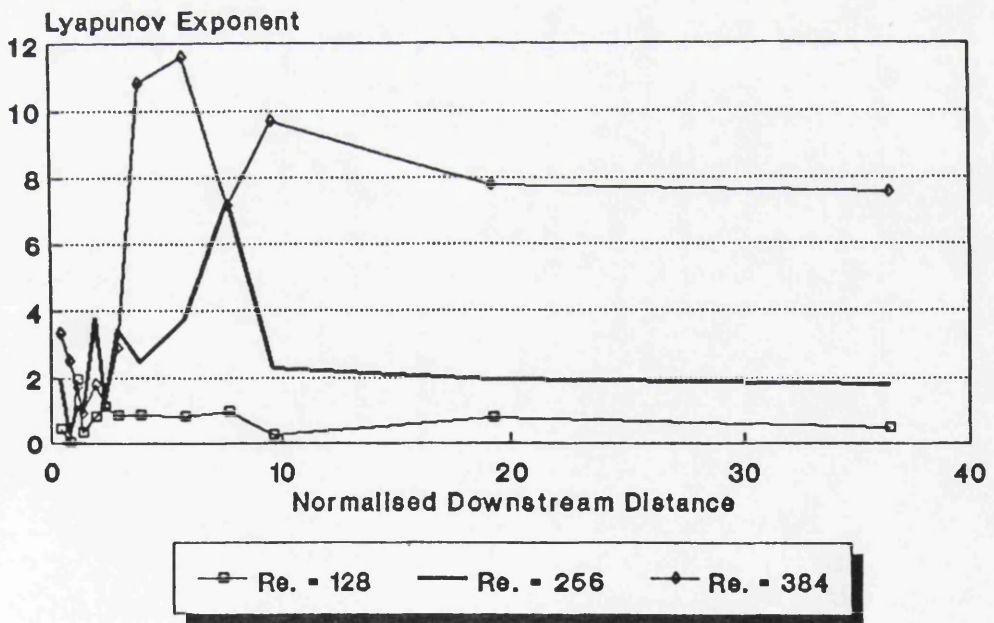


Figure 6-44: Lyapunov Exponent Results - 9.75mm Orifice  
Various Reynolds Numbers

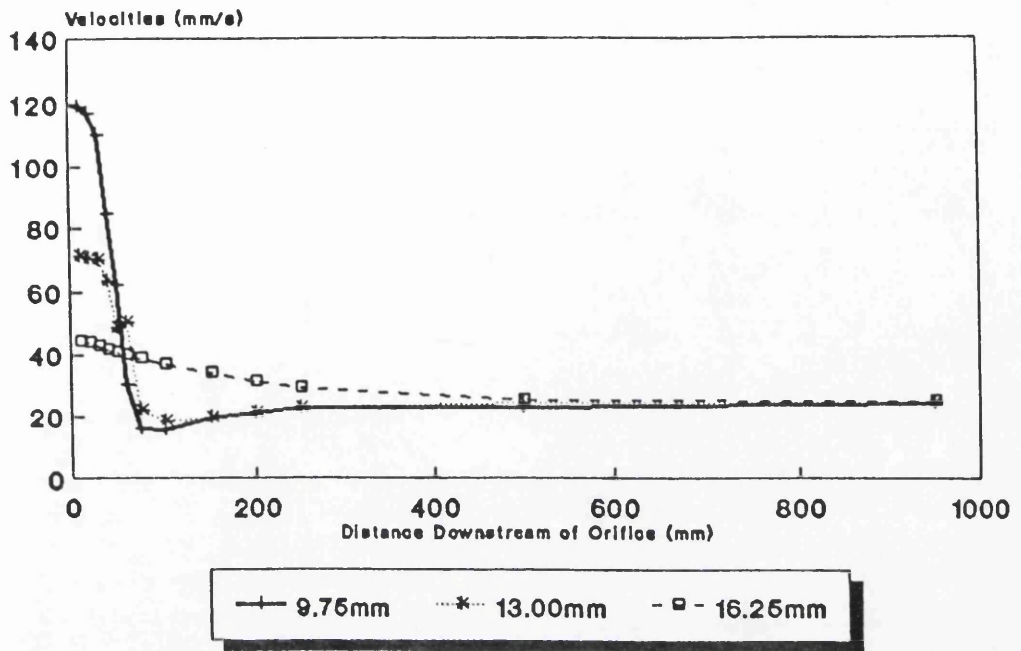


Figure 6-45: Centreline Velocities -  $Re_p = 256$   
 9.75, 13.00 & 16.25mm Orifice Plates

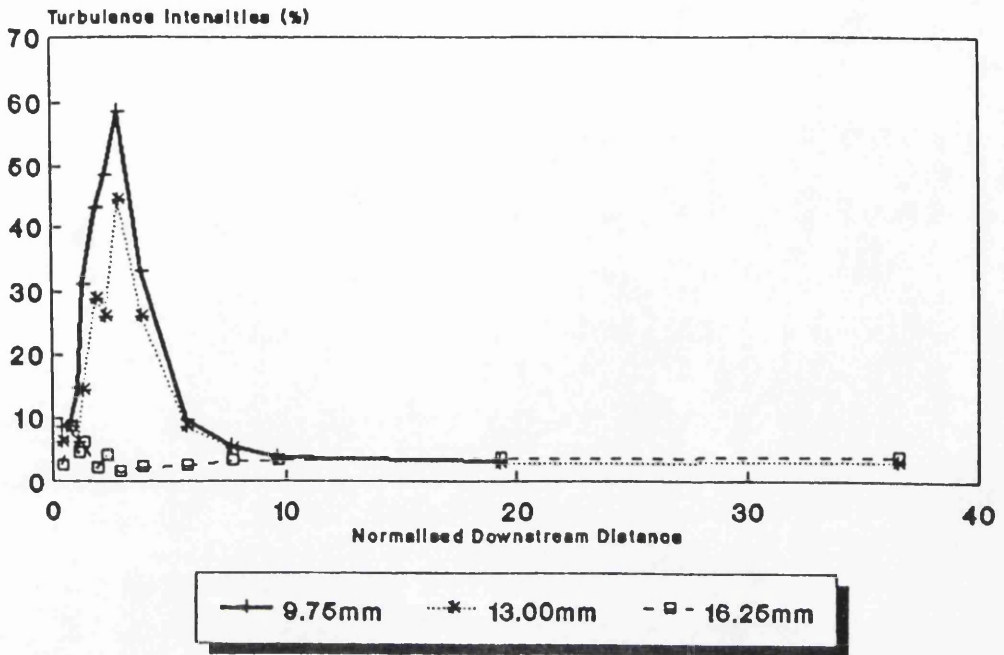


Figure 6-46a: Point-Turbulence Intensities -  $Re_p = 256$   
 9.75, 13.00 & 16.25mm Orifice Plates

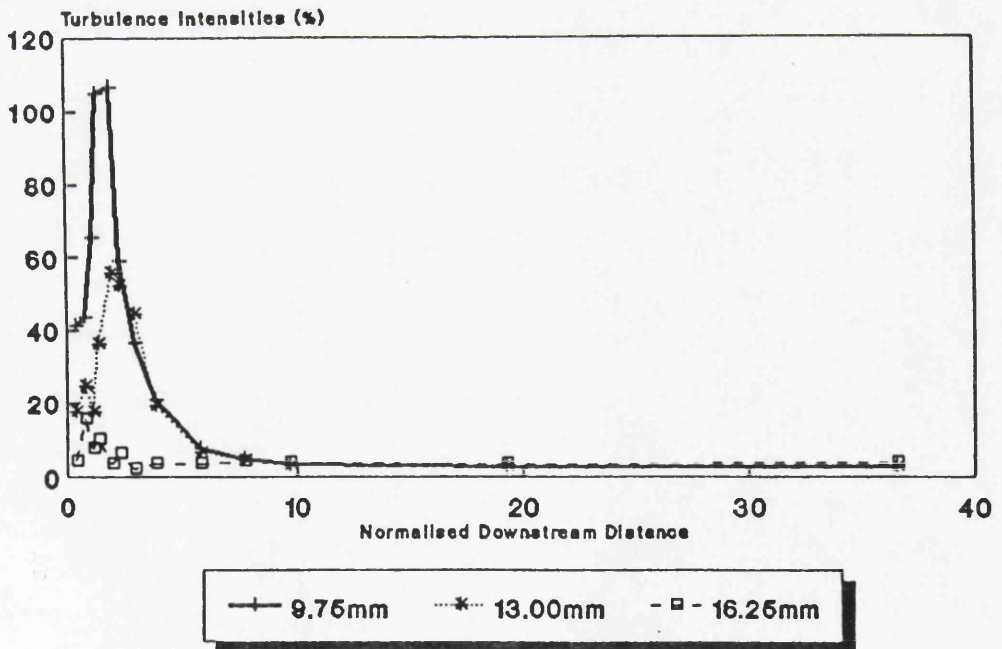


Figure 6-46b: H.G.-Turbulence Intensities -  $Re_p = 256$   
 9.75, 13.00 & 16.25mm Orifice Plates

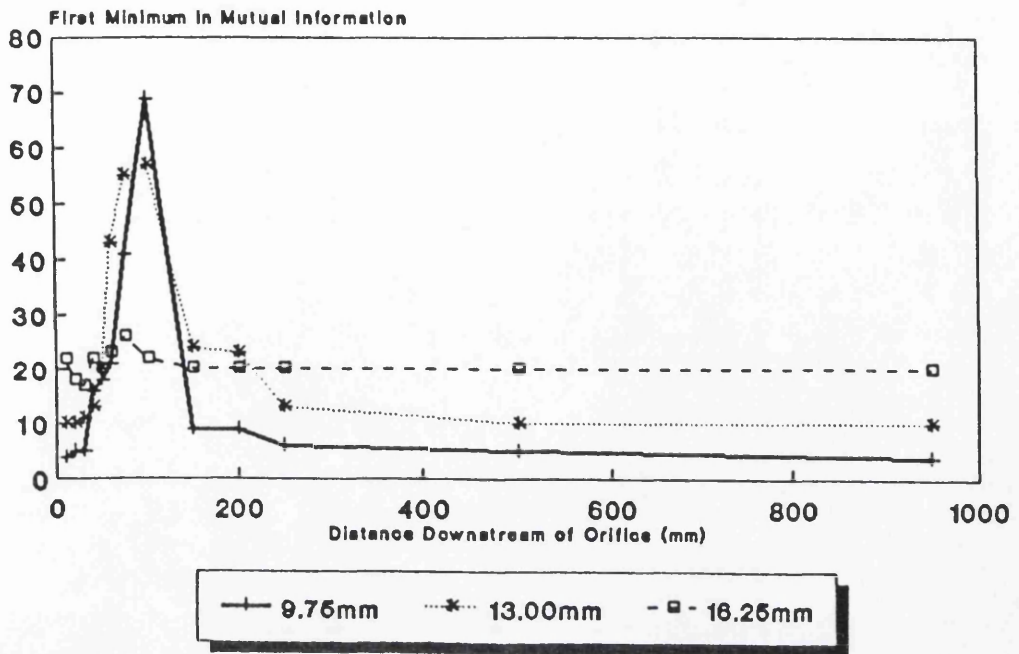


Figure 6-47a: Minimum Mutual Information -  $Re_p = 256$   
 9.75, 13.00 & 16.25mm Orifice Plates

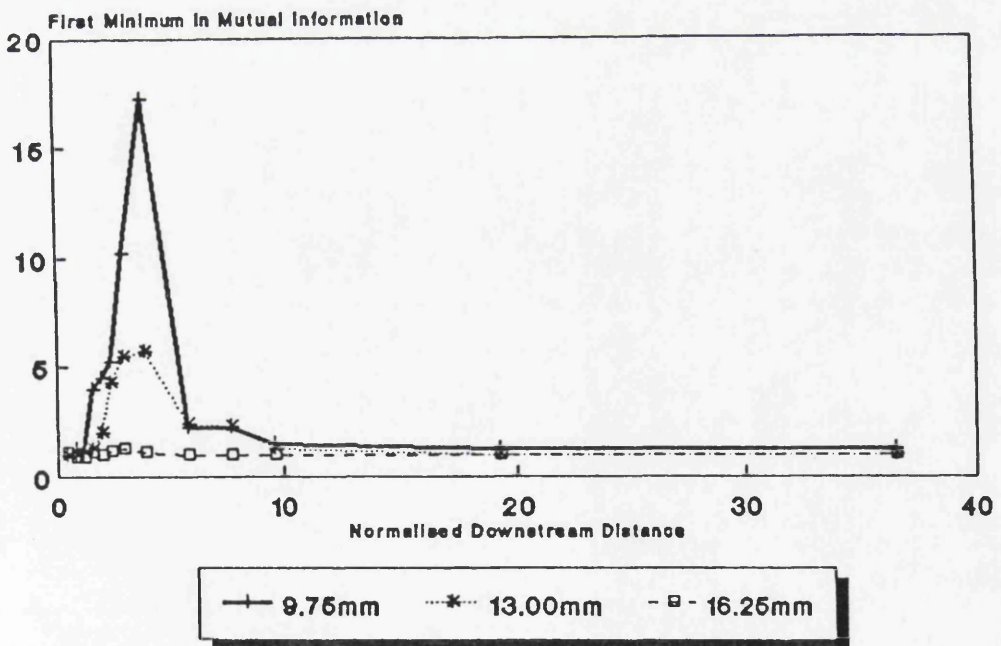


Figure 6-47b: Normalised Minimum Mutual Information -  $Re_p = 256$   
 9.75, 13.00 & 16.25mm Orifice Plates

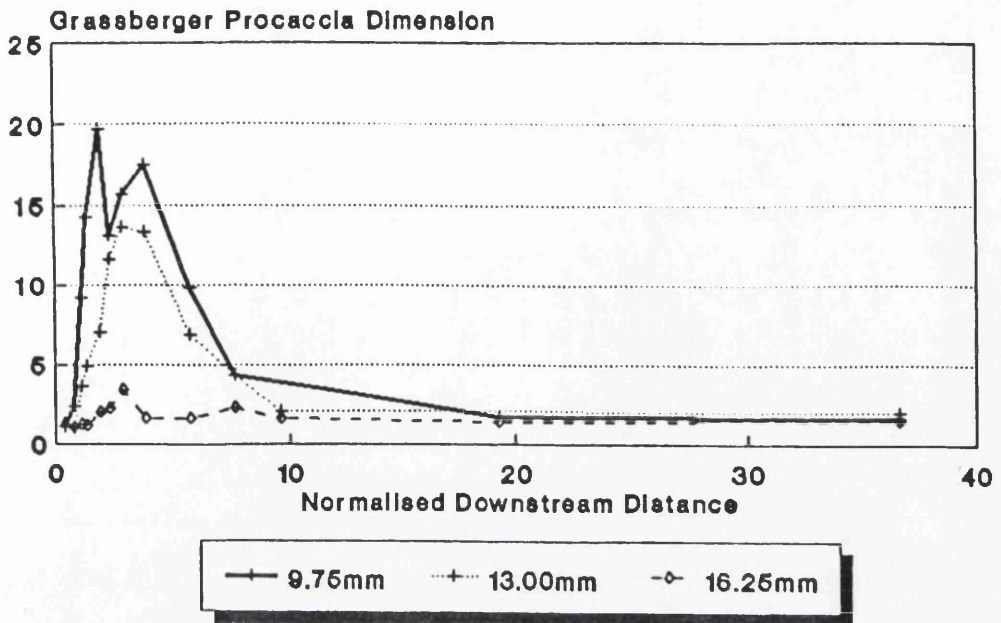


Figure 6-48: Dimension Results -  $Re_p = 256$   
 9.75, 13.00 & 16.25mm Orifice Plates

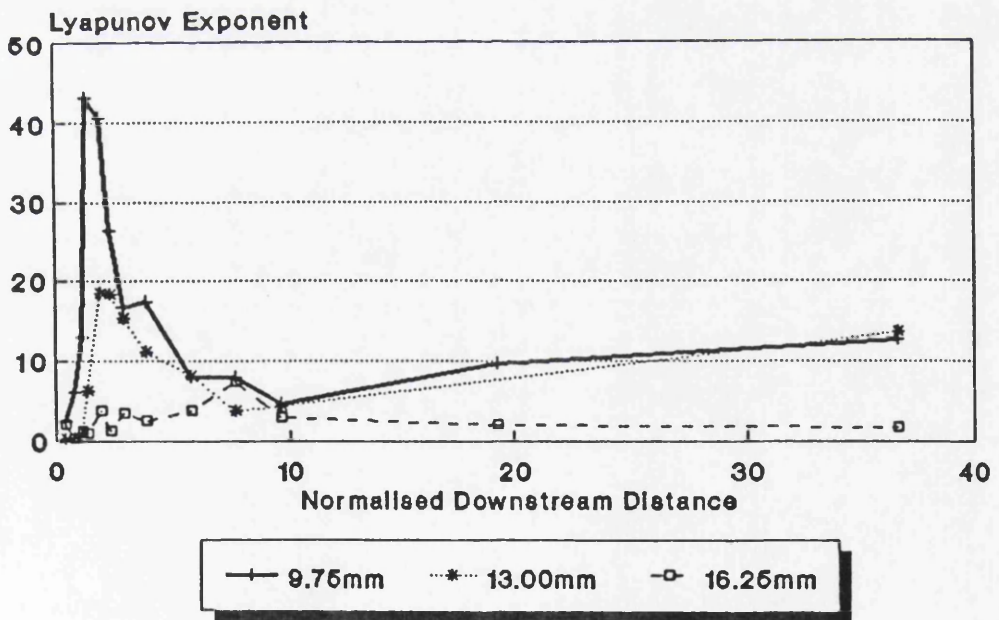
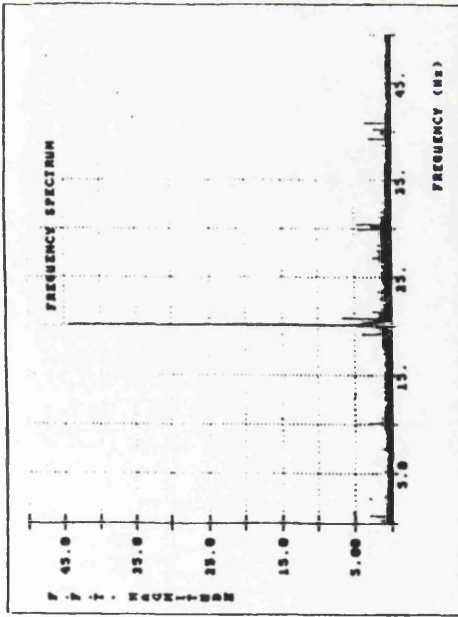
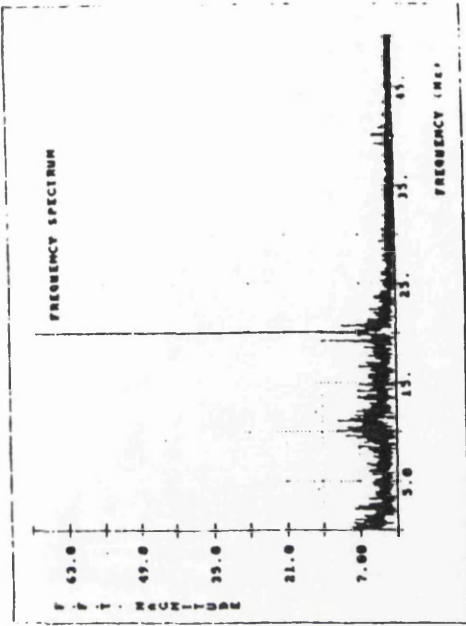


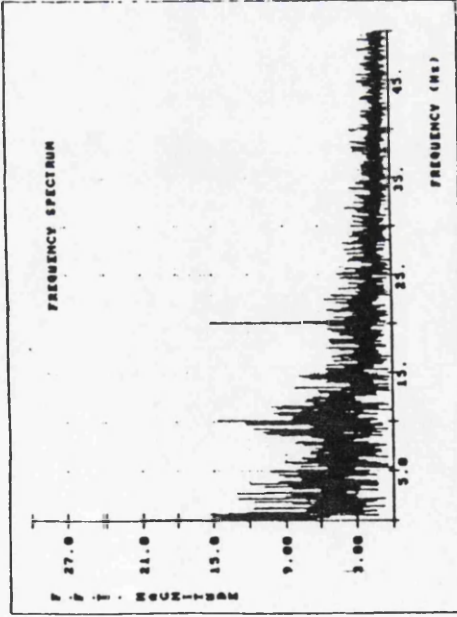
Figure 6-49: Lyapunov Exponent, Results -  $Re_p = 256$   
 9.75, 13.00 & 16.25mm Orifice Plates



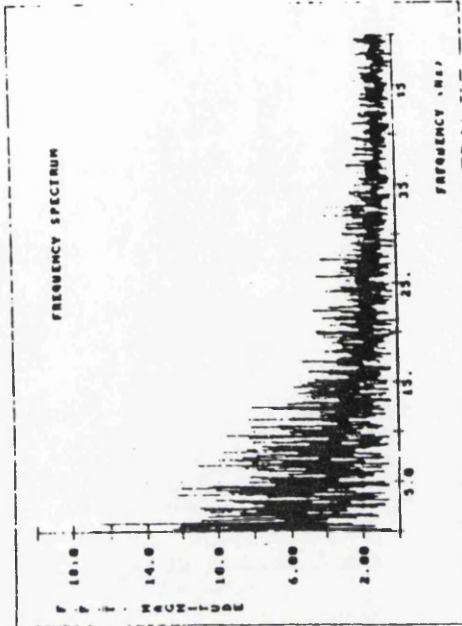
(a) 10mm Downstream



(b) 20mm Downstream



(c) 30mm Downstream



(d) 40mm Downstream

Figure 6-50: Frequency Spectra - 6.50mm Orifice -  $Re_p = 256$

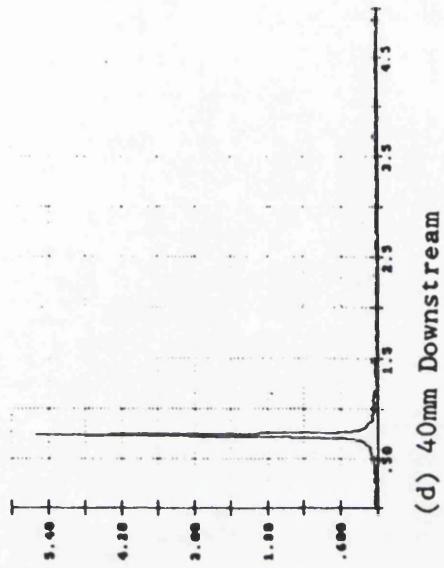
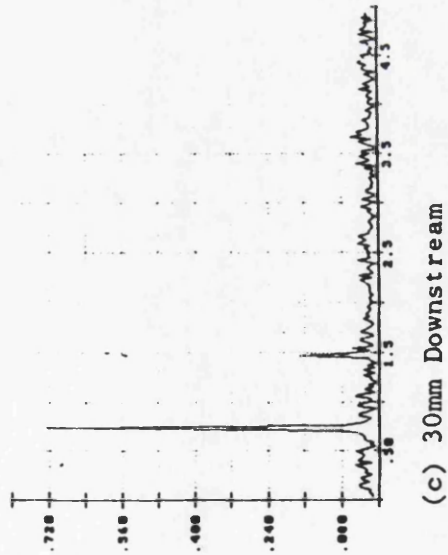
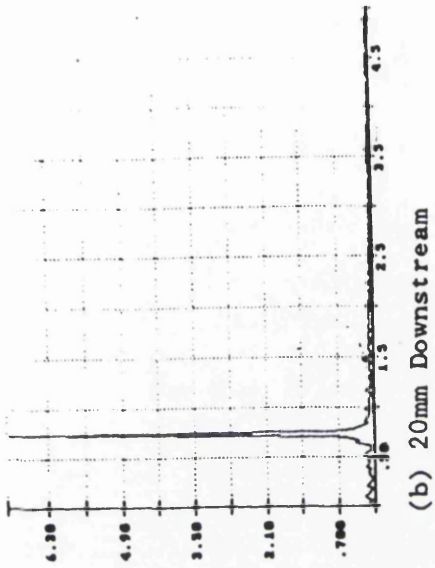
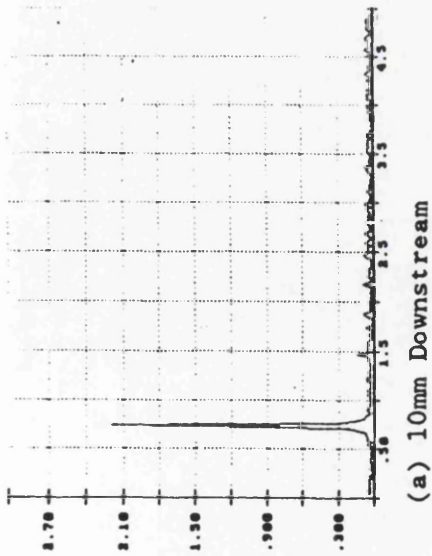


Figure 6-51: Frequency Spectra - 19.50mm Orifice - Rep - 256

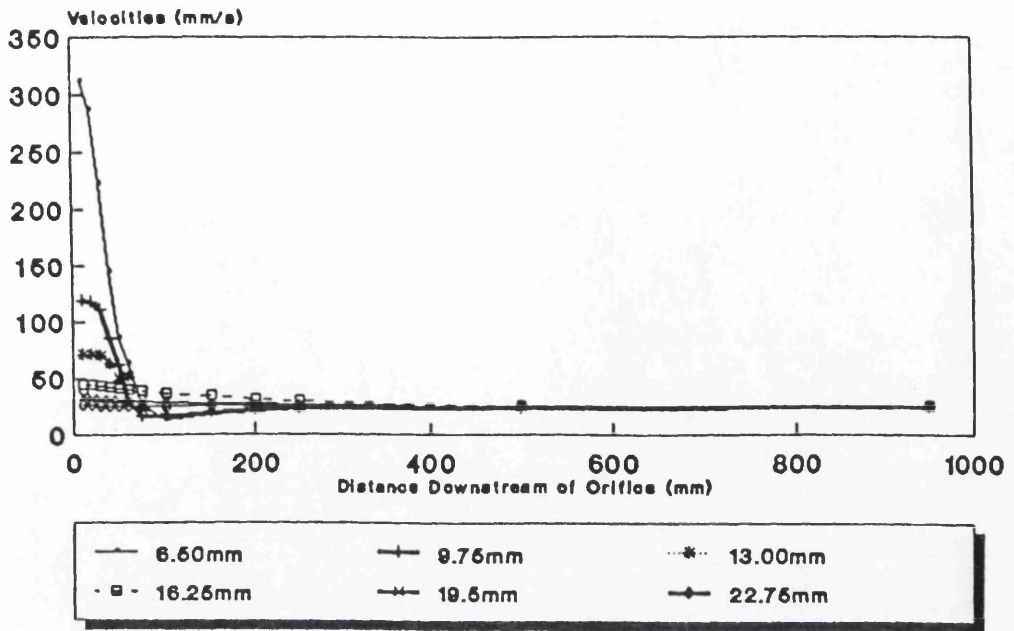


Figure 6-52: Centreline Velocities -  $Re_p = 256$   
All Orifice Plates

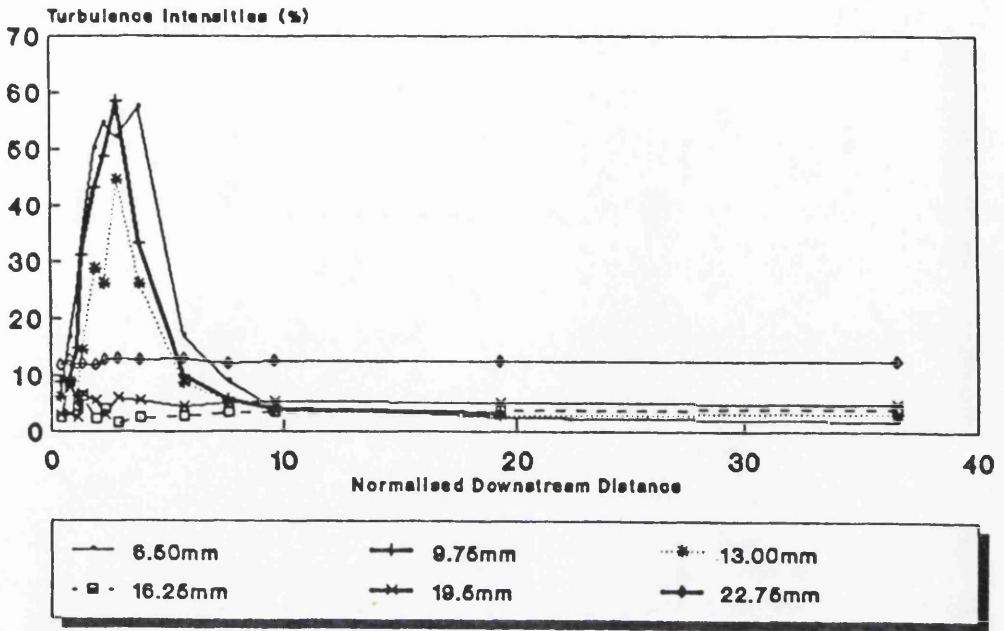


Figure 6-53a: Point-Turbulence Intensities -  $Re_p = 256$   
All Orifice Plates

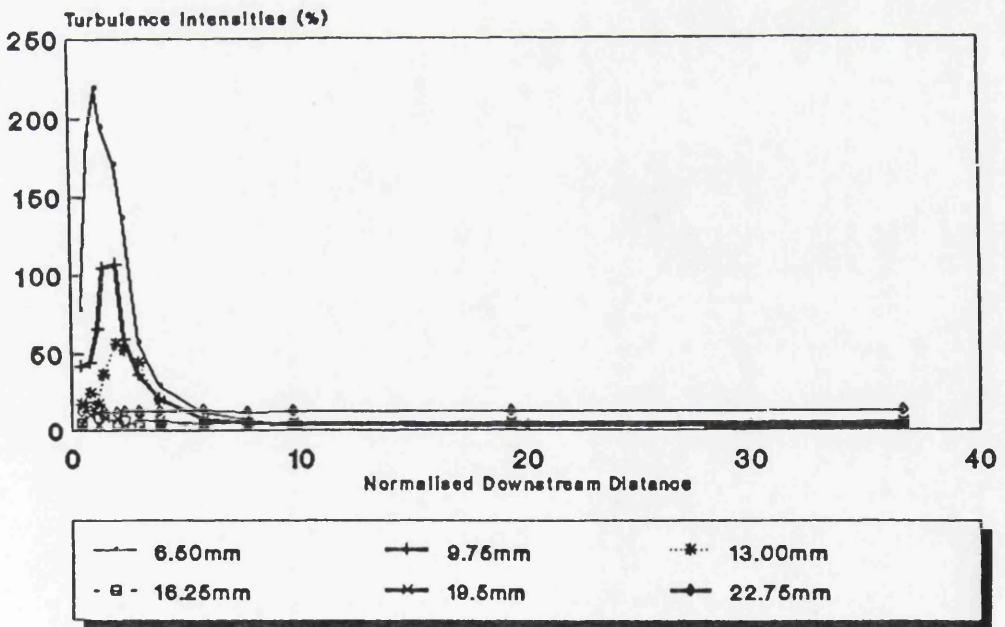


Figure 6-53b: H.G.-Turbulence Intensities -  $Re_p = 256$   
All Orifice Plates

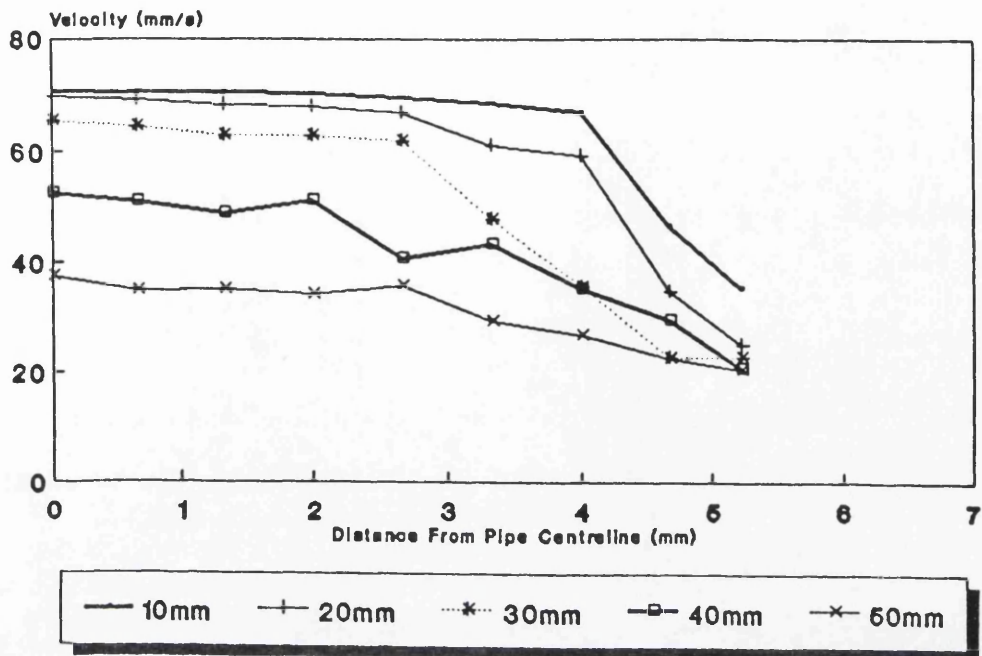


Figure 6-54a: Across-Flow Velocities -  $Re_p = 256$   
13mm Orifice Plate

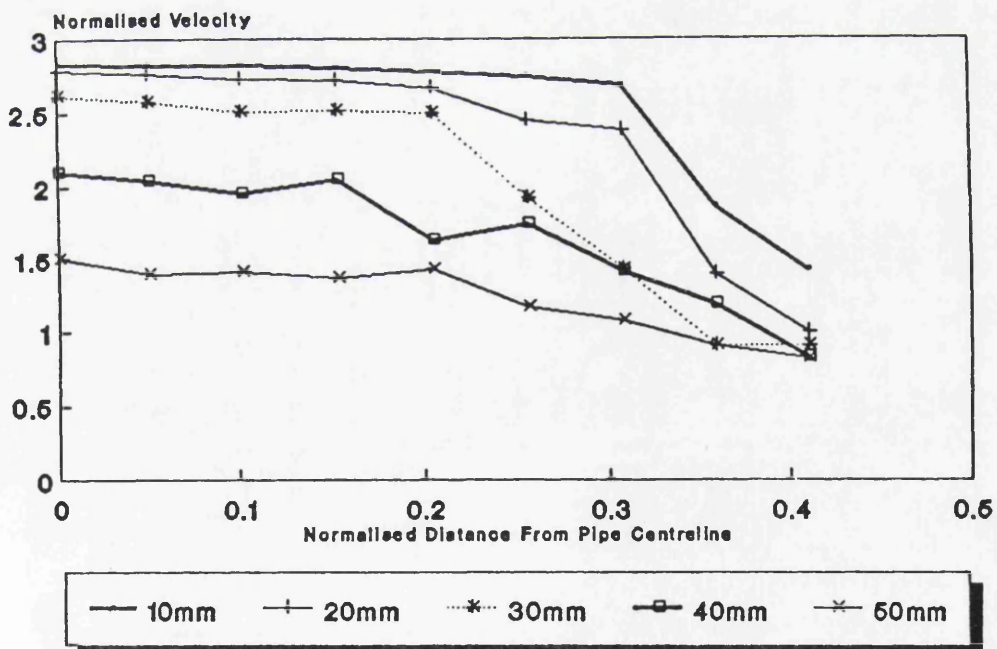


Figure 6-54b: Normalised Across-Flow Velocities -  $Re_p = 256$   
13mm Orifice Plate

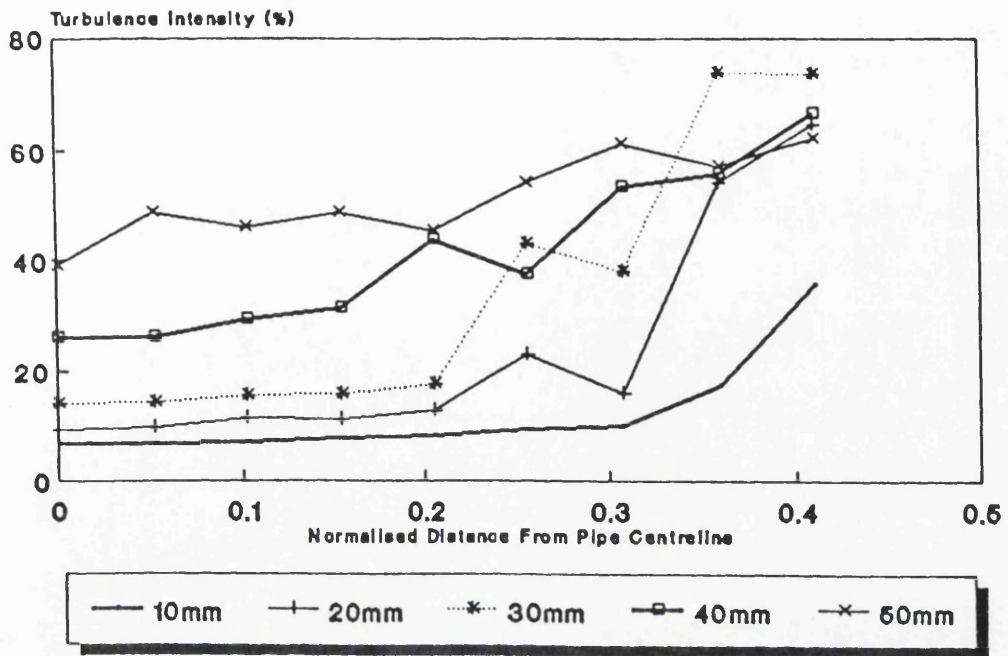


Figure 6-55a: Across-Flow Point-Turbulence Intensities  
 13.00 Orifice Plate -  $Re_p = 256$

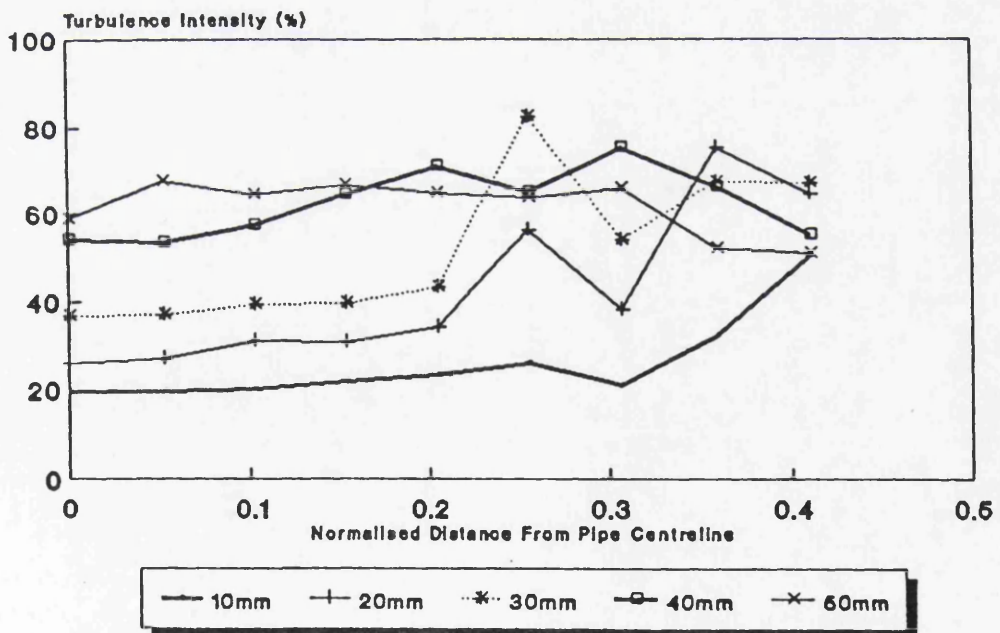


Figure 6-55b: Across-Flow H.C.-Turbulence Intensities  
 13.00 Orifice Plate -  $Re_p = 256$

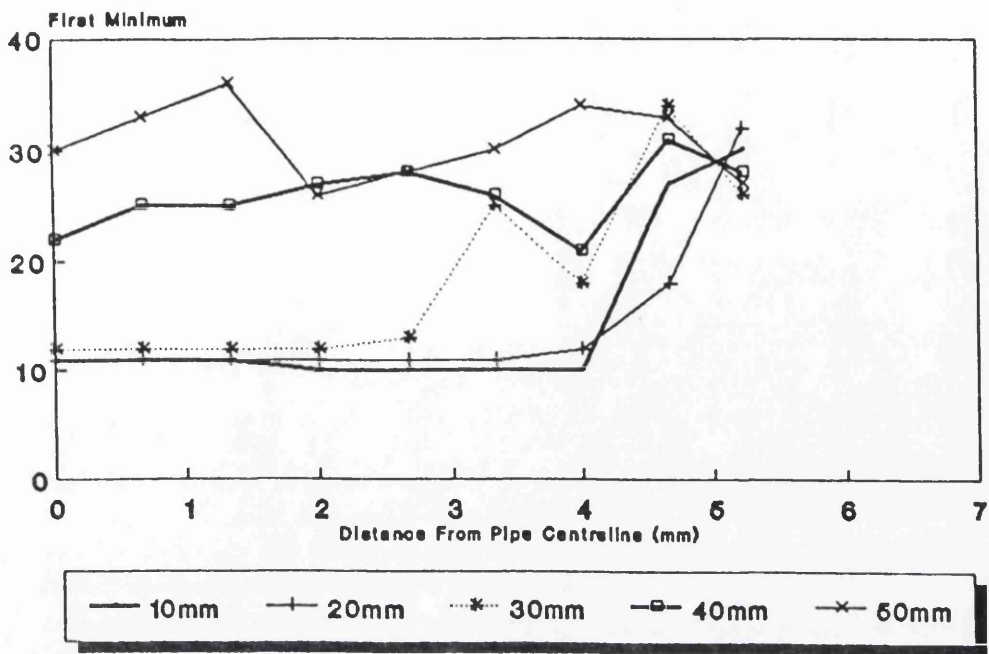


Figure 6-56a: Across-Flow Minimum Mutual Information  
13.00 Orifice Plate -  $Re_p = 256$

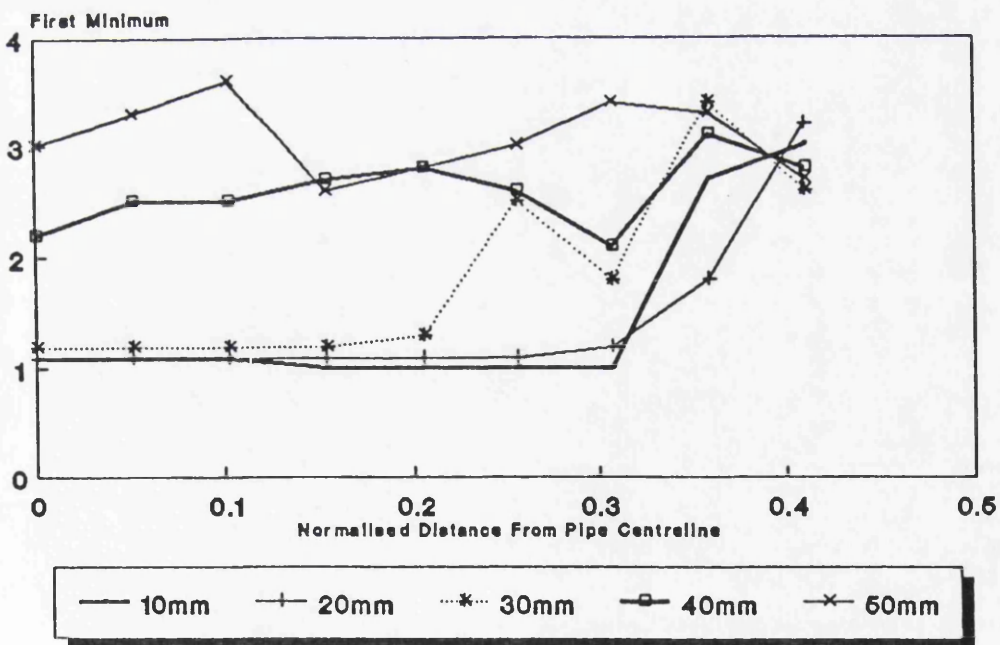


Figure 6-56b: Across-Flow Normalised Minimum Mutual Information  
13.00 Orifice Plate -  $Re_p = 256$

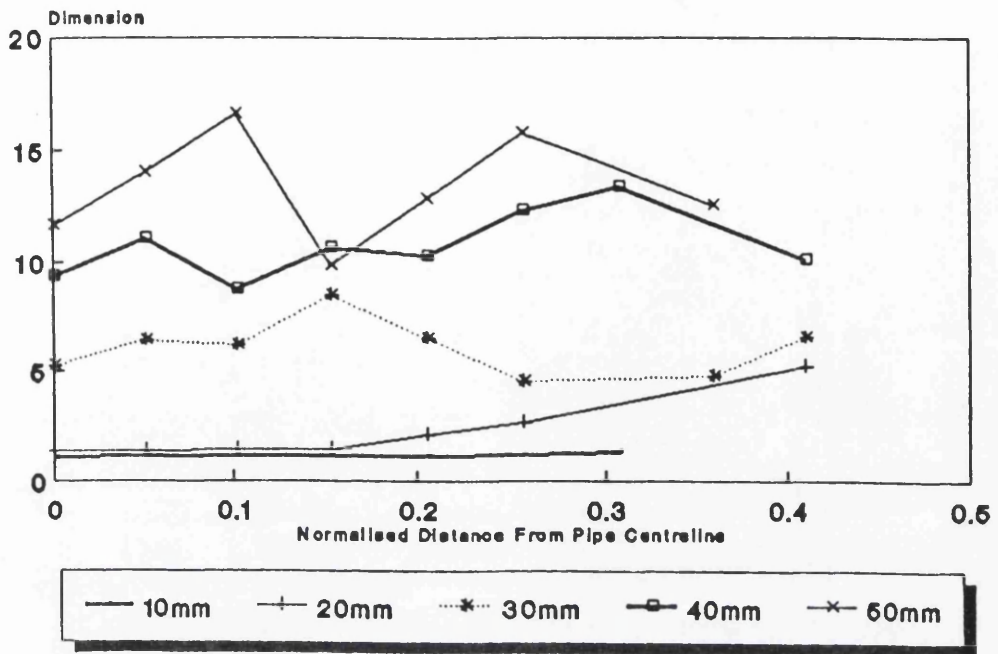


Figure 6-57: Across-Flow Dimension Results  
 13.00mm Orifice Plate -  $Re_p = 256$

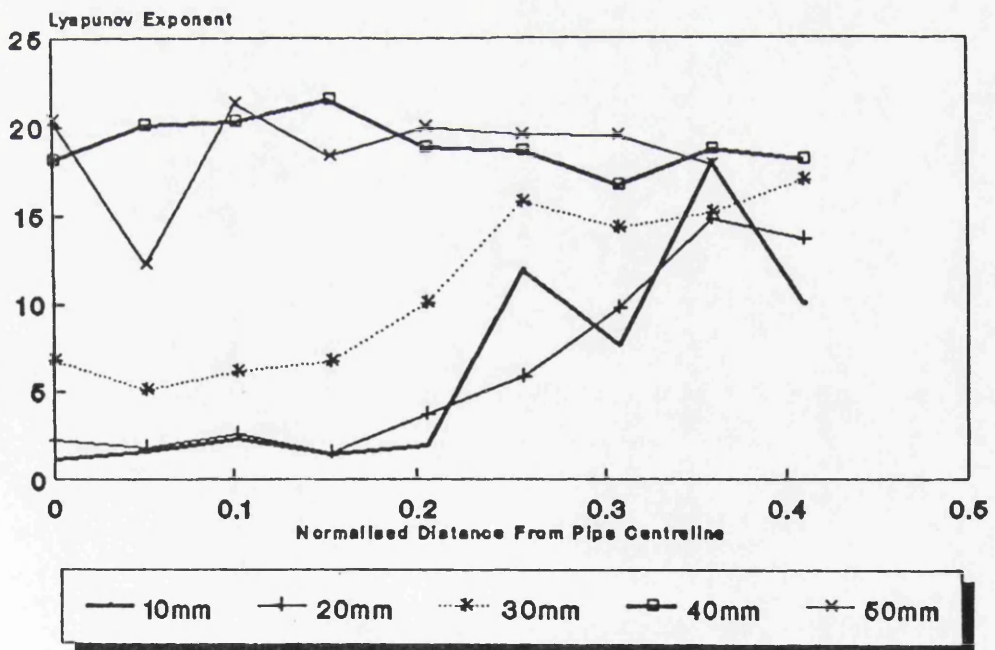


Figure 6-58: Across-Flow Lyapunov Exponent Results  
 13.00 Orifice Plate -  $Re_p = 256$

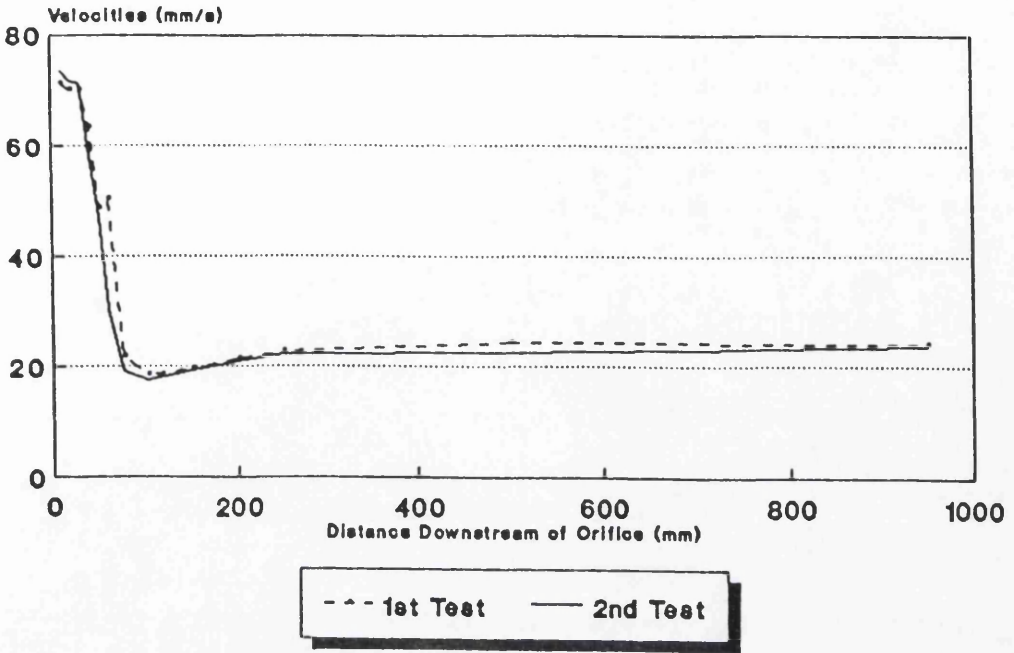


Figure 6-59: Repeated Centreline Velocity Results  
 13mm Orifice Plate -  $Re_p = 256$

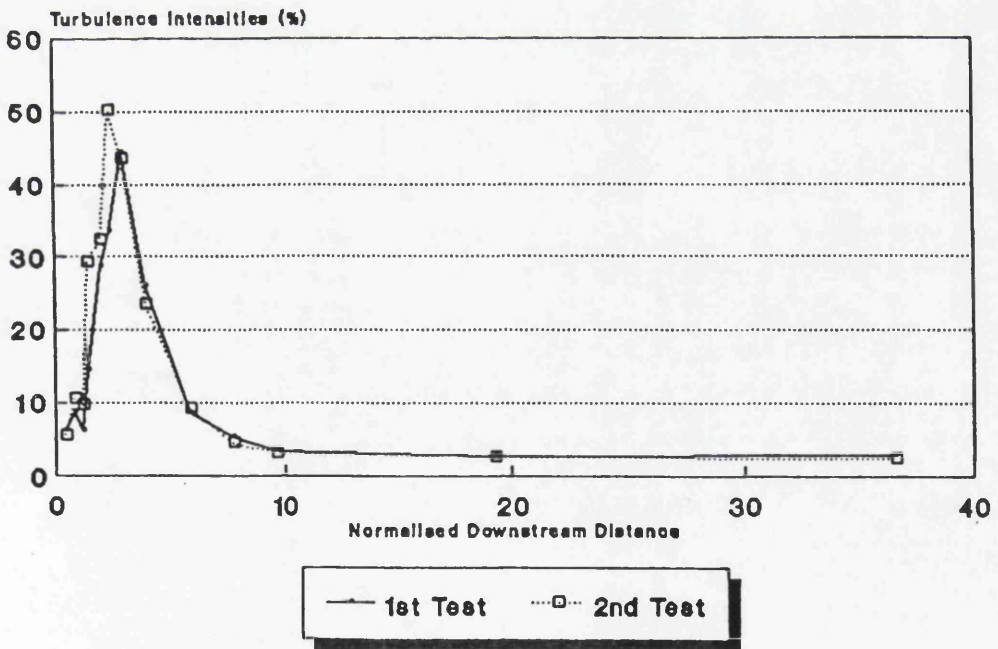


Figure 6-60: Repeated Point-Turbulence Intensities  
 13.00 Orifice Plate -  $Re_p = 256$

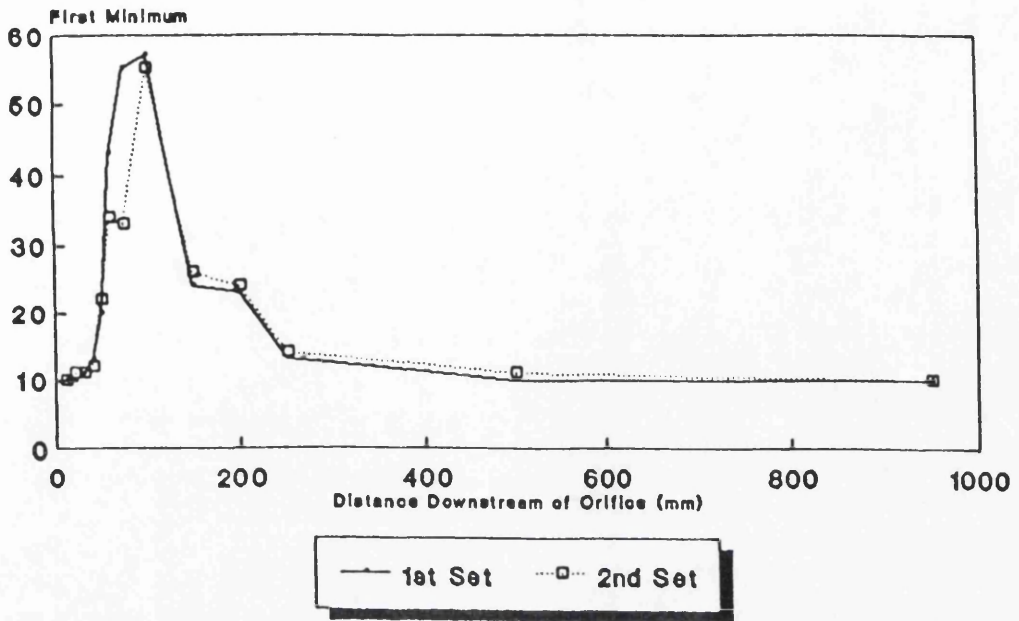


Figure 6-61: Repeated Minimum Mutual Information  
 13.00 Orifice Plate -  $Re_p = 256$

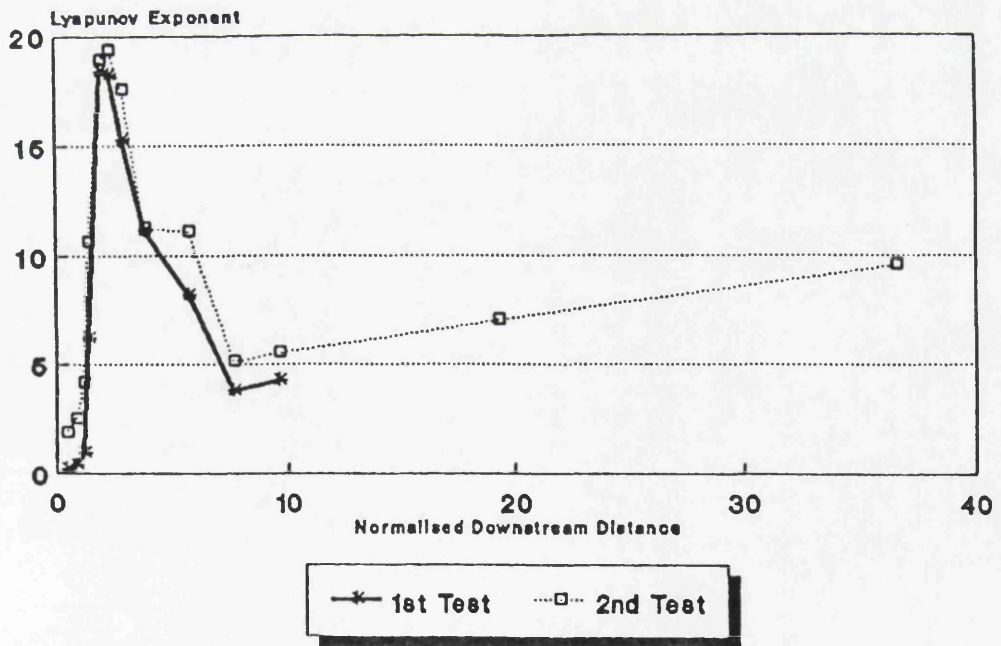
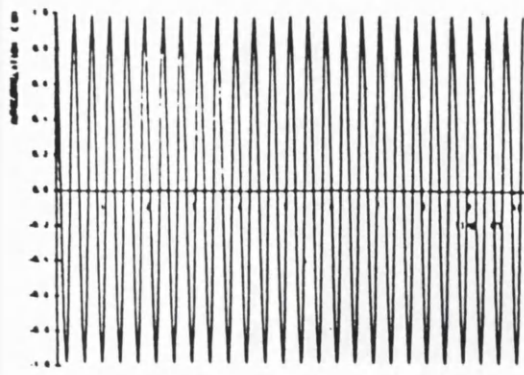
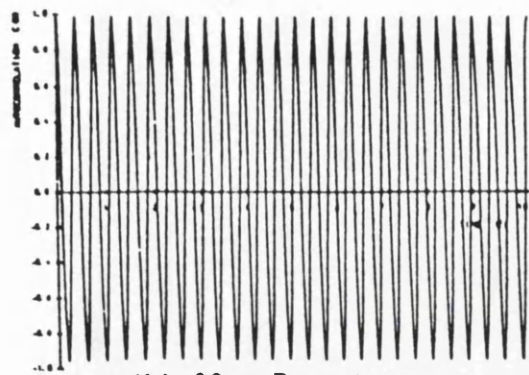


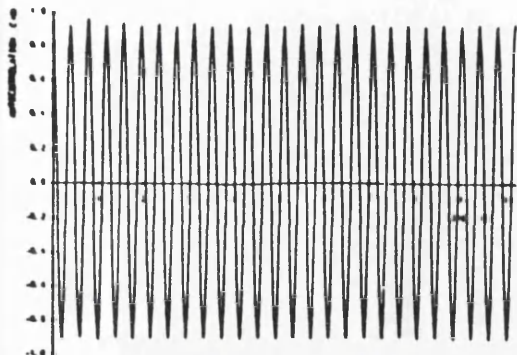
Figure 6-62: Repeated Lyapunov Exponent Results  
 13.00 Orifice Plate -  $Re_p = 256$



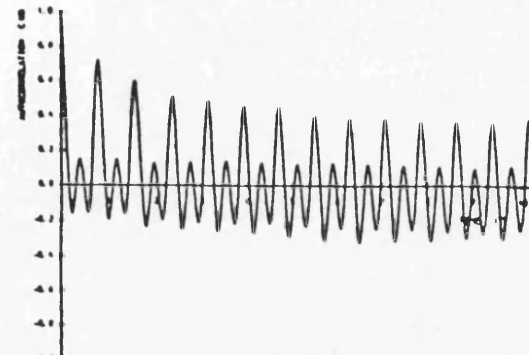
(a) 10mm Downstream



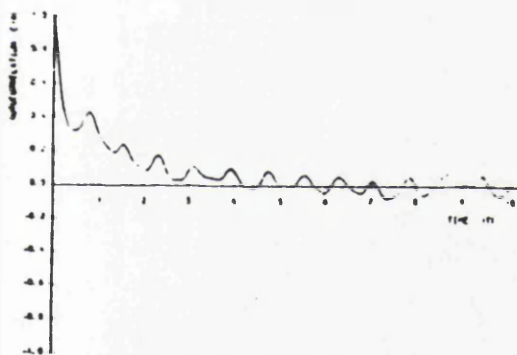
(b) 20mm Downstream



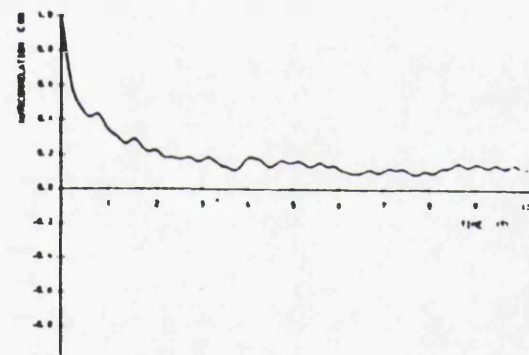
(c) 30mm Downstream



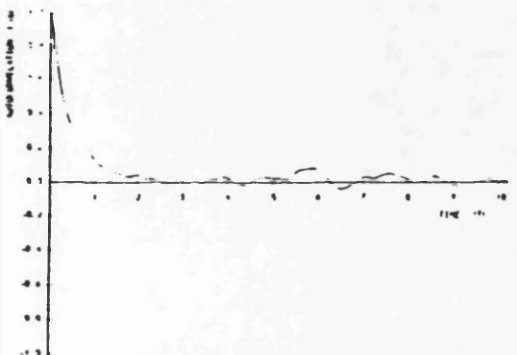
(d) 40mm Downstream



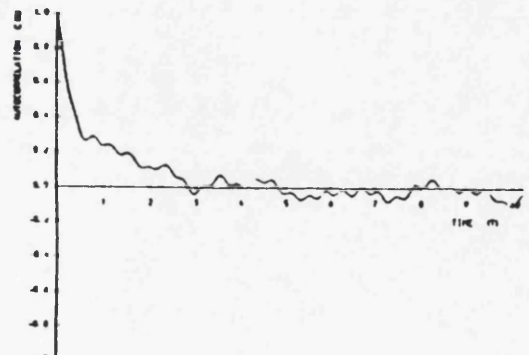
(e) 50mm Downstream



(f) 60mm Downstream



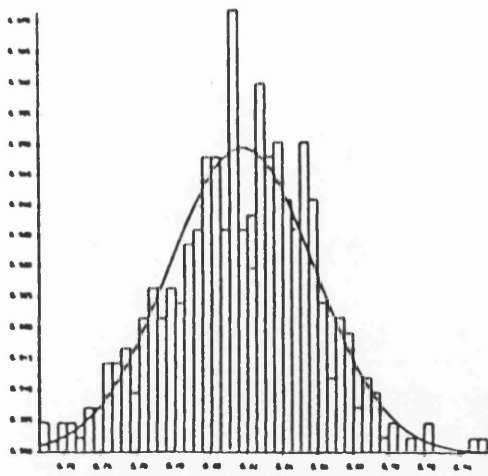
(g) 75mm Downstream



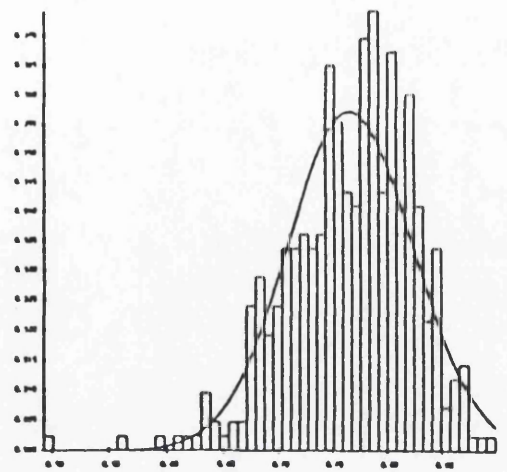
(h) 100mm Downstream

Figure 6-63: Autocorrelation Results - 13mm Orifice Plate

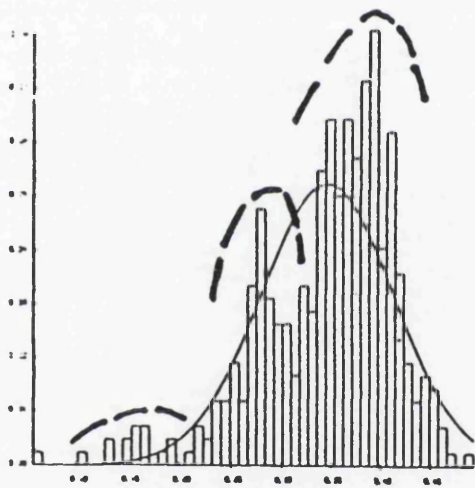
$Re_p = 256$



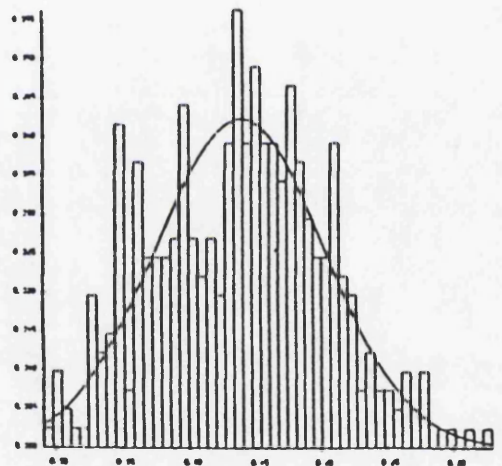
(a) 10mm Downstream



(b) 20mm Downstream

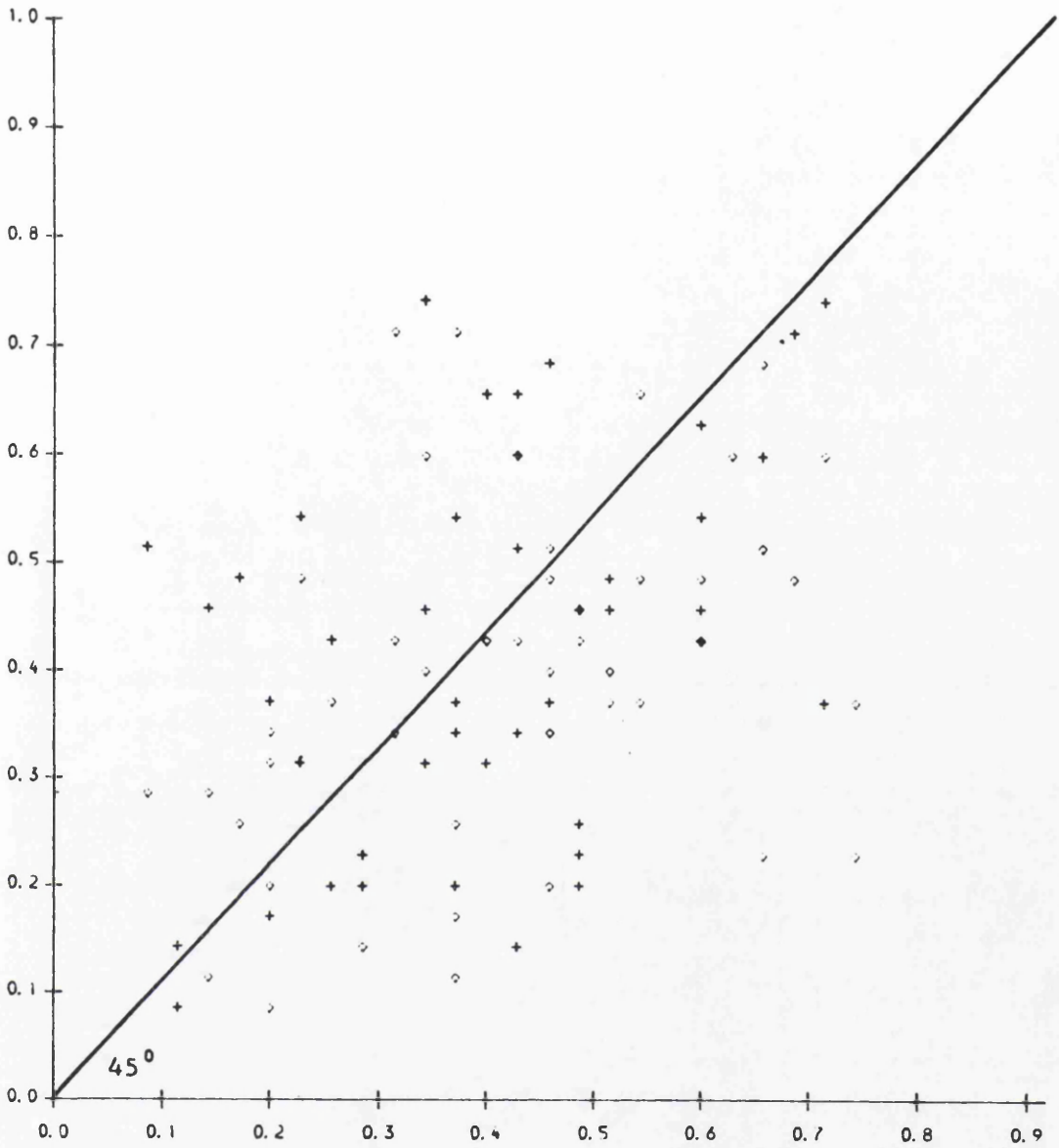


(c) 30mm Downstream



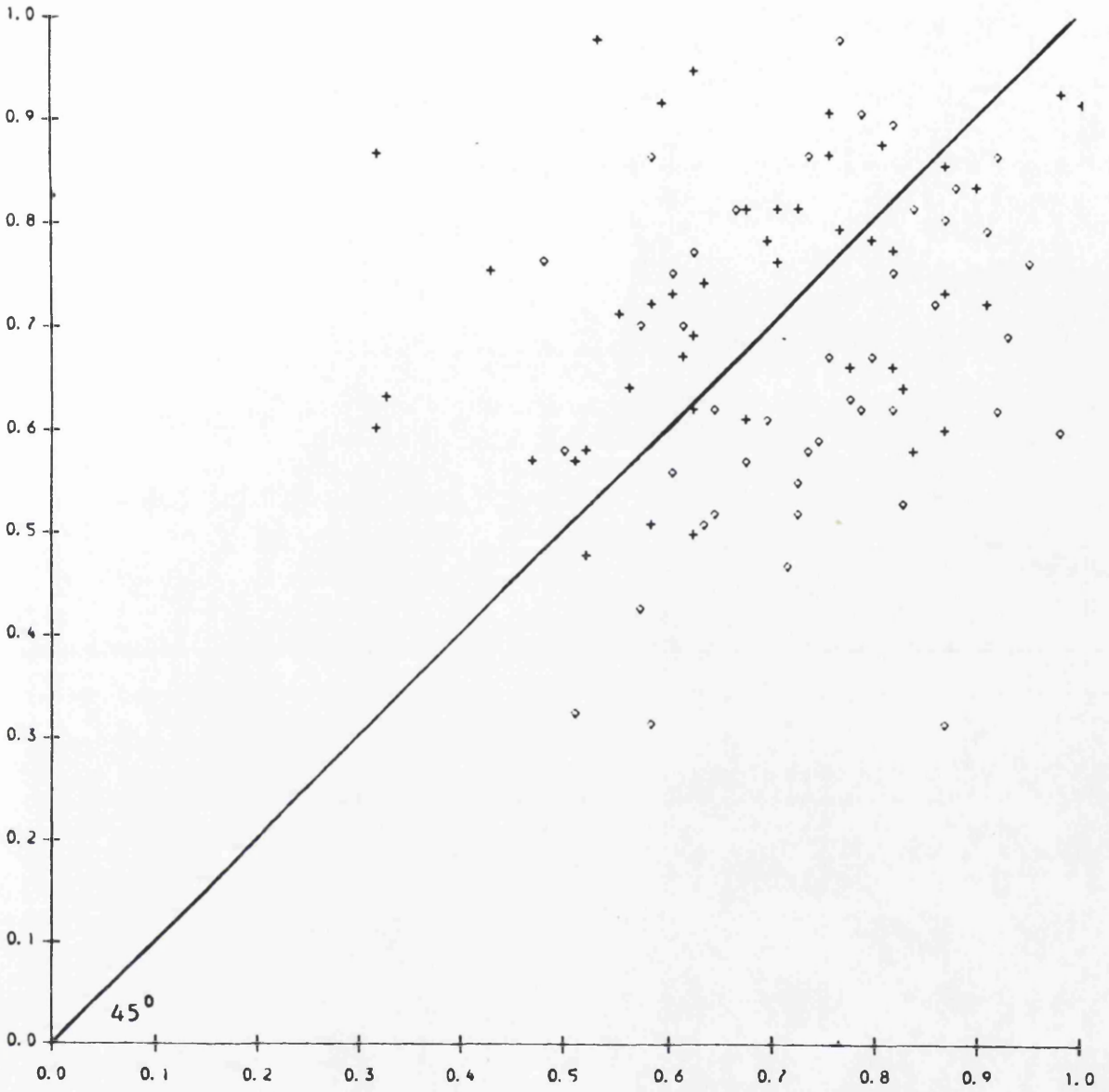
(d) 40mm Downstream

**Figure 6-64: Attractor Trajectory Histogram**  
13.00mm Orifice -  $Re_p = 256$



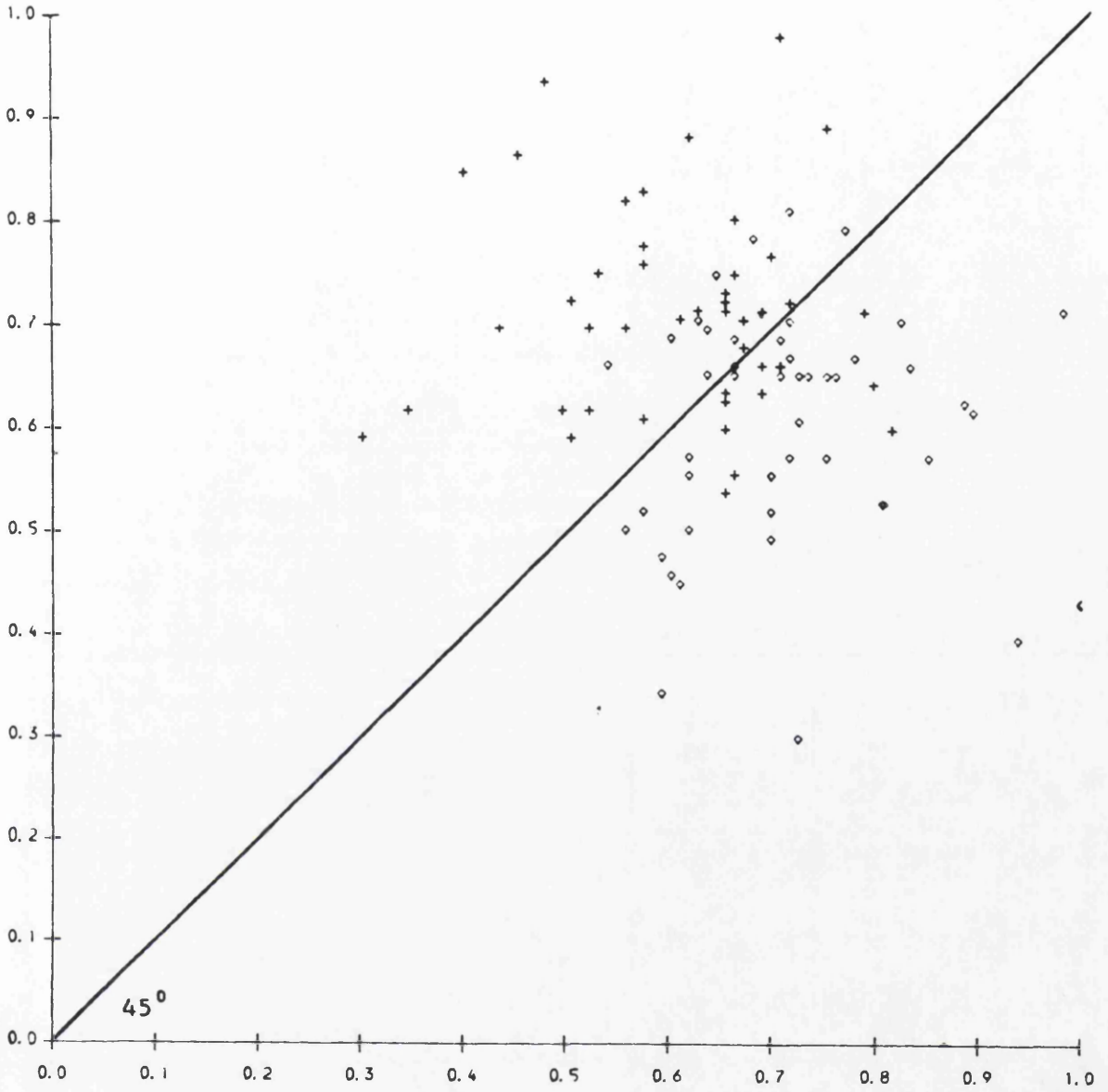
(a) 10mm Downstream

Figure 6-65: Return Mappings - 13.00mm Orifice -  $Re_p = 256$



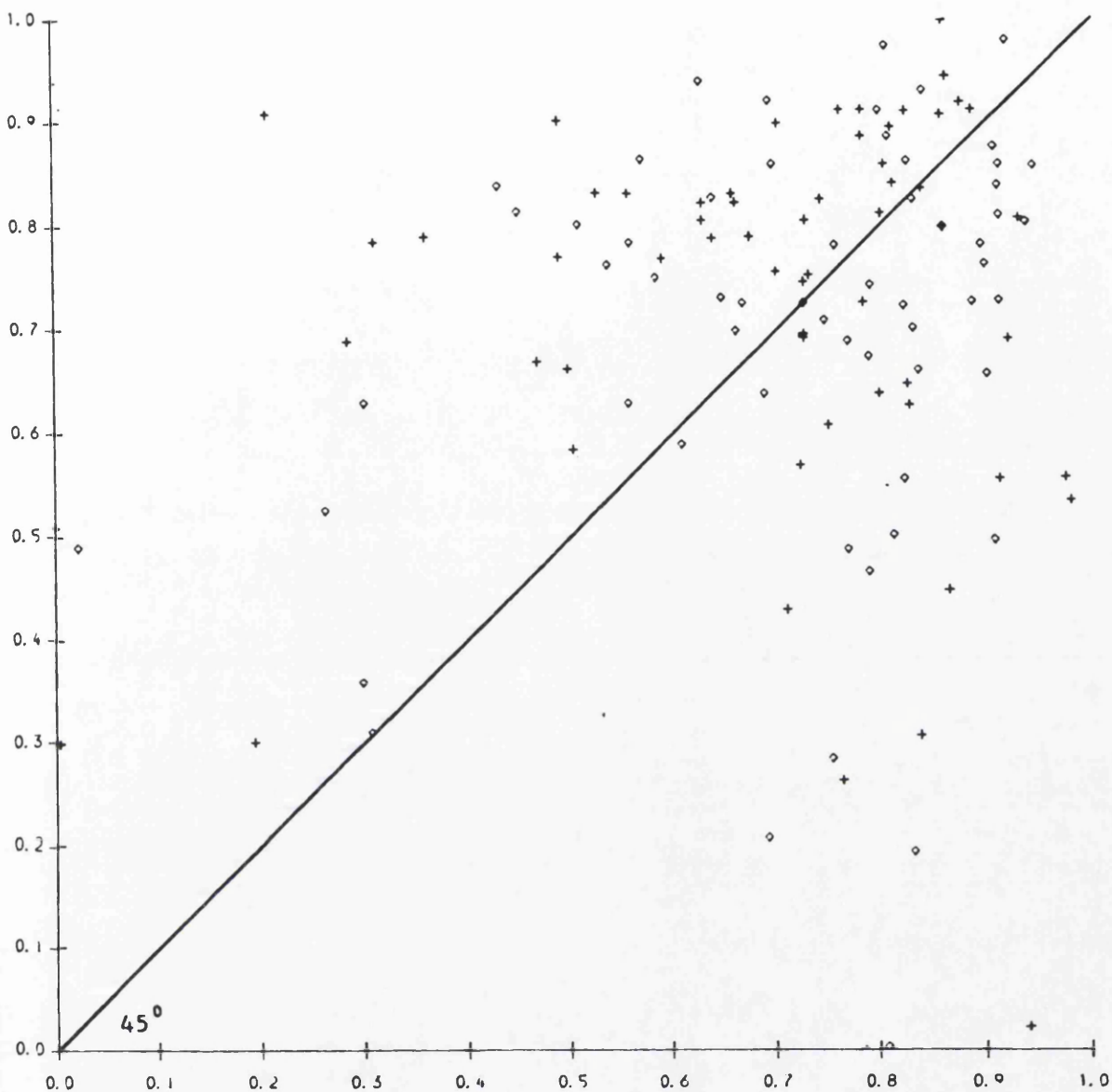
(b) 20mm Downstream

Figure 6-65: Return Mappings - 13.00mm Orifice -  $Re_p = 256$



(c) 30mm Downstream

Figure 6-65: Return Mappings - 13.00mm Orifice -  $Re_p = 256$



(d) 40mm Downstream

Figure 6-65: Return Mappings - 13.00mm Orifice -  $Re_p = 256$

## CHAPTER 7

## CHAPTER 7

### ANALYSIS OF THE RESULTS

#### 7.1 INTRODUCTION

#### 7.2 ANALYSIS OF PULSATILE FLOW BEHAVIOUR AT A PIPE ORIFICE AT LOW REYNOLDS NUMBERS

##### 7.2.1 An Overview of the Flow Mechanisms

###### 7.2.1.1 The Flow Processes in the Pipe Generated by the Orifice Plate

###### 7.2.1.2 The Evolution of Shed Vortices

###### 7.2.1.3 The Relationship Between Flow Type, Orifice Diameter and Reynolds Number

##### 7.2.2 The Centre-Line Velocity and Turbulence Intensity

###### 7.2.2.1 Directly Dissipating Flows

###### 7.2.2.2 Initially Interacting Flows

##### 7.2.3 Transverse Measurements of Velocity and Turbulence Intensity for Initially Interacting Flows

#### 7.3 THE EVIDENCE FOR CHAOTIC BEHAVIOUR

##### 7.3.1 Preliminary Analyses: The First Minimum in Mutual Information, Autocorrelation Function, Attractor Plots, Return Maps and Probability Density Functions

##### 7.3.2 Downstream Development of the Lyapunov Exponent, Dimension and Turbulence Intensity

**7.4 THE ROLE OF THE NEW TECHNIQUES IN DESCRIBING  
TRANSITIONAL FLUID PHENOMENA**

**7.4.1 Introduction**

**7.4.2 The Description of Non-Random Flows**

**7.4.3 The Practical Application of the Techniques  
from Non-Linear Dynamics**

**7.5 FURTHER NOTES ON THE CHARACTERISATION ALGORITHMS**

**7.5.1 Introduction**

**7.5.2 The Grassberger-Procaccia Dimension  
Algorithm and Noise**

**7.5.3 The Lyapunov Exponent Algorithm and Noise**

**7.5.3.1 Positive Lyapunov Exponents Caused by Noise**

**7.5.3.2 Coincident Trajectories**

**7.6 SUMMARY**

## 7.1 INTRODUCTION

The aim of this chapter is to present the results of analyses performed on the observations and data presented in chapters five and six respectively. A coherent picture of events at the orifice plate will be presented.

An overall picture of the flow mechanisms at the orifice plate is presented in section 7.2. In particular, the evolution of the shed vortices and the route taken by the vortices, to either of the two types of flow identified in the study, is described. The evidence for the existence of chaotic behaviour is presented in section 7.3. This involves the use of preliminary analysis techniques in addition to the Lyapunov exponent and Grassberger–Procaccia dimension characterisation techniques. The role of that the new techniques from the field of non-linear dynamics have to play in fluid flow problems is identified in section 7.4. Section 7.5 contains some additional notes on the behaviour of the two characterisation techniques, namely the Lyapunov exponent and the Grassberger–Procaccia dimension algorithms.

## 7.2 ANALYSIS OF PULSATILE FLOW BEHAVIOUR AT A PIPE ORIFICE AT LOW REYNOLDS NUMBERS

### 7.2.1 An Overview of the Flow Mechanisms

#### 7.2.1.1 The Flow Processes in the Pipe Generated by the Orifice Plate

As described in chapter 5, section 5.7.4, two types of flow were encountered at the orifice lip depending on the flow Reynolds number. At low flow velocities the flow would remain axisymmetric, and dissipate out immediately after leaving the orifice plate. This type of flow was named Directly Dissipative flow. The other type of flow occurs at higher flow velocities, whereby the flow breaks down into a more complex, turbulent form downstream of the orifice plate. This type of flow was named Initially Interacting flow, and may be further subdivided into three

sub-categories, (as defined in section 5.7.4), these are:

- 1 - Unstable Slow Jet Flow,
- 2 - Interacting Vortex Flow, and
- 3 - Confined Jet Flow.

Flows 1, 2 and 3 occurring for respectively higher values of Reynolds number.

Figure 7-1 presents an overall picture of the flow processes at a pipe orifice. Typical frequency spectra for the centre-line velocity traces are given in figure 7-2. The flow breakdown shown in figure 7-1 is for a typical Interacting Vortex Flow. This type of flow was by far the most common encountered during the experimental investigation. However, the flow processes within such a flow cover those present within all other types of flow. As can be seen from figure 7-1 there are seven distinct regions of behaviour, these are:

#### 1 - Upstream Laminar Pulsatile Pipe Flow.

This region contains the undisturbed, (by the orifice plate), pulsatile pipe flow, far upstream of the orifice plate. Centre-line velocity measurements indicated that the mean centre-line velocity for the pulsed flows were equal to the centre-line velocity of the unpulsed Hagen-Poiseuille flow at an equivalent mass flux rate. The frequency spectrum for the upstream laminar pulsatile pipe flow contains a single spike at the forcing frequency  $f_f$ , as shown in figure 7-2a.

#### 2 - Converging Flow.

Prior to passing through the orifice plate, the flow streamlines converge, and the flow accelerates, to allow passage of the fluid through the constriction. This region is very short, from flow visualisation studies obvious flow convergence was not observed beyond a distance of one pipe diameter upstream of the orifice plate. With the streamlines converging nearer to the orifice plate as the orifice aperture increases in diameter. The frequency spectrum again consists of a single peak at the forcing frequency, (figure 7-2a).

#### 3 - Region of Axisymmetric Vortex Production and Growth together with the Recirculation Zone.

The vortices generated at the orifice lip, roll up and are convected away by the

main flow streaming through the orifice aperture. These vortices increase in size as they proceed downstream, due to entrainment of the fluid, both from the flow passing through the orifice plate and the recirculation zone. A more detailed picture of the development of the shed vortices and flow entrainment is given below in section 7.2.2. Within this region of initial growth of the shed vortices the frequency spectrum contains only one spike at the forcing frequency  $f_f$ , as depicted in figure 7-2a.

#### 4 – Non-Axisymmetric Vortex Growth, Interaction and Breakdown.

Towards the end of region 3, the vortices begin to merge in pairs, this is indicated by a period doubling peak occurring in the frequency spectra in region 4, (figure 7-2b). The merging of the shed vortices produces larger vortices which continue to grow and eventually interact with each other and result in a loss of axisymmetry, leading to a broadening of the  $f_f/2$  spectral peak, (the frequency spectrum of the centre-line velocity fluctuations is given in figure 7-2c).

#### 5 – Weakly Turbulent Flow Region.

Once the size of the evolving vortices increases to that comparable with the pipe internal diameter, they interact with each other becoming noticeably non-axisymmetric. This process leads to rapid breakdown of the resultant large coherent structures into the more complex flow composed of low frequency broad band spectra, as shown in the frequency plot of region 5. The broadening of the frequency spectra as the shed vortices break down to a more incoherent, weakly turbulent flow eventually swamps the  $f_f/2$  and  $f_f$  peaks. This is shown in figure 7-2d. Subsequent to the vortices reaching their maximum size, and breaking down, a turbulent flow region ensues. It is this region where most of the energy dissipation will take place. The region is relatively short, and contains highly complex motion, as observed during the flow visualisation studies.

#### 6 – Region of Dissipation and Decay.

The flow now begins its transition from the turbulent state back to the downstream condition of pulsatile laminar flow. This takes place by a gradual decrease in the amplitudes of the broad band spectral components, the higher frequencies dying out first. This leaves a frequency spectrum with low frequency broad band noise and a re-emergence of the forcing frequency peak, this is shown in figure 7-2e. From the flow visualisation studies it is apparent that the flow becomes noticeably less

energetic with large, slowly moving, coherent structures dominating the flow field. This was most apparent from the video film of the downstream dissipation of the disturbances. The large flow structures gradually die out due to the action of viscosity.

#### **7 - Downstream Laminar Pulsatile Flow.**

Once the disturbances, caused by the orifice plate, have died out, the flow once again resumes its upstream boundary condition, (region-1), of pulsatile laminar flow, and the frequency spectrum again consists of the single peak at  $f_f$ , (figure 7-2a).

These flow processes, described above, are present in the other flow types. All the flows investigated were composed of regions 1 and 2 upstream, (i.e. no disturbances were generated upstream of the orifice plate).

Downstream of the orifice plate the directly dissipating flow is basically composed of a region 3 flow, in which the vortices die out as they proceed downstream, at which point the flow has reached its downstream condition, region 7.

The initially interacting unstable jet flow has a region of vortex production, (region 3), and then dissipation, (region 6), whereby, the vortices die out as do the low frequency fluctuations, caused by the unstable jet. Downstream the flow reverts back to that of region 7.

Lastly, the initially interacting confined jet flow, immediately upon issuing from the orifice plate, breaks down to a flow similar to that of region 5, with a very turbulent recirculation zone. This is followed by flows typical of regions 6 and 7 respectively.

#### **7.2.1.2 The Evolution of Shed Vortices**

The evolution of shed vortices in directly dissipating and initially interacting vortex flows are shown in figures 7-3 and 7-4 respectively.

In directly dissipating flows the vortices shed from the orifice lip initially grow in size reaching a limiting size downstream of the orifice plate, as shown in figure 7-3. Eventually viscous diffusion causes the solid body rotation present at the centre of each shed vortex to spread to the entire vortex. Eventually the vortices cease to rotate and the vortex structure is merely stretched by the velocity profile as the flow proceeds downstream.

Figure 7-4 gives details of the processes involved in the evolution and breakdown of vortices shed from the orifice plate lip. The downstream flow processes, that is vortex production, evolution, breakdown and dissipation, are driven by the main flow streaming through the orifice aperture.

Once the vortices are shed from the lip, they increase in size as they proceed downstream. The outer limits of the vortices define a vortex envelope as shown in figure 7-4. The increase in size of the vortices is due primarily to entrainment of fluid from the main flow passing through the orifice aperture. However, some fluid is also entrained from the recirculation zone. This is apparent from the breakdown pattern of the vortices observed in the flow visualisation studies. Some of the fluid from the degenerated vortices has been observed, during flow visualisation, to pass back into the recirculation zone. Thus there must be a movement of fluid upstream from the recirculation zone into the evolving vortices.

The boundary of the recirculation zone, is therefore, very complex. This is due to the flow in the recirculation zone, being entrained by the cylindrical vortex street, spreading across the whole vortex envelope due to the rotation of the vortices. The fluid entering the recirculation zone downstream, at the breakdown point, will be composed of the main flow passing through the orifice plate, and also some of the flow entrained upstream from the recirculation zone. The effective boundary of the recirculation zone could be determined from a knowledge of the actual fluid in the vortex envelope, which originated from within the recirculation zone itself.

Viscous diffusion does not play an important part in the overall increase in size of the vortices as they proceed downstream. The main role played by viscous diffusion is to increase the volume of fluid undergoing solid body rotation at the centre of each vortex.

Three dimensional schematics of the vortex shedding for directly dissipating and initially interacting flows are given in figures 7-5a and 7-5b respectively.

### 7.2.1.3 The Relationship between Flow Type, Orifice Diameter and Reynolds Number

It is clear from the flow visualisation and Laser Doppler Anemometry studies, of chapters 5 and 6 respectively, that two types of flow regimes occur – directly dissipating and initially interacting flows.

In general directly dissipating flows occur for lower orifice Reynolds numbers, which may be achieved by either, reducing the pipe Reynolds number for a constant orifice diameter, or, increasing the orifice diameter for a constant pipe Reynolds number. It is most probable that forcing amplitude would also have an effect on the flow regime present, however, as only one set of tests on the forcing amplitude was undertaken, no firm conclusions may be reached as to its effect. (For the case of a constant pipe and orifice Reynolds number, an increase in the forcing amplitude was seen to bring the breakdown region closer to the pipe orifice, see chapter 6, section 6.3.) In addition, the forcing frequency during the tests was kept to the natural frequency of the pipe orifice system, and thus no conclusions may be drawn as to the effect of the forcing frequency on the breakdown mechanism.

The effect of Reynolds number and orifice diameter on the flow regime is given in figures 7-6a and 7-6b, using two definitions of Reynolds number – orifice Reynolds number,  $Re_o$ , and Wake Reynolds Number,  $Re_w$ , respectively. These Reynolds numbers have been used to give two different perspectives of the results. ( $Re_o$  and  $Re_w$  have been defined in expressions 4.7b and 4.10 respectively in chapter 4, and the relationship between them is shown in section 4.4.2 and table 4.1.)

Figure 7-6a, plots the normalised orifice diameter,  $D_o/D_p$ , versus the orifice Reynolds Number,  $Re_o$ . (Lines of constant pipe Reynolds numbers are superimposed on the diagram.) From the plot there appears to be two distinct regions, one of

directly dissipating flows for low pipe Reynolds numbers and large orifice diameters, as expected, the other region of initially interacting flow appears for higher Reynolds numbers and smaller orifice diameters. However, the boundary separating the two flow regimes is not clearly defined.

Figure 7-6b, plots the normalised lip height,  $h/D_p$ , versus the wake Reynolds Number,  $Re_w$ . Where the lip height is the distance into the flow that the orifice plate protrudes and the wake Reynolds number is defined using the equivalent Hagen-Poiseuille flow velocity at the lip height in the absence of the orifice plate. Both the lip height and the wake Reynolds number are defined in detail in chapter 4, section 4.4.2 and equations 4.10 and 4.13. In figure 7-6b, the regions of directly dissipating and initially interacting flows are again quite distinct. This time, the directly dissipating flows occupy a region close to the origin, where  $h$  and  $Re_w$  are both small.

In light of these results, it was decided to perform more flow visualisation studies to clarify the boundary between the directly dissipating flows and the initially interacting flows. Thus all the orifices used in the study were briefly re-examined to look for the boundary between these two flow regimes. These additional results are plotted in figures 7-6c and 7-6d, which are essentially the same plots as those of figures 7-6a and 7-6b respectively, with the additional data collected superimposed upon them.

One aspect of the flow behaviour that became apparent from these extra studies was that there are clearly defined regions of directly dissipating and initially interacting flows, labelled D.D. and I.I. in the figures. Another feature of the results is that the initially interacting region's border with the directly dissipating region is composed of unstable slow jet flow, (see section 7.2.1.1). These unstable jet flows were clearly distinguishable from interacting vortex flows. However, the distinction was not as clear between interacting vortex flows and confined jet flows. Figures 7-6c and d show the results of these additional tests. In these figures, the unstable jet flows are distinguished from the other initially interacting flow types.

Figure 7-6c plots the non-dimensional orifice diameter against the orifice Reynolds number. From the figure, a clearly defined border between directly dissipating and initially interacting flows may be observed. Along this border

unstable slow jet flows occur. The simplest expression that may be found which defines this border adequately is

$$\frac{D_o}{D_p} = \tanh \left[ \frac{Re_o}{820} \right] \quad (7.1)$$

this expression is plotted on figure 7-6c. This expression gives a value close to unity, (0.993), for a critical pipe Reynolds number of 2300, (chapter 2, section 2.2.1), as one would expect.

The initially interacting flows occupy a region at the bottom left hand of figure 7-6c which corresponds to high orifice Reynolds numbers and small orifice diameters. Whereas, the directly dissipating flows occur at low orifice Reynolds numbers and large orifice diameters. The plot of the non-dimensional lip height versus the wake Reynolds number (figure 7-6d) shows a directly dissipating region which bulges from the vertical axis. Also plotted on the figure is the line corresponding to the critical pipe Reynolds number of 2300. Below this line all flows will be turbulent. This is assuming that superlaminar flow does not occur, which should be the case as the flow pulsations will be sufficient to trigger the transition process.

## 7.2.2 Centre-Line Velocity and Turbulence

### Intensity Results

#### 7.2.2.1 Directly Dissipating Flows

The variation in the centre-line velocity and turbulence intensities as the directly dissipating flow proceeds downstream from the orifice plate is given in figure 7-7. For a directly dissipating flow the velocity profile decreases gradually from its maximum value as the flow passes through the orifice to its minimum value which is the downstream boundary condition. The peak in both turbulence intensities, Point-T.I. and H.P.-T.I., occurs soon after the flow leaves the orifice

plate, generally within one pipe diameter downstream. From this point the turbulence intensities decrease smoothly to the downstream condition. The maximum in the turbulence intensities corresponds to the point of maximum growth of the vortices, from which point they begin to decay. A more complex picture for the centre-line velocity and turbulence intensities occurs for the initially interacting flows and will be discussed in the next section.

### 7.2.2.2 Initially Interacting Flows

A schematic picture of the variation of centre-line velocity and turbulence intensities, as the flow proceeds downstream, is given in figure 7-8. From the figure, one may see the typical initially interacting velocity profile, that is the increasingly rapid decrease in flow velocity as the flow emanates from the orifice plate, reaching a minimum downstream, before increasing back to the downstream condition.

The velocity minimum corresponds to the turbulent region, (region 5, as defined above). This is probably due to a flattening of the velocity profile by the turbulent Reynolds stresses, see figure 7-9. The initially axisymmetric fluctuations,  $u_z^2$ , will cause radial fluctuations,  $u_r^2$ , to be set up. It is likely that the radial fluctuations will be a function of the axial fluctuations, i.e.  $u_r^2 = F(u_z^2)$ . The radial fluctuations cause the flattening of the flow profile, thus a link between the axial fluctuations and the profile flattening might be found. However, the simultaneous measurement of  $u_z^2$  and  $u_r^2$  would require a two-component laser system, it was, therefore, outside the scope of the work presented herein.

Both the Point-T.I. and the H.P.-T.I. are also plotted on figure 7-8. In general, for the results obtained, the H.P.-T.I. peaked at the point of maximum slope of the velocity profile, i.e. maximum value of  $-dU/dz$ . The Point-T.I., on the other hand, peaked at the point of minimum velocity, i.e.  $dU/dz = 0$ . The reason for the different position in the T.I. peaks may be explained in the following way.

The H.P.-T.I. is a normalised measure of the absolute velocity fluctuations, since  $u_z^2$  is normalised by dividing it by the centre-line velocity of

Hagen-Poiseuille flow, for the equivalent mass flux. A value which remains constant for each Reynolds number. Therefore, the peak value of the H.P.-T.I., corresponds to the maximum velocity fluctuation. The velocity fluctuations cause Reynolds stresses within the flow, which lead to the flattening of the velocity profile radially. Thus, the maximum value of the H.P.-T.I. should correspond to the maximum flattening of the velocity profile, i.e. a maximum value of  $-dU/dz$  at the centre-line. This phenomena can also be observed in the replotted results of Khezzar et al [1986], which are discussed in chapter 2, section 2.3.7 and shown in figure 2-33.

The Point-T.I. is a measure of the magnitude of the velocity fluctuations relative to the flow velocity at the local point measured. Thus, this definition will give very large values for areas of low mean flow with large fluctuations. In certain circumstances, the average flow velocity may be zero, (i.e. within the recirculation zone), this case would give an infinite value of Point-T.I. Therefore, it is not surprising that the maximum value of Point-T.I. occurs at the position of minimum velocity. (However, this need not be the case, it is easy to envisage circumstances where the Point-T.I. maximum is not at the flow velocity minimum. Suffice to say that it does have a 'tendency' to move towards the velocity minimum.)

There has been considerable interest in recent years in confined jet flows, it would therefore be useful to compare the results of chapter 6 with submerged jet flow data. In general, for confined jet flows the centre-line turbulence intensity is normalised to the mean jet velocity. In the case of an orifice flow this would be the mean velocity through the orifice plate. This orifice Turbulence Intensity is then defined as,

$$\text{Orifice T.I.} = \frac{u'_{rms}}{\bar{U}_o} \quad (7.2)$$

Figure 7-10a gives details of the turbulence intensity variation of a submerged jet downstream of the jet entrance, as given by Withers [1991]. It can be seen that the peak in the Orifice-T.I. for the three types of jets shown is approximately

15% ± 1%.

The forced vortex flows investigated in this study behaved in two distinct ways, depending on whether the flow was Directly Dissipating or Initially Interacting. This is shown in figure 7.10b, on which is plotted the maximum value of turbulence intensity obtained against the normalised orifice diameter,  $(D_o/D_p)$ . In the figure both the H.P.—Turbulence Intensity and the Orifice—Turbulence Intensity are plotted.

From the figure one may see that the Orifice T.I. remains constant over the range of Initially interacting flows, (from 27.4% to 30.1%), and the H.P.—T.I. remains constant, (from 10.1% to 13.0%), over the directly dissipating flow range. Two main conclusions may be drawn from the results of figure 7-10b, these are:

- 1 - The peak values of the centre—line orifice turbulence intensity for Initially Interacting flows, as defined in equation 7.2, are approximately twice that of those found in submerged turbulent jets, (figure 7-10a). However, the jet data is for fully turbulent unpulsed jet flows, whereas the results reported herein are for initially laminar, pulsed orifice flows which break down to the turbulent state on leaving the orifice plate. The pulsations themselves contribute to the turbulence intensities obtained by enhancing the vortex growth mechanism prior to breakdown.
- 2 - The downstream centre—line turbulence intensity depends on the downstream flow regime. For the case of initially interacting flows, the maximum value of the root mean square of the turbulent fluctuations,  $(u'_{rms})$ , is linearly related to the mean orifice flow velocity, and hence the Orifice Reynolds number. This is shown in figure 7-10b, by the constant Orifice—T.I. value in this region. The turbulent fluctuations in Directly Dissipating flows are, however, independent of the orifice plate used. This is probably due to the fact that the vortices generated in directly dissipating flows die out shortly after leaving the orifice plate and, unlike the Initially Interacting flows, do not grow to a size whereby they interact and cause large turbulent fluctuations at the centre—line.

### 7.2.3 Transverse Measurements of Velocity and Turbulence Intensity for Initially Interacting Flows

Transverse measurements were taken for only one set of flow parameters, namely a pipe Reynolds number of 256, an orifice diameter of 13mm and a pulsation frequency of 2.54 Hz and amplitude of 0.6 Volts. These correspond to the standard set as defined in chapter 4, section 4.5. These results were only taken for the first 50mm, (or two times the pipe diameter), downstream of the orifice plate.

The behaviour of the velocity across the central part of the jet is shown in figure 7-11a. Initially as the jet of fluid streams through the orifice the mean velocity profile consists of a fairly flat central region with a steep velocity gradient at the edge of this central jet. As the fluid proceeds downstream the central region decreases as more of the fluid in the jet is retarded at the sides, and the velocity gradient across the retarded zone becomes less steep, as shown in figure 7-11a.

Typical behaviour of the Point Turbulence Intensities downstream of the orifice plate are shown in figure 7-11b. The turbulence intensities over the central core of the fluid emanating from the orifice plate tend to be fairly constant over that part corresponding to the constant velocity profile. However, at the jet edge the turbulence intensities increase dramatically. This increase in the turbulence intensities corresponds to the vortex structures which surround the jet core.

It would seem, therefore, that the issuing jet has a fairly flat velocity profile across its central core, with a steep velocity gradient bringing the velocity down to the much slower velocities attained in the slower moving fluid in the recirculation zone. This steep velocity gradient is gradually lessened, as the fluid moves downstream, by the action of the growing vortex structures at the jet edge. The eventual breakdown of these structures leads to a rapid flattening of the velocity profile induced by the Reynolds stresses in the turbulent region. The overall results compare well with those of Sibulkin, (Chapter 2, figure 2-34c), where he investigated the relaminarisation of turbulent jet flows at a pipe expansion.

### 7.3 THE EVIDENCE FOR CHAOTIC BEHAVIOUR

In this section the evidence for the existence of chaotic behaviour of the forced vortex flow system is summarised from the results of chapter 6.

#### 7.3.1 Preliminary Analyses: The First Minimum in Mutual Information, Autocorrelation Function, Attractor Plots, Return Maps and Probability Density Functions

The route to chaotic behaviour for the forced vortex system may be seen by using preliminary analysis techniques. These are discussed below:

##### The First Minimum in Mutual Information

The first minimum in the mutual information function as defined in chapter 2, equation 2.46, is used to determine a suitable time delay for the construction of an attractor. In general, oscillator systems with a dominant forcing frequency will have a first minimum in mutual information at one quarter of the forcing time period. Using this time period as the delay time to reconstruct the attractor will lead to the most 'spread out' attractor in phase space, making the structure of the attractor amenable to being probed by the characterisation technique, i.e. a fractal dimension or Lyapunov exponent algorithm.

The time series analysed in this study were of forced vortex flows through a pipe orifice. These flows formed vortex rings immediately on leaving the orifice lip, the shedding of the rings occurred at the forcing frequency of the flow pulsations, which in turn was kept at the natural shedding frequency of vortex shedding for each specific flow Reynolds number. The shed ring vortices behaved in two generally distinct ways depending on the flow parameters:

1 – they either enlarged to a point whereafter they dissipated out, retaining their axisymmetry throughout their evolution and decay, (Directly Dissipating Flow),  
or,

2 - they merged into larger structures and further enlarged to a point where their size was of the order of the pipe internal diameter whereby they lost their axisymmetry and broke down into a complicated, turbulent flow regime, which dissipates out further downstream, (Initially Interacting Flow).

For the case of directly dissipating flows the mutual information function gave a distinct minimum at one quarter of the forcing period throughout the evolution of the flow.

A more complex picture appeared for the initially interacting flow, (see for example figure 6-9). For the initially interacting flows the first minimum in the mutual information function appeared at one quarter of the forcing cycle time period just downstream of the orifice plate, where the vortex rings are still intact and increasing in size rapidly. Then, as the vortices breakdown into a turbulent regime, the first minimum in mutual information rapidly increases with a maximum value of up to 17 times the original minimum due to the forcing function being observed, (see figure 6-29b).

However, the minimum mutual information function did seem to decay in an exponential manner for very complex flow regimes and the calculated minimum may have been no more than a slight undulation in the decaying minimum mutual information function caused by the forcing pulsations.

A novel non-dimensional complexity parameter, based on the minimum mutual information function, was used in the study. This was obtained by dividing the first minimum in mutual information obtained from the time series, by the first minimum in mutual information that would be given by the forcing period, i.e. one quarter of the forcing period. If this is labelled the non-dimensional, mutual information complexity parameter,  $M^*$ , then

$$M^* = \frac{\text{First Minimum in Mutual Information obtained from the Time Series}}{\text{First Minimum in Mutual Information of the Forcing Function}} \quad (7.3a)$$

or,

$$M^* = \frac{\text{First Minimum in Mutual Information}}{1/4 \text{ Forcing Period}} \quad (7.3b)$$

Thus, for a flow where the forcing frequency dominates  $M^*$  is equal to unity. More complex flows produce values of  $M^*$  greater than unity. The significance of this parameter is that it allows the variation in minimum mutual information to be compared between flows with different forcing frequencies.

### Autocorrelation Function

The autocorrelation function was not used to determine the attractor construction time delay. This is because the first minimum in the mutual information is the preferred method, as the autocorrelation function cannot 'see' the non-linear correlations that can be picked up by the mutual information function, (see chapter 2, section 2.5.3). However, much information may be gained from the autocorrelation function, and thus it was calculated for all the time series produced. The results of the autocorrelation function for one initially interacting flow, the standard set (as defined in chapter 4, section 4.5), were presented at the end of chapter 6, (figure(6- 63.)

Referring to figure 6- 63. The autocorrelation function exhibits periodic behaviour for a dominant forcing function. However, the effect of period doubling due to vortex merging is much in evidence, giving a two period waveform. The effect of other, noisy frequencies in the flow causes the autocorrelation function to decay as the delay time is increased. Once the flow has broken down to the turbulent state, the autocorrelation function exhibits a rapidly decaying form typical of turbulent flow. With the first zero being a temporal measure of the largest structures within the flow.

### Attractor Plot

Again attractors were plotted for all the results obtained, some of which are presented in chapter 6. In regimes where there is a dominant forcing frequency,

i.e. in directly dissipating flows and the preliminary ring vortex growth in initially interacting flows, the attractors are of a coherent, periodic nature with a thickening of the attractor band due to the presence of noise in the system. Good examples of such attractors may be seen in figures 6-11a, 6-21a, 6-30a and 6-31a. A schematic diagram of a noisy periodic attractor is shown in figure 7-12a.

One other feature of the noisy periodic attractors which may be observed from those plotted in chapter 6 is the change in overall shape of the attractor as it develops. The noisy periodic attractors tended to a rounded triangular shape as the attractor developed downstream, before becoming more complex. This may be observed by following the attractors plotted in figures 6-11a to 6-11c. The attractors obtained bear a striking resemblance to the locked, forced attractor obtained by Williams-Stuber and Gharib [1990], which is plotted in chapter 2, figure 2-59b.

Once the vortices enlarge and interact, the attractor band tends to lose its shape and in certain instances a period doubled attractor may be observed. A schematic diagram of an initially noiseless, periodic attractor, before and after it has period doubled, is shown in figures 7-12b and 7-12c respectively.

Finally, at breakdown of the flow, a very complex time series is obtained which gives an similarly complex attractor as depicted in figure 7-12d. However, as the attractors are plotted in two dimensions, it is impossible to discern a higher dimensional structure with the naked eye. In such cases dimension algorithms are required to probe the underlying structure of the attractor.

### Return Map

Return maps are useful for observing period doubling routes to chaotic flow. However, the presence of noise may completely obscure the period doubling. In this thesis only one return map was presented, (figure 6-65). The presence of noise completely obscured the period doubling plot, however, by using different markers for each alternate peak a 'tendency' for each alternate peak to visit a different section of the return map was observed, indicating that a period doubling had occurred. Return maps may also show up underlying structure in chaotic flows, however, the presence of noise did much to prevent the return map being used

more often in the analysis of the data.

### Probability Density Function

An attempt was made to probe the attractor band during its initial noisy, periodic structure. To do this the attractor band was sampled once per cycle on the attractor. By doing this, a probability density histogram,  $\Phi(x)$ , may be built up of the trajectory crossings. As far as the author is aware this technique has not been used before.

The results of the probability histograms showed the development of the attractor band as the vortex system evolved downstream. For the case examined in detail in chapter 6, section 6.9.2, (standard set, chapter 4, section 4.5), the following was observed in the histogram as the flow developed downstream of the orifice plate:

- 1 - The probability histogram of the attractor band initially had a Gaussian distribution, indicating that the attractor was of a noisy, singly periodic structure, (figure 7-13a).
- 2 - The histogram then became skewed, (figure 7-13b).
- 3 - The histogram then developed two peaks, indicating a period doubling of the system, (figure 7-13c).
- 4 - The histogram developed an additional peak indicating a further bifurcation in the band, (figure 7-13d).
- 5 - The histogram then degenerated into a random shape, tending back towards the initial Gaussian shape of the band, (figure 7-13e). However, at this point the attractor has an indistinguishable shape, (figure 7-12d), and this Gaussian distribution indicates a completely random, (noisy), time series rather than a periodic times series with a noisy spreading of the attractor band, (figure 7-12a). (See also chapter 6, figure 6-64.)

#### 7.3.2 Downstream Development of the Lyapunov Exponent, Dimension and Turbulence Intensity

Many of the flows investigated by the author and described in this thesis did

exhibit behaviour which gave broad band frequency spectra. However, investigation of the Lyapunov exponents and Grassberger–Procaccia dimension of the resulting time series suggest that these flows were in fact chaotic at certain spatial positions within the flow field.

Figure 7–14 presents the general trends of the Dimension, Lyapunov Exponent and Turbulence Intensity results, plotted against downstream distance for initially interacting flows. The figure is a summary of the salient details of these characterisation techniques. All the values are normalised by setting the maximum value of each variable equal to unity. (A similar plot for a directly dissipating flow contains no interesting features as the Lyapunov exponent and dimension of such flows remains fairly constant over the downstream region, since the flow remains periodic.)

From figure 7–14, the following may be discerned:

#### 1 – Lyapunov Exponents

The most obvious feature of the Lyapunov exponent plot is that it is always positive. However, one would expect a negative Lyapunov exponent for a periodic flow. The reason for this discrepancy is the presence of noise in the signal, which blurs the paths of the trajectories. Thus two initially very close trajectories will statistically appear to have separated due to the presence of noise. More will be said on this topic in section 7.5.3.1.

In general the Lyapunov Exponent peaks first. This occurs at the point where the vortices are just beginning to lose their simple axisymmetric structure. The rapid increase in the Lyapunov exponent indicates that the trajectories are now separating beyond the noise level and a chaotic attractor has appeared. The Lyapunov exponent plot then seems to cut-off. A result one may attribute to the attractor dimension exceeding that of the reconstruction phase space. The reconstruction phase space remained at four for all results reported.

The results of the Lyapunov exponent calculations do, therefore, imply that a strange attractor is forming as the vortex system evolves downstream of the orifice plate.

## 2 - H.P.-Turbulence Intensity

The peak in the H.P.-T.I. occurs between the Lyapunov exponent and both the Point-T.I. and Dimension, (which occur at approximately the same position). The peak corresponds to the maximum actual fluctuation in the flow, which occurs at the point of vortex breakdown, i.e. the boundary between regions 4 and 5, as described in section 7.2.1.1 and shown in figure 7-1. The H.P.-T.I. peak occurs on the up slope of the attractor dimension plot, but after the peak cut-off value of the Lyapunov exponent, which suggests that the attractor at this point has exceeded the embedding dimension of the Lyapunov exponent calculation, which is equal to four. It also implies that the flow at this point of breakdown has not yet reached its maximum complexity as the dimension is still increasing.

## 3 - Point-Turbulence Intensity and Grassberger-Procaccia Dimension

These peak last, at approximately the same downstream position. Both peak within the fully turbulent region. The Point-T.I. peaks at this point due to the presence of the velocity minimum at this point, (see section 7.2.2.2). The peak in the Grassberger-Procaccia dimension plot at this point suggests that the highest dimensional attractor, and hence maximum flow complexity coincides with the maximum value of the Point-T.I..

The value of the dimension is very difficult to accurately obtain from the ' $\log(r)-\log(Cr)$ ' plot for high dimensional attractors. This is due to the steepness of the slope, the presence of associated noise and the fact that fewer points are used in the plot at higher embedding dimensions.

## 7.4 THE ROLE OF THE NEW TECHNIQUES IN DESCRIBING TRANSITIONAL FLUID PHENOMENA

### 7.4.1 Introduction

The experiment set up and reported upon within this thesis has sought to induce a turbulent state downstream of an axisymmetric disturbance in flows with pipe Reynolds numbers much below the critical value. The aim has been to produce a flow system where the salient features of the breakdown to turbulence

may be observed.

The field of non-linear dynamics has much to offer the study of flow transition and turbulence. Much knowledge about the behaviour of complex systems has been forthcoming from the study of non-linear systems.

#### 7.4.2 The Description of Non-Random Flows

Until recently it was thought that a broad band frequency spectra indicated that the time signal, from which the frequency spectra was constructed, was random, or at least had some element of randomness connected with it. It followed from this that the evolution through time of the system, or variable, described by the time series had randomness associated with its motion. This randomness was either attributed to the unpredictable nature of the system itself or to external noise (randomness) influencing the system.

When mathematicians and scientists discovered non-linear phenomena which exhibited seemingly unpredictable behaviour, they either ignored it, blaming it on external noise, and concentrated on the well behaved regions of behaviour, or alternatively, they used a statistical approach to characterise the behaviour. However, with the discovery of chaotic motion, researchers realised that it was possible for a dynamical system to behave in a seemingly unpredictable way, exhibiting a broad band frequency spectrum, and yet be governed by relatively simple dynamical rules. It was also possible for a highly complex system, such as a fluid flow, to behave in a relatively simple way, which although seemed unpredictable, could be described by a low dimensional dynamical system.

Once chaotic motion was established as a phenomenon scientists sought, ways to characterise it. The frequency spectra is of limited use, as both random noise and deterministic chaotic motion exhibit broad band frequency spectra. The two main methods in use at present are the Lyapunov exponent and the Grassberger-Procaccia dimension. With these techniques, one may determine whether the system observed is behaving chaotically or randomly, as described chapter 2, section 2.5.1. Positive, non-infinite values of the Lyapunov exponent and the Dimension indicate a chaotic flow.

### **7.4.3 The Practical Application of the Techniques from Non-Linear Dynamics**

Once an experimental time series has been probed and found to behave chaotically this provides the investigator with the knowledge that the underlying dynamics may be described by a relatively simple model. Such models may then be constructed in a variety of ways, some of which are described in chapter 2, section 2.4.8. This is a major step forward in the understanding of many systems, as prior to the understanding of chaotic dynamics the investigator would be forced to conclude that the system was behaving randomly and therefore employed a statistical approach to model, or predict, the evolution of the system.

In the investigation presented herein the construction of a model system was outside the scope of the project due to the constraint of time. This thread of investigation may lead to subsequent work in the area.

During the course of the investigation another possible practical application of the techniques came to light. This is by using the techniques to the predict flow complexity and linking this to the energy loss associated with them. This could be done by setting up an experimental investigation to monitor the Reynolds stresses induced by flows of varying complexity, using a two component L.D.A. system. The information gained would be of direct use in turbulent flow models for transitional flow regimes. (See chapter 8, section 8.3, 'Suggestions for Future Research'.)

## **7.5 FURTHER NOTES ON THE CHARACTERISATION ALGORITHMS**

### **7.5.1 Introduction**

During the course of the investigation and analysis of the results a few points came to light about the behaviour of the characterisation techniques. The presence of noise affected both the dimension and Lyapunov exponent algorithms. Some notes on the effect of noise will be presented in section 7.5.2 and 7.5.3.

In addition the author undertook some preliminary studies on the Grassberger–Procaccia dimension algorithm, when applied to two separate systems, both based on the Duffing oscillator. These are:

- 1 – Two multiple oscillator systems with different modes of coupling,
- 2 – The transients produced by a linear oscillator.

This work was done subsequent to the main work of this thesis and will not be presented in full herein, however, a brief summary of the two pieces of work is given in appendix 6.

### 7.5.2 The Grassberger–Procaccia Dimension Algorithm and Noise

Noise is the main source of uncertainty in most signal analysis. Noise has the effect of obscuring the true picture, however, when the noise is below an acceptable level, the underlying dynamics of a system may still be discerned. One is required to know precisely the effect that noise has on the characterisation technique, in order to discount its effect.

The effect that noise in the signal has on the Grassberger–Procaccia dimension plot is to increase the attractor dimension estimate with the embedding dimension. This occurs at scales below the noise level. Above the noise level the attractor's structure may be observed. This effect is much documented in the literature and has previously been described in Chapter 2, section 2.5.5.2 and also chapter 4, section 4.2.5 and figure 4.5c.

### 7.5.3 The Lyapunov Exponent Algorithm and Noise

The effect of noise on the Lyapunov exponent estimate is not documented in the literature. The author has conducted some preliminary work into the subject, which will be described below.

The Lyapunov exponent measures the divergence of initially close points on an

attractor. For a chaotic attractor this divergence is exponential giving a positive Lyapunov exponent. It is this divergence property of the trajectories on a chaotic attractor which causes the rapid decorrelation of points on a chaotic time series and leads to the seemingly unpredictable nature of chaotic flows. (See section 2.5.6.1).

### 7.5.3.1 Positive Lyapunov Exponents Caused by Noise

The presence of noise is almost certainly responsible for the positive Lyapunov exponent found for all flow results obtained in this study and presented in chapter 6. This effect was also found by Williams—Stuber and Gharib [1990] in their investigation into the chaotic vortex shedding downstream of an airfoil, and is shown in figure 2-60 of chapter 2. In such a case where the noisy periodic attractor gives a positive (largest) Lyapunov exponent, the chaotic system may still be readily distinguished as it gives a markedly larger exponent value.

The positive Lyapunov exponent obtained from a noisy periodic attractor may be explained using a simple model, the details of which are shown in figures 7-15a and b. In figure 7-15a two noiseless trajectories on a periodic attractor are shown. Let trajectory 1 be the periodic attractor trajectory of the system in question and trajectory 2 be a slightly perturbed trajectory of the system.

On these trajectories two extremely close points are depicted at time '0', denoted point  $x_1$  and  $x_2$ , and are separated by a distance  $\epsilon_0$ . (See the explanation of the Lyapunov exponent in chapter 2, section 2.5.6.1.) If the attractor in figure 7-15a was noiseless, then at time 't' the two points would be at position  $x_1'$  and  $x_2'$  respectively, separated by a distance  $\epsilon_t$ . Since the attractor is not chaotic, there is no divergence of initially close points, thus  $\epsilon_t$  is not greater than  $\epsilon_0$ . In fact, since  $x_2$  is a perturbation to the periodic trajectory on which  $x_1$  lies, and assuming the periodic attractor to be stable, then the perturbed trajectory through which  $x_2$  passes will tend back to the periodic trajectory on which  $x_1$  lies. Therefore,  $\epsilon_t$  is less than or equal to  $\epsilon_0$ . Thus, the Lyapunov exponent for the system is, (equation 2.55, chapter 2),

$$L = \frac{1}{t} \cdot \ln \left[ \frac{\epsilon_t}{\epsilon_0} \right] \quad (7.4)$$

and since  $\epsilon_t < \epsilon_0$ , this expression must be less than or equal to zero. Thus, for a noiseless, periodic flow the Lyapunov exponent should be less than or equal to zero.

If the above picture is complicated by noise associated with the attractor trajectories, this causes a blurring of the trajectories which thickens the attractor band, (as described in section 7.3.1 and figure 7-12), this is shown schematically in figure 7-15b. Thus, at time 't' the separation of the two points becomes indeterminate, as they have a random distribution described by the characteristics of the noise. The noise will have a probability density function,  $\Phi(x)$ , associated with it. If the trajectories are sufficiently close together, then it is reasonable to assume that the two probability distribution functions associated with them are the same, i.e.

$$\Phi(x_1) = \Phi(x_2) = \Phi(x) \quad (7.5)$$

The Lyapunov exponent of the noisy system is again calculated by using expression 7.4, which may be written,

$$L = \frac{1}{t} \cdot \ln \left[ \frac{|x'_1 - x'_2|}{|x_1 - x_2|} \right] \quad (7.6)$$

However, it is usual, in practise, to estimate the mean Lyapunov exponent of an attractor. This is done by calculating the Lyapunov exponent of many diverging pairs of trajectories on the attractor and taking the average. This type of averaging was performed for the Lyapunov exponent results given in chapter 6. Thus, the mean Lyapunov exponent of the system is then,

$$\bar{L} = \frac{1}{t} \cdot \ln \left[ \frac{\epsilon_t}{\epsilon_0} \right] \quad (7.7)$$

where the time delay 't' is constant, and also specifying the initial separation of the trajectories,  $\epsilon_0$ , to be a constant value, then,

$$\bar{L} = \frac{1}{t} \left[ - \ln \left[ \epsilon_0 \right] + \left[ \overline{\ln(|x_1' - x_2'|)} \right] \right] \quad (7.8)$$

This expression requires that the time average of the logarithm of the trajectory separation at time 't' is found, this may be done, knowing the probability distribution function of the noise,  $\Phi$ , as follows,

$$\begin{aligned} \overline{\ln(|x_1' - x_2'|)} &= \overline{\ln(\epsilon_t)} \\ &= \int_{-\infty}^{\infty} \int_{-\infty}^{\infty} \ln(|x_1 - x_2|) \cdot \Phi(x_1) \cdot \Phi(x_2) \, dx_1 \, dx_2 \quad (7.9) \end{aligned}$$

Thus, if the average value of equation 7.9 is greater than  $\ln(\epsilon_0)$ , then equation 7.8 gives a positive number. This is the mechanism by which noise in the system causes the Lyapunov exponent calculation to produce a positive value for a noisy, periodic waveform.

Assuming the noise affecting the trajectories to be completely random and thus decorrelation of the time signal occurring instantaneously, then equation 7.9 is completely independent of the time separating the initial and final trajectory points, and is therefore a constant for a particular noisy periodic attractor system. In other words, the final trajectory separation  $\epsilon_t$  is independent of the time 't' and is only a function of the probability density function of the noise affecting the system.

Thus, according to equation 7.7, the average Lyapunov exponent of the system must be inversely proportional to the separation time 't', as both  $\epsilon_0$  and  $\epsilon_t$  are constants. If this is the case, then one would expect the Lyapunov exponent calculated from such a noisy periodic signal to vary inversely with the time taken between the initial and final sampling of  $x_1$  and  $x_2$ . Such behaviour is depicted in figure 7-16. A chaotic flow would give a Lyapunov exponent which remained constant with a variation in 't', this is also depicted in figure 7-16. A noiseless, periodic flow would give a constant negative Lyapunov exponent, also shown in the figure.

To test this model, the Lyapunov exponent was calculated over a large range of evolution times for the initial vortex growth and breakdown for the standard flow set, (see chapter 4, section 4.5). The standard flow set is for a 13.0mm orifice plate at a Pipe Reynolds number of 256, and has a forcing period of 2.54 Hertz and a forcing amplitude of 0.6 Volts.

The time series at 10mm, 20mm, 30mm, 40mm and 100mm downstream of the orifice plate were used. This corresponds to the vortex growth range (10mm-40mm) and a time series taken downstream of the complete breakdown of the flow, (100mm). The frequency spectra, time series, attractor plots, autocorrelation functions and probability distribution functions for this flow type are given in chapter 6, figures 6-2, 6-10, 6-11, 6-63 and 6-64 respectively.

Figure 7-17 plots out the variation in the Lyapunov exponent against delay time, on a log-log graph. Immediately apparent from the figure is the similar slope followed by all five curves. The slope of these curves is -0.44, which indicates that the average Lyapunov exponent varies inversely with delay time to the power of 0.44, i.e.,

$$\bar{\lambda} \propto t^{-0.44} \quad (7.10a)$$

The reason for this relationship is not obvious. The occurrence of the -0.44 power law needs further interpretation, this is given below.

In the latter stages of the 40mm and 100mm traces, (the two traces at the top of the figure), the average Lyapunov exponent does vary inversely with the delay time, i.e.,

$$\bar{\lambda} \propto \tau^{-1.0} \quad (7.10b)$$

This suggests that the signal has completely decorrelated over these larger delay times, as one would expect.

The 30mm trace is the only plot with a substantial range of constant Lyapunov exponent, as indicated on the figure, i.e.,

$$\bar{\lambda} \propto \tau^{0.0} \quad (7.10b)$$

The Lyapunov exponent for the 30mm trace remaining constant over a range of time delays from 0.05 to 0.15 seconds which is approximately 1/8 to 3/8 of the forcing period. The time taken for one cycle of forcing is  $1/f_f$  which is approximately 0.4 seconds, thus one quarter of the forcing cycle time is 0.1 seconds. This is the recommended delay time for the reconstruction of chaotic periodically forced attractors, i.e. one quarter of the forcing cycle period, [Guckenheimer, 1986], (chapter 2, section 2.5.3). It would seem, therefore, that the 30mm attractor is chaotic with a dominant periodic forcing function. It would also appear that the calculated Lyapunov exponent remains fairly constant for attractors reconstructed using a time delay around the recommended one quarter of the forcing cycle period.

There are no similarly recognisable constant Lyapunov exponent plateaus for the 40mm or 100mm results, which exhibit similar behaviour over the plot. However, the dimension of the flow for these results is probably higher than the embedding dimension, (of 4), used in the attractor reconstruction for the Lyapunov exponent calculation.

The variation in the Lyapunov exponent with time to the power of  $-0.44$  is

not immediately apparent. Combining this result with equation 7.4 leads to,

$$\left[ \ln \left[ \frac{\epsilon_t}{\epsilon_0} \right] \right]^{0.56} \propto t \quad (7.11)$$

The presence of noise is the probable cause of this reduction in the divergence properties of the trajectories.

Figure 7-18 shows schematically a possible mechanism for this occurrence. In the figure, the separation for a pair of noisy trajectories is shown. The trajectories are considered far enough apart for their respective probability density functions to be independent, i.e.  $\phi_1$  is not coincident with  $\phi_2$ . (Compare with figure 7-15b, in which coincident probability distributions were assumed.) As the probability density functions drift further and further apart then the average separation of the trajectories tends to the mean distance between them, as depicted on the figure. After a time delay,  $t$ , the average separation of the trajectories  $\epsilon_t$  becomes simply the separation between the mean path of the two trajectories.

Now, the Lyapunov exponent, as defined in equations 7.7 and 7.8, requires the average of the logarithm of the final separation to be computed, i.e.,

$$\overline{\ln(\epsilon_t)} \quad (7.12)$$

This expression will weight, more heavily, the trajectory separations which end up very close to each other, than those which appear further apart. This will, in turn, reduce the average value of the Lyapunov exponent obtained from the calculations.

This increased emphasis placed on very close trajectories, caused by the logarithm in equation 7.9, could be the cause of the power law relationships of equation 7.10a and 7.11. More work will have to be done in this area to investigate the cause of the relationship between the trajectory separation and the time delay in the presence of noise. However, time does not allow for this work to be taken further herein.

### 7.5.3.2 Coincident Trajectories

The averaging of the Lyapunov exponent of a signal in the presence of noise has a major undesirable effect. The noise superimposed on the signal is random, thus, the possibility arises for the two trajectories to coincide, i.e.  $x_1' = x_2'$ , (refer to figure 7-15). If this occurred, then  $\epsilon_t$  would equal zero and the Lyapunov exponent would appear to be negative infinity according to equation 7-2. To overcome this problem, the author suggests that a more convenient measure of the divergence properties of a noisy trajectory could be obtained by taking the Lyapunov exponent of the average trajectory separation, i.e.,

$$L^* = \frac{1}{t} \cdot \ln \left[ \frac{\overline{\epsilon_t}}{\epsilon_0} \right] \quad (7.13)$$

This type of averaging would eliminate the possibility of a singularity appearing in the calculations. If one characterises the noise in the trajectories by a probability density function,  $\Phi(x)$ , which may be found by taking attractor slices, as described in chapter 6, section 6.9.2. Then the mean separation of the trajectories may be obtained by integrating the following expression:

$$\overline{|x_1 - x_2|} = \int_{-\infty}^{\infty} \int_{-\infty}^{\infty} |x_1 - x_2| \cdot \Phi(x_1) \cdot \Phi(x_2) \, dx_1 \, dx_2 \quad (7.14)$$

This expression may be directly integrated for many types of theoretical noises. For example, if the probability density function of the noise is assumed to be a Gaussian distribution of the type,

$$\Phi(x) = \frac{1}{\sqrt{2 \cdot \pi \cdot \sigma}} \cdot e^{-\frac{1}{2} \left[ \frac{x - \mu}{\sigma} \right]^2} \quad (7.15)$$

Then, combining 7.15 with equation 7.14, and assuming expression 7.5 to be valid, (i.e. coincident probability distribution functions), leads to an average separation of two trajectories with a coincident Gaussian distribution of noise of,

$$\overline{\epsilon_t} = \overline{|x_1' - x_2'|} = \frac{2 \cdot \sigma}{\pi^{1/2}} \quad (7.16)$$

It should therefore be possible to obtain a value of  $L^*$  analytically, if the characteristics of the noise in the attractor band can be defined. However, it should still be possible to obtain a value of  $L^*$  using a numerically obtained probability distribution functions found by slicing through the attractor band.

## 7.6 SUMMARY

In chapter 7, the author has attempted to bring together, and present in a coherent format, the main features of low Reynolds number, pulsed, vortex flows at a pipe orifice. The salient features of such flows were probed using relatively new techniques from the field of non-linear dynamical systems. The emphasis was both on the characteristics of the flow regimes investigated, and, the applicability of the new analysis techniques in describing such flows.

The two flow types found in the study, (directly dissipating and initially interacting), were clearly identifiable using both flow visualisation techniques and the new techniques from the field of non-linear dynamics. The turbulence intensity of the flow does not, in itself, provide enough information to discern the complexity of the flow. The more traditional technique does not reveal the nature of the fluctuations, i.e. whether the fluctuations are periodic, chaotic or random. However, the shape of the centre-line velocity profile does change according to the downstream flow regime.

The main distinction between the directly dissipating and initially interacting flows is the complexity of the downstream flow regime. The orifice plate placed in the pipe acts as a trigger mechanism for the production of vortices. Vortices which

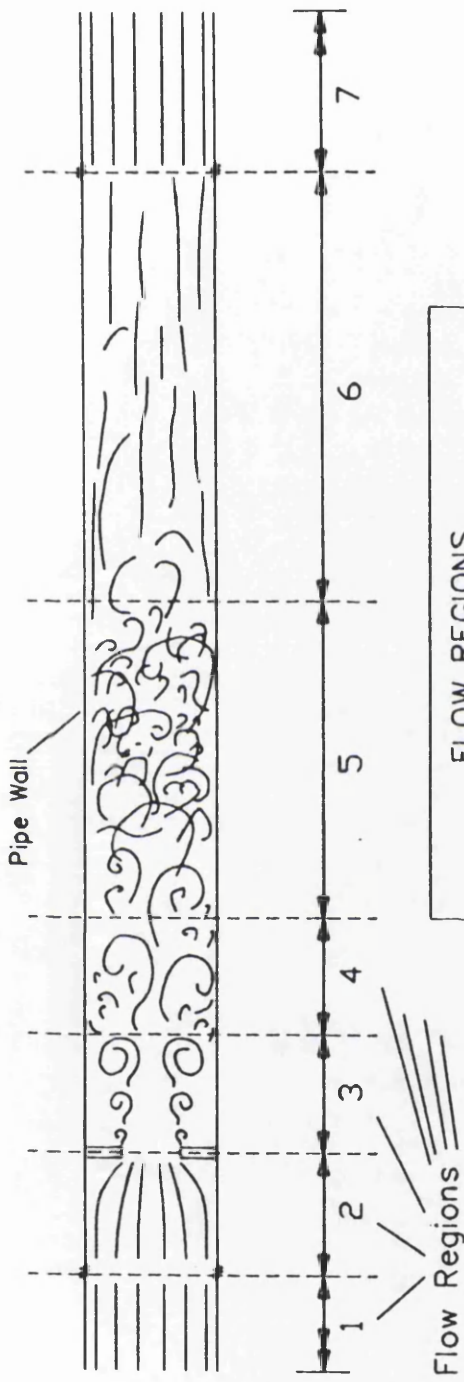
die out downstream of the orifice plate, while remaining axisymmetric, lead to a directly dissipating flow. Initially interacting flows occur where there is a complete breakdown of the vortex flow producing a turbulent region downstream of the orifice plate. Thus, directly dissipating flows are composed solely of the pulsation frequency,  $f_f$ , and in some cases subharmonics of  $f_f$ , (due to vortex merging). Initially interacting flows possess a highly complex, non-axisymmetric structure within the region of vortex breakdown and decay. It is this turbulent region which leads to a rapid flattening of the velocity profile downstream of the orifice plate.

The two techniques from non-linear dynamics used in this study, namely the Lyapunov exponent and Grassberger-Procaccia dimension algorithm, are particularly successful at detecting changes in flow complexity. Using these techniques evidence was found for the existence of low dimensional chaotic flows occurring prior to the breakdown of initially interacting flows.

In addition to the investigation of the flow phenomena, an examination of the two characterisation techniques was also undertaken. In particular, the effect of noise on both the Lyapunov exponent and dimension was discussed. Some theoretical advances on the Lyapunov exponent and noise were put forward.

The main conclusions of the study, together with recommendations for future research, will be presented in chapter 8.

**CHAPTER 7**  
**FIGURES**



- FLOW REGIONS
- 1: Upstream Laminar Pipe Flow
  - 2: Converging Flow Streamlines
  - 3: Axisymmetric Vortex Growth and Recirculation Zone
  - 4: Non-Axisymmetric Vortex Growth and Breakdown
  - 5: Turbulent Flow Region
  - 6: Dissipation and Decay
  - 7: Downstream Laminar Pipe Flow

(Not to scale)

**Figure 7-1: Regions of Flow Behaviour**

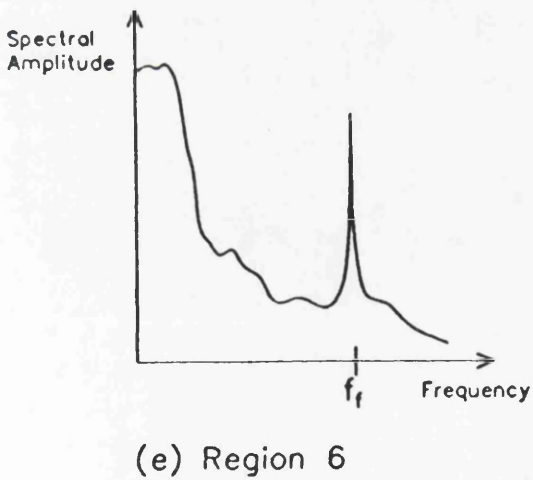
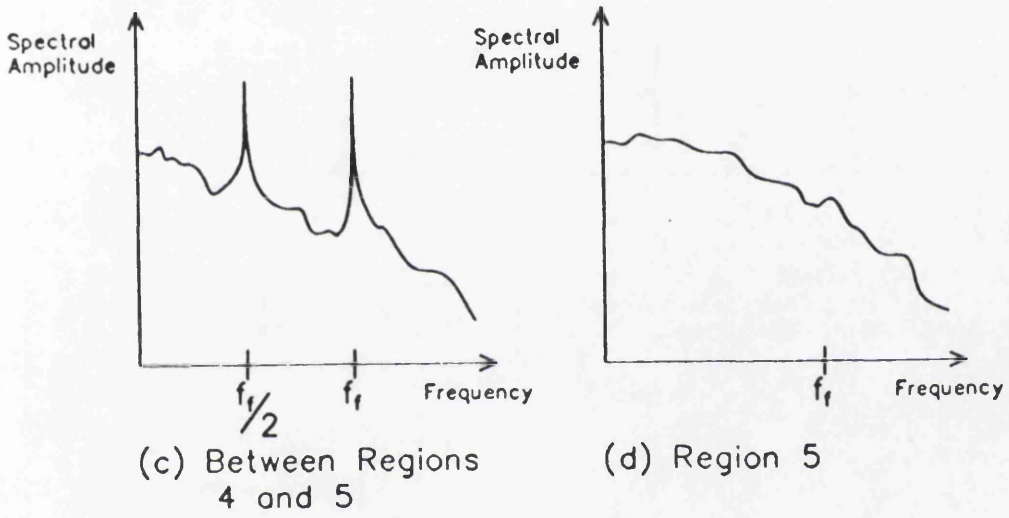
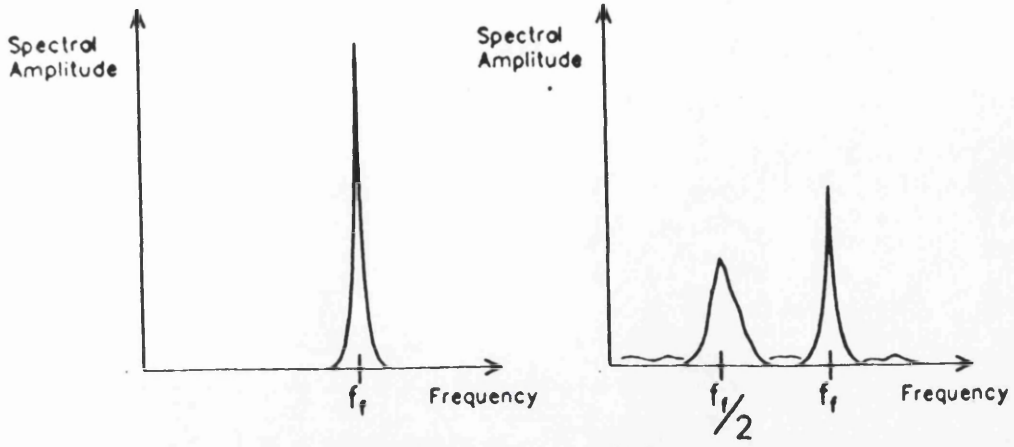


**Figure 7-2: Typical Frequency Spectra Corresponding to the Flow Regions Identified in Figure 1**

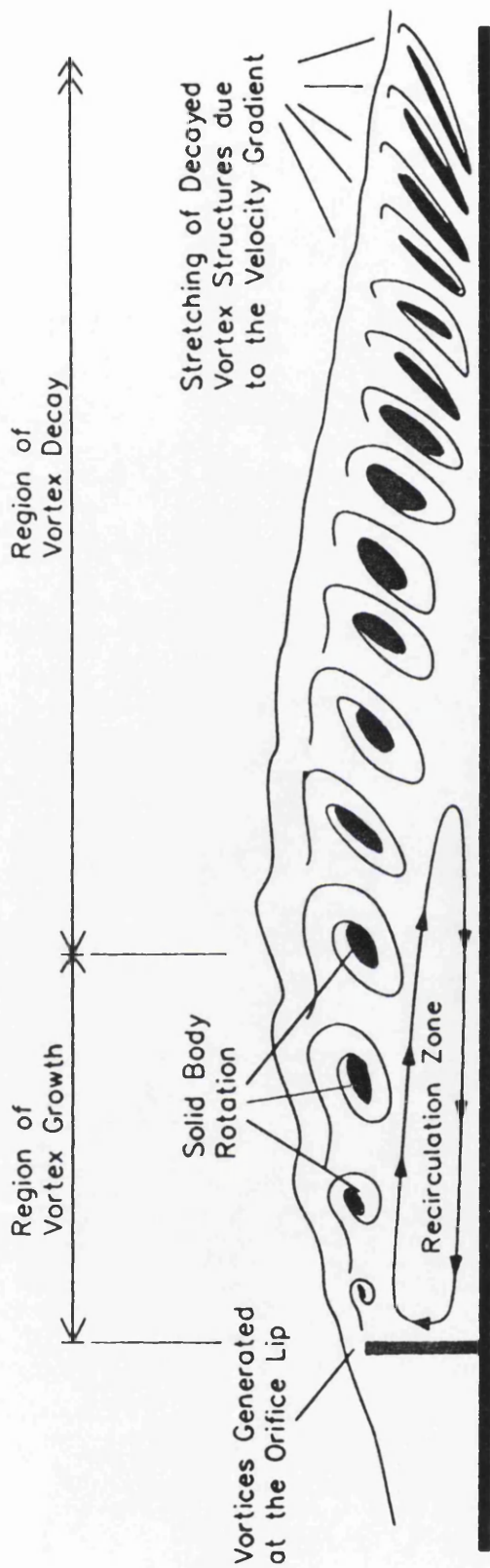


**Figure 7-3: Vortex Evolution in Directly Dissipating Flow**

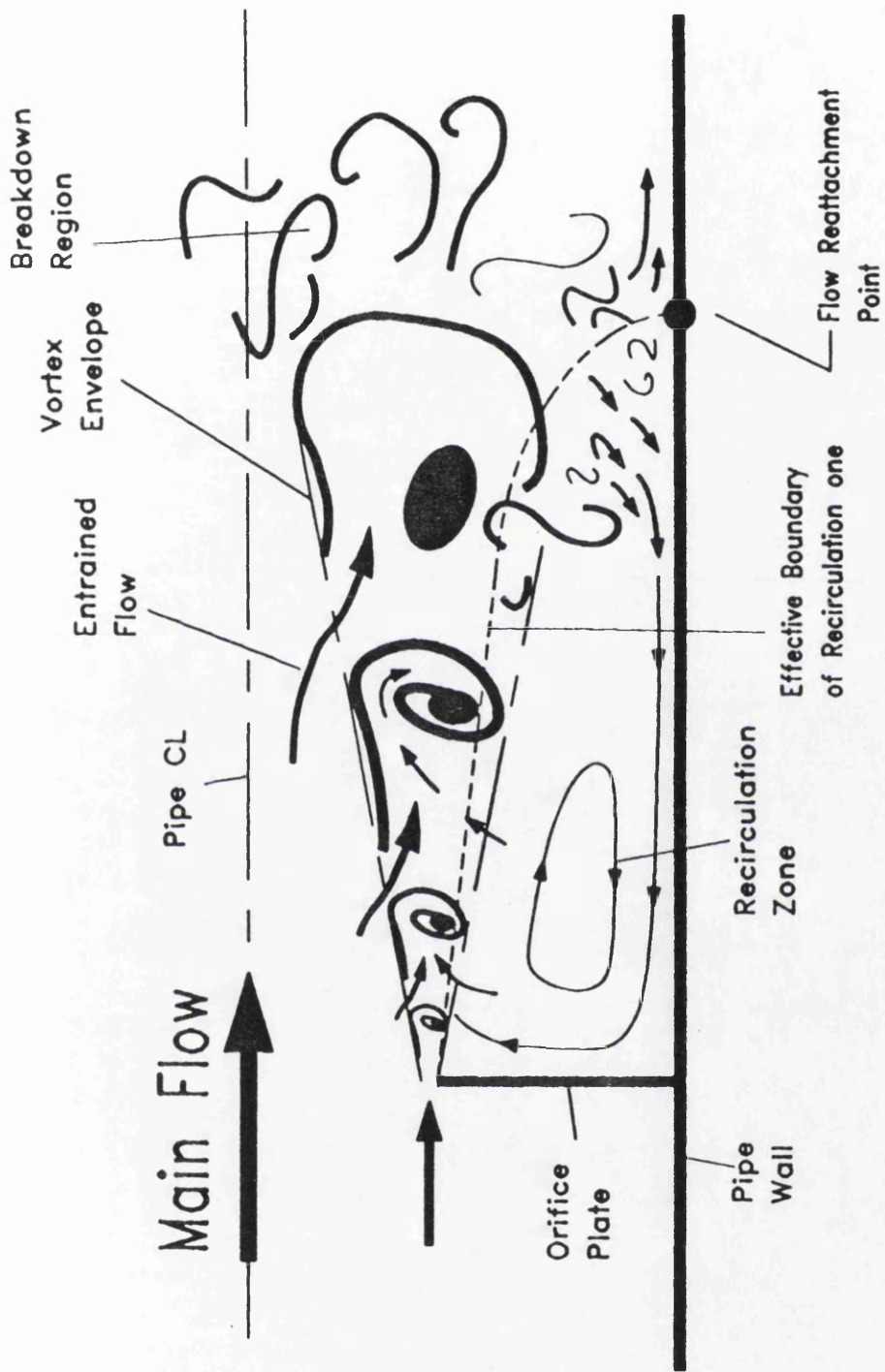
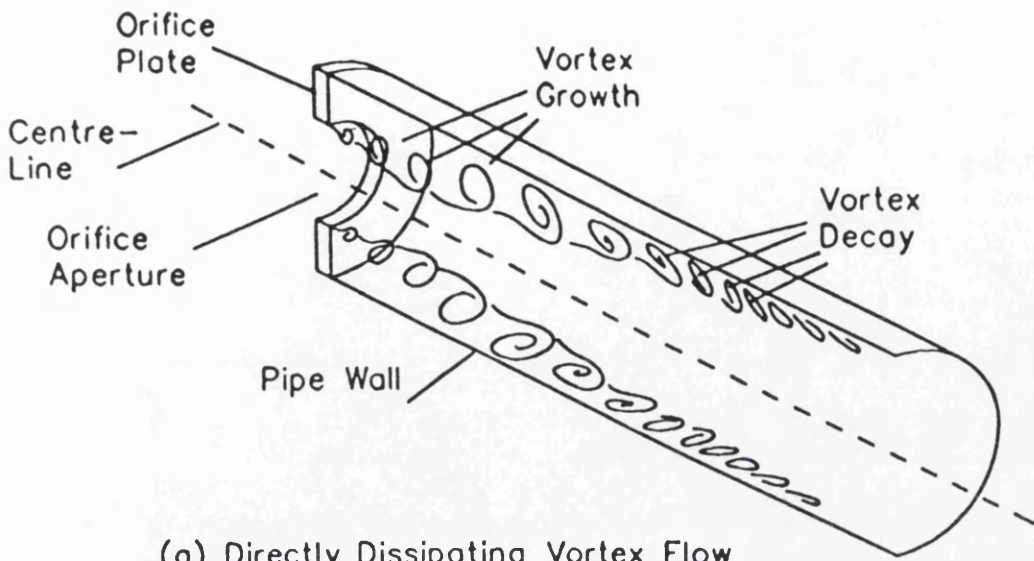
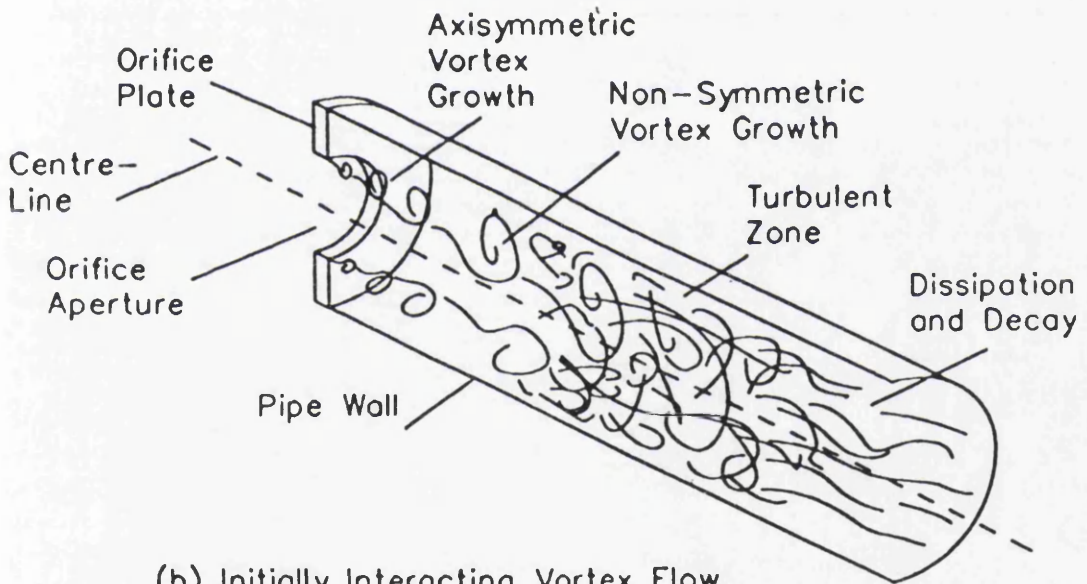


Figure 7-4: Vortex Evolution in Initially Interacting Vortex Flow

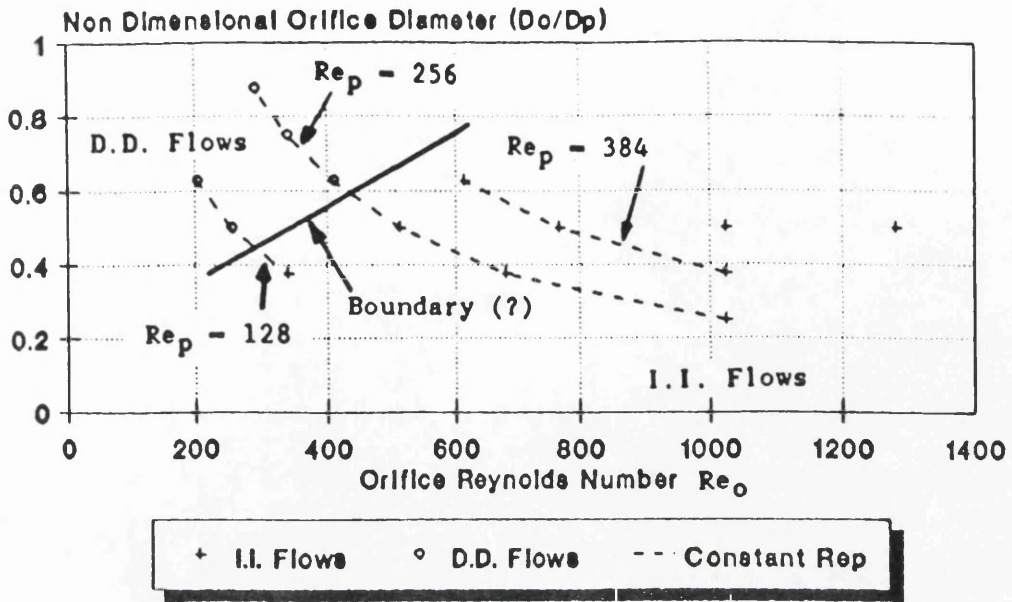


(a) Directly Dissipating Vortex Flow

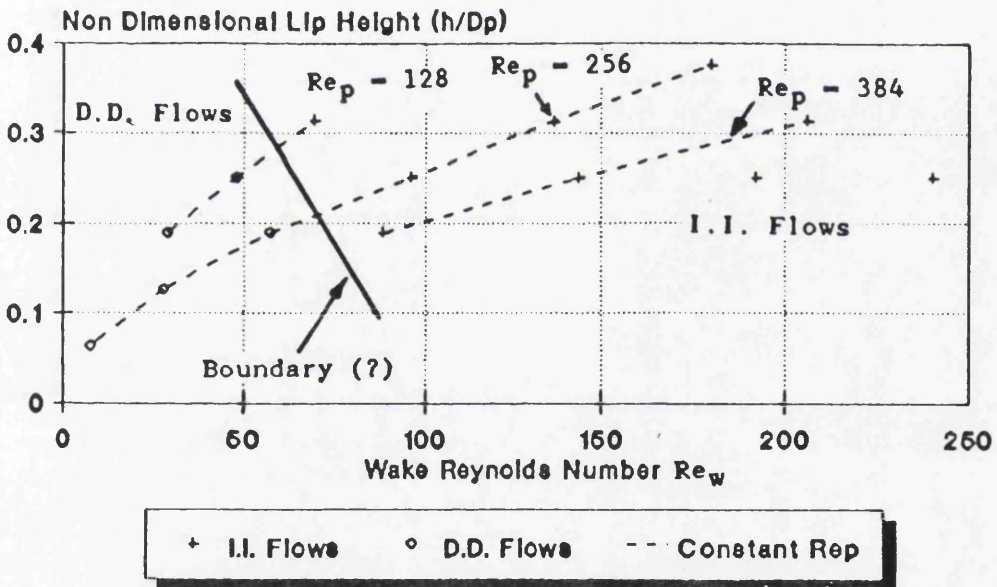


(b) Initially Interacting Vortex Flow

**Figure 7-5: Schematic Isometric Views of Directly Dissipating and Initially Interacting Vortex Flows**

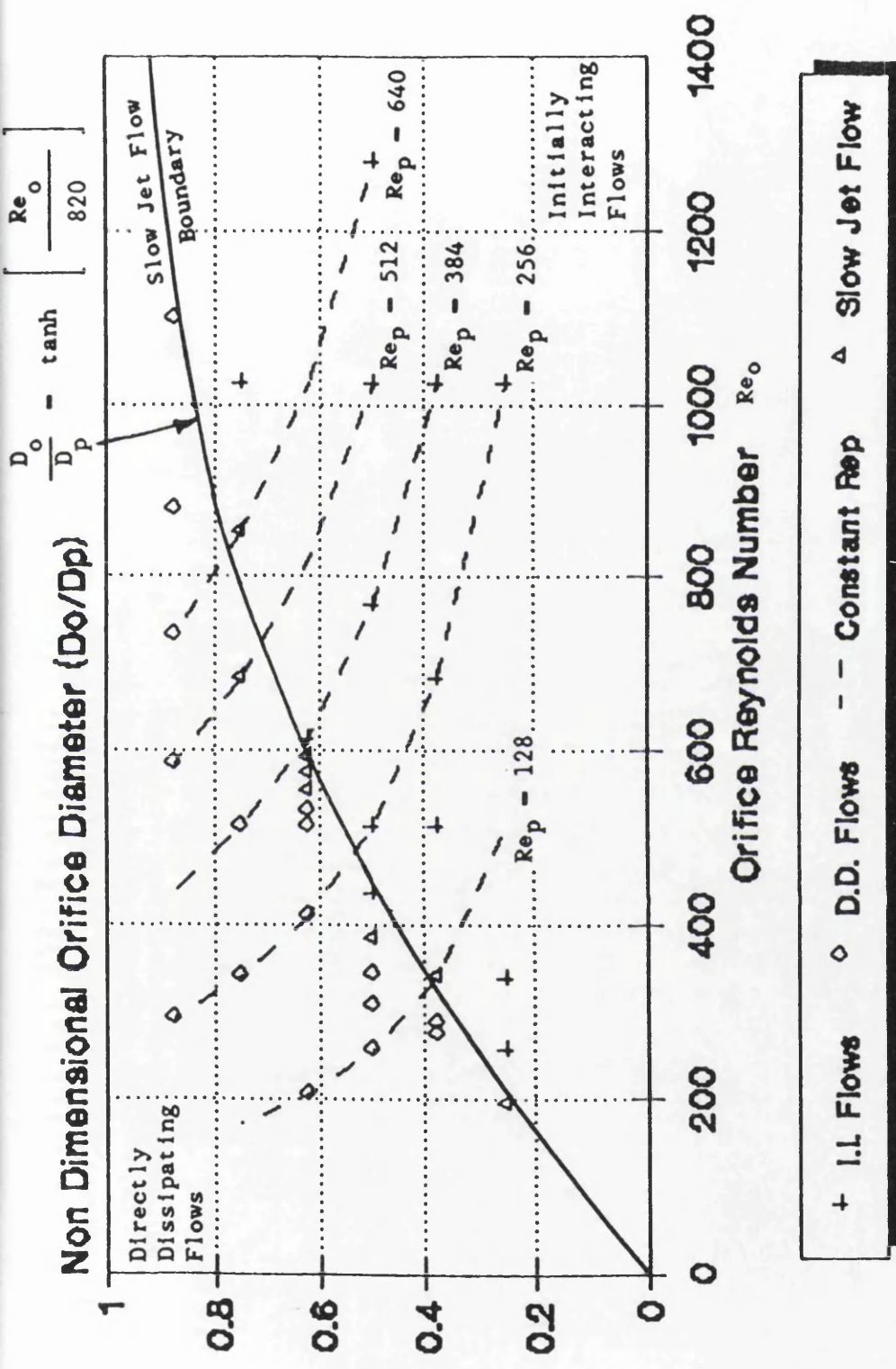


(a)  $D_o/D_p$  versus  $Re_o$



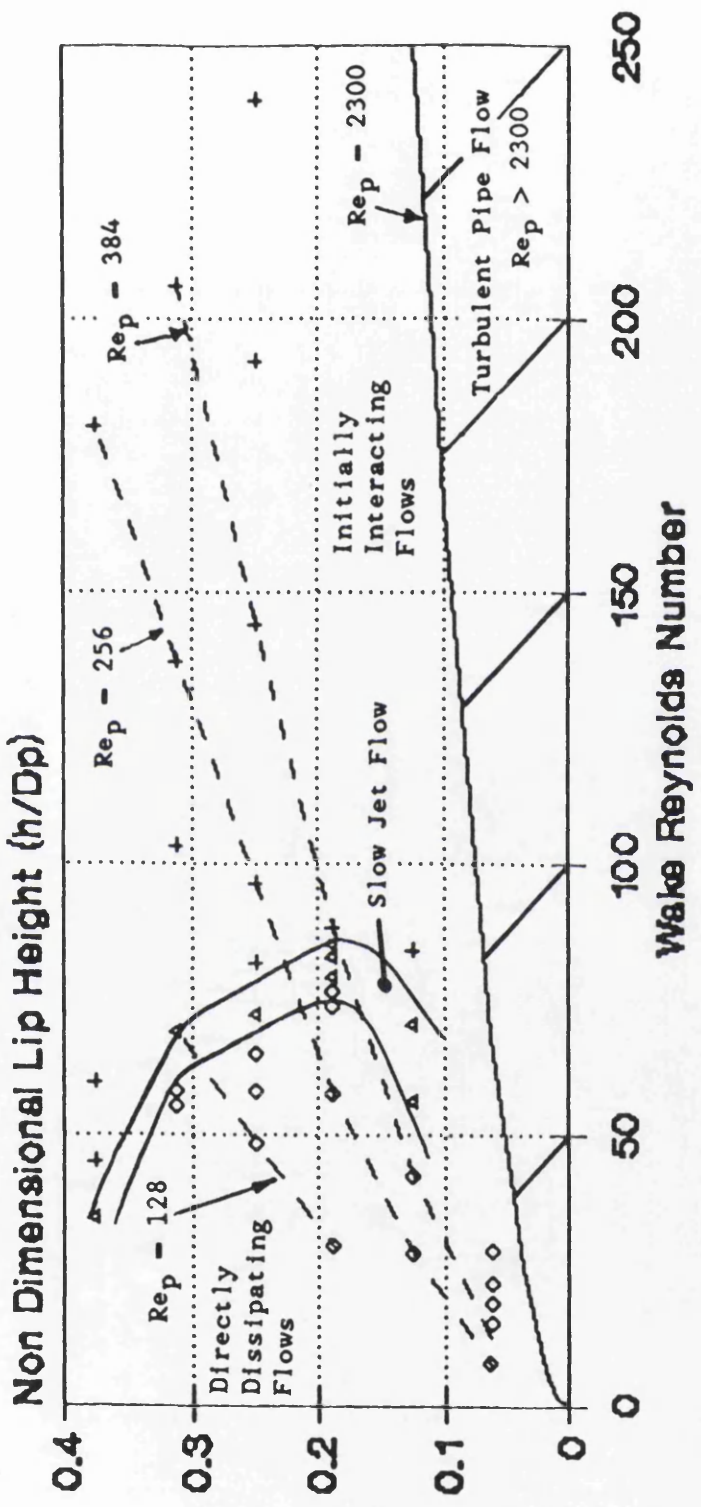
(b)  $h/D_p$  Versus  $Re_w$

Figure 7-6: The Relationship Between Flow Type, Orifice Diameter and Reynolds Number



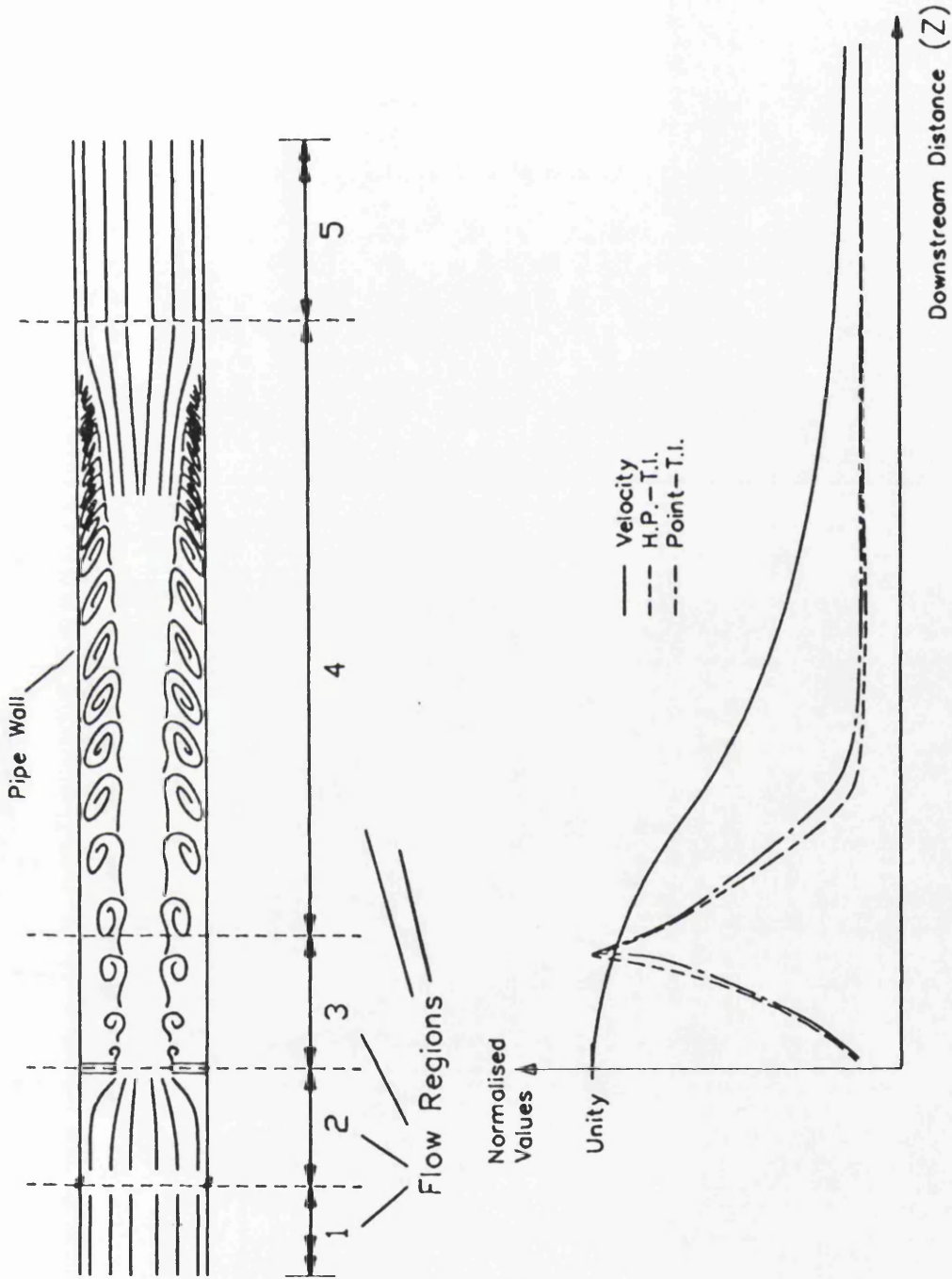
(c)  $D_o/D_p$  versus  $Re_o$  with Additional Results

Figure 7-6: The Relationship Between Flow Type, Orifice Diameter and Reynolds Number



(d)  $h/D_p$  Versus  $Re_w$  with Additional Results

Figure 7-6: The Relationship Between Flow Type, Orifice Diameter and Reynolds Number



**Figure 7-7: The Variation in Centre-Line Velocity and Turbulence Intensity Downstream of the Orifice Plate in Directly Dissipating Flows**

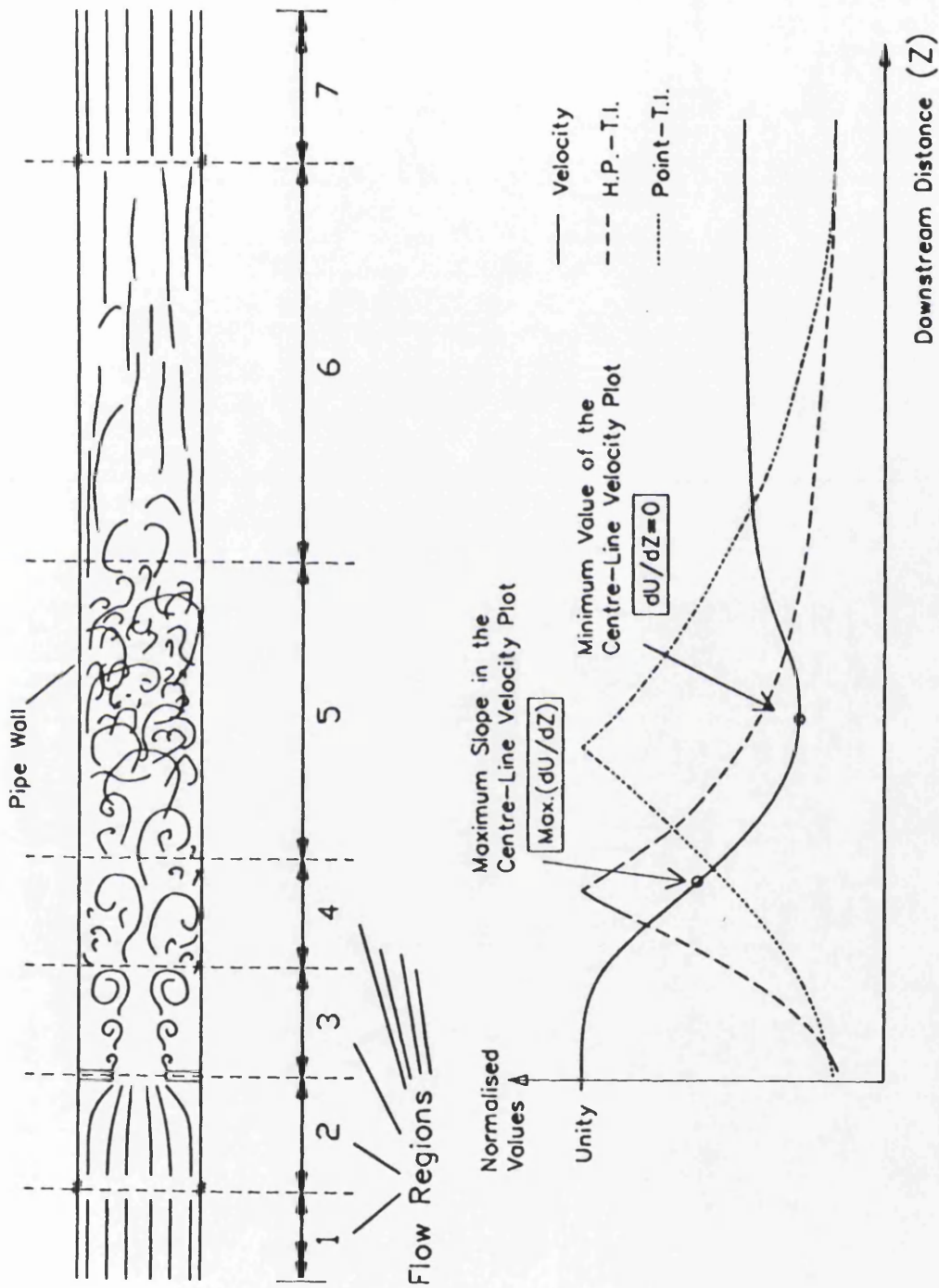
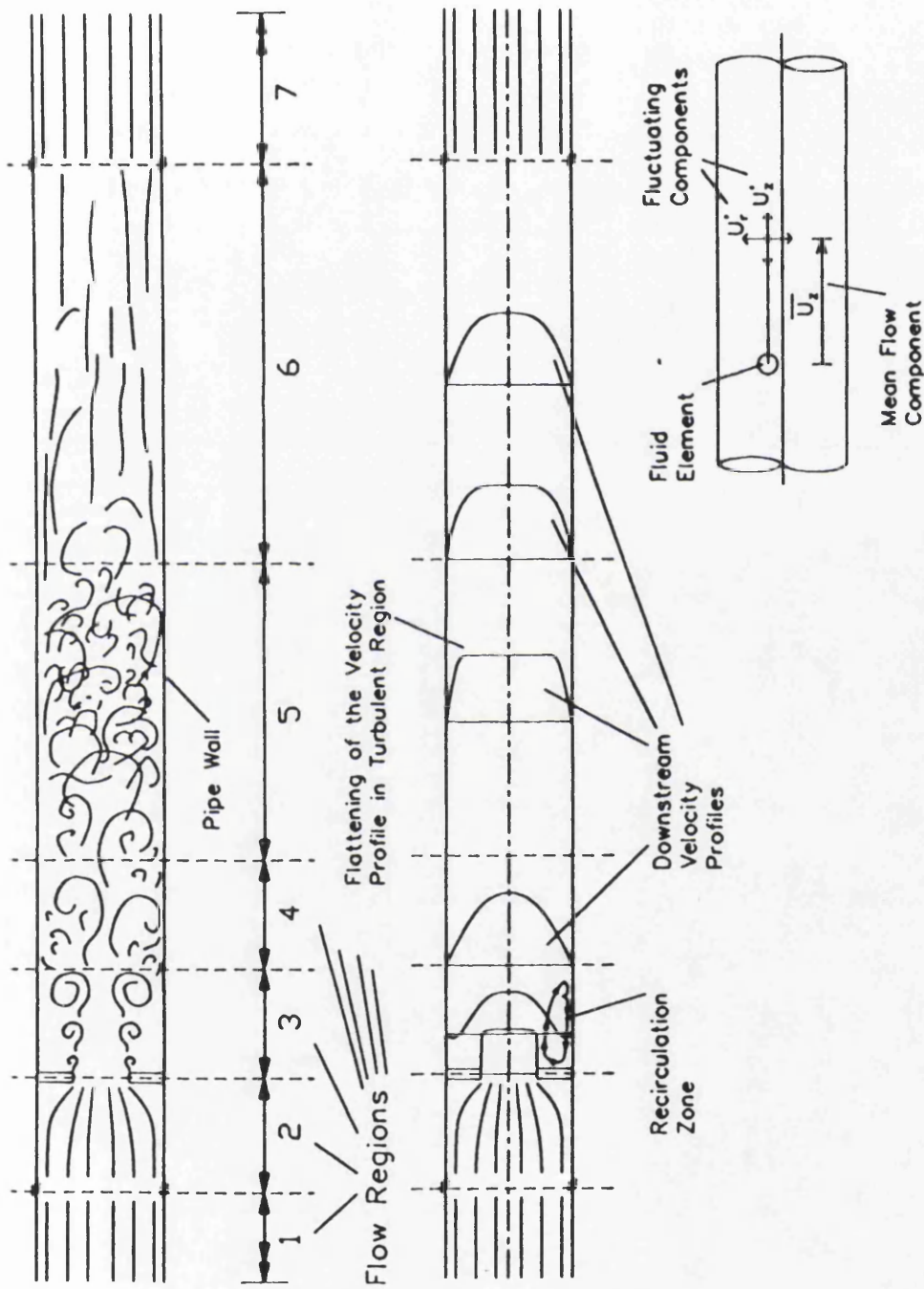
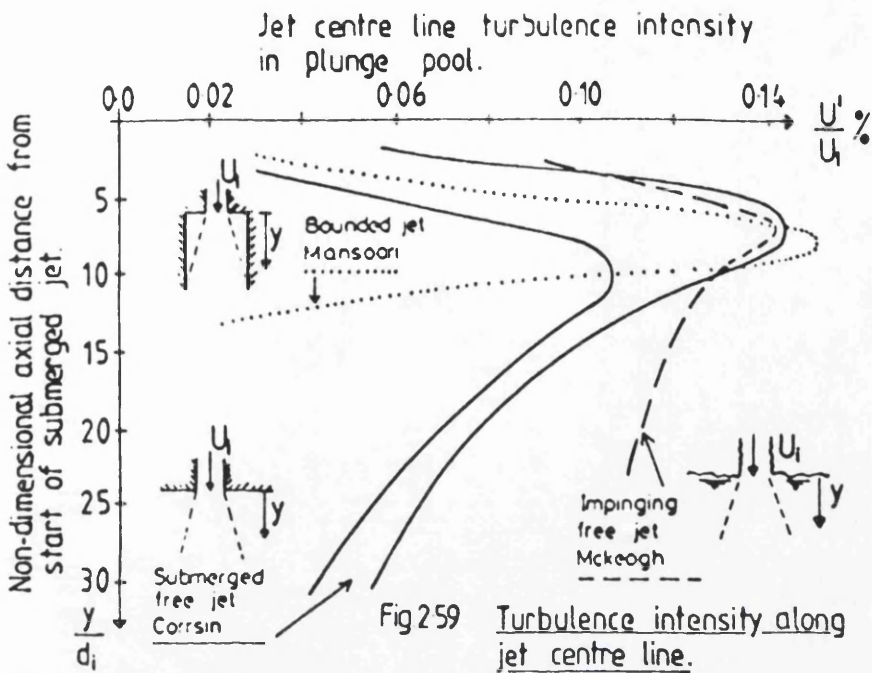


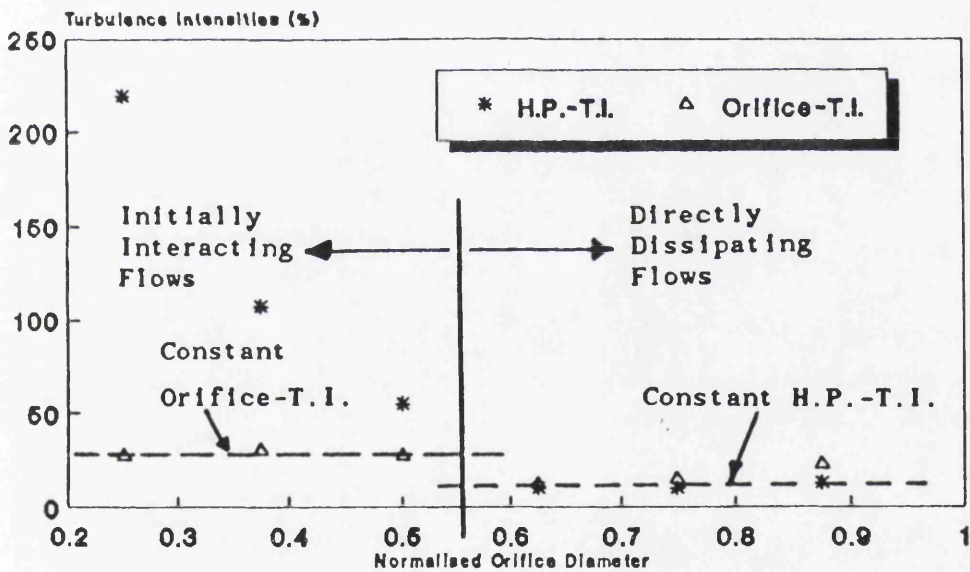
Figure 7-8: The Variation in Centre-Line Velocity and Turbulence Intensity Downstream of the Orifice Plate in Initially Interacting Flows



**Figure 7-9: The Flattening of the Velocity Profile due to the Reynolds Stresses in the Flow**

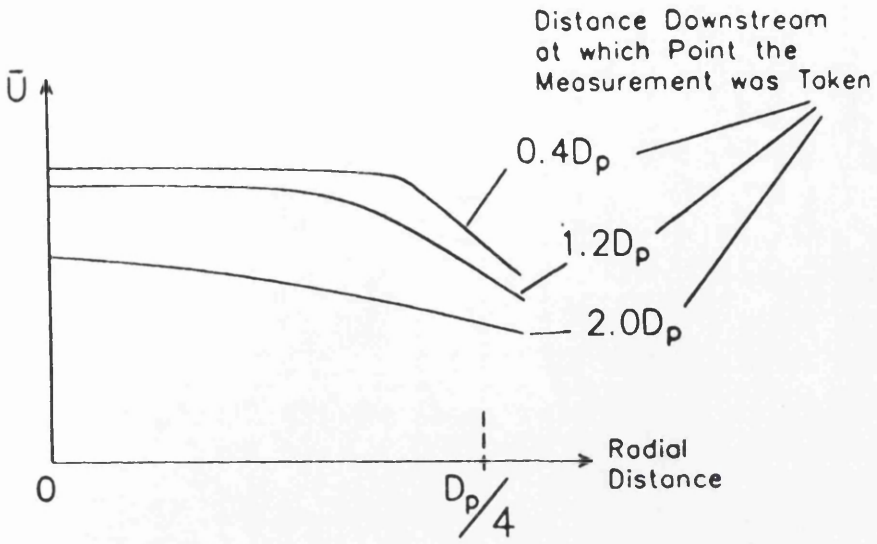


(a) Turbulence Intensity along Submerged Jet Centre Line (After Withers, 1992)



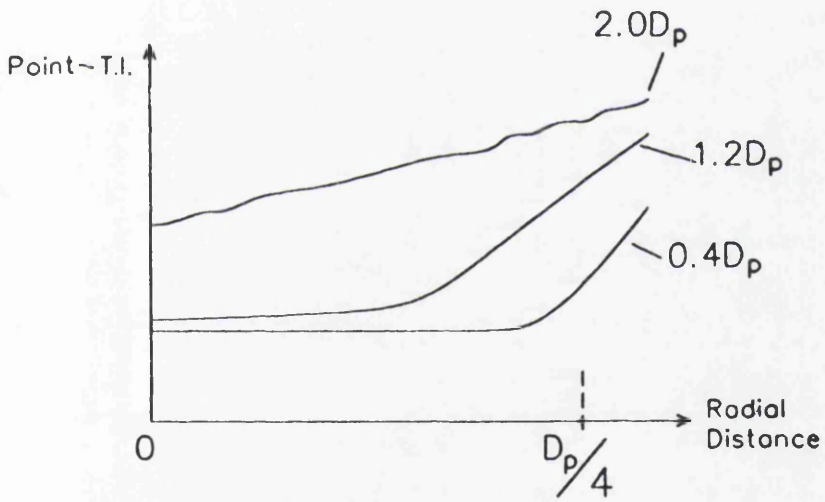
(b) Maximum Turbulence Intensities versus  $D_o/D_p$

Figure 7-10: Turbulence Intensities of Submerged Jet Flows Compared to Experimental Results



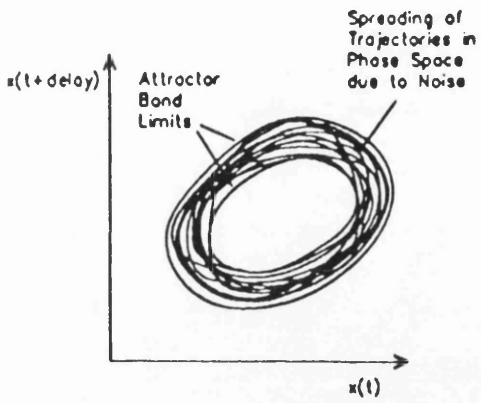
(a) Mean Flow Velocity

$$D_o = \frac{D_p}{2}$$

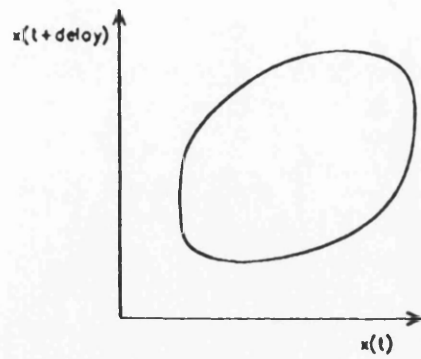


(b) Point Turbulence Intensity

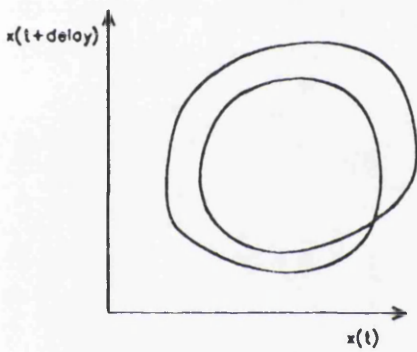
**Figure 7-11: Transverse Flow Measurements**



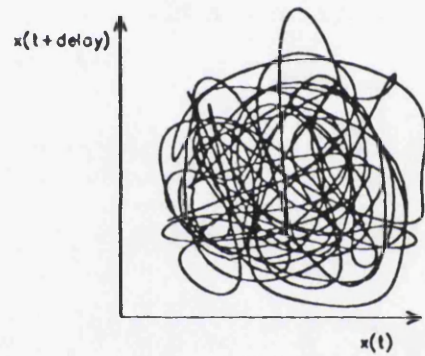
(a) Noisy, Periodic Attractor



(b) Initial, Noiseless, Singly Periodic Attractor

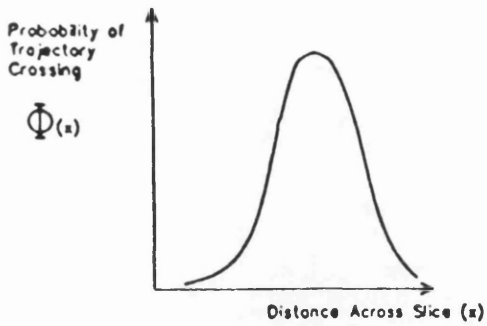


(c) Period-Doubled Attractor

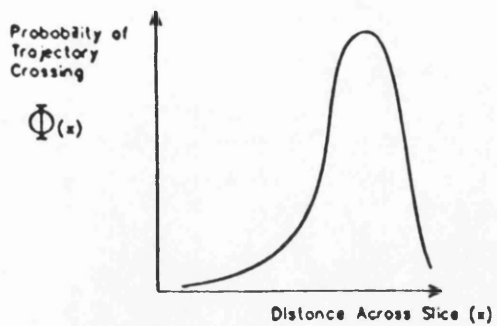


(d) Seemingly Random - High-Dimensional Attractor

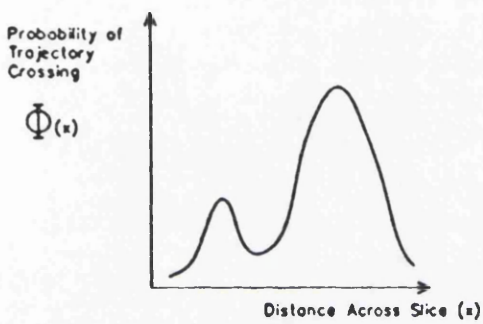
**Figure 7-12: Phase Portraits of Typical Attractor Types**



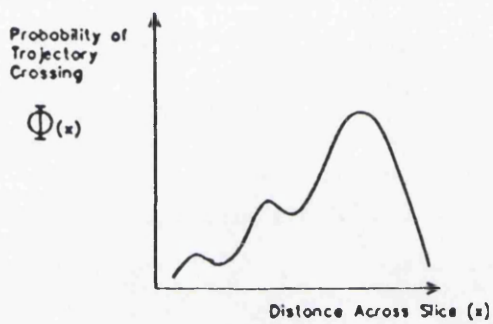
(a) Initial Gaussian Distribution



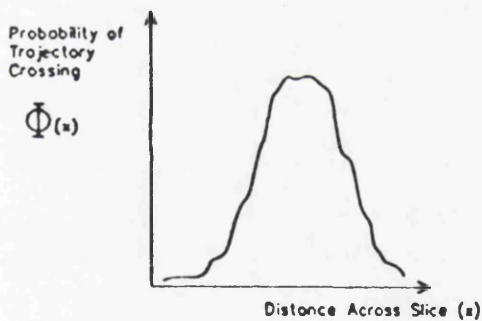
(b) Skewed Distribution



(c) Development of Second Peak



(d) Third Peak Appearing



(e) Tending Back to Gaussian

**Figure 7-13: The Behaviour of the Attractor Band Probability Distribution Function as the Vortices Develop Downstream of the Orifice Plate**  
**(See Text for Details)**

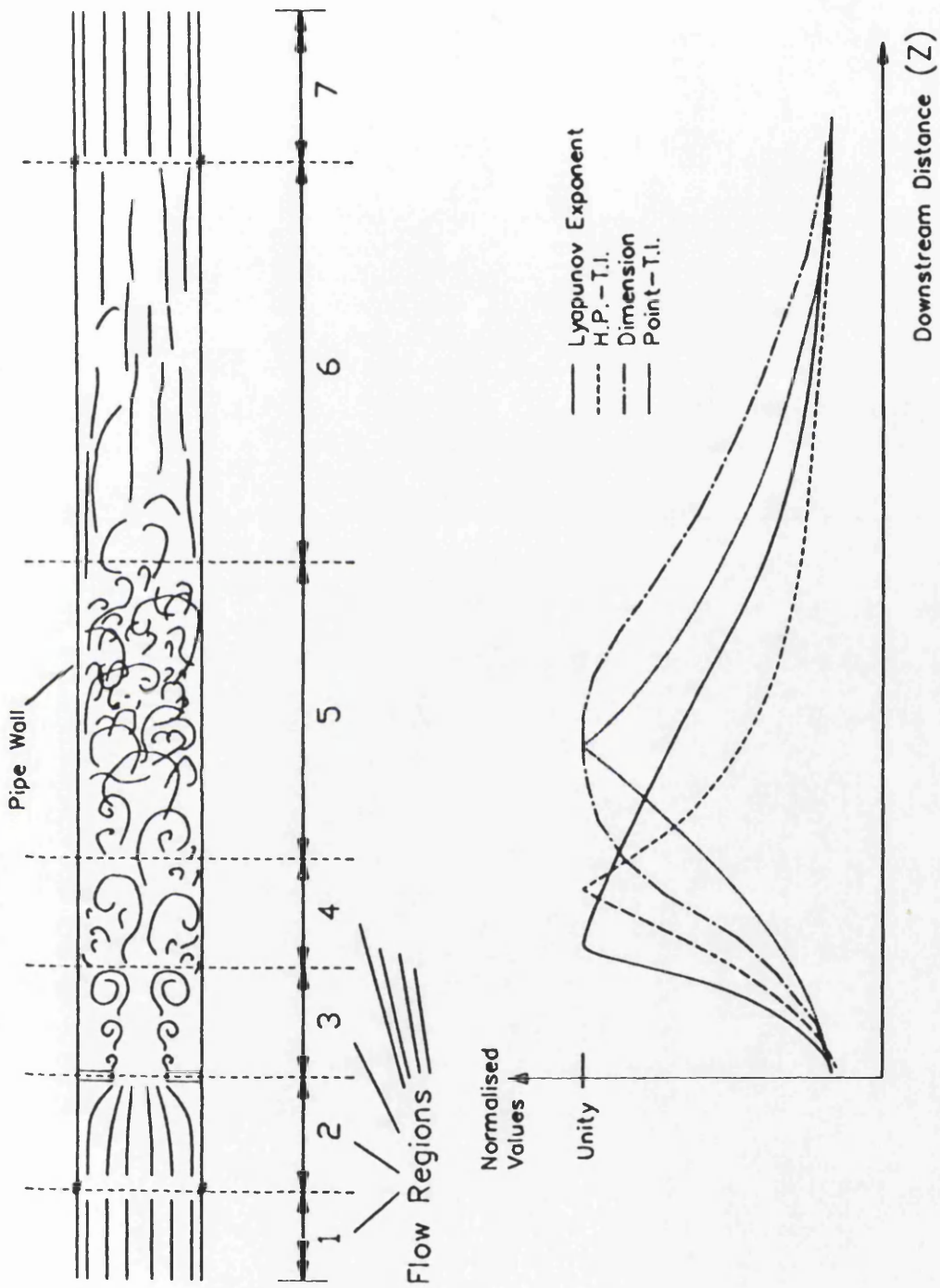
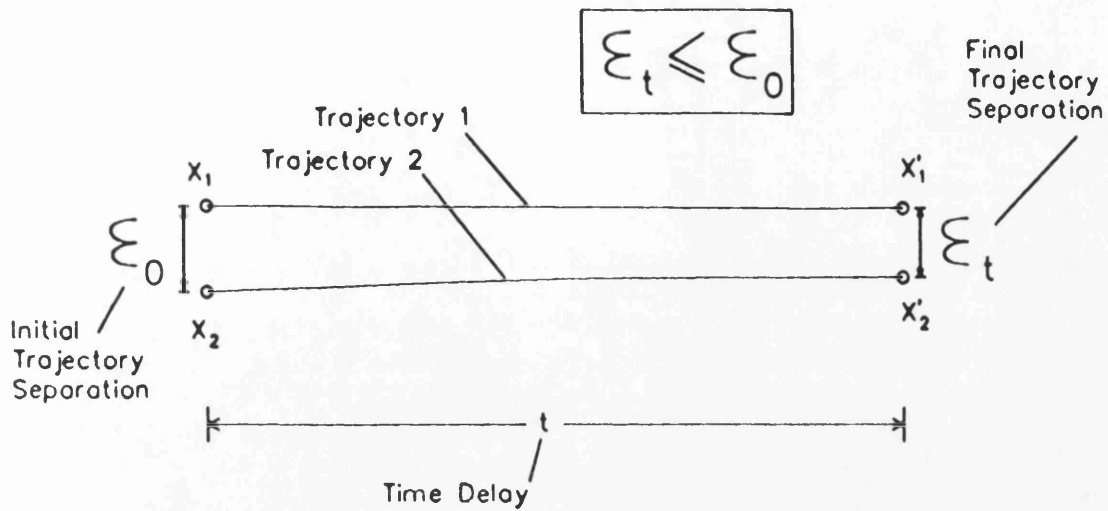
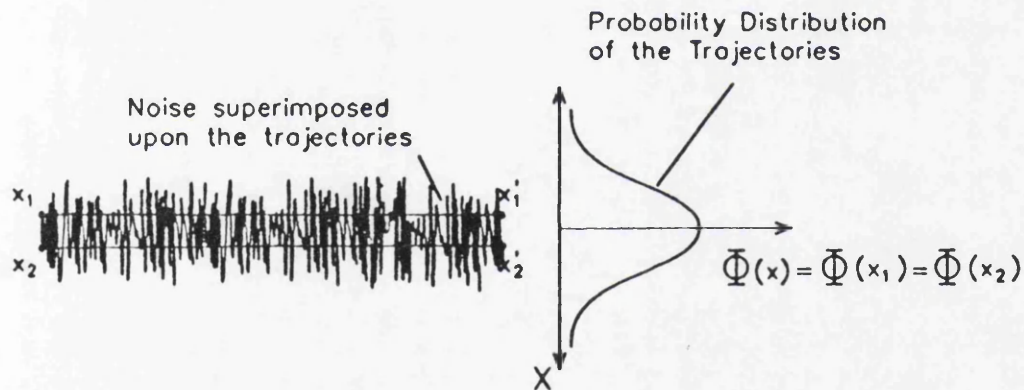


Figure 7-14: The Downstream Development of the Lyapunov Exponent, Grassberger-Procaccia Dimension and Turbulence Intensity



(a) Periodic Noiseless Attractor



(b) Periodic Noisy Attractors

Figure 7-15: The Lyapunov Exponent and Noise

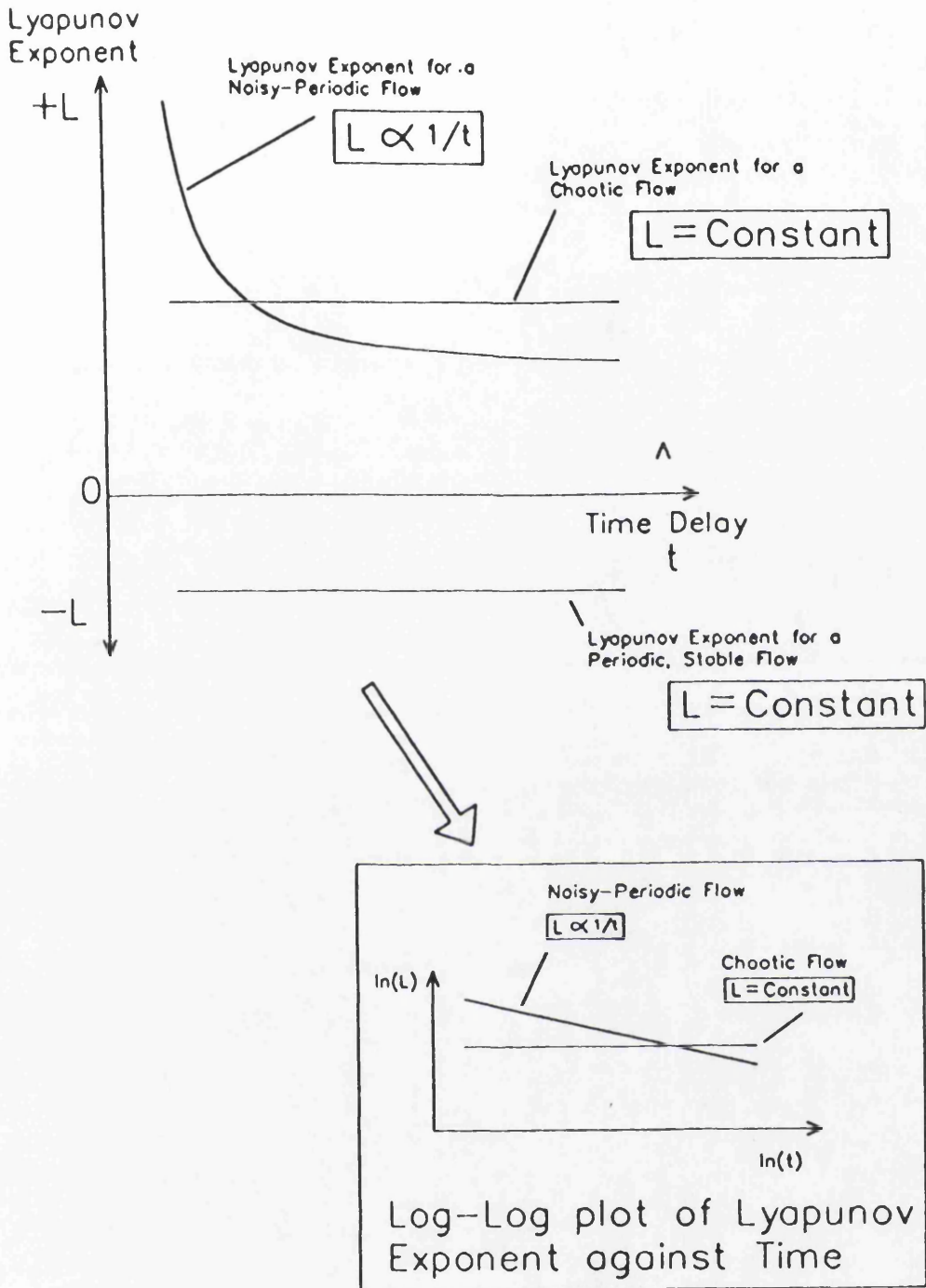


**Figure 7-16: The Behaviour of the Average Lyapunov Exponent Calculation**

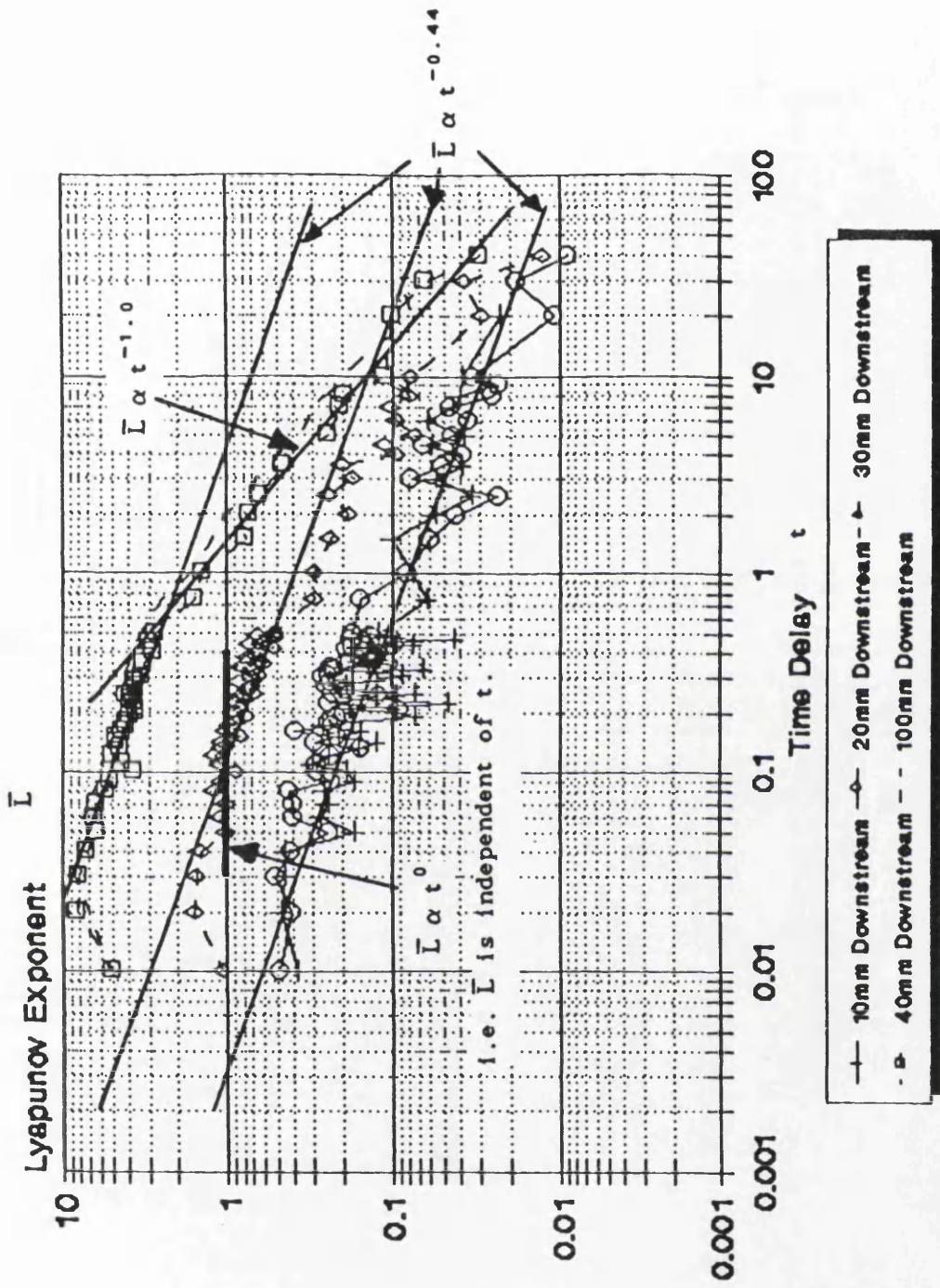
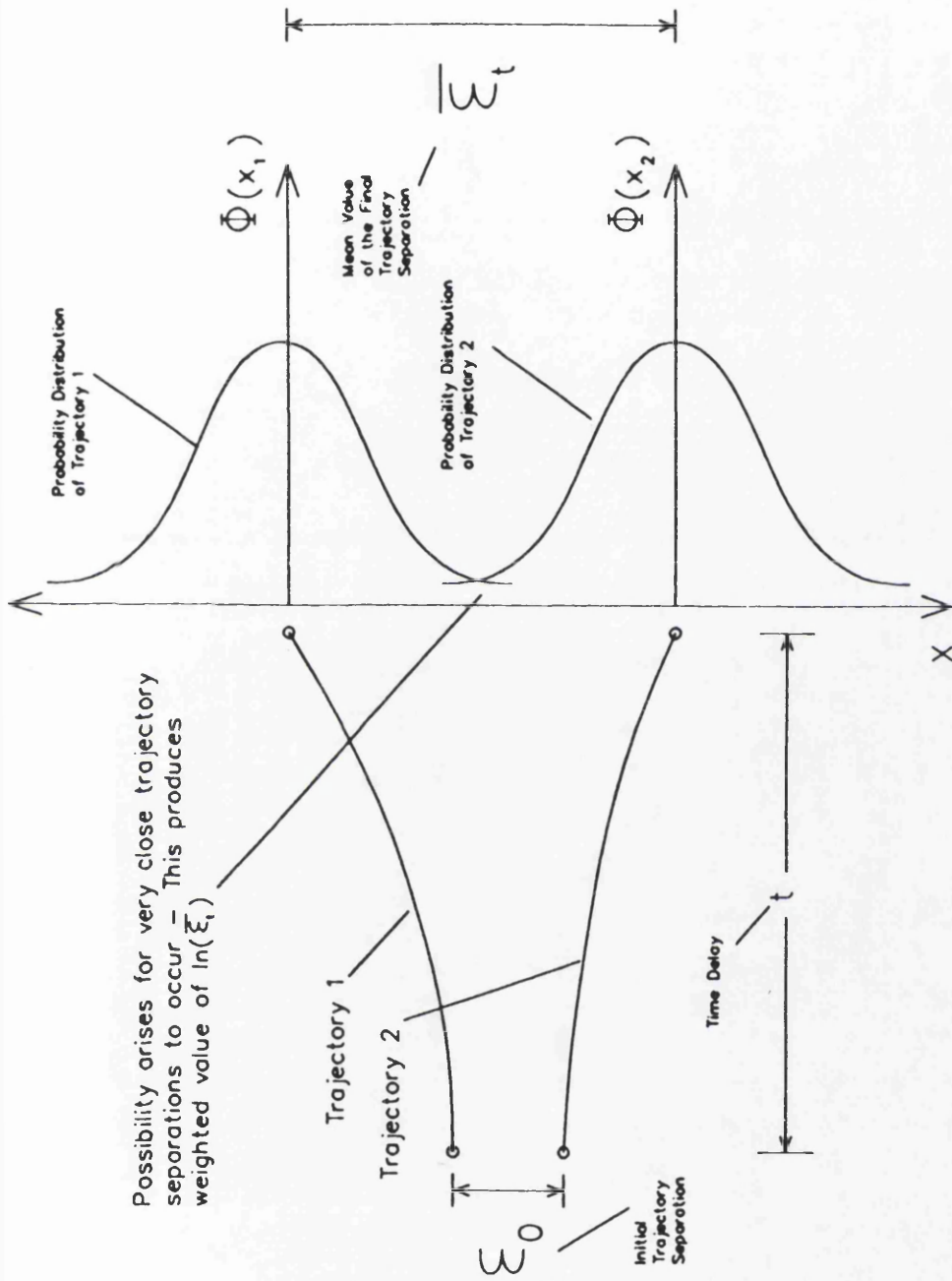


Figure 7-17: Lyapunov Exponent versus Time Delay for the Standard Test Results



Possibility arises for very close trajectory separations to occur. This produces weighted value of  $\ln(\bar{\xi}_t)$

Figure 7-18: The Effect of Noise on the Lyapunov Exponent Calculation

## CHAPTER 8

## CHAPTER 8

### CONCLUSIONS

#### 8.1 INTRODUCTION

#### 8.2 MAIN CONCLUSIONS

##### 8.2.1 Non-Linear Dynamics and Fluid Flow

##### 8.2.2 The Characterisation Techniques

#### 8.3 SUGGESTIONS FOR FUTURE RESEARCH

## 8.1 INTRODUCTION

The study of non-linear dynamics and fluid flow are inextricably linked. It is widely felt, throughout the scientific community, that the transition to turbulence may be understood using the theories and techniques from non-linear dynamics. This project sought to use characterisation techniques from the field of non-linear dynamics to probe the breakdown to turbulence of a forced vortex flow. In addition, the project sought to investigate the applicability of these techniques to the area of Civil Engineering Hydraulics.

The following general points can be made on the overall research project:

- 1 - A sophisticated experimental rig was built which produced constant mean mass flux rates upon which controllable fluctuations could be superimposed.
- 2 - A wide range of flow parameters were studied, including the pipe Reynolds number, forcing frequency, forcing amplitude and orifice diameter.
- 3 - A Laser table was constructed to allow accurate positioning within the pipe of the Laser Doppler Anemometer system.
- 4 - A method of flow visualisation was devised and successfully implemented. Flow visualisation was used in a photographic study of the various flow phenomena present in the vicinity of the orifice plate. In addition, video footage was taken of the flow processes using the flow visualisation apparatus.
- 5 - A sophisticated data acquisition system was designed to read in the flow velocity data, obtained from the Laser Doppler anemometer, and convert it to a suitable digital format for subsequent data analysis.
- 6 - Most of the analysis techniques were performed using programs written by the author, (with the exception of the Lyapunov exponent algorithm). Most notable of these was the Grassberger-Procaccia dimension algorithm which was successfully written, tested and used in the study. The dimension algorithm was also used successfully in an external collaborative study with D. Brown of Heriot-Watt University, [Brown, Addison and Chan, 1992].

7 – The use of an orifice to produce an axisymmetric disturbance in the flow was a novel method by which to control the transition process, which then could be investigated using methods from the field of non-linear dynamics. The use of an orifice plate allows turbulence to be generated in a distinct spatial location within the flow field at sub-critical pipe Reynolds numbers. The breakdown and re-laminarisation processes are also spread spatially downstream of the orifice plate, this allows for detailed investigation of these flow processes at each position.

8 – The control of the transition process, obtained by using an orifice plate and pulsations on the mean mass flux rate, led to the experiment being easily repeatable.

The main criticism of the work might centre on the inability, as yet, to expand on non-linear dynamics theory to produce practically useful methods for the hydraulics engineer.

The main conclusions of the work are summarised in section 8.2 and recommendations for future research into topics related to the work presented herein are given in section 8.3

## 8.2 MAIN CONCLUSIONS

### 8.2.1 Non-Linear Dynamics and Fluid Flow

1 – It was clear that the combined effect of the orifice and flow pulsations led to enhanced breakdown of the flow in a pipe. In addition, further enhancement of the breakdown process was caused by the following:

- (1) An increase in the pipe Reynolds Number
- (2) A reduction in the orifice diameter
- (3) An increase in the forcing amplitude

2 – Two distinct flow regimes were found. These were **Directly Dissipating** and **Initially Interacting** flows. Directly dissipating flow occurs when the vortices

generated at the orifice plate remain coherent downstream and dissipate out with the flow remaining axisymmetric throughout the flow field. Initially interacting flows occur when the generated vortices increase in size and interact with each other, leading to a loss of axisymmetry and an eventual breakdown to a more complex low regime.

Initially interacting flows may further be broken up into three sub-groups, these are:

- (1) Unstable Jet Flow
- (2) Interacting Vortex Flow
- (3) Confined Jet Flow

In addition, it was found that unstable jet flows occurred at the boundary between the Directly Dissipating and Initially Interacting flow regimes.

3 - It was found that both directly dissipating and initially interacting flow regimes could be described by up to seven distinct flow regions. With each region identified by a combination of flow visualisation and their respective frequency spectra.

4 - Two turbulence intensities were used in the study. These were the H.P.-T.I. and the Point-T.I., which are measures of the local velocity fluctuations compared to the average maximum pipe velocity and the local velocity respectively. The H.P.-T.I. and the Point-T.I. were linked respectively, with the maximum rate of velocity reduction and the velocity minimum downstream of the orifice plate which occurs in initially interacting flows.

5 - It was found that the maximum turbulence intensity for breakdown flows obtained in the study for each orifice diameter was approximately twice that found for submerged jet flows. This was attributed to the enhancement of the turbulent fluctuations caused by the flow pulsations and the relatively large coherent vortex structures in the flow field.

6 - Low dimensional chaotic behaviour was observed for Initially Interacting flow regimes. There was strong evidence to indicate that the initial periodic, axisymmetric vortex flow regime became chaotic, as it destabilised, en route to becoming turbulent. This was observed from a rapid increase both in the Lyapunov

exponent and the dimension estimate in the region of axisymmetric vortex growth. The techniques also highlighted the reduction in flow complexity as the turbulent regime dissipated back to the laminar condition.

7 — The techniques from non-linear dynamics enabled the flow complexity to be monitored throughout the flow field. Thus, the flow could be categorised into either directly dissipating or initially interacting without resorting to flow visualisation. The traditional technique of using the turbulence intensity to give information about the flow pattern cannot predict whether the fluctuations are coherent vortex structures or more complex turbulent eddies.

8 — The Lyapunov exponent and the Grassberger-Procaccia dimension estimate both provide ways to characterise the complexity of flows, leading to categorisation of the flow types. However, these techniques provide much information on the complexity of dynamics of the flow, however, as yet no information may be obtained from these techniques which is particularly useful to the modelling of such flows. The next step to be taken in the investigation of the applicability of the techniques from non-linear dynamics in fluid flow problems would be to link the output from such techniques to directly quantifiable variables, useful in the modelling and prediction of such flows.

The author feels that the ability of the characterisation techniques to quantify the complexity of the flows is a valuable asset of the techniques. The Reynolds stresses within turbulent flows must depend not only on the intensity of the turbulent fluctuations in each spatial direction, but also on the complexity of the turbulent fluctuations, linked through spatial correlations. A technique linking the complexity of the turbulent interactions with the turbulence intensity may provide a useful way to predict the Reynolds stresses within the flow.

### 8.2.2 The Characterisation Techniques

1 — The effect of noise on the Lyapunov exponent estimate was investigated analytically and numerical results were obtained. This investigation indicated that the Lyapunov exponent may be positive for a stable periodic trajectory subject to noise, which thickens the attractor band.

2 - A constant Lyapunov exponent was found for a small range of reconstruction time delays for attractors whose dimension do not exceed the embedding dimension of the phase space. This plateau of constant Lyapunov exponent was centred upon one quarter of the forcing cycle time.

3 - Further investigation into the effect of noise on the Lyapunov exponent showed that for large time delays, where the trajectories became completely decorrelated, the Lyapunov exponent tended to be inversely proportional to the delay time, i.e.,

$$\bar{L} \propto t^{-1.00}$$

However, for shorter time periods the Lyapunov exponent was inversely proportional to the delay time to the power of 0.44, i.e.,

$$\bar{L} \propto t^{-0.44}$$

An explanation was put forward to explain each of these relationships in terms of both the averaging involved in the Lyapunov exponent algorithm, and the presence of noise.

4 - A new Lyapunov exponent type measure of the trajectory divergence was proposed which avoids the possibility of singularities appearing in the calculations. This exponent,  $L^*$ , measures the Lyapunov exponent of the average separation of the trajectories rather than the more usual method of taking the average of the Lyapunov exponents each of the trajectory separations, ( $\bar{L}$ ).  $L^*$  is defined as,

$$L^* = \frac{1}{t} \ln \left[ \frac{\overline{\epsilon_t}}{\epsilon_0} \right]$$

5 - A novel method of probing the attractor band structure was proposed. Slicing

through the attractor band and constructing probability distribution histograms of the trajectory crossings gives visual information about the attractor development. In addition, the probability distribution information present in the histogram may then be used in the calculation of  $L^*$ .

6 - The minimum mutual information function was successfully used in obtaining attractor time delays. A novel non-dimensional complexity parameter was used in the study. This mutual information complexity parameter,  $M^*$ , is obtained by dividing the first minimum in mutual information obtained, from the time series, by the first minimum in mutual information that would be given by the forcing period, i.e. one quarter of the forcing period. Thus,

$$M^* = \frac{\text{First Minimum in Mutual Information}}{1/4 \text{ Forcing Period}}$$

This parameter allows the variation in minimum mutual information to be compared between flow with different forcing frequencies.

### 8.3 SUGGESTIONS FOR FUTURE RESEARCH

During the course of the investigation many interesting areas of associated research came to light. However, due to the time limitation imposed on the research project, many of these areas could not be adequately covered by the author. The following is a list of topics that the author suggests could lead to further understanding of non-linear dynamics and fluid flow phenomena.

#### 1 - Flow Complexity, Turbulence Intensity and the Reynolds Stresses

One possible direction for further research to aim for would be a study to link the flow complexity, (as defined by the techniques from non-linear dynamics), and the turbulence intensity, to the actual Reynolds stresses in the flow. This would be particularly useful to the modelling of flow regimes, where the flow is not fully turbulent, but rather, consists of large coherent structures of low complexity.

## **2 – Flow Complexity and Sediment Transport Properties**

One immediately obvious result from the investigations presented herein, is that pulsing the flow of fluid through an orifice plate, in low flow Reynolds numbers, changes the subsequent flow pattern downstream. The flow exhibits enhanced vortex growth which, under suitable conditions, breaks down to a region of turbulence. Both enhanced vortex flows and turbulent flows have increased sediment transport properties. In pipe systems, in which the fluid carries particles, obstacles cause a build up of sediment. It would be valuable to investigate the effect that flow pulsation has both on the dispersal of sediment at obstacles and on the sediment carrying properties of the flow as a whole, especially for low Reynolds number flows.

## **3 – Non-linear Oscillator Systems**

It would be useful to investigate the behaviour of non-linear oscillator systems in chaotic mode, leading to the possibility of modelling the evolution of vortex streets with such a system. Once such a flow loses its axisymmetry, and evolves into a highly complex spatial structure, the modelling of the flow using a simple chain of non-linear oscillators would not be applicable. However, over the initial region of axisymmetric development such a model may be possible.

## **4 – The Grassberger-Procaccia Dimension Estimate and Transients in the Signal**

A study into the effect of transients in the time trace signal, used to reconstruct the attractor, would be of benefit in locating weaknesses in the Grassberger-Procaccia dimension algorithm. The author has already found apparent fractal dimensions in a simple transient, periodic signal, (Appendix 6). Further research should concentrate on the effect on the dimension estimate of intermittent perturbations to the signal, (in the form of noise), and the subsequent transients caused.

## **5 – The Lyapunov Exponent and Noise**

Further research into the behaviour of the Lyapunov exponent estimate in the presence of noise should be undertaken. In particular, various types and levels of noise could be investigated. This research would lead to a better understanding of the ability of the technique to identify precisely the difference between periodic, chaotic and purely noisy flows.

## **APPENDICES**

**APPENDIX 1 : DERIVATION OF THE LAMINAR PIPE FLOW EQUATION  
FROM THE NAVIER STOKES EQUATIONS EXPRESSED  
IN CYLINDRICAL COORDINATES.**

**Navier Stokes Equations in Cylindrical Coordinates:**

**r-momentum:**

$$\frac{\partial U_r}{\partial t} + (U \cdot \nabla) U_r - \frac{1}{r} U_\theta^2 = - \frac{1}{\rho} \frac{\partial P}{\partial r} + g_r + \nu \left[ \nabla^2 U_r - \frac{U_r}{r^2} - \frac{2}{r^2} \frac{\partial U_\theta}{\partial \theta} \right] \quad (A1.1)$$

**$\theta$ -momentum:**

$$\frac{\partial U_\theta}{\partial t} + (U \cdot \nabla) U_\theta - \frac{1}{r} U_r U_\theta = - \frac{1}{\rho} \frac{\partial P}{\partial \theta} + g_\theta + \nu \left[ \nabla^2 U_\theta - \frac{2}{r^2} \frac{\partial U_r}{\partial \theta} - \frac{U_\theta}{r^2} \right] \quad (A1.2)$$

**z-momentum:**

$$\frac{\partial U_z}{\partial t} + (U \cdot \nabla) U_z = - \frac{1}{\rho} \frac{\partial P}{\partial z} (U_\theta) + g_z + \nu \nabla^2 U_z \quad (A1.3)$$

**Continuity:**

$$\frac{1}{r} \frac{\partial}{\partial r} (r \cdot U_r) + \frac{1}{r} \frac{\partial}{\partial \theta} (U_\theta) + \frac{\partial}{\partial z} (U_z) = 0 \quad (A1.4a)$$

**Laplacian Operator**

$$\nabla^2 = \frac{1}{r} \cdot \frac{\partial}{\partial r} \left[ r \cdot \frac{\partial}{\partial r} \right] + \frac{1}{r} \cdot \frac{\partial^2}{\partial \theta^2} + \frac{\partial^2}{\partial z^2} \quad (A1.4b)$$

**Consider Laminar Flow Case, ( Steady state in pipe ):**

**ASSUMPTIONS:**

**Flow Velocities:**

$$U_r = 0$$

$$U_\theta = 0$$

$$U_z = U_z(r)$$

Boundary conditions:  $U_z \left[ \pm \frac{D}{2} \right] = 0$  (A1.5)

Pressure:  $P = a_1 z + a_0$  (A1.6)

Consider z-momentum ( equation A4 ) :

$$\frac{\partial U_z}{\partial t} + (U \cdot \nabla) U_z = - \frac{1}{\rho} \frac{\partial P}{\partial z} + g_z + \nu \nabla^2 U_z$$

$V_z$  Steady state hence equation (A4) reduces to:

$$0 = - \frac{1}{\rho} (a_1) + \nu \left[ \frac{1}{r} \frac{\partial}{\partial r} \left[ r \frac{\partial U_z}{\partial r} \right] + \frac{\partial^2 U_z}{\partial \theta^2} + \frac{\partial^2 U_z}{\partial z^2} \right]$$

$$0 = - a_1 + \mu \left[ \frac{1}{r} \frac{\partial}{\partial r} \left[ r \frac{\partial U_z}{\partial r} \right] \right]$$

$$0 = - a_1 + \mu \left[ \frac{1}{r} \frac{\partial U_r}{\partial r} + \frac{\partial^2 U_z}{\partial r^2} \right]$$

Thus :  $\frac{a_1}{\mu} = \frac{\partial^2 U_z}{\partial r^2} + \frac{1}{r} \frac{\partial U_z}{\partial r}$  (A1.7)

Let :  $y = \frac{\partial U_z}{\partial r}$  (A1.8)

Hence :  $\frac{a_1}{\mu} = \frac{\partial y}{\partial r} - \frac{y}{r}$  (A1.9)

Equation (A1.8) is a First Order Linear Differential Equation,

Integrating Factor:  $G(r) = e^{\int \frac{1}{r} dr}$  (A1.10)

So equation (A1.8) becomes:

$$\frac{\partial}{\partial r} \left[ y e^{\int \frac{1}{r} dr} \right] = \frac{a_1}{\mu} e^{\int \frac{1}{r} dr}$$

Integrating both sides :

$$\int e^{\int \frac{1}{r} dr} dy = \int \frac{a_1}{\mu} e^{\int \frac{1}{r} dr} dr$$

$$ye^{\int \frac{1}{r} dr} = \frac{a_1}{\mu} \int r dr$$

$$y = \frac{a_1}{\mu} e^{-\int \frac{1}{r} dr} \left[ \frac{r^2}{2} + C_1 \right]$$

$$y = \frac{a_1}{\mu} \frac{1}{r} \left[ \frac{r^2}{2} + C_1 \right]$$

$$y = \frac{a_1}{\mu} \frac{r}{2} + \frac{C_1}{r} \quad (\text{A1.11})$$

using equation (A1.7) we get:

$$\frac{dU_z}{dr} = \frac{a_1}{\mu} \frac{r}{2} + \frac{C_1}{r} \quad (\text{A1.12})$$

Integrating equation (A1.11):

$$\int dU_z = \int \left[ \frac{a_1}{\mu} \frac{r}{2} + \frac{C_1}{r} \right] dr \quad (\text{A1.13})$$

$$U_z = \frac{a_1}{\mu} \frac{r^2}{4} + C_1 \ln(r) + C_2 \quad (\text{A1.14})$$

$C_1 = 0$  as  $U_z$  is finite.

So :

$$U_z = \frac{a_1}{\mu} \frac{r^2}{4} + C_2$$

We know :  $U_z \left[ \begin{matrix} + D \\ - \frac{D}{2} \end{matrix} \right] = 0$  ( equation A1.5 )

So :  $C_2 = - \frac{a_1 D^2}{4\mu}$

Hence,  $U_z = \frac{a_1}{4\mu} \left[ r^2 - \frac{D^2}{4} \right]$  (A1.15)

From the Velocity Equation ( equation A1.15 ) now calculate the Mean Velocity  $\bar{U}_z$ .

$$\bar{U}_z = \frac{\int_0^{2\pi} \int_0^{D/2} U_z r dr d\theta}{\frac{\pi D^2}{4}} \quad (A1.16)$$

Where  $\frac{\pi \cdot D^2}{4}$  is the pipe cross sectional area.

$$\bar{U}_z = \frac{8}{\pi D^2} \int_0^{\pi} \int_0^{D/2} \frac{a_1}{4\mu} \left( r^2 - \frac{D^2}{4} \right) r dr d\theta$$

This reduces to:

$$\bar{U}_z = \frac{2a_1}{\pi\mu D^2} \int_0^{\pi} \frac{D^4}{64} d\theta$$

Hence :  $\bar{U}_z = \frac{a_1 D^2}{32\mu}$  (A1.17)

Pipe head loss :  $h_l = \frac{\lambda L \bar{U}_z^2}{2g}$  (A1.18)

Also :  $h_l = \frac{1}{\rho g} \left( \frac{dP}{dL} L \right) = \frac{1}{\rho g} ( a_1 )$  (A1.19)

Hence : 
$$\lambda = \frac{2a_1}{\rho \bar{U}_z^2} \quad (\text{A1.20})$$

Combining equations (A1.17) and (A1.20) to get :

$$\lambda = \frac{64}{R} \quad (\text{A1.21})$$

as required.

## APPENDIX 2: COMPUTER PROGRAMS AND ALGORITHM CONSTRUCTION

### A2.1 Introduction

In this appendix an explanation of the computer programs, used in the study presented within this thesis, is given. The main programs are listed.

### A2.2 Data Acquisition Programs

The ASYST language was used to write the data acquisition programs. The two main programs used for this purpose were LASERP4 and SETUP4.

LASERP4 is the main acquisition program which interfaces with the Burr-Brown data acquisition card within the IBM P.C.. The data is stored in the array POSITIONA which contains 16384 data points of the time series. The program also computes the average flow velocity and the turbulence intensity for each data acquisition run.

SETUP4 is mainly for the presentation and manipulation of the data, and contains many user defined F.F.T. routines to plot out frequency spectra with linear and logarithmic scales. The program also contains a routine to plot out the velocity-time traces of the first 500 data points, which serves as a check during the experimentation.

In the following four pages the program LASERP4 is listed together with a typical plotting routine from SETUP4.

### A2.3 Data Analysis Programs

Programs were written by the author to perform all of the data analysis requirements. These techniques were: F.F.T., Autocorrelation function, Grassberger-Procaccia dimension estimate, Lyapunov exponent measurement, the first minimum in mutual information, the probability distribution of attractor slices and first return maps.

However, in two cases, programs not written by the author were eventually used. These were to calculate the F.F.T. and the Lyapunov exponent of the time series. The Fourier transform of the time series was obtained using the user-defined routine in the ASYST language called 'FSPECTRUM'. Whereby the F.F.T. of the time series could be calculated, viewed on screen and plotted whilst the experiment was being run. This gave instant feedback of the results.

### A2.3.1 The Lyapunov Exponent

Originally a program to determine the largest Lyapunov exponent was also written by the author. However, the author subsequently obtained a software package, FET, from Prof. Alan Wolf [1991], a co-author of the paper, 'Determining Lyapunov Exponents from a Time Series', Wolf<sup>et al</sup> [1985], from which the author's Lyapunov exponent program was originally written. The FET program was much faster than the one developed by the author due to a box assisted search, preprocessing routine. Therefore, the author used this routine for the computation of the time series exponent. The acquired package was run on the OPUS-V P.C., and the author's original program was used merely to check the results obtained. For speed, the Lyapunov exponents were calculated for up to 10, or more, experimental time series results at a time. This was done by running the FET program simultaneously on some of the many IBM PS2 personal computers to be found in the computer laboratory, situated elsewhere in the civil engineering department building. (Although this had to be done at times of low usage of the computer laboratory, i.e. at nights and weekends.)

### A2.3.2 The Calculation of the Mutual Information and the Grassberger-Procaccia Dimension

Program XD6, written by the author, is the most recent version of the computer program used to determine the dimension of the attractors reconstructed from the time series. A listing of the subroutines contained within the program are as follows:

PROGRAM XD6: Main program block.

MUTINFO: Subroutine to calculate the mutual information of the time series for

various values of time delay. The first minimum in the mutual information function then determines the value of time delay to be used in the attractor construction.

**MUTGRAPH:** Subroutine to plot out the results of the minimum mutual information calculations.

**DROPALG:** Subroutine to check the time series for drop-outs in the signal. These drop-out sections are subsequently labelled, and ignored in the attractor construction. (See section A2.5 for more details).

**EXPTDIM:** This subroutine sets up the initial data required for the Grassberger-Procaccia dimension calculation.

**GBDIM:** Subroutine to calculate the Grassberger-Procaccia dimension.

**DIMGRAPH:** Subroutine to plot out the resulting ' $\log(r) - \log(Cr)$ ' graph.

Program **XD6** is listed at the end of this section.

### **A2.3.3 Attractor Slicing and Probability Distribution**

Program **X\_PDF4** slices through the attractor, and using a box-counting algorithm, produces a probability histogram of the likelihood of the trajectory crossing each part of the slice. The mean and standard deviation of the crossing points are then calculated and an 'equivalent' Normal, or Gaussian, distribution is calculated. This Normal distribution is then superimposed on top of the histogram results for comparison purposes. Program **X\_PDF4** is listed at the end of section 2.3.

### **A2.3.4 First Return Map and Autocorrelation Function**

Programs were produced to calculate the first return map and the autocorrelation function from a time series, these programs were **X\_RET4** and **X\_CORR2** respectively. The first return map was produced by plotting each peak of the time series against each subsequent peak. The autocorrelation function was calculated by applying the formula given in chapter 2, section 2.7.3, to the time series. Both these programs are not listed herein, due to their simplicity.

Program LASERP4

```

\ PROGRAM LASERP4
\ THIS PROGRAM USED TO DETERMINE
\ THE FLOW VELOCITIES AND TURBULENCE INTENSITIES
\ FROM THE VOLTAGE OUTPUT OF THE LASER TRACKER
\
INTEGER SCALAR ERROR.CODE
INTEGER SCALAR SEGMT
INTEGER SCALAR CHN
INTEGER SCALAR GAIN
INTEGER SCALAR Z.CHN
INTEGER SCALAR RANGE
INTEGER SCALAR W
INTEGER SCALAR ADATA
REAL DIM[ 16384 ] ARRAY POSITIONA
\
\ DEFINE A GENERAL PURPOSE ERROR PROCESSING ROUTINE.
\
: ERROR? \ (STRING _____)
CALL[ PCI46S , ERR.SYS , ERROR.CODE ]
ERROR.CODE 0 <> IF
"TYPE ERROR.CODE . CR
ELSE
"DROP
THEN
;
: LASER
CR ." SETTING ARRAYS TO ZERO"
0 POSITIONA :=
\
\ INITIALIZE THE PCI-20046S-4 SYSTEM. THIS SEQUENCE
MUST BE
\ GIVEN PRIOR TO CALLING ANY OTHER PCI-20046S-4
INSTRUCTION.
CR
" 61"H SET.VECT
CALL[ PCI46S , SYSINIT ]
\
\ SEGMT, DEFINE BELOW, CONTAINS THE BASE ADDRESS OF THE
CARRIER
\ WE USE " C000"H, BUT YOU CAN SET IT ANY WHERE. REFER
TO THE
\ CARRIER MANUAL FOR MORE INFORMATION.
\ [ PCI46S , INIT , SEGMT ] MUST BE CALLED ONCE FOR EACH
CARRIER
\ IN THE SYSTEM, EACH WITH ITS OWN ADDRESS
\
" C000"H SEGMT :=
CALL[ PCI46S , INIT , SEGMT ]
\
\ CHECK FOR A SYSTEM ERROR. DURING DEBUG, CALL ERR.SYS
OFTEN,
\ POSSIBLY AFTER EVERY CALL TO THE PCI-20046S-4. IT IS A
GOOD
\ IDEA TO LEAVE A FEW ERR.SYS CALLS IN A FINISHED
PROGRAM TO
\ MONITOR THE STATUS OF THE SYSTEM.
\
" ERROR FOUND DURING INIT" ERROR?

```

Program LASERP4 Continued

```

CR ." PROGRAM LASERP4"
CR
CR ." SETTING GAIN AND RANGE"
0 CHN :=
1 GAIN :=
-1 Z.CHN :=
1 RANGE :=
\ W IS THE NUMBER OF READINGS +1 ON CHANNEL
16385 W :=
CR
CR ." CONFIGURING CHANNEL 0"
CALL[ PCI46S , CNF.AI , CHN , GAIN , Z.CHN , RANGE ]
" ERROR FOUND DURING CNF.AI" ERROR?
\
\ READ THE ANALOG INPUT CHANNEL
\
CR
CR ." READING CHANNEL"
\ SET FREQUENCY OF SAMPLING
SYNC.ERROR.ON
INV 1000. *
SYNC.PERIOD
CR ." DATA AQUISITION LOOP"
W 1 DO
SYNCHRONIZE
CALL[ PCI46S , READ.CH , AI.T , CHN , ADATA ]
\
\ GIVEN THE ADC READING, ADATA, TO ARRAY AND CONVERT
\
\ THE ASSUMPTION IS THAT THE PCI-20002M-1 MODULE IS SET
\ UP FOR +\ - 10 VOLTS
\ THE PREVIOUS PROGRAME GIVES THE EQUATION TO BE USED IN
PLACE
\ OF THE ABOVE LINE FOR OTHER THAN +\ - 10 VOLTS
\
ADATA POSITIONA [ I ] :=
LOOP
;

\
INTEGER SCALAR W2
REAL DIM[ 4096 ] ARRAY POSITIONO
: LASER2
CR ." DATA CONVERSION AD INPUT TO DIGITISED VOLTAGES"
CR
\
\ CONVERT ARRAY FROM ANALOG VOLTAGE TO DIGITAL VOLTAGE
TO VELOCITY
\
4097 W2 :=
POSITIONA SUB[ 1 , 4096 ] POSITIONO :=
POSITIONO 20.0 * 4096.0 / 10.0 - GAIN / POSITIONO :=
CR ." NUMBER OF READINGS ON CHANNEL 0 WAS" W2 1 - .
CR
;

```

Program LASERP4 Continued

```

\ EXPERIMENTAL ANALYSIS
\
REAL SCALAR RANGE2
20 STRING TESTRUN
20 STRING DATE
\
: INPUTSO
CR ." DATA CONVERSION VOLTAGES TO VELOCITIES"
CR
\
CR ." FREQUENCY RANGE (MAX) =" RANGE2 . ." Hz"
CR
W2 1 DO
\
POSITIONO [ I ] .0000006328 * RANGE2 * 1.98986836 /
POSITIONO [ I ] :=
\
LOOP
;

\
\ DETERMINE STATICAL PROPERTIES AND RESULTS
\
REAL DIM[ 3 ] ARRAY TEMPO
: RESULTSO
\
INPUTSO
\
CR ." LASER MEASUREMENTS (m/s)"
CR
\
POSITIONO MEAN TEMPO [ 1 ] :=
POSITIONO VARIANCE SQRT TEMPO [ 2 ] :=
TEMPO [ 2 ] TEMPO [ 1 ] / 100 * TEMPO [ 3 ] :=
CR ." POINT VELOCITY IN THE CHANNEL=" TEMPO [ 1 ] . ."
m/s"
CR
CR ." TURBULENCE INTENSITY U' AT THE SAME POINT=" TEMPO [
3 ] . ." %"
CR
;
CR
;
;

" %"
CR
\
;

```

A Typical Plotting Routine from the Program Setup4  
from the Program Setup4

```
\ PLOT FREQUENCY SPECTRUM
\
REAL DIM[ 4096 ] ARRAY FSPECTRUM
: FS
  VERTICAL LINEAR
  -1.2 0 5 LABEL.FORMAT
  HORIZONTAL LINEAR
  VERTICAL LINEAR
  -1.2 0 5 LABEL.FORMAT
  HORIZONTAL LINEAR
  -.5 -.8 4 LABEL.FORMAT
  -.5 -.8 4 LABEL.FORMAT
  FREQS SUB[ 2 , 2048 ]
  POSITION0 FFT ZMAG FSPECTRUM :=
  FSPECTRUM SUB[ 2 , 2048 ]
  XY.AUTO.PLOT
  NORMAL.COORDS
  0 LABEL.DIR 0 CHAR.DIR
  .5 .9 POSITION " FREQUENCY SPECTRUM" LABEL
  .7 .05 POSITION " FREQUENCY (Hz)" LABEL
  270 LABEL.DIR 0 CHAR.DIR
  .03 .90 POSITION " F.F.T. MAGNITUDE" LABEL
  OUTLINE
  CURSOR.OFF
  WORLD.COORDS
;
```



Program XD6 continued

```

REAL MINMUT(0:150),MMUTOLD
C
NBOX   =   100
MMAX   =   100
MSTEP  =    1
MMUTOLD = 10000000000000.0
MINFLAG = 0
PRINT *, 'MMUTINFO'  NSTEP=' ',NSTEP
C
C..CALL ALGORITHM TO LABEL DROPOUTS IN THE SIGNAL.
C
CALL DROPALG(X,NSTEP)
C
DO 100 M = 0 , MMAX
  XMAX = -100.0
  XMIN =  100.0
  YMAX = -100.0
  YMIN =  100.0
  DEL = M * MSTEP
  STEP = REAL(NSTEP-DEL)
C
C..FIND MAX + MIN OF THE TWO TIME SERIES
C..HENCE FIND THE SIZE OF THE GRID SPACES
C
DO 10 I = 1,NSTEP - DEL
  IF(X(I).LT.0)GOTO10
  IF(XMAX.LT.X(I)) XMAX = X(I)
  IF(XMIN.GT.X(I)) XMIN = X(I)
10  CONTINUE
C
DO 20 I = 1 + DEL,NSTEP
  IF(X(I).LT.0)GOTO20
  IF(YMAX.LT.X(I)) YMAX = X(I)
  IF(YMIN.GT.X(I)) YMIN = X(I)
20  CONTINUE
BOXSIZEX = (XMAX-XMIN)/REAL(NBOX)
BOXSIZEY = (YMAX-YMIN)/REAL(NBOX)
C
C..INITIALIZE THE BOX COUNTING ARRAYS
C
ISUMX = 0
ISUMY = 0
ISUMXY = 0
DO 30 I = 1,NBOX
  ICOUNTX(I)=0
  ICOUNTY(I)=0
  DO 40 J = 1,NBOX
    ICOUNTXY(I,J)=0
40  CONTINUE
30  CONTINUE
C
C..COUNT UP THE NUMBER OF POINTS IN EACH ROW AND COLUMN
C
STEPCOUNT = 0
DO 50 I = 1,NSTEP-DEL
  IF(X(I).LT.0 .OR. X(I+DEL).LT.0)GOTO50
  STEPCOUNT = STEPCOUNT + 1
  K = INT((X(I) - XMIN) / BOXSIZEX) + 1
  L = INT((X(I+DEL) - YMIN) / BOXSIZEY) + 1
  ICOUNTX(K) = ICOUNTX(K) + 1
  ICOUNTY(L) = ICOUNTY(L) + 1
  ICOUNTXY(K,L) = ICOUNTXY(K,L) + 1
50  CONTINUE
C..CHECK
DO 51 I = 1,NBOX
  ISUMX = ISUMX + ICOUNTX(I)
  ISUMY = ISUMY + ICOUNTY(I)
51  CONTINUE

```

Program XD6 continued

```

C
CCCCCCCCCCCCCCCCCCCCCCCCCCCCCCCCCCCCCCCCCCCCCCCCCCCCCCCCCCCC
C
C          CALCULATE MUTUAL INFORMATION          C
C
CCCCCCCCCCCCCCCCCCCCCCCCCCCCCCCCCCCCCCCCCCCCCCCCCCCCCCCCCCCC
C
      MINMUT(M)=0.0
      DO 60 I = 1,NBOX
        IF (ICOUNTX(I).EQ.0) GOTO 60
        DO 70 J = 1,NBOX
          IF (ICOUNTY(J).EQ.0 .OR. ICOUNTXY(I,J).EQ.0) THEN
            GOTO 70
          ELSE
            LOGVAL=(ICOUNTXY(I,J)/REAL(STEPCOUNT))*
            LOG(REAL(ICOUNTXY(I,J)*REAL(STEPCOUNT)) /
            REAL(ICOUNTX(I)*ICOUNTY(J)))
            ENDIF
            MINMUT(M) = MINMUT(M) + LOGVAL
70      CONTINUE
60      CONTINUE
C
      MINMUT(M) = MINMUT(M)/LOG(2.0)
      IF (MMUTOLD.LT.MINMUT(M) .AND. MINFLAG.EQ.0)THEN
        DELAY = DEL - 1
        PRINT *,'*MUTINFO*** *** FIRST MINIMUM REACHED *** *** '
        PRINT *,'*MUTINFO*          TIME DELAY = ',DELAY
        MINFLAG = MINFLAG + 1
        IF (SKIPGRAP.EQ.1) GOTO 110
      ENDIF
      PRINT *,M,'DEL,MINMUT =',DEL,MINMUT(M)
      MMUTOLD = MINMUT(M)
C
100 CONTINUE
C
C...CALL GRAPHICS SUBROUTINE
C
      CALL MUTGRAPH(MINMUT,MMAX,MSTEP,DT,DELAY)
C
110 CONTINUE
C
      RETURN
      END
C
C*: ~XXXXXXXXXXXXXXXXXXXXXXXXXXXXXXXXXXXXXXXXXXXXXXXXXXXXXXXXXXXX
C
      SUBROUTINE MUTGRAPH(MINMUT,MMAX,MSTEP,DT,DELAY)
C
C..SUBROUTINE TO PLOT OUT THE MUTUAL INFO. RESULTS
C
      INTEGER MMAX,MSTEP,DELAY
      REAL MINMUT(0:50)
C
      CALL PSPACE(0.30,1.10,0.25,0.70)
      CALL MAP(0.0, REAL(MMAX*MSTEP), 0.0,1.2*MINMUT(0))
      CALL AXESSI(1.0,1.0)
      CALL POSITN(0.0,MINMUT(0))
      DO 10 I = 1,MMAX*MSTEP
        CALL JOIN(REAL(I),MINMUT(I))
10     CONTINUE
C
      CALL PSPACE(0.10,1.30,0.10,0.90)
      CALL MAP (0.10,1.30,0.10,0.90)
      CALL PCSCEN(0.70,0.70,' H010105          ')
      CALL BORDER
      CALL CTRMAG(15)
      CALL PCSCEN(0.70,0.82,'MUTUAL INFORMATION OF THE EXPERIMENTAL ')
      CALL PCSCEN(0.70,0.77,'TIME SIGNAL WITH DROP OUTS NOT INCLUDED ')

```

Program XD6 continued

```

CALL CTRMAG(10)
CALL PCSCEN(0.95,0.18,'UNITS OF TIME DELAY')
CALL PCSCEN(0.95,0.65,'TIME INCREMENT =  ')
CALL PLOTNF(1.05,0.65,DT,3)
CALL PCSCEN(0.95,0.70,'FIRST MIN. =  ')
CALL PLOTNI(1.00,0.70,DELAY)
CALL CTRORI(90.0)
CALL PCSCEN(0.21,0.60,'MUTUAL INFORMATION (I)')
CALL CTRORI( 0.0)

C
CALL FRAME
RETURN
END

C
C *****
C
SUBROUTINE DROPALG(XX,NSTEP)
C
C...THIS SUBROUTINE - 1. CHECKS DATA FOR DROPOUTS
C                   2. LABELS DROPOUTS BY MAKING THEM NEGATIVE
C
IMPLICIT NONE
INTEGER NMAX
PARAMETER (NMAX=16384)
DOUBLE PRECISION SCALEX,PP
REAL XX(NMAX)
INTEGER N,I,K,ICOL,NXPPIX,NYPPIX,ICLEAN,IREP,J,MM,MARK,KMIN
INTEGER KMAX,KK(NMAX),KSUM,KTOL,SMAX,S,L,NW,SS
PARAMETER (SMAX=100)
INTEGER SLOT(2,SMAX)
REAL XNEW(NMAX)
INTEGER NSTEP,MARKDROP
COMMON/DROPVAR/KTOL,MM,PP,NW

C
MARKDROP = 0
PRINT *,'*DROPALG***** SEARCHING FOR DROPOUTS *****'
PRINT *, 'KTOL,NW,PP,MM', KTOL,NW,PP,MM
N=0
KSUM=0
DO 10 I = 1,NMAX
    KK(I) = INT(XX(I))
10 CONTINUE
DO 20 N=1,NMAX
    K = KK(N)
    KSUM=KSUM+K
    IF (N.EQ.1) THEN
        KMIN=K
        KMAX=K
    ELSE
        KMIN=MIN(K,KMIN)
        KMAX=MAX(K,KMAX)
    END IF
20 CONTINUE

C
MARK=0
DO 150 I=2,N
    KK(I)=ABS(KK(I))
    IF (MARK.EQ.0.AND.ABS(KK(I)-KK(I-1)).LE.KTOL) THEN
        MARK=I-1
    ELSE IF (MARK.EQ.0) THEN
        CONTINUE
    ELSE IF (ABS(KK(I)-KK(MARK)).GT.KTOL) THEN
        IF (I-MARK-1.GE.MM) THEN
            S=0
            DO 140 J=MARK,I-1
                DO 130 K=1,S
                    IF (SLOT(1,K).NE.KK(J)) GOTO 130
                    SLOT(2,K)=SLOT(2,K)+1
                130 CONTINUE
            140 CONTINUE
        END IF
    END IF
150 CONTINUE

```

Program XD6 continued

```

                GOTO 135
130             CONTINUE
                DO 160 K=1,S
                    IF (KK(J).LT.SLOT(1,K)) GOTO 170
160             CONTINUE
                K=S+1
170             CONTINUE
                DO 180 L=S,K,-1
                    SLOT(1,L+1)=SLOT(1,L)
                    SLOT(2,L+1)=SLOT(2,L)
180             CONTINUE
                S=S+1
                slot(1,k)=kk(j)
                SLOT(2,K)=1
135             CONTINUE
140             CONTINUE
                SS=0
                DO 300 J=1,MAX(1,S-NW+1)
                    K=0
                    DO 290 L=J,MIN(S,J+NW-1)
                        K=K+SLOT(2,L)
290             CONTINUE
                    SS=MAX(SS,K)
300             CONTINUE
                IF (SS.GT.PP*(I-MARK)) THEN
                    MARKDROP = MARKDROP + 1
                    DO 310 J=MARK,I-1
                        KK(J)=-KK(J)
310             CONTINUE
                END IF
            END IF
            MARK=0

            END IF
150         CONTINUE
            MARK=1
C
            DO 800 I = 1,NMAX
                XX(I) = REAL(KK(I))
800         CONTINUE
            PRINT *,'*DROPALG* NO OF DISCRETE DROPOUTS =',MARKDROP
            RETURN
            END
C
C *****
C
            SUBROUTINE EXPTDIM(NSTEP,DELAY,X,MAX_EMBED,M_DEL,DT)
C
C ..THIS SUBROUTINE SETS UP INITIAL DATA FOR THE DIMENSION ALGORITHM
C
            IMPLICIT NONE
            INTEGER I,DELAY,MAX_EMBED,M_DEL,NSTEP
            REAL XL,XR,YY,YT,FINAL,X(16384),DT
            REAL XPOINT(30,30000),CORPLOT(30,1000),RPLLOT(30,1000)
C
            FINAL = REAL(NSTEP)*DT
            PRINT *,'*EXPTDIM* FINAL=',FINAL
C
            DO 10I = 1,NSTEP,1024
                PRINT *,'*EXPTDIM*',I,'X(I) =',X(I)
10         CONTINUE
C
C ..INITIAL VALUES
C
C ..XPOINT=X
C
            DO 20 I = 1,NSTEP
                XPOINT(1,I) = X(I)

```

Program XD6 continued

```

20 CONTINUE
C
C..CALL THE GRASSBERGER-PROCACCIA DIM. ALG.
C
    CALL GBDIM(XPOINT,NSTEP,MAX_EMBED,M_DEL,DELAY,RPLOT,CORPLOT)
C
C..LARGE AXIS DIMENSIONS
C
    XL= - 8.0
    XR=  0.0
    YY= -20.0
    YT=  0.0
C
C..CALL GRAPHICS ROUTINE
C
    CALL DIMGRAPH(MAX_EMBED,NSTEP,XL,XR,YY,YT,FINAL,DELAY,
    RPLOT,CORPLOT,M_DEL)
C
    RETURN
    END
C
C*****
C
    SUBROUTINE GBDIM(XPOINT,NSTEP,MAX_EMBED,M_DEL,DELAY,RPLOT,CORPLOT)
C
C..SUBROUTINE TO CALC. THE DIM. OF AN ATTRACTOR USING THE GRASSBERGER-
C..PROCACCIA DIMENSION ALGORITHM
C
    IMPLICIT NONE
    INTEGER I,J,M,M_EMBED,MAX_EMBED,M_DEL,N,NRSTART,NPOINT,STPVAL
    INTEGER NSTEP,MOD_NSTEP,DELAY,NCOUNT
    REAL RARR(1000)
    REAL XDISTSQ,CORINT,R,DIST,RMAX,XMAX,XMIN,XMEDIAN
    REAL XPOINT(30,30000),CORPLOT(30,1000),RPLOT(30,1000)
    COMMON/DIMVAR/STPVAL,NCOUNT,RMAX
C
    NPOINT = 1000 !..NO. OF POINTS USED FOR PLOT
    XMAX = -1000000.0
    XMIN = 1000000.0
    MOD_NSTEP = NSTEP - (MAX_EMBED-1)*DELAY !..MODIFIED NSTEP
    PRINT *, 'EXPTDIM' RMAX = ',RMAX
    PRINT *, 'EXPTDIM' MOD_NSTEP = ',MOD_NSTEP
C
C..FIND MAX ABSOLUTE VALUE OF INPUT TIME SERIES
C
    DO 10 I = 1,NSTEP
        IF(XPOINT(1,I).LT.0) GOTO 10
        IF(XMAX .LT. XPOINT(1,I) ) XMAX = XPOINT(1,I)
        IF(XMIN .GT. XPOINT(1,I) ) XMIN = XPOINT(1,I)
10 CONTINUE
    XMEDIAN = (XMAX + XMIN) /2.0
    PRINT *, 'XMAX = ',XMAX
    PRINT *, 'XMIN = ',XMIN
    PRINT *, 'XMEDIAN = ',XMEDIAN
    XMAX = ABS(XMAX - XMEDIAN)
C
C..NORMALISE INPUT TIME SERIES, EXCEPT FOR DROPOUTS
C
    NCOUNT = 0
    DO 20 I = 1,NSTEP
        IF(XPOINT(1,I).LT.0) GOTO 20
        XPOINT(1,I) = (XPOINT(1,I) - XMEDIAN) / XMAX
        NCOUNT = NCOUNT + 1
20 CONTINUE
    PRINT *, 'NO OF GOOD POINTS = ',NCOUNT
C
C..GENERATE THE REMAINING SERIES UP TO DIMENSION M_EMBED

```

Program XD6 continued

```

C
DO 30 I = 1,MOD_NSTEP
DO 40 M = 2,MAX_EMBED
XPOINT(M,I) = XPOINT(1,I+(M-1)*DELAY)
40 CONTINUE
30 CONTINUE
C
C...CALCULATE THE CORRELATION INTEGRAL FOR EACH (R)
C
DO 50 M_EMBED = 2,MAX_EMBED,M_DEL
NCOUNT = 0
DO 60 I = 1,MOD_NSTEP
DO 65 M = 1,M_EMBED
IF(XPOINT(M,I).LT.-1) GOTO 60
65 CONTINUE
DO 70 J = 1,MOD_NSTEP,STPVAL
IF (IABS(I-J).LT.DELAY) GOTO70
XDISTSQ = 0.0
DO 75 M = 1,M_EMBED
IF(XPOINT(M,J).LT.-1) GOTO 70
75 CONTINUE
DO 80 M = 1, M_EMBED
XDISTSQ = (XPOINT(M,I)-XPOINT(M,J))**2 + XDISTSQ
80 CONTINUE
DIST = SQRT(XDISTSQ)
IF (DIST.GT.0.0 .AND. DIST.LE.RMAX) THEN
NCOUNT = NCOUNT + 1
NRSTART = 1 + INT((REAL(NPOINT))*(DIST/RMAX)))
DO 90 N = NRSTART,NPOINT
RARR(N) = RARR(N) + 1.0
90 CONTINUE
ENDIF
70 CONTINUE
60 CONTINUE
C
C...CHECK TO SEE IF THE EFFECT OF THE DROPOUTS HAS SPREAD TO THE
C...WHOLE DATA SET
C
PRINT *,M_EMBED,'**** *** ** * NCOUNT =',NCOUNT
IF(NCOUNT.EQ.0)THEN
PRINT *,'DROPOUTS HAVE LIMITED EMBEDDING DIMENSION'
MAX_EMBED = M_EMBED - M_DEL
GOTO 110
ENDIF
C
DO 100 N = 1,NPOINT
CORINT = RARR(N)/ REAL(NCOUNT)
RARR(N) = 0.0
R = (RMAX/REAL(NPOINT))*REAL(N)
IF (CORINT,GT.0.0) THEN
CORPLOT(M_EMBED,N) = LOG10(CORINT)/LOG10(2.0)
C
C..NOW CHOOSE BETWEEN THE ORIGINAL ALGORITHM OR THE MODIFICATION
C..OF DVORAK & KLASHKA. SEE ALSO SMITH.
C
C..ORIGINAL
C
RPLOT(M_EMBED,N)=LOG10(R/RMAX)/LOG10(2.0)
C
C..MODIFIED
C
CCC RPLOT(M-EMBED,N)=LOG10((R*(2.0*RMAX-R))/RMAX**2)/LOG10(2.0)
C
ENDIF
100 CONTINUE
50 CONTINUE
110 CONTINUE
RETURN

```

Program XD6 continued

```

END
C
C*****
C
SUBROUTINE DIMGRAPH(MAX_EMBED,NSTEP,XL,XR,YY,YT,FINAL,DELAY,
    2 RPLLOT,CORPLOT,M_DEL)
C
C..SUBROUTINE TO PLOT OUT THE 'LOG(R)-LOG(CR)' RESULTS
C
IMPLICIT NONE
INTEGER IBEGIN,ISUM,J,JCOUNT,M,MAX_EMBED,NSTEP
INTEGER I,JMAX,DELAY,M_DEL,MCOUNT
INTEGER LINE1,LINE2,LINE3,JSTART
REAL XPLOT(1000),YPLOT(1000),YPLT(2:10,1:1000)
REAL XL,XR,YY,YT
REAL BEGIN,SUM,XXSUM,YSUM,XXSUM,XXSUM,B(30),A(30)
REAL K2DAT(2:30)
REAL FINAL,TAU,TIME_STEP
REAL RPLLOT(30,1000),CORPLOT(30,1000)
INTEGER KTOL,MM,NW,STPVAL,NCOUNT
REAL RMAX,DT
DOUBLE PRECISION PP
COMMON/DROPVAR/KTOL,MM,PP,NW
COMMON/DIMVAR/STPVAL,NCOUNT,RMAX
COMMON/EMBVAR/DT
C
JMAX = 0
MCOUNT = 0
TIME_STEP = (FINAL/REAL(NSTEP))
TAU = (FINAL/REAL(NSTEP)) * REAL(DELAY)
PRINT *,'*DIMGRAPH* TAU ',TAU
PRINT *,'*DIMGRAPH* MAX_EMBED = ',MAX_EMBED
C
CALL PSPACE(0.15,0.75,0.15,0.75)
CALL MAP (XL,XR,YY,YT)
CALL AXESSI(2.0,5.0)
C
SUM = 400.0 !..THE NUMBER OF POINTS USED IN ESTIMATING THE SLOPE
ISUM= 400 !.. " " " " " " " " " " " " " " " " " " " " " "
BEGIN = 150.0 !..THE POINT PRECEDING THE POINT TO BE
IBEGIN= 150 !..USED IN THE SLOPE CALCS.
C
DO 10 M = 2,MAX_EMBED,M_DEL
PRINT *,'*DIMGRAPH* M = ',M
JCOUNT = 0
XXSUM = 0.0
YSUM = 0.0
XXSUM = 0.0
XXSUM = 0.0
DO 20 J = 1,1000
IF (CORPLOT(M,J) .NE. 0.0) THEN
JCOUNT = JCOUNT + 1
XPLOT(JCOUNT) = RPLLOT(M,J)
YPLOT(JCOUNT) = CORPLOT(M,J)
20 CONTINUE
C
C..*** PLOT OUT LINES ***
C
C..3 POINTS AT WHICH THE LINE DRAWING INTERVAL IS CHANGED
C
LINE1 = 100
LINE2 = 200
LINE3 = 400
C
CALL POSITN (XPLOT( 1),YPLOT( 1))
DO 30 J = 1,JCOUNT
JSTART = J
IF(J.GT.LINE1) GOTO 31

```

Program XD6 continued

```

        CALL JOIN(XPLOT(J),YPLOT(J))
30     CONTINUE
        GOTO 100
31     CONTINUE
        DO 40 J = JSTART,JCOUNT,2
            JSTART = J
            IF(J.GT.LINE2) GOTO 41
            CALL JOIN(XPLOT(J),YPLOT(J))
40     CONTINUE
        GOTO 100
41     CONTINUE
        DO 50 J = JSTART,JCOUNT,4
            JSTART = J
            IF(J.GT.LINE3) GOTO 51
            CALL JOIN(XPLOT(J),YPLOT(J))
50     CONTINUE
        GOTO 100
51     CONTINUE
        DO 60 J = JSTART,JCOUNT,8
            CALL JOIN(XPLOT(J),YPLOT(J))
60     CONTINUE
100    CONTINUE
10    CONTINUE
C
    CALL PSPACE(0.1,1.3,0.1,0.9)
    CALL MAP (0.1,1.3,0.1,0.9)
    CALL PLOTCS(0.9,0.80,'H010105 * XD6 *          ')
    CALL PLOTCS(0.9,0.80,'                                DELAY = ')
    CALL PLOTNI(1.20,0.80,DELAY)
    CALL PLOTCS(0.9,0.77,'MAX_EMBED,M_DEL =          ')
    CALL PLOTNI(1.10,0.77,MAX_EMBED)
    CALL PLOTNI(1.20,0.77,M_DEL )
    CALL CTRMAG(13)
    CALL PLOTCS(0.15,0.78,'LOG(R) ')
    CALL PLOTCS(0.71,0.12,'LOG(CR)')
C
    CALL CTRMAG(12)
    CALL PLOTCS(0.12,0.86,'KTOL,MM,PP,NW='')
    CALL PLOTNI(0.30,0.86,KTOL)
    CALL PLOTNI(0.35,0.86,MM )
    CALL PLOTNF(0.40,0.86,PP,4)
    CALL PLOTNI(0.48,0.86,NW )
    CALL PLOTCS(0.12,0.82,'STPVAL,NCOUNT,RMAX='')
    CALL PLOTNI(0.40,0.82,STPVAL)
    CALL PLOTNI(0.49,0.82,NCOUNT)
    CALL PLOTNF(0.59,0.82,RMAX,4)
    CALL PLOTCS(0.9,0.87,'EXPERIMENTAL TIME SERIES DATA ')
    CALL PLOTCS(0.9,0.83,'GRASSBERGER-PROCCACIA DIMENSION ')
    CALL PLOTCS(0.9,0.71,'N-DATA =')
    CALL PLOTNI(1.05,0.71,NSTEP)
C
    CALL POSITN(0.85,1.00)
    CALL JOIN (0.85,0.00)
    CALL POSITN(0.85,0.75)
    CALL JOIN (1.30,0.75)
    CALL BORDER
    CALL FRAME
C
    RETURN
    END

```

Program X-PDF4

```

PROGRAM X-PDF4
C
C..PROGRAM TO CALC. THE P.D.F. OF AN ATTRACTOR SLICE
C
    IMPLICIT NONE
    INTEGER I,J,K,L,BOXARRAY(50),NBOXES,NCROSS,IBOX,NSTEP,DELAY
    REAL XCMAX,XCMIN,XCROSS(16384),X(16384),DELTAC,FBOXES
    REAL XDAT(16384),XDIFF1,XDIFF2,XDIFF,XMEAN,XML
    REAL CMULT,FBOX,EDLTAX,FRACTX,DELTAXC,XCDIFF
    REAL XMAX,XMIN,XTOTAL,DELTAX,P(50),PSUM,DT
    REAL XC,CMEAN,CSUM,CSUMSQ,SIGMA,CONST1,DISTNORM(51)
    REAL ALTSIG
C
    NSTEP = 16384
    DT = 0.01
    ALTSIG = 1.0
    DELAY = 4
C
C..READ IN TIME SERIES
C
    OPEN (20,FILE='M309050B ')
    READ (20,101) (XDAT(I), I = 1,NSTEP)
101  FORMAT (6F12.1)
C
C..NORMALISE THE TIME SERIES FLUCTUATIONS ABOUT THE MEAN
C
    XMAX = -1000000.0
    XMIN = 1000000.0
    XTOTAL = 0.0
    DO 10 I = 1,NSTEP
        IF(XMAX.LT.XDAT(I)) XMAX = XDAT(I)
        IF(XMIN.GT.XDAT(I)) XMIN = XDAT(I)
        XTOTAL = XTOTAL + XDAT(I)
10  CONTINUE
    XMEAN = XTOTAL/REAL(NSTEP)
    XDIFF1 = XMAX - XMEAN
    XDIFF2 = XMEAN - XMIN
    IF(XDIFF1.GE.XDIFF2)THEN
        XDIFF = XDIFF1
    ELSE
        XDIFF = XDIFF2
    ENDIF
    DO 20 I = 1,NSTEP
        X(I) = (XDAT(I)-XMEAN)/XDIFF
20  CONTINUE
C
C...FIND THE ARRAY OF ALL POINTS CROSSING THE +VE X-AXIS
C
    J = 0
    DO 30 I = 1, NSTEP - (1 + DELAY)
        IF(X(I+DELAY+1).LT.0.0 .AND. X(I+DELAY).GT.0.0) THEN
            IF(X(I).GT.0)THEN
                J = J + 1
                DELTAX = X(I+1) - X(I)
                FRACTX = -(X(I+DELAY))/(X(I+DELAY+1)-X(I+DELAY))
                XCROSS(J) = X(I) + DELTAX * FRACTX
            ENDIF
        ENDIF
30  CONTINUE
    NCROSS = J
    PRINT *, 'NCROSS = ', NCROSS
    XCMIN = 1000000.0
    XCMAX = -1000000.0
    DO 40 J = 1, NCROSS
        IF(XCMAX.LT.XCROSS(J)) XCMAX = XCROSS(J)
        IF(XCMIN.GT.XCROSS(J)) XCMIN = XCROSS(J)
40  CONTINUE
    PRINT *, 'MIN X-CROSS VALUE =', XCMIN

```

Program X-PDF4 continued

```

PRINT *, 'MAX X-CROSS VALUE =', XCMAX
DELTAC = XCMAX - XCMIN
PRINT *, 'MAX - MIN VALYE  =', DELTAC
NBOXES = 50
FBOXES = REAL(NBOXES)
CMULT = FBOXES/DELTAC
C
C...INITIALIZE BOX COUNTING ARRAY
C
DO 50 K = 1 , NBOXES
  BOXARRAY(K) = 0.0
50 CONTINUE
C
C...COUNT NUMBER OF CROSSINGS PER BOX
C
DO 60 J = 1,NCROSS
  FBOX = (XCROSS(J)-XCMIN)*CMULT
  K = INT(FBOX) + 1
  BOXARRAY(K) = BOXARRAY(K) + 1
60 CONTINUE
C
C...CALCULATE THE PROBABILITIES OF EACH BOX BEING VISITED
C
PSUM = 0.0
DO 70 K = 1,NBOXES
  P(K) = REAL(BOXARRAY(K))/NCROSS
  PSUM = PSUM + P(K)
70 CONTINUE
DELTAXC = DELTAC / FBOXES
PRINT *, 'DELTAXC = ',DELTAXC
PRINT *, 'SUM OF PROBABILITIES = ',PSUM
C
C...CALCULATE THE MEAN SEPARATION OF THE X-CROSSINGS (XML)
C
XML = 0.0
DO 80 K = 1,NBOXES
  DO 90 L = 1,NBOXES
    IF(L.GT.K)THEN
      XCDIFF = REAL(L-K)
    ELSE
      XCDIFF = REAL(K-L)
    ENDIF
    XML = XML + P(L)*P(K)*XCDIFF*DELTAXC
90 CONTINUE
80 CONTINUE
C
CCCCCCCCCCCCCCCCCCCCCCCCCCCCCCCCCCCCCCCCCCCCCCCCCCCCCCCCCCCC
C
C..CALCULATE THE NORMAL DISTRIBUTION USING THE MEAN AND
C..STANDARD DEVIATION OF THE POINTS
C
CCCCCCCCCCCCCCCCCCCCCCCCCCCCCCCCCCCCCCCCCCCCCCCCCCCCCCCCCCCC
C
C..FIND THE MEAN CROSSING VALUE
C
CSUM = 0.0
CMEAN = 0.0
DO 100 I = 1,NCROSS
  CSUM = CSUM + XCROSS(I)
100 CONTINUE
CMEAN = CSUM/REAL(NCROSS)
C
C..CALCULATE THE STANDARD DEVIATION
C
CSUMSQ = 0.0
DO 110 I = 1,NCROSS
  CSUMSQ = CSUMSQ + (XCROSS(I)-CMEAN)**2
110 CONTINUE

```

Program X-PDF4 continued

```

        SIGMA = ((CSUMSQ/REAL(NCROSS))**.5) * ALTSIG
C
C...FIND THE NORMAL DISTRIBUTION OF THE POINTS
C
        CONST1 = DELTAXC/(SIGMA*2.506628275)
        PRINT *,'CONST1 = ',CONST1
        DO 120 I = 1,NBOXES + 1
            XC = XCMIN + REAL(I-1) * DELTAXC
            DISTNORM(I) = CONST1*EXP(-0.5*((XC-CMEAN)/SIGMA)**2)
            PRINT *,'XC = ',XC
            PRINT *,'DISTNORM = ',DISTNORM(I)
            PRINT *,'PROB      = ',P(I)
120    CONTINUE
C
C...PLOT OUT THE P(X) HISTOGRAM
C
        CALL PDFPLOT(XCMIN,XCHAX,DELTAXC,P,NBOXES,XML,DISTNORM,ALTSIG)
C
        CALL GREND
C
        STOP
        END
C*****
        SUBROUTINE PDFPLOT(XCMIN,XCHAX,DELTAXC,P,NBOXES,XML,DISTNORM,
            *                ALTSIG)
C
C..SUBROUTINE TO PLOT OUT THE PROBABILITY HISTOGRAM OF SLICE
C..INTERSECTIONS AND SUPERIMPOSE NORMAL DISTRIBUTION
C
        IMPLICIT NONE
        INTEGER I,NBOXES
        REAL XC(51),XCMIN,XCHAX,DELTAXC,P(50),PMAX,XML
        REAL DISTNORM(51),ALTSIG
C
        PMAX = -100000.000
        DO 10 I = 1,NBOXES
            IF(P(I).GT.PMAX) PMAX = P(I)
10    CONTINUE
        PRINT *,'MAX. PROBABILITY = ', PMAX
C
        CALL PSPACE(0.1,1.3,0.1,0.9)
        CALL MAP   (0.1,1.3,0.1,0.9)
        CALL BORDER
        CALL CTRMAG(14)
        CALL PCSCEN(1.0,0.8,'PROBABILITY HISTOGRAM OF ATTRACTOR SLICE')
        CALL PCSCEN(1.0,0.76,'FILE = M309050B,    DELAY=11  ')
        CALL PCSCEN(1.0,0.72,'MEAN SEPERATION =')
        CALL PLOTNF(1.15,0.72,XML,4)
        CALL PCSCEN(1.0,0.66,'          ALTSIG =')
        CALL PLOTNF(1.15,0.66,ALTSIG,4)
        CALL PSPACE(0.2,0.8,0.2,0.8)
        CALL MAP   (XCMIN,XCHAX,0.0,PMAX)
        CALL AXORIG(XCMIN,0.0)
        CALL AXES
C
C...PLOT THE NORMAL DISTRIBUTION OF THE POINTS
C
        DO 20 I = 1,NBOXES + 1
            XC(I) = XCMIN + REAL(I-1) * DELTAXC
20    CONTINUE
        CALL CURVED (XC,DISTNORM,1,NBOXES+1)
        CALL HISTGM(XCMIN,0.0,DELTAXC,P,1,50)
        CALL FRAME
C
        RETURN
        END

```

## **A2.4 Testing of the Programs**

### **A2.4.1 Testing the Grassberger–Procaccia Dimension Algorithm**

The algorithm to calculate the Grassberger–Procaccia algorithm was extensively tested prior to its use on the experimental data. The algorithm underwent many revisions in the process. The algorithm was tested on a wide variety of data sets, the main ones are given in the following.

1 – Sine wave time series data. This is possibly the simplest of tests for a dimension estimate. A data set comprising a sinusoidal wave form should give a one dimensional estimate. The results of the test may be seen in figure A2–1. The results are for an embedding dimension of 2 to 29 in steps of 3. It can be seen from the figure that the dimension algorithm predicts the actual dimension of one fairly accurately.

2 – The Lorenz system. The chaotic Lorenz system, (for the parameters outlined in section 2.6.4) has a theoretical dimension of 2.07, [Wolf et al, 1985]. The results of the Grassberger–Procaccia for a data set of 10,000 points is given in figure A2–2, for an embedding dimension of one to ten. The average slope of the plots is approximately 2.05.

3 – The Rossler equations. The theoretical dimension of the chaotic Rossler system, is 2.01. The dimension estimate obtained by the author was 2.012, figure A2–3. This for 5,000 data points and an embedding dimension of 6.

4 – The Rossler–Hyperchaos equations. The theoretical dimension of the chaotic Rossler–Hyperchaos equations, is 3.005. The dimension estimate obtained by the author was 3.0037, figure A2–4. This for 30,000 data points and an embedding dimension of 4.

5 – Lorenz system with added noise. It was decided by the author to test the dimension algorithm on the chaotic solution to the Lorenz equations with different levels of noise added to the equations. Figure A2–5 gives the results for a very large noise level of 0.3 times the attractor radius. As can be seen from the figure the slope of the plots, and hence the dimension of the attractor is scaling with the

embedding dimension, and shows no sign of levelling off.

#### **A2.4.2 Testing of the Lyapunov Exponent Program**

The Lyapunov exponent program, FET, was tested using both the sample data supplied with the program, by Wolf, [1991], and on test data produced by the author. The test data supplied with the program consisted of time series for the Lorenz and Rossler attractors, as well as the logistic equation. The program was also tested on sine wave data manufactured by the author, with, and without, added noise. Exponents close to zero were found for such data sets.

#### **A2.5 Signal Dropouts**

For time signals with reverse flow components, and rapidly fluctuating velocities, the tracker would momentarily lose the signal, causing a dropout to occur in the velocity time trace. Figure A2-6a gives an example of such a time trace with dropouts. As is evident from the figure, the time signal is fairly constant over the dropout portion of the time series. Thus the reconstructed part of the attractor, pertaining to the dropouts, consists of localised 'spots' containing many points, as shown in figure A2-6b. At small length scales, the dimension algorithm gives a lower value of dimension than would otherwise be the case if the time trace contained no drop outs. This is because the spots are essentially of zero dimension.

An algorithm was written by the author to look for, and label the dropouts in the signal, figure A2-6c. These labelled points were then ignored during the construction process of the attractor. An example of the modified, reconstructed attractor with the dropouts omitted is given in figure A2-6d. Data analysis techniques, such as the Mutual Information calculation, Dimension estimate etc. were then calculated using this labelled time series, whereby the dropout regions were ignored.

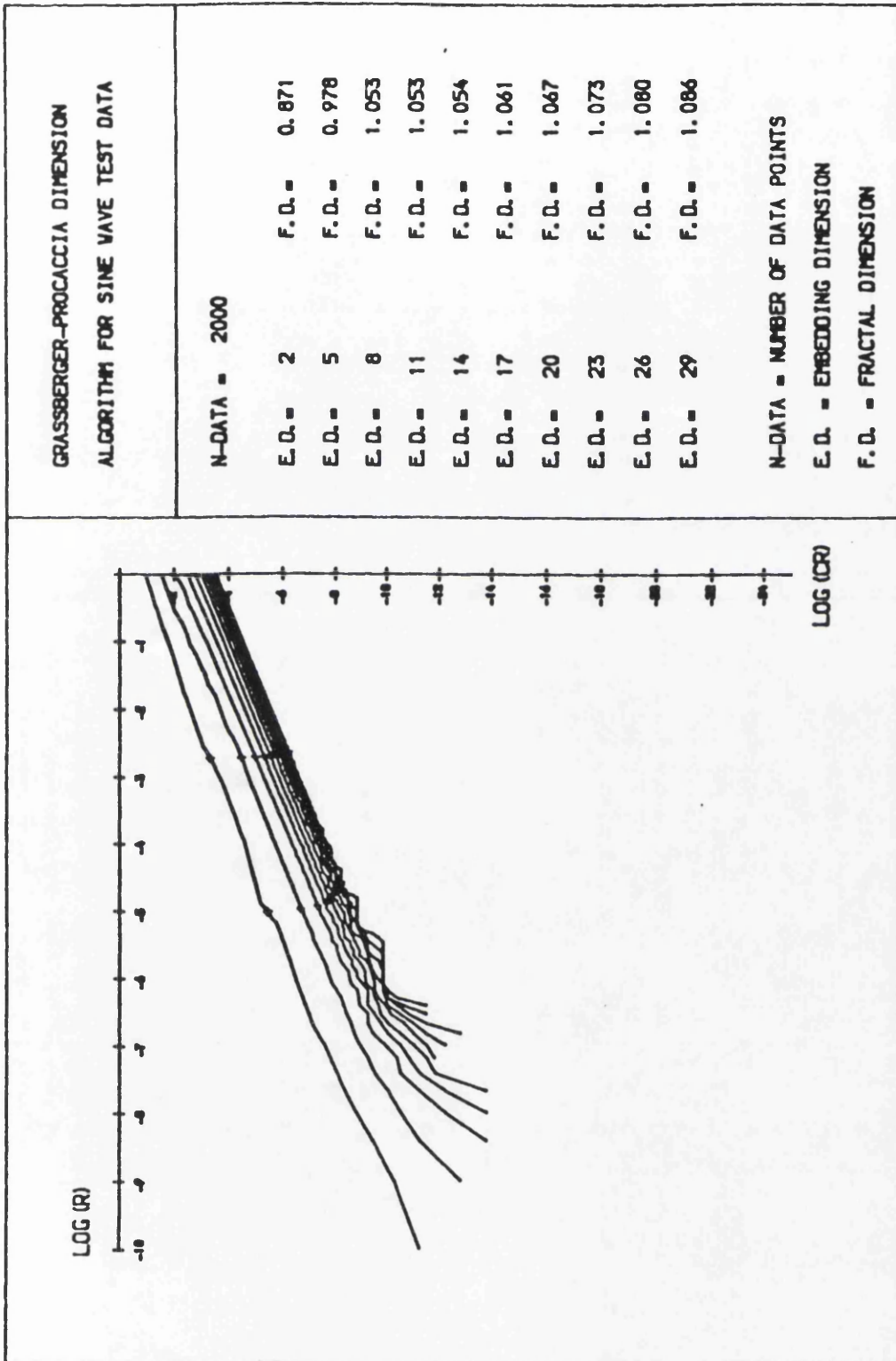


Figure A2-1: 'log(r)-log(C<sub>r</sub>)' Plot for Sine Wave Test Data

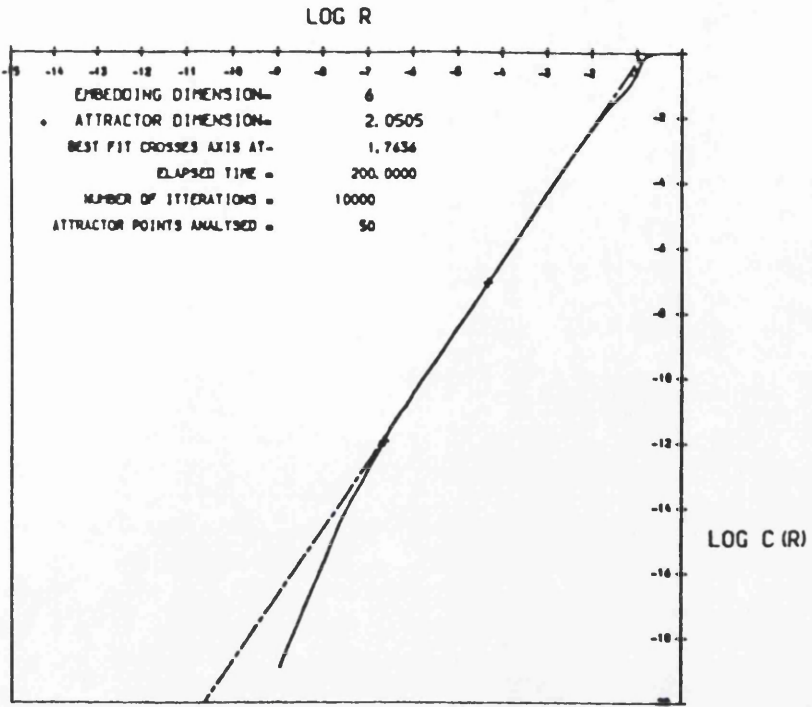


Figure A2-2: ' $\log(r)-\log(C_r)$ ' Plot for the Lorenz Attractor

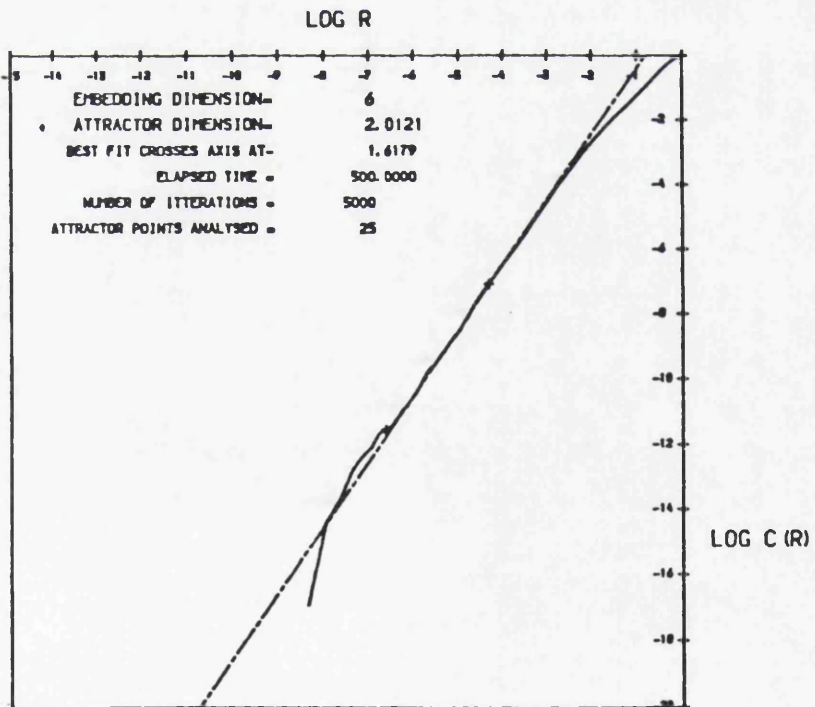


Figure A2-3: ' $\log(r)-\log(C_r)$ ' Plot for the Rossler Attractor

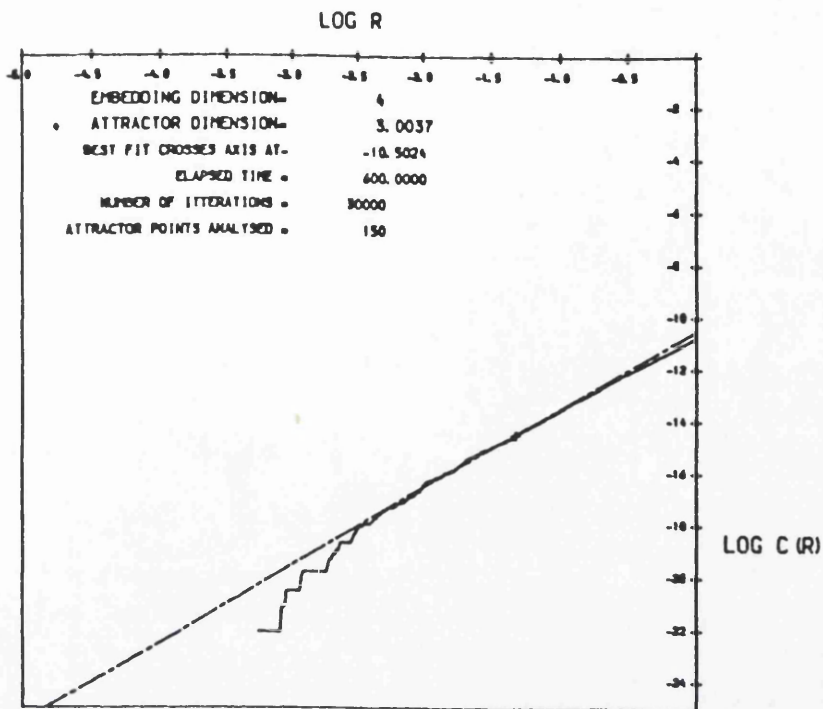


Figure A2-4: ' $\log(r)-\log(C_r)$ ' Plot for the Rossler Hyper-Chaos Attractor

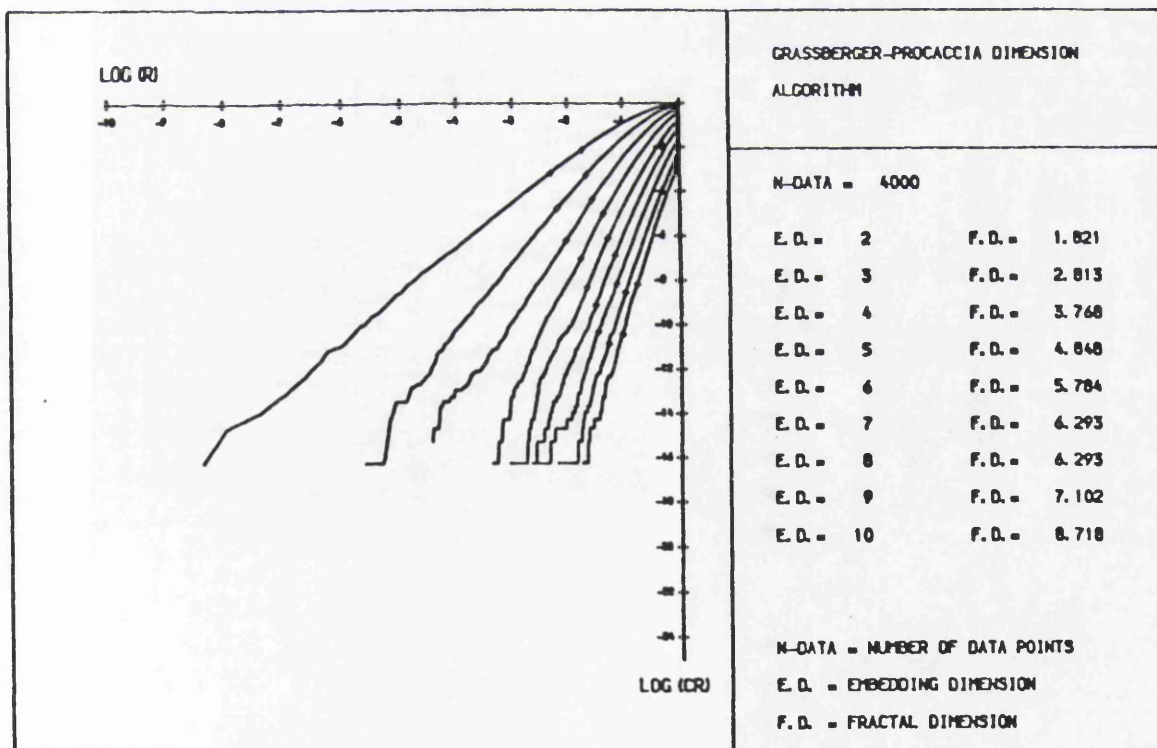
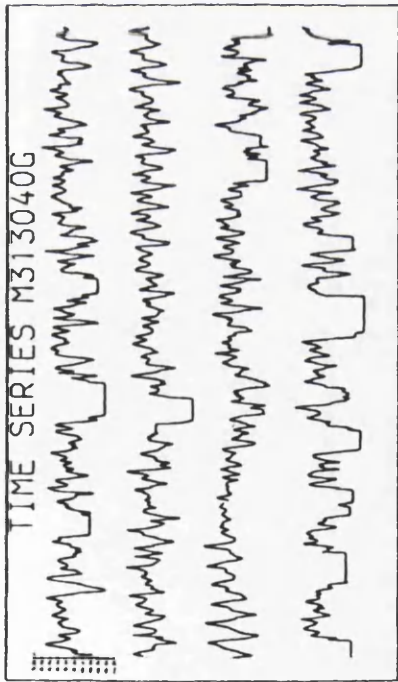
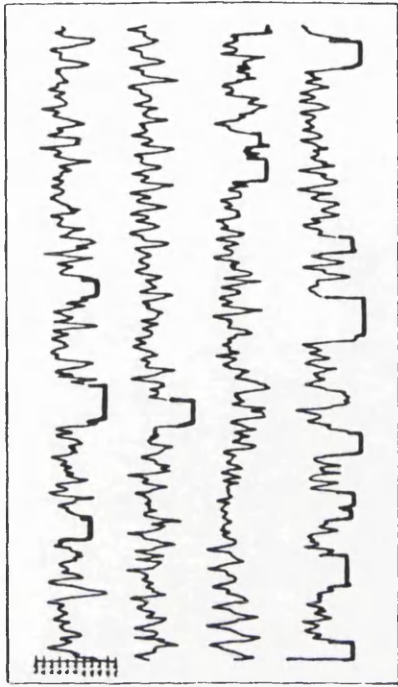


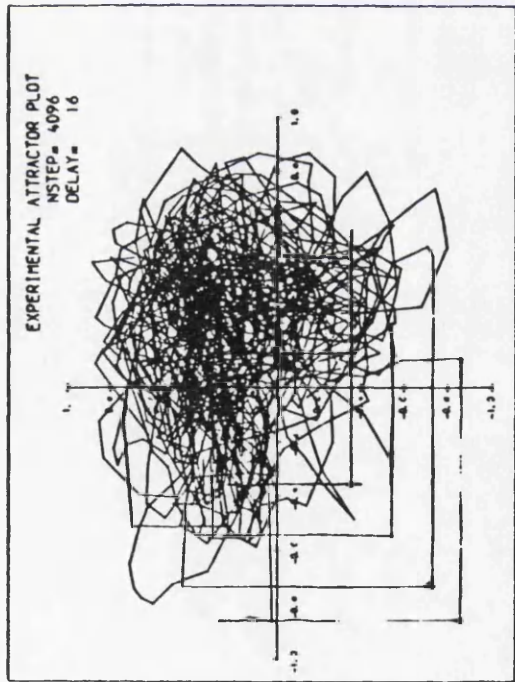
Figure A2-5: ' $\log(r)-\log(C_r)$ ' Plot for Noisy Sine Wave Data



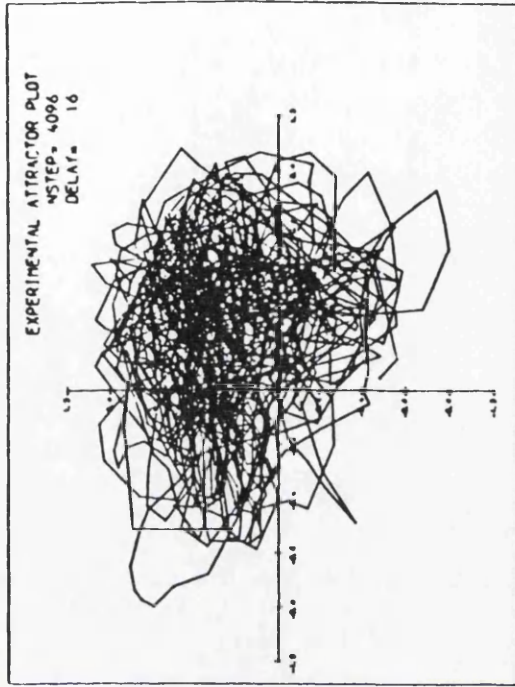
(a)



(c)



(b)



(d)

Figure A2-6: The Elimination of Signal Dropouts in the Time Series

## APPENDIX 3: A NOTE ON THE GEOMETRIC AND REFRACTIVE PROPERTIES OF THE PIPE

### A3.1 Actual and Apparent Images

The flow visualisation results, described in chapter 5, were obtained by illuminating the flow within the pipe with a sheet of light passing through the pipe on one of the main diameters. (Either in the horizontal or vertical plane.) The resulting photographs and video film were then analysed visually to elucidate qualitatively the flow mechanisms involved at the orifice plate within the pipe. Also quantitative measurements were made of the vortex wavelengths by measuring directly from the photographic and video film. However, when one views the illuminated sheet from outside the pipe, the resulting picture is distorted by the geometrical and refractive properties of the pipe and fluid. These distortions are outlined in this appendix.

Referring to figure A3-1, we may see that a ray of light coming from a flow visualisation particle on the illuminated diameter, (marked  $Y_{act}$ ), is refracted first by the inner pipe wall-fluid interface. Then again by the outer surface of the pipe wall-air interface. Thus the apparent position of the flow visualisation particle appears at  $Y_{app}$ .

Knowing the initial value of the apparent position of the particle,  $Y_{app} = H_2$ , and the distance from the observer to the pipe centre-line,  $D_{total}$ , the actual position of the particle ( $Y_{act} = H_1$ ) may be found by the following series of formulae.

Knowing  $D_{total} = D_{out} + t_w + D_{in}$ ,  $D_{in} = R_2$  and  $H_2$ , and referring to figure A3-1, one proceeds as follows.

$$\tan(\theta_e) = \frac{H_2}{D_{total}} \quad \text{hence} \quad \theta_e \quad (A3.1)$$

$$\text{Sine Rule: } \frac{\sin(\theta_{i1})}{R_1} = \frac{\sin(180 - \theta_{i1})}{D_{\text{total}}} \quad (\text{A3.2})$$

hence  $\theta_{i1}$

$$\theta_{i1} = \alpha_1 + \theta_e \quad \text{hence } \alpha_1 \quad (\text{A3.3})$$

$$\text{Snell's law: } \frac{\sin(\theta_{r1})}{\sin(\theta_{i1})} = \frac{n_i}{n_r} \quad (\text{A3.4})$$

hence  $\theta_{r1}$

$$\text{Sine Rule: } \frac{\sin(\theta_{r1})}{R_2} = \frac{\sin(180 - \theta_{i2})}{R_1} \quad (\text{A3.5})$$

hence  $\theta_{i2}$

$$\text{Snell's law: } \frac{\sin(\theta_{r2})}{\sin(\theta_{i2})} = \frac{n_i}{n_r} \quad (\text{A3.6})$$

hence  $\theta_{r2}$

$$\text{Position 1: } x = D_{\text{total}} - R_1 \cdot \cos(\alpha_1) \quad (\text{A3.7a})$$

$$y = R_1 \cdot \sin(\alpha_1) \quad (\text{A3.7b})$$

$$\text{Position 2: } x = D_{\text{total}} - R_2 \cdot \cos(\alpha_2) \quad (\text{A3.7c})$$

$$y = R_2 \cdot \sin(\alpha_2) \quad (\text{A3.7d})$$

$$\text{Where, } \alpha_2 = \alpha_1 + \theta_{i2} + \theta_{r1} \quad (\text{A3.7e})$$

Therefore the actual position of the particle,  $Y_{\text{act}}$ , is at a height of  $H_1$ , where  $H_1$  is obtained from the expression:

$$\frac{\sin(90 - \theta_{r2} + \alpha_2)}{R_2} = \frac{\sin(\theta_{r2})}{H_1} \quad (\text{A3.8})$$

Using the above expressions one may transform an apparent image into an actual image. This could be done by digitising the photograph, or video film frame, and applying a transformation to the digitised points based on the above formulae. Thus, the actual image could be produced.

### A3.2 Laser Intersection Point Error

In normal operation to detect axial velocities, the laser is set up so that the centre-line of the two beams intersects the pipe centre-line at right angles, as shown in figure A3-2. It was decided to investigate the effect that a slight deviation in the angle of the laser centre-line,  $\theta_{\text{dev}}$ , would have on the actual position of the intersection point within the fluid.

The position of the front lens, to allow the intersection of the beams to fall on the pipe centre-line, must first be calculated. The distance of the front lens ( $D_{\text{total}}$ ) from the pipe centre-line to allow this to happen is calculated as follows.

(Refer also to figure A3-2.)

$$\theta_3 = 5.71^\circ \text{ and } Y_3 = 30.00\text{mm} \text{ (Manufacturers Data - DISA)}$$

$$R_2 = 13.00\text{mm} \quad t_w = 2.00\text{mm}$$

$$\text{Snell's Law: } \theta_2 = \sin^{-1} \left[ \frac{n_a}{n_g} \cdot \sin(\theta_3) \right] \quad (\text{A3.9})$$

$$\text{Snell's Law: } \theta_1 = \sin^{-1} \left[ \frac{n_g}{n_w} \cdot \sin(\theta_2) \right] \quad (\text{A3.10})$$

Where the indices of refraction are

$$n_g = 1.473$$

$$n_w = 1.333$$

$$n_a = 1.000$$

$$x_1 = \tan(\theta_1) \cdot R_2 = 0.9730\text{mm} \quad (\text{A3.11})$$

$$x_2 = 0.9730 + \tan(\theta_2) \cdot t_w = 1.1084\text{mm} \quad (\text{A3.12})$$

$$x_3 = 30\text{mm} \rightarrow x_3 - x_2 = 28.8916 \quad (\text{A3.13})$$

$$D_{\text{out}} = \frac{28.8916}{\tan(\theta_3)} \quad (\text{A3.14})$$

$$D_{\text{total}} = D_{\text{out}} + t_w + R_2 \quad (\text{A3.15})$$

$$= 288.95 + 2.00 + 13.00 = 303.95$$

Thus, starting with the lens mid-point at this position of 303.95mm from the pipe centre-line, the deviation, or error, angle,  $\theta_{\text{dev}}$ , was varied and the new intersection points calculated. Figure A3-3 contains the results of these calculations. The curved line running up and down the page represent the movement of the intersection points as the deviation angle is increased from zero, both in a clockwise (below the  $r$ -axis) and an anti-clockwise (above the  $r$ -axis) direction.  $\theta_{\text{dev}} = 0$  is represented by the horizontal  $r$ -axis.

An intersection line has been calculated for points initially on the pipe centre-line ( $r = 0$ ). In addition, intersection lines have been calculated for a movement of the lens in the direction of the laser beam intersection line, i.e. perpendicular to the pipe axis. These lines are also drawn on figure A3-3 and represent incremental movements of 2.00mm of the laser front lens both towards, and away from, the pipe. The horizontal lines in the figure denote the incremental points at which  $\theta_{\text{dev}}$  has been varied by  $1^\circ$ , or 0.01745 radians. Note that in the figure the  $z$ -axis and the  $r$ -axis are not to the same scale, this has the effect of accentuating the curvature of the intersection lines as one moves away from the correct position.

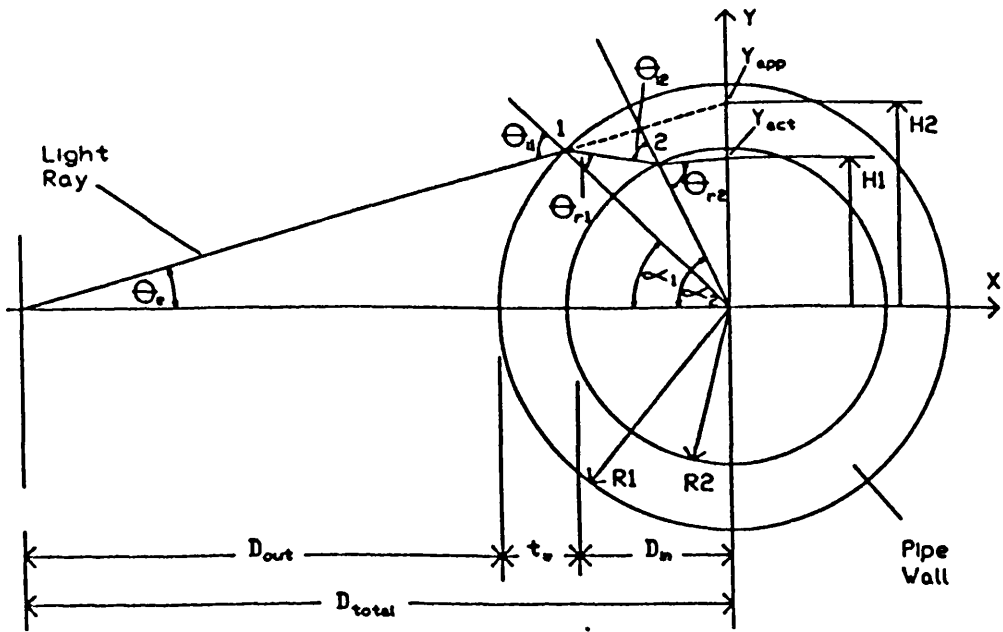


**Figure A3-1: Refraction of Light Rays Through the Pipe Wall (1)**

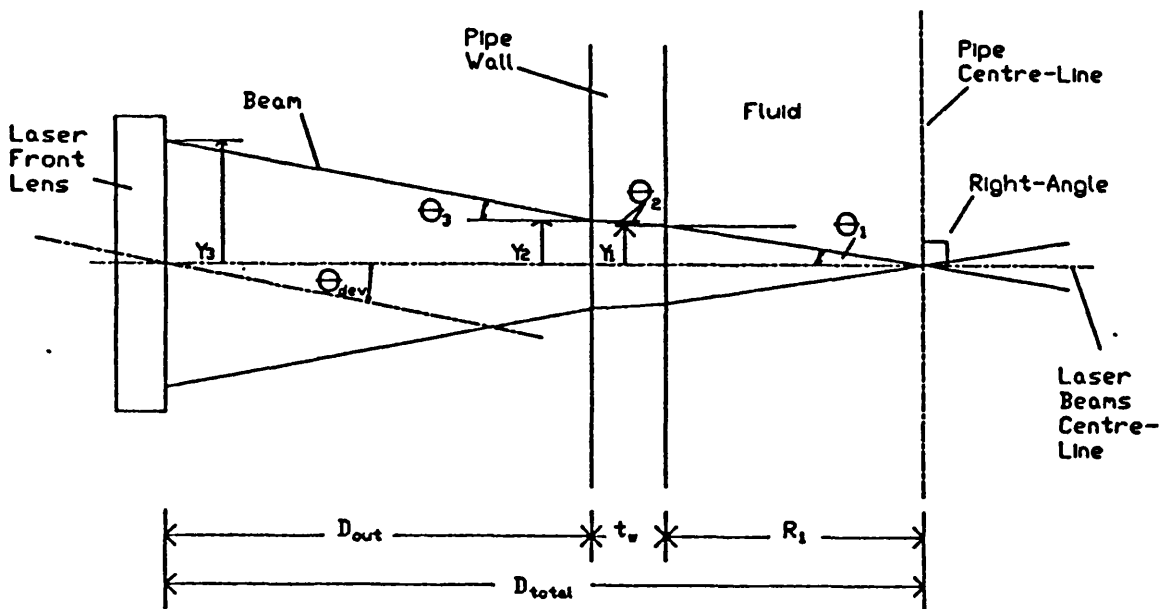
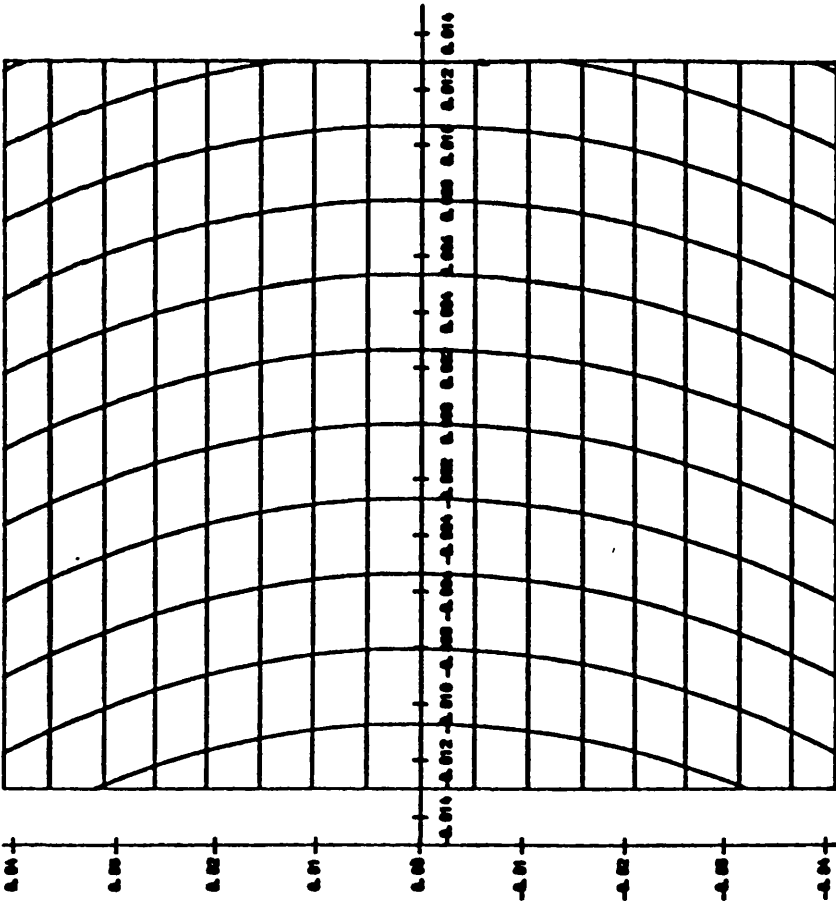


**Figure A3-2: Refraction of Light Rays Through the Pipe Wall (2)**

# LASER INTERSECTION DEPENDENCE GRAPH 11



LASER INTERSECTION DUE TO DEVIATION IN LENS X-COORDINATE AND THE LENS ANGLE

## \*\*\* INITIAL DATA \*\*\*

INTERNAL XLINE = 0.1300E-01  
 WALL THICKNESS = 0.2000E-02  
 THETA-INC. OUTSIDE 0.1745E-01  
 X-INC. OUTSIDE = 0.2000E 01

AIR REF. INDEX = 0.1000E 01  
 GLASS REF. INDEX = 0.1475E 01  
 WATER REF. INDEX = 0.1335E 01

Figure A3-3: Laser Intersection Dependence Graph

## APPENDIX 4: OBSERVATIONS ON NUMERICAL METHOD DEPENDENT SOLUTIONS OF A MODIFIED DUFFING OSCILLATOR

During the course of the author's main work of the thesis, some additional work was done in the area of non-linear oscillators. Some interesting results came to light regarding the effect of numerical schemes on the subsequent solutions of a modified version of the Duffing oscillator. A paper was produced describing the main points discovered during this additional piece of work. A summary of this paper is given in what follows in this Appendix.

### ABSTRACT

Numerical solutions of a non-linear oscillator have been produced by various methods. Some unexpected discrepancies have been found in the solutions obtained. This behaviour is reported herein and the implications to the application of numerical methods to non-linear dynamical systems are discussed.

### A4.1: INTRODUCTION

Since the discoveries of Edward Lorenz [1963] regarding the order present within the complex structure of the apparently random solutions (now called chaotic solutions) to a set of non-linear differential equations, many papers have emerged in the field of non-linear dynamical systems. As with Lorenz's work, many of the important discoveries in this area have been possible only with the availability of computer generated solutions to the non-linear equations and mappings considered.

One of the most extensively studied of all non-linear systems is the Duffing equation [Duffing, Date Unknown and Dinca and Teodosiu, 1973]:

$$\ddot{x} + k\dot{x} + x^3 = B \cos(t) \quad (\text{A4.1})$$

which is an example of a damped, periodically forced non-linear oscillator with a cubic elastic restoring force. This form of equation is found in engineering and might, for instance, model the motion of a sinusoidally forced structure undergoing large elastic deformations. Depending on the choice of the parameters  $k$  and  $B$ , the solution to Equation A4.1 can exhibit periodic or chaotic motion [Thompson and Stuart, 1986].

For the purposes of the investigation presented herein, it was decided to investigate the properties of a modified version of Equation A4.1, given as follows;

$$\ddot{x} + k\dot{x} + x^3 = -\cos(t) - k.\sin(t) + \cos^3(t) \quad (\text{A4.2})$$

where the viscous damping parameter  $k$  has a value of 0.05, giving periodic solutions to equation A4.2. This value of  $k$  was kept constant for the investigation reported here.

Equation(2) has an obvious exact solution:

$$x = \cos(t) \quad (\text{A4.3})$$

with the appropriate initial conditions of:

$$x = 1 \quad \text{and} \quad \dot{x} = 0 \quad (\text{A4.4})$$

The numerical integration procedures for all the results reported in this paper were started on this known solution. Equation A4.2 was solved using the standard numerical integration schemes outlined in part A4.2.

## A4.2. NUMERICAL SCHEMES INVESTIGATED

It is surprising to note that a substantial number of papers in the non-linear

dynamics field reporting on phenomena which require the use of a numerical integration scheme fail to name the scheme used or the time step chosen. As will be seen subsequently, the magnitude of the time step itself can have a controlling effect on the solution produced.

Previous studies by Wood and Oduor, [1988], have shown that the time stepping schemes which are stable for the linear equations can exhibit unstable behaviour for the non-linear equations. Moreover, a number of previous studies, (by Wood and Odour, [1988], Park, [1975] and Bert and Stricklin [1975]), have concentrated on homogeneous ordinary differential equations, (i.e. without forcing terms). Although, in the work by Bert and Stricklin, an equation similar to the Duffing equation used in this study was employed, the time integration was only carried out for 2 cycles of the forcing function, which is insufficient to reveal instability or non-unique behaviour.

To integrate equation A4.2, two commonly used numerical integration schemes were tried, namely: the fourth-order Runge-Kutta method and the Newmark direct integration method. In this investigation the parameters of the integration schemes were varied and the parameters in equation A4.2 were kept constant, thus enabling the influence of the actual integration scheme on the solution to be discerned.

Whilst Runge-Kutta methods with higher degrees of accuracy are available, the amount of algebraic computation required to achieve a specified order of accuracy greater than four becomes proportionally greater in terms of the number of function evaluations. It is this reason which accounts for the popularity of the fourth-order method.

A detailed account of the Runge-Kutta method used in the study reported here is given by Gerald and Wheatley, [1984]. In the method, the second order differential equation of equation A4.2 is treated as a system of first order

differential equations, as follows.

$$y = \dot{x} \quad (A4.5a)$$

$$y = -\cos(t) - k.\sin(t) + \cos^3(t) - k\dot{x} - x^3 \quad (A4.5b)$$

The Newmark direct integration method is another popular approximation scheme available for computing the time derivatives of differential equations. This investigation has made use of the method as outlined by Bert and Stricklin [1971] and Hughes [1987], where the parameters  $\beta$  and  $\gamma$  control the stability and accuracy of the scheme.  $\beta = 1/4$ ,  $\gamma = 1/2$  is known to be unconditionally stable for *linear* problems and corresponds to the 'Constant Average Acceleration Method'.  $\beta = 1/6$ ,  $\gamma = 1/2$  corresponds to the 'Linear Acceleration Method', which is conditionally stable for linear problems. However, unlike the investigation of Bert and Stricklin, our interest lies with the post transient solution of non-linear equations. A generalisation of the Newmark method is given by Katona and Zienkiewicz [1985].

The generalised Newmark method for equation A4.2 may be expressed as

$$\ddot{X}_{n+1} = \ddot{X}_n + \Delta\ddot{X}_n \quad (A4.6a)$$

$$\dot{X}_{n+1} = \dot{X}_n + \ddot{X}_n \Delta t + \gamma \Delta\ddot{X}_n \Delta t \quad (A4.6b)$$

$$X_{n+1} = X_n + \dot{X}_n \Delta t + \ddot{X}_n \Delta t^2 / 2 + \beta \Delta\ddot{X}_n \Delta t^2 \quad (A4.6c)$$

and

$$\ddot{X}_{n+1} + k\dot{X}_{n+1} + X_{n+1}^3 = \cos(t_n) - k.\sin(t_n) + \cos^3(t_n) \quad (A4.6d)$$

When  $\beta$  is not equal to zero, a cubic equation in terms of  $\Delta\ddot{X}_n$  has to be solved.

It can be shown that the equation has only one real root. This cubic equation was first solved by the classical solution of Cardan [Low, 1931]. However, even with REAL\*8 accuracy, (16 significant figures), the solution can be inaccurate. It was decided that a further refinement was required. This was done by employing both the Newton-Raphson method and the interval halving method. For the Newton-Raphson method the solution obtained from the linearised equation, (neglecting coefficients of the second and third order), is input as the initial guess, and the value of  $\ddot{\Delta X}_n^r$  is refined until  $\ddot{\Delta X}_n^{r+1}$  is equal to  $\ddot{\Delta X}_n^r$  for the full machine precision.

$$\ddot{\Delta X}_n^{r+1} = \ddot{\Delta X}_n^r + \frac{f(\ddot{\Delta X}_n^r)}{f'(\ddot{\Delta X}_n^r)} \quad (\text{A4.7a})$$

Where

$$\begin{aligned} f(\ddot{\Delta X}_n^r) = & -\cos(t_n) - k \sin(t_n) + \cos^3(t_n) \\ & - (\ddot{X}_{n+1} + k\dot{X}_{n+1} + X_{n+1}^3) \end{aligned} \quad (\text{A4.7b})$$

There is no difference between the results obtained with the Newton-Raphson refinement and the interval-halving method, although the CPU time required for the interval-halving method is much greater.

### A4.3. RESULTS

The modified Duffing oscillator, equation A4.2, was numerically integrated using

the schemes outlined in section A4.2. It was found that the solution obtained by the Runge–Kutta method and the Newmark method generally took on one of five forms. All computed solutions were started on the exact solution, equation A4.3, and proceeded to follow this solution for some time. Thereafter, the solution would always become unstable, pass through a transition period, and switch to one of three final solutions (Type A,B,C), as shown in figure A4.1. In fact, the Runge–Kutta and Newmark methods usually gave quite dissimilar results for the same value of the time step  $\Delta t$

### A4.3.1 PHASE SPACE DIAGRAMS

The phase space diagrams for the final solutions depicted in figure A4.1 are given in figure A4.2. The initial circular phase space trajectory shown in figure 2a clearly indicates that the solution does indeed follow the initial cosine waveform solution of equation A4.3. The behaviour of the final solutions, types A, B and C, are seen to be more complex than the initial exact solution and seem to incorporate two or more commensurate frequencies. All phase diagrams shown have been drawn by running the calculations for a time  $T$ , where  $T \gg 2\pi$ .

### A4.3.2 FAST FOURIER ANALYSIS OF RESULTS

Figure A4.3 shows typical frequency spectra for the solutions using a Fast Fourier Analysis algorithm, as given by Cooley *et al* [1969]. From the spectra, it can be seen that all solutions exhibit a dominant peak at a circular frequency of 1 cycles/sec, and that the cosine solution, figure A4.3a, consists of this alone. In addition to this dominant frequency, the final solutions (figures A4.3b, A4.3c and A4.3d) have peaks at 3 cycles/sec for all three types with the type B solution

having a third peak at 1/3 cycles/sec. The amplitudes of the solutions, calculated by the F.F.T. analysis, are given in table 1.

A much more satisfactory method of classification of the solutions is the invariant measure:

$$X_{sq} = \frac{1}{2} \sum_{k=0}^{n-1} |X_k|^2 = \frac{1}{2N} \sum_{r=0}^{n-1} |x_r|^2 \quad (A4.8)$$

where  $X_k$  is the time series of the solution and  $x_r$  is the Fourier transform of the solution. The values of  $X_{sq}$  computed for each scheme, at various arbitrary time steps, were approximately 0.018, 0.028 and 0.377 for final solution types A, B and C respectively.

Solution	Amplitudes for given frequencies.			$X_{sq}$
	$\omega = 1/3$	$\omega = 1$	$\omega = 3$	
Initial Cosine Exact Solution	—	0.500	—	0.125
Final Solution Type A	—	0.133	0.014	0.018
Final Solution Type B	0.075	0.141	0.014	0.028
Final Solution Type C	—	0.607	0.031	0.377

Table A4.1: Amplitudes of the frequency components of the solutions, obtained by the F.F.T. analysis.

### A4.3.3 METHODS OF SOLUTION

Initially, both methods were run with various values of the time step  $\Delta t$ . It was found that the two Newmark methods (analytical and Newton–Raphson) would give the same solutions for large time steps ( $\Delta t > 0.004$ ) but would seldom agree with the Runge–Kutta solutions produced using the same time step. All three of these methods could be made to produce all three of the characteristic final solutions of figure 1 by altering the value of  $\Delta t$  used. For the case of  $\Delta t < 0.004$ , all three solutions vary independently of each other and in a seemingly random fashion. It was found that every possible combination of solutions occurred for the schemes as the time step was varied. It was also found that the Runge–Kutta method in all cases was the last method to lose its initial stability and depart from the  $x = \cos(t)$  curve – a result one would expect from the method's fourth order accuracy.

For all methods, as one would expect, the initial solution becomes unstable at progressively later points with decreasing values of the time step  $\Delta t$ .

### A4.3.4 SMALLER VALUES OF $\gamma$

The use of the linear acceleration Newmark method, which has a reduction in the stability parameter  $\gamma$  in the approximation of the solution i.e.  $\gamma = 1/6$ , and the case for the explicit solution i.e.  $\gamma = 0$ , both result in the highest amplitude solution (figure A4.1c), regardless of time step chosen. The latter case results in not having to solve a cubic equation. This indicates that a value of  $\gamma = 1/2$  allows the solution to take on forms with less amplitude than would be obtained with lower values of  $\gamma$ , namely the highest amplitude type C solution.

#### A4.3.5 COMPUTER ACCURACY AND PROCESSING TIMES

The computer used in all calculations was an IBM 3090 VF 150E, and the compiler used was the IBM 'V.S. FORTRAN', Version 2.4. All the results presented here were produced by algorithms written in FORTRAN 77 code where REAL\*8 accuracy was employed. REAL\*4 and REAL\*16 were also tried but all the behaviours found with the REAL\*8 accuracy could be obtained with both the lower and higher accuracy real numbers, though not necessarily for the same value of time step. However, the higher accuracy solutions generally took a longer time to lose their initial stability. This would tend to suggest that the initial cosine solution, equation A4.3, loses its stability due to round-off error present within the computer. This error grows exponentially, characteristic of non-linear equations, and results in the solution moving to one of the three stable final solutions.

Typical processing times of the Runge-Kutta method and the Newmark scheme with the cubic solved analytically and explicitly are given in table A4.2. The Runge-Kutta methods fourth order accuracy accounting for the longest solution time. The results given in the table are for a time step of 0.1257, (or  $2\pi/50$ ), and run for 24 cycles or 1200 time steps.

Solution Schemes	C.P.U. Times (Seconds)	C.P.U. Times as a Percentage of the Runge Kutta Time
Runge-Kutta Method	0.7310	100 %
Newmark, Analytic Method	0.4797	65 %
Newmark, Newton-Raphson Method	0.2339	32 %
Newmark, Explicit Method	0.1635	22 %

Table A4.2: Typical C.P.U. times required for various schemes.

#### A4.3.6 SEARCH FOR A BASIN OF ATTRACTION

A search was conducted to find out how the initial conditions affected the final solution and, more precisely, to check whether the initial conditions used for the previous analyses were in an unstable region. The initial conditions were varied over the  $x, \dot{x}$  plane from  $-1.0$  to  $1.0$  using a  $81 \times 81$  point grid, this giving an incremental increase of  $0.025$ . A central difference scheme was used which was exactly equivalent to the Newmark explicit method, with  $\beta = 0$ ,  $\gamma = 1/2$ .

Figure A4.4 gives results for a time step  $\Delta t$  of  $2\pi/25$ . In the figure, type A solution initial conditions are denoted by a circle, type B solutions by a cross and the initial conditions giving a type C solution have been left blank. From the figure, it can be seen that a pattern emerges, whereby the type C solution predominates and forms a 'sea' around an 'island' made up of type A and B solutions.

The boundaries to the island appear to be quite broken, and in fact could be of a fractal nature. More work will be done, to follow on from these preliminary results on the effect of the initial conditions, to elucidate the further the nature of these basins of attraction.

#### A4.3.7 NEWMARK EXPLICIT SCHEME SOLVED AS A SET OF NONLINEAR EQUATIONS

A matrix method was used in order to locate the steady state periodic solution for the Newmark explicit scheme. This is done to verify the existence of the periodic solution of types A, B and C. When the Newmark explicit method is used with  $\beta=0$  and  $\gamma=1/2$  this is equivalent to the Central Difference method and equation 2 may be expressed as

$$a_n x_{n-1} + b_n x_n + c_n x_{n+1} = d_n \quad (\text{A4.9a})$$

where

$$a_n = \left[ \begin{array}{cc} \frac{1}{\Delta t^2} & - \frac{k}{2\Delta t} \end{array} \right] \quad (\text{A4.9b})$$

$$b_n = \left[ \begin{array}{cc} x_n^2 & - \frac{2}{\Delta t^2} \end{array} \right] \quad (\text{A4.9c})$$

$$c_n = \left[ \frac{1}{\Delta t^2} + \frac{k}{2\Delta t} \right] \quad (\text{A4.9d})$$

and  $d_n$  is the forcing function:

$$d_n = -\cos(t_n) - k \cdot \sin(t_n) + \cos^3(t_n) \quad (\text{A4.9e})$$

The period of the steady state response, if it exists, must be an integral multiple of the period of the forcing function  $2\pi$  by choosing the time step to be a submultiple of the period of the forcing function:

$$\Delta t = T/N$$

The value of  $X_i$  will repeat itself in a definite pattern. For a single period, for instance,  $X_{N+i}$  should be the same as  $X_i$ . For the multiple period  $n$ ,  $X_{nN+i}$  should be the same as  $X_i$ . By letting  $X_N, X_{2N}, \dots$  be equal to  $X_0$ , in turn, the steady state periodic solution, (e.g. for a single period) may be obtained by solving the following set of equations:

$$\begin{bmatrix} b_1 & c_1 & 0 & 0 & \dots & \dots & 0 & 0 & a_1 \\ a_2 & b_2 & 0 & 0 & 0 & \dots & 0 & 0 & 0 \\ 0 & a_3 & b_3 & c_3 & 0 & 0 & & & \\ \vdots & \vdots & \vdots & & & & & & \vdots \\ \vdots & \vdots & \vdots & & & & & & \vdots \\ \vdots & \vdots & \vdots & & & & & & \vdots \\ c_N & 0 & 0 & \dots & & & a_{N-1} & b_{N-1} & c_{N-1} \\ & & & & & & a_N & b_N & b_N \end{bmatrix} \begin{bmatrix} x_1 \\ x_2 \\ \vdots \\ \vdots \\ \vdots \\ \vdots \\ x_N \end{bmatrix} = \begin{bmatrix} d_1 \\ d_2 \\ \vdots \\ \vdots \\ \vdots \\ \vdots \\ d_N \end{bmatrix}$$

$$(\text{A4.10})$$

A NAG library routine, C05PBF, was employed to find the solutions to the

above set of non-linear equations. It was found that this resulted in a quick method for finding the possible sets of solutions that the system may settle down to, the final solution depending on the initial guess chosen for the non-linear equation solver. As a system of non-linear equations, there is not necessarily a unique solution. A brief description of the ones we have discovered are as follows:

Briefly summarised, the results indicate that, through this matrix-solver method, all three types of solution given in figure 1 may be obtained with the appropriate initial conditions. The initial conditions used were either various amplitude cosine solutions or one of the final solutions, shown in figure 1. More interesting perhaps is that a cosine solution is obtained when the initial condition is a cosine wave of amplitude of unity or larger. A type B solution may only be obtained by expanding the matrix solver method to encompass a time of three cycles or  $6\pi$ .

#### A4.4. CONCLUDING REMARKS

Most physical systems are non-linear, hence the current interest in the new theories emerging in the field of non-linear dynamics. Nonlinear models of real systems are generally solved using numerical algorithms which have been proved to give acceptable solutions to linear problems, and there is a considerable amount of literature around to this effect. However, it has been shown in this paper that the solving of a non-linear equation, equation A4.2, with such methods, can present its own problems. The scheme used, the chosen value for the time step and the values of the stability and accuracy parameters can all have a significant effect on the solution produced.

It would seem prudent, therefore, to suggest that when using a numerical

method to approximate the solution to a non-linear equation (or system of equations), one should include the following when reporting the results:

- 1 - The numerical integration scheme used.
- 2 - The value of the time step chosen.
- 3 - The value of the parameters chosen within the scheme.
- 4 - The type and accuracy of the computer used.

With regard to suggestion number (2), it would also be advisable to try out various values of time step for a particular problem to see if this has an effect on the solution.

For linear equations, it is known that the solution will converge to a unique solution if the scheme is consistent and stable. However, as is shown by the results presented in this paper, new methods for the analysis of non-linear equations will have to be found, where the possibility of multiple solutions must be taken into account. For the modified Duffing oscillator investigated herein, equation (2), three solution types were found, and there appears to be no obvious method for predicting in advance which solution a specific run will tend to settle on to.

By varying the initial conditions, all three types of final solution have been found for the explicit scheme and there exists a definite basin of attraction for the solution types. As the viscous damping parameter  $k$  was not changed during the course of the study, we cannot comment on its effect on the solutions obtained.

Some other questions yet to be addressed on the problem are as follows:

- 1 - The lack of conclusive proof that the exact solution, equation 3, is unstable.
- 2 - The effects of round off error, it is, however, presumed that the results will not change qualitatively, as indicated by the use of variables with varying precision. There may be programming strategies which may minimise this sort of diversion of the result.
- 3 - The lack of an obvious reason for the Newton-Raphson method taking less

CPU time than the analytical solution. It seems possible that the linearised solution is close to the exact answer, so less algebraic effort is required by the Newton-Raphson method.

Many people are now using numerical schemes such as those investigated here, to produce nonperiodic, or chaotic, solutions to non-linear equations where it is difficult to see at a glance, whether the choice of the integration scheme will greatly affect the solution and, more importantly, the properties of the solution. This is a problem which warrants further study.

### REFERENCES

- [ 1 ] - E.N. Lorenz, 'Deterministic Nonperiodic Flow', J. Atmos. Sci.,20, 130-141 (1963).
- [ 2 ] - G. Duffing, 'Erzwungene Schwingungen bei Veranderlicher Eigenfrequenz', Vieweg: Braunschweig.
- [ 3 ] - F. Dinca & C. Teodosiu, 'Nonlinear and Random Vibrations', Academic Press, 253-277 (1973).
- [ 4 ] - J.M.T. Thompson & H.B. Stuart, 'Nonlinear Dynamics and Chaos', John Wiley and Sons,1-26 (1986).
- [ 5 ] - W.L. Wood and M.E. Oduor, 'Stability Properties of some Algorithms for the Solution of Nonlinear Dynamic Vibration Equations', Comm. Applied Num. Meth., 4, 205-212, 1988.
- [ 6 ] - K.C. Park, 'An Improved Stiffly Stable Method for the Direct Integration of Nonlinear Structural Dynamic Equations', Journal of Applied Mechanics, 42, 464-470, June, 1975.
- [ 7 ] - C.W. Bert and J.D. Stricklin, 'Evaluation of Various Numerical

Integration Methods for Nonlinear Systems', 24th Annual technical Meeting, Society of Engineering Science, Sept. 20-30, 1987, University of Utah, Salt Lake City, Utah

[ 8 ] - C.F. Gerald & P.O. Wheatly, 'Applied Numerical Analysis', Addison-Wesley Publishing Company, 15-20 & 306-312, 1984.

[ 9 ] - T.J.R. Hughes, 'The Finite Element Method', Prentice-Hall Inc., 490-513, 1987.

[ 10 ] - M.G. Katona and O.C. Zienkiewicz, 'A Unified Set of Single Step Algorithms Part 3: The Beta-m method, a Generalization of the Newmark Scheme', Int. J. Num. Meth. Engng., 21, 1345-1359, 1985.

[ 11 ] - B.B. Low, 'Mathematics', Longman Green & Co., 1931.

[ 12 ] - J.W. Cooley, P.A.W. Lewis and P.D. Welsch, 'The Fast Fourier Transform and its Applications', I.E.E.E. Transactions on Education, 12, 27-34, 1969.

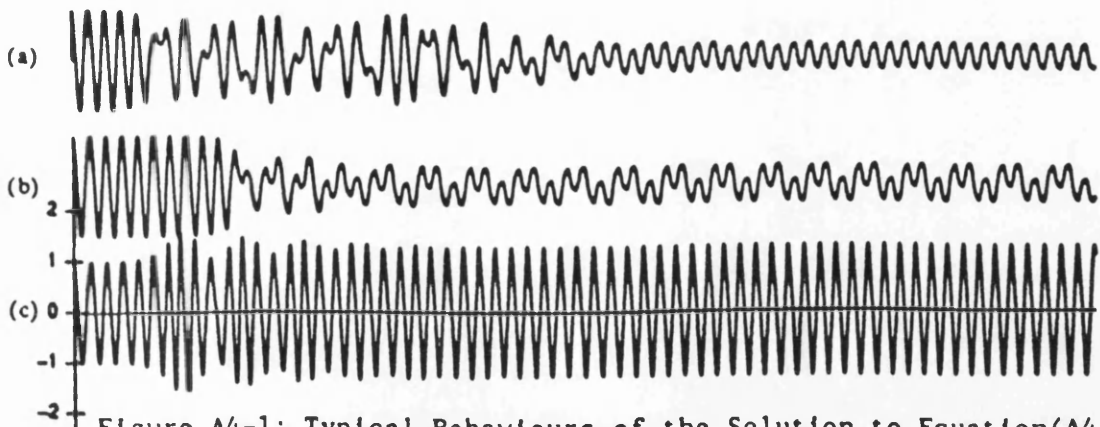
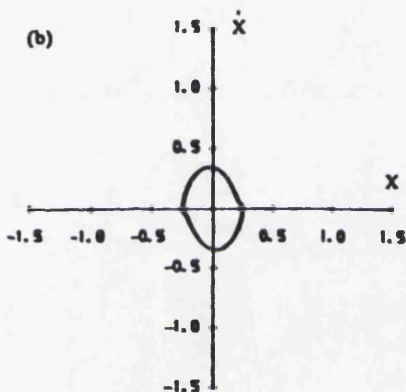
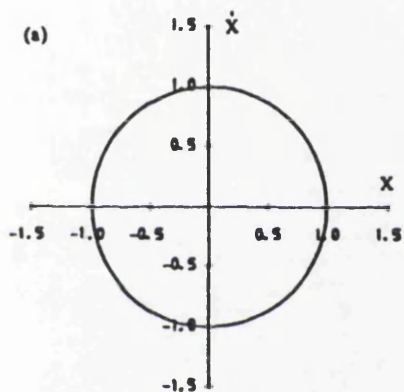


Figure A4-1: Typical Behaviours of the Solution to Equation (A4-2)

All three of these solutions are begun on the exact solution ' $x = \cos(t)$ ', then pass through a transition phase and end up on one of the final solutions shown.

- (a) Type A
- (b) Type B
- (c) Type C



- (a) The Initial Solution ' $x = \cos(t)$ '
- (b) Type A Solution
- (c) Type B Solution
- (d) Type C Solution

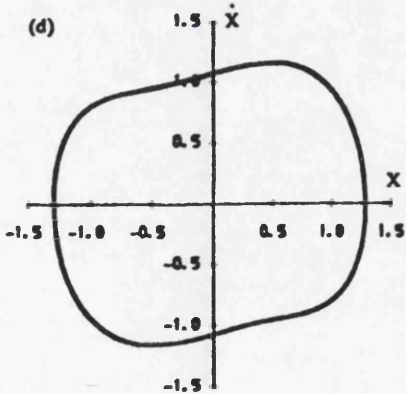
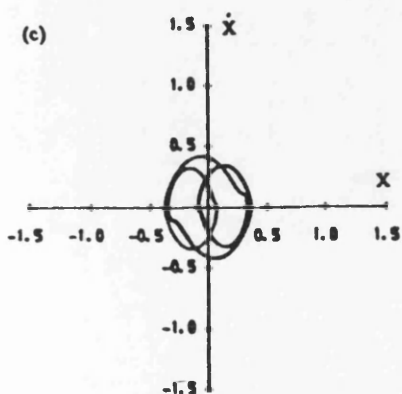


Figure A4-2: Phase Space Representations of the Solutions Shown in figure A4-1

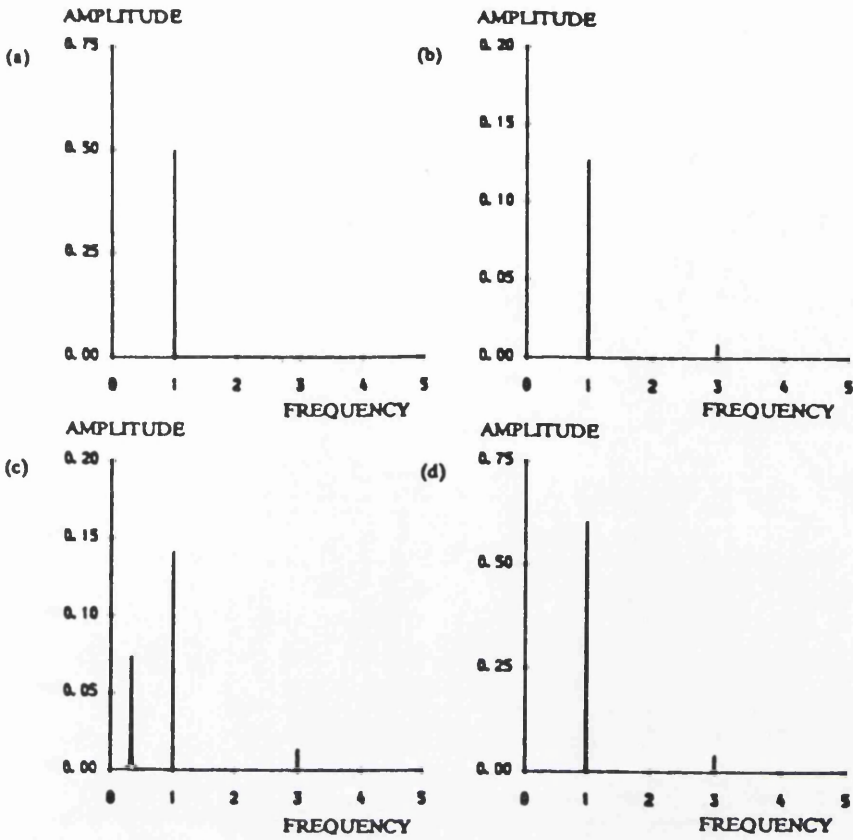


Figure A4-3: Frequency Spectra of the Solutions to Equation A4-2  
 (a)  $x = \cos(t)$  Initial Solution      (c) Type B Solution  
 (b) Type A Solution      (d) Type C Solution

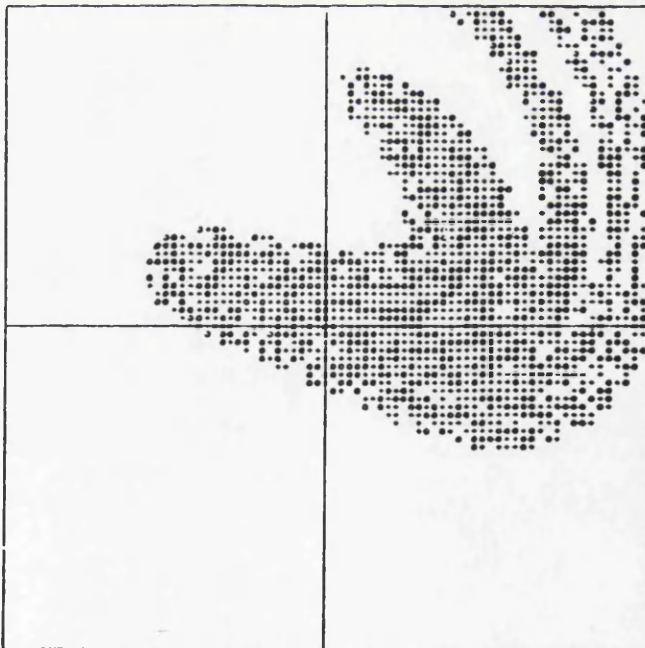


Figure A4-4: Mapping of the Final Solution Obtained to the Initial Conditions on the Unit Square  
 Abscissa =  $x_0$  , Ordinate =  $x_0$  .

**APPENDIX 5: A NOTE ON THE USE OF THE GRASSBERGER–PROCACCIA DIMENSION ALGORITHM TO CHARACTERISE THE SOLUTION OF A NUMERICALLY MODELLED JOURNAL BEARING SYSTEM**

The Grassberger–Procaccia dimension algorithm developed by the author was used to test the seemingly random solutions of a modelled journal bearing system. This work was done in conjunction with Mr. R.D. Brown of the Mechanical Engineering Department at Heriot–Watt University, Edinburgh.

The response of a journal bearing, to a variation in rotational speeds and degrees of unbalance, were obtained using a numerical model developed by Mr. Brown at Heriot–Watt University. The displacements  $x$  and  $y$  of the centre of the bearing were monitored, and also the speed of the displacements  $\dot{x}$  and  $\dot{y}$ . These time series were then used to construct attractors using the method of time delays. These attractors were then tested using the Grassberger–Procaccia dimension algorithm written by the author. A typical ' $\log(r) - \log(Cr)$ ' plot is given in figure A5–1, giving a dimension of approximately 2.16 for the chaotic response of the journal bearing system. A boundary between regular and chaotic behaviour was obtained in the parameter space of the system, which compared very well with plots obtained by other workers, using other methods of analysis, [Holmes et al, 1978].

The full results are reported in the literature, see Brown, Addison and Chan [1992].

JOURNAL BEARING SOLUTION DATA  
 GRASSBERGER-PROCCACCIA DIMENSION

N-DATA = 29441	
E.D. = 2	F.D. = 1.331
E.D. = 3	F.D. = 1.597
E.D. = 4	F.D. = 1.811
E.D. = 5	F.D. = 2.025
E.D. = 6	F.D. = 2.168
E.D. = 7	F.D. = 2.200
E.D. = 8	F.D. = 2.160
E.D. = 9	F.D. = 2.165
E.D. = 10	F.D. = 2.144
E.D. = 11	F.D. = 2.132
E.D. = 12	F.D. = 2.098

N-DATA = NUMBER OF DATA POINTS

E.D. = EMBEDDING DIMENSION

F.D. = FRACTAL DIMENSION

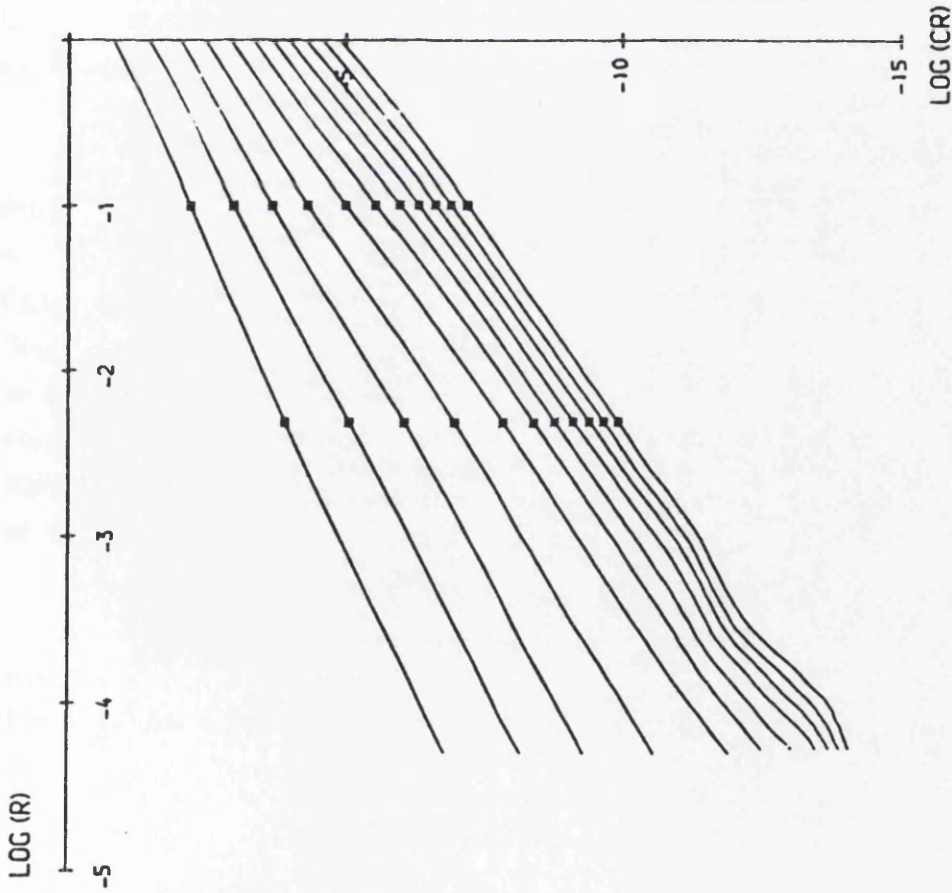


Figure A5-1: 'log(r)-log(C<sub>r</sub>)' Plot for the Journal Bearing Model in Chaotic Mode

## APPENDIX 6: FURTHER NOTES ON THE GRASSBERGER-PROCACCIA DIMENSION ALGORITHM

In this section a brief summary of some preliminary investigations into two areas of research currently pursued by the author will be given.

### A6.1 The Grassberger Procaccia Dimension Algorithm and Transient Signals

The dimension of an attracting set may be found using the Grassberger-Procaccia dimension algorithm. This algorithm is employed by many researchers investigating the fractal properties of reconstructed attractors, obtained from dynamical systems operating in chaotic mode. With a non-integer dimension estimate indicating the presence of a strange attractor. However, the author has found evidence that non-integer dimension estimates can occur for periodic attractors exhibiting transient motion.

A linear version of the Duffing oscillator was used to produce a transient signal decaying onto a periodic attractor. The exact form of the oscillator is not necessary for the discussion. A typical transient time series is shown in figure A6-1a, with its 'spiral' phase portrait in figure A6-1b. The ' $\log(r) - \log(C_T)$ ' plots for varying lengths of time series are given in figures A6-2a to d. The dimension estimate, obtained from the slope of the plots, (see chapter 2, section 2.5.5), are 1.94, 1.60, 1.26 and 1.11 for time series of length 2000, 5000, 10000 and 15000 points respectively. Most surprising is the consistency of the ' $\log(r) - \log(C_T)$ ' plot lines over a wide range of length scale.

This initial investigation underlines the fact that long time series are required to negate the effect of transients in the signal. This point has been expounded in the literature by many workers in the field. However, the consistency of the dimension estimate over a wide range of length scales is a mystery.

This work into transients is, as yet, in its infancy. The author hopes to extend the work to trajectories perturbed intermittently by noise, resulting in transient behaviour occurring as the perturbed trajectory approaches the attractor.

## A6.2 The Grassberger–Procaccia Dimension Algorithm and Multiple Oscillator Systems

Most work in the field of non-linear dynamics has either been performed numerically on simple mathematical oscillator systems, or, has involved the investigation of complex natural phenomena, which exhibits seemingly low dimensional dynamics under certain operating conditions. The author has conducted some initial research into the possible chaotic behaviour of multiple oscillator systems.

The research looked at two distinct oscillator systems, both based on the Duffing oscillator, but with different modes of coupling. The work was stimulated by a paper from Burton and Anderson, (1989), who found chaotic motion occurring in a chaotically excited chain of Duffing oscillators, whereby the output from oscillator was used to force the next oscillator in the chain:

$$x_n + \delta x_n + x_n^3 = x_{n-1} \quad (\text{A6.1})$$

where,  $n = 1, 2, 3, 4 \dots N$ , and,  $x_0 = \cos(\Omega t)$

Thus, for  $N = 1$  one gets the single Duffing oscillator. However, this type of system does not allow for feedback from the  $(n+1)$ th oscillator to the  $n$ th oscillator.

The author decided to investigate a more realistic method of coupling, whereby each oscillator is linked by the elastic restoring components. This non-linearly coupled system is given below:

$$\begin{array}{cccc}
x_1 + \delta x_1 + \cos(\Omega t) & - & (x_2 - x_1)^3 & \\
\vdots & & \vdots & \\
\vdots & & \vdots & \\
x_n + \delta x_n + (x_n - x_{n-1})^3 & - & (x_{n+1} - x_n)^3 & \\
\vdots & & \vdots & \\
\vdots & & \vdots & \\
x_N + \delta x_N + (x_N - x_{N-1})^3 & - & x_N^3 & \text{(A6.2)}
\end{array}$$

again,  $n = 1, 2, 3, 4, \dots, N$

This system does allow for feedback from the  $(n+1)$ th oscillator to the  $n$ th oscillator in the chain, (and vice versa).

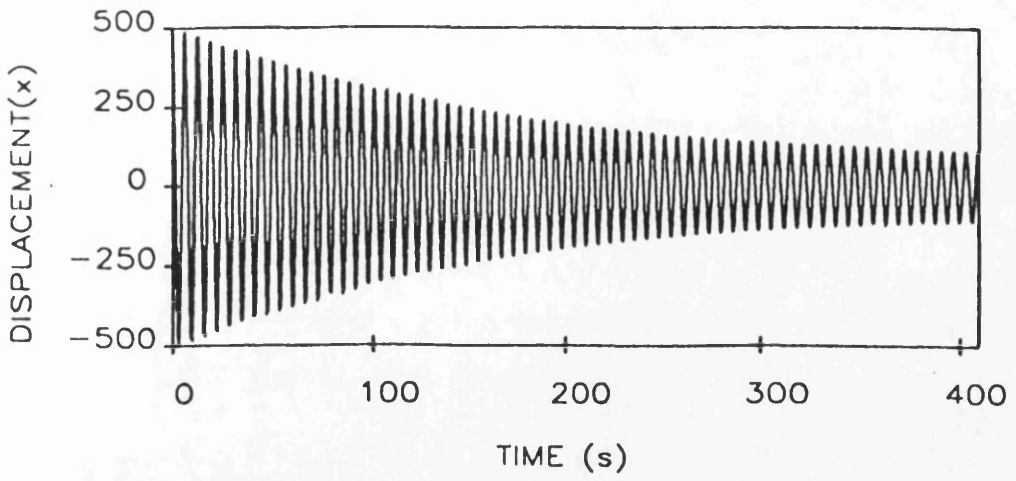
In short, both systems were run with the parameters,  $\Omega$  and  $\delta$ , set equal to values which give chaotic motion for a single Duffing oscillator, ( $\delta = 0.04496$  and  $\Omega = 0.44964$ ). This was done for,  $N$ , (the number of oscillators), from 1 to 10. The subsequent behaviour of the time series, frequency spectra, phase portraits and the Grassberger–Procaccia dimension algorithm was monitored. The time series for the two systems for  $N = 1$  to 10 are presented in figure A6–3a and b, the corresponding phase portraits for  $N = 1, 2, 3, 4, 5$  and 10 are presented in figure A6–4a and b. The dimension estimate for the chaotically excited oscillator is given in figure A6–5 and for the non-linearly coupled oscillator in figure A6–6. Notice that a two dimensional plot is used in figure 6–5 and a three dimensional plot in figure 6–6. The reason for this is that since the chaotically excited oscillator system, (equation A6.1), has no feedback then the behaviour of the  $n$ th oscillator remains constant for all  $N > n$ . However, in the non-linearly coupled system the feedback through the cubic elastic terms means that the behaviour changes for all the oscillators in the chain for each value of  $N$ .

The research work cited above is attempting to address the dual problem of systems of non-linear oscillators operating in chaotic mode, together with the use of the Grassberger–Procaccia dimension estimate in probing the complexity of the

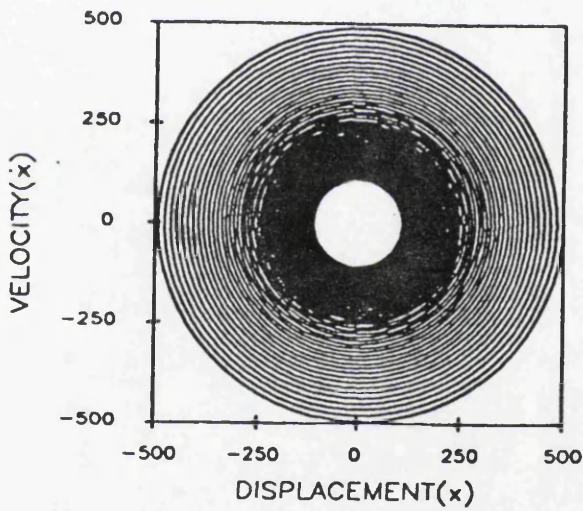
output of such systems.

It has been shown that the increase in the number of oscillators in the case of the chaotically excited system leads to a rapid increase in the dimension estimate, reaching a limit between 10.0 and 12.0. However, the same is not true for the more realistic, non-linearly coupled system. In this case, the increase in the number of oscillators in the system first led to a rapid decrease in the systems complexity, with  $N = 3$  providing a periodic response. Increases in  $N$  above 3 then led to an increase in the average dimension estimate, again a limiting value of the estimate was reached at between 10.0 and 12.0.

Further studies should investigate the apparent maximum dimension obtained, between 10.0 and 12.0 to see if this is a maximum dimension of such oscillator systems or rather an inherent limit to the Grassberger-Procaccia dimension estimate. In addition, the  $N = 3$ , non-linearly coupled system is particularly interesting, as the system reverts from a chaotic response at  $N = 2$  to a periodic response. In this case, the act of increasing the number of degrees of freedom of the system, and therefore the intrinsic complexity of the system, has the counter-intuitive effect of decreasing the complexity of the system. This effect in itself warrants further study.

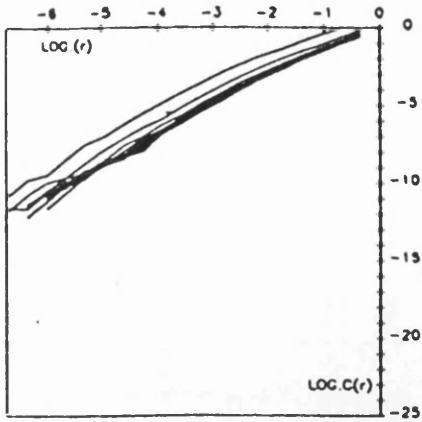


(a) Time Series

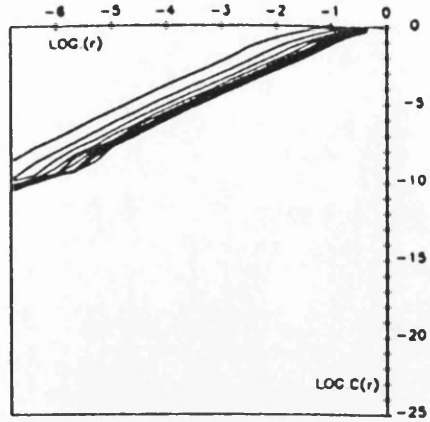


(b) Phase Portrait

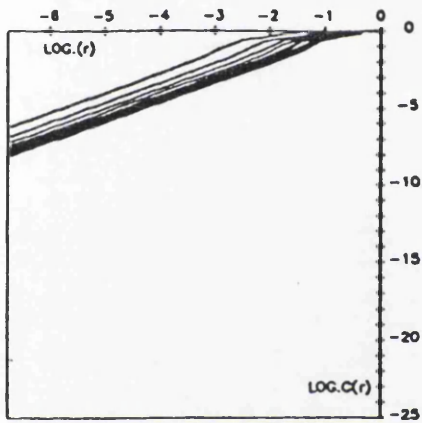
Figure A6-1; Typical Transient, Time Series with Phase Portrait



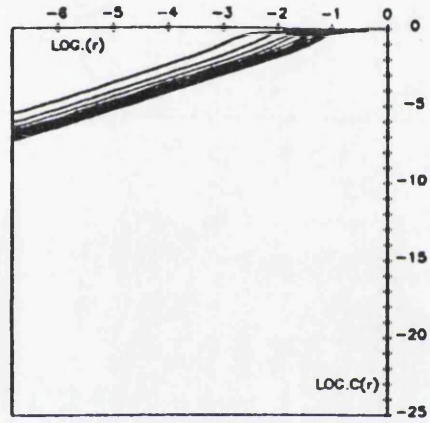
(a) 2000 points



(b) 5000 points

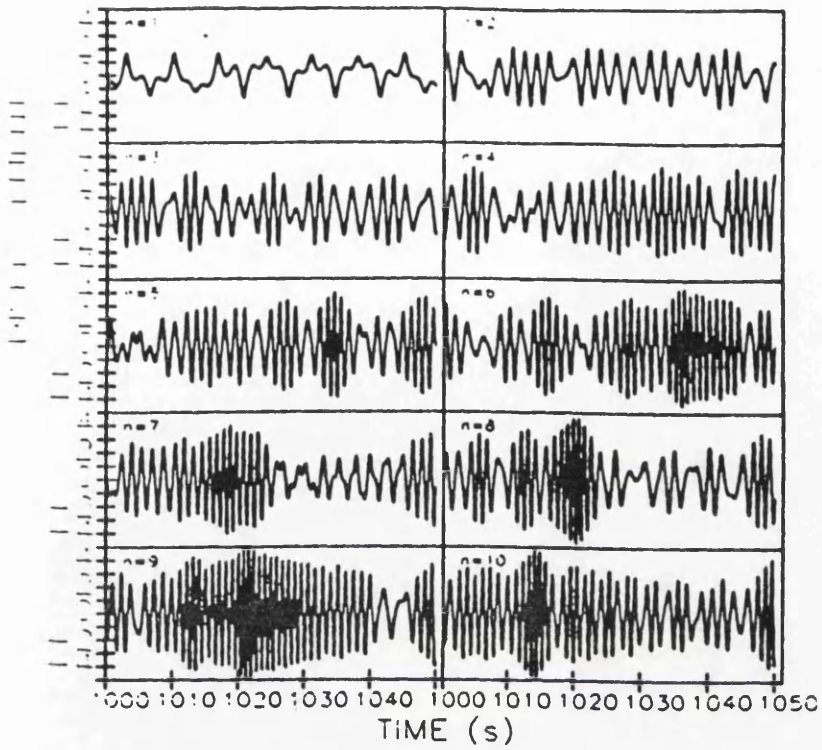


(c) 10,000 points

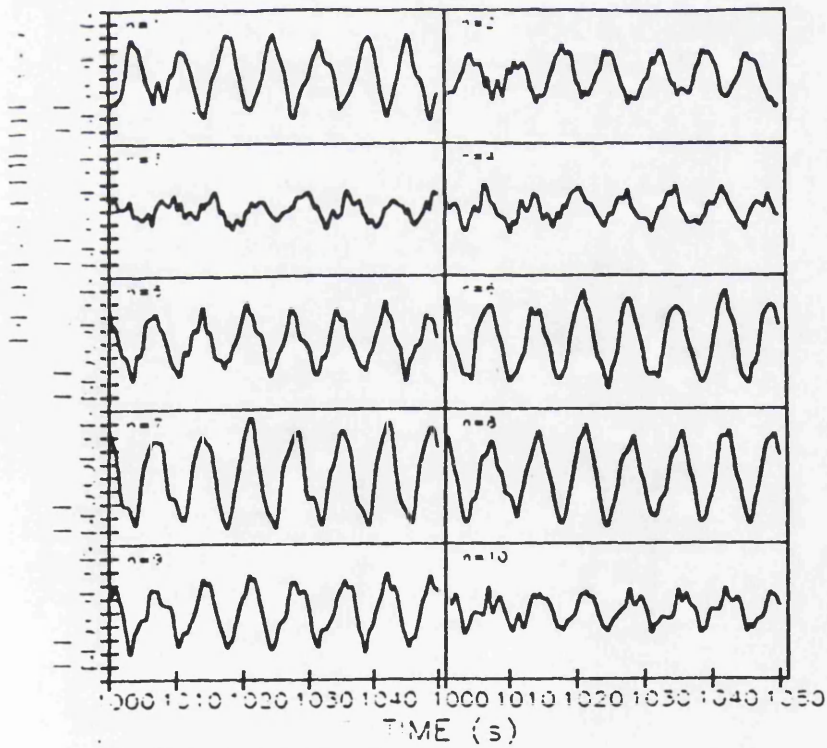


(d) 15,000 points

Figure A6-2: 'log(r)-log(C<sub>r</sub>)' Plot for Various Lengths of the Time Series of figure A6-1a

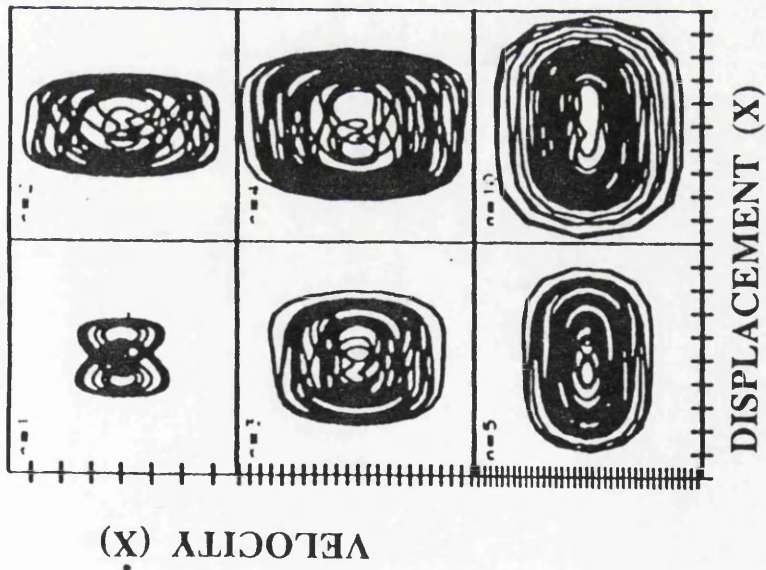


(a) Chaotically Excited

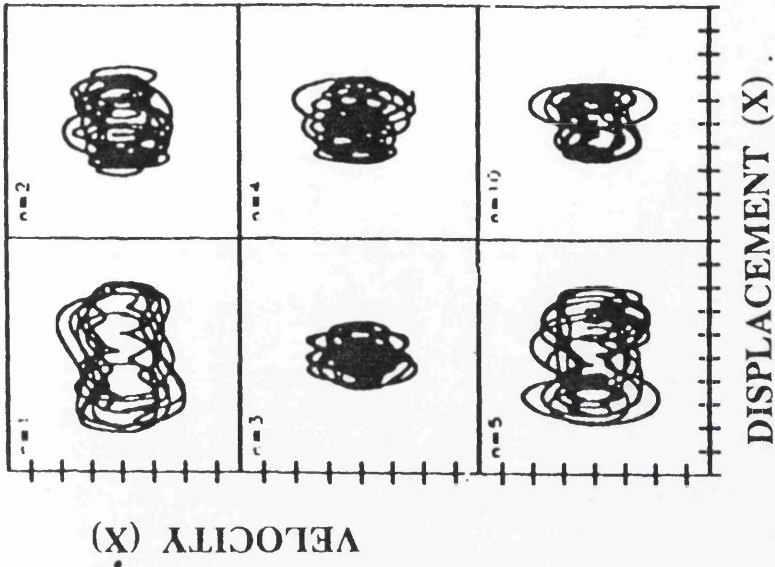


(b) Non-Linearly Coupled

**Figure A6-3: Time Series of the First Ten Oscillators**



(a) Chaotically Excited ( $n = 1, 2, 3, 4, 5$  and  $10$ )



(b) Non-Linearly Coupled ( $n = 1, 2, 3, 4, 5$  and  $10$ )

Figure A6-4: Phase Portraits of the First Ten Oscillators

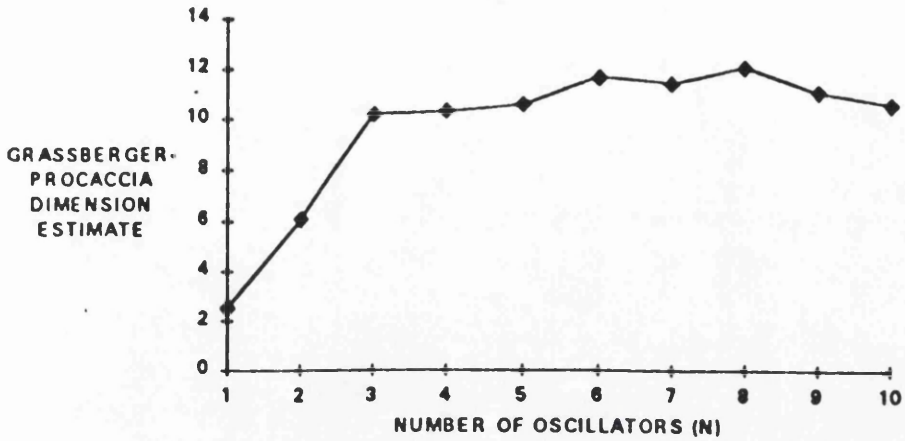


Figure A6-5: The Variation in the Average Grassberger-Procaccia Dimension Estimate with the Number of Oscillators in the Chaotically Excited System

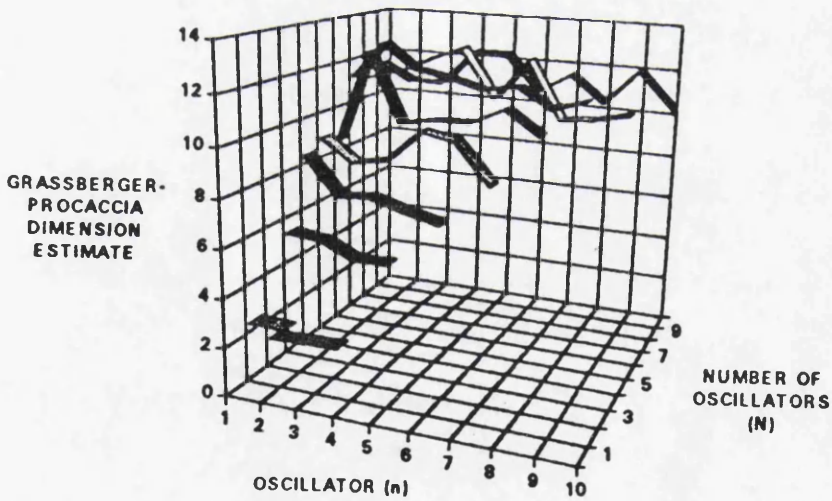


Figure A6-6: The Variation in the Grassberger-Procaccia Dimension Estimate with the Number of Oscillators in the Non-Linearly Coupled System

## REFERENCES

## REFERENCES

- Abraham N.B. & Gollub J.P., "Testing Non-linear Dynamics", *Physica-D*, 1984, Vol.11, pp 252-264.
- Abraham N.B., Albano A.M., Das B., De Guzman G., Yong S., Gioggiars R.S., Puccioni G.P. & Tredicce J.R., "Calculating the Dimension of Attractors from Small Data Sets", *Phys. Lett. A*, 1986, Vol.114, pp 217-221.
- Addison P.S., "A Report on Work Done to Date on an Experimental Investigation into Vortex Dominated Flows at a Pipe Orifice", Research Report No.2, August 1991, Civil Engineering Department, University of Glasgow.
- Addison P.S., Chan A.H.C., Ervine D.A. & Williams K.J., "On the Numerical Method Dependant Solutions of a Modified Duffing Oscillator", *Communications in Applied Numerical Methods*, 1992, Vol.8, pp519-528.
- Arecchi F.T., "Hyperchaos and  $1/f$  spectra in Non-linear Dynamics", from "Chaos, Noise and Fractals", edited by E.R. Pike & L.A. Lugiato, 1987, Adam Hilger, pp 1-14.
- Aref H., Jones S.W., Mofina S. & Zawadzki I., "Vortices, Kinematics and Chaos", *Physica D*, 1989, pp 423-440.
- Argoul F, Arneodo A, Grasseau G., Gaone Y., Hopfinger E.J. & Frisch U., "Wavelet Analysis of Turbulence Reveals the Multifractal Nature of the Richardson Cascade", *Nature*, 1989, Vol.338, pp 51-53.

Argoul F., Arneodo A., Elezgaray J, Grasseau G. & Murenzi R., "Wavelet Transforms of Fractal Aggregates", Phys. Lett. A, 1989, Vol.135, pp327-336.

Arneodo A., Couillet P. & Tresser C., "On the Observation of an Uncompleted Cascade in a Rayleigh-Benard Experiment", Physica-D, 1983, Vol.6, pp 385-392.

Arneodo A, Grasseau G. & Holschneider M., "Wavelet Transform of Multifractals", Phys. Rev. Lett., 1988, Vol.61, pp 2281-2284.

Asfar K.R. and Masoud K.K., 'On the Period-Doubling Bifurcations in the Duffing's Oscillator with Negative Linear Stiffness', A.S.M.E., Journal of Vibration and Acoustics, Vol.114, 1992, pp489-494.

B.S. 188:1977, "Methods for Determination of the Viscosity of Liquid", British Standards Institution.

B.S.1042:1989, "Pressure Differential Devices", British Standards Institution.

Back L.H. & Roschke E.J., "Shear-Layer Flow Regimes and Wave Instabilities and Reattachment Lengths Downstream of an Abrupt Circular Channel Expansion", Trans. A.S.M.E, Journal of Applied Mechanics, 1972, pp 677-681.

Baird M.H.I., Round G.F. & Cardenas J.N., "Friction Factors in Pulsed Turbulent Flow", The Canadian Journal of Chemical Engineering, 1971, Vol.49, pp 220-223.

Bak P. & Chen K., "The Physics of Fractals",  
Physica-D, 1989, Vol.38, pp 5-12.

Bak P., Chen K. & Tang C., "A Forest Fire Model and  
Some Thoughts on Turbulence", Phys. Lett A, 1990,  
Vol.147, pp 297-300.

Baker G.L. & Gollub J.P., "Chaotic Dynamics - an  
Introduction", Cambridge University Press, 1990.

Bakhmeteff B.A., "The Mechanics of Turbulent Flow",  
Princeton University Press, 1936.

Bandyopadhyay P.R., "Aspects of the Equilibrium Puff  
in Transitional Pipe Flow", J. Fluid Mech., 1986,  
Vol.163, pp 439-458.

Bandyopadhyay P.R., Private Communication,  
April, 1989.

Barford N.C., "Experimental Measurements: Precision  
Error and Truth", John Wiley and Sons, 1985.

Barr D.I.H., "Two Additional Methods of Solution of  
the Colebrook-White Function", Proc. Inst. Civ.  
Engrs., 1975, Part2, Vol.59, pp827-835.

Batchelor G.K., "The Theory of Homogeneous  
Turbulence", Cambridge Monographs on Mechanics and  
Applied Mathematics, Cambridge University Press,  
1960.

Baumann N., Joseph D.D., Mohr P. & Renardy Y.,  
"Vortex Rings of One Fluid Inside Another in Free  
Fall", Phys. Fluids. A, 1992, Vol.4, pp 567-580.

Bell K.J. & Bergelin O.P., "Laminar and Transition  
Flow in Annular Orifices of Fine Clearance", from,  
"Flow Measurement in Closed Conduits", Proc.  
Symposium N.E.L. 27th-30th Sept. 1960, H.M.S.O.,  
1962, pp 439-456.

Belytschko T. & Schoeberle D.F., 'On the  
Unconditional Stability of an Implicit Algorithm for  
Non-linear Structural Dynamics', Transactions  
A.S.M.E., Journal of Applied Mechanics, 1975, pp865-  
869.

Ben-Mizrachi A., Procaccia I. & Grassberger P.,  
"Characterisation of Experimental (Noisy) Strange  
Attractors", Phys. Rev. A, 1984, Vol.29, pp 975-977.

Berge P., Pomeau Y. & Vidal C., "Order Within  
Chaos", John Wiley & Sons, 1984, pp 111-123.

Bert C.W. & Stricklin J.D., "Evaluation of Various  
Numerical Integration Methods for Non-linear Dynamic  
Systems", 24th Annual Technical Meeting, Society of  
Engineering Science, Sept 20-23rd, 1987, University  
of Utah, Salt Lake City, Utah.

Binnie A.M. & Fowler J.S., "A Study by a Double  
Refraction Method of the Development of Turbulence  
in a Long Circular Pipe", Proc. Royal Society, 1947-  
48, Vol.A192, pp 32-44.

Blevins R.D., "Flow Induced Vibration", Van Nostrand  
Reinhold, 1977, pp 1-54.

Boldrighini C. & Franceschini V., "A Five Dimensional Truncation of the Plane Incompressible Navier Stokes Equations", Comm. Math. Phys., 1979, Vol.64, pp159-170.

Boussinesq M.J., Comptes Rendus, 1891, pp 9-15 & 49-51.

Bradley T.A. & Ng T.T., "Phase Locking in a Jet Forced with Two Frequencies", Experiments in Fluids, 1989, Vol.7, pp 38-48.

Brandstater A., Swift J., Swinney H.L., Wolf A., Farmer J.D. & Jen E., "Low-Dimensional Chaos in a Hydrodynamical System", Phys. Rev. Lett., 1983, Vol.51, pp 1442-1445.

Brown R.D., Addison P.S. & Chan A.H.C., "Chaos in the Unbalance Response of Journal Bearings", presented at the "Fourth Conference on Non-linear Vibrations, Stability and Analysis of Structures and Mechanisms", Virginia Polytechnic Institute and State University, Blacksburg, Virginia, June 7-11, 1992, (To be published in the journal-Non-linear Dynamics).

Buckingham E., "Notes on Some Recently Published Experiments on Orifice Meters", Trans. Am. Soc. Mech. Eng., 1956, Vol.78(2), pp 379-387.

Bullock K.J., Lai J.C.S. & Walker T.B, "Flow Measurement Behind Attached Ring-Type Turbulence Promoters", Phys. Fluids, 1990, Vol.2, pp 390-399.

Burton T.D. & Anderson M., "On Asymptotic Behaviour in Cascaded Chaotically Excited Non-Linear Oscillator", Journal of Sound and Vibration, 1989, Vol.133, pp253-258.

Casperen C., "The Vortex Flowmeter", Paper C-1, from, "Fluid Measurement in the Mid 1970's, 1977, edited by E.A. Spencer & W.J. Ramsay, H.M.S.O., pp 147-166.

Chadwick A. & Morfett J., "Hydraulics in Civil Engineering", Allen and Unwin, 1986.

Chen J.J.J. & Ackland A.D., "Correlation of Laminar, Transitional and Turbulent Flow Friction Factor", Proc. Inst. Civ. Eng., Part 2, 1990, Vol.89, pp573-576.

Choi H.S. & Lou J.Y.K., 'Non-linear Behaviour of an Articulated Offshore Loading Platform', Journal of Applied Ocean Research, 1991, Vol.13, pp 63-74.

Colebrook C.F., "Turbulent Flow in Pipes, with Particular Reference to the Transition Between the Smooth and Rough Pipe Laws", J. Inst. Civ. Eng., 1939, Vol.11, pp 135-156.

Conlisk A.T., Guezennec Y.G. & Elliott G.S., "Chaotic Motion of an Array of Vortices Above a Flat Wall", Phys. Fluids A, 1989, Vol.1, pp 704-717.

Conrad M., "What is the Use of Chaos ?", from "Chaos", edited by A.V. Holden, Manchester University Press, 1986, pp 3-14.

Cooley J.W., Lewis P.A.W. & Welch P.D., "The Fast Fourier Transform and its Applications", I.E.E.E. Transactions on Education, 1969, Vol.2, pp27-34.

Corcos G.M. & Sellars J.R., "On the Stability of Fully Developed Flow in a Pipe", J. Fluid Mech., 1959, Vol.5, pp 97-112.

Crutchfield J., Farmer D., Packard N., Shaw R., Jones G. & Donnelly R.J., "Power Spectral Analysis of a Dynamical System", Phys. Lett., 1980, Vol.76A, pp 399-401.

Cvitanovic P., "Universality in Chaos", from "Universality in Chaos", edited by P. Cvitanovic, Adam Hilger Ltd., Bristol, 1984.

D'Netto W. & Weaver D.S., "Divergence and Limit Cycle Oscillations in Valves operating at Small Openings", J. Fluids and Structures, 1987, Vol.1, pp 3-18.

Davies J.T., "Turbulence Phenomena", Academic Press, 1972, pp 1-39, 47-62, 121-136.

Deissler R.J. & Kaneko K., "Velocity Dependent Lyapunov Exponents as a Measure of Chaos in Open Flow Systems" Phys. Lett. A, 1987, Vol.119, pp397-401.

Detemple-Laake E. & Eckelmann H., "Phenomenology of Karman Vortex Streets in Oscillatory Flow", Experiments in Fluids, 1989, Vol.7, pp 217-277.

Dinca F. & Teodosiu C., "Non-linear and Random Vibrations", 1973, Academic Press, pp 253-277.

Dowell E.H. and Pezeshki C., 'On Necessary and Sufficient Conditions for Chaos to Occur in Duffing's Equation: An Heuristic Approach', Journal of Sound and Vibration, Vol.121, 1988, pp195-200.

Downing P.M. & Mottram R.C., "The Effects of Flow Pulsations on Orifice Plate Flowmeters", from, "Fluid Measurement in the Mid 1970's, 1977, edited by E.A. Spencer & W.J. Ramsay, H.M.S.O.

Drazin P.G & Reid W.H., "Hydrodynamic Stability", Cambridge University Press, 1981.

Duffing G., "Erzwungene Schwingungen bei Veranderlicher Eigenfrequenz", Vieweg: Braunschweig.

Durst F. & Ruck B., "Effective Particle Size Range in Laser-Doppler Anemometry", Expts. in Fluids, 1987, Vol.5, pp 305-314.

Durst F., Maxworthy T. & Pereira J.C.F., "Piston-Driven, Unsteady Separation at a Sudden Expansion in a Tube: Flow Visualization and L.D.A. Measurements", Phys. Fluids A, 1989, Vol.1, pp1249-1260.

Dvorak I. & Klaschka J., "Modification of the Grassberger-Procaccia Algorithm for Estimating the Correlation Exponent of Chaotic Systems with High Embedding Dimension", Physics Letters A, 1990, pp 225-231.

El Masry O.A. & El Shobaki K., "Pulsating Slurry Flows in Pipelines", Experiments in Fluids, 1989, Vol.7, pp 481-486.

Elgar S. & Mayer-Kress G., "Observation of the Fractal Dimension of Deep- and Shallow-Water Ocean Surface Gravity Waves", Physica-D, 1989, Vol.37, pp 104-108.

Elgar S., Van Atta C.W. & Gharib M., "Bispectral Analysis of Ordered and Chaotic Vortex Shedding from Vibrating Cylinders at Low Reynolds Numbers", Physica-d, 1989<sup>b</sup>, Vol.39, pp 281-286.

Emrich R.J., "Flow Field Measurement by Tracer Photography", Experiments in Fluids", 1983, Vol.1, pp 179-184.

Everson R. & Sirovich L., "A Survey of Wavelet Analysis Applied to Turbulence Data", Report No. 89-182, 1989, Centre for Fluid Mechanics, Turbulence and Computation, Brown University, Providence, U.S.A.

Everson R., Sirovich L. & Sreenivasan K.R., "Wavelet Analysis of the Turbulent Jet", Phys. Lett. A, 1990, Vol.145, pp 314-322.

Faler J.H. & Leibovich S., "An Experimental Map of the Internal Structure of a Vortex breakdown", J.F.M., 1978, Vol.86, pp 313-335.

Farmer J.D. , "Spectral Broadening of Period-Doubling Bifurcation Sequences", Phy. Rev. Lett., 1981, Vol.47, pp 179-182.

Farmer J.D., "Chaotic Attractors of an Infinite Dimensional Dynamical System", Physica-D, 1982<sup>a</sup>, Vol.4, pp 366-393.

Farmer J.D., "Dimension, Fractal Measures and Chaotic Dynamics", from "Evolution of Order and Chaos in Physics, Chemistry and Biology", Editor H. Haken, Proceedings of the International Symposium of Synergetics, at Schloss Elmau, Bavaria, April 26th - May 1st, 1982a, Springer Verlag, 1982b, pp 174-182.

Farmer J.D., Ott E. & Yorke J.A., "The Dimension of Chaotic Attractors", Physica-D, 1983, Vol.7, pp 153-180.

Feigenbaum M.J., "Universal Behaviour in Non-linear Systems", Los Alamos Science, 1980, Vol.1, pp 4-27.

Fishler L.S. & Brodkey R.S., "Transition, Turbulence and Oscillating Flow in a Pipe", Experiments in Fluids, 1991, Vol.11, pp 388-398.

Fox J.A., Lessen M. & Bhat W.V., "Experimental Investigation of the Stability of Hagen Poiseuille Flow", Phys. Fluids, 1968, Vol.2, pp 1-4.

Franceschini V. & Tebaldi C., "Sequences of Infinite Bifurcations and Turbulence in a Five-Mode Truncation of the Navier Stokes Equations", J. Stat. Phys., 1979, Vol.21, pp 207-213.

Fraser A.M. & Swinney H.L., "Independent Coordinates for Strange Attractors from Mutual Information", Phys. Rev. A, 1986, Vol.133, pp 1134-1140.

Fraser A.M., "Reconstructing Attractors from Scalar Time Series: A Comparison of Singular System and Redundancy Criteria", Physica-D, 1989, Vol.34, pp 391-404.

Freidmann M., Gillis J. & Liron N., "Laminar Flow in a Pipe at Low and Moderate Reynolds Numbers", App. Sci. Res., 1968, Vol.19, pp 426-438.

Froehling H., Crutchfield J.P., Farmer D., Packard N.H. & Shaw R., "On Determining the Dimension of Chaotic Flows", Physica-D, Vol.3, 1981, pp 605-617.

Fukuda K., Inouye A., Kawabe Y & Hirai A., "Transition from Laminar to Turbulent Flow of Water in a Pipe Measured by a Pulsed N.M.R. Method", J. Phys. Soc. Japan, 1985, Vol.54, pp 4555-4560.

Gardarvsky J., Hrbek J., Chara Z. & Severa M., "Refraction Corrections for L.D.A. Measurements in Circular Tubes Within Rectangular Optical Boxes", Dantec Information, No.8, Nov.1989.

Gaster M., "A Note on the Relation Between Temporally Increasing and Spatially Increasing Disturbances in Hydrodynamic Stability", J. Fluid Mech., 1962, Vol.5, pp 222-224.

Gerald C.F. & Wheatley P.O., "Applied Numerical Analysis", 1984, Addison-Wesley Publishing Company, pp 15-20 & 306-312.

Gershenfeld N.A., "Dimension Measurement on High-Dimensional Systems", Physica-D, 1992, Vol.55, pp 135-154.

Gharib M., Williams-Stuber K., "Experiments on the Forced Wake of an Airfoil", J.F.M., 1989, Vol.208, pp 225-255.

Ghez J.M. & Vaienti S., "On the Wavelet Analysis of Multifractal Sets", J. Stat. Phys., 1989, Vol.57, pp 415-420.

Giglio M., Musazzi S. & Perini U., "Onset of Chaos in Fluid Dynamics", from "Evolution of Order and Chaos in Physics, Chemistry and Biology", Editor H. Haken, Proceedings of the International Symposium of Synergetics, at Schloss Elmau, Bavaria, April 26th - May 1st, 1982, Springer Verlag, 1982, pp 174-182.

Giglio M., Musazzi S. & Perini U., "Transition to Chaotic Behaviour via a Reproducible Sequence of Period Doubling Bifurcations", Phys. Rev. Lett., 1981, Vol.47, pp 243-246.

Glass L., Shrier A. & Belair J., "Chaotic Cardiac Rhythms", from, "Non-linear Science: Theory and Applications", edited by A. Holden, Manchester University Press, 1986, pp 237-256.

Goldburg W.I., Pak H.K. & Tong P., "A Light Scattering Study of Turbulence", Physica-D, 1989, Vol.38, pp 134-140.

Goldstein S. (Editor), "Modern Developments in Fluid Dynamics", 1938, Vol.1, Oxford University Press, pp 299-308.

Gollub J.P. & Benson S.V., "Many Routes to Turbulent Convection", J. Fluid Mech., 1980, Vol.100, pp 449-470.

Gottwald J.A., Virgin L.N. and Dowell E.H.,  
'Experimental Mimicry of Duffing's Equation',  
Journal of Sound and Vibration, Vol.158, 1992,  
pp447-467.

Grassberger P. & Procaccia I., "Characterisation of  
Strange Attractors", Phys. Rev. Lett., 1983<sup>a</sup>, Vol.50,  
pp 346-349.

Grassberger P. & Procaccia I., "Estimation of the  
Kolmogorov Entropy from a Chaotic Signal", Phys.  
Rev. A, 1983<sup>b</sup>, Vol.28, pp 2591-2593.

Grassberger P. & Procaccia I., "Measuring the  
Strangeness of Strange Attractors", Physica-D, 1983<sup>c</sup>,  
Vol.9, pp 183-208.

Grassberger P., "Generalised Dimensions of Strange  
Attractors", Phys. Lett. A, 1983, Vol.97,  
pp 227-230.

Grassberger P., "An Optimised Box-Assisted Algorithm  
for Fractal Dimensions", Phys. Lett. A, 1990,  
Vol.148, pp 63-68.

Grey F. & Kjemis J.K., "Aggregates, Broccoli and  
Cauliflower", Physica-D, 1989, Vol.38, pp 154-159.

Grossman A., Holschneider M., Kronland-Martinet R. &  
Morlet J., "Detection of Abrupt Changes in Sound  
Signals with the Help of Wavelet Transforms", from  
"Advances in Electronics and Electron Physics",  
Supplement 19, "Inverse Problems: An  
Interdisciplinary Study", edited by P.C. Sabatier,  
Academic Press, 1987, pp 289-306.

Guckenheimer J. & Buzyna G., "Dimension Measurements for Geostrophic Turbulence", Phys. Rev. Lett., 1983, Vol.51, pp 1438-1441.

Guckenheimer J., "Strange Attractors in Fluids: Another View", Ann. Rev. Fluid Mech., 1986, Vol.18, pp 15-31.

Guevara M.R., Glass L. & Shrier A., "Phase Locking, Period Doubling Bifurcations, and Irregular Dynamics in Periodically Stimulated Cardiac Cells", Science, 1981, Vol.214, pp 1350-1353.

Gursul I. & Rockwell D., "Effect of Concentration of Vortices on Streakline Patterns", Experiments in Fluids, 1991, Vol.10, pp 294-296.

Gursul I., Lusseyran D. & Rockwell D., "On Interpretation of Flow Visualization of Unsteady Shear Flows", Experiments in Fluids, 1990, Vol.9, pp 257-266.

Hama F.R., "Streaklines in Perturbed Shear Flow", Physics of Fluids, 1962, Vol.5, pp 644-650.

Haward R.N., "The Strength of Plastics and Glass : A Study of Time Sensitive Materials", Clever-Hume Press Ltd., 1949, pp 74-75.

Hernan M.A. & Jiminez J., "Computer Analysis of a High Speed Film of the Plane Turbulent Mixing Layer", J.F.M., 1982, Vol.119, pp 323-345.

Higuchi T., "Relationship Between the Fractal Dimension and the Power Law Index for a Time Series: A Numerical Investigation", *Physica-D*, 1990, Vol.46, pp 254-264.

Hinze J.O., "Turbulence: An Introduction to its Mechanism and Theory", McGraw-Hill, 1959.

Ho Chih-Ming + Huang Lein-Sang, 'Subharmonics and Vortex Merging in Mixing Layers', *J.F.M.*, 1982, Vol.119, pp 443-473.

Hodgson J.L., "The Laws of Similarity for Orifice and Nozzle Flows", *Trans. Am. Soc. Mech. Eng.*, 1929, Vol.51, pp 303-332.

Holden A.V. & Muhamad M.A., "A Graphical Zoo of Strange and Peculiar Attractors", from "Chaos", edited by A.V. Holden, Manchester University Press, 1986, pp 15-35.

Holmes A.G., Ettles C.M.M. & Mayes I.W., "The Aperiodic Behaviour of a Rigid Shaft in Short Journal Bearings", *I.J.N.M.E.*, 1978, Vol.12, pp 695-707.

Huang Y. & Huang Y., "On the Transition to Turbulence in Pipe Flow", *Physica-D*, 1989, Vol.37, pp 153-159.

Huberman B.A. & Rudnick J., "Scaling Behaviour of Chaotic Flows", *Phys. Rev. Lett.*, 1980, Vol.45, pp 154-156.

Huberman B.A. & Zisook A.B., "Power Spectra of Strange Attractors", Phys. Rev. Lett., 1981, Vol.40, pp 626-628.

Hudson J.L., Mankin J., McCulloch J. & Lamba P., "Experiments on Chaos in a Continuous Stirred Reactor", from "Non-linear Phenomena in Chemical Dynamics", Proceedings of an International Conference, Bordeaux, France, Sept. 7-11th, 1981, editors C. Vidal & A. Pascault, Springer Verlag, 1981.

Hughes T.J.R., "The Finite Element Method", Prentice-Hall Inc., 1987, pp 490-513.

Iguchi M., Ohmi M. & Kimura H., "Behaviour of Turbulent Slugs in Pulsatile Pipe Flow", from, "Fluid Control and its Measurement", Vol.2, 1985, Pergamon Press, edited by M. Harada, pp 951-956.

Infeld E. & Rowlands G., "Non-linear Waves, Solitons and Chaos", Cambridge University Press, 1990.

Iversen H.W., "Orifice Coefficients for Reynolds Numbers from 4 to 50,000", Trans. A.S.M.E., 1956, Vol.78(2), pp359-364.

Japan Society of Mechanical Engineers, The, "Visualized Flow: Fluid Motion in Basic and Engineering Situation Revealed by Flow Visualization", Pergamon Press, 1988.

Johansen F.C., "Flow Through a Pipe Orifice at Low Reynolds Numbers", Aeronautical Research Committee, Reports and Memoranda, No. 1252, June 1929, H.M.S.O., Published 1930.

Johansen F.C., "Flow Through Pipe Orifices at Low Reynolds Numbers", Proc. Roy. Soc., 1933, Vol.126a, pp 231-245. ((read 20/7/90))

Jones (Jr.) E.H. & Bajura R.A., "A Numerical Analysis of Pulsating Laminar Flow Through a Pipe Orifice", Trans. A.S.M.E., Journal of Fluids Eng., 1991, Vol.113, pp199-205.

Kaolin R., Turkevich L.A., Putterman S.J., Rudnick I. & Rudnick J.A., "Subharmonic Sequences in the Faraday Experiment : Departures from Period Doubling", Phys. Rev. Lett., 1981, Vol.47, p 1133.

Kaplan J.L. & Yorke J.A., "Chaotic Behaviour of Multidimensional Difference Equations", from "Functional Differential Equations and Approximations to Fixed Points", Edited by H.O. Peitgen & H.-O. Walther, Lecture Notes in Mathematics, P 730, Springer, Berlin, 1979.

Katona M.G. & Zienkiewicz O.C., "A Unified Set of Single Step Algorithms. Part 3: The Beta-m method, a Generalization of the Newmark Scheme", International Journal for Numerical Methods in Engineering, 1985, Vol.21, pp 1345-1359.

Kay J.M., "An Introduction to Fluid Mechanics and Heat Transfer", Second Edition, Cambridge University Press, 1963, pp 66-69.

Kestin J., Sokolov M. & Wakeham W.A., "Viscosity of Liquid Water in the Range - 8C to 150C", Journal of Physical Chemistry Reference Data, 1978, Vol.7, No.3, pp 941-948.

Keuthe A.M., "Some Features of Boundary Layers and Transition to Turbulent Flow", J. Aero. Sciences, 1962, Vol.14, pp 444-452.

Khezzar L., Whitelaw J.H. & Yanneskis M., "Round Sudden-Expansion Flows", Proc. Instn. Mecg. Engrs., 1986, Vol.200, pp 447-455.

Kida S., Yamada M. & Ohkitani K., "A Route to Chaos and Turbulence", Physica-D, 1989, Vol.37, pp 116-125.

Kirmse R.E., "Investigations of Pulsating Turbulent Pipe Flow", Trans. A.S.M.E., Journal of Fluids Engineering, 1979, Vol.101, pp 436-442.

Klebanoff P.S., Tidstrom K.D. & Sargent L.M., "The Three Dimensional Nature of Boundary Layer Instability", J. Fluid Mech., 1962, Vol.12, pp 1-34.

Konishi I, Shiraishi N. & Matsumoto M., "Vortex Shedding Oscillations of Bridge Deck Sections", from I.A.H.R. and I.U.T.A.M. Symposium, "Practical Experiences with Flow Induced Vibrations", Karlsruhe/Germany, Sept. 3-6, 1979, University of Karlsruhe, edited by E. Naudascher & D. Rockwell, pp 619-624.

Kostelich E.J. & Yorke J.A., "Noise Reduction: Finding the Simplest Dynamical System Consistent with the Data", Physica-D, 1990, Vol.41, pp 183-196.

- Kowalke O.L., "Manner of Liquid Flow Through a Pipe Orifice", Industrial and Engineering Chemistry, 1938, Vol.30, pp216-222.
- Kronland-Martinet R., "The Wavelet Transform for the Analysis, Synthesis and Processing of Speech and Music Sounds", Computer Music Journal, 1988, Vol.12, pp 11-20.
- Kuramoto Y., "Meeting Report: The 6th Kyoto Summer Institute. Chaos and Statistical Mechanics", Physica D, 1984, Vol.11, pp 384-386.
- Kurzweg U.H., Lindgren E.R. & Lothrop B. , "Onset of Turbulence in Oscillating Flow at Low Wormsley Numbers", Phys. Fluids A, 1989, Vol.1, pp 1972-1975.
- Landau L., "On the Problem of Turbulence", C.R. Acad. Sciences U.R.S.S., 1944, Vol.44, pp 311-316.
- Lanford O.E., "Strange Attractors and Fluid Turbulence", from "Hydrodynamic Instabilities and the Transition to Turbulence", edited by H.L. Swinney and J.P. Gollub, Springer-Verlag, 1981, Chapter 2, pp7-26.
- Langhaar H.L., "Steady Flow in the Transition Length of a Straight Tube", Trans. A.S.M.E., J. Appl. Mech., 1942, Vol.64, pp A55-A58.
- Lau J.C., Whiffen M.C, Fisher M.J. & Smith D.M., "A Note on Turbulence Measurements with a Laser Velocimeter", J. Fluid Mech., 1981, Vol.102, pp 353-366.

Leiber B.B. & Giddens D.P., "Autoregressive Spectral Estimation in Transitional Pulsatile Flow", Experiments in Fluids, 1989, Vol.8, pp 209-215.

Leite R.J., "An Experimental Investigation into the Stability of Poiseuille Flow", J. Fluid Mech., 1959, Vol.5, p 81.

Leite R.J., "An Experimental Investigation of the Stability of Axisymmetric Poiseuille Flow", Report No. OSR-TR-56-2, University of Michigan, Ann Arbor, Nov. 1957.

Lesieur M., "Turbulence in Fluids", Nijhoff Publishers, 1987.

Lessen M., Fox J.A., Bhat V.W. & Ting-Yung L., "Stability of Hagen Poiseuille Flow", The Physics of Fluids, Vol.7, 1964, pp 1384-1385.

Lewis R.D., Foreman J.W., Watson H.J. & Thornton J.R., "Laser Doppler Velocimeter for Measuring Flow-Velocity Fluctuations", Phys. Fluids, 1968, Vol.2, pp 433-435.

Lighthill J., "An Informal Introduction to Theoretical Fluid Mechanics", Clarendon Press, Oxford, 1986, pp 59-75.

Lin C.C., "The Theory of Hydrodynamic Stability", Cambridge Monographs on Mechanics and Applied Mechanics, Cambridge University Press, 1966.

Lindgren E.R., "Propagation Velocity of Turbulent Slugs and Streaks in Transition Pipe Flow", The Physics of Fluids, 1969, Vol.12, pp 418-425.

Lindgren E.R., "The Transition Process and Other Phenomena in Viscous Flow", Arkiv for Fysik, 1957, Vol.12, pp 1 -169.

Linford A., "Flow Measurement and Meters", 1961, 2nd edition, E. & F.N. Spon Ltd., pp 84-99.

Lorenz E.N., "Deterministic Nonperiodic Flow", J. Atmos. Sciences, 1963, Vol.20, pp 130-141.

Low B.B., "Mathematics", Longman Green & Co., 1931, pp 23,61,74.

Lugt H.J., "The Influence of Swirling Flow on the Discharge Coefficients of Standard Pressure Differential Flow Meters", The British Hydromechanics Research Association, Report T716, Feb., 1962.

Lugt H.J., "Vortex Flow in Nature and Technology", John Wiley and Sons, 1983, pp 1-126 (Part One).

Mackey M.C. & Glass L., "Oscillation and Chaos in Physiological Control Systems", Science, 1977, Vol.197, pp 287-289.

Mair W.A. & Maul D.J., "Bluff Bodies and Vortex Shedding - A Report on Euromech 17", Journal of Fluid Mechanics, 1971, Vol.45, pp 209-224.

Mandelbrot B.B., "The Fractal Geometry of Nature", W.H. Freeman & Co., 1977.

Mansoori A., "On the Turbulent Velocity and Pressure Fluctuations Occurring in Water at a Sudden Enlargement", Ph.D. Thesis, University of London, July 1988.

Martinez-Val R., Viedma A. & Cuerno C., "Eulerian and Lagrangian Description of a Pulsatile, Partially Turbulent Flow", Experiments in Fluids, 1990, Vol.9, pp 129-136.

Matisse P. & Gorman M., "Neutrally Buoyant Anisotropic Particles for Flow Visualization", The Physics of Fluids, 1984, Vol.27, pp 759-760.

Mayer-Kress G., "Application of Dimension Algorithms to Experimental Chaos", from "Directions in Chaos" edited by Hao Bai-Lin, World Scientific; 1987, pp 122-147.

Mercader I., Massaguer J.M. & Net M., "Hysterisis on the Transition to Chaos", Phys. Lett A, 1990, Vol.149, pp 195-199.

Merzkirch W., "Flow Visualization", 1987, Second Edition, Academic Press, pp 1-82.

Miles J., "Strange Attractors in Fluid Dynamics", Advances in Applied Mechanics, 1983, Vol.24, pp 189-214.

Miller D.S., "Internal Flow Systems", 1978, Vol.5, B.H.R.A. Fluid Engineering Series, pp276-281.

Mills R.D., "Numerical Solution of Viscous Flow Through a Pipe Orifice at Low Reynolds Numbers", J. Mech. Eng. Sci., 1968, Vol.10, No.2, pp 133-140.

Mitchell A.R., Stein G & Maritz M., 'Periodic Structure Beyond a Hopf Bifurcation', Communications in Applied Numerical Methods, Vol.4, 1988, pp 263-272.

Moss E.A., "The Identification of Two Distinct Laminar to Turbulent Transition Modes in Pipe Flows Accelerated from Rest", Expts. in Fluids, 1989, Vol.7, pp 271-274.

Mottram R.C. & Robatti B., "A Comparison of Effects on Vortex and Orifice Flowmeters", from, "Fluid Control and its Measurement", Vol.2, 1985, Pergamon Press, edited by M. Harada, pp 957-963.

Mullin T. & Price T.J., "An Experimental Investigation of Chaos Arising from the Interaction of Steady and Time Dependent Flows", nature, 1989, Vol.340, pp 294-296.

Newland D.E., "Random Vibrations and Structural Analysis", Longman, 1975, 1st edition, Ch.4,10,12.

Nigro F.E.B., Strong A.B. & Alpay S.A., "A Numerical Study of the Laminar Viscous Incompressible Flow Through a Pipe Orifice", Trans. A.S.M.E., Journal of Fluids Engineering, 1978, Vol.100, pp 467-472.

Novikov E.A., "Chaotic Vortex-Body Interaction", Phys. Lett. A, 1991, Vol.152, pp 393-396. ((read 1/11/91))

Oppenheim A.K. & Chilton E.G., "Pulsating Flow Measurement - A Literature Survey", Trans. A.S.M.E., 1955, Vol.77(2), pp231-245.

Osborne A.R. & Provenzale A., "Finite Correlation Dimension for Stochastic Systems with Power law spectra", Physica-D, 1989, Vol.35, pp 357-381.

Owen P.R., "Buffeting Excitation of Boiler Tube Vibration", J. Mech. Eng Sci., 1985, Vol.7, pp 431-439.

Packard N.H., Crutchfield J.P., Farmer J.D. & Shaw R.S., "Geometry from a Time Series", Phys. Rev Lett., 1980, Vol.45, pp 712-716.

Paidoussis M.P. & Moon F.C., 'Nonlinear and Chaotic Fluidelastic Vibrations of a Flexible Pipe Conveying Fluid', J.Fluid and Structures, 1988, Vol.2, pp 567-591.

Park K.C., 'An Improved Stiffly Stable Method for Direct Integration of Nonlinear Structural Dynamic Equations', Transactions A.S.M.E, Journal of Applied Mechanics, 1975, pp464-470.

Patel V.C. & Head M.R., "Some Observations on Skin Friction and Velocity Profiles in Fully Developed Pipe and Channel Flows"; J. Fluid Mech., 1969, Vol.38, pp 181-202.

Percival I. & Richards D., "Introduction to Dynamics, Cambridge University Press, 1982.

Peitgen H.O. & Richter P.H., "The Beauty of Fractals", Springer- Verlag, 1986, pp 1-26.

Perry A.E. & Fairlie B.D., "Critical Points in Flow Patterns", Adv. in Geophys., 1974, Vol.B18, pp 299-315.

Perry A.E. & Lim T.T., "Coherent Structures in Coflowing Jets and Wakes", J. Fluid Mech., 1978, Vol.88, pp 451-463.

Perry A.E., Lim T.T. & Chong M.S., "The Instantaneous Vector Fields of Coherent Structures in Coflowing Jets and Wakes", J. Fluid Mech., 1980, Vol.101, pp 243-256.

Peterson G.S., "Orifice Discharge Coefficients in the Viscous Flow Range", Trans. A.S.M.E., 1947, Vol.69, pp765-768.

Pomeau Y., "Front Motion, Metastability and Subcritical Biufurcations in Hydrodynamics", Physica\_D, 1986, Vol.23, pp 3-11.

Prenel J.P., Porcar R. & Rhassouli A.E.L., "Three Dimensional Flow Analysis by Means of Sequential and Volumic Laser Sheet Illumination", Experiments in Fluids, 1989, Vol.7, pp 133-137.

Pressing J., "Nonlinear Maps as Generators of Musical Design", Computer Music Journal, 1988, Vol.12, pp 35-46.

Rahman Z. and Burton T.D., 'Large Amplitude Primary and Superharmonic Resonances in the Duffing Oscillator', Journal of Sound and Vibration, 1986, Vol.110(3), pp363-380.

Ramaprian B.R. & Tu S., "An Experimental Study of Oscillating Pipe Flow at Transitional Reynolds Numbers", Journal of Fluid Mechanics", 1980, Vol.100, pp 513-544.

Rao N.S.L. & Sridharan K., "Orifice Losses for Laminar Approach Flow.", Proc. A.S.C.E., J. Hyd. Div., 1972, Vol.98, pp2015-2034.

Reddy J.N., "An Introduction to the Finite Element Method", McGraw-Hill, 2nd Edition, 1986, pp 54-57.

Renyi A., "Probability Theory", North Holland Publishing Co., 1970, pp 540-554.

Reshotko E., "Experimental Study of the Stability of Pipe Flow. 1. The Establishment of an Axially Symmetric Poiseuille Flow.", Progress Report No. 20-304, 1958, Jet Propulsion Lab., Caltech, California, U.S.A.

Reshotko E., "Remark on Engineering Aspects of Transition", from "Transition and Turbulence" edited by Meyer R.E., Academic Press, 1981, pp 147-148.

Reynolds O., "An Experimental Investigation of the Circumstances which Determine Whether the Motion of Water Shall be Direct or Sinuous and of the Law of Resistance in Parallel Channels", Phil. Trans. Roy. Soc., 1883, Vol.174, pp 935-982.

Rhee H.S., Koseff J.R. & Street R.L., "Flow Visualization of a Recirculating Flow by Rheoscopic Liquid and Liquid Crystal Techniques", Experiments in Fluids, 1984, Vol.2, pp 57-64.

Robertson J.M., "A Turbulence Primer", Engineering Experimental Station Circular, Number 79, (date unknown).

Rockwell D, Nuzzi F. & Magness C., 'Period Doubling in the Wake of a Three-Dimensional Cylinder', Phys. Fluids A, 1991, Vol.3, pp 1477-1478.

Rosenhead L., "Laminar Boundary Layers", Oxford, 1963.

Rossler O.E., "An Equation for Hyperchaos", Phys. Lett., 1979, Vol.71a, pp 155-157.

Rotta J., "Experimenteller Beitrag zur Entstehung Turbulenter Stromung im Rohr", Ing. Archiv, 1956, Vol. 24, pp 258-281.

Rouse H. & Ince S., "History of Hydraulics", Dover Publications Inc., 1957.

Roux J.C. & Swinney H.L., "Topology of Chaos in a Chemical reaction", from "Nonlinear Phenomena in Chemical Dynamics", Proceedings of an International Conference, Bordeaux, France, Sept. 7-11th, 1981, editors C. Vidal & A. Pascault, Springer Verlag, 1981.

Roux J.C., Rossi A., Batchelart S. & Vidal C., "Representation of a Strange Attractor from an Experimental Study of Chemical Turbulence", Physics Letters, 1980, Vol.77a, pp 391-393.

Roux J.C., Simoyi R.H. & Swinney H.L., "Observation of a Strange Attractor", Physica-d, 1983, Vol.8, pp 257-266.

Rubin Y., Wignanski I. & Haritonidis J.H., "Further Observations on Transition in a Pipe", from I.U.T.A.M. Conference Proceedings, "Laminar Turbulent Transition", Stuttgart, Germany, Sept. 16-22, 1979, edited by R. Eppler & H. Fusel, Springer-Verlag, pp 17 - 26.

Ruelle D., "Chaotic Evolution and Strange Attractors", Cambridge University Press, 1989.

Ruelle D., "Chemical Kinetics and Differentiable Dynamical Systems", from "Nonlinear Phenomena in Chemical Dynamics", Proceedings of an International Conference, Bordeaux, France, Sept. 7-11th, 1981, editors C. Vidal & A. Pascault, Springer Verlag, 1981.

Ruelle D., "Five Turbulent Problems", Physica-7D, 1983A, pp 40-44.

Ruelle D., "Strange Attractors", Math. Intell., 1980, Vol.2, pp 126-137.

Ruelle D., "Turbulent Dynamical Systems", Proceedings of the International Congress of Mathematicians, 1983b, August 16-24, Warsaw, pp 271-286.

Russel D.A., "Dimension of Strange Attractors", Phys. Rev. Lett., 1980, Vol.45, pp 1175-1177.

Sagdeev R.Z., Usikov D.A. & Zaslavsky G.M., "Nonlinear Physics: From the Pendulum to Turbulence and Chaos", Harwood Academic Publishers, 1988.

Sano M. & Sawada Y., "Measurement of the Lyapunov Spectrum from a Chaotic Time Series", Phys. Rev. Lett., Vol.55, 1985, pp 1082-1085.

Schiller L., "Die Entwicklung der Laminaren Geschwindigkeits- Verteilung und Ihre Bedeutung fur Zahigkeitsmessungen", Zeitschrift fur Angewandte Mathematik und Mechanik, 1922, pp 96-106.

Schlichting S., "Boundary Layer Theory", McGraw Hill, 1979, 7th Edition.

Schlien D.J., "Inexpensive Method of Generation of a Good Quality Laser Light Sheet for Flow Visualization", Expts. in Fluids, 1987, Vol.5, pp 356-358.

Schuster H.G., "Deterministic Chaos: An Introduction", Physik-Verlag, 1984.

Seino M. & Sawada Y, "Chaotic Attractors in Rayleigh Benard Systems", from Chaos and Statistical Methods", Proceedings of the Sixth Kyoto Summer Institute, Kyoto, Japan, Sept. 12-15, 1983, editor Y. Kurimoto, Springer Verlag, 1984, pp 167-169.

Sexl T., "Uber Dreidimensionale Storungen der Pousseuilleschen Stromung", Ann. Phys., 1927b, Vol.84, pp 807-822.

Sexl T., "Zur Stabilitatsfrage der Pousseuilleschen und Couetteschen Stromung", Ann. Phys., 1927a, Vol.83, pp 835-848.

Shannon C.E. & Weaver W., "The Mathematical Theory of Communication", The University of Illinois Press: Urbana, 1949.

Shaw R., "The Dripping Faucet as a Model Chaotic System", Aerial Press, 1984.

Sibulkin M., "Transition from Turbulent to Laminar Pipe Flow", Phys. of Fluids, 1962, Vol.5, pp 280-284.

Smith A.M.O., "Remarks on Transition in a Round Tube", J. Fluid Mech., 1960, Vol.17, pp 565-576.

Smith L.A., "Intrinsic Limits on Dimension Calculations", Physics Letters A, 1988, Vol.133, pp 283-288.

Snedecor G.W. & Cochran W.G., "Statistical Methods", The Iowa State University Press, Ames, Iowa, U.S.A., 1967, pp 59-62.

Soliman M.S. & Thompson J.M.T., 'Transient and Steady State Analysis of Capsize Phenomena', Applied Ocean Research, 1991, Vol.13, pp82-92.

Sprenkle R.E., "The Thin-Plate Orifice for Flow Measurement", from "Flow Measurement in Closed Conduits", Proc. Symposium N.E.L., 27th-30th Sept., 1960, H.M.S.O. 1962, pp125-137.

Sreenivasan K.R. & Ramshyankar R., "Transmission Intermittency in Open Flows and Intermittency Routes to Chaos", Physica-D, 1986, Vol.23, pp 246-258.

Sreenivasan K.R., "Fractals and Multifractals in Fluid Turbulence", Annual Revue of Fluid Mechanics, 1991, Vol.23, pp 539-600.

Stuart J.S., "Stability and Transition: Some Comments on the Problems", from I.U.T.A.M. Conference Proceedings, "Laminar Turbulent Transition", Stuttgart, Germany, Sept. 16-22, 1979, edited by R. Eppler & H. Fusel, Springer Verlag, pp 1 - 13.

Swinney H.L., "Observations of Order and Chaos in Nonlinear Systems", Physica-D, 1983, Vol.7, pp 3-15.

Swinney H.L. & Gollub J.P., "Introduction", from "Hydrodynamic Instabilities and the Transition to Chaos", Springer-Verlag, 1981, Chapter 1, pp 1-6.

Swinney H.L., Simoyi R.H. & Roux J.C., "Instabilities and Chaos in a Chemical Reaction", from Chaos and Statistical Methods", Proceedings of the Sixth Kyoto Summer Institute, Kyoto, Japan, Sept. 12-15, 1983, editor Y.Kurimoto, Springer-Verlag, 1984, pp 167-169.

Tabeling P., Cardoso O. & Perrin B., "Chaos in a Linear Array of Vortices", J.F.M., 1990, Vol.213, pp 511-530.

Tatsumi T., "Stability of the Laminar Inlet-Flow Prior to the Formation of Poiseuille Regime, 1", J. Phys. Soc. Japan, 1952, Vol.7, pp 489-495.

Tatsumi T., "Stability of the Laminar Inlet-Flow Prior to the Formation of Poiseuille Regime, 2", J. Phys. Soc. Japan, 1952, Vol.7, pp 495-502.

Teitgen R., "Laminar-Turbulent Transition in Pipe Flow. Development and Structure of the Turbulent Slug", from I.U.T.A.M. Conference Proceedings, "Laminar Turbulent Transition", Stuttgart, Germany, Sept. 16-22, 1979, edited by R. Eppler & H. Fusel, Springer-Verlag, pp 27-36.

Tennent R.M., "Science Data Book", 1986, Oliver and Boyd.

Thompson J.M.T. & Stewart H.B., "Nonlinear Dynamics and Chaos", John Wiley and Sons, 1986, pp 1-131.

Velarde M.G. & Antoranz J.C., "Strange Attractor (Optical Turbulence) in a Model Problem for the Laser with Saturable Absorber and Two Component Benard Convection" Prog. Theor. Phys., 1981, Vol.66, No.2, Progress Letters, pp 717-720.

Voss R.F., "Random Fractals: Self Affinity in Noise, Music, Mountains and Clouds", Physica-D, 1989, Vol.38, pp 362-371.

Waldner F., Barberis D.R. & Yamazaki H., 'Route to Chaos by Irregular Periods: Simulations of Parrallel Pumping in Ferromagnets', Phys. Rev. A, 1985, Vol.31, pp420-431.

Ward-Smith A.J., "Pressure Losses in Ducted Flows", Butterworths, London, 1971, pp1-27 & 135-191.

Ward-Smith A.J., "Internal Fluid Flow: The Fluid Dynamics of Flow in Pipes and Ducts", Clarendon Press, Oxford, 1980.

Weaver D.S., Adubi F.A. & Kouwen N, "Flow Induced Vibration of a Hydraulic Valve and their Elimination", J.Fluids Eng., 1978, Vol.100, pp 239-245.

Webb W.H. & Harrington R.P., "Vortex Structures in Pipe Flow", J. Aero. Sciences, 1956, Vol.23, pp 792-793.

West G.S. & Apelt C.J., "Measurements of Fluctuating Effects on Circular Cylinder in a Uniform Flow at Subcritical Reynolds Number. Part 1: The Pressure Distribution and Lift and Drag forces on an Elemental Cross Section", University of Queensland, Dept. of Civil Engineering, Research Report, No. CE109, July 1990.

West R.G., "Developments in Flow Metering by Means of Orifice Plates", from "Flow Measurements in Closed Conduits" Proc. Sympoium N.E.L., 27th-30th Sept., 1960, H.M.S.O., 1962, pp165-186.

White F.M., "Viscous Fluid Flow", McGraw Hill , 1974, pp 1-25, 61-77, 385-452.

Wigner E.P., "The Unreasonable Effectiveness of Mathematics in the Natural Sciences", Comm. Pure & Appl. Math., 1960, pp 1-14.

Willert C. & Gharib M., "A New Video Technique to Capture Images Generated by a Smoke Wire", Experiments in Fluids, 1989, Vol.8, pp 236-237.

Williams-Stuber K. & Gharib M., "Transition from Order to Chaos in the Wake of an Airfoil", J.F.M., 1990, Vol.213, pp 29-57.

Withers W. J., "Pressure Fluctuations in the Plunge Pool of an Impinging Jet Spillway", Ph.D. Thesis No. 8913, University of Glasgow, 1991.

Wolf A., "LYAPU-NEWS: Documentation for F.E.T., a Program that Quantifies Chaos in a time Series", supplied by A.Wolf, Dept. of Physics, The Cooper Union, 51, Astor Place, New York, N.Y., 10003, 1991.

Wolf A., "Quantifying Chaos with Lyapunov Exponents", from "Nonlinear Science: Theory and Applications", edited by A. Holden, Manchester University Press, 1986, pp 273-290.

Wolf A., Swift J.B., Swinney H.L. & Vastano J.A., "Determining Lyapunov Exponents from a Time Series", Physica-D, 1985, Vol.61, p 285.

Wood W.L. & Oduor M.E., 'Stability Properties of Some Algorithms for the Solution of Nonlinear Dynamic Vibration Equations', Comm. App. Num. Meth., 1988, Vol.4, pp 205-212.

Wynanski I., Sokolov M. & Friedman D., "On Transition in a Pipe. Part 2. The Equilibrium Puff", J. Fluid Mech., 1975, pp 283-304..

Wynanski I.J. & Champagne F.H., "On Transition in a Pipe. Part 1. The Origin of Puffs and Slugs and the Flow in a Turbulent Slug", J. Fluid Mech., 1973, Vol.59, pp 281-335.

Yamada T. & Fujisaka H., "Coupled Chaos", from Chaos and Statistical Methods", Proceedings of the Sixth Kyoto Summer Institute, Kyoto, Japan, Sept. 12-15, 1983, editor Y.Kurimoto, Springer-Verlag, 1984, pp 167-169.

Yorke J.A. & Yorke E.D., "Chaotic Behaviour and Fluid Dynamics", from "Hydrodynamic Instabilities and the Transition to Turbulence", edited by H.L. Swinney & J.P. Gollub, Springer-Verlag, 1981, Chapter 4, pp 77-95.

Yoshitani Y., Sakuta H. & Koba T., "Flexible Orifice Flowmeter" from, "Fluid Control and its Measurement", Vol.2, 1985, Pergamon Press, edited by M. Harada, pp 893-899.

Zanker K.J. & Cousins T., "The Performance and Design of Vortex Meters", Paper C-3, from, "Fluid Measurement in the Mid 1970's, 1977, edited by E.A. Spencer & W.J. Ramsay, H.M.S.O., pp 147-166.

Zdravkovich M.M., "Smoke Observations of the Formation of a Karman Vortex Street", J. Fluid Mech., 1969, Vol.37, pp 491-496.

## ADDITIONAL REFERENCES

- Birkhoff G. & Zarantonello E.H., 'Jets, Wakes and Cavities', New York Academic Press, 1957.
- Bullock K.J., Lai J.C.S. & Walker T.B., 'Flow Measurement behind Attached Ring-type Turbulence Promoters', Phys. Fluids A, Vol.2, 1990, pp390-399.
- Chen K. & Bak P., 'Is the Universe Operating at a Self Organised State?', Phys. Lett. A, Vol.140, 1989, pp299-302.
- Duncan W.J., Thom A.S. & Young A.D., 'Mechanics of Fluids', Arnold, 2nd Edition, 1970.
- Baker G.L. & Gollub J.P., 'Chaotic Dynamics', Cambridge University Press, 1990.
- Hanko Z.G., 'Vortex Induced Oscillations at low Head Weirs', Proc. Am. Soc. Civil Engineers, Journal of the Hydraulics Division, Vol.6, 1967, pp255-270.
- Iguchi M., Ohmi M. & Kimura H., 'Behaviour of Turbulent Slugs in Pulsatile Pipe Flow', from 'Fluid Control and Its Measurement', Vol. 2, Pergamon Press, Edited by M. Harada, 1985, pp951-956.
- Hunt J.C.R., Abell C.J., Peterka J.A. & Woo H., 'Kinematical Studies of the Flows Around Free or Surface Mounted Obstacles: Applying Topology to Flow Visualization', Journal of Fluid Mechanics, Vol.86, 1978, pp179-200.
- Marris A.W., 'A review of Vortex Streets, Periodic Wakes, and Induced Vibration Phenomena', Trans. A.S.M.E., Journal of basic Engineering, June 1964, pp185-196.
- Massey B.S., 'Mechanics of Fluids', 5th Edition, Van Nostrand Reinhold (UK), 1984.
- O'Neill P.V., 'Advanced Engineering Mathematics', Wadsworth Pub. Co., 1987.
- Prandtl L., 'Essentials of fluid Dynamics: With Applications to Hydraulics, Aeronautics, Meteorology and other Subjects', Blackie, 1952.
- Russel D.A., 'Dimension of Strange Attractors', Phys. Rev. Lett., Vol.45, 1980, p1175.
- Sarpkaya T., 'Experimental Determination of the Critical Reynolds Number for Pulsating Poiseuille Flow', Trans. A.S.M.E., Journal of Basic Engineering, Sept.1966, pp589-598.
- Schaefer J.W. & Eskinazi S., 'An Analysis of the Vortex Street Generated in a Viscous Fluid', Journal of Fluid Mechanics, Vol.16, 1959, pp241-260.
- Smith D., 'How to Generate Chaos at Home', Scientific American, January 1992, pp121-123.
- Tomita K., 'Periodically Forced Nonlinear Oscillators', from 'Chaos', edited by A.V. Holden, Manchester University Press, 1986.